Technische Universität München
Institut für Energietechnik

Lehrstuhl für Thermodynamik

Linear Stability Assessment of Cryogenic Rocket Engines

Moritz Schulze

Vollständiger Abdruck der von der Fakultät für Maschinenwesen der Technischen Universität München zur Erlangung des akademischen Grades eines

Doktor – Ingenieurs

genehmigten Dissertation.

Vorsitzender:
Univ.-Prof. Dr.-Ing. Hans-Jakob Kaltenbach
Prüfer der Dissertation:
Univ.-Prof. Dr.-Ing. Thomas Sattelmayer
Univ.-Prof. Dr.rer.nat. Michael Oschwald
Rheinisch-Westfälische Technische Hochschule Aachen

Die Dissertation wurde am 05.04.2016 bei der Technischen Universität München eingereicht und durch die Fakultät für Maschinenwesen am 14.07.2016 angenommen.

Danksagung

Diese Dissertation entstand im Rahmen meiner Tätigkeit als wissenschaftlicher Mitarbeiter und Assistent in den Jahren 2012 bis 2016 am Lehrstuhl für Thermodynamik der Technischen Universität München. Ich möchte mich deshalb zuerst bei meinem Doktorvater Prof. Dr.-Ing. Thomas Sattelmayer für sein entgegengebrachtes Vertrauen bedanken. Ich habe mich stets wertgeschätzt und hervorragend betreut gefühlt. Ich wünsche Prof. Sattelmayer alles Gute.

Weiterhin möchte ich mich bei Prof. Dr. Michael Oschwald für die Übernahme der Zweitbegutachtung meiner Dissertation bedanken. Mit Prof. Oschwald verbinde ich nicht nur angenehme und konstruktive Besprechungen im Rahmen des DFG SFB Transregio 40, sondern auch viele interessante Diskussionen in zahlreichen Treffen der Rocket Engine Stability Initiative (REST). Über den Transregio 40 habe ich auch Prof. Dr.-Ing. Oskar Haidn kennengelernt, dem ich für die Übernahme des Vorsitzes der Prüfungskommission danke.

Während meiner Zeit am Lehrstuhl durfte ich knapp 4000 Studenten im Grundlagenfach Wärmetransportphänomene betreuen. Bei Prof. Wolfgang Polifke (Ph.D.) bedanke ich mich für die gute und entspannte Zusammenarbeit bei der Gestaltung der Lehre, die mir immer viel Spaß gemacht hat.

Manchmal erschien mir die Bürokratie herausfordender als die Fragestellungen des Forschungsprojektes. Für die Unterstützung bei der Lösung nicht-wissenschaftlicher Aufgaben aller Art am Lehrstuhl möchte ich mich herzlich bei Helga Basset und Sigrid Schulz-Reichwald bedanken.

Bei Dr.-Ing. Christoph Hirsch und allen anderen Kollegen bedanke ich mich für die angenehme Arbeitsatmosphäre und guten Diskussionen. Namentlich möchte ich meine ehemaligen Kollegen Dr.-Ing. Martin Schmid und Dr.-Ing. Daniel Morgenweck erwähnen, die mit ihrer Arbeit wichtige Grundsteine für das Gelingen dieser Dissertation gelegt haben, sowie Dr.-Ing. Thomas Fiala, dem ich für die konstruktive Zusammenarbeit im Transregio 40 danke. Auf dem von Dr.-Ing. Robert Kathan konstruierten Prüfstand konnte ich wertvolle Validierungsdaten für die Entwicklung des numerischen Verfahrens generieren. Außerdem möchte ich meine Wertschätzung gegenüber der kollegialen Kooperation mit Dipl.-Ing. Stefan Gröning und der gesamten HF Gruppe beim DLR Lampoldshausen ausdrücken, die mir darüber hinaus experimentelle Daten für die Validierung des numerischen Verfahrens zu Verfügung gestellt haben. Dr.-Ing. Nancy Kings danke ich für das intensive Korrekturlesen meiner Dissertation und die hilfreichen Anmerkungen.

Meiner Familie danke ich für die stetige Unterstützung. Zuletzt gilt mein besonderer Dank meiner Frau Rebecca, die mich über die Jahre uneingeschränkt gestärkt und immer für die notwendige Work-Life-Balance gesorgt hat.

Moritz Schulze München, im Juli 2016

Abstract

The linear high frequency stability of DLR's cryogenic H_2/O_2 BKD test chamber is assessed using a hybrid Computational Fluid Dynamic/Computational Aeroacoustic methodology, which is based on single flame considerations for the generation of an adequate mean flow and for the calibration of feedback models as well as on frequency space transformed linearized Euler equations. Successful validation on the basis of non-reactive conditions reveals high suitability for the description of acoustic propagation in three-dimensional space comprising nozzle, chamber, propellant domes and absorber rings. It is found that resonating cavities may significantly alter the mode shape such that the risk of thermo-mechanical engine failures due to unbearable acoustic pressure and temperature loads rises. The application of a realistic mean flow field including combustion and real gas effects explains the spatial separation of transverse modes into a near face plate mode, which is found linearly unstable under certain operation conditions for the first transverse, and a rear part mode. The axial mode shape length as well as eigenfrequencies are affected by propellant injection specifications and, in consequence, decisively influence pressure and transverse velocity sensitive dynamic flame response. Lorentzian fitting and a parameter extraction method are employed to extract linear damping rates from experimental pressure recordings, which are subsequently used to validate the CFD/CAA results.

Zusammenfassung

Die lineare Stabilität für den Hochfrequenzbereich der kryogenen H_2/O_2 DLR Testkammer BKD wird untersucht. Dazu wird ein hybrider Ansatz verwendet, der aus der getrennten Auswertung von Strömungsmechanik zur Berechnung eines adäquaten mittleren Strömungsfeldes sowie für die Kalibrierung von Rückkopplungsmodellen in Einzelflammensimulationen und aus einer Beschreibung der Aeroakustik mithilfe von linearisierten Eulergleichungen besteht. Die erfolgreiche Validierung unter nicht-reagierenden Bedingungen verdeutlicht die Eignung des Verfahrens zur Simulation dreidimensionaler Wellenausbreitung in der Düse und Kammer sowie in den Treibstoffdomen und Absorberringen. Es wird gezeigt, dass resonante Kavitäten die Modenform beträchtlich beeinflussen können, so dass das Risiko eines thermomechanischen Versagens des Motors aufgrund von untragbaren akustischen Druck- und Temperaturlasten steigt. Die Berücksichtigung eines realistischen reagierenden Strömungsfeldes mit Realgaseffekten bewirkt eine räumliche Trennung der transversalen Moden in eine einspritzkopfnahe Mode, die unter bestimmten Lastpunktspezifikationen instabiles Verhalten der ersten Transversalen erzeugt, sowie einer zweiten Mode, die hauptsächlich im hinteren Bereich der Kammer auftritt. Die Einspritzbedingungen der Treibstoffe beeinflussen die axiale Länge der Moden und damit die druck- und transversal geschwindigkeitssensitive Flammendynamik. Lorentzfits sowie eine Parameter Extraktionsmethode werden angewendet, um lineare Dämpfungs- und Wachstumsraten aus experimentell gemessenen dynamischen Druckaufzeichnungen für die Validierung des numerischen Verfahrens zu bestimmen.

Contents

1 Introduction **1**
1.1. Combustion Instabilities in Rocket Engines 1
1.2. Modeling Approach 4
1.3. Thesis Scope and Structure 5

2 Rocket Engine Acoustics **9**
2.1. General Form of Governing Equations 9
2.2. Fundamentals of Linear Acoustics 10
2.3. LEE in Frequency Space 13
2.4. Acoustic Propagation in Uniform Mean Flow 15
2.5. Propagation and Evanescence of Higher-Order Modes 17
2.6. Fluctuating Energy and Intensity Flux 19
2.7. Boundary Conditions 20
2.7.1. Slip Wall 21
2.7.2. Reflection Coefficient, Admittance and Impedance 21
2.7.3. Nozzle 23
2.7.4. Absorbers 23
2.7.5. Dome Coupling 25
2.7.6. Further Boundary Conditions 28
2.7.6.1. Energetically Neutral Boundary with Flow 29
2.7.6.2. Non-Reflective Boundary Condition 29
2.8. Dynamic Flame Modeling 30

3 Solution of LEE in Time Domain and Frequency Space **35**
3.1. Time Domain Solver PIANO 35
3.2. Solution Technique in Frequency Space 36
3.2.1. Stabilized Finite Element Method 36
3.2.2. Solution Procedures 39
3.2.2.1. Frequency Response 40
3.2.2.2. Eigenvalue Problem 41
3.3. Frequency Dependent Boundary Conditions 42
3.3.1. General Considerations and Application to Frequency Space . . . 42
3.3.2. Digital Filters in Time Domain 46
3.4. Comparison of Time Domain and Frequency Space Methods and Perspective Towards Non-Linearity 51

4 Non-Reactive Acoustic Analysis **55**
4.1. Nozzle Acoustics . . . 55
4.1.1. Nozzle Configurations and Modeling . . . 55
4.1.2. Mode Decomposition . . . 58
4.1.3. Validation of Mode Decomposition . . . 58
4.1.4. Admittances . . . 59
4.1.5. Use of the Nozzle Admittance as Boundary Condition . . . 61
4.2. Dome Coupling and Determination of Damping Rates . . . 63
4.2.1. Reconstruction of the Scattering Matrix . . . 64
4.2.2. Determination of Damping Rates with Dome Coupling . . . 68
4.2.2.1. Types of Inlet Boundary Treatments . . . 68
4.2.2.2. Modeling of Scattering Properties in Time Domain . . . 70
4.2.2.3. Complex Frequencies and Mode Shapes . . . 72
4.2.2.4. Influence of Grid Resolution and Stabilization Parameter on Eigenfrequency and Damping Rate . . . 76
4.3. Absorbers under Grazing Flow Conditions . . . 77
4.3.1. Longitudinal Wave Propagation - GIT Test Case . . . 77
4.3.1.1. Test Case Description . . . 78
4.3.1.2. Exit and Liner Impedances . . . 79
4.3.1.3. Mean Flow Profiles . . . 81
4.3.1.4. Numerical Setup . . . 81
4.3.1.5. Acoustic Pressure Distributions . . . 81
4.3.1.6. Results . . . 83
4.3.2. Absorber Influence on First Transverse Mode . . . 88
4.3.2.1. Test Configurations . . . 88
4.3.2.2. Computational Setup and Absorber Model . . . 88
4.3.2.3. Frequency Response for Absorber Ring Position 1 . . . 93
4.3.2.4. Eigenfrequencies and Damping Rates for Absorber Ring Position 1 . . . 95
4.3.2.5. Eigenfrequencies and Damping Rates for Absorber Ring Position 2 . . . 98
4.4. Remarks for the Non-Reactive Acoustic Analyses . . . 100

5 Validation Data for Reactive Conditions **103**
5.1. Rocket Test Chamber BKD . . . 103
5.2. Operating Conditions . . . 106
5.3. Verification of BKD's Stability Behavior . . . 108
5.4. Determination of Linear Growth and Damping Rates . . . 110
5.4.1. Lorentzian Fitting . . . 110
5.4.2. Parameter Extraction Method . . . 112

6 Stability Assessment Procedure **119**
6.1. Extended Methodology for the Incorporation of Reactive Flow into the Simulation . . . 119
6.1.1. Scope of the Stability Assessment Procedure . . . 120
6.1.2. Separation of Scales . . . 120

6.1.3. Essential Steps of the Stability Assessment Procedure 122
6.2. Single Flame Simulation and Mean Flow Computation 123
6.2.1. Computational Domain and Boundary Conditions 123
6.2.2. Real Gas Description 124
6.2.2.1. Real Gas Equations of State 126
6.2.2.2. Caloric Equation of State, Entropy and Speed of Sound 127
6.2.2.3. Comparison of Equation of States 129
6.2.3. Multi-Component Flow and Combustion 131
6.2.3.1. Turbulence Modeling and Mixing 132
6.2.3.2. Combustion Modeling 134
6.2.4. Mean Flow Computation 141
6.3. Determination of Dome Coupling Scattering Matrices 142
6.4. Acoustic Simulation 144
6.5. Modeling of the Dynamic Heat Release Rate $\hat{\dot{q}}$ 148
6.5.1. Pressure Coupling and FTF^{p} Modeling 153
6.5.2. Velocity Coupling and FTF^{v} Modeling 157
6.6. Assessment of Linear Stability 162

7 Thermoacoustic Characterization of the Test Chamber BKD 165
7.1. Mean Flow Fields 166
7.1.1. Injection Temperatures of H_2 and O_2 166
7.1.2. O_2 Dome and Injector Flow 167
7.1.3. Reactive Field in the Chamber 169
7.2. Dome Coupling Properties 171
7.2.1. Scattering Matrices of the Impedance Change Element and the Pressure Loss Element 171
7.2.2. Dome Coupling Scattering Matrices 174
7.3. Eigenfrequencies and Mode Shapes 177
7.3.1. BKD Eigenfrequencies and Visualization of Mode Shapes 177
7.3.2. Investigation of T_1^{α} Mode Shapes 184
7.3.2.1. Mode Shape Amplitude Distributions 184
7.3.2.2. Analysis of Axial Decay Rates 186
7.3.2.3. Influence of the Mean Flow on the T_1^{α} Mode Damping . 189
7.4. Impact of the Injection Conditions on T_1^{α} and $T_1^{\beta}L_1$ Eigenfrequencies . . 192
7.4.1. Influence of the H_2 Temperature on T_1^{α} and $T_1^{\beta}L_1$ Eigenfrequencies 193
7.4.2. Influence of ROF on T_1^{α} and $T_1^{\beta}L_1$ Eigenfrequencies 198
7.5. Flame Dynamics and Flame Transfer Functions 202
7.5.1. Pressure Coupling 202
7.5.1.1. Coupling Mechanisms 204
7.5.1.2. Flame Transfer Functions for Pressure Coupling 207
7.5.1.3. Nearfield FTF_n^p 208
7.5.1.4. Farfield FTF_f^p 210
7.5.1.5. Influence of the O_2 Injector 211
7.5.2. Velocity Coupling 211
7.5.2.1. Slip Effect between Flame and Acoustic Displacement . 212

7.5.2.2. Flame Transfer Functions of Velocity Coupling 214
7.5.3. Heat Release Source Terms for Pressure Coupling and Velocity Coupling in the Acoustic Simulations 215
7.5.4. Rayleigh Integrals 216
7.6. Stability Behavior of the BKD Test Chamber 218
7.6.1. Linear Stability Assessment 218
7.6.2. Identification of Main Contributors to Damping and Amplification 220
7.6.2.1. Dampening Effects 222
7.6.2.2. Amplification Effects 223
7.6.3. Final Remarks on the Stability Assessment 224
7.6.4. Sensitivity Studies 224
7.6.4.1. Dependence of T_1^α Mode Eigenfrequency and Damping Rate on Grid Resolution and Stability Coefficient 224
7.6.4.2. Dependency of Damping Rate on FTF^p 225

8 Conclusions and Future Work **227**

Appendix **231**

A LEE Compact Matrix Notation **232**

B Supplement for Rocket Engine Acoustics **233**

C Non-reactive Nozzle Acoustics **237**

D Geometrical Specifications of the Perforated Plate **241**

E Dome Coupling **242**

F T_1 Mode Filter Coefficients for Perforated Plate **243**

G L Modes – Non-Reactive Case **244**

H GIT Test Case **245**

I Perforated Plate: Reflection Coefficients **247**

J Derivation of Equivalent Absorber Ring Reflection Coefficient **248**

K Effect of Systematic Noise Excitation **249**

L Additional Real Gas Relations **250**

M Molecular Transport Properties **252**

N Axial Distributions of Mean Quantities for LP1-4 **253**

O $T_1^\beta L_x$ Modes in the BKD Test Chamber **255**

P Derivative of $\mathfrak{Im}(k^{+}_{\mathrm{T}^{\alpha}_{1}})$ at Cut-on **257**

Q Open and Closed Loop Mode Shapes **258**

R Quantitative Contributions of Damping and Amplification Effects for LP1-4 **259**

Supervised Student Theses **261**

Previous Publications **262**

List of Figures **267**

List of Tables **274**

References **276**

Nomenclature

Latin letters

$\dot{I}$	momentum	$[(\mathrm{kg\ m})/\mathrm{s}^2]$
$\dot{m}$	mass flow	$[\mathrm{kg/s}]$
$\dot{Q}$	heat release rate	$[\mathrm{W}]$
$\dot{q}$	volumetric heat release rate	$[\mathrm{W/m}^3]$
$\mathbf{W}$	molar mass	$[\mathrm{kg/kmol}]$
$\mathcal{C}$	prefactor	$[-]$
$\mathcal{D}$	source term	$[\mathrm{W/m}^3]$
$\mathcal{F}, \mathcal{G}$	Riemann invariants	$[\mathrm{m/s}]$
$\mathcal{H}$	finite element size	$[\mathrm{m}]$
$\mathcal{R}$	gas constant	$[\mathrm{J/(kg\ K)}]$
$\mathfrak{R}$	universal gas constant	$[\mathrm{J/(mol\ K)}]$
$\mathfrak{s}$	shape function	$[-]$
ω_a	acentric factor	$[-]$
$\mathbf{M}$	delay multiplicator	$[-]$
$\underline{\mathcal{W}}$	weighting function	$[-]$
$\underline{\underline{A}}, \underline{\underline{B}}, \underline{\underline{C}}$	convective matrices	$[-]$
$\underline{\underline{D}}$	reactive matrix	$[-]$
$\underline{\underline{E}}$	assembly matrix	$[-]$
$\underline{\underline{I}}$	identity matrix	$[-]$
$\underline{\underline{K}}$	stiffness matrix	$[-]$
$\underline{\underline{L}}$	boundary condition matrix	$[-]$
$\underline{\underline{P}}$	matrix of pressure measurements	$[\mathrm{Pa}]$
$\underline{\underline{Q}}$	feedback matrix	$[-]$
a	empirical coefficient	$[-]$
a_0	empirical factor of real gas equation	$[-]$
A_1, A_2, B_1, B_2	amplitudes of circumferential pressure distribution	$[-]$
A_e	amplitude of excitation	$[\mathrm{Pa}]$
a_k, b_k	filter coefficients	$[-]$
a_q	strain rate at extinction	$[1/\mathrm{s}]$
A_{EDM}	EDM model constant	$[-]$
A_{FR}	Finite rate model constant	$[-]$
b	co-volume	$[\mathrm{m}^3]$

c	speed of sound	[m/s]
c_k	complex-valued fit coefficients	[−]
c_p	isobaric specific heat capacity	[J/(kg K)]
c_v	isochoric specific heat capacity	[J/(kg K)]
D	diameter	[m]
DF	down-sampling factor	[−]
E	fluctuating energy density	[J/m^3]
e	internal energy	[J/kg]
E_{FR}	activation energy of finite rate reaction	[J/kg]
f	frequency/eigenfrequency of harmonic oscillation	[Hz]
F, G	complex wave amplitudes	[m/s]
H	transfer function	[−]
h	enthalpy	[J/kg]
h_0^k	mass formation enthalpy	[J/kg]
I	fluctuating intensity flux	[W/m^2]
I, J, K	number of points in each spatial direction	[−]
J_m	Bessel function	[−]
K	non-linear saturation coefficient	$\left[1/(s\,\mathrm{Pa}^2)\right]$
k	wave number	[1/m]
k^{r}	radial wave number	[1/m]
K^f	order of complex fit	[−]
$k^{\mathrm{x}\pm}$	axial wave number	[1/m]
k_{f}	fitted wave number	[1/m]
L	Lagrange ansatz function	[−]
l	length	[m]
l_e	effective length	[m]
N	shape function	[−]
n	number of moles	[−]
n_i	surface normal vector	[−]
N_{SA}	number of single absorbers	[−]
p	pressure	[Pa]
p_a	cohesion pressure	[Pa]
P_{mn}	axial pressure function	[Pa]
R	reflection coefficient	[−]
r	radial coordinate	[m]
r_v	radius of circular excitation boundary	[m]
$R_{e/L}$	resistance of exit/liner	[−]
R_{mn}	radial pressure function	[−]
r_{mn}	impulse response of reflection coefficient	[−]
S	external excitation function	[−]
s	entropy	[J/(kg K)]
$s(t)$	uncorrelated white noise	[Pa/s]
s_{mn}	n-th root of the m-th derivate Bessel function	[−]

T	temperature	[K]
t	time	[s]
T_s	acoustic period	[s]
$T_{u/d}$	transmission coefficient	[−]
u_i	i-th velocity component	[m/s]
U_{mn}	axial velocity function	[m/s]
V	volume	[m^3]
v	specific volume	[m^3/kg]
V_{mn}	radial velocity function	[−]
W_{mn}	circumferential velocity function	[−]
x	spatial coordinate	[m]
$X_{e/L}$	reactance of exit/liner	[−]
Y	acoustic admittance	[−]
Y_k	mass fraction of k-th species	[−]
Z	acoustic impedance	[−]
z	variable in z space	[−]
Z_r	real gas factor	[−]
Z_{st}	mixture fraction at stoichiometry	[−]
A/B	nozzle A/B	[−]
i	imaginary unit	[−]
M,N	number of filter coefficients	[−]
n	discrete time step	[−]
ROF	ratio of oxidizer to fuel	[−]
SM	scattering matrix	[−]
TM	transfer matrix	[−]

Greek letters

α_A	area ratio	[−]
α_τ	stabilization coefficient	[−]
β	volume expansivity	[1/K]
β_{FR}	Finite rate model constant	[−]
χ	scalar dissipation rate	[1/s]
Δt	computational time step	[s]
Δ	displacement	[m]
δ	relative change	[−]
δ_m	angle between pressure nodal line and frame of reference	[rad]
$\dot{\omega}$	reaction rate	[kg/(s m^3)]
ϵ	turbulent dissipation	[J/(kg s)]
ϵ_{nl}	non-linear factor	[−]
η_a/η_b	Fourier coefficients	[Pa]
Γ	noise intensity	[Pa^2/s]
κ	isentropic exponent	[−]
$\kappa_{mn}^{\pm}$	axial ratio of wave numbers	[−]
λ	damping rate	[rad/s]

λ_i	spectral radius	[m]
$\mathcal{K}_s$	isentropic compressibility	[m^2/N]
$\mathcal{K}_T$	isothermal compressibility	[m^2/N]
$\mathcal{T}$	time delay	[s]
μ	dynamic viscosity	[Pa s]
$\mu_{mn}^{\pm}$	radial ratio of wave numbers	[−]
ν	kinematic viscosity	[m^2/s]
ν'/ν''	stoichiometric coefficients of educts/products	[−]
Ω	complex frequency	[rad/s]
ω	angular frequency/eigenfrequency of harmonic oscillation	[rad/s]
Φ	acoustic scalar potential	[m^2/s]
ϕ	phase	[rad]
$\phi_a(t)/\phi_b(t)$	phase of Fourier coefficients	[rad]
ρ	density	[kg/m^3]
σ	heat conductivity	[W/(m K)]
σ_d	collision diameter	$\left[\text{cm/mol}^{-1/3}\right]$
τ	viscous stress tensor	[Pa]
$\tau_\mathrm{t}/\tau_\mathrm{c}$	turbulent/chemical time scale	[s]
θ	circumferential coordinate	[rad]
Θ_{mn}	circumferential pressure function	[−]
$\underline{\Lambda}$	vector of Lagrange multipliers	[−]
$\underline{\phi}$	vector of unknowns	[−]
$\underline{\underline{\eta}}$	matrix of Fourier coefficients	[Pa]
$\underline{\underline{\theta}}$	matrix of circumferential pressure sensor locations	[rad]
τ	stabilization parameter	[−]
Γ	molecular diffusion coefficient	[kg/(m s)]
ξ	vorticity	[1/s]
ξ, η	spatial coordinates of single flame domain	[−]
ζ_l	loss coefficient	[−]
$A(t)/B(t)$	amplitude of Fourier coefficients	[Pa]
k_t	turbulent kinetic energy	[J/kg]

Superscripts

$()'$	acoustic fluctuation in time
$()''$	turbulent fluctuating quantity
$()^*$	complex conjugation
$()^\circ$	original definition of reflection coefficient
$(\bar{})$	mean quantity
$(\breve{})$	quantity on the single flame domain axis
$(\hat{})$	complex amplitude
$(\tilde{})$	Favre average
$(\widetilde{})$	radial average
$+/-$	additional modes in the presence of an absorber ring
α/β	acoustic modes in regions of different speed of sound

Δ	displacement
$\pm$	positive/negative axial direction
ρc	impedance change
a	acoustic
A/B	excitation state A/B
co	cut-on/off
E	finite element
e	entropic
h	discrete approximation
s	system frequency
T	transpose
v	vortical
AC	area change
DE	duct element
EVA	eigenvalue analysis
I,II,III	different configurations
p	pressure
v	transverse velocity

Indices

$1/2$	inner/outer nozzle radius
$\mathcal{A}$	nodal value
$\mathcal{B}$	weighting function value
$\mathcal{C}$	prefactor
ϕ	all unknowns
τ	stabilization parameter
A	absorber
b	baroclinique
c	critical
cc	combustion chamber
d	downstream
e	exit
i	inlet
L	liner
n	n-th step of iterative calculation of the eigenfrequency
q	at extinction
r	radially integrated quantity
s	isentropic
T	isothermal
t	throat
u	upstream
u/d	spatially decoupled modes in the presence of an absorber ring
v	velocity excitation
x	x-longitudinal order

mn	mode class
0	ideal gas state
A	nozzle A
ac	acoustic
AR	absorber ring
B	nozzle B
BL	boundary layer
c	chemical
e	excitation
eff	effective
F	feed line
f	farfield
fl	flame
inj	injection
LP	load point
m	molar volume
mech	mechanism
n	nearfield
p	plateau
P1	absorber ring position 1
P2	absorber ring position 2
post	O_2 post
red	reduced
ref	reference state
S	shell
SA	single absorber
SF	single flame
St	Strouhal number
st	stoichiometric
t	turbulent

Operators

δ_{ij}	Kronecker delta
$\mathcal{O}$	Landau operator (order of magnitude)
$\mathfrak{Im}$	imaginary part
$\mathfrak{Re}$	real part
$\underline{\underline{\mathcal{L}}}$	LEE operator
$\underline{\underline{\mathcal{R}}}$	residuum
ε_{ijk}	Levi-Civita symbol

Letter-like symbols

$\mathcal{A}$	acoustic amplitude for fitting
$\mathcal{F}$	Fourier transform
$\mathcal{S}$	force term

Non-Dimensional numbers

M	Mach number
Da	Damköhler number
Le	Lewis number
Pe	Péclet number
Pr	Prandtl number
Ra	Rayleigh integral
$\mathrm{Re_t}$	Turbulent Reynolds number
Sc	Schmidt number

Abbreviations

BaZ	Bell and Zinn
BKD	Brennkammer D
CAA	Computational Aeroacoustics
CEA	Chemical Equilibrium with Applications
CFD	Computational Fluid Dynamics
CPIA	Chemical Propulsion Information Analysis Center
DLR	German Aerospace Center
DOF	Degrees of Freedom
DRP	Dispersion Relation Preserving
EDM	Eddy-Dissipation Model
EOS	Equation of State
FEM	Finite Element Method
FIR	Finite Impulse Response
FR	Finite Rate
FTF	Flame Transfer Function
GIT	Grazing-Incidence-Tube
GLS	Galerkin/Least-squares
HF	high frequency
IG	Ideal Gas
IIR	Infinite Impulse Response
L	longitudinal mode
LEE	Linearized Euler Equations
LES	Large Eddy Simulation
LP	Load point
MUMPS	Multifrontal Massively Parallel sparse direct Solver
NIST	National Institute of Standards and Technology
P1	absorber ring position 1
P2	absorber ring position 2
PDF	Probability Density Function
PIANO	Perturbation Investigation of Aerodynamic Noise
PR	Peng-Robinson
R	radial mode
REST	Rocket Engine Stability Research Initiative
SPL	Sound Pressure Level

SRK	Soave-Redlich-Kwong
T	transverse mode
TDIBC	Time-Domain Impedance Boundary Conditions
URANS	Unsteady Reynolds Averaged Navier-Stokes Simulations

1 Introduction

1.1. Combustion Instabilities in Rocket Engines

Efficient and profitable commercial space transportation systems demand enormous thrust to weight ratios. Depending on the targeted orbit, a payload of only 10-20 tons already requires a Ariane 5 total lift-off weight of approximately 780 tons. The necessary thrust is conventionally generated through the chemical conversion of fuel into hot products establishing tremendous volumetric power densities in the combustion chamber. In fact, the Ariane 5 Vulcain II main stage engine provides 3 GW of power while facing extreme thermal loads on highly weight optimized walls of up to $100\,\mathrm{MW/m^2}$. Operating pressures of several MPa and temperatures of approximatively 3600 K bring technical feasibilities to absolute limits and give rocket science and development rise to one of the most ambitious disciplines in engineering.

The Vulcain II engine is shown in Fig. 1.1. It consists of two main systems. The feed and injection system, which delivers the oxygen and hydrogen propellants at suitable temperature and pressure to the combustion and thrust system. Oxygen is provided by the feed lines from the tanks and fed first into the oxygen dome. In this confinement, the splitter plate homogenizes the oxygen flow and hence leads to an equal pressure distribution on the face plate. Subsequently, oxygen is injected into the combustion chamber through a high number of small injectors. Hydrogen is delivered by cooling channels in the combustion chamber wall to the face plate and finally injected coaxially to the oxygen. Thrust is generated by volume expansion of the burned gas in the cylindrical combustion chamber and its acceleration in the convergent - divergent nozzle.

By nature, combustion in rocket engines such as shown in Fig. 1.1 are permanently subjected to disturbances originating from a variety of possible sources. Therefore, a certain level of combustion noise is always present in the chamber. For peak-to-peak values below 5 % of the mean chamber pressure, steady state engine operation is characterized to be *smooth* (Sutton and Biblarz 2001). If higher sound pressure levels with several bar peak-to-peak amplitude at a discrete frequency occur, critical thermo-mechanical loads might arise and the integrity of the solid walls might be endangered. Furthermore, control systems and payload cargo could potentially be exposed to unbearable vibrational loads. In consequence, the engine operation might either be restricted to lower power output or, at the worst, the engine could be destroyed leading to a mission

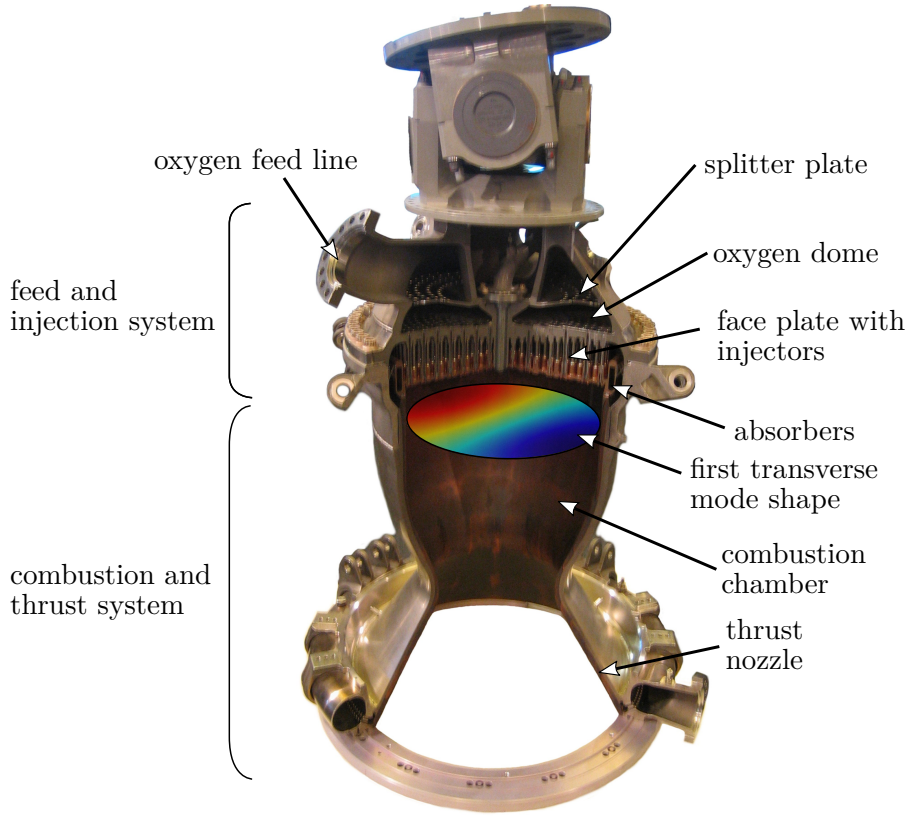

Fig. 1.1.: Vulcain II rocket engine configuration, adapted from (Kathan 2013).

failure and the loss of valuable payload.

Such high energy acoustic motion is often associated with a high-frequency (HF) combustion instability. Due to the enormous damping effect on axially oriented acoustic modes through convective transport in the thrust nozzle, longitudinal modes are usually irrelevant. In turn, high frequency motions associated with transverse modes are most destructive for rocket engines, see Fig. 1.1. Conventional chamber diameters and combustion temperatures lead to typical oscillation frequencies in the range of 3000 to 10,000 Hz. The acoustic propagation is usually not limited to the combustion chamber, but the entire feed and injection system may alter the system dynamics, which makes the understanding of HF instabilities highly challenging.

The fundamental mechanism of acoustic amplitude amplification is based on an internal feedback loop, which contains the interaction of fluctuating pressure and velocity with combustion including several sub-processes. Under unfavorable conditions, acoustically modulated unsteady heat release feeds energy back into critical oscillation frequencies and natural damping capabilities inherently present in the system can be exceeded. At high amplitudes, reduced feedback and enhanced damping simultaneously balance amplification and damping, limiting further growth. Stable engine operation can either be reached by establishing a weak modulability of the heat release rate or

by increasing the system damping by passive or active means (Culick 2006).

Acoustic absorbers are widely used as additional damping devices, which influence acoustic propagation in multiple ways (Culick 1988; Culick and Yang 1995). A typical absorber device is shown in Fig. 1.1. Different absorber cavity configurations exist, e.g. $\lambda/4$ absorbers (Oschwald et al. 2008b) and Helmholtz resonators (Keller and Zauner 1995). Another type of auxiliary damping devices are so-called baffles, which are located directly at the face plate (Culick and Yang 1995). Due to the complex interaction of absorbers with the acoustic field in the chamber and the combustion process, an effective design is difficult to achieve and the development process is usually accompanied with extensive testing. Furthermore, their numerical evaluation in terms of damping capabilities as well as their incorporation into stability assessment tools is especially challenging, since dissipation of acoustic energy is partially based on small-scaled shear-layer - acoustic interactions, which promote the occurrence of numerical instabilities (Richter et al. 2007).

Unexpected combustion instabilities during the development of rocket thrust systems put due-dates at risk and became apparent as critical cost driver since the 1930s (Harrje and Reardon 1972). For instance, a number of 2000 full scale, hot fire tests were necessary to establish stable operation conditions for the Rocketdyne F-1 liquid engine. In 1980 a combustion instability in one of the four Viking engines powering the Ariane 1 led to the automatic self-destruction of the rocket due to the loss of maneuverability (Leitenberger 2013). As a counter measure the injection system was redesigned and a more stable propellant combination was introduced during a one-year phase without any take-off. Recently, unstable operation of a cryogenic liquid oxygen/liquid methane engine occurred during the start sequence of NASA's planetary vehicle Morpheus (Melcher and Morehead 2014). Chug instabilities at low frequencies as well as HF (*screech*) instabilities were both prevented by an elevated pressure start sequence and modified fuel injection temperatures.

The necessity of reliable and efficient assessment tools for combustion instabilities in rocket engines becomes further evident with the trend towards the usage of the thermoacoustically more critical methane propellant as well as with the reduction of pressure drop over the injectors in order to improve thrust efficiency.

Understanding the thermoacoustic processes in rocket engines is demanding due to multiple reasons: (1) Interactions between turbulent fluid dynamics, combustion kinematics, heat transfer, acoustics, viscosity and further physical phenomena indicate their multidisciplinary complexity. (2) It is unlikely that a unique mechanism is responsible for the appearance of high acoustic amplitudes in unstable systems. Instead, the interplay of different mechanisms plays a role and may differ in strength and relevance for each system leading to different types of instabilities. (3) Full-scale experiments are required, which are critical in terms of costs and limited in diagnostic accessibility restricting the available data for analysis. (4) The presence of different physical processes creates a huge dispersity of scales both in time and space which needs to be resolved. Numerical approaches available today are not yet able to capture all relevant processes to a sufficient degree.

Nevertheless, pursuing the understanding for unstable engine operation continues to be worthwhile as the benefit of each new insight brings scientists closer to the ultimate goal of an a priori predictive engineering level tool. Therefore, concentrated research activities are found in countries launching rockets on a regular basis.

The development of numerical methods to assess HF combustion stability is still an unfulfilled task (Culick and Yang 1995). However, the necessity of such prediction tools has not changed. Especially the trend towards alternative fuels such as methane (Melcher and Morehead 2014) requires reliable predictions since the wealth of experience in this field is less than for conventional propellants like hydrogen/oxygen. Methods for assessing the potential of thermoacoustic instabilities need to be applied from the beginning of a new engine design and reused in an iterative process during the entire development providing reliable stability assessments. At the same time, these methods are supposed to be lean in terms of computational time and effort.

Different numerical methods for the prediction of thermoacoustic stability have been developed. Analytical derivations allow for the calculation of nozzle admittances and the system damping without flame response (Köglmeier et al. 2010). Furthermore, flame response models can be applied to include the effect of the acoustically modulated heat release fluctuations on the dynamic amplitude behavior (Frezzotti et al. 2014). On the contrary, high quality but time consuming LES (Large Eddy Simulation) computations were conducted to reproduce a self-excited thermoacoustic loop (Urbano et al. 2014, 2015). As a compromise, the decomposition of the governing fluid-dynamic quantities into a mean flow state including combustion and the acoustic propagation was applied to benefit from separation of scales. Such methods are commonly referred to as CFD/CAA (Computational Fluid Dynamics/Computational Aeroacoustics) hybrid approaches (Köglmeier et al. 2014a; Morgenweck 2013; Pieringer 2008; Schulze et al. 2012, 2013b; Schulze and Sattelmayer 2014). However, the recently held 3rd modeling workshop on combustion instabilities[1] in the framework of the French-German research initiative REST evidently showed that a predictive level is not yet reached by any type of simulation.

1.2. Modeling Approach

Due to the lack of availability of predictive HF stability assessment tools for rocket engines, the CFD/CAA approach is further developed in this thesis. The essential ingredient to reduce computational effort is to exploit separation of small scale effects such as turbulent combustion from considerably bigger scales of acoustic propagation. The scale separation is motivated by the geometrical arrangements of typical industrial rocket engine configurations as shown in Fig. 1.1. Different numerical environments are applied to establish the most suitable techniques for the description of the different scales. Therefore, high quality results can be achieved in each computation including all relevant effects. Especially for the determination of dynamic response models in terms of *Flame Transfer Functions* (FTF), a significant reduction of computational

[1] Held in Vernon, France, 2014

effort is achieved when their determination is separated from the stability assessment procedure using CAA. The links between the CFD and CAA computations are shaped into transfer functions which include the essential mechanisms of the thermoacoustic feedback phenomena.

For the description of acoustic propagation, linearized governing equations are especially suitable. On a basic level the convective wave equation describes the acoustic propagation without considering spatial mean flow gradients and is therefore not applicable for stratified flow as well as nozzle flows. Therefore, linearized Euler equations (LEE) are used to describe the acoustic propagation in three-dimensional space in order to account for higher-order modes and relevant mean flow effects.

Linearized Euler equations describe the conservations of mass, momentum and energy in time and space. In the linear regime acoustic modes are orthogonal and therefore independent of each other. An alternative description of the same physics is hence achieved by the transformation of the time (t) dependence of the LEE into a complex frequency (Ω) dependency, viz.

$$\frac{\partial(\,)}{\partial t} \rightarrow \mathrm{i}\Omega(\,), \tag{1.1}$$

where i denotes the imaginary unit. Time domain and frequency space based equations are used in this thesis in order to highlight their strengths, differences and potential advantages for the assessment of combustion instabilities in rocket engines.

1.3. Thesis Scope and Structure

The goal is the development and implementation of a CFD/CAA hybrid stability assessment procedure into a modular environment, which allows for the determination of combustion stability margins of a rocket engine system. The thesis focus is on cryogenic rocket engines, since supercritical combustion is better suited for model development purposes due to the absence of complex droplet atomization and evaporation processes. Studies on combustion dynamics for liquid driven engines on the basis of the same numerical methodology can be found in (Sattelmayer et al. 2015a,b; Schulze et al. 2016b).

Since longitudinal acoustic modes are usually uncritical, the stability assessment procedure is implemented such that higher-order modes can be simulated. The procedure is explained and validated on the basis of the first transverse mode, cf. Fig. 1.1. Furthermore, the developed method is capable of describing the system dynamics at low amplitudes, i.e. in the linear regime. Specifically, eigenfrequencies and damping rates can be calculated. The damping rates are employed to assess the linear stability of the combustion system.

In contrast, it is not intended to determine limit cycle amplitudes. Such simulations require the incorporation of non-linear saturation effects. However, procedures to incorporate non-linearity on the basis of the presented stability assessment procedure will be depicted.

Basically, this thesis covers four essential steps for the development of an extended hybrid CFD/CAA stability assessment procedure:

1. The presentation of suitable governing equations for the usage of CFD/CAA in rocket engines and the implementation of high-fidelity techniques for their numerical solution.
2. The validation of the methods on the basis of non-reactive conditions supported by comprehensive experimental procedures for the generation of validation data. The non-reactive setup allows for comparably simple pre- and post-processing procedures.
3. An investigation of dynamic flame processes under artificially excitation using CFD together with the calibration of suitable dynamic feedback models.
4. The validation of the assessment tool for linear stability using a representative rocket engine configuration.

Consequently, the thesis is structured as follows:

In Chapter 2, the fundamental acoustic equations in different forms are introduced together with the modeling of the dynamic heat release response and suitable boundary conditions for the incorporation of the nozzle, absorbers and the oxidizer dome into the stability assessment.

Chapter 3 presents the numerical techniques for the simulation of the LEE in time domain and frequency space as well as the discussion of advantages and disadvantages of the respective methodology.

Subsequently, Chapter 4 is concerned with the validation of the LEE in time domain and frequency space on the basis of non-reactive conditions. Experimental results are used for full verification of the suitability of the chosen solution techniques.

In Chapter 5, the reactive BKD test chamber is presented and its main characteristics are explained. Additionally, Lorentzian fitting and parameter extraction procedures are employed to extract linear damping rates from dynamic pressure measurements.

Chapter 6 introduces the stability assessment procedure. This concerns the presentation of the CFD model including the governing equations for the simulation of cryogenic H_2/O_2 combustion, the methodology for the determination of scattering matrices for the acoustic coupling of the chamber with the oxidizer dome, the numerical setup for the acoustic simulations under reactive conditions as well as the modeling strategy of the flame feedback and its incorporation into the acoustic simulations.

Finally, Chapter 7 deals with the validation of the stability assessment procedure. The validation is conducted on different levels. First the mean flow results for the BKD is validated on the basis of combustion temperatures and pressures. Afterwards, the dome coupling scattering matrices for the BKD test chamber are presented. Subsequently, the eigenfrequencies of the BKD test chamber are determined numerically and compared to experimental findings. Furthermore, the mode shapes are intensively analyzed and discussed. In the next step, the dependency of eigenfrequencies and mode shapes on injection conditions is studied revealing the numerical accuracy necessary for

meaningful stability predictions. The subsequent subsection is concerned with the analysis of dynamic flame behavior. Fundamental coupling mechanisms between acoustics and combustion are identified and suitable transfer functions are determined. Finally, the linear stability of the BKD test chamber is determined on the basis of the developed stability assessment procedure. The calculated damping rates are compared to experimental findings presented in Chapter 6.

Chapter 8 concludes the thesis and explains further development and validation possibilities in the future.

2 Rocket Engine Acoustics

In this Chapter the fundamental equations for the description of rocket engine acoustics are introduced. First, the general equations are presented and subsequently converted into their linearized form for the simulation of acoustic propagation for small amplitudes. Afterwards, analytical solutions for the wave propagation in uniform flow are presented. Additionally, boundary conditions are introduced. Special attention is paid to the acoustic coupling of combustion chamber and oxidizer dome. In the last section, the modeling strategy for the dynamic flame response is described.

2.1. General Form of Governing Equations

The general description of the unsteady dynamic fluid field including acoustic propagation within a rocket thrust system is given by the Navier-Stokes equations. The spatiotemporal behavior (x_i,t) of a reactive multi-component Newtonian fluid neglecting volumetric force terms is governed by the conservation of mass, momentum and energy:

$$\frac{\partial \rho}{\partial t} + \frac{\partial (\rho u_i)}{\partial x_i} = 0, \tag{2.1}$$

$$\frac{\partial (\rho u_j)}{\partial t} + \frac{\partial (\rho u_i u_j)}{\partial x_i} + \frac{\partial p}{\partial x_j} = \frac{\partial \tau_{ij}}{\partial x_j}, \tag{2.2}$$

$$\frac{\partial (\rho e)}{\partial t} + \frac{\partial (\rho u_i e)}{\partial x_i} = \frac{\partial}{\partial x_i}\left(\sigma \frac{\partial T}{\partial x_i} + \sum_k^N \Gamma_k h_k \frac{\partial Y_k}{\partial x_i}\right) + \left(\tau_{ij} - p\delta_{ij}\right)\frac{\partial u_i}{\partial x_j} + \dot{q}, \tag{2.3}$$

with the definition of the viscous stress tensor

$$\tau_{ij} = \mu\left(\frac{\partial u_i}{\partial x_j} + \frac{\partial u_j}{\partial x_i} - \frac{2}{3}\frac{\partial u_k}{\partial x_k}\delta_{ij}\right), \tag{2.4}$$

where ρ denotes density, u_i the velocity components, p pressure, e internal energy, Y_k the mass fraction of the k-th species, Γ the molecular diffusion coefficient and N the

number of species involved. Heat conductivity σ and dynamic viscosity μ are mass averaged, i.e.

$$\sigma = \sum_{k}^{N} Y_k \sigma_k \; ; \qquad \mu = \sum_{k}^{N} Y_k \mu_k. \tag{2.5}$$

The dynamic viscosity is related to the kinematic viscosity ν by

$$\mu = \nu \rho. \tag{2.6}$$

Additionally, the species transport equation reads

$$\frac{\partial(\rho Y_k)}{\partial t} + \frac{\partial(\rho u_i Y_k)}{\partial x_i} = \frac{\partial}{\partial x_i}\left(\Gamma_k \frac{\partial Y_k}{\partial x_i}\right) + \dot{\omega}_k, \tag{2.7}$$

where $\dot{\omega}_k$ states the reaction rate due to combustion.

Closure of the system of equations is provided by a thermal equation of state relating pressure, density and temperature, i.e.

$$p = p(\rho, T), \tag{2.8}$$

where the detailed form depends on the considered temperature and pressure conditions and will be introduced when appropriate.

2.2. Fundamentals of Linear Acoustics

If the acoustic fluctuations $()'$ are assumed to be small compared to the mean flow state $(\bar{})$, i.e.

$$\rho' << \bar{\rho}, \quad u_i' << c, \quad p' << \bar{p} \;\text{ and }\; \dot{q}' << \bar{\dot{q}}, \tag{2.9}$$

the general equations (2.1)-(2.8) can be evaluated in their linearized form for the description of acoustic propagation. For small amplitudes, heat conduction and viscous effects can be neglected in rocket engines (Culick 2006). Also, for the description of linear acoustic propagation, the variation of species composition due to diffusion and chemical reaction is not accounted for. In consequence, the species transport equation is excluded. Assuming the validity of the ideal gas relation, i.e.

$$\bar{p} = \bar{\rho} \mathcal{R} \bar{T}, \tag{2.10}$$

where $\mathcal{R}$ denotes the gas constant, the linearized set of the Euler equations (LEE) can be derived (Gikadi 2014; Schulze 2012):

$$\frac{\partial \rho'}{\partial t} + \bar{u}_i \frac{\partial \rho'}{\partial x_i} + \bar{\rho} \frac{\partial u_i'}{\partial x_i} + u_i' \frac{\partial \bar{\rho}}{\partial x_i} + \rho' \frac{\partial \bar{u}_i}{\partial x_i} = \mathcal{S}_\rho', \tag{2.11}$$

$$\frac{\partial u_i'}{\partial t} + \bar{u}_j \frac{\partial u_i'}{\partial x_j} + u_j' \frac{\partial \bar{u}_i}{\partial x_j} + \frac{1}{\bar{\rho}} \frac{\partial p'}{\partial x_i} - \frac{\rho'}{\bar{\rho}^2} \frac{\partial \bar{p}}{\partial x_i} = \frac{\mathcal{S}'_{u_i}}{\bar{\rho}}, \tag{2.12}$$

$$\frac{\partial p'}{\partial t} + \bar{u}_i \frac{\partial p'}{\partial x_i} + u_i' \frac{\partial \bar{p}}{\partial x_i} + \kappa \left(\bar{p} \frac{\partial u_i'}{\partial x_i} + p' \frac{\partial \bar{u}_i}{\partial x_i} \right) - \left(\frac{\bar{p} u_i' + p' \bar{u}_i}{\kappa - 1} \right) \frac{\partial \kappa}{\partial x_i} = (\kappa - 1)\, \dot{q}' + \mathcal{S}'_p, \tag{2.13}$$

where $\mathcal{S}'$ denotes force terms potentially applicable for external acoustic excitation.

In Eq. (2.13) the spatial variation of the isentropic exponent κ is included. This is necessary to account for its dependency on temperature and species composition in reactive fields. In case of single species dynamics and only weak temperature dependence, κ may be set constant simplifying Eq. (2.13) to

$$\frac{\partial p'}{\partial t} + \bar{u}_i \frac{\partial p'}{\partial x_i} + u_i' \frac{\partial \bar{p}}{\partial x_i} + \kappa \left(\bar{p} \frac{\partial u_i'}{\partial x_i} + p' \frac{\partial \bar{u}_i}{\partial x_i} \right) = (\kappa - 1)\, \dot{q}' + \mathcal{S}'_p. \tag{2.14}$$

The perturbed energy term $\dot{q}'$ in Eq. (2.13) and Eq. (2.14), respectively, accounts for a fluctuating heat release source. In the context of combustion instabilities, heat release is modulated by acoustic perturbation.

In general, the mean flow quantities ($\bar{}$) can be determined analytically, numerically or experimentally. For complex mean flows, numerical evaluations are preferable. For this purpose, Eq. (2.1)-(2.8) are evaluated using appropriate CFD tools. Euler Equations (laminar), Reynolds Averaged Navier-Stokes (RANS), Large Eddy Simulation (LES) or Direct Numerical Simulations (DNS) can be used.

The fluctuating fields are composed of three general types of fluctuations. Firstly, the acoustic fluctuations, which are further subdivided into different modes. The acoustic modes propagate with speed of sound superimposed by the mean flow velocity. In consequence, the acoustic modes are able to propagate against the mean flow only for Mach numbers below unity. Changes of thermodynamic state due to the acoustic modes are isentropic. Secondly, the vorticity fluctuations are transported convectively with the mean flow altering only the fluctuating velocity field. Finally, the entropy fluctuations describe non-acoustic fluctuations of density, i.e. its non-isentropic changes, and also propagate with the mean flow.

Combustion instabilities are associated with the impact of the acoustic modes on the system. However, vorticity fluctuations and entropy fluctuations may intrinsically modulate the feedback mechanism or attribute to enhanced damping (Föller and Polifke 2012; Gikadi et al. 2012; Shipley et al. 2014).

The LEE are capable of describing the interaction of the different types of fluctuations. Shaping the LEE into a different form by a decomposition of variables, the main effects can be highlighted and discussed. The transformation of the equations was suggested in (Ewert and Schröder 2003; Ewert et al. 2002a,b), applied to thermoacoustics in

(Pankiewitz 2004; Pieringer 2008) and is extended in terms of the spatial dependence of κ in this thesis.

Density fluctuations are decomposed into an isentropic part, which is attributed to the acoustic fluctuations (^{a}), and a non-isentropic part, attributed to entropy fluctuations (^{e}), viz.

$$\rho' = \rho^a + \rho^e. \tag{2.15}$$

Isentropically relating the *acoustic* density with the pressure fluctuations yields

$$p' = c^2 \rho^a, \tag{2.16}$$

as pressure is purely acoustic. Finally, the vorticity fluctuations (^{v}) are identified with the rotational flow component of the fluctuating velocity field, while the irrotational (acoustic) part is given as gradient field of a scalar potential Φ, viz.

$$u_i' = \nabla\Phi + u_i^v. \tag{2.17}$$

Furthermore, a relation between Φ and p' is employed (Pankiewitz 2004; Pieringer 2008):

$$p' = -\bar{\rho}\frac{D\Phi}{Dt}, \tag{2.18}$$

where the material derivative is used for the sake of simplicity, viz.

$$\frac{D()}{Dt} = \frac{\partial()}{\partial t} + \bar{u}_i \frac{\partial()}{\partial x_i}. \tag{2.19}$$

Inserting Eq. (2.15)-(2.19) into the LEE (2.11)-(2.13) and rearranging yields transport equations for the acoustic potential, the rotational velocity component and the non-isentropic density fluctuation:

$$\bar{\rho}\frac{D}{Dt}\left(\frac{1}{c}\frac{D\Phi}{Dt}\right) - \frac{\partial}{\partial x_i}\left(\bar{\rho}\frac{\partial\Phi}{\partial x_i}\right) = \mathcal{S}^a(u_i^v, \rho^e), \tag{2.20}$$

$$\frac{Du_k^v}{Dt} + u_i^v \frac{\partial \bar{u}_k}{\partial x_i} = \mathcal{S}^v(\Phi, \rho^e), \tag{2.21}$$

$$\frac{D\rho^e}{Dt} + \rho^e \frac{\partial \bar{u}_i}{\partial x_i} = \mathcal{S}^e(\Phi, u_i^v, \dot{q}'). \tag{2.22}$$

The source terms are given by

$$\mathcal{S}^a(u_i^v, \rho^e) = \frac{\partial \rho^e}{\partial t} + \bar{u}_i \frac{\partial \rho^e}{\partial x_i} + \rho^e \frac{\partial \bar{u}_i}{\partial x_i} + \frac{\partial}{\partial x_i}(u_i^v \bar{\rho}), \tag{2.23}$$

$$\mathcal{S}^v(\Phi, \rho^e) = \varepsilon_{ijk}\bar{\xi}_i \frac{\partial\Phi}{\partial x_j} + \frac{\rho^e}{\bar{\rho}^2}\frac{\partial \bar{p}}{\partial x_k} + \frac{1}{\bar{\rho}}\frac{D\Phi}{Dt}\left(\frac{\partial\bar{\rho}}{\partial x_k} - \frac{1}{c^2}\frac{\partial \bar{p}}{\partial x_k}\right), \tag{2.24}$$

$$\begin{aligned}\mathcal{S}^e(\Phi, u_i^v, \dot{q}') = &\left(\frac{1}{c^2}\frac{\partial \bar{p}}{\partial x_i} - \frac{\partial\bar{\rho}}{\partial x_i} + \frac{\bar{p}}{c^2(\kappa-1)}\frac{\partial\kappa}{\partial x_i}\right)\left(\frac{\partial\Phi}{\partial x_i} + u_i^v\right) + \\ &- \frac{\bar{\rho}}{c^2}\left((\kappa-1)\frac{\partial \bar{u}_i}{\partial x_i} + \frac{2\bar{u}_i}{c}\frac{\partial c}{\partial x_i} + \frac{\bar{u}_i}{\kappa-1}\frac{\partial\kappa}{\partial x_i}\right)\frac{D\Phi}{Dt} - \frac{(\kappa-1)}{c^2}\dot{q}',\end{aligned} \tag{2.25}$$

and highlight the interaction mechanisms: The acoustic fluctuations exchange energy with the fluctuating vorticity and the non-isentropic density fluctuations through the mean flow velocity as well as through the density field and corresponding gradients. The vorticity fluctuations are coupled with the acoustic fluctuations on the basis of the mean flow vorticity $\bar{\xi}$ and the gradients of the mean density and pressure. Furthermore, the entropy fluctuations also interact with the vorticity fluctuations depending on the mean flow pressure gradient. The source term of the entropy fluctuations shows the most complex behavior: Gradients of mean flow pressure, density, velocity, speed of sound and κ interact with the acoustic fluctuations yielding a variety of possible energy transfer mechanisms between those types of fluctuations. A rather complex interaction with the vorticity fluctuations are present as well. Lastly, a fluctuating heat release source provides an energy transfer from combustion into the strongly coupled fluctuating components. In fact, the entropy fluctuations are primarily driven by dynamic heat release fluctuations. The acoustic fluctuations and vorticity fluctuations are coupled to combustion indirectly via source terms.

2.3. LEE in Frequency Space

By definition, linear acoustics allow for a decomposition of the fluctuating variables into space and time dependency. Assuming harmonicity in time leads in complex notation to

$$\begin{aligned} \rho'(x_i,t) &= \mathfrak{Re}\left[\hat{\rho}(x_i)e^{\mathrm{i}\Omega t}\right], \quad u_i'(x_k,t) = \mathfrak{Re}\left[\hat{u}_i(x_k)e^{\mathrm{i}\Omega t}\right], \\ p'(x_i,t) &= \mathfrak{Re}\left[\hat{p}(x_i)e^{\mathrm{i}\Omega t}\right], \quad \dot{q}'(x_i,t) = \mathfrak{Re}\left[\hat{\dot{q}}(x_i)e^{\mathrm{i}\Omega t}\right], \end{aligned} \tag{2.26}$$

where $(\hat{})$ denotes the complex amplitude and Ω the complex frequency containing the frequency of harmonic oscillation ω as well as the damping rate λ, viz.

$$\Omega = \omega + \mathrm{i}\lambda. \tag{2.27}$$

For instance, pressure fluctuations are given by

$$p'(x_i,t) = \mathfrak{Re}\left[\hat{p}(x_i)e^{\mathrm{i}\Omega t}\right] = \mathfrak{Re}\left[\hat{p}(x_i)e^{\mathrm{i}\omega t-\lambda t}\right]. \tag{2.28}$$

Velocity, density and heat release fluctuations behave equally. Eq. (2.28) shows that acoustic amplitudes decay exponentially if the damping rate is positive. In contrast, for a negative damping rate, acoustic amplitudes grow exponentially in time. Hence, the linear stability of a combustion system can be characterized as follows:

- $\lambda > 0$:
  The combustion system operates stable.
- $\lambda < 0$:
  The linear system is unstable and high acoustic amplitudes must be expected.
- $\lambda = 0$:
  Quasi steady state oscillations and constant amplitudes. This state is referred to as limit cycle.

Negative damping rates are often referred to as growth rates. However, in this thesis λ is only referred to as damping rate. Its sign determines if amplitudes decay or grow in time. Furthermore, the frequency of harmonic oscillation is regularly given in [Hz], i.e.

$$f = \frac{\omega}{2\pi}. \tag{2.29}$$

Inserting Eq. (2.26) into the LEE (2.11)-(2.13) and using the time derivative according to Eq. (1.1) yields the equivalent set of equations in frequency space

$$\mathrm{i}\Omega\hat{\rho} + \bar{u}_i \frac{\partial \hat{\rho}}{\partial x_i} + \bar{\rho}\frac{\partial \hat{u}_i}{\partial x_i} + \hat{u}_i \frac{\partial \bar{\rho}}{\partial x_i} + \hat{\rho}\frac{\partial \bar{u}_i}{\partial x_i} = \hat{\mathcal{S}}_\rho, \tag{2.30}$$

$$\mathrm{i}\Omega\hat{u}_i + \bar{u}_j \frac{\partial \hat{u}_i}{\partial x_j} + \hat{u}_j \frac{\partial \bar{u}_i}{\partial x_j} + \frac{1}{\bar{\rho}}\frac{\partial \hat{p}}{\partial x_i} - \frac{\hat{\rho}}{\bar{\rho}^2}\frac{\partial \bar{p}}{\partial x_i} = \frac{\hat{\mathcal{S}}_{u_i}}{\bar{\rho}}, \tag{2.31}$$

$$\mathrm{i}\Omega\hat{p} + \bar{u}_i \frac{\partial \hat{p}}{\partial x_i} + \hat{u}_i \frac{\partial \bar{p}}{\partial x_i} + \kappa\left(\bar{p}\frac{\partial \hat{u}_i}{\partial x_i} + \hat{p}\frac{\partial \bar{u}_i}{\partial x_i}\right) - \left(\frac{\bar{p}\hat{u}_i + \hat{p}\bar{u}_i}{\kappa - 1}\right)\frac{\partial \kappa}{\partial x_i} = (\kappa - 1)\,\hat{\dot{q}} + \hat{\mathcal{S}}_p. \tag{2.32}$$

In matrix-vector notation the LEE can be written in a compact form. For future reference, this form is introduced as well:

$$\underline{\underline{\mathcal{R}}} = \underline{\underline{\mathcal{L}}}(\underline{\hat{\phi}}) - \underline{\hat{\mathcal{S}}} = \mathrm{i}\Omega\underline{\hat{\phi}} + \underline{\underline{A}}\,\frac{\partial \underline{\hat{\phi}}}{\partial x} + \underline{\underline{B}}\,\frac{\partial \underline{\hat{\phi}}}{\partial y} + \underline{\underline{C}}\,\frac{\partial \underline{\hat{\phi}}}{\partial z} + \underline{\underline{D}}\,\underline{\hat{\phi}} - \underline{\underline{Q}}\,\underline{\hat{\phi}} - \underline{\hat{\mathcal{S}}} = 0, \tag{2.33}$$

where $\underline{\underline{\mathcal{R}}}$ denotes the residuum, $\underline{\underline{\mathcal{L}}}$ the LEE operator on $\underline{\hat{\phi}}$, and $\underline{\hat{\phi}}$ itself the vector of unknowns, viz.

$$\underline{\hat{\phi}} = (\hat{\rho}, \hat{u}, \hat{v}, \hat{w}, \hat{p})^T, \tag{2.34}$$

in a three-dimensional space. Due to their physical meaning, the matrices $\underline{\underline{A}}$-$\underline{\underline{C}}$ are referred to as convective matrices, $\underline{\underline{D}}$ as reactive matrix and $\underline{\underline{Q}}$ as feedback matrix. The matrices $\underline{\underline{A}}$-$\underline{\underline{D}}$ and $\underline{\underline{Q}}$ as well as the vector $\underline{\hat{\mathcal{S}}}$ are given in App. A.

Solving the frequency space transformed LEE for the complex frequency Ω on the basis of an eigenvalue problem formulation accounting for adequate boundary conditions without external excitation, i.e. $\hat{\mathcal{S}} = 0$, yields the system's eigenfrequencies, damping rates as well as the associated acoustic mode shapes. In time domain, corresponding results are determined by exciting the system acoustically via external or volumetric impulse forcing and analyzing e.g. the pressure signal using different post-processing techniques (Oppenheim et al. 1999; Schulze et al. 2014a). Generating the frequency response at zero damping rate requires harmonic forcing in frequency space, which can

also be established through external excitation or with volumetric source terms. However, in time domain, the frequency response can be generated on the basis of impulse forcing and harmonic excitation (Morgenweck 2013).

Fluctuating temperature and entropy are given by

$$\frac{\hat{T}}{\bar{T}} = \frac{\hat{p}}{\bar{p}} - \frac{\hat{\rho}}{\bar{\rho}}, \tag{2.35}$$

and

$$\hat{s} = c_v \frac{\hat{p}}{\bar{p}} - c_p \frac{\hat{\rho}}{\bar{\rho}}, \tag{2.36}$$

where c_p and c_v denote the isobaric and isochoric specific heat capacities. If only isentropic variations are present, the entropy is set to zero, $\hat{s} = 0$, and Eq. (2.36) reduces to

$$\hat{p} = c^2 \hat{\rho}, \tag{2.37}$$

which can be used to reduce the number of equations in (2.30)-(2.32) to only four.

2.4. Acoustic Propagation in Uniform Mean Flow

While the impact of vorticity and entropy complicates the analysis of the fluctuating fields, uniform mean flow considerations are most appropriate to establish profound knowledge about the acoustic mode propagation. Since it is of substantial relevance for rocket engine acoustics, a cylindrical configuration is considered. Assuming constant mean flow velocity in axial direction in a cylindrical frame of reference ($\bar{u}_x = \bar{u}, \bar{u}_r = \bar{u}_\theta = 0$), uniformly distributed mean density and speed of sound as well as in the absence of a fluctuating heat release source, the LEE reduce to

$$-k^2\hat{p} + \mathrm{i}2kMc\frac{\partial \hat{p}}{\partial x} + M^2\frac{\partial \hat{p}}{\partial x} = \frac{\partial^2 \hat{p}}{\partial r^2} + \frac{1}{r}\frac{\partial \hat{p}}{\partial r} + \frac{1}{r^2}\frac{\partial^2 \hat{p}}{\partial \theta^2} + \frac{\partial^2 \hat{p}}{\partial x^2}. \tag{2.38}$$

Eq. (2.38) is referred to as Helmholtz equation. In Eq. (2.38), k denotes the wave number given by

$$k = \frac{\omega}{c}, \tag{2.39}$$

and M the Mach number, viz.

$$M = \frac{\bar{u}}{c}. \tag{2.40}$$

The general solution of Eq. (2.38) reads

$$\hat{p}\,(x, r, \theta) = \sum_{m=0}^{\infty}\sum_{n=0}^{\infty} \hat{p}_{mn}\,(x, r, \theta) = \sum_{m=0}^{\infty}\sum_{n=0}^{\infty} P_{mn}\,(x)\,R_{mn}\,(r)\,\Theta_{mn}\,(\theta)\,, \tag{2.41}$$

and states the multiplication of the ansatz functions in axial, radial and circumferential direction. Furthermore, m denotes the transversal order and n the radial order. Higher-order acoustic modes are defined by $m > 0$ and/or $n > 0$.

Eq. (2.41) shows that the acoustic fluctuations are composed of an infinite number of different modes, which are subcategorized into the mn-th class. For instance, the class of the first transverse mode, generally denoted with $\mathrm{T_1L}_x$, is given by the pressure field $\hat{p}_{10}$ and is influenced by the x-th longitudinal structure. However, this does not implicate that the $\mathrm{T_1L_0}$ mode amplitude is independent of axial direction. In fact, both the mean flow and the boundary conditions influence the axial distribution of $\hat{p}_{10}$ (Schmid 2014).

The axial pressure ansatz function is given by (Ehrenfried 2003; Kathan 2013)

$$P_{mn}\left(x\right) = \bar{\rho}c\left(\hat{F}_{mn}\mathrm{e}^{-\mathrm{i}k_{mn}^{\mathrm{x}+}(x-x_0)} + \hat{G}_{mn}\mathrm{e}^{-\mathrm{i}k_{mn}^{\mathrm{x}-}(x-x_0)}\right), \tag{2.42}$$

where $\bar{\rho}c = \mathcal{Z}$ denotes the characteristic (field) impedance of the medium and x_0 a reference position. The quantities $\hat{F}_{mn}$ and $\hat{G}_{mn}$ are referred to as the complex amplitudes of the waves propagating in positive and negative x-direction, respectively (Kathan 2013).

The axial wave numbers in Eq. (2.42) are defined by

$$k_{mn}^{\mathrm{x}\pm} = \frac{k}{1-M^2}\left(-M \pm \sqrt{1-\left(\frac{k_{mn}^{\mathrm{r}}}{k}\right)^2\left(1-M^2\right)}\right), \tag{2.43}$$

where the radial wave number is given by

$$k_{mn}^{\mathrm{r}} = \frac{s_{mn}}{R_{\mathrm{cc}}}. \tag{2.44}$$

In Eq. (2.44), s_{mn} denotes the n-th root of the m-th derivative Bessel function J_m (see App. B.1) and R_{cc} the radius of the combustion chamber.

The radial pressure distribution in cylindrical geometries with solid casing reads

$$R_{mn}\left(r\right) = \mathrm{J}_m\left(k_{mn}^{\mathrm{r}}r\right). \tag{2.45}$$

In azimuthal direction different forms are used. Each provides certain advantages in terms of interpretation. In general, the distribution can be given by

$$\Theta_m(\theta) = A_1 e^{\mathrm{i}m\theta} + B_1 e^{-\mathrm{i}m\theta}, \tag{2.46}$$

or alternatively by

$$\Theta_m(\theta) = A\cos(m\theta) + \mathrm{i}B\sin(m\theta), \tag{2.47}$$

with

$$A = A_1 + B_1 \quad \text{and} \quad B = A_1 - B_1, \tag{2.48}$$

where A_1, A_2, B_1, B_2 denote the amplitudes of circumferential pressure distribution. A third alternative is given if a standing transverse mode pattern is assumed. In this case the circumferential pressure distribution reads

$$\Theta_m(\theta) = \sin(m\theta + \delta_m), \tag{2.49}$$

where δ_m describes the difference between a pressure nodal line and the frame of reference.

According to Eq. (2.47) two solutions in azimuthal direction exist. However, due to circumferential periodicity, these solutions are shifted by $\pi/2$ and may differ in amplitude.

The velocity distributions $\hat{u}_i$ are related to pressure and read:

$$\hat{u}\left(x,r,\theta\right) = \sum_{m=0}^{\infty}\sum_{n=0}^{\infty}\hat{u}_{mn}\left(x,r,\theta\right) = \sum_{m=0}^{\infty}\sum_{n=0}^{\infty}U_{mn}\left(x\right)R_{mn}\left(r\right)\Theta_{mn}\left(\theta\right), \tag{2.50}$$

$$\hat{v}\left(x,r,\theta\right) = \sum_{m=0}^{\infty}\sum_{n=0}^{\infty}\hat{v}_{mn}\left(x,r,\theta\right) = \sum_{m=0}^{\infty}\sum_{n=0}^{\infty}V_{mn}\left(x\right)\frac{\mathrm{d}R_{mn}\left(r\right)}{\mathrm{d}r}\Theta_{mn}\left(\theta\right), \tag{2.51}$$

$$\hat{w}\left(x,r,\theta\right) = \sum_{m=0}^{\infty}\sum_{n=0}^{\infty}\hat{w}_{mn}\left(x,r,\theta\right) = \sum_{m=0}^{\infty}\sum_{n=0}^{\infty}W_{mn}\left(x\right)\frac{R_{mn}(r)}{r}\frac{\mathrm{d}\Theta_{mn}\left(\theta\right)}{\mathrm{d}\theta}, \tag{2.52}$$

with

$$U_{mn}\left(x\right) = \kappa_{mn}^{+}\hat{F}_{mn}\,\mathrm{e}^{-\mathrm{i}k_{mn}^{\mathrm{x}+}(x-x_0)} + \kappa_{mn}^{-}\hat{G}_{mn}\,\mathrm{e}^{-\mathrm{i}k_{mn}^{\mathrm{x}-}(x-x_0)}, \tag{2.53}$$

$$V_{mn}\left(x\right) = \mu_{mn}^{+}\hat{F}_{mn}\,\mathrm{e}^{-\mathrm{i}k_{mn}^{\mathrm{x}+}(x-x_0)} + \mu_{mn}^{-}\hat{G}_{mn}\,\mathrm{e}^{-\mathrm{i}k_{mn}^{\mathrm{x}-}(x-x_0)}, \tag{2.54}$$

$$W_{mn}\left(x\right) = \mu_{mn}^{+}\hat{F}_{mn}\,\mathrm{e}^{-\mathrm{i}k_{mn}^{\mathrm{x}+}(x-x_0)} + \mu_{mn}^{-}\hat{G}_{mn}\,\mathrm{e}^{-\mathrm{i}k_{mn}^{\mathrm{x}-}(x-x_0)}. \tag{2.55}$$

Furthermore, the axial ratio of wave numbers $\kappa_{mn}^{\pm}$ and the radial ratio of wave numbers $\mu_{mn}^{\pm}$ are given by

$$\kappa_{mn}^{\pm} = \frac{k_{mn}^{x\pm}}{k - Mk_{mn}^{x\pm}}, \tag{2.56}$$

$$\mu_{mn}^{\pm} = \frac{\pm\mathrm{i}}{k - Mk_{mn}^{x\pm}}. \tag{2.57}$$

2.5. Propagation and Evanescence of Higher-Order Modes

The propagation of higher-order modes in cylindrical confinements is restricted by the so-called cut-on condition. If the wavelength is larger than the confinement, the mode cannot freely propagate in space. This can be explained by the wave number according to Eq. (2.43). Essentially, the wave number becomes complex valued, if

$$\left(\frac{k_{mn}^{\mathrm{r}}}{k}\right)^2\left(1 - M^2\right) > 1. \tag{2.58}$$

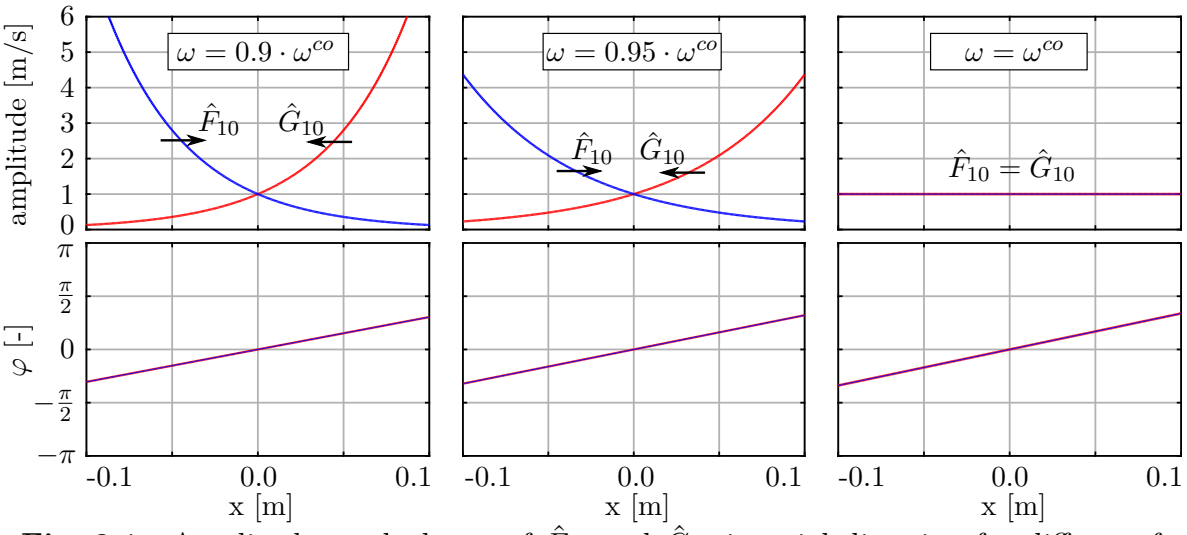

Fig. 2.1.: Amplitudes and phases of $\hat{F}_{10}$ and $\hat{G}_{10}$ in axial direction for different frequencies.

For complex valued wave numbers, the axial pressure distribution according to Eq. (2.42) depends on the exponential terms

$$e^{-\mathfrak{Im}(k^{x+})(x-x_0)} \text{ and } e^{-\mathfrak{Im}(k^{x-})(x-x_0)}, \tag{2.59}$$

which indicate an exponential decay of amplitudes in space. In consequence, unrestrictive propagation of an acoustic mode requires real-valued axial wave numbers $k_{mn}^{x\pm}$. In turn, a decay of amplitudes of a specific mode occurs if the mode frequency is below the cut-on frequency ω_{mn}^{co}

$$\omega < \omega_{mn}^{co} = \frac{c\, s_{mn}}{R_{cc}} \sqrt{1 - M^2}, \tag{2.60}$$

cf. Eq. (2.58).

The effect of the cut-on condition on the wave propagation is visualized in Fig. 2.1 for the first transverse mode, i.e. $mn = 10$. The plots show the amplitude and phase of the complex amplitudes $\hat{F}_{10}$ and $\hat{G}_{10}$ in axial direction for different frequencies. The reference location is $x_0 = 0$ m. Typical combustion chamber conditions in the burned gas region are applied, i.e. $\bar{\rho} = 4$ kg/m^3, $c = 1500$ m/s and $M = 0.225$. Furthermore, a chamber radius of $R_{cc} = 0.04$ m is assumed.

The axial decay of the $\hat{F}_{10}$ amplitude is given by the imaginary part of the wave number $\mathfrak{Im}(k^{x+})$. For a frequency below the cut-on frequency of $\omega = 0.9 \cdot \omega^{co}$, $\mathfrak{Im}(k^{x+})$ yields

$$\mathfrak{Im}(k^{x+}) \approx 20.6 \text{ 1/m}. \tag{2.61}$$

In consequence, the $\hat{F}_{10}$ amplitude reduces over a distance of 0.1 m, by

$$\left| \frac{\hat{F}_{10}(x = 0.1)}{\hat{F}_{10}(x = 0)} \right| \approx e^{-20.6 \cdot 0.1} \approx 0.127, \tag{2.62}$$

cf. Fig. 2.1 (left). Therefore, the amplitude reduces by almost 90 %.

If the frequency is only 5 % below the cut-on frequency, the reduction is still significant, cf. Fig. 2.1 (center). The amplitude reduces by almost 80 %. For a frequency equal to the cut-on frequency, $\mathfrak{Im}(k^{\mathrm{x}+})$ is zero and, in consequence, the amplitude of $\hat{F}_{10}$ does not decay. The same behavior holds true for the amplitudes of the Riemann invariant $\hat{G}_{10}$. The phase distributions of $\hat{F}_{10}$ and of $\hat{G}_{10}$ are similar for all frequencies considered. Therefore, the cut-off condition primarily leads to a reduction of the amplitudes only.

Higher-order modes which are cut-off are referred to as *evanescent* modes. In rocket combustion chambers, evanescent modes may occur due to the increase of temperature and hence of speed of sound in axial direction. For example, a transverse mode may be cut-on in the region of injection, where temperatures are still low, but cut-off in the region further downstream. The mode shape may then be dominated by a strong axial decay of amplitudes, cf. Fig. 2.1.

2.6. Fluctuating Energy and Intensity Flux

The fluctuating field energy is difficult to analyze due to its dependence on second order terms, which are neglected in the LEE. However, (Myers 1991) and (Brear et al. 2012) show that the disturbance energy density E can be derived on the basis of first order quantities and balanced with a disturbance intensity flux vector I_i across the boundaries as well as a source term $\mathcal{D}$:

$$\frac{\partial E}{\partial t} + \frac{\partial I_i}{\partial x_i} = \mathcal{D}. \tag{2.63}$$

The individual terms in Eq. (2.63) are given in first order quantities exclusively by

$$E = \frac{p'^2}{2\bar{\rho}c^2} + \frac{1}{2}\bar{\rho}u_i'^2 + \rho'\bar{u}_i u_i' + \frac{\bar{\rho}\bar{T}s'^2}{2c_p}, \tag{2.64}$$

$$I_i = p'u_i' + \bar{u}_i\frac{p'\rho'}{\bar{\rho}} + \bar{\rho}\bar{u}_j u_j' u_i' + \rho'\bar{u}_j u_j'\bar{u}_i + \bar{\rho}\bar{u}_i T's', \tag{2.65}$$

$$\mathcal{D} = \bar{\rho}\bar{u}_i\,\varepsilon_{ijk}\xi_j' u_k' + \rho' u_i'\,\varepsilon_{ijk}\bar{\xi}_j\bar{u}_k - s'(\bar{\rho}u_i' + \rho'\bar{u}_i)\frac{\partial\bar{T}}{\partial x_i} + s'\bar{\rho}\bar{u}_i\frac{\partial T'}{\partial x_i} + \frac{\dot{q}'T'}{\bar{T}} - \frac{\bar{\dot{q}}T'^2}{\bar{T}^2}, \tag{2.66}$$

where ξ_i is given by

$$\xi_i = \varepsilon_{ijk}\frac{\partial u_k}{\partial x_j}. \tag{2.67}$$

and denotes the vorticity, i.e. the rotation of the velocity field.

The source term $\mathcal{D}$ describes both dissipation and amplification of the energy E. The first two terms in Eq. (2.66) describe the generation of disturbance energy due to the interaction of the mean flow field with fluctuating vorticity as well as due to the interplay of fluctuating velocity and density with the mean vorticity. These interaction

processes are often present in situations where acoustic fluctuations modulate shear layer instabilities (Föller and Polifke 2012; Gikadi et al. 2012, 2013; Schulze 2012). The third and fourth terms reflect the influence of entropy fluctuations and their interaction with gradients of mean temperature and fluctuating temperature as well as with velocity and density disturbances. The last two terms represent the effect of mean heat release and fluctuating heat release on the disturbance energy and are therefore of major interest for thermoacoustic considerations. Especially the fifth term is directly related to the so-called *Rayleigh criterion*, which indicates the potential of the feedback system to amplify disturbance energy, see Sec. 2.8.

For a quiescent and isothermal flow, the source term $\mathcal{D}$ vanishes. Consequently, for the generation of a source term, a mean flow with heat release needs to be present.

It is convenient to consider only the energy balance of the acoustic fluctuations. The set of equations (2.63)-(2.66) then reduces to

$$\frac{\partial E^a}{\partial t} + \frac{\partial I_i^a}{\partial x_i} = 0, \tag{2.68}$$

where the energy density and intensity flux are given in acoustic quantities exclusively:

$$E^a = \frac{p'^2}{2\bar{\rho}c^2} + \frac{1}{2}\bar{\rho}u_i'^a u_i'^a + \rho'\bar{u}_i u_i'^a, \tag{2.69}$$

$$I_i^a = p' u_i'^a + \bar{u}_i \frac{p'^2}{\bar{\rho}c^2} + \bar{\rho}\bar{u}_j u_j'^a u_i'^a + \frac{p'}{c^2}\bar{u}_j u_j'^a \bar{u}_i. \tag{2.70}$$

Eq. (2.68) - Eq. (2.70) show that for a homentropic, irrotational flow the change of acoustic energy density depends only on the flux of acoustic intensity across the boundaries.

Fluctuating energy considerations are most feasible for periodically averaged quantities. The average of the product of two harmonic quantities $\hat{\phi}_1$ and $\hat{\phi}_2$ (ϕ_1' and ϕ_2') reads (Pieringer et al. 2005)

$$< \hat{\phi}_1 \cdot \hat{\phi}_2 >= \frac{1}{T_s}\int_0^{T_s} \phi_1' \cdot \phi_2' \, dt = \frac{1}{2}\mathfrak{Re}\left(\hat{\phi}_1 \cdot \hat{\phi}_2^*\right), \tag{2.71}$$

where $\mathfrak{Re}$ denotes the real part, T_s the acoustic period and $(^*)$ complex conjugation. Eq. (2.71) can directly be applied to Eq. (2.69) and Eq. (2.70).

2.7. Boundary Conditions

Evaluating the particular solution of the LEE system of partial differential equations, analytically or numerically, requires the definition of adequate boundary conditions. In time domain initial conditions have to be imposed. Choosing adequate, physically motivated boundary descriptions is of substantial importance for meaningful stability assessments, since often additional damping, energy preserving time lags, which influence the frequency ω and the distribution of amplitudes, and possibly even amplifying effects are attributed to the boundary conditions.

Different types of boundary conditions are required with the frequency dependency being the most important source of numerical difficulties and inaccuracies. Furthermore, for time domain and frequency space simulations, respectively, different techniques in terms of boundary treatment need to be applied. In the following, the boundary conditions are presented in order of increasing complexity. The definitions are given in terms of complex amplitudes for reasons of simplicity. A technique for the application of the boundary conditions in time domain is presented in Sec. 3.3.2.

2.7.1. Slip Wall

Basically, the solid walls represent the only frequency independent boundaries, since viscous boundary layer effects are neglected in the LEE. This slip condition reads in frequency space

$$\hat{u}_i \, n_i = 0, \tag{2.72}$$

and restricts the acoustic velocity direction to be perpendicular to the wall normal vector n_i.

As neither mass nor energy is transported across the walls, zero gradient boundary conditions are applied for $\hat{\rho}$ and $\hat{p}$:

$$\frac{\partial \hat{\rho}}{\partial x_i} n_i = 0 \tag{2.73}$$

and

$$\frac{\partial \hat{p}}{\partial x_i} n_i = 0. \tag{2.74}$$

Applying Eq. (2.72)-(2.74) to the LEE (2.30)-(2.32) allows to determine a unique solution at the corresponding wall boundaries.

2.7.2. Reflection Coefficient, Admittance and Impedance

The remaining boundary conditions are described on the basis of a reflection coefficient R, which generally depends on complex frequency, viz.

$$R = R(\Omega) = R(\omega + \mathrm{i}\lambda), \tag{2.75}$$

The reflection coefficient according to Eq. (2.75) relates reflected and incident acoustic waves to each other in terms of amplitude and phase at the boundary and is therefore a complex-valued quantity. The reflection coefficient inherently contains absorption properties and time lags generated by the modeled acoustic component.

It was shown that the reflection coefficient may be determined by (Fiala 2010; Kathan 2013)

$$R^{\circ}_{mn} = \frac{\hat{F}_{mn}}{\hat{G}_{mn}}. \tag{2.76}$$

However, this representation is not sufficient for higher-order modes. In general, the reflection coefficient is given by the ratio of the Riemann invariants $\hat{\mathcal{F}}_{mn}$ and $\hat{\mathcal{G}}_{mn}$, which describe the waves propagating in positive and negative x-direction. In contrast to the complex amplitudes used in Eq. (2.42), the Riemann invariants take the non-parallel alignment of the boundary surface and the wave front into account. In terms of acoustic pressure and velocity, $\hat{\mathcal{F}}_{mn}$ and $\hat{\mathcal{G}}_{mn}$ are given for longitudinal modes in (Polifke et al. 1997). For higher-order modes, the Riemann invariants can be written as

$$\hat{\mathcal{F}}_{mn} = \frac{\hat{p}_{mn}}{\bar{\rho}c} - \hat{u}_{i,mn} n_i, \tag{2.77}$$

$$\hat{\mathcal{G}}_{mn} = \frac{\hat{p}_{mn}}{\bar{\rho}c} + \hat{u}_{i,mn} n_i. \tag{2.78}$$

Based on the Riemann invariants, the reflection coefficient reads

$$R_{mn} = \frac{\hat{\mathcal{F}}_{mn}}{\hat{\mathcal{G}}_{mn}} = \frac{\hat{p}_{mn} - \bar{\rho}c\, \hat{u}_{i,mn} n_i}{\hat{p}_{mn} + \bar{\rho}c\, \hat{u}_{i,mn} n_i}. \tag{2.79}$$

Restricting the definition to the axial direction, i.e. $\hat{u}_i = \hat{u}_x$, evaluating conveniently at $x = x_0$ and inserting Eq. (2.41) and Eq. (2.53)-(2.55), yields for an inlet ($n_i = n = -1$)

$$R_{mn} = \frac{\hat{F}_{mn} + \hat{G}_{mn} + (\kappa^+_{mn}\hat{F}_{mn} + \kappa^-_{mn}\hat{G}_{mn})}{\hat{F}_{mn} + \hat{G}_{mn} - (\kappa^+_{mn}\hat{F}_{mn} + \kappa^-_{mn}\hat{G}_{mn})}. \tag{2.80}$$

For a longitudinal mode, i.e. $mn = 00$, it holds that $\kappa^+_{00} = 1$ and $\kappa^-_{00} = -1$. In this case, Eq. (2.80) yields

$$R_{00} = \frac{\hat{F}_{00}}{\hat{G}_{00}}, \tag{2.81}$$

which is equal to Eq. (2.76). Furthermore, for longitudinal modes holds that

$$\hat{F}_{00} = \hat{\mathcal{F}}_{00}, \tag{2.82}$$

$$\hat{G}_{00} = \hat{\mathcal{G}}_{00}. \tag{2.83}$$

For higher-order modes, e.g. $mn = 10$, Eq. (2.80) implies that

$$R_{10} = \frac{(1 + \kappa^+_{10})R^\circ_{10} + (1 + \kappa^-_{10})}{(1 - \kappa^+_{10})R^\circ_{10} + (1 - \kappa^-_{10})}, \tag{2.84}$$

and for an outlet

$$R_{10} = \frac{(1 - \kappa^-_{10})R^\circ_{10} + (1 - \kappa^+_{10})}{(1 + \kappa^-_{10})R^\circ_{10} + (1 + \kappa^+_{10})}. \tag{2.85}$$

However, according to Eq. (2.76), the reflection coefficient would read

$$R_{10}^{\circ} = \frac{\hat{F}_{10}}{\hat{G}_{10}}. \tag{2.86}$$

Ultimately, this is not the same as Eq. (2.85), since

$$\hat{F}_{10} \neq \hat{\mathcal{F}}_{10}, \tag{2.87}$$

$$\hat{G}_{10} \neq \hat{\mathcal{G}}_{10}. \tag{2.88}$$

In consequence, for the usage of the reflection coefficient as boundary condition as well as for its determination in experimental or numerical studies, it is necessary to apply Eq. (2.79) instead of Eq. (2.76) for higher-order modes.

Instead of a reflection coefficient, acoustic boundary characteristics may be described in terms of the acoustic impedance Z reading in non-dimensional form

$$Z_{mn} = \frac{\hat{p}_{mn}}{\hat{u}_{i,mn} n_i} \frac{1}{\bar{\rho} c}, \tag{2.89}$$

or by the admittance, which is given by $Y = Z^{-1}$, i.e.

$$Y_{mn} = \frac{\hat{u}_{i,mn} n_i}{\hat{p}_{mn}} \bar{\rho} c. \tag{2.90}$$

Both impedance and admittance can be defined on the basis of Riemann invariants, see App. B.2.1. Furthermore, R_{mn}, Y_{mn} and Z_{mn} can be converted into each other, see App. B.2.2.

2.7.3. Nozzle

It might appear consequentially to model the nozzle acoustics in form of a reflection coefficient. For reasons however discussed in Sec. 4.1.5, the nozzle volume is included into the computational LEE domain.

The LEE allow to account for a representative mean nozzle flow. In the divergent part of the nozzle, supersonic flow conditions prevent acoustic fluctuation from propagating back upstream, establishing natural non-reflectivity. For a well-defined supersonic flow to be present, a sufficient axial extend of the supersonic nozzle part is incorporated. Since the outlet boundary condition does not influence the acoustic propagation inside the combustion chamber, its description is somewhat arbitrary. However, the optimal solution procedure could be achieved if non-reflectivity is applied. Consequently, the reflection coefficient is set to zero at the outlet of the nozzle, i.e. $R_{mn} = 0$, see also Sec. 2.7.6.2.

2.7.4. Absorbers

Accounting for absorber cavities such as shown in Fig. 1.1 in terms of reflection coefficients in the acoustic simulations is complicated due to two reasons:

1. In comparison to the geometric scale of the chamber, cavity inlet sections are rather small, potentially leading to excessively refined computational grids in these regions.

However, the cavity diameter is small compared to the acoustic wavelength in the chamber. The compactness of the cavity is used to keep the minimal resolution necessary in a reasonable limit. The absorber reflection coefficient is not imposed on the cavity mouth in accordance with the true geometrical arrangement, but it is mapped onto the corresponding cylindrical shell surface and an equivalent coefficient R_{AR} is defined accordingly. This procedure is explained in more detail for a specific test configuration in Sec. 4.3.2.2.

2. Depending on the geometrical arrangement, absorber cavities are potentially subjected to grazing flow. In this situation, acoustic fluctuations at the cavity mouth interact with the emerging shear layer leading to the generation of vorticity, which in turn may scatter energy back into the acoustic modes establishing a feedback loop. Due to the absence of non-linear saturation terms limiting the growth of these *hydrodynamic instabilities*, the acoustic fields predicted by the LEE might be rapidly overlaid by unphysical contributions, which drastically reduce the correctness and usability of the results.

As discussed in (Morgenweck 2013), an efficient stabilization can be achieved through the implementation of spatial low-pass filter techniques when time domain simulations are performed. In frequency space in turn the unbounded temporal growth of hydrodynamic instabilities is naturally prevented. (Gikadi et al. 2013; Schulze et al. 2013a; Zahn et al. 2015) show the great potential of frequency space transformed LEE for the description of the interaction of acoustic fluctuations with a free shear layer flow. In (Gikadi et al. 2014), a T-junction configuration was characterized using the frequency space transformed LEE and good agreement with experimental findings in terms of reflection and transmission of acoustic waves was found.

The shear layer across the absorber cavity mouth is not resolved in the simulations. However, as pointed out in (Myers 1980), incident waves are partially reflected at the shear layer and are therefore not completely subjected to attenuation by the absorbers. Furthermore, transmission through the shear layer is accompanied by refraction effects altering the velocity component relevant for the interaction with the absorber and the boundary condition, respectively. To account for these scattering effects, (Myers 1980) suggested a modified impedance boundary condition:

$$n_i \hat{u}_i \bar{\rho} c = \frac{\bar{p}}{Z} + \frac{\bar{u}_i}{\mathrm{i}\Omega} \frac{\partial}{\partial x_i} \left(\frac{\hat{p}}{Z} \right) - \frac{1}{\mathrm{i}\Omega} \frac{\hat{p}}{Z} n_i \left(n_j \frac{\partial \bar{u}_i}{\partial x_j} \right). \tag{2.91}$$

The modified condition includes the classical impedance definition (first term on the r.h.s), but furthermore accounts for effects of convection (second term) and streamline curvature (third term). As shown in (Morgenweck 2013), the Myers boundary condition relates the normal acoustic velocity component in the mean flow, with the corresponding normal velocity directly at the boundary, while acoustic pressure is not affected.

Two test configurations for longitudinal and transverse modes with absorbers under grazing flow conditions will be investigated and used to validate the LEE in Sec. 4.3.

2.7.5. Dome Coupling

In order to include the dynamics of the feed and injection system into the computation, unfeasible fine grid resolutions would be needed to solve the acoustic propagation within each small injectors, cf. Fig. 1.1. It might appear obvious to model the feed and injection system as reflection coefficient, which could be imposed directly at the interface between combustion chamber and face plate. However, the three-dimensional acoustic field in the oxidizer dome provides wave propagation across the injectors violating the requirement of *local reactivity* for classical boundary conditions. To circumvent this issue, a different approach is chosen in this thesis.

First, the complex acoustic coupling behavior between combustion chamber and oxidizer dome is illustrated for a simplified face plate configuration in Fig. 2.2. Ignition tube elements possibly located in the center of the face plate are not shown and the dome is assumed to be of cylindrical shape. For illustrative purposes, the acoustic propagation path of only incident wave initiated at an arbitrarily chosen injector on the combustion chamber side is considered.

The three-dimensional acoustic field in the combustion chamber initiates longitudinal wave propagation inside the injector domain, locally affecting pressure and velocity on the dome side. Higher-order modes, denoted by $\hat{\mathcal{F}}^u_{mn}$ and $\hat{\mathcal{G}}^u_{mn}$, provide a cross transfer of acoustic energy to the other injectors, which in turn feed energy back into the combustion chamber. Incident and reflected waves are therefore no longer locally related.

The reflection and transmission properties of the dome coupling depend on the area ratios between combustion chamber and the injectors as well as oxidizer dome and the injectors, respectively. Small injector diameters and a low number of injection elements reduce the intensity of the coupling. Furthermore, the injector interior itself consists of area changes, which provide further scattering of acoustic waves. As shown in Fig. 2.2, the incident wave already gets reflected at the pressure loss element, which consists of an orifice configuration and is conventionally mounted into the injector at the dome side. The scattering properties of a typical pressure loss element will be analyzed in more detail in Sec. 7.2.

Besides geometrical effects, the influence of the oxidizer mean flow in the injectors has to be taken into account. Due to the area changes and accompanied streamline curvatures as well as shear layer effects, especially in the region of the pressure loss element, reductions of 15-25 % of the mean chamber pressure are realized across the face plate to avoid the propagation of acoustic waves into the dome.

To include the dome coupling into the acoustic simulations without resolving each single injector, a combined approach is applied, consisting of a low-order model of the face plate and the incorporation of the oxidizer volume into the CAA. The frequency dependent scattering properties of the face plate are lumped into a scattering matrix relating the acoustic pressure and velocity on dome and chamber side to each other. Using the representation in form of reflection $R_{u/d}$ and transmission coefficients $T_{u/d}$,

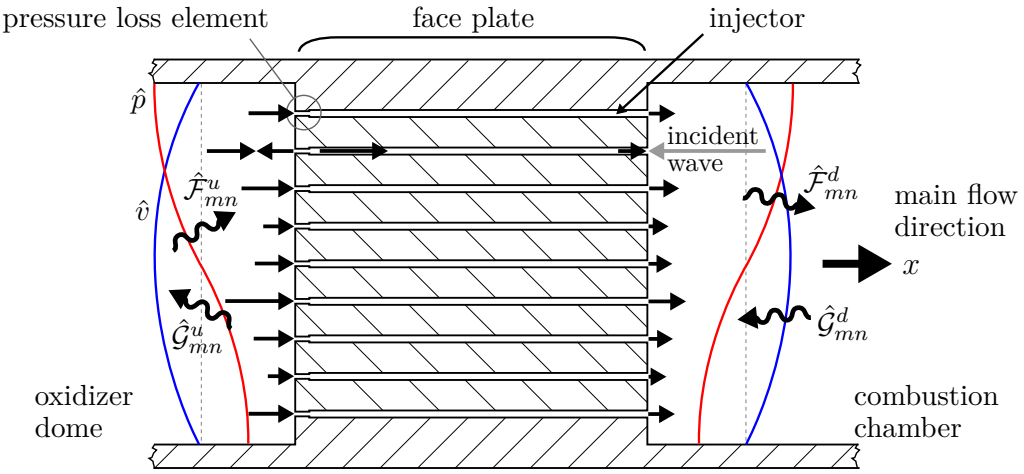

Fig. 2.2.: Illustration of dome coupling with complex acoustic scattering processes involved.

the scattering matrix SM reads

$$\begin{pmatrix} \hat{\mathcal{F}}_{d,mn} \\ \hat{\mathcal{G}}_{u,mn} \end{pmatrix} = \underbrace{\begin{pmatrix} T_u(\Omega) & R_d(\Omega) \\ R_u(\Omega) & T_d(\Omega) \end{pmatrix}}_{\mathrm{SM}(\Omega)} \begin{pmatrix} \hat{\mathcal{F}}_{u,mn} \\ \hat{\mathcal{G}}_{d,mn} \end{pmatrix}, \tag{2.92}$$

where $()_u$ denotes the upstream dome side and $()_d$ the downstream chamber side.

In the CAA code the scattering matrix is used to realize a one-dimensional point-to-point coupling in axial direction between the boundary at the dome side and the boundary at the chamber side in terms of amplitude and phase differences, see Fig. 2.3. The detailed injector contours on the boundaries are not resolved, but the entire surface is assumed to be acoustically active[2]. The corresponding area changes between the injector tubes and the chamber and dome, respectively, are directly mapped into the scattering matrix in order to account for the solid wall regions at the face plate.

The application of a point-to-point relation of acoustic quantities is only justified as long as the wave propagation inside the injectors is longitudinal. Considering the small diameter of the injector tubes and the high cut-on frequencies of higher-order modes, see Eq. (2.60), acoustics are effectively one-dimensional for a sufficiently wide frequency range containing relevant higher-order mode propagation only in the chamber and the dome, respectively.

A more stringent restriction for the validity of the scattering matrix approach is given by the fact that the radial wavelength of the chamber mode and dome mode, respectively, needs to be sufficiently large in comparison to the injector diameter. If this is fulfilled, the distributions of acoustic pressure and axial velocity in the immediate vicinity of the injector are constant. Otherwise, detailed profiles of pressure and velocity

[2] In this context, *active* does not mean an introduction of additional energy, as it is the case for active acoustic elements.

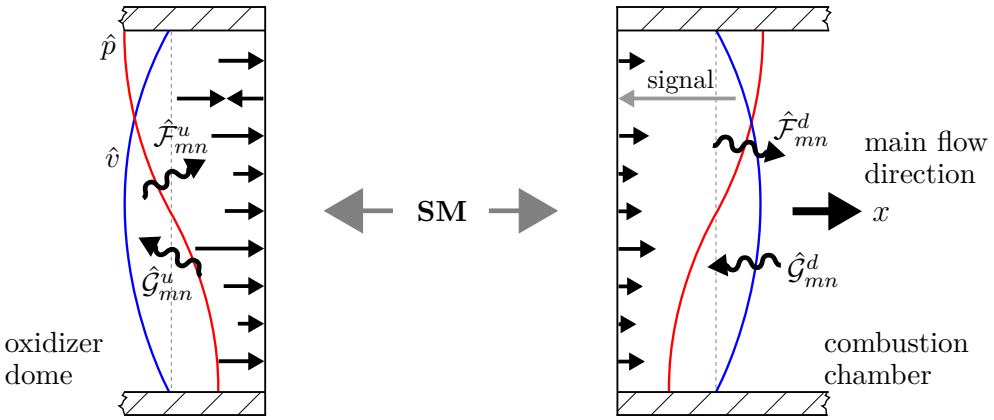

Fig. 2.3.: Illustration of the scattering matrix (SM) approach.

across a single injector inlet and outlet area would be required during the characterization process of the reflection and transmission coefficients. Such profiles are, however, not unique and the scattering matrix would become dependent on injector location making this approach inefficient and probably inaccurate. Furthermore, as long as the injector inlets and outlets are acoustically compact, the scattering matrix does not depend on the chamber mode and dome mode, respectively, but only on frequency. The independence of the SM on the mode shape will be shown in Sec. 4.2.1.

In Fig. 2.2, pressure $\hat{p}$ (red) and velocity $\hat{v}$ (blue) center line profiles of the first transverse mode are depicted. It can be seen that the injector tube diameter is reasonably compact in comparison to the T_1 wavelength and that the changes of $\hat{p}$ and $\hat{v}$ in vertical direction are sufficiently small across a single injector section. Furthermore, realistic engines are equipped with an even higher number of injectors than sketched in Fig. 2.2, justifying the validity of the acoustic compactness assumption further, cf. Fig. 1.1. In this situation, the scattering matrix approach becomes more and more beneficial while injector resolving methods become grossly ineffective.

Inherently, the scattering matrix approach assumes that all injectors are equal in terms of geometrical configuration and fluid dynamical behavior. In consequence, the mass flow of oxidizer and therefore pressure drop are the same for all injectors. Furthermore, it is assumed that heat transfer to or from the environment equally affects the oxidizer temperature in the injectors. In typical rocket engines, the splitter plate within the oxidizer dome ensures a homogeneous distribution of propellant across the injectors (Sutton and Biblarz 2001), which reasonably justifies the assumption, cf. Fig. 1.1. Equivalent acoustic scattering properties of each injector induce locally equal amplitude and phase ratios of $\hat{\mathcal{F}}^{u/d}_{mn}$ and $\hat{\mathcal{G}}^{u/d}_{mn}$ between dome side and chamber side at each surface location.

For the characterization of coefficients for reflection $R_{u/d}$ and transmission $T_{u/d}$, experimental, numerical and analytical methods are applicable. Experimental procedures allow for the direct determination of the coefficients for the entire face plate configu-

ration using e.g. the two-source location method (Åbom 1992; Åbom and H. Bodén 1988; Lung and Doige 1983; Munjal and Doige 1990; Paschereit et al. 2002). Numerical methods in turn are most efficient when evaluated on the basis of single injector configurations. As explained before, the consideration of only one injector is justified by its acoustic compactness with respect to the chamber mode and dome mode. Following the reasoning of homogeneously distributed pressure and velocity in the vicinity of the injector given before, adequate excitation routines can be derived. The frequency dependent acoustic fields can then be computed using URANS (Unsteady Reynolds Averaged Navier-Stokes Simulations) or LES methods applying broadband excitation (Föller et al. 2010).

To reduce computational efforts, LEE can be used for the determination of the scattering matrix elements. Several studies show that the unidirectional coupling between the steady state mean flow and the acoustic perturbation provided by the isentropic LEE approach accurately describes acoustically modulated shear layer mechanisms in case of isentropic, single species systems (Gikadi et al. 2012, 2014; Schulze 2012). The application of the LEE for rocket engine injectors requires their extension towards a real gas description, if non-isentropic variations are relevant. In this case, the isentropic relation between acoustic fluctuations of pressure and density according to Eq. (2.37) is no longer valid. In consequence, the energy equation takes a different form than shown in Eq. (2.32), since the ideal gas law cannot be applied, see also Sec. 6.2.2. In this thesis only isentropic variations are assumed within the dome and the injectors. The assumption is motivated by the fact that only small amplitudes are considered and that the temperature is approximately constant within the injectors and oxidizer dome.

Finally, the injector scattering matrix may be determined using a low-order, acoustic network model. Herein, the injector is decomposed into its components. Each of the components provide certain scattering properties. At the intersecting connections, the continuity of pressure and acoustic mass flow ensures consistency. Elementary scattering matrices are given analytically and depend only on geometric dimensions and mean flow conditions, which can be evaluated from experimental measurements or steady state CFD results. For the treatment of conventional injectors, area change elements with acoustic losses, straight duct elements and impedance change elements are used and assembled by multiplication into the injector scattering matrix, viz.

$$\mathrm{SM}(\Omega) = \prod_{k=1}^{J} \mathrm{SM}_{J-k}(\Omega), \tag{2.93}$$

where J denotes the total number of acoustic elements. The order of multiplication is not arbitrary but reflects the arrangement in the injector configuration. The analytical representation of the k-th element is shown in App. B.3. The network model of a typical rocket engine injector configuration is presented in Sec. 6.3.

2.7.6. Further Boundary Conditions

To study numerically single components of a rocket engine configuration, additional types of boundary conditions are required, which are introduced in this section.

2.7.6.1. Energetically Neutral Boundary with Flow

In order to investigate the impact of single components on the acoustic fields, it is often advantageous to set boundaries energetically neutral in terms of acoustic intensity flux, i.e. $I_i^a = 0$, cf. Eq. (2.70). Under the assumption that entropy fluctuations are zero at the boundary, i.e.

$$\hat{s} = 0, \tag{2.94}$$

algebraic manipulation of Eq. (2.70) reveals that the acoustic intensity flux consists of a fluctuating mass flow rate per unit area $\dot{m}_i'$ and a fluctuating stagnation enthalpy $\hat{h}_0$:

$$I_i^a = \underbrace{(\bar{\rho}\hat{u}_i^a + \hat{\rho}^a \bar{u}_i)}_{\dot{m}_i'} \underbrace{\left(\frac{\hat{p}}{\bar{\rho}} + \bar{u}_j \hat{u}_j^a\right)}_{\hat{h}_0}. \tag{2.95}$$

Eq. (2.95) shows that a zero acoustic intensity flux requires vanishing fluctuating mass flow rate or fluctuating stagnation enthalpy. Setting $\dot{m}_i'$ to zero yields

$$(\bar{\rho}\hat{u}_i^a + \hat{\rho}^a \bar{u}_i)\, n_i = 0. \tag{2.96}$$

A zero mass flow condition can also be derived by the linearization of the continuity equation, see App. B.4.

Inserting Eq. (2.96) into Eq. (2.79) yields the representation of an energetically neutral boundary condition in terms of a reflection coefficient:

$$R_{mn} = \frac{1 - M}{1 + M}. \tag{2.97}$$

Eq. (2.97) shows that a vanishing mass flow condition is independent of the acoustic mode.

The application of energetically neutral conditions to the chamber inlet on the basis of the reflection coefficient can conveniently be used to decouple acoustically the combustion chamber from the feed and injection system. This procedure allows to evaluate the influence of the feed and injection system on eigenfrequencies and damping rates. The corresponding dome coupling scattering matrix yields:

$$\mathrm{SM} = \begin{pmatrix} 0 & \frac{1-M}{1+M} \\ 0 & 0 \end{pmatrix}, \tag{2.98}$$

and is independent of frequency.

2.7.6.2. Non-Reflective Boundary Condition

Non-reflective boundary conditions are advantageous for the determination of scattering matrices in experimental and numerical procedures. The system under consideration is then not influenced by reflected waves and can conveniently be analyzed. Although

not ultimately necessary, the determination of scattering matrices of acoustic elements is often based on anechoic conditions at inlet and outlet. Non-reflective conditions are given by

$$R_{mn} = 0, \tag{2.99}$$

and by

$$Y_{mn} = Z_{mn} = 1, \tag{2.100}$$

respectively. Non-reflecting conditions are energetically not neutral.

2.8. Dynamic Flame Modeling

For the simulation of the wave propagation inside the combustion chamber, the interaction of acoustic fluctuations with combustion needs to be described. As the combustion process is nonlinear, the interaction cannot directly be described by the LEE. Instead, a general fluctuating heat release source term $\dot{q}'$ is included into the energy Eq. (2.13) and $\hat{\dot{q}}$ in Eq. (2.32), respectively. In the following, the general modeling approach of this source term is presented.

As already explained in Sec. 1, the interplay of acoustic fluctuations in the chamber and combustion can be described in form of a feedback loop, see Fig. 2.4. Specifically, the dynamic heat release rate may act as driver of the acoustic amplitudes. However, the dynamic heat release rate itself is modulated by the influence of acoustic fluctuations and hence a self-sustained feedback cycle is established. In consequence, for the modeling of the dynamic heat release rate, $\dot{q}'$ needs to be formulated as a function of the acoustic fluctuations, which are in turn described by the LEE.

In general, the dynamic heat release rate is sensitive to fluctuations of density ρ', velocity u_i' and pressure p', see Fig. 2.4. The response of heat release to these acoustic fluctuations in terms of amplitude and phase is expressed in form of a frequency-dependent Flame Transfer Function, which is given in frequency space by

$$\hat{\dot{q}} = \mathrm{FTF}(\Omega, \hat{p}, \hat{\rho}, \hat{u}_i). \tag{2.101}$$

In the linear regime of small acoustic amplitudes, it is assumed that the FTF can be decomposed in terms of its dependency on each acoustic fluctuation and subsequently superimposed. Furthermore, it is assumed that the individual FTF relate linearly the acoustic fluctuation to the dynamic heat release rate. The dynamic heat release source term is hence given in non-dimensionalized form by

$$\frac{\hat{\dot{q}}}{\bar{\dot{q}}} = \mathrm{FTF}^{\rho}(\Omega)\,\frac{\hat{\rho}}{\bar{\rho}} + \mathrm{FTF}^{\mathrm{p}}(\Omega)\,\frac{\hat{p}}{\bar{p}} + \mathrm{FTF}^{\mathrm{v}}(\Omega)\,\frac{\hat{u}_i}{\bar{u}_i}. \tag{2.102}$$

According to Eq. (2.102), the heat release rate can generally be modulated by density, velocity and pressure fluctuations. However, it is assumed that only acoustic fluctuations lead to a modulation of heat release. As acoustic pressure and density are related

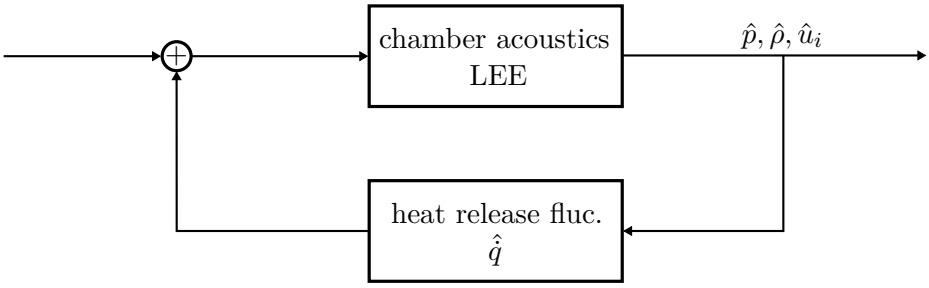

Fig. 2.4.: Interplay between wave propagation inside the chamber and dynamic heat releaser rate.

by the isentropic relation, cf. Eq. (2.37), their individual FTF can be combined into a single term. In consequence, the fluctuating heat release is modeled to be sensitive towards pressure and velocity modulation. Eq. (2.102) reduces hence to

$$\frac{\hat{\dot{q}}}{\bar{\dot{q}}} = \mathrm{FTF}^{\mathrm{p}}(\Omega)\,\frac{\hat{p}}{\bar{p}} + \mathrm{FTF}^{\mathrm{v}}(\Omega)\,\frac{\hat{u}_i}{\bar{u}_i}. \tag{2.103}$$

The decomposition allows for the characterization of each dependency individually. Nevertheless, a variety of feedback mechanisms may be attributed to each single FTF.

For the determination of the FTF, both experimental and numerical procedures could be used. However, the measurement of dynamic heat release under typical rocket engine chamber pressure and temperature conditions is extremely challenging. (Fiala 2015) suggests a radiation-based methodology. Its application requires a wide optical access to the chamber. Due to the extreme pressure and temperature conditions, sufficient optical access can usually not be provided. Hence, for the generation of the FTF, CFD simulations are conducted in this thesis. The applied methodology is explained in detail in Sec. 6.5.

For the occurrence of an energy transfer from the dynamic heat release into the feedback loop, the phase difference between the fluctuations of the dynamic heat release rate $\hat{\dot{q}}$ and pressure $\hat{p}$ is decisive. (Rayleigh 1896) shows that energy is fed into the feedback loop over one acoustic period if the Rayleigh integral Ra is larger than zero, i.e.

$$\mathrm{Ra} = \frac{1}{T_s}\int_0^{T_s}\int_V \dot{q}' \cdot p'\, dV dt > 0, \tag{2.104}$$

which is given in frequency space by

$$\mathrm{Ra} = \frac{1}{2}\mathfrak{Re}\int_V \hat{\dot{q}} \cdot \hat{p}^*\, dV > 0, \tag{2.105}$$

where V denotes the combustion chamber volume, see also Eq. (2.71). The necessary condition of $\mathrm{Ra} > 0$ is also referred to as Rayleigh *criterion*.

Rewriting Eq. (2.105) into amplitude - phase form yields

$$\mathrm{Ra} = \frac{1}{2}\mathfrak{Re}\int_V |\hat{\dot{q}}| \cdot |\hat{p}| \cdot e^{\mathrm{i}\left(\varphi_{\hat{\dot{q}}} - \varphi_{\hat{p}}\right)}\, dV = \frac{1}{2}\int_V |\hat{\dot{q}}| \cdot |\hat{p}| \cdot \cos\left(\varphi_{\hat{\dot{q}}} - \varphi_{\hat{p}}\right) dV > 0. \tag{2.106}$$

Eq. (2.106) shows that the integrand of the Rayleigh integral is positive if

$$\cos\left(\varphi_{\hat{\dot{q}}} - \varphi_{\hat{p}}\right) > 0 \tag{2.107}$$

and hence

$$|\varphi_{\hat{\dot{q}}} - \varphi_{\hat{p}}| < \frac{\pi}{2}. \tag{2.108}$$

In consequence, the energy contained in the feedback loop is increased over one acoustic period if the fluctuations of heat release and pressure are in phase. In contrast, if the Rayleigh integral is negative, heat release rate and pressure fluctuate out of phase and the combustion dynamics cannot amplify acoustic amplitudes. Instead energy is extracted from the feedback loop increasing the overall damping.

It is important to realize that the pressure coupling quantity in Eq. (2.103) is not necessarily the same as the pressure fluctuation in the Rayleigh integral according to Eq. (2.105). The $\mathrm{FTF^p}$ relates $\hat{p}$ to $\hat{\dot{q}}$ on the basis of a coupling mechanism. This mechanism might be influenced by convective transport, spatially separating the initiation at a position x_1, i.e. $\hat{p}(x_1)$, from the actual location of the heat release at x_2, i.e. $\hat{\dot{q}}(x_2)$. The $\mathrm{FTF^p}$ model for the heat release rate is then given by

$$\frac{\hat{\dot{q}}(x_2)}{\bar{\dot{q}}} = \mathrm{FTF^p}\frac{\hat{p}(x_1)}{\bar{p}}, \tag{2.109}$$

if it is assumed that only pressure fluctuation are relevant. In contrast, the Rayleigh integral relates dynamic heat release and pressure fluctuation locally, i.e.

$$\mathrm{Ra} = \frac{1}{2}\mathfrak{Re}\int_V \hat{\dot{q}}(x_2)\,\hat{p}^*(x_2)dV. \tag{2.110}$$

Inserting Eq. (2.109) into Eq. (2.110) yields

$$\mathrm{Ra} = \frac{1}{2}\mathfrak{Re}\int_V \mathrm{FTF^p}\hat{p}(x_1)\frac{\bar{\dot{q}}}{\bar{p}}\,\hat{p}^*(x_2)\,dV. \tag{2.111}$$

Eq. (2.111) indeed shows that the pressure fluctuation for the modeling of the dynamic heat release rate using a FTF and the pressure fluctuations for the calculation of the Rayleigh integral are not the same.

If the processes of the coupling mechanism occur in an acoustically compact region or if convective transport of perturbations is negligible, it can be assumed that $\hat{p}(x_1) = \hat{p}(x_2)$. In this case, the Rayleigh criterion for the coupling of heat release with pressure can be reformulated. In fact, since $\mathrm{FTF^p}$ then locally relates the dynamic heat release rate to the pressure fluctuation, energy is fed into the feedback loop if

$$|\varphi_{\mathrm{FTF^p}}| < \frac{\pi}{2}, \tag{2.112}$$

or alternatively if

$$\mathfrak{Re}(\mathrm{FTF^p}) > 0. \tag{2.113}$$

As the real part of the $\mathrm{FTF}^{\mathrm{p}}$ is crucial for the feedback in case of an acoustically compact coupling mechanism, it is referred to as *response factor* (RF), i.e.

$$\mathrm{RF} = \mathfrak{Re}(\mathrm{FTF}^{\mathrm{p}}). \tag{2.114}$$

The response factor can be used as a first indicator of the potential amplification of acoustic amplitudes by the flame.

Since the dynamic flame response may be the active driver for combustion instabilities, its comprehensive understanding, adequate modeling and accurate characterization is crucial for the realization of reliable stability assessment procedures. Sec. 6.5 and Sec. 7.5 are thus dedicated to present and discuss these aspects in more detail on the basis of a realistic test configuration.

3 Solution of LEE in Time Domain and Frequency Space

The LEE in time domain and frequency space describe the same physical processes. However, differences must be expected as soon as different numerical discretization schemes and resolutions in terms of space and time or frequency are applied. While in the time domain, the temporal evolution of the primary variables have to be calculated, in frequency space the acoustic field is either solved for a given complex frequency Ω or an eigenvalue problem is formulated in order to determine the eigenfrequency and corresponding mode shape.

Adequate solution techniques are very different leading to additional discrepancies in terms of numerical damping or amplification, respectively. This section summarizes and compares the solution procedures for time domain and frequency space indicating advantages and disadvantages of each methodology. Since the usage of LEE in frequency space is a new methodology in the field of rocket engine thermoacoustics its application is explained in detail within this thesis. Special focus is on the applicability of frequency dependent boundary conditions in time domain and frequency space.

3.1. Time Domain Solver PIANO

The time domain solver PIANO[3] used in this thesis solves the LEE (2.11)-(2.13) on the basis of a Dispersion Relation Preserving (DRP), 7-point stencil finite difference spatial discretization scheme (Delfs et al. 2008). The computational grid requires a block-structured topology. In the interior of each block, centered schemes are used. However, at the boundaries of the blocks as well as of the computational domain centered schemes are not applicable. Here, unsymmetrical stencils increase the dispersion leading to enhanced damping or amplification of unresolved wavelength. Explicit time integration is based on a standard Runge-Kutta procedure. Both discretization schemes in time and space provide 4th order accuracy (Delfs et al. 2008; Morgenweck 2013).

Spatially and temporally unresolved wavelengths may destabilize the solution process. Furthermore, the absence of non-linear saturation terms lead to the unlimited growth of hydrodynamic modes, which additionally obscure the acoustic fields. Effecti-

[3]PIANO is provided by the DLR Braunschweig, Prof. Delfs

ve stabilization can be achieved by spatially low-pass filtering the acoustic fields during the computation, e.g. on the basis of a Padé-filter design (Lele 1992). As shown in (Morgenweck 2013; Pieringer 2008), this type of filter introduces additional numerical damping due to its permanent influence for a high number of necessary time integration steps. Typically, numerical dissipation and physical damping are of the same order of magnitude, which reduces the accuracy of determined damping or amplification rates significantly. An improved stabilization procedure based on implicit filters was implemented into PIANO by (Morgenweck 2013).

Further information about the time solver PIANO and implemented extensions for thermoacoustic purposes can be found in (Delfs et al. 2008; Morgenweck 2013; Pieringer 2008).

3.2. Solution Technique in Frequency Space

Solving the LEE for the acoustic field in frequency space is fundamentally different from the time domain solution technique. Since time dependence is a priori assumed to be of harmonic character, the spatial distribution of the acoustic variables has to be solved exclusively.

3.2.1. Stabilized Finite Element Method

The frequency space transformed LEE are discretized on the basis of a stabilized Finite Element Method (SFEM), which was proven to be very effective for aeroacoustic (Gikadi et al. 2012; Schulze et al. 2013a; Ullrich et al. 2014; Zahn et al. 2015) and thermoacoustic problems (Gikadi 2014; Schulze and Sattelmayer 2015a). To briefly illustrate the basic principle, the governing Eq. (2.33) is first formulated in standard weak Galerkin form. Herein, Eq. (2.33) is multiplied by a weighting function $\underline{\mathcal{W}}$ for mass, momentum and energy equation individually, i.e.

$$\underline{\mathcal{W}} = (\mathcal{W}_\rho, \mathcal{W}_u, \mathcal{W}_v, \mathcal{W}_w, \mathcal{W}_p), \tag{3.1}$$

and integrated over the entire computational domain, which reads in compact matrix notation

$$\int_V \underline{\mathcal{W}} \left(\mathrm{i}\Omega \underline{\hat{\phi}} + \underline{\underline{A}} \frac{\partial \underline{\hat{\phi}}}{\partial x} + \underline{\underline{B}} \frac{\partial \underline{\hat{\phi}}}{\partial y} + \underline{\underline{C}} \frac{\partial \underline{\hat{\phi}}}{\partial z} + \underline{\underline{D}}\, \underline{\hat{\phi}} - \underline{\underline{Q}}\, \underline{\hat{\phi}} - \underline{\hat{\mathcal{S}}} \right) dV = \int_V \underline{\mathcal{W}}\, \underline{\underline{\mathcal{R}}}\, dV = 0. \tag{3.2}$$

Therefore, the FEM satisfies the equations in integral sense. The discretized system is obtained by replacing the continuous variables by their discrete approximations, viz.

$$\underline{\hat{\phi}} \rightarrow \underline{\hat{\phi}}^{\mathcal{H}}, \tag{3.3}$$

which are defined as sum of shape functions $N_{\mathcal{A}}$ and nodal values $\underline{\hat{\phi}}_{\mathcal{A}}$, viz.

$$\underline{\hat{\phi}}^{\mathcal{H}} = \sum_{\mathcal{A}=1}^{\mathrm{DOF}} N_{\mathcal{A}} \underline{\hat{\phi}}_{\mathcal{A}}, \tag{3.4}$$

and equivalently for the weighting functions

$$\underline{\mathcal{W}}^{h} = \sum_{\mathcal{B}=1}^{\mathrm{DOF}} N_{\mathcal{B}} \underline{\mathcal{W}}_{\mathcal{B}}, \tag{3.5}$$

where DOF denotes the degrees of freedom, which depends on the number of volume elements and boundary elements. In this thesis, Lagrange polynomials of order one are used as shape functions, viz.

$$N_{\mathcal{A}/\mathcal{B}} = L_1(x_i)_{\mathcal{A}/\mathcal{B}}. \tag{3.6}$$

The nodal values $\underline{\hat{\phi}}_{\mathcal{A}}$ state the results of the computation.

Solving the LEE in frequency space inherently describes the propagation of hydrodynamic modes. However, as time dependence is a priorly defined to be harmonic, see Eq. (2.26), the unbounded temporal growth of hydrodynamic modes is naturally prevented. Nevertheless, stabilization is still required to eliminate spurious oscillations in the solution due to unresolved scales and unlimited growth of hydrodynamic modes in space.

Essentially, unstable discretization schemes originate from the introduction of negative numerical diffusion, see (Donea and Huerta 2003) and the examples given therein. A necessary condition to guaranteed non oscillating solutions reads

$$\mathrm{Pe}^{E} < 1, \tag{3.7}$$

where Pe^{E} denotes the Péclet number based on the finite element size $\mathcal{H}$, viz.

$$\mathrm{Pe}^{E} = \frac{\bar{u}\mathcal{H}}{2\nu}. \tag{3.8}$$

The Péclet number shows that the stability criterion depends on the ratio between convection ($\bar{u}$) and diffusion (ν). If the effect of convection dominates the problem, numerical instability issues arise.

The absence of viscous dissipation in the LEE, i.e. $\nu = 0$, leads to

$$\mathrm{Pe}^{E} \to \infty, \tag{3.9}$$

indicating that advanced numerical schemes are absolutely necessary. The stabilization of the FEM formulation can be achieved in different ways. A comprehensive illustration is given in (Donea and Huerta 2003; Gikadi 2014).

Introducing viscosity on a physically motivated order of magnitude increases computational efforts for two reasons. On the one hand, the viscous term has to be incorporated into the governing equations leading to the linearized Navier-Stokes Equations

(LNSEs). On the other hand, to fulfill condition (3.7) requires additionally fine element dimensions leading to a significant increase of the number of degrees of freedom.

The compensation of negative diffusion by artificially increased viscosity is somewhat obvious. However, combustion stability prediction tools fundamentally depend on the accurate balance between physical amplification and damping. Artificially introduced viscosity tends to stabilize the thermoacoustic system. In consequence, stability reserves might be overrated leading to incorrect stability predictions.

Motivated by the fact that stabilization needs to be introduced only if convection is present, streamline upwind weighting functions were defined. Numerical dissipation is therefore incorporated only in streamline direction and not in transversal, which significantly reduces the overall added dissipation. Consistent stabilization is then achieved by introducing an extra term into the weak Galerkin form of the LEE, which is a function of the residuum. For an exact solution, defined by a residuum of zero, the influence of the stabilization term vanishes. In this thesis the so-called Galerkin/Least-squares (GLS) method is utilized for stabilization. It features additional stability advantages in contrast to the Streamline-Upwind/Petrov-Galerkin formulation (Donea and Huerta 2003).

The Galerkin/Least-squares method minimizes the residuum norm $||\underline{\underline{\mathcal{R}}}||_2$, viz.

$$\frac{\mathrm{d}}{\mathrm{d}\underline{\underline{\mathcal{R}}}} \int_V \underline{\underline{\mathcal{R}}}^2 \, dV = 2 \int_V \underline{\underline{\mathcal{R}}} \, \delta\underline{\underline{\mathcal{R}}} \, dV = 0 \tag{3.10}$$

Variations $\delta\underline{\underline{\mathcal{R}}}$ are given by $\underline{\underline{\mathcal{L}}}(\delta\underline{\hat{\phi}})$, which corresponds to $\underline{\underline{\mathcal{L}}}(\underline{\mathcal{W}})$ (Gikadi 2014).

The stabilized FEM form finally reads

$$\int_V \underline{\mathcal{W}}^{\mathcal{H}} \, \underline{\underline{\mathcal{L}}}(\underline{\hat{\phi}}^{\mathcal{H}}) \, \mathrm{d}V + \underbrace{\int_{V^{\mathcal{H}}|\partial V^{\mathcal{H}}} \underline{\underline{\tau}} \, \underline{\underline{\mathcal{L}}}(\underline{\hat{\phi}}^{\mathcal{H}}) \, \underline{\underline{\mathcal{L}}}(\underline{\mathcal{W}}^{\mathcal{H}}) \mathrm{d}V^{\mathcal{H}}}_{\text{GLS term}} = 0, \tag{3.11}$$

where the GLS term is symmetrical, which contributes to robust solution procedures (Hughes et al. 1989). The GLS term is evaluated element-wise and integrated only over its interior (i.e. over $V^{\mathcal{H}}|\partial V^{\mathcal{H}}$), since the modified weighting function is discontinuous along the element boundaries. To control the influence of GLS, a stabilization matrix $\underline{\underline{\tau}}$ is added, which plays a crucial role for robust and accurate stabilization. The stabilization matrix is of diagonal form imposing a scalar value to each individual equation. For simple one- and two-dimensional convection-diffusion problems, $\underline{\underline{\tau}}$ can be derived analytically yielding nodally exact results. However, for three-dimensional LEE problems, analytical definitions do not exist. Optimal stabilization parameters therefore have to be empirically optimized on the basis of existing definitions. For instance, (Hughes et al. 1989) derive an analytical expression for the stabilization parameter according to

$$\mathrm{diag}(\underline{\underline{\tau}}) = \alpha_{\tau,\phi} \frac{\mathcal{H}}{2||\bar{u}_i||_2} \underline{\underline{I}}, \tag{3.12}$$

where $\underline{\underline{I}}$ denotes the identity matrix and $\alpha_{\tau,\phi}$ a certain stabilization coefficient, which depends on the problem. It was shown that $\alpha_{\tau,\phi}$ might be varied over a wide range with

only minor influence on the results for aeroacoustic scattering problems involving shear layer interactions (Schulze 2012).

In (Beau et al. 1993; Rao and Morris 2006) a more advanced definition for the stabilization parameter is proposed. It is derived analytically and takes into account the three-dimensionality of the problem yielding

$$\underline{\underline{\tau}} = \max\left(\alpha_{\tau,\phi}\frac{\mathcal{H}_i}{\lambda_i}\right)\underline{\underline{I}}. \tag{3.13}$$

In Eq. (3.13) $\mathcal{H}_i$ states the finite element size in i-th direction and λ_i the spectral radius of the convection matrices $\underline{\underline{A}}$-$\underline{\underline{C}}$, see Sec. 2.3 and App. A. The spectral radius can be directly evaluated yielding an explicit formulation of the stabilization parameter (Ullrich and Sattelmayer 2015):

$$\underline{\underline{\tau}} = \alpha_{\tau,\phi}\max\left(\frac{\mathcal{H}_i}{|\bar{u}_i| + c}\right)\underline{\underline{I}}. \tag{3.14}$$

The acoustic simulations conducted in this thesis are based on definition (3.14).

The stabilization coefficient $\alpha_{\tau,\phi}$ can be chosen differently for each equation, which brings a certain flexibility. Nevertheless, $\alpha_{\tau,\phi}$ is restricted to be equal for all equations in this thesis, viz.

$$\alpha_{\tau,\phi} \rightarrow \alpha_\tau, \tag{3.15}$$

for reasons of simplicity.

Nevertheless, the stabilization coefficient α_τ remains a factor of uncertainty. Although lower limits can be found empirically (Gikadi 2014; Hughes et al. 1986), α_τ still needs to be calibrated for each problem. Inevitably, stabilization adds a certain (small) amount of numerical damping to the computation, which, as already discussed, might decisively influence the stability predictions. It is therefore essential to apply the best approximation for α_τ as possible.

In this thesis an optimal value of α_τ is determined on the basis of non-reactive rocket-engine-like configurations involving choked nozzle flow, transverse chamber modes and frequency dependent boundary conditions at the face plate and for absorbers under grazing flow situations. For non-reactive conditions, mode frequencies and damping rates can accurately be determined (Kathan 2013) and serve as a validation base. A sensitivity analysis is performed to show the influence of α_τ on the complex frequency Ω, i.e. on the damping rate λ and frequency ω. Furthermore, empirically determined rules for finding an optimal value are proposed. For reactive conditions, where damping measurements are considerably more difficult to perform, the optimized α_τ is used for stability predictions and further investigations. Furthermore, the adequateness of the chosen value of α_τ is again investigated.

3.2.2. Solution Procedures

On the basis of a SFEM discretization, different scenarios can be investigated. If the equations are solved for a given complex or real-valued frequency of excitation, its

spatial response can be analyzed in terms of density, velocity and pressure fluctuations. Such procedures are used to characterize the frequency response of acoustic elements, e.g. in form of reflection coefficients or scattering matrices, but are also applicable for the approximative determination of eigenfrequencies (Haimerl 2013). The approximative character stems from the fact that the excitation itself influences the system yielding potentially different eigenfrequencies and mode shapes. A consistent way to determine the true eigenfrequencies is to formulate and solve the equations in form of an eigenvalue problem. In the following, both scenarios are discussed in more detail.

3.2.2.1. Frequency Response

For a given frequency of excitation Ω the discretized system (3.11) can directly be integrated element-wise and assembled into a linear system of equations:

$$\begin{pmatrix} \underline{\underline{K}} & \underline{\underline{L}} \\ \underline{\underline{L}} & \underline{\underline{0}} \end{pmatrix} \begin{pmatrix} \underline{\hat{\phi}}_A \\ \underline{\Lambda} \end{pmatrix} = \begin{pmatrix} \underline{\hat{\mathcal{S}}}_A \\ \underline{h} \end{pmatrix}, \tag{3.16}$$

where $\underline{\underline{K}}$ denotes the so-called stiffness matrix, $\underline{\underline{L}}$ the boundary condition matrix, $\underline{\Lambda}$ a vector of Lagrange multipliers, $\underline{\hat{\mathcal{S}}}^h$ the nodal values of the load vector and $\underline{h}$ a vector, which lists the imposed constraints on the system. The boundary condition matrix $\underline{\underline{L}}$ and the vector $\underline{h}$ are used to impose directly the *essential* boundary constraints as known values of $\underline{\hat{\phi}}^{\mathcal{H}}$ at the Dirichlet boundary or linear combinations of different degrees of freedom. Essentially, reflection coefficients and scattering matrices are of the latter type stating a linear combination of velocity $\hat{u}_i^{\mathcal{H}}$ and pressure $\hat{p}^{\mathcal{H}}$. The Lagragian multiplier technique requires the boundary constraints to be fulfilled and provides therefore an elegant and flexible procedure of incorporating boundary conditions into the system (Donea and Huerta 2003). However, depending on the number of constraint relations to be imposed, the order of the system increases accordingly and higher computational efforts are necessary. Furthermore, the resulting matrix might lose its predominantly banded structure typically attributed to Finite Element discretization, which extends simulation times further. Nevertheless, frequency space solution procedures provide generally short turnaround times, which makes Lagrange multipliers affordable.

The linear system of equations (3.16) is solved for $(\underline{\hat{\phi}}_A, \underline{\Lambda})^T$ using either direct or iterative methods. After the solution is obtained, the Lagrange multipliers $\underline{\Lambda}$ are deleted, as they do not fullfill any further purpose. In this thesis only direct solution techniques are applied. For a comprehensive overview of iterative methods for the solution of the LEE it is referred to (Gikadi 2014) and the references therein.

Direct solvers for linear system of equations are widely explained and studied in literature (Schenk and Gärtner 2004). A detailed introduction is therefore not given in this thesis. For the solution of the LEE the direct solver MUMPS (MUltifrontal Massively Parallel sparse direct Solver) is used in the readily available simulation platform COMSOL. MUMPS is based on the Gaussian LU (lower-upper) factorization providing efficient solution procedure for huge sparse systems (Amestoy et al. 2001; Enseeiht 2015). Other algorithms, such as SPOOLES (Ashcraft 1999) and PARADISO (Schenk

and Gärtner 2004), were tested and found equally suitable for the problems dealt with in this thesis.

3.2.2.2. Eigenvalue Problem

The eigenvalue solution delivers both the complex eigenfrequencies as well as the eigenvectors, which correspond to the spatial distributions of the acoustic modes in terms of pressure, velocity and density. Therefore, it is not possible to formulate a linear system of equations according to (3.16), which can directly be solved. Instead, the system to be solved reads

$$\begin{pmatrix} \mathrm{i}\Omega\underline{\underline{I}} + \underline{\underline{E}} - \underline{\underline{Q}} & \underline{\underline{L}} \\ \underline{\underline{L}} & \underline{\underline{0}} \end{pmatrix} \begin{pmatrix} \underline{\hat{\phi}}_A \\ \underline{\Lambda} \end{pmatrix} = \begin{pmatrix} 0 \\ \underline{h} \end{pmatrix}, \tag{3.17}$$

where Ω is the eigenvalue and the feedback matrix $\underline{\underline{Q}}$ is explicitly shown. Convection matrices and reaction matrix are assembled into the matrix $\underline{\underline{E}}$. Furthermore, Lagrange multipliers are again used to impose boundary conditions. As explained before, external forcing is not present for eigenvalue studies and, consequently, volumetric source terms $\underline{\hat{\mathcal{S}}}_A$ are set to zero. The solution procedure finally reads:

$$\text{Find } \Omega \,\epsilon\, \mathbb{C} \text{ and } \underline{\hat{\phi}}_A \neq \underline{0} \text{ such that Eq. (3.17) is fullfilled.}$$

The process can, in principle, be conducted on the basis of the well-known QR-Algorithm (Demmel 1997) or Arnoldi procedure (Lehoucq et al. 1997). To generate meaningful results, such algorithms require that the matrices $\underline{\underline{E}}$, $\underline{\underline{Q}}$ and $\underline{\underline{L}}$ are independent of the eigenvalue, i.e. independent of the eigenfrequency. The matrix $\underline{\underline{E}}$ contains only mean flow values and is therefore uncritical. However, the frequency response of the modeled subcomponents such as absorbers or the dome coupling, represented by boundary conditions in $\underline{\underline{L}}$, as well as the Flame Transfer Function contained in $\underline{\underline{Q}}$, depend in fact non-linearly on Ω. According to (Nicoud et al. 2007), a suitable algorithm to directly account for such dependencies does not exist.

An iterative procedure to circumvent the deficiencies of the eigenvalue solution algorithm is proposed in (Nicoud et al. 2007; Schulze and Sattelmayer 2015a) and illustrated in Fig. 3.1. Starting with a guess of ω, which can e.g. be generated by evaluating the cut-on condition for higher-order acoustic modes, a solution is found iteratively. Herein, the frequency dependency of $\underline{\underline{L}}$ and $\underline{\underline{Q}}$ is eliminated in each eigenvalue solution by describing directly the last known frequency. The prescribed frequency is corrected in the subsequent eigenvalue solution step. This is repeated until the change of frequency is within a defined threshold and convergence is reached. The final solution reveals the complex frequency Ω and the corresponding mode shape $\underline{\hat{\phi}}_A$ for the considered problem, accounting for frequency dependent flame dynamics and boundary conditions of any kind. If several acoustic modes are of interest, the procedure has to be applied repeatedly. Unfortunately, due to significantly different mode structures, converged results for an acoustic mode cannot be used as initial solution for another mode. However, (Nicoud et al. 2007) and (Gikadi 2014) report that a low number of iterations is necessary to reach sufficient convergence for longitudinal modes.

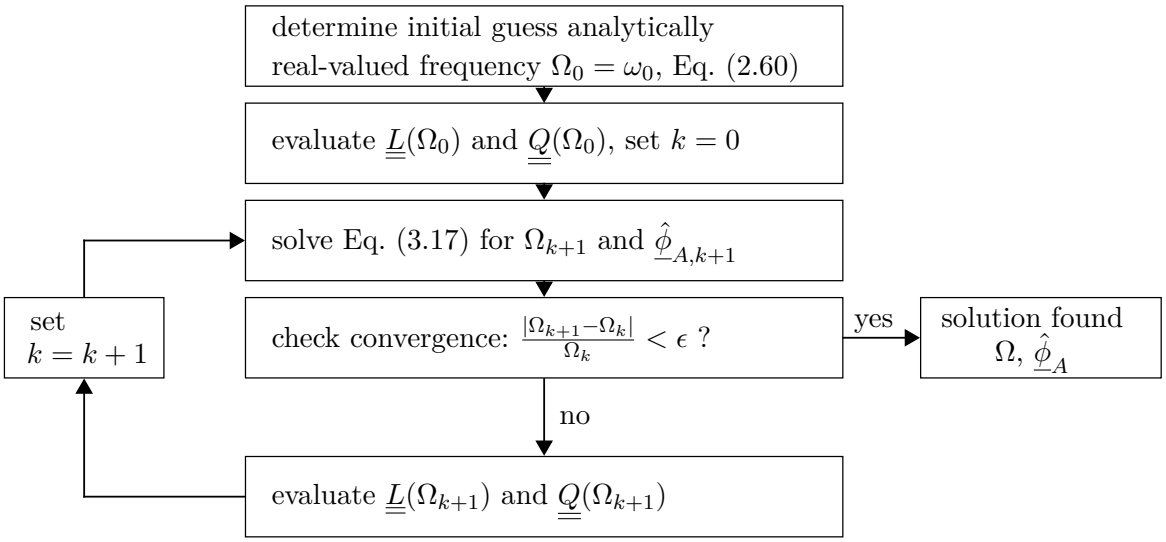

Fig. 3.1.: Procedure for the iterative determination of the eigenfrequency and the corresponding mode shape.

3.3. Frequency Dependent Boundary Conditions

The application of frequency dependent boundary conditions for rocket engine applications is not straight-forward, especially for higher-order modes. Conveniently, boundary conditions are usually given in terms of frequency ω, which already indicates that frequency space considerations provide certain advantages in terms of boundary modeling. This section discusses general modeling issues and introduces modeling strategies both in frequency space and time domain.

3.3.1. General Considerations and Application to Frequency Space

As comprehensively discussed in the previous section, boundary conditions generally depend on the complex frequency Ω. To perform the iterative procedure for frequency dependent boundary conditions and Flame Transfer Functions, the acoustic properties of each component must be available, i.e. $\underline{\underline{L}}(\Omega_k)$ has to be evaluable, see Fig. 3.1. In particular, it is necessary to provide a meaningful description of $\underline{\underline{L}}(\Omega_k)$ for each iterative step. If inadequate values are used for the k-th intermediate solution, the convergence process is prone to be slowed down or might even fail entirely. Furthermore, if different acoustic modes are analyzed, $\underline{\underline{L}}$ has to be provided for a wider range of frequencies and, as shown in Eq. (2.75), (2.89), (2.90), and (2.92), $\underline{\underline{L}}$ is then mode dependent.

Difficult circumstances arise: As a rule, reflection coefficients are characterized for frequencies ω employing experimental (Kathan 2013; Wagner et al. 2013a), numerical (Föller and Polifke 2010; Gikadi et al. 2012; Kierkegaard et al. 2010) or analytical methods (Bade 2014) and λ dependent characterizations are usually not available. While experimental procedures cannot be conducted for arbitrary damping rates, but only for the inherently present system damping, numerical and analytical methods allow

for the systematic characterization of an acoustic element for any pair of frequency ω and damping rate λ by solving e.g. Eq. (3.16) for Ω. However, theoretical procedures are not always applicable. Moreover, despite the immense progress, the state of the art CFD methods are not capable to simulate complicated geometries and complex physical processes with sufficient accuracy within reasonable turnaround times by all means. Experimental data is therefore still indispensable.

Experimentally determined reflection coefficients are usually only given in terms of ω. However, it can be shown that the knowledge of the reflection coefficient for frequencies ω is sufficient to evaluate its amplitude and phase at complex frequency Ω: For a given frequency response of an acoustic element, i.e. $R_{mn}(\omega)$, the impulse response $h(t)$ in time domain is calculated by applying the inverse Fourier-Transform ($\mathcal{F}^{-1}$) (Oppenheim et al. 1999):

$$r_{mn}(t) = \mathcal{F}^{-1}(R_{mn}(\omega)) = \frac{1}{2\pi}\int_0^\infty R_{mn}(\omega)e^{\mathrm{i}\omega t}d\omega. \tag{3.18}$$

For linear time-invariant (LTI) systems, the impulse response $r(t)$ is an equivalent representation of the acoustic properties of the acoustic element. Subsequently, the impulse response is Laplace transformed for complex frequencies Ω, viz.

$$R_{mn}(\Omega) = \int_0^\infty r_{mn}(t)e^{\mathrm{i}\Omega t}dt. \tag{3.19}$$

The two-folded transformation shows conclusively that the real-valued frequency dependence of $R_{mn}(\omega)$ contains the essential acoustic properties necessary for the application to damped and amplified systems, respectively. In fact, frequency ω and complex frequency Ω can simply be interchanged:

$$R_{mn}(\omega) \rightarrow R_{mn}(\Omega) \tag{3.20}$$

However, a direct evaluation of $R_{mn}(\Omega)$ is, strictly speaking, only allowed when the transformations (3.18), (3.19) are finite, which ultimately requires the knowledge of $R_{mn}(\omega)$ over the entire frequency range.

In practice, reflection coefficients are typically not available for the entire frequency range and only determinable for distinct frequencies. This is especially obvious for higher-order modes, which are present merely at and beyond their cut-on frequency, cf Eq. (2.60). For lower frequencies, information about scattering properties cannot be obtained. Therefore, methods are necessary allow for the determination of amplitude and phase of the reflection coefficients although only discrete frequency response data in a limited frequency range is available.

(Schmid 2014; Schmid et al. 2013a,b) reported that a certain circle of confidence can be established for a given data set of R on the basis of frequencies ω: Fig. 3.2 shows point-wise data of R (real part only) in the complex ω, λ-plane. This point-wise data can be obtained from experiments or numerical procedures. To make R continuously available for the covered real-valued frequency range and therefore feasible for Eq. (3.20), a polynomial fit of the order K^f with complex-valued coefficient c_k is generated,

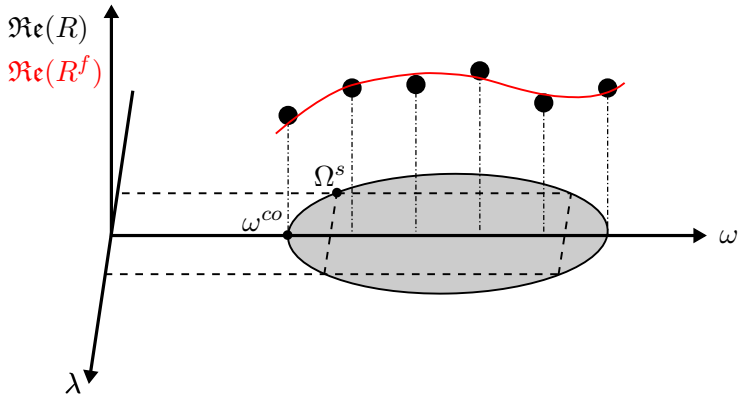

Fig. 3.2.: Point-wise data of R (real part) for frequencies ω and confidence circle in the ω, λ-plane, adapted from (Schmid 2014). Furthermore, a exemplary continuous fit is shown in red.

viz.

$$R^f(\mathrm{i}\omega) = \sum_{k=1}^{K^f} c_k(\omega)^k, \tag{3.21}$$

which is highlighted in Fig. 3.2 in red. The error of $R^f(\Omega)$, if evaluated at arbitrary complex frequency Ω within this circle, depends on the error introduced on the real-valued frequency axis (Schmid 2014). Consequently, the quality of the fit in (ω) influences the accuracy of $R^f(\Omega)$. The fit quality can be improved by increasing the density of given data points on the ω axis and a higher polynomial order.

Large polynomial orders tend by using to generate strong oscillations for frequencies outside of the circle of confidence. For simulations in frequency space, the behavior of $R^f(\Omega)$ in the exterior is irrelevant. However, in time domain simulations such oscillatory behavior may immensely alter the accuracy of the results.

For meaningful stability predictions, the circle of confidence for each modeled component and the Flame Transfer Function necessarily needs to cover the system's complex eigenfrequency Ω^s. A sufficient dimension of the circle is therefore crucial, which depends on the available data range of R in terms of ω.

For the determination of an adequate circle radius, indicative values for the eigenfrequency and damping rate are necessary. Based on the CPIA rules (Priem 1997), (Schmid 2014) determined typical values of λ for unstable rocket engine operation of

$$-500 \text{ rad/s} < \lambda < -200 \text{ rad/s} \tag{3.22}$$

at approximately 3000 Hz.

For frequencies close to the cut-on frequency, viz.

$$\omega \to \omega^{co}, \tag{3.23}$$

the confidence spread in λ direction significantly reduces, which requires a large circle radius to ensure accuracy. In fact, if the eigenfrequency coincides with the cut-on frequency, a singularity is present and the confidence spread is lost. The resulting inaccuracies can potentially be unacceptable large.

Under certain conditions, acceptable results can be expected for frequencies close to the cut-on frequency:

1. The system is dominated by higher-order modes at high frequency. Variations of R in terms of ω occur at a higher scale than for λ, i.e.

$$\omega >> \lambda \rightarrow R(\omega + \mathrm{i}\lambda) \approx R(\omega). \tag{3.24}$$

2. $R(\mathrm{i}\omega) \approx$ constant for a sufficient frequency range starting from the cut-on frequency. The change of R with respect to ω is then

$$\frac{\partial R}{\partial \omega} \approx 0, \tag{3.25}$$

and the Cauchy-Riemann operation (Schmid et al. 2013b) indicates that the change with respect to λ accordingly reads

$$\frac{\partial R}{\partial \mathrm{i}\lambda} = 0. \tag{3.26}$$

$R(\Omega)$ can then confidently be evaluated at the real-valued cut-on frequency, viz.

$$R(\Omega) = R(\omega^{co}), \tag{3.27}$$

as long as $|\lambda|$ is not too large.

3. If the derivatives cannot be set to zero, the Cauchy-Riemann operation enables the expansion of R in a Taylor-Series around the cut-on frequency both in ω and λ direction (Schmid et al. 2013b) and $R(\Omega)$ can be estimated:

$$\begin{aligned}\mathfrak{Re}\{R(\lambda,\omega)\} &= \mathfrak{Re}\{R(0,\omega)\} + \frac{\partial \mathfrak{Re}\{R(0,\omega)\}}{\partial(\mathrm{i}\lambda)}(\mathrm{i}\lambda) + \frac{\partial^2 \mathfrak{Re}\{R(0,\omega)\}}{2\partial(\mathrm{i}\lambda)^2}(\mathrm{i}\lambda)^2 + \mathcal{O}((\mathrm{i}\lambda)^3) \\ &= \mathfrak{Re}\{R(0,\omega)\} - \frac{\partial \mathfrak{Im}\{R(0,\omega)\}}{\partial \omega}(\mathrm{i}\lambda) + \frac{\partial^2 \mathfrak{Re}\{R(0,\omega)\}}{2\partial \omega^2}(\mathrm{i}\lambda)^2 + \mathcal{O}((\mathrm{i}\lambda)^3)\end{aligned} \tag{3.28}$$

4. The system oscillates at limit cycle, which is defined by

$$\lambda \rightarrow 0, \tag{3.29}$$

i.e. quasi steady state conditions are present, which again yields

$$R(\omega + \mathrm{i}\lambda) \approx R(\omega). \tag{3.30}$$

The conditions need to be equally valid for $\mathfrak{Re}(R)$ and $\mathfrak{Im}(R)$.

If none of the described conditions are valid, the determination of $R(\omega)$ needs to be performed on the basis of a modified configuration, which allows for the excitation of frequencies below the cut-on frequency of the original configuration. The circle can then be extended towards lower frequencies shifting Ω^s into the confidence region. According to the cut-on condition (2.60), a higher chamber radius, for example, is feasible. However, this technique is only applicable if the acoustic element under consideration can be assumed as acoustically compact, so that the modified mode shape due to the change of frequency and geometry alters the acoustic response only marginally. Absorbers are of this type due to their small diameter, see Fig. 1.1.

Finally, if the acoustic element depends on mode shape, it ultimately needs to be incorporated into the three-dimensional discretization to fully account for its dependency on the complex frequency. Thrust nozzles typically fall into that category. Its relevant acoustic length scale is obviously equivalent to the chamber radius. A complete discussion about the nozzle acoustics is given in Sec. 4.1.

The presented consideration are generally valid. The joint application of the iterative algorithm, see Fig. 3.1, Eq. (3.20) and (3.21) for the generation of boundary conditions and for Flame Transfer Functions at complex frequency Ω_k, together with a suitable assumption from (3.24)-(3.30), if necessary, forms a consistent boundary conditions treatment for frequency space simulations. For time domain computations, in contrast, additional modeling is necessary to provide efficient and stable procedures, which will be explained in the next section.

3.3.2. Digital Filters in Time Domain

For the usage of frequency dependent boundary conditions in time domain, a transformation of these into their time dependent representation is required. Such Time-Domain Impedance Boundary Conditions (TDIBC) are widely discussed in literature and different approaches are proposed. If an analytical description of the boundary condition is available, the inverse Fourier transformation is applied according to Eq. (3.18) to directly obtain the impulse response, (Richter et al. 2007). For absorbers a variety of models exist, which are applicable for a direct usage, see (Cárdenas 2014) and the references therein.

However, as discussed before other boundaries or the flame description are given at discrete frequencies for a limited range only. An approach to use this data in time domain was proposed in (Özyörük and Long 1996, 2000; Özyörük et al. 1998), extended and applied in (Huber and Polifke 2007; Kaess et al. 2008) for considerations of longitudinal wave propagation in gas turbines and adapted for the usage for three-dimensional acoustic fields in rocket engine configurations in (Morgenweck 2013). Furthermore, (Schmid 2014) proposes the application of the same approach for the description of flame models. The method is based on digital filters, which are commonly used in signal processing theory (Oppenheim et al. 1999; Proakis and Manolakis 1996).

Digital filters represent a class of transfer functions, which can conveniently be trans-

formed between frequency space and time domain, providing modeling flexibility for given frequency response functions. The transfer behavior to be captured is shaped into the form of an Infinite Impulse Response filter (IIR), which reads in discrete frequency space ($\omega \rightarrow z$)

$$H(z) = \frac{\sum\limits_{k=0}^{\mathrm{M}} b_k z^{-k}}{1 + \sum\limits_{k=1}^{\mathrm{N}} a_k z^{-k}}. \tag{3.31}$$

The rational structure of Eq. (3.31) allows to define different polynomial orders M and N. In general, $H(z)$ is interpreted as ratio between input and output signal.

Using the definition of the reflection coefficient according to Eq. (2.75), incoming and outgoing waves are related to each other through the IIR filter representation of R

$$\hat{\mathcal{F}}_{mn}(z) = \underbrace{\frac{\sum\limits_{k=0}^{\mathrm{M}} b_{k,R} z^{-k}}{1 + \sum\limits_{k=1}^{\mathrm{N}} a_{k,R} z^{-k}}}_{H(z)=R_{mn}(z)} \hat{\mathcal{G}}_{mn}(z), \tag{3.32}$$

where the filter coefficients $b_{k,R}$ and $a_{k,R}$ are calibrated such that the frequency response of R_{mn} is adequately reproduced. Applying the convolution theorem (Oppenheim et al. 1999; Proakis and Manolakis 1996) to Eq. (3.32) yields the corresponding transformation in discrete time domain ($t \rightarrow \mathrm{n}$)

$$\mathcal{F}'_{mn}[\mathrm{n}] = -\sum_{k=1}^{\mathrm{N}} a_{k,R}\, \mathcal{F}'_{mn}[\mathrm{n}-k] + \sum_{k=0}^{\mathrm{M}} b_{k,R}\, \mathcal{G}'_{mn}[\mathrm{n}-k], \tag{3.33}$$

where n denotes the discrete time step. The filter coefficients are conserved, which makes this transformation very feasible to apply. The polynomial order M, N in frequency space representation translates into time delayed responses in time domain. Higher-order polynomials therefore require a larger amount of stored data during the simulation for reference. Furthermore, the delayed responses are weighted by the filter coefficients $a_{k,R}$ and $b_{k,R}$.

The representation (3.33) can readily be incorporated in time domain simulations. Assuming that accurately determined data is provided for the filter generation, the correctness of the acoustic scattering depends on the chosen filter coefficients and on the adequateness of a rational structure for the representation of the respective acoustic transfer behavior. Therefore, the filter has to be carefully designed.

Instead of a reflection coefficient, the impedance or admittance can be used as well. However, (Rienstra 2006) and (Morgenweck 2013) report difficulties arising from possible violations of causality. Although causality can be achieved through further modification, (Morgenweck 2013) suggests to use a reflection coefficient.

As indicated in Eq. (3.32) and Eq. (3.33), the IIR filter relates the modified Riemann invariants mode-dependently. In consequence, for each acoustic mode a different IRR filter and hence a different set of filter coefficients must be defined.

The digital filter approach can be generalized. In fact, a Flame Transfer Function for pressure coupling in IIR filter representation reads

$$\dot{q}'[\mathrm{n}] = -\sum_{k=1}^{\mathrm{N}} a_{k,\mathrm{FTF}}\, \dot{q}'[\mathrm{n}-k] + \sum_{k=0}^{\mathrm{M}} b_{k,\mathrm{FTF}}\, p'[\mathrm{n}-k], \tag{3.34}$$

relating pressure perturbations to heat release rate fluctuations. The representation of displacement coupling is slightly more complicated since the acoustic displacement has to be calculated. The integration of velocity to obtain displacement is defined by an additional filter structure (Oppenheim et al. 1999):

$$H(z) = \frac{b_0}{1 - a_1 z^{-1}}. \tag{3.35}$$

Finally, each scattering matrix element for dome coupling, see Eq. (2.92), is given by an input-output relation. The incidenting waves $\hat{\mathcal{F}}^u$ and $\hat{\mathcal{G}}^d$ are reflected as well as transmitted and the outgoing waves $\hat{\mathcal{F}}^d$ and $\hat{\mathcal{G}}^u$ are formed, viz[4].

$$\hat{\mathcal{F}}^d = \frac{\sum_{k=0}^{\mathrm{M}_{T_u}} b_{k,T_u} z^{-k}}{1 + \sum_{k=1}^{\mathrm{N}_{T_u}} a_{k,T_u} z^{-k}} \hat{\mathcal{F}}^u + \frac{\sum_{k=0}^{\mathrm{M}_{R_d}} b_{k,R_d} z^{-k}}{1 + \sum_{k=1}^{\mathrm{N}_{R_d}} a_{k,R_d} z^{-k}} \hat{\mathcal{G}}^d, \tag{3.36}$$

$$\hat{\mathcal{G}}^u = \frac{\sum_{k=0}^{\mathrm{M}_{R_u}} b_{k,R_u} z^{-k}}{1 + \sum_{k=1}^{\mathrm{N}_{R_u}} a_{k,R_u} z^{-k}} \hat{\mathcal{F}}^u + \frac{\sum_{k=0}^{\mathrm{M}_{T_d}} b_{k,T_d} z^{-k}}{1 + \sum_{k=1}^{\mathrm{N}_{T_d}} a_{k,T_d} z^{-k}} \hat{\mathcal{G}}^d, \tag{3.37}$$

and in time domain

$$\mathcal{F}^{d\,\prime}[\mathrm{n}] = -\sum_{k=1}^{\mathrm{N}_{T_u}} a_{k,T_u} \mathcal{F}^{d\,\prime}[\mathrm{n}-k] + \sum_{k=0}^{\mathrm{M}_{T_u}} b_{k,T_u} \mathcal{F}^{u\,\prime}[\mathrm{n}-k] + \tag{3.38}$$

$$- \sum_{k=1}^{\mathrm{N}_{R_d}} a_{k,R_d} \mathcal{F}^{d\,\prime}[\mathrm{n}-k] + \sum_{k=0}^{\mathrm{M}_{R_d}} b_{k,R_d} \mathcal{G}^{d\,\prime}[\mathrm{n}-k], \tag{3.39}$$

$$\mathcal{G}^{u\,\prime}[\mathrm{n}] = -\sum_{k=1}^{\mathrm{N}_{R_u}} a_{k,R_u} \mathcal{G}^{u\,\prime}[\mathrm{n}-k] + \sum_{k=0}^{\mathrm{M}_{R_u}} b_{k,R_u} \mathcal{F}^{u\,\prime}[\mathrm{n}-k] + \tag{3.40}$$

$$- \sum_{k=1}^{\mathrm{N}_{T_d}} a_{k,T_d} \mathcal{G}^{u\,\prime}[\mathrm{n}-k] + \sum_{k=0}^{\mathrm{M}_{T_d}} b_{k,T_d} \mathcal{G}^{d\,\prime}[\mathrm{n}-k]. \tag{3.41}$$

Conclusively, for the modeling of the scattering matrix, the filter coefficients depend additionally on the individual element. Furthermore, the order of polynomials and the number of filter coefficients, respectively, can be chosen differently for each element.

[4]Note: for the sake of better readability the mode indicator $()_{mn}$ is omitted here. The filter coefficients for the scattering matrix elements are, in general, mode-dependent as well.

The complex filter structure for the dome coupling already indicates rather high preprocessing efforts.

The IIR filter employs past output and input values as well as the current input value to calculate the output at an instant of time. This leads to a low number of filter coefficients required to model the respective transfer behavior but stability issues may arise. In fact, for stable filter designs, poles may exist only within the unit circle of the complex z plane, which is a stringent requirement for robust computational routines.

By definition, excluding poles from the filter, i.e.

$$\hat{\mathcal{F}}_{mn}(z) = \sum_{k=0}^{\mathrm{M}} b_{k,R} z^{-k}\, \hat{\mathcal{G}}_{mn}(z), \tag{3.42}$$

provides an unconditional stable transfer behavior. The corresponding time domain representation reads

$$\mathcal{F}'_{mn}[n] = \sum_{k=0}^{\mathrm{M}} b_{k,R}\, \mathcal{G}'_{mn}[n-k]. \tag{3.43}$$

However, experience shows that Finite Impulse Response (FIR) filter structures require a higher number of coefficients to capture the transfer behavior to be modeled, compared to IIR filters. Consequently, increased memory is required during the simulations. Therefore, IIR filter structures are generally the preferred choice.

The set of filter coefficients are generated on the basis of an optimization procedure minimizing the error between the given frequency-wise data points and the filter values. For a scattering matrix the coefficients of each element are fitted individually. To sustain causality, amplitude and phase or real and imaginary part of the transfer function have to be fitted simultaneously, which complicates the determination of the coefficients substantially.

Between the fitting procedure employed in frequency space, see Eq. (3.21), and the generation of the filter coefficients for the usage in time domain, significantly different requirements arise influencing the flexibility and accuracy of the fits:

(1) The filter coefficients for the IIR filters have to be found such that stability and causality are fulfilled. Fitting in frequency space according to Eq. (3.21) does not demand for these restrictions, offering more flexibility and potentially more accurate fit results.

(2) While eigenfrequency studies in frequency domain require adequate representations of the transfer function for frequencies only within the circle of confidence or, at most, frequencies occurring during the iterative convergence process, see Fig. 3.2 and Fig. 3.1, time domain filters have to provide a conservative transfer behavior for frequencies outside of the circle as well. That means, for eigenfrequencies not covered by a priori given frequency-wise input data, the filter must be designed such that these eigenmodes are not amplified. Otherwise, the solution might rapidly get dubious. This behavior can be interpreted as artificial feedback introduced by the filter and needs to be avoided.

The potential risk of artificial amplification is obvious considering the cut-on condition for higher-order modes, see Eq. (2.60) and Fig. 3.2. The generation of filter coefficients can only be based on frequencies above the cut-on frequency of higher-order modes. The amplitude transfer behavior in the lower frequency range is not restricted giving rise to potentially high values. Longitudinal modes, typically propagating at frequencies below the cut-on frequency of higher-order modes and containing high acoustic energy might then be artificially amplified. Fortunately, thrust nozzles provide strong damping for longitudinal modes. A certain artificial amplification for such modes can hence be tolerated for linear considerations.

To circumvent unfavorable transfer behavior for undefined frequency ranges, different types of filters might be used, e.g. band-pass filters restrict the presence of relevant amplitudes of the transfer behavior to the frequency range of interest. However, band-pass structures are even less flexible and potentially prone to introduce significant errors into the transfer behavior within the relevant frequency range.

Finally, the iterative algorithm used for eigenfrequency analysis in frequency space can be applied to time domain considerations. Thus, the filter is not designed to directly capture the entire frequency range of interest accounting for the influence of the system damping and growth, respectively, but a simple delay model is employed describing a constant amplitude and linear phase, which are valid only at a distinct frequency. In this case, the filter contains only one coefficient and time delay pair, which reduces the general form to

$$\hat{\mathcal{F}}_{mn}(z) = b_{\mathbf{M},R} z^{-\mathbf{M}}\, \hat{\mathcal{G}}_{mn}(z), \tag{3.44}$$

and in time domain to

$$\mathcal{F}'_{mn}[\mathrm{n}] = b_{\mathbf{M},R}\, \mathcal{G}'_{mn}[\mathrm{n} - \mathbf{M}]. \tag{3.45}$$

Herein, the coefficient $b_{\mathbf{M},R}$ corresponds to the amplitude of the reflection coefficient and $\mathbf{M}$ represents the delay multiplicator, i.e. the physical time delay $\mathcal{T}$ is given by

$$\mathcal{T} = \mathbf{M}\Delta t, \tag{3.46}$$

where Δt denotes the computational time step. The time delay $\mathcal{T}$ directly depends on the phase behavior of the reflection coefficient, viz.

$$\mathcal{T} = -\frac{d\phi(R(\Omega))}{d\Omega}. \tag{3.47}$$

The iterative procedure leads to a converged solution using Eq. (3.21) to evaluate the amplitude and phase in each step. However, this method is extremely time-consuming since it loses its capability to determine the system's stability within a single computational run. Furthermore, the attributed constant amplitude and phase behavior for all frequencies effects the entire mode spectrum covered in the simulation. Nevertheless, irrelevant modes are prone to be amplified more intensely due to a more unbalanced situation between amplification and damping.

3.4. Comparison of Time Domain and Frequency Space Methods and Perspective Towards Non-Linearity

This section provides a discussion about strengths and disadvantages of frequency space based computations in comparison to time domain procedures. The potential scope of application of each approach is presented and their respective extensibility of to non-linearity is revealed. Tab. 3.1 summarizes the main statements and provides additional comparisons concerning the applied numerical methods.

In time domain the time series of the primary variables have to be computed until sufficient data is available for meaningful post-processing purposes. Although linearized equations reduce computational efforts significantly, time domain simulations still take a couple of hours. However, time domain calculation techniques allow for strongly parallelized solution procedures on multiple cores. In contrast, the solution of the eigenvalue problem on typically sized grids in frequency space is performed within minutes.

The restrictions of FIR and IIR filter techniques for the modeling of frequency dependent boundary conditions and source terms makes the generation of meaningful filter coefficients difficult. Frequency domain based simulations are much more flexible and robust for the incorporation of frequency dependent boundaries and source terms.

The time domain solver PIANO is based on structured grids, which are inefficient for more complex geometries. The frequency domain solver, based on an unstructured methodology, allows to reduce the number of degrees of freedom whilst providing sufficient resolution for the acoustic propagation, which again reduces computational turnaround times.

A considerable advantage of low computational times in frequency space is the possibility to apply a high repetition rate of simulations, which allows for the validation and improvement of the model very efficiently.

The post-processing of results is simpler and faster in frequency space than in time domain since final results are often presented in terms of frequency. Time consuming methods such as Proper Orthogonal Decomposition (POD) or Dynamic Mode Decomposition (DMD) are regularly used for time series analyses.

In the linear regime the time domain approach theoretically yields the same results in terms of complex amplitudes and complex eigenfrequencies. Because of modeling issues, however, inaccuracies should be expected, which depend on the considered configuration. For linear acoustic propagation the evaluation of the LEE in frequency space is therefore beneficial. The time domain approach becomes ultimately necessary when the acoustic propagation itself depends on the acoustic amplitude and requires therefore the incorporation of non-linear effects. The transformation of the Euler equations into a non-linear formulation, which is still based on a hybrid approach, results in the PErturbed Nonconservative Nonlinear Euler (PENNE) equations (Long 2000). This set of equations also requires a mean flow field as input. In contrast to the LEE, the PENNE are able to capture non-linear effects such as acoustic mode interaction, i.e. the energy transfer between acoustic modes, as well as wave steepening (Köglmeier et al. 2011).

Tab. 3.1.: Summary and comparison of time domain and frequency space simulation techniques.

	time domain (PIANO)	frequency space
governing equations	LEE	LEE
spatial discretization	DRP, Finite Difference, 4th order	Finite Elements, 1st order[5]
temporal discretization	LDDRK, 4th order	∞
mean flow interpolation	linear	linear
mesh topology	block-structured	unstructured
element types	hexagonal in 3D	tetrahedral or hexagonal
parallelizable	yes	limited
numerical stabilization	spatial filtering	GLS, SUPG
mode decomposition	no	no (forcing); yes (eigenvalue)
feedback models	pressure coupling	pressure/velocity coupling
dome coupling	yes	yes
axially dependent mean flow	yes	yes
non-linear wave propagation	no (LEE); yes (PENNE)	no
mode interaction	no (LEE); yes (PENNE)	no
simulation time	-	+
boundary treatment	0	+
post-processing	0	+
extensibility	0	+
non-linear flame feedback & boundaries	0	0
amplitude dependent mean flow	0	0
characterization of linear transfer functions	0	+

Such effects are especially important when high acoustic amplitudes are present in a rocket engine, e.g. in case of bomb tests (Priem 1997).

However, non-linearity does not only affect the acoustic propagation, boundary conditions and source terms have to be modeled adequately as well. While the definition of transfer functions and their incorporation into frequency and time domain approaches is state of the art, non-linearity cannot as easily be captured. Essentially, the amplitude dependence of the transfer behavior has to be included.

In terms of thermoacoustic feedback modeling, a frequency-dependent transfer function for the source term according to Eq. (2.103), relates the fluctuating heat release rate linearly to an acoustic coupling quantity. While the stable operation is related to small amplitudes, which can be described by linear models, unstable operation may lead to

[5] higher-order discretization can be used as well.

significantly higher amplitudes. In order to account for non-linear effects, the Flame Transfer Function has to be extended to be dependent of pressure amplitude, as well. The transfer function is then referred to as Flame Describing Function and depends on both frequency and amplitude. As discussed before, a Flame Transfer Functions can easily be included into the frequency space based simulation, while certain inaccuracies are incorporated through the filter representation of the Flame Transfer Function in time domain. Flame Describing Function, in contrast, require a higher modeling effort. For example, the amplitude dependency of the Flame Describing Function can be stored in a library yielding a set of Flame Transfer Functions, where each of them is valid for a single amplitude. The solution of the eigenvalue problem on the basis of the frequency space transformed LEE is then obtained for different amplitudes by varying the Flame Transfer Functions. When the damping rate is zero, the limit cycle condition of equalized thermoacoustic driving and damping, is reached. The limit cycle amplitude can then be found in the library at the corresponding Flame Transfer Function.

However, the non-linear propagation of acoustics is neglected when calculating the limit cycle amplitude in frequency domain. In time domain, the non-linearity of acoustic propagation can also be considered yielding a powerful stability assessment tool. The Flame Describing Function is then e.g. modeled in terms of pressure dependence as an amplitude saturation model of cubic type (Noiray and Schuermans 2013), viz.

$$\dot{q}' = \mathcal{F}^{-1}(\mathrm{FTF}) \cdot p' \frac{\bar{\dot{q}}}{\bar{p}} - K \cdot p'^3, \tag{3.48}$$

where K is a constant coefficient, which needs to be fitted to the library data of Flame Transfer Functions. However, such an approach is not capable to take the frequency dependency into account without further modeling efforts.

In general, hybrid approaches are based on a steady mean flow field as input. However, high amplitude acoustics may affect the mean flow field considerably, which may also be referred to as a non-linear behavior. For instance, in (Sattelmayer et al. 2015a), a shift of the flame and therefore high temperatures towards the face plate due to the influence of transverse acoustic velocity for high amplitudes is observed. Such effects cannot directly be incorporated into hybrid approaches. A possible concept is based on the parametrization of the mean flow field. The parameters may depend on amplitude and therefore account for mean flow variations. This concept can be realized both in frequency space and time domain, making both approaches equally suitable for this particular area.

The concepts of Flame Transfer Function and Flame Describing Function can be transferred into a general concept for modeling source terms as well as boundary conditions. Reflection coefficients and scattering matrix elements are determined for different amplitudes as well. Conclusively, as long as the non-linearity of acoustic propagation can be neglected, frequency space based codes are advantageous due to the accurate modeling of source terms and boundary conditions as well as the fast turnaround times. The non-linearity of transfer functions can be considered, as well. The time domain approach is favorable when non-linear acoustic propagations need to be taken into account with the disadvantage of increased turnaround times.

4 Non-Reactive Acoustic Analysis

Linear stability assessments demand an adequate description of the acoustic propagation including boundary conditions for rocket engine relevant configurations. This Chapter deals with the validation of the numerical approaches presented in Chap. 3 for a non-reactive environment and the interpretation of the results in terms of modeling strategies under reactive, closed feedback loop conditions. Furthermore, the influence of different design aspects on acoustic damping is discussed. Since the time domain code was validated intensively in previous investigations (Kaess et al. 2010; Köglmeier et al. 2014a; Morgenweck 2013; Pieringer 2008), the focus is on the frequency space LEE description.

4.1. Nozzle Acoustics

The supersonic thrust nozzle flow establishes a natural decoupling of the chamber acoustics from influences originating from downstream of the sonic line. Acoustic waves are partly reflected or transmitted by the nozzle. The capability of the frequency space LEE to capture such effects for longitudinal and transverse modes is analyzed in this section, followed by an investigation of the results.

Validation and interpretation of the frequency space transformed LEE results are conducted for ambient temperature and slightly elevated pressure conditions on the basis of a well-studied experimental chamber configuration (Kathan 2010, EADS Astrium, Ottobrunn, 2013). To characterize the scattering properties of the nozzle, its admittance is determined at the interface between the cylindrical chamber part and nozzle inlet. The admittance is especially useful to determine the flux of acoustic energy across the surface according to Eq. (B.22). Such analyses were already conducted in time domain for longitudinal excitation and for the T_1 eigenfrequency (Kathan et al. 2011; Morgenweck 2013; Pieringer 2008). However, the admittance for frequencies above the cut-on frequency of the T_1 mode were not calculated and validated.

4.1.1. Nozzle Configurations and Modeling

Two different nozzle configurations are considered. While the chamber dimensions are the same, nozzle A is considerable shorter than nozzle B, see Fig. 4.1. The geometrical dimensions are given in Tab. 4.1. For further information about the nozzle design it is

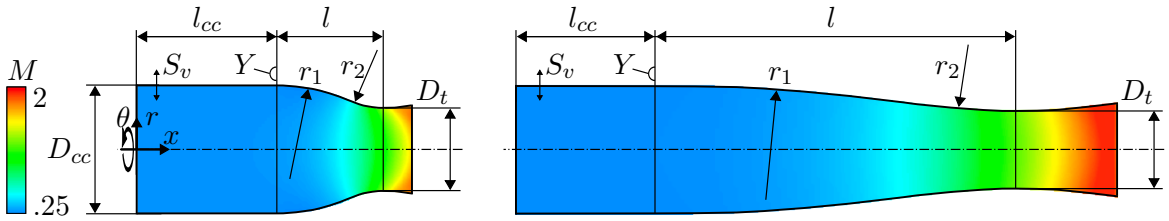

Fig. 4.1.: Geometry and Mach number distribution of nozzle A (left) and nozzle B (right).

referred to (Morgenweck et al. 2011) and (Kathan 2013).

The absence of acceleration due to combustion requires high Mach numbers in the chamber to establish supersonic flow conditions at the nozzle outlet. In fact, a Mach number of 0.25 in the chamber is present in case of nozzle A. In contrast, a slightly lower Mach numbers of 0.22 establishes in case of nozzle B (Kathan 2013). Further flow conditions are given in Tab. 4.1. Fig. 4.1 shows the Mach number distribution for isentropic flow conditions in the nozzle.

According to Eq. (2.60), the cut-on frequencies for the configurations are slightly above 2100 Hz, see also Tab. 4.1. The eigenfrequency of the first longitudinal mode is approximately 1000 Hz.

The excitation of acoustics within the domain is performed similarly to the experimental configuration to provide an adequate acoustic field consisting of the desired modes (Kathan 2010, EADS Astrium, Ottobrunn). On an ellipsoidal curved small area on the wall close to the inlet of the domain, a harmonically fluctuating velocity com-

Tab. 4.1.: Specifications, flow conditions and the cut-on frequencies and of the nozzles A and B.

		nozzle A	nozzle B
nozzle length [mm]	l	73	273
chamber length [mm]	l_{cc}	107	
chamber diameter [mm]	D_{cc}	92	
throat diameter [mm]	D_t	60	56
inner nozzle radius [mm]	r_1	119	1469
outer nozzle radius [mm]	r_2	53	544
mach number in the chamber [-]	M	0.25	0.22
mean pressure in the chamber [bar]	$\bar{p}$	1.65	1.66
mass flow [kg/s]	$\bar{m}$	1.15	1.00
mean density [kg/m^3]	$\bar{\rho}$	1.94	2.03
speed of sound [m/s]	c	341	
mean air inlet temperature [K]	$\bar{T}$	290	
cut-on frequency T_1 mode [Hz]	$f^{co}_{T_1}$	2103	2119

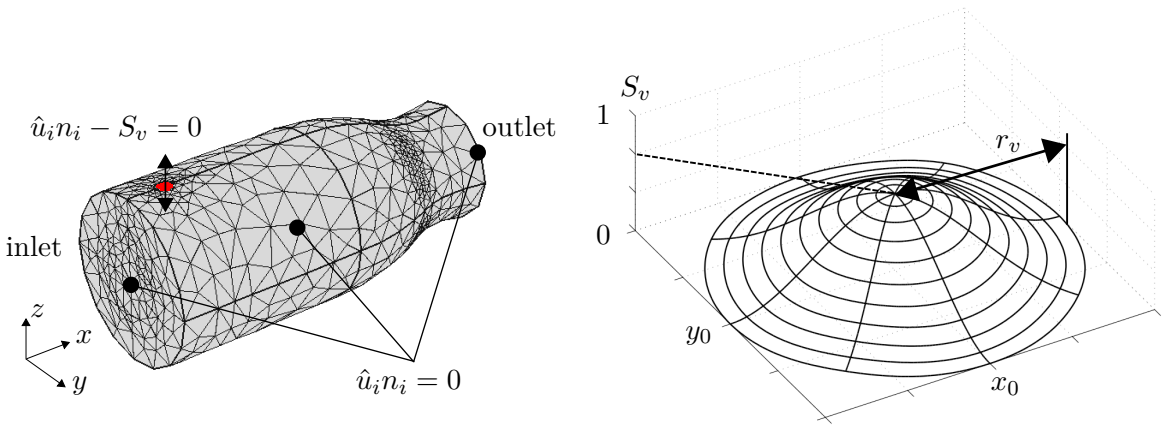

Fig. 4.2.: Left: Location of the excitation, boundary conditions and computational grid. Right: Shape of the excitation function.

ponent normal to the surface is imposed. The excitation surface is highlighted in red in Fig. 4.2. To provide a consistent boundary treatment at the edge of the excitation surface, the shape S_v of the excitation is defined such that the slip-wall condition is fulfilled. A smooth shape function on the excitation surface is defined by

$$S_v = 0.5 \left[\cos\left(\frac{\pi(x - x_0)}{r_v}\right) + 0.5\right] \left[\cos\left(\frac{2\pi(y - y_0)}{r_v}\right) + 0.5\right], \tag{4.1}$$

where (x_0, y_0) denote the center and r_v the radius of the in z-direction projected circular surface of the excitation boundary, see Fig. 4.2 (right). The boundary condition for the excitation finally reads

$$\hat{u}_i n_i - S_v = 0, \tag{4.2}$$

as indicated in Fig. 4.1 (left).

The small area ensures a low influence of the excitation on the acoustic mode shapes. On the rigid wall, free slip boundary conditions according to Eq. (2.72) are applied. At the inlet, the air flow enters the domain with a homogeneously distributed axial velocity component. As described in Sec. 2.7.3, the outlet is prescribed as non-reflective. Energetically neutral conditions for the acoustic flux are set here according to Eq. (2.96).

The frequency response of the nozzle is determined on the basis of the isentropic LEE (2.30)-(2.31) and (2.37), employing the methodology introduced in Sec. 3.2.2.1. The computational grid is shown in Fig. 4.2 (left) as well. A rather coarse resolution is chosen to provide short turnaround times. Altogether the acoustic field is solved for approximately 7400 degrees of freedom using linear shape functions on tetrahedral elements in a unstructured grid. Tetrahedral elements are required here to adequately resolve the excitation boundary. In the region close to the excitation and within the subsonic region slightly upstream of the nozzle throat, the grid is refined to provide a higher resolution of the acoustic waves. The time consumption for a single frequency

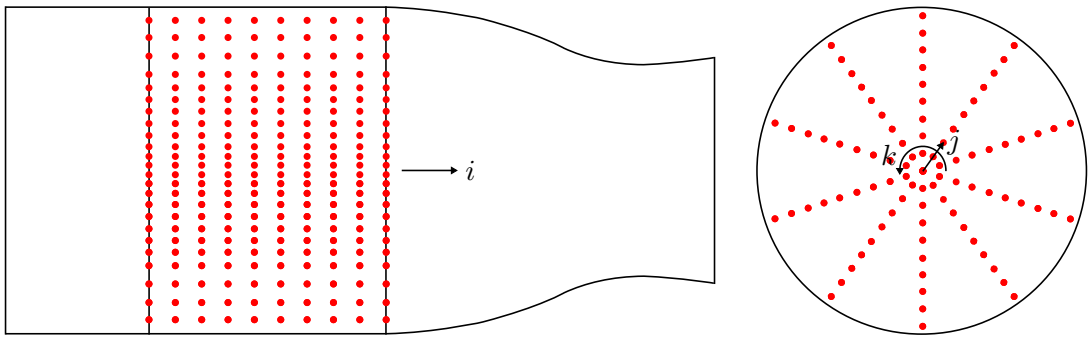

Fig. 4.3.: Distribution of spatial monitor points $I, J, K = (10, 8, 10)$ in the cylindrical part of nozzle A.

calculation on a standard 2.6 GHz, 8 Gbyte RAM machine is about 2 s, which allows for a very fine frequency resolution.

4.1.2. Mode Decomposition

In order to determine the nozzle admittance for each acoustic mode, the acoustic pressure field $\hat{p}$ is decomposed into the individual mode-dependent contributions $\hat{p}_{mn}$, see Eq. (2.41). The mode separation is achieved by fitting the computed pressure values $\hat{p}$ to the general ansatz for the acoustic pressure field, see Sec. 2.4, accounting for modes which are cut-on. The definition according to Eq. (2.49) for the azimuthal pressure distribution is used. For the present investigation, frequencies are limited to the T_1 mode yielding for the fitting procedure in a cylindrical frame of reference:

$$\sum_{i=1}^{I}\sum_{j=1}^{J}\sum_{k=1}^{K}\left[\hat{p}(x_i, r_j, \theta_k) - \left(\hat{p}_{00}(x_i, r_j, \theta_k, \hat{\phi}) + \hat{p}_{10}(x_i, r_j, \theta_k, \hat{\phi})\right)\right]^2 \stackrel{!}{=} \min, \tag{4.3}$$

where $\hat{\phi} = (\hat{\mathcal{F}}_{00}, \hat{\mathcal{G}}_{00}, \hat{\mathcal{F}}_{10}, \hat{\mathcal{G}}_{10}, \delta)$ denotes the vector of unknowns to be solved for. Furthermore, i, j, k indicate the spatial coordinates which are used for the fitting procedure. The optimization problem is solved by utilizing the Newton-Raphson-Method in MATLAB. A high number of $I, J, K = (10, 8, 10)$ monitor points is used in axial, radial and azimuthal direction to provide adequate fitting results, see Fig. 4.3.

4.1.3. Validation of Mode Decomposition

In the following, the mode decomposition method is validated for nozzle A. The volume integrated periodically averaged acoustic energy of the extracted modes stored within the cylindrical section x = 50-107 mm is determined over frequency and compared to the overall acoustic energy $< E^a >$ within the same volume for nozzle A, see Eq. (2.69).

Fig. 4.4 shows the contribution of the longitudinal $< E^a_{00} >$ and first transverse mode

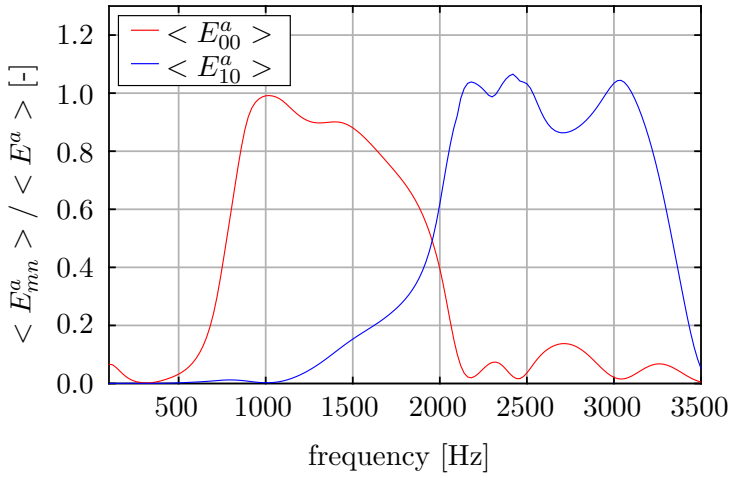

Fig. 4.4.: Energy ratio of the extracted modes and the entire acoustic energy in the specified volume between $x = 50$-107 mm for nozzle A.

$< E^a_{10} >$ to the total acoustic energy $< E^a >$, which is also determined by Eq. (2.69) using the acoustic quantities $\hat{u}_i$ and $\hat{p}$, respectively.

Below approximately 2100 Hz transverse modes are cut-off and only longitudinal wave propagation is present. Close to 1000 Hz the first longitudinal mode stores more and more energy until it contains the entire amount at about 1000 Hz, which corresponds to the L_1 eigenfrequency. In the range from 1000 Hz to about 2100 Hz the energy of the transverse mode increases in the volume. At higher frequencies the transverse mode dominates. Further mixed modes with longitudinal components are present as well. Above 3000 Hz radial modes propagate in the system, which are not accounted for in the ansatz function. Minor overestimations of the energy occur. Nevertheless, the mode decomposition method captures the relevant modes with sufficient precision for the determination of nozzle admittances.

4.1.4. Admittances

Fig. 4.5 presents the obtained nozzle admittances for nozzle A (top) and B (bottom) concerning both the longitudinal Y_{00} (left) and first transverse Y_{10} (right) mode with a frequency resolution of $\Delta f = 10$ Hz. In general, excellent agreement is achieved in comparison with the analytical solution by (Bell and Zinn 1973) (BaZ) and experimental data by (Kathan 2010, EADS Astrium, Ottobrunn) (exp.). Also, the available data for $Y_{00,A}$ and $Y_{10,A}$ of nozzle A compares well with results calculated in time-domain by (Kathan et al. 2011; Morgenweck 2013) (LEE-t).

Considering the admittances $Y_{00,\mathrm{A/B}}$ of the longitudinal mode for nozzle A and B, similarities are observed. The real parts are positive showing a peak value of about $Y_{00,A/B} \approx 2.5$. The imaginary parts are mainly positive with a peak value of $Y_{00,\mathrm{A/B}} \approx 1.8$ but also minimum values of $Y_{00,A/B} \approx -0.6$ are observed. Furthermore, the peak values of the imaginary part occur at the same frequency at which the real part shows

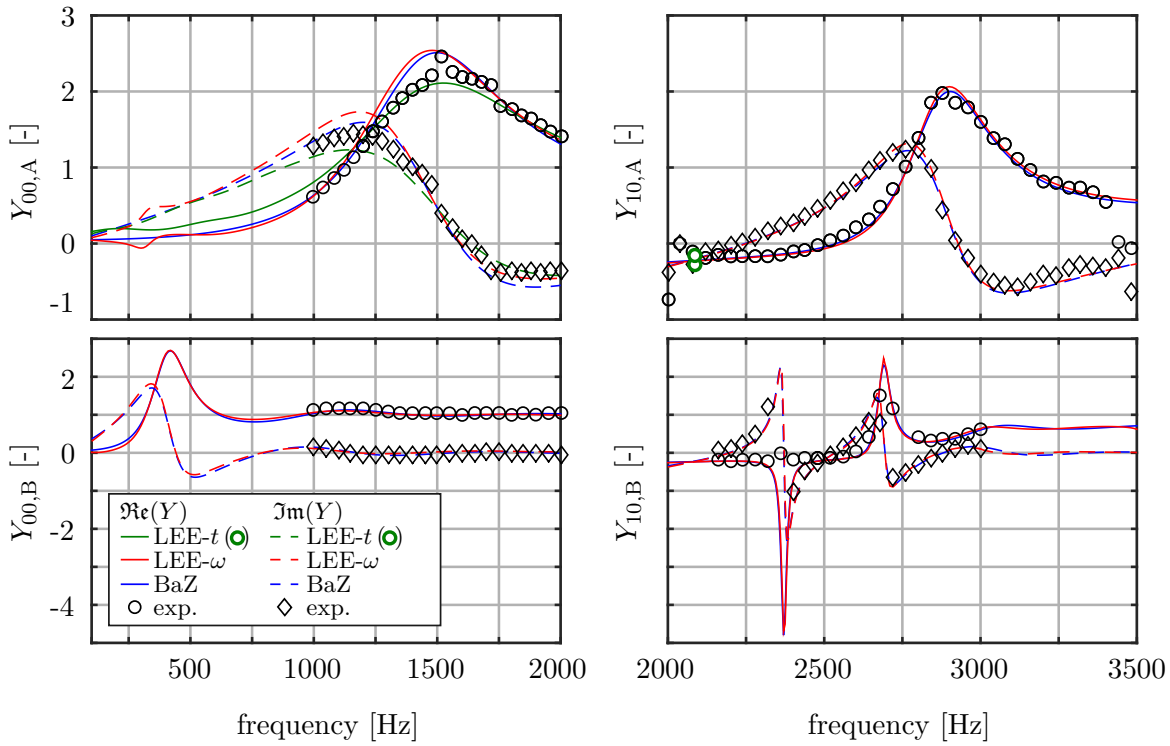

Fig. 4.5.: Admittances of nozzle A (top) and nozzle B (bottom). Left: First longitudinal mode ($mn = 00$). Right: First transverse mode ($mn = 10$).

an inflection point. Therefore, the change of the real part with respect to frequency is highest when the value of the imaginary part is highest and its slope is zero. In turn, the change of imaginary part is highest at the peak frequency of the real part.

The frequencies at which the maximum and minimum values occur are different for both nozzle designs.

Moreover, the admittance of nozzle A varies over a wide frequency spectrum of over 2000 Hz, while nozzle B shows the variation of admittance in a considerably more narrow frequency range. For higher frequencies only weak variations are observed both for the real part and for the imaginary part. For very high frequencies, the longitudinal mode becomes a purely running wave, i.e. $Y_{00,\mathrm{A/B}} \to 1+0\mathrm{i}$, which can be seen especially for nozzle B.

The same observations as for the Y_{00} mode are made for the first transverse mode but at higher frequencies. However, the nozzle B admittance shows very strong variations and two maxima and minima of the real and imaginary part are found within the considered frequency range.

A strong damping effect of the nozzle is established for high acoustic intensity flux through the nozzle, see App. B.5. According to Eq. (B.22), the flux is defined by the absolute pressure value $|\hat{p}|^2$. The pressure distribution depends, however, on the entire

system including consistent boundary conditions at the inlet. Consequently, the numerical model for the determination of the nozzle admittance cannot be employed to calculate acoustic pressure at the admittance reference plane.

However, high damping can also be realized by maximized values of the nozzle admittance in terms of its real part and absolute value. For this purpose, a rule to rapidly determine the frequencies of the maximum admittance values is derived and presented in App. C.2.

4.1.5. Use of the Nozzle Admittance as Boundary Condition

Although the nozzle admittance for a specific acoustic mode is homogeneously distributed in cross-section, see App. C.1, it is unfavorable to use the nozzle admittance as a boundary condition for various reasons:

In time domain, all eigenmodes which oscillate with a frequency resolved by the numerical time step are present simultaneously. The usage of an admittance boundary condition, however, requires the decomposition of the acoustic field into its eigenmodes in order to account adequately for each mode admittance, see App. C.1. The mode separation method needs to be applied at each time step decelerating the solution process and attributing to potential errors.

The usage of the composed admittance is in turn complicated, since the pre-processing for the characterization of Y needs to be based on the actual pressure and velocity field in the full system. However, the actual distributions are given by the solution of the stability prediction procedure and are not a priori known. Consequently, an iterative procedure would be required. Furthermore, the composed admittance depends on cross-sectional coordinates, see App. C.1, which both complicates the characterization further and requires great modeling effort in the subsequent simulations.

In rocket engines, the nozzle usually provides enormous damping on longitudinal modes reducing the attributed amplitudes significantly (Morgenweck et al. 2010). Therefore, only the admittance of the higher-order modes appear to be relevant and might be used as outlet boundary condition. However, higher-order modes still need to be decomposed and the error introduced by neglecting the longitudinal part needs to be validated for each configuration.

Eigenvalue studies in frequency space, in turn, inherently describe decomposed mode results. It might appear plausible to impose the admittance for the mode under consideration and investigate the results for this specific mode. However, as discussed before, the higher-order modes admittance can be characterized for frequencies above the cut-on frequency only and the circle of confidence is limited accordingly, see Sec. 3.3.1. Besides, for longitudinal modes the dimension of the circle is restrictive due to the zero frequency limit. An accurate evaluation of the admittance at any complex frequency Ω is therefore not possible using a complex fit according to Eq. (3.21).

The influence of an insufficiently large circle of confidence on the accuracy of the transfer behavior is demonstrated for $\mathfrak{Re}(Y_{00,\mathrm{A}})$. To generate a reference data set, the admittance is determined for different complex frequencies including damping rates

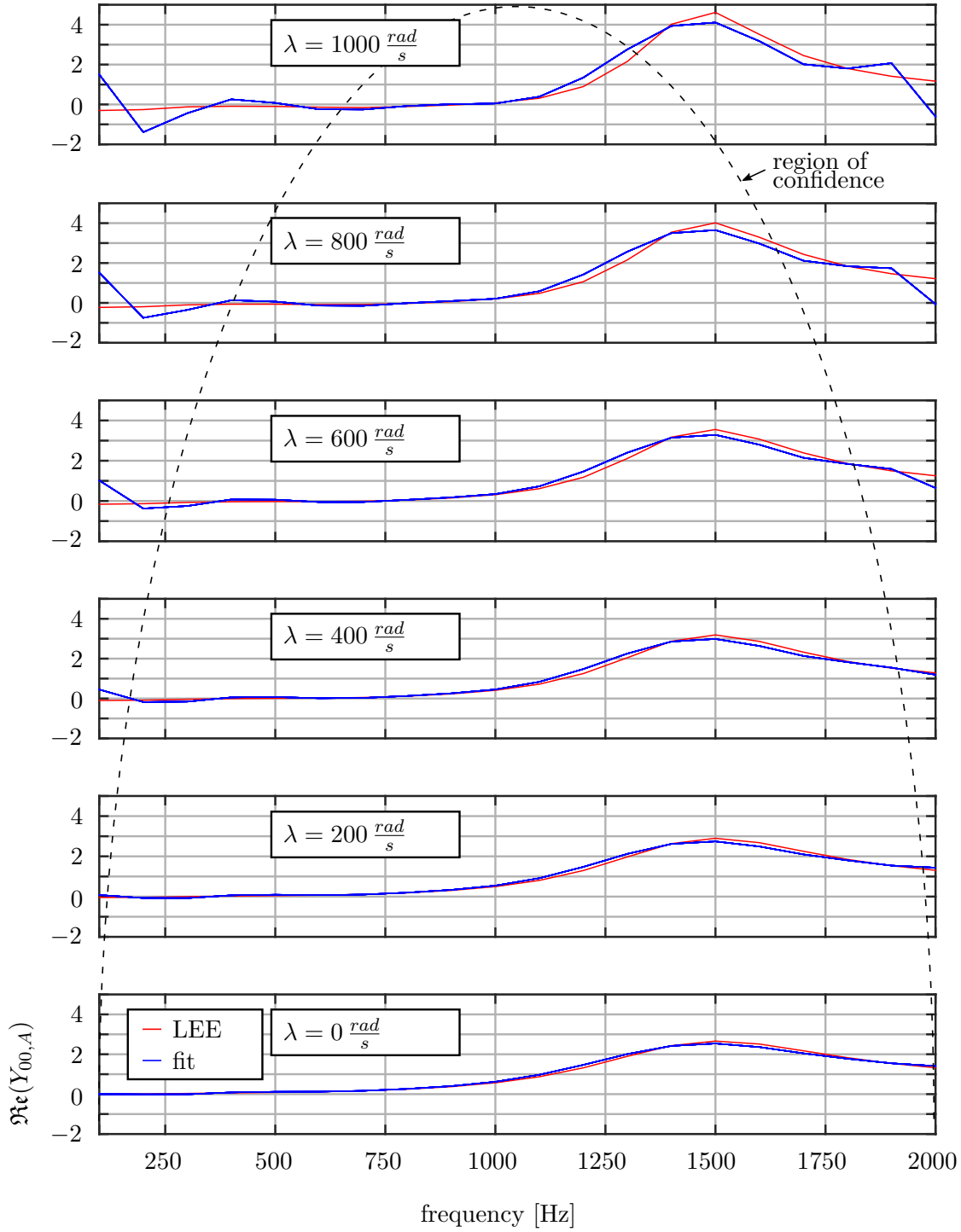

Fig. 4.6.: Direct LEE computation results compared to the application of the fit of the nozzle admittance: Real part for the longitudinal mode evaluated at different damping rates.

up to $\lambda = 1000$ rad/s on the basis of LEE field solutions including the nozzle. For the determination of the complex fit according to Eq. (3.21), the previously presented nozzle A admittances are employed, see Sec. 4.1.4. A polynomial order of $K^f = 5$ is used. The fitted function is evaluated to determine the admittance for complex frequencies. Finally, the admittance evaluated by the fitting function for complex frequencies is compared to the admittance findings from the LEE field results.

A comparison between both approaches is shown in Fig. 4.6. For the undamped case the results coincide well. For increased damping rates, however, deviations occur, which are initially observed at the frequency bounds. For higher damping rates, the deviations increase narrowing the frequency range with accurate results further. The comparison indicates that for high damping rates in the middle of the frequency range and for already moderate damping rates for frequencies close to the bounds, significant errors are introduced yielding an incorrect nozzle damping influence.

In Fig. 4.6 the circle of confidence is also indicated. Since frequency and damping rate are not plotted with the same grid spacing, the confidence region appears elliptical and not circular, cf. Fig. 3.2. It can be seen that the error propagation from the frequency bounds towards the center with increasing damping rate corresponds approximatively to the circumference of the region of confidence. For high damping rates the region of confidence is narrow. Correspondingly, the range of accurately determined acoustic admittance is limited to a small frequency range.

In conclusion, the incorporation of the thrust nozzle into the computational domain yields accurate damping rates and avoids modeling issues concerning the usage of the nozzle admittance. For the incorporation of the nozzle, only low computational resolution is required, increasing turnaround times only insignificantly for frequency space consideration as well as for time domain simulations. Therefore, the direct simulation of the nozzle is highly beneficial and most accurate.

4.2. Dome Coupling and Determination of Damping Rates

The numerical model of the nozzle configuration with chamber element investigated in the previous section is extended towards a more realistic rocket engine design upstream of the chamber and used to demonstrate the capabilities of the dome coupling concept introduced in Sec. 2.7.5 in time domain and frequency space. The experimental configuration upstream consists of a perforated plate, a pipe element and a thin annular slit in which choked conditions are established to decouple the chamber acoustically from the supply system, see Fig. 4.7 (left). The perforated plate imitates the face plate comprising a high number of injectors. The Mach number in the holes is 0.4, which is significantly larger than in case of a realistic injector flow, but necessary to generate choked nozzle conditions. Further geometrical specifications of the perforated plate are given in App. D. Otherwise the same conditions as before are applied using nozzle A, see Tab. 4.1. In the simulations, the perforated plate is replaced by a representative scattering matrix, which couples the chamber with the upstream pipe element, cf. Sec. 2.7.5.

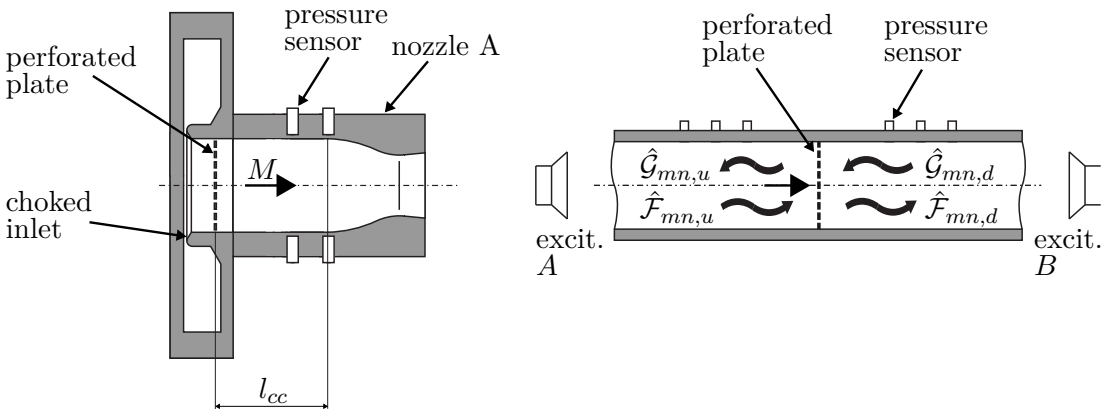

Fig. 4.7.: Extended non-reactive rocket engine system (left) and pipe element with perforated plate (right).

The dome coupling concept is demonstrated in two steps. First, the perforated plate is considered in a simple pipe configuration, see Fig. 4.7 (right). The goal is to impose the experimentally determined scattering matrix of the perforated plate in the computation and to reconstruct the transfer behavior from the simulation data. The numerical findings are finally compared to the experimental results. Afterwards, the eigenfrequency and the damping rate of the T_1 mode propagating in the extended rocket engine system are determined and validated against experimental findings.

4.2.1. Reconstruction of the Scattering Matrix

The experimental procedure for the determination of reflection and transmission coefficients of the perforated plate is briefly described first. The perforated plate is placed in a simple pipe element with an equal diameter of 92 mm and a flow with a Mach number of 0.25 as in the extended rocket engine system, see Fig. 4.7 (right) and Tab. 4.1 . It is assumed that the perforated plate sufficiently decouples the upstream and downstream transverse acoustic motion and that the propagation of acoustic fluctuations is strictly longitudinal in the single holes. In this situation the scattering matrix is capable of describing the transfer behavior.

For the determination of the scattering matrix of the perforated plate, the two-source location method is applied, which is based on two independent excitation states denoted with A and B in Fig. 4.7 (right) (Åbom 1992; Åbom and H. Bodén 1988; Bodén and Åbom 1986; Kathan 2013; Lung and Doige 1983; Munjal and Doige 1990; Paschereit et al. 2002). A detailed description of the siren excitation method can be found in (Kathan 2013). The calculation of the generalized Riemann invariants for each excitation state upstream and downstream, i.e.

$$\hat{\mathcal{F}}_{mn,u}^{A/B},\ \hat{\mathcal{G}}_{mn,u}^{A/B},\ \hat{\mathcal{F}}_{mn,d}^{A/B} \text{ and } \hat{\mathcal{G}}_{mn,d}^{A/B}, \tag{4.4}$$

is obtained employing the fitting-procedure according to Eq. (4.3). The dynamic pres-

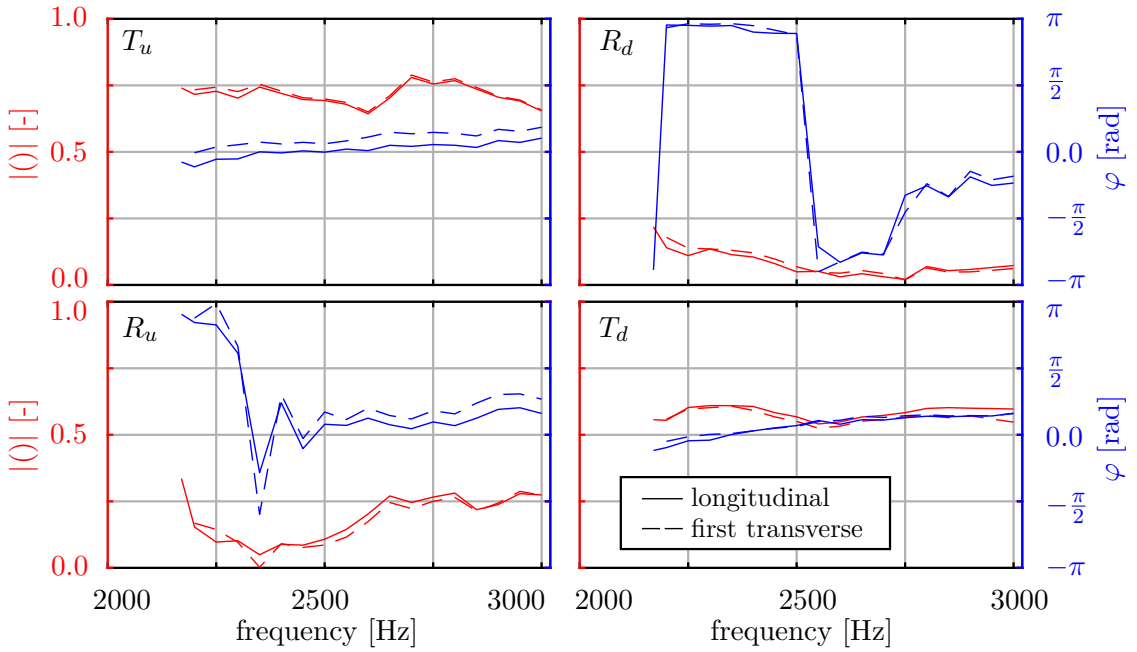

Fig. 4.8.: Comparison of scattering matrices of the perforated plate for the longitudinal and first transverse modes calculated from experimental measurements in the simple pipe element, cf. Fig. 4.7 (right).

sure is recorded at ten sensor locations upstream and downstream which are distributed axially and circumferentially at the walls close to the perforated plate. The scattering matrix is finally determined from the solution of

$$\begin{pmatrix} T_u(\omega) & R_d(\omega) \\ R_u(\omega) & T_d(\omega) \end{pmatrix} = \begin{pmatrix} \hat{\mathcal{F}}^A_{mn,d}(\omega) & \hat{\mathcal{F}}^B_{mn,d}(\omega) \\ \hat{\mathcal{F}}^A_{mn,u}(\omega) & \hat{\mathcal{F}}^B_{mn,u}(\omega) \end{pmatrix} \begin{pmatrix} \hat{\mathcal{G}}^A_{mn,u}(\omega) & \hat{\mathcal{G}}^B_{mn,u}(\omega) \\ \hat{\mathcal{G}}^A_{mn,d}(\omega) & \hat{\mathcal{G}}^B_{mn,d}(\omega) \end{pmatrix}^{-1} . \tag{4.5}$$

As explained in Sec. 2.7.5, the dome coupling concept is based on a mode independent scattering matrix. However, according to Eq. (4.5), the calculation of the matrix elements involves mode dependent Riemann invariants. Consequently, for frequencies above the cut-on frequencies of higher-order modes, the scattering matrix can be determined for each mode individually. To show that the scattering matrix is in fact mode independent, the matrix elements are calculated for both the longitudinal ($mn = 00$) and the first transverse ($mn = 10$) mode in the range between the cut-on frequencies of T_1 and T_2 using the experimentally measured pressure data. The comparison is shown in Fig. 4.8. Overall, the mode dependent amplitudes and phases compare excellently. Small discrepancies are observed for the phases of T_u and R_d, which might originate from insufficiently accurate mode decomposition procedures. Nevertheless, it can be concluded that the acoustic coupling of the pipe sections provided by the perforated plate does not depend on a specific mode but only on frequency. Furthermore, longitudinal or higher-order modes, if they are cut-on, can be used to determine the scattering matrix. In the following, the scattering matrix determined for the first transverse mode is employed.

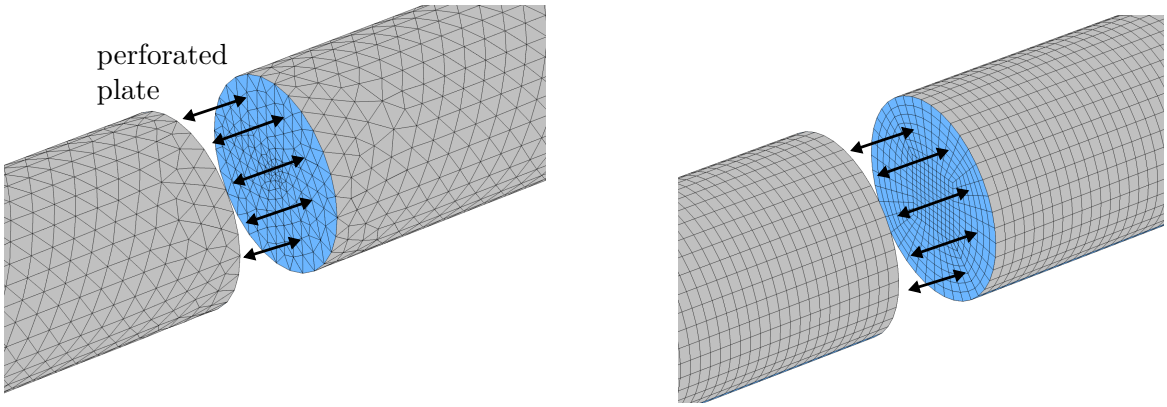

Fig. 4.9.: Computational grid for frequency space (left) and time domain solver (right).

In the next step, the simulations of the simple pipe configuration including the perforated plate in form of the scattering matrix are conducted. The computational domain consists of two separated co-axially arranged pipe sections, which are coupled by means of the scattering matrix. The used computational domain are shown in Fig. 4.9. The gap between the sections represents the perforated plate. The single holes are not resolved, but the connection is applied to the entire coupling surface. Consequently, the scattering matrix is determined such that the area ratio between the single holes and the pipe cross-section is inherently included.

The application of the scattering matrix allows for coarse grids. Fig. 4.9 illustrates that the grid resolution is chosen such that the T_1 mode is just sufficiently resolved in cross-section and the axial element size is not refined at the coupling boundary. Tetrahedral elements are chosen again in frequency space, see Fig. 4.9 (left). In time domain, only hexagonal block-structured grids are applicable, see Fig. 4.9 (right). Altogether, approximately 70,000 degrees of freedom are solved for in frequency space and in time domain.

For the reconstruction of the scattering behavior from numerically determined pressure $\hat{p}$, the same procedure used for the experimental analysis is employed, see Eq. (4.5). In contrast to the experiments, a higher number of data extraction positions is used in the simulations to reduce potential errors originating from the post-processing procedures.

The comparison between experimental findings and reconstructed data for the T_1 mode is shown in Fig. 4.10. It can be seen that for the rather complex scattering behavior excellent agreement of amplitude and phase is achieved for all matrix elements over the entire frequency range. Small deviations originate from minor discretization errors and slightly inaccurate fitting procedures.

The time domain results are shown in Fig. 4.15 together with the IIR filter representation. Discrepancies between the reconstruction and the experimental values are observed, which affect the accuracy of subsequent calculations of damping and growth rates, respectively. For reasons discussed before, the constraints of the filter design restrict its flexibility and applicability. If unacceptable errors are introduced, frequen-

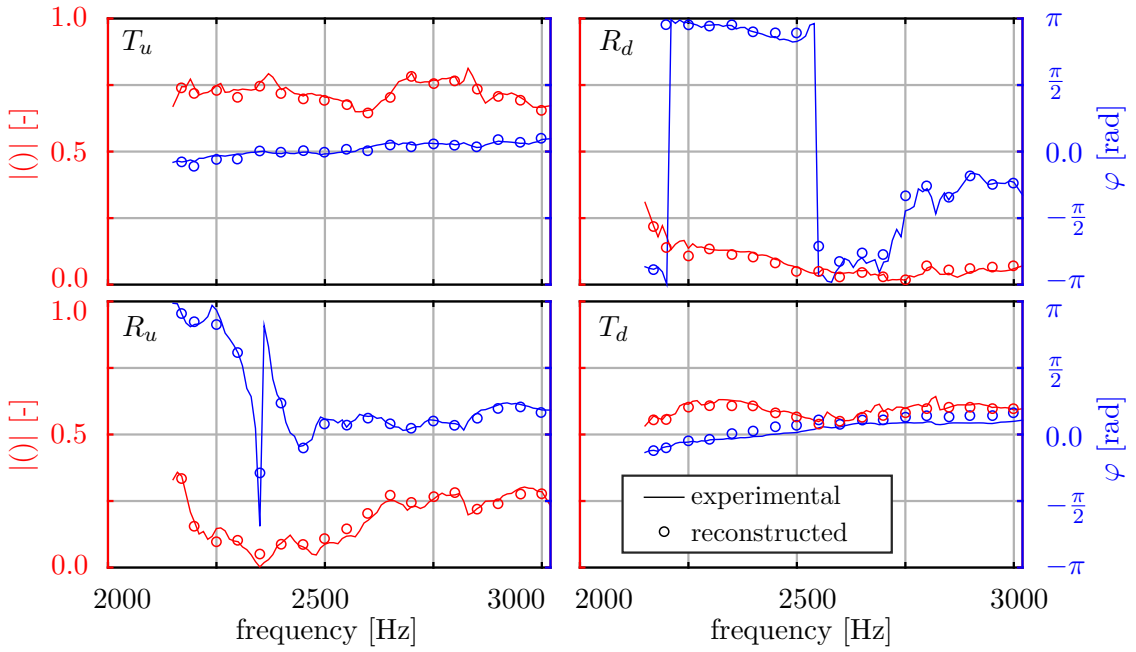

Fig. 4.10.: Comparison between experimental findings and reconstructed data for the scattering matrix SM in case of T_1 mode propagation.

cy space simulations should be preferred, which allow for accurate modeling of the scattering properties, see Fig. 4.10.

Studies show that the virtual gap realized between the domains in the simulation does not effect the results. Furthermore, the grid does not necessarily have to be chosen equally on both surfaces. However, equal grid point patterns minimizes interpolation errors.

A visualization of the coupling for the T_1 mode at 2110 Hz is presented in Fig. 4.11. It shows the normalized amplitude distribution of the generalized Riemann invariant propagating in positive x-direction $|(\hat{\mathcal{F}}_{10})|$ on the interface between the pipe sections (left). The excitation is applied upstream and generates an asymmetric distribution of $|(\hat{\mathcal{F}}_{10})|$ over the cross-section. Nevertheless, the scattering matrix approach couples the upstream and downstream surface adequately. Due to the bi-directional coupling, the impact of any boundary condition in the downstream section is well described in the upstream part and vice versa. The amplitude of transmission from upstream to downstream reads $|T_u\,(2110\text{ Hz})| = 0.71$. The transmission amplitude and phase is homogeneous across the interfacing surfaces describing the longitudinal, point-wise coupling.

To quantitatively illustrate the behavior of $\hat{\mathcal{F}}_{10}$ in more detail, it is plotted along the axial direction for an exemplary location in cross-section in the pipe elements, see gray line in Fig. 4.11 (left). The corresponding distribution is shown in Fig. 4.11 (right). Close to the lower x-limit, the influence of the excitation can be observed. The right-running wave then propagates towards the coupling condition, where it gets transmitted to the

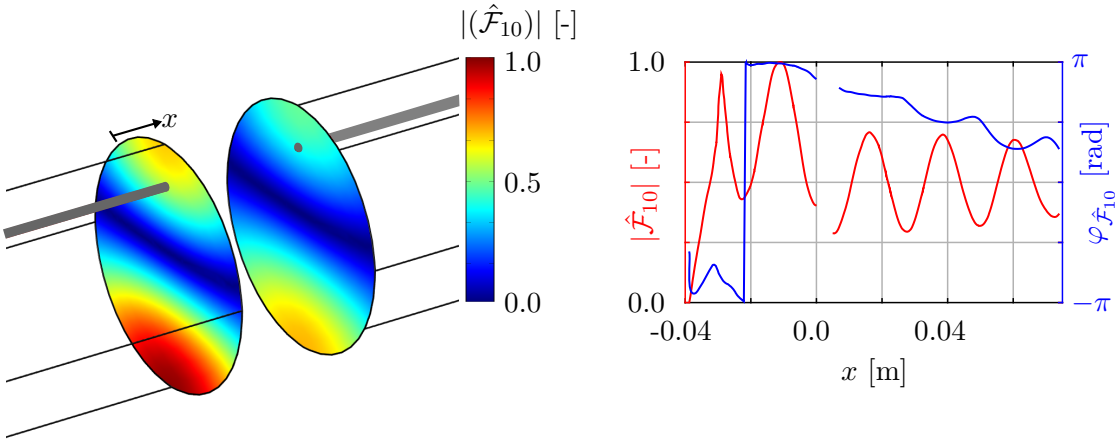

Fig. 4.11.: Distribution of normalized $|(\hat{\mathcal{F}}_{10})|$ at the interfacing surfaces (left) as well as axial distribution of $\hat{\mathcal{F}}_{10}$ in terms of amplitude and phase (right) for a frequency of 2110 Hz.

downstream section while exhibiting a reduction of amplitude of $|T_u\,(2110\text{ Hz})| = 0.71$ and a small phase shift of $\varphi_{T_u}(\,(2110\text{ Hz})) = -0.16$ rad. Afterwards the wave travels further downstream.

The same accuracy is achieved for longitudinal wave propagation in the pipe sections, i.e. for excitation frequencies below the cut-on frequency of the T_1 modes. The corresponding results are presented in App. E.

As long as the point-wise interface between two domains can be described via a longitudinal propagation, the scattering matrix approach represents an efficient and accurate realization of the coupling condition, especially for frequency space considerations. Furthermore, it provides fast turnaround times while accounting for the acoustic damping mechanisms described by the scattering matrix.

4.2.2. Determination of Damping Rates with Dome Coupling

Modeling concepts for dome coupling and the thrust nozzle were introduced above. To demonstrate the validity of the approaches for eigenvalue studies, the damping rates are determined for the non-reactive test case and compared to experimental findings. The study is primarily focused on the T_1 mode. Different types of boundary treatment are used to highlight the influence of the dome coupling. Both frequency space and time domain are compared again on the basis of nozzle A. The specifications and flow conditions are given in Tab. 4.1.

4.2.2.1. Types of Inlet Boundary Treatments

Fig. 4.12 shows the different types of inlet boundary treatment. In a first step (I), the dome is not included and the chamber inlet condition is modeled energetically neutral

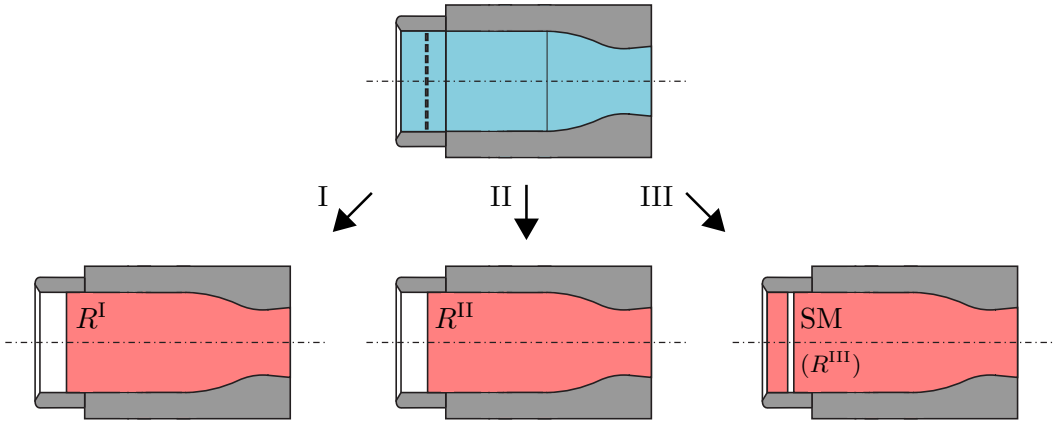

Fig. 4.12.: Step-wise approach for the modeling of dome coupling: Computational domain and inlet boundary treatment for I-III.

according to Eq. (2.96). The boundary condition at the inlet is imposed in form of Eq. (2.97) yielding

$$R_{\mathrm{i}} = R^{\mathrm{I}} = \frac{1-M}{1+M} = 0.6. \tag{4.6}$$

This configuration is referred to as reference case, in which only the nozzle attributes to acoustic damping. The influence of the subsequently incorporated dome coupling is revealed by comparing eigenfrequencies and damping rates to the reference case.

In a second step (II), the acoustic reflection coefficient R^{II} of the entire dome subsystem is imposed at the inlet. Since the pipe element upstream of the perforated plate is not included in this simulation, the non-local reactivity of the dome coupling is not accounted for and its influence can be analyzed, cf. Sec. 2.7.5. This case is referred to as partially reflecting inlet. Ad hoc measured values of the admittance for the T_1 mode at the inlet are taken from (Kathan 2013) and transformed into a reflection coefficient, viz.

$$R_{\mathrm{i}} = R^{\mathrm{II}}. \tag{4.7}$$

In a third and last step (III), the dome coupling is fully included. For this purpose, the scattering matrix for the T_1 mode presented in the previous section is applied to the numerical setup, which accordingly reads

$$\mathrm{SM} = \begin{pmatrix} T_u^{\mathrm{III}} & R_d^{\mathrm{III}} \\ R_u^{\mathrm{III}} & T_d^{\mathrm{III}} \end{pmatrix}. \tag{4.8}$$

The matrix reflection coefficient downstream R_d^{III} is not the same as R^{II}. While R_d^{III} contains the downstream reflection properties of the perforated plate only, R^{II} describes the reflection properties of the entire dome subsystem upstream of the chamber including further scattering effects at the choked circular ring and phase differences generated by the upstream pipe section. For the simulations, the computational domain used for the characterization of the nozzle admittances, cf. Fig. 4.2, is extended

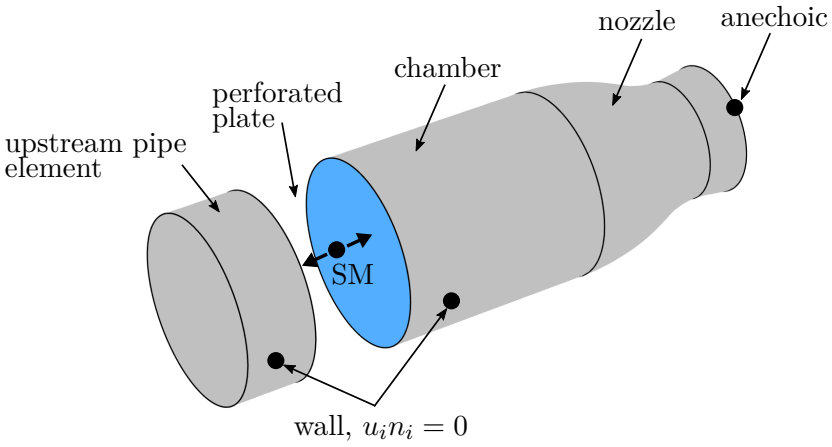

Fig. 4.13.: Extended computational domain including dome coupling.

in upstream direction to incorporate the dome volume, see Fig. 4.13. Altogether, a total number of approximately 100,000 DOF is solved for. Due to the non-isentropic flow in the perforated plate and the accompanied reduction in the total pressure, a slightly higher Mach number of 0.262 is present in the upstream pipe section than in the downstream section of 0.25. Furthermore, slip wall conditions are imposed to its remaining boundaries excluding potential damping mechanisms generated at its inlet.

4.2.2.2. Modeling of Scattering Properties in Time Domain

For the numerical simulations in time domain, the acoustic properties of the inlet are converted into a digital filter formulation. The experimental values and the corresponding filters for the reflection coefficient at the chamber inlet are shown in Fig. 4.14.

For case (I) the reflection coefficient R^{I} has a constant amplitude and a zero phase over the entire frequency range, which can conveniently be represented as a IIR filter with a single coefficient $b_0 = 0.6$, see Eq. (3.43) and Eq. (3.45).

The experimentally determined reflection coefficient $R^{\mathrm{II}}_{\mathrm{exp}}$ for case (II) is taken from (Kathan 2013), which is also referred to for further information about the measurement techniques. For modeling purposes an IIR filter $R^{\mathrm{II}}_{\mathrm{IIR}}$ is used with $M = 2$ and $N = 1$. The filter coefficients b_k and a_k are given in App. F. The experimental findings and the most accurate filter design found out are shown in Fig. 4.14. The IIR filter matches the experimental values only to a limited extent, which highlights the inflexibility of the filter generation. More accurate filter designs are possible for increasing polynomial order, i.e. a higher number of filter coefficients. However, as discussed before, in the frequency range below 2000 Hz and beyond 3500 Hz, spurious amplification of acoustic amplitudes due to artificially high values for the reflection coefficients is likely to occur. In frequency domain, in turn, the experimental values can directly be used or interpolated in between the given frequency points, which is a great advantage in terms

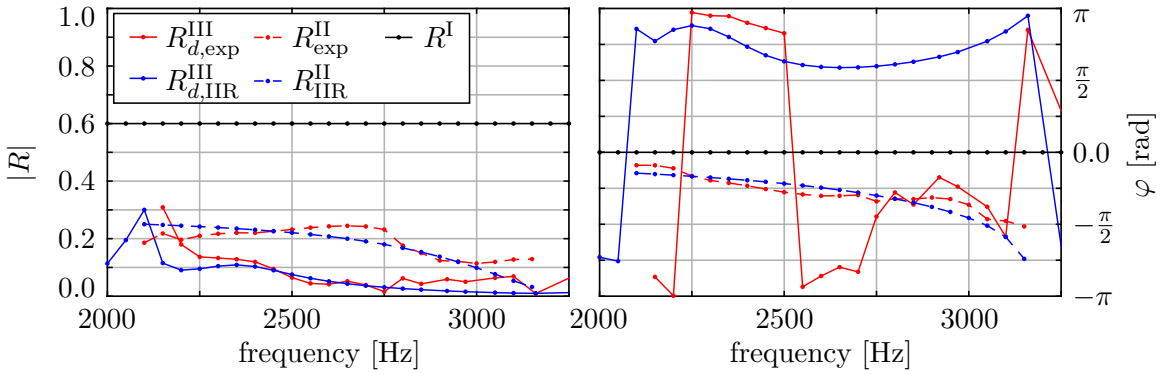

Fig. 4.14.: Experimentally evaluated reflection coefficient for the cases (I)-(III) together with their IIR filter representation.

of pre-processing efforts and accuracy in the simulation.

Finally, for case (III) the scattering matrix of the perforated plate is imposed on the interface between chamber and the upstream pipe element. First, the corresponding IIR filter for the matrix reflection coefficient downstream $R^{III}_{d,IIR}$, which is based on polynomials orders of $M = 5$ and $N = 5$, as well as its corresponding experimental values $R^{III}_{d,exp}$ are compared to R^{II}_{exp} and R^{II}_{IIR}, respectively, in Fig. 4.14. The filter accuracy is rather poor in the lower frequency range. Moreover, in the higher frequency range especially the phase values deviate strongly from the experimental findings. To increase accuracy, a higher filter order was investigated and turned out as inadequate due to the already described artificial strong amplification at very low frequencies.

In Fig. 4.15 the entire scattering matrix is shown in terms of experimental values and IIR filter designs. Besides the already discussed discrepancies in case of R^{III}_{d}, stronger deviations are found for the phase of the reflection coefficient upstream R^{III}_{u}. The overall accuracy for the remaining coefficients is rather high. The polynomial orders of the filters are reported in Tab. 4.2 and the coefficients are explicitly given in App. F.

In Sec. 3.3.1, different strategies were suggested to circumvent the problematic evaluation of boundary conditions at complex frequencies for the T_1 mode in case of eigenfrequency studies. Considering R^{II}_{exp} as well as SM^{III}_{exp} and their corresponding filter representations around the T_1 eigenfrequency, see Fig. 4.14 and Fig. 4.15, a rather constant behavior is observed. Probably, this is due to the compactness of the perforated plate in axial direction and the therefore very small time delays between ingoing and

Tab. 4.2.: Polynomial orders for the cases (I)-(III) and each scattering matrix element for the perforated plate.

	R^{I}	R^{II}_{IIR}	$T^{III}_{u,IIR}$	$R^{III}_{d,IIR}$	$R^{III}_{u,IIR}$	$T^{III}_{d,FIR}$
M	0	2	2	5	2	0
N	0	1	0	5	2	0

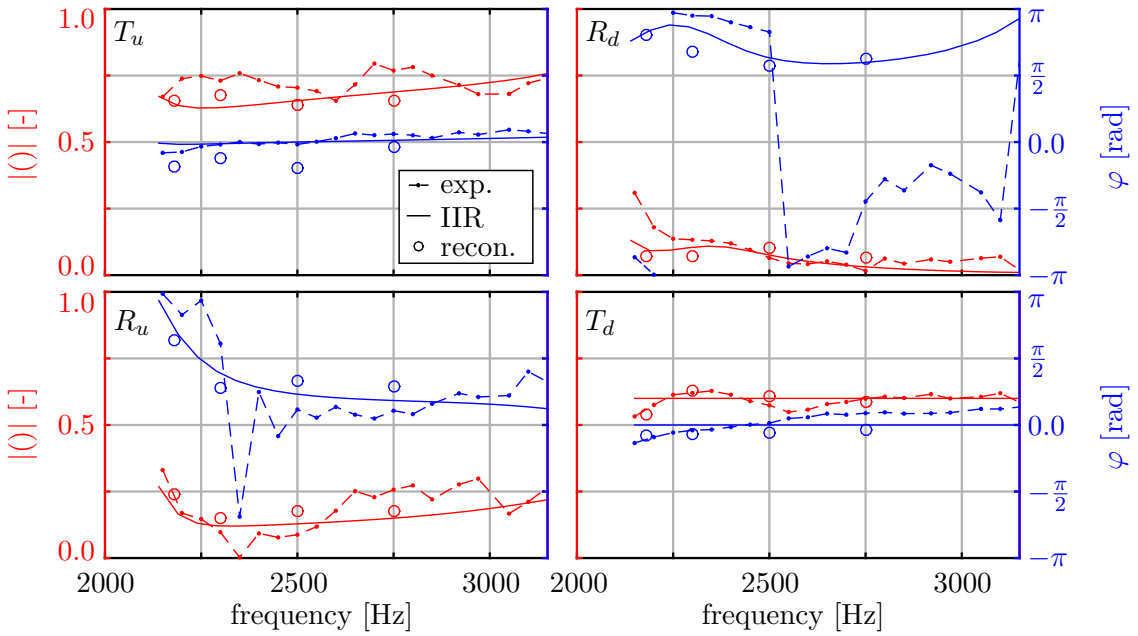

Fig. 4.15.: T_1 scattering matrix for the perforated plate: Experimental findings, IIR filter representation and reconstruction in time domain for case (III).

reflected or transmitted waves. Consequently, it is assumed that amplitude and phase do not change with damping rate, which corresponds to modeling strategy 2 in Sec. 3.3.1.

4.2.2.3. Complex Frequencies and Mode Shapes

While eigenvalue studies are performed in frequency space, decaying pressure signals, initially modulated by an impulse excitation, are monitored and a windowing FFT procedure is applied to compute the mode frequency and damping rate in time domain (Morgenweck 2013; Schulze et al. 2013b). The experimental findings are taken from (Kathan 2010) and compared to numerical findings for the T_1 mode in Tab. 4.3. In case (I), the time domain results already reported in (Morgenweck 2013) are presented, which are based on the same modeling and computational procedures as applied in this thesis. Furthermore, eigenvalue studies are also conducted on the basis of the time domain IIR filter values, which allows for a direct comparison between the numerical methodologies.

Overall, the simulated eigenfrequencies f for (I)-(III) are in good agreement with the experimental results. Time domain and frequency space consistently predict the frequency slightly too low for case (I). In contrast, small overpredictions are observed for case (II). Apparently, R^{I} and R^{II} do not fully reflect the time lags of the dome subsystem. Especially the phase information seems to be inaccurate. In case (III), excellent agreement of f is observed for the eigenvalue solution in frequency space. Essentially, the direct computation of the wave propagation in the dome and chamber

Tab. 4.3.: Comparison of eigenfrequencies f [Hz] and damping rates λ [rad/s] for the considered cases (I)-(III). The experimental data of (III) is also used for the comparison with the numerical results of (II) and of (III)/filter

	(I)		(II)		(III)		(III)/filter	
	f	λ	f	λ	f	λ	f	λ
experiment	2160	63			2160	585		
time domain	2134	35	2207	680	2207	347	2207	347
frequency space	2141	37	2215	583	2158	480	2177	291

together with the coupling description of the perforated plate captures the relevant phase dynamics in the dome subsystem accurately. In contrast, the direct incorporation of the dome in time domain still overpredicts the frequency, which is the consequence of the inaccurate IIR filter representation.

Concerning the damping rates, time domain and frequency space results are in very good agreement for case (I), but deviate from the experimental findings. However, another analytical methodology predicts the damping rate considerably lower as well (Köglmeier et al. 2010). It is therefore concluded that the numerical findings describe the realistic damping rate accurately. The reason for the experimental inaccuracy probably originates from the intensity flux based post-processing method, used to approximately determine the damping rate under the hypothesis of an energetically neutral inlet boundary (Kathan 2010).

Experimental findings are more trustful for case (II), since assumptions for the intensity fluxes do not have to be made. Excellent agreement with experimental data in terms of damping rates is obtained on the basis of the eigenvalue solution. Therefore, the applied modeling strategy for the frequency dependent boundary conditions seems to be adequate in frequency space. In contrast, in time domain considerable discrepancies are observed again. Apparently, the insufficient accuracy of the IIR filter in terms of both amplitude and phase is accompanied with an overprediction of damping.

In case (III), both time domain and frequency space simulations consistently predict the damping rate too low. A difference between the experiment and the numerical case (III) is, however, that the acoustic loss mechanism present at the choked inlet including strong spatial mean flow gradients, is not incorporated in the numerical simulations, cf. Fig. 4.7. Apparently, approximately 20 % of the system damping originates from the choked inlet region. In case (II) the applied reflection coefficient R^{II} also contains the choked inlet effects and the damping rates in the numerical simulations, especially in the frequency based approach, agree therefore well with the experimental findings.

Applying the filter values in frequency domain for case (III) yields considerably better agreement between eigenvalue study and time domain for both mode frequency and damping rate. Both methodologies provide similar results if the boundary conditions are equivalent. This conclusion is confirmed by case (I), which is also based on a consistent boundary treatment.

Altogether, frequency space simulations on the basis of eigenvalue studies provide more accurate results than the time domain simulations if frequency dependent boundary conditions are required. The dome coupling concept provides an adequate method to incorporate the dome dynamics into the computation. The presented test case indicates that it is generally not sufficient to lump the dome dynamics into a single reflection coefficient. Although excellent agreement with experimental findings is observed for the damping rate, the mode frequency is predicted more accurately when the wave propagation within the dome is directly computed and relevant time lags are therefore consistently described. In consequence, further modeling of additional boundary conditions in the dome itself is then necessary, which might considerably attribute to the overall damping.

Fig. 4.16 presents a comparison of the mode shapes of the cases (II) (left) and (III) (right) in order to illustrate the effect of dome coupling on the pressure distribution. The mode shapes are taken from the frequency space based computations and plotted in terms of normalized pressure amplitude $|\hat{p}|$ (top) and its real part $\mathfrak{Re}(\hat{p})$ (bottom). Both cases (II) and (III) clearly show the typical T_1 mode structure over the cross-section. However, while case (II) exhibits acoustic amplitudes only in the chamber and nozzle sections, the coupling allows for the propagation of acoustic fluctuations into the dome in case (III). The point-to-point coupling can be observed again showing that the T_1 modes in chamber and dome are oriented in the same direction. Furthermore, the reduction of amplitudes from the chamber into the dome according to the scattering matrix is visible.

In both cases (II) and (III) the pressure amplitude is not constant in axial direction, which is a direct consequence of the mean flow on the mode shape in the chamber and nozzle section. The influence of the mean flow on the distribution of acoustic amplitudes plays a crucial role for the understanding of the interaction between acoustics and combustion, see Sec. 6.5 and Sec. 7.5.

Furthermore, the axial pressure distribution is considerably affected by the dome coupling. Especially $\mathfrak{Re}(\hat{p})$ shows that in case (III) the real part is considerably shifted upstream. This behavior is explained by the axial extension of the domain, which changes the amplitude and phase distribution. A different domain length and an altered mode shape also influence the eigenfrequency, which explains why only case (III) provides accurate predictions of f, see Tab. 4.3.

The decoupling of the acoustic system from the environment at the nozzle is also visible. Downstream of the sonic line only insignificant pressure amplitudes are found, indicating that this region is irrelevant for the T_1 mode. The boundary condition at the nozzle exit can thus be set arbitrarily. In terms of computational effectiveness, however, non-reflecting conditions show best properties resulting in faster convergence and shorter computational times.

From the experimental and numerical results important insights into the system damping are obtained. The findings indicate a significant increase of damping by almost a factor of 20 as soon as the partially reflecting boundary condition is included. The additional dissipation of acoustic energy is probably provided by shear layer instabilities

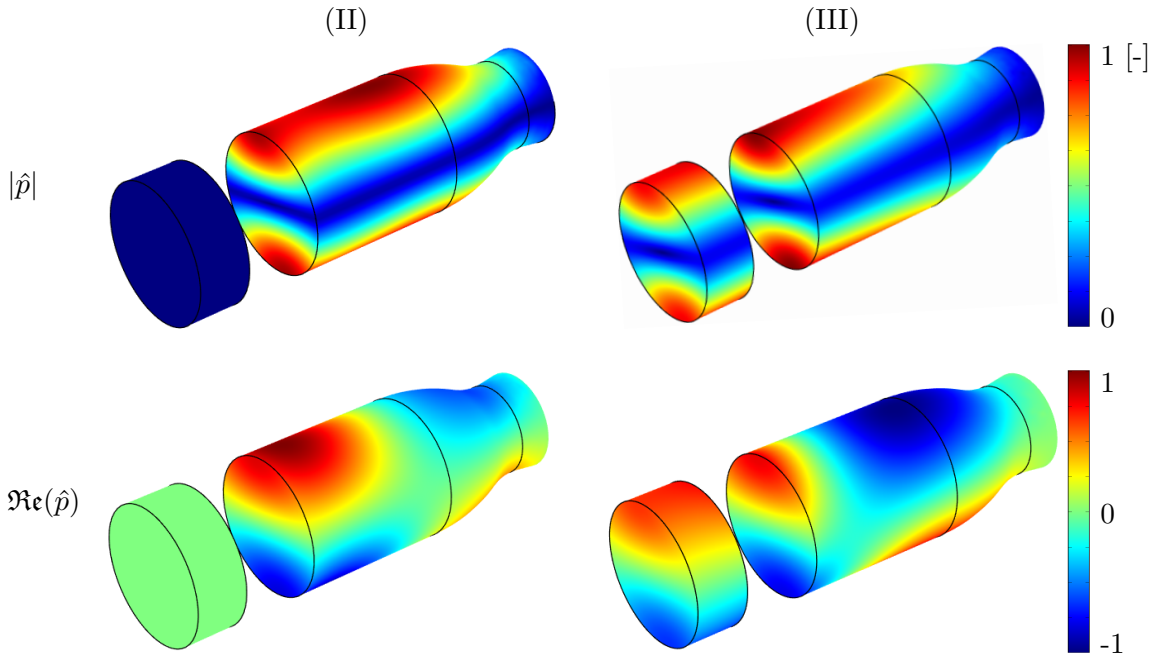

Fig. 4.16.: Mode shapes of case (II) (left) and case (III) (right) taken from the eigenvalue studies: Normalized pressure amplitudes $|\hat{p}|$ (top) and its real part $\mathfrak{Re}(\hat{p})$ (bottom).

(Schulze et al. 2015b; Temmler et al. 2015; Wagner et al. 2013a) downstream of to the perforated plate and also at the choked condition at the inlet of the system, see Fig. 4.7. As described in Sec. 2.2, the transfer of acoustic energy into fluctuating vortical structures dominates the damping mechanism.

Another essential conclusion is drawn on the basis of case (I): The flux of acoustic intensity through the nozzle is the only damping mechanism involved, which is dominated by the convective transport of acoustic energy. Comparing the computed damping rate for (I) with (II) and (III) shows that the damping capabilities of the nozzle flow is weak for the T_1 mode. The low nozzle damping can essentially be explained by perpendicularly oriented transverse acoustic motion and mean flow. In contrast, longitudinal modes are drastically damped by the nozzle, since mean flow and acoustic motion are aligned in parallel, see App. G. In terms of modeling, especially in the time domain, the high damping rates for longitudinal modes is advantageous. Essentially, the influence of inaccurate filter designs potentially amplifying amplitudes in the longitudinal frequency regime, i.e. the low frequency range, is compensated to a certain degree. Furthermore, the impact of longitudinal modes propagating close to the eigenfrequency of the T_1 mode can be neglected, which allows for an adequate characterization of boundary conditions and Flame Transfer Functions.

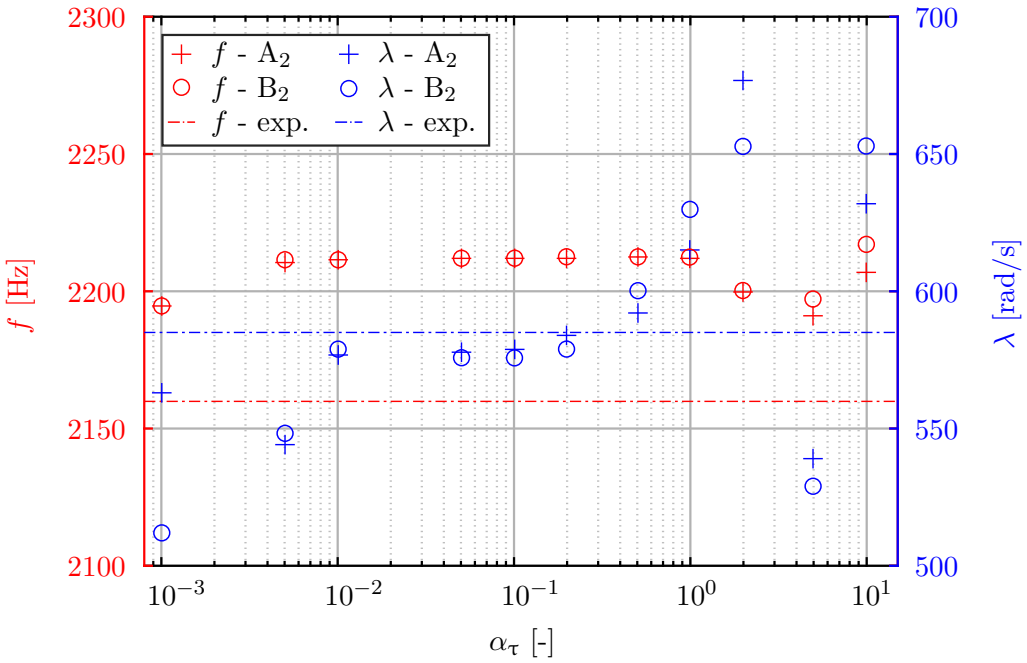

Fig. 4.17.: Dependence of T_1 eigenfrequency and damping rate on stabilization coefficient α_τ for mode A_2 and mode B_2.

4.2.2.4. Influence of Grid Resolution and Stabilization Parameter on Eigenfrequency and Damping Rate

On the basis of stabilized finite element Method, the frequency space LEE provide accurate predictions of the damping rates and frequency for the T_1 mode for the non-reactive experimental configuration. However, the involved stabilization coefficient α_τ, see Eq. (3.13) and Eq. (3.14), is so far not uniquely defined and appears as a source of uncertainty. Hence, a study of the α_τ influence on the eigenfrequency and damping rate was conducted.

According to Eq. (2.47), two solutions A_2 and B_2 for the T_1 mode exist, which are shifted by $\pi/2$ in azimuthal direction. Since in the investigated configuration provides rotational symmetrical conditions both in terms of the geometry but also for the mean flow, see Fig. 4.1 and Fig. 4.13, it is expected that the damping rates for the A_2 and B_2 modes are equal. This criterion is used to find an optimum value for the stabilization coefficient α_τ. To demonstrate the procedure, the non-reactive test case configuration (II) from the previous section is investigated.

In Fig. 4.17 the frequencies and damping rates for mode A_2 and mode B_2 are presented for increasing values of the stabilization coefficient starting from a lower limit of $\alpha_\tau = 10^{-3}$. The experimental comparison data is also shown. It can be seen that the eigenfrequencies f for A_2 and B_2 are constant and in very good agreement for a wide range of α_τ. At the lower limit of α_τ deviations occur. Furthermore, for very high values, variations of frequencies and discrepancies between both modes are observed, which indicate that the optimum range for α_τ is already exceeded.

In general, the behavior of the damping rates is comparable between mode A_2 and mode B_2. However, strong deviations between mode A_2 and B_2 occur both in the lower and higher limits of α_τ. Nevertheless, constant damping rates within the interval $\alpha_\tau = [10^{-2}\,;\, 2 \cdot 10^{-1}]$ can be identified, in which also good agreement between both modes is present. Furthermore, the simulated damping rates match the experimental comparison data.

In conclusion, an optimum stabilization coefficient α_τ can be found iteratively on the basis of minimized discrepancies between the complex frequencies of mode A_2 and mode B_2. This procedure is especially independent of experimental comparison data and allows for the predictive usage of the eigenvalue solution technique.

4.3. Absorbers under Grazing Flow Conditions

In rocket engines, absorbers are used to damp acoustic amplitudes. Often, absorbers are located close to the face plate, see Fig. 1.1. In this region, the Mach number is usually low. However, acoustic simulations including absorbers might still be subjected to unphysical growth of numerical instabilities, cf. Sec. 2.7.4. Hence, the capabilities of the LEE to describe the influence of such lateral boundary conditions under grazing flow situations is discussed in this section.

As shown in the previous sections, frequency space LEE are more suitable for linear acoustic analysis and provide shorter turnaround times. The following investigations are therefore based on frequency space evaluations and time domain simulations are not conducted.

First, longitudinal wave propagation over an absorbing liner configuration for different Mach number flows is considered to highlight the general applicability of the LEE under grazing flow conditions. Afterwards, the non-reactive test case equipped with an absorber ring is considered to validate the LEE for the prediction of the absorber influence on the T_1 mode.

4.3.1. Longitudinal Wave Propagation - GIT Test Case

With focus on the investigation and development of liners for aero-engine applications, the Grazing-Incidence-Tube (GIT) test case was operated at the NASA Langley Research Center to provide experimental data for the validation of frequency dependent, impedance boundary conditions under grazing flow situations in numerical tools for longitudinal wave propagation (Jones et al. 2003, 2005). For given mean flow states, excitation amplitude and frequency, the numerical simulations seek for the detailed distribution of pressure in terms of Sound Pressure Level (SPL) and phase along the liner. Since absolute values of pressure are of interest, accurate boundary conditions at inlet, exit and at the liner are of particular importance. Furthermore, the acoustic pressure excitation amplitude and phase has to match experimentally imposed values.

Several approaches were reported to describe the liner effect on pressure amplitudes

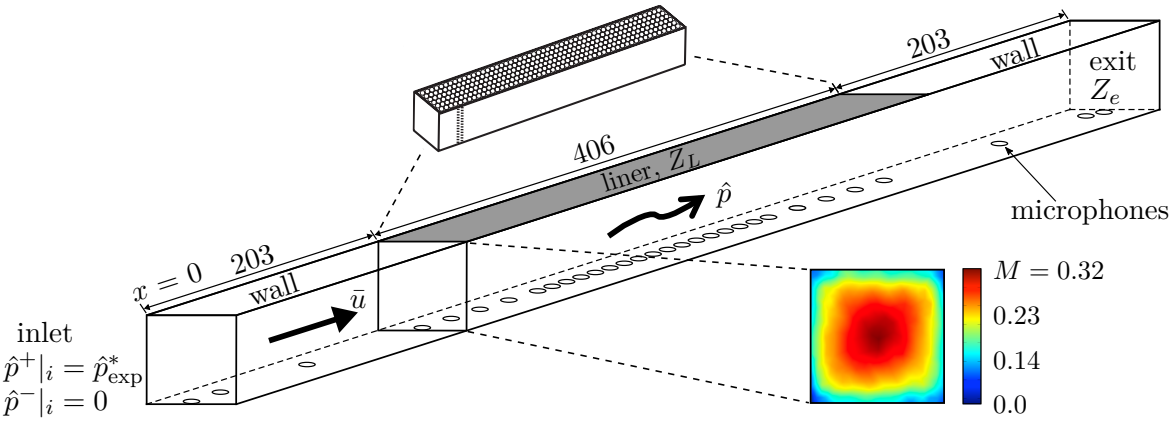

Fig. 4.18.: Detailed illustration of the GIT test case including the location of the liner, boundary conditions, microphone positions as well as the Mach number profile in the duct (Jones et al. 2005). Dimensions are given in [mm].

with different levels of accuracy (Li and Thiele 2004; Morgenweck 2013; Richter et al. 2007). Such simulations are time consuming and require a rather complex modeling of the frequency dependent boundary conditions. The results are, however, in good agreement with the experimental data.

4.3.1.1. Test Case Description

The GIT test rig consists of a ceramic tubular liner matrix, which is mounted to the top wall of a rectangular duct of quadratic cross-section with 51 mm side length, see Fig. 4.18. The liner matrix with a length of 406 mm consists of parallel, cylindrical cavities, each with a diameter of 0.6 mm and depth of $l = 85.6$ mm, which are arranged perpendicular to the wall. Altogether, the surface porosity amounts 57 %.

The sinusoidal, single frequency excitation is located 203 mm upstream of the liner. The outlet is 203 mm downstream, where a silencer reduces reflections to nearly anechoic conditions. At the bottom wall, 31 microphones are used to record the dynamic pressure over the entire test rig length. Opposite to the liner the measurements locations are concentrated.

For the numerical studies, the impedances of the liner and the exit are directly applied to the corresponding boundaries. The liner impedance is experimentally determined at the liner surface and assumed to be homogeneously distributed over the entire liner surface. As shown in the test case description (Jones et al. 2005), the liner impedance is obtained through the solution of a discretized convective Helmholtz equation, cf. Eq. (2.38), by iteratively varying the impedance value at the boundary until the complex pressure amplitudes match the given experimental measurements. Two- and three-dimensional computations were performed for that purpose.

The measurements were conducted for different operation points. The operational

Tab. 4.4.: Operational conditions for the GIT test case.

$\bar{T}$ [°C]	$\bar{p}$ [Pa]	M [−]
22.6	101,945	0.0
23.0	109,501	0.079
23.6	103,434	0.172
23.6	107,473	0.255

conditions in terms of temperature $\bar{T}$, pressure $\bar{p}$ and Mach number M of the air flow are given in Tab. 4.4. The SPL is set to 120 dB ($\hat{=} 20\,\mathrm{Pa}$) throughout the entire study and the frequencies $f = 700, 1000, 2000$ and $3000\,\mathrm{Hz}$ are simulated. The Mach number distribution was experimentally determined and is given in the test case description (Jones et al. 2005).

The Mach number is varied in order to investigate the influence of grazing flow on the damping properties of the liner as well as on the numerical stability. A maximum frequency of 3000 Hz is considered. Variations of sound pressure levels are not subject to the present investigation. However, conclusions of the presented numerical methodology's suitability are equally valid for different amplitudes, as long as the assumption of linear acoustics is not violated. The excitation amplitude is set to 120 dB throughout the entire investigation.

4.3.1.2. Exit and Liner Impedances

The impedances of the exit and the liner are given in the test case description (Jones et al. 2005). The frequency dependent exit impedance Z_e is shown in Fig. 4.19 in terms of its resistance R_e and its reactance X_e, hence

$$Z_e = R_e + \mathrm{i}X_e. \tag{4.9}$$

The mode index mn is dropped here, since only longitudinal modes are present.

The reactance manifests the temporal storage of acoustic energy and shows only weak dependence on both frequency and Mach number. The resistance, in turn, represents the loss of acoustic energy and clearly depends on frequency and Mach number. Overall, the exit impedance for the considered frequency and Mach number range can roughly be estimated by

$$Z_e = 1 + \mathrm{i}0, \tag{4.10}$$

for low Mach numbers, which corresponds to the condition of an anechoic exit, cf. Eq. (2.100). For higher Mach numbers the deviations of the exit impedance from an anechoic exit condition become larger. To fully account for the reflection properties of the exit, the given values for the exit impedance are used in the simulations.

The liner impedance Z_L is shown in Fig. 4.19 and is equivalently defined by

$$Z_L = R_L + \mathrm{i}X_L, \tag{4.11}$$

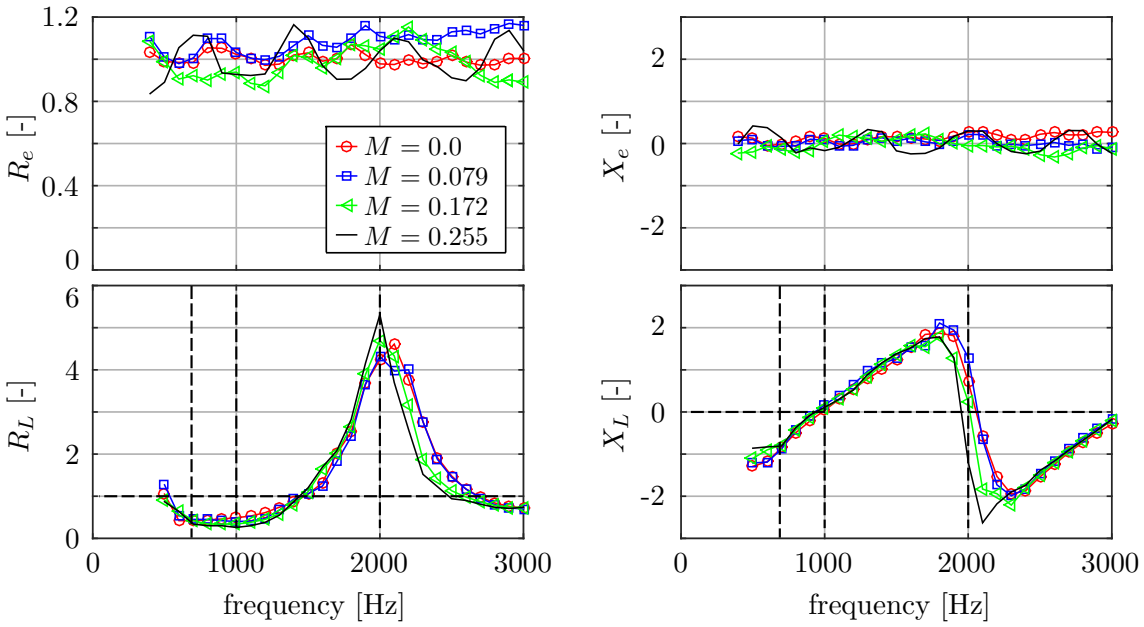

Fig. 4.19.: Exit (top) and liner (bottom) impedances in terms of resistance (left) and reactance (right) for different Mach numbers (Jones et al. 2005).

In general, strong damping of acoustic waves is expected if the liner impedance matches non-reflecting conditions according to Eq. (4.10) best. Among the considered frequencies, these conditions are approached closest by resonant frequencies of 1000 Hz and 3000 Hz. For a frequency of 700 Hz considerably higher values than unity for the liner resistance and significant contributions from the liner reactance lead to only weak damping capabilities. An anti-resonant frequency is found at approximately 2000 Hz, where maximal values for the resistance are reached, while the reactance shows an inflection point. Therefore, in case of an excitation frequency of 2000 Hz weak damping of acoustic waves is expected.

In general, the x-th eigenfrequency for a single liner hole is given by

$$f_{L,x} = \frac{(2x-1)c}{4l}. \tag{4.12}$$

Considering the length of a single hole l, the first and second harmonics are found at frequencies of $f_{L,1} = 1002$ Hz and $f_{L,2} = 3006$ Hz. As discussed before, high damping capabilities are expected for these frequencies. In case of an eigenfrequency, a standing mode pattern is established in the single hole. On the one hand, viscous dissipation inside the hole contributes to damping. On the other hand, the velocity anti-node at the single hole exit leads to a strong coupling between the hole acoustics and grazing flow and damping is greatly enhanced due to the generation of vortical structures in the vicinity of the hole exit. In turn, for the anti-resonant frequency at 2000 Hz, the single hole can hardly be excited by the acoustic waves. Consequently, dissipative effects due to the coupling do not occur. In that situation the liner essentially acts similar to a slip

wall, which is defined as the limit case of

$$Z_L \to \infty. \tag{4.13}$$

For an excitation of 2000 Hz, high values for the liner resistance are confirmed in Fig. 4.19.

4.3.1.3. Mean Flow Profiles

For the different Mach numbers detailed two-dimensional mean flow profiles are provided for the GIT test case at axial positions of $x = 203, 356, 559$ mm. The Mach numbers listed in Tab. 4.4 represent averaged values over the three measurement planes. In Fig. 4.18 the mean Mach number distribution is illustratively shown at an axial position of $x = 203$ mm for the case of $M = 0.255$. The maximal Mach number in the center reaches 0.32. The measured profiles can directly be used in the simulations and the generation of a mean flow by CFD means is not necessary here. Furthermore, mean density is determined by

$$\bar{\rho} = \frac{\bar{p}}{\mathcal{R}\bar{T}}, \tag{4.14}$$

cf. Eq. (2.10), and speed of sound by

$$c = \sqrt{\kappa \mathcal{R} \bar{T}}, \tag{4.15}$$

for an ideal gas.

4.3.1.4. Numerical Setup

The pressure distributions are determined on the basis of isentropic LEE in frequency space. Since the frequencies are explicitly given, the frequency response is calculated using Eq. (3.16).

To show the influence of the numerical grid on the results, three stages of resolution are used reaching from approximately 50,000 elements for the coarsest grid to approximately 210,000 elements for the highest resolution, see App. H. For all grids linear shape functions are used on tetrahedral elements in an unstructured pattern. The time consumption for a single frequency calculation on a standard 2.6 GHz, 8 Gbyte RAM machine varies between 5-30 s.

4.3.1.5. Acoustic Pressure Distributions

For the simulation of the GIT test case the following boundary conditions are applied, see Fig. 4.18. An acoustic driver is used at the inlet to emit acoustic waves propagating

in positive x-direction. Using the decomposition of an acoustic wave into downstream ($\hat{p}^+$) and upstream ($\hat{p}^-$) running waves by[6]

$$\frac{\hat{p}^{\pm}}{\bar{\rho}c} = \frac{1}{2}\left(\frac{\hat{p}}{\bar{\rho}c} \pm \hat{u}\right), \tag{4.16}$$

the source is modeled conveniently by setting the downstream running wave at the inlet $\hat{p}^+|_i$ according to the experimentally given sound pressure level $\hat{p}|_{\text{exp}}$ with zero phase, viz.

$$\hat{p}^+|_i = \hat{p}|_{\text{exp}}, \tag{4.17}$$

see Tab. 4.4, and the upstream running wave at the inlet surface accordingly to zero, viz.

$$\hat{p}^-|_i = 0. \tag{4.18}$$

At the exit the acoustic impedance is imposed according to Eq. (2.89), i.e.

$$\left.\frac{\hat{p}}{\hat{u}_i n_i \bar{\rho}c}\right|_e = Z_e. \tag{4.19}$$

Motivated by the purely longitudinal wave propagation, it can be assumed that the impedance is homogeneously distributed over the exit plane.

In the simulations the liner structure is not resolved, but its impedance is used as boundary condition. As stated in the test case description (Jones et al. 2005), locally reacting properties of the liner cavities can be assumed. It is therefore sufficient to prescribe the liner impedance at the corresponding location. Furthermore, the given impedances are determined such that a single value represents the entire liner surface. In the simulation, the impedance value for a given frequency is hence homogeneously distributed over the entire liner plane.

The boundary layer at the liner surface is not resolved in the simulation. In general, the influence of the boundary layer on the acoustic propagation can be accounted for by a modified impedance boundary condition, which is proposed by (Myers 1980) and was already explained in Eq. (2.91). To use the modified boundary condition in the GIT test case, it is applied in a different form. As shown in (Morgenweck 2013) and (Schulze and Sattelmayer 2015b), an effective impedance can be derived, which reads

$$Z_{L,\text{eff}} = \frac{Z_L}{1 - M}, \tag{4.20}$$

and is based on the assumption that the axial wave number k_x and the free space wave number k are equivalent. The justification of this assumption can be found in (Schulze and Sattelmayer 2015b).

[6]Riemann invariants may be used as well, cf. Eq. (2.77) and Eq. (2.78).

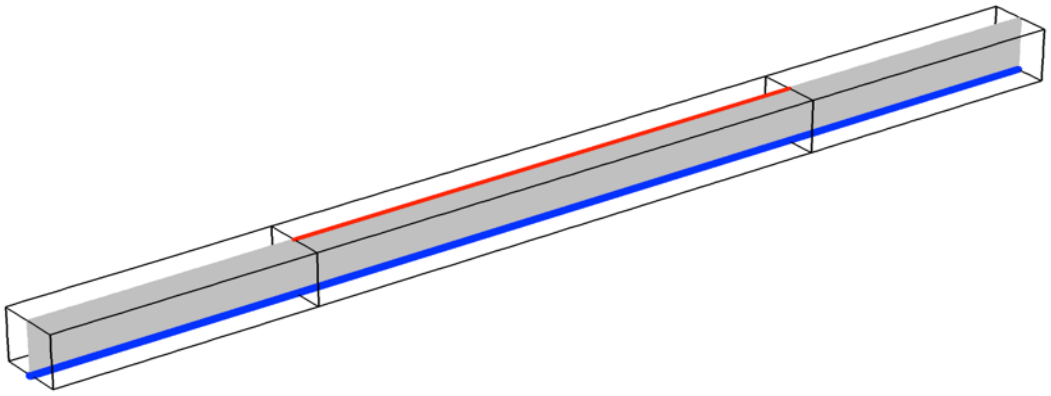

Fig. 4.20.: Cut-plane used to visualize pressure distribution (gray). Visualization lines used to plot surface normal velocity (red) and to compare numerical and experimental pressure values (blue).

In the simulation the effective impedance boundary condition is applied to the liner surface, viz.

$$\left.\frac{\hat{p}}{\hat{u}_i n_i \bar{\rho} c}\right|_L = Z_{L,\text{eff}}. \tag{4.21}$$

The remaining boundaries are modeled as free slip walls, cf. Eq. (2.72).

4.3.1.6. Results

In a first step, the fields of the acoustic pressure distributions are analyzed. For that purpose a representative cut-plane in the center of the computational domain is utilized, see Fig. 4.20. At the liner segment's surface the normal velocity component is considered as well. It is highlighted as a red line in Fig. 4.20.

For the following considerations a constant Mach number and hence constant axial mean velocity is used. Fig. 4.21 shows the real part of the pressure distribution $\mathfrak{Re}(\hat{p})$ in [Pa] for the excitation frequencies of 1000 Hz and 2000 Hz for the two Mach numbers $M = 0.0$ (top) and $M = 0.172$ (bottom). In general, the acoustic simulations on the basis of frequency space transformed LEE provide stable solution procedures and meaningful field results.

In Fig. 4.21, the propagation of a longitudinal wave is clearly visible with a wavelength according to the frequency. In case of a resonant frequency at 1000 Hz the acoustic wave is rapidly damped in the liner segment leading to almost complete attenuation at the exit for both Mach numbers $M = 0.0$ and $M = 0.172$. In turn, for an anti-resonant frequency at 2000 Hz, high pressure amplitudes are observed throughout the entire liner length with only moderate attenuation. It is also shown for both frequencies that the mode shape is influenced by the liner, leading to a slightly bowed wave front. Possible higher-order modes, however, are strongly damped due to the fact that the considered

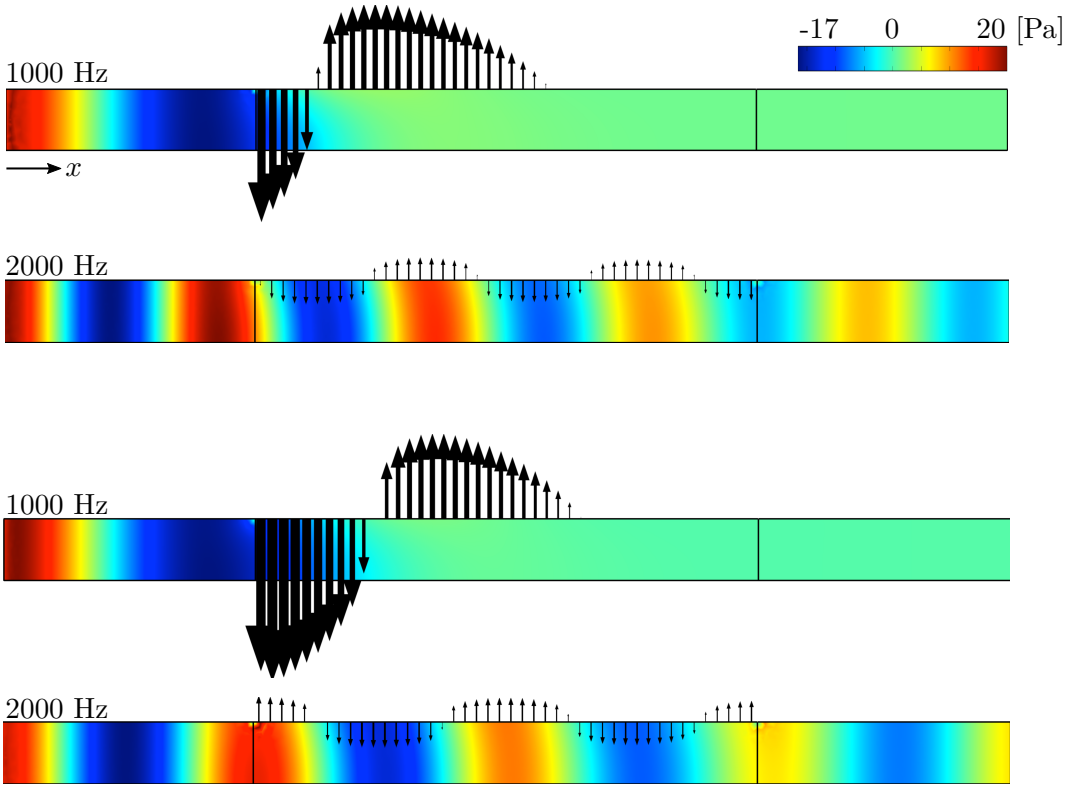

Fig. 4.21.: Pressure distribution $\mathfrak{Re}(\hat{p})$ for $M = 0.0$ (top) and $M = 0.172$ (bottom) together with liner surface normal acoustic velocity (arrows).

frequencies are well below the respective cut-on frequency, which is approximately 3400 Hz for the GIT test case. For that reason, higher-order modes do not play a role. In the segments upstream and downstream of the liner only planar waves are traveling.

To illustrate the liner effect, the transverse velocity pointing into and out of the liner, respectively, is also presented in Fig. 4.21 in form of arrows. The length of the arrows is equally normalized for all plots. Significantly higher velocities at the liner surface are observed for the resonant frequency at 1000 Hz than for the anti-resonant frequency at 2000 Hz for both Mach numbers $M = 0.0$ and $M = 0.172$. Furthermore, for the 1000 Hz case, relevant velocity contributions are only present until the wave is almost completely attenuated. For the anti-resonant case at 2000 Hz, velocities are observed within the entire liner length, which get only weakly reduced. As explained before, at the eigenfrequency of the liner holes, a velocity anti-node is established at the hole exit leading to high velocities, cf. Sec. 4.3.1.2. For an excitation of 2000 Hz, the single liner hole acoustics cannot considerably be excited, leading to rather transverse acoustic velocities at the hole exit. Consequently, the interaction of the single hole acoustics with the grazing flow is weak. Therefore, only low damping effects are present.

Similar observations are made for the other Mach numbers of $M = 0.079$ and $M = 0.255$ and frequencies of 700 Hz and 3000 Hz (not shown). Due to the influence of

convective transport by the mean flow the wavelengths is slightly higher for increased Mach numbers. Consequently, also the distribution of the transverse velocity over the liner segment is affected.

Altogether the conclusions drawn from the experimentally determined liner impedance in terms of damping properties before are clearly confirmed by the investigations of the field pressure distribution and transverse velocity, cf. Sec. 4.3.1.2.

The obtained pressure distributions are compared to experimental values using a constant Mach number distribution. For that purpose the computed pressure values are taken along the blue line illustrated in Fig. 4.20, which coincides with the microphone locations, see Fig. 4.18. In Fig. 4.22 the pressure distributions are shown in form of SPL with a reference pressure of 20 [μPa], viz. Ehrenfried (2003)

$$\mathrm{SPL} = 20 \log_{10} \left(\frac{\mathfrak{Re}(\hat{p})/\sqrt{2}}{20[\mu\mathrm{Pa}]} \right), \tag{4.22}$$

together with the comparison data for all frequencies and the two highest Mach numbers (left column). Additionally, the phase of pressure is shown (right column). Altogether, an excellent agreement between the numerical results and the measured data for both SPL and phase is obtained. The complex interaction between the liner influence on the wave propagation and the impact of the exit impedance is accurately predicted by the frequency transformed isentropic LEE. The excellent comparison is, of course, also a result of the accurate liner and exit impedances given in the test case description (Jones et al. 2005).

Three different numerical resolutions are tested to analyze grid convergence, see App. H. The impact of the grid resolution is exemplarily shown in Fig. 4.22 in case of $M = 0.172$ and for two frequencies of 1000 Hz and 2000 Hz. For both SPL and phase a very good agreement between the different grid resolutions is obtained.

Therefore, it can be concluded that grid convergence is reached for this Mach number and frequency. Consequently, the coarsest grid is used for all simulations of the GIT test case. The chosen excitation method seems to adequately represent the experimental excitation procedure. The rather coarse discretization is sufficient to describe accurately the wave propagation and capture the impedance boundary condition, see App. H. The numerical data reproduces small variations very accurately and even captures the sharp interfaces between the wall segments and the liner segment.

Concerning the relevance of the mean Mach number profile, a weak influence on the pressure distribution is observed in this study. Especially the phase values, which strongly depend on the mean axial velocity, are met quite well using a constant Mach number distribution. However, small deviations between the numerical results and the experimental measurements of the phase are sometimes observed in the section downstream of the liner, see e.g. $M = 0.172$ as well as $M = 0.255$ for a frequency of 1000 Hz in Fig. 4.22.

For the case of a resonant frequency at 3000 Hz small deviations for the SPL are observed for Mach numbers of $M = 0.172$ and $M = 0.255$. Particularly the slope of SPL with respect to the axial coordinate seems to be slightly underpredicted by the calcu-

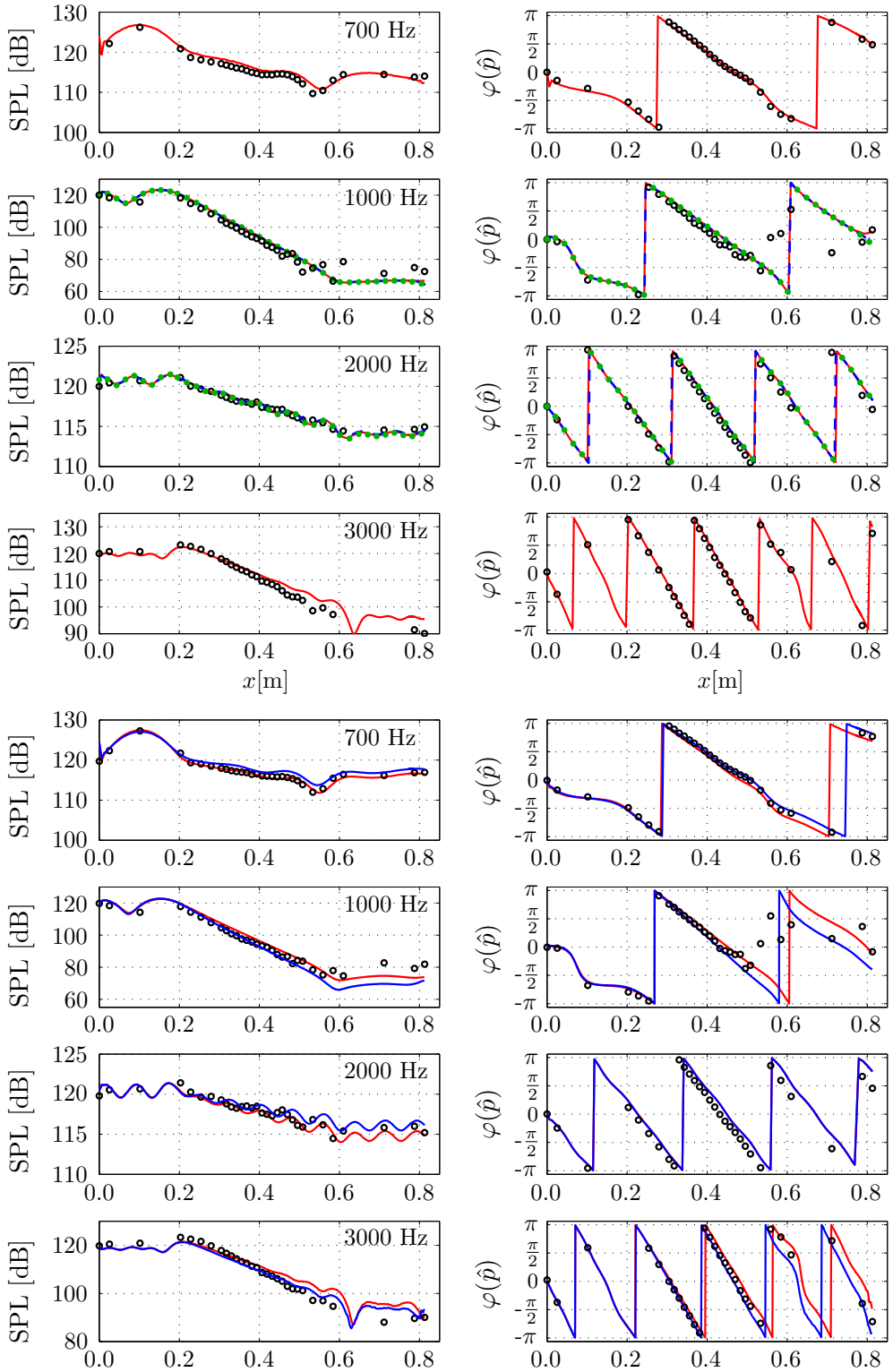

Fig. 4.22.: SPL (left) & phase (right) of $\hat{p}$; $M = 0.172$ (top) & $M = 0.255$ (bottom): Exp. (∘); coarse grid (•), medium grid (–), fine grid (--); effective imped. (–).

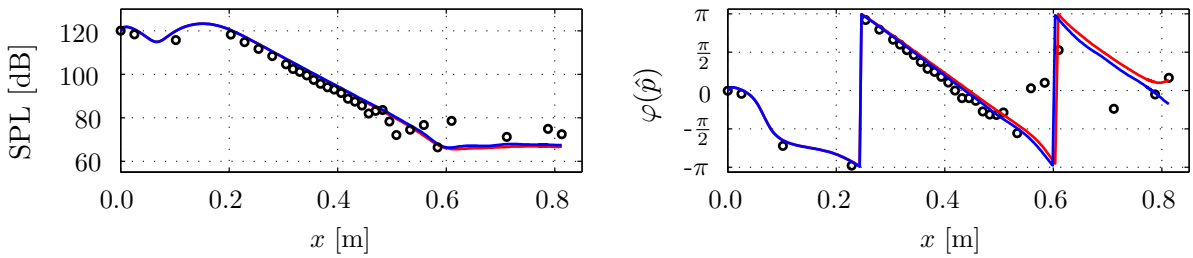

Fig. 4.23.: Comparisons of constant Mach number distribution and detailed profile for SPL (left) and phase (right): experimental values (∘); constant Mach number (–); detailed Mach number profile (–).

lations. Small errors in the educed liner impedances from experimental considerations, however, might yield to such deviations in the numerical results.

In case of $M = 0.255$ the impact of the effective impedance on the SPL is analyzed, cf. Eq. (4.20). Fig. 4.22 shows the results in comparison to the results on basis of the unmodified impedance. Small deviations are found both for the SPL and for the phase. In general, the effective impedance seems to be better suited for a more accurate representation of the slope of SPL over axial distance for 1000 Hz and 3000 Hz. Interestingly, for increasing axial distance the inaccuracy of the calculated phase values seem to increase in case of the unmodified impedance, while the effective impedance predicts accurate results for almost all cases. For 2000 Hz excitation the deviations between both impedance formulations are barely noticeable, which can be explained by the only weak damping effects for this frequency.

From the results, strong damping properties of the liner for wave propagation in case of resonant frequencies at 1000 Hz and 3000 Hz are observed once again. For the anti-resonant frequency at 2000 Hz the liner damping capabilities are low for all Mach numbers. For increasing Mach numbers the damping of the acoustic waves is reduced, yielding higher SPL values downstream of the liner, except for an excitation frequency of 3000 Hz, for which the exit SPL values are roughly the same for all Mach numbers.

Additionally, the comparison of SPL and phase for $M = 0.0$ and $M = 0.079$ is given in App. H.

Finally, the influence of the mean flow profile on the pressure distribution is studied. For this purpose, the case of a resonant frequency at 1000 Hz and a Mach number of $M = 0.172$ is employed considering the detailed Mach number distribution. A comparison is given in Fig. 4.23. Clearly, the influence of the detailed mean axial velocity distribution is of minor importance. The SPL is only slightly changed in the section downstream of the liner. The deviations of the phase increases in axial direction. Overall, the discrepancies are very small. The influence of the mean flow profile on the damping properties of the GIT test case was also consistently reported in (Jones and Nark 2010).

4.3.2. Absorber Influence on First Transverse Mode

In this section, the interaction of absorbers under grazing flow conditions with transverse modes is investigated. Time domain results were presented in (Schulze et al. 2012) and (Köglmeier et al. 2014a). In (Schulze et al. 2012) quite inaccurate results for the T_1 mode damping rate were reported and the results could only be analyzed qualitatively. In turn, (Köglmeier et al. 2014a) presented reasonable results on the basis of quiescent flow conditions without considering any grazing flow.

To demonstrate the capabilities of the chosen modeling approach to capture the influence of an absorber ring under grazing flow conditions on the T_1 mode and investigate the impact of an absorber ring on the system dynamics, the frequency response is determined and compared to experimental findings for different absorber cavity lengths in a first step. Afterwards, eigenfrequencies and damping rates for the T_1 mode are validated. Finally, the impact of the absorber ring position and the cavity length on acoustic damping are analyzed.

4.3.2.1. Test Configurations

The validations and investigations are carried out for the non-reactive test case described in Sec. 4.1 for nozzle A. Mass flow, mean pressure and temperature are the same, see Tab. 4.1. However, the chamber is additionally equipped with an absorber ring, which comprises 20 cavities with a diameter of $D_A = 8$ mm. The cavities are equidistantly distributed in circumferential direction and set to the same length, which is varied between $l_A = 30$ mm and 45 mm in 5 mm steps. At first, to simulate a typical rocket engine arrangement, the absorber ring is located closely to the face plate, i.e. to the perforated plate. This absorber ring location is referred to position 1 (P1), see Fig. 4.24 (left). The distance between the perforated plate and the absorber ring amounts $l_{\mathrm{P1}} = 36$ mm. Experimental validation data for this arrangement in terms of frequency response as well as eigenfrequencies and damping rates for the T_1 mode is taken from (Kathan 2013).

Experimental findings showed that an absorber ring arranged according to configuration P1 reduces the damping rate of the T_1 mode (Kathan 2013). Further experimental evaluations indicate significant influence of the absorber ring's axial location on the damping properties (Kathan 2013; Schulze et al. 2015a). To investigate this phenomena, a second configuration P2 is considered as well, where the absorber ring is located at position 2, which is close to the nozzle, see Fig. 4.24 (right). In this case, l_{P2} is 102 mm.

4.3.2.2. Computational Setup and Absorber Model

The computational domain is shown in Fig. 4.24 in red and corresponds essentially to the domain used in the previous sections, see Sec. 4.1 and Sec. 4.2. A detailed overview of boundary conditions and the grid topology is shown in Fig. 4.25.

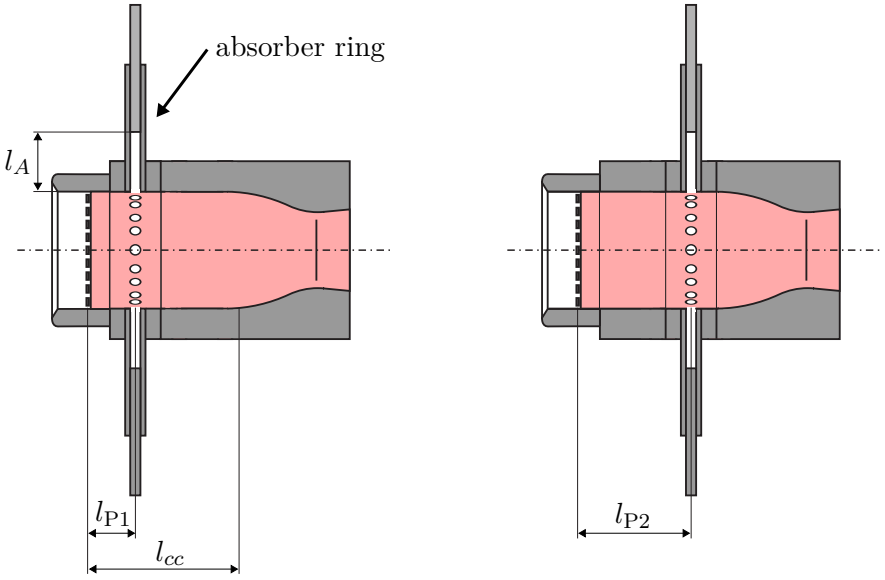

Fig. 4.24.: Experimental test configuration and computational domain (red) for absorber ring positions P1 (left) and P2 (right).

Since frequencies and damping rates can be predicted reasonably accurate on the basis of a reflection coefficient for the entire dome sub system, see Tab. 4.3 case (II), the dome volume is not included in the following analysis. Instead, the reflection coefficient $\mathrm{R}_{\mathrm{exp}}^{II}$ is imposed at the inlet boundary conditions, cf. Fig. 4.14.

Acoustic excitation is necessary to determine the frequency response. In the experimental procedure, broadband excitation using natural flow noise is employed to provide a fast procedure for the determination of the Power Spectral Density (PSD) (Kathan 2013; Schulze et al. 2015a). The high Mach number flow, especially in the single holes of the perforated plate, generates a satisfying acoustic signal-to-noise ratio. In the numerical evaluations, however, flow noise is not included. Acoustic excitation is provided by velocity modulation on a small circular region, which is eccentrically located at the inlet surface, see red circle at the inlet in Fig. 4.25. In comparison to the procedure employed for the determination of the nozzle admittance in 4.1.1, the location for excitation at the inlet is advantageous here, since it provides a larger distance to the absorber ring and reduces unwanted interactions with the cavities. Furthermore, it models the flow noise excitation more realistically. The boundary condition reads

$$\hat{u}_i n_i|_{\text{exc. inlet}} = \hat{u}_v. \tag{4.23}$$

Modeling the velocity excitation amplitude $\hat{u}_v$ is difficult, since the frequency spectrum of the flow noise modulation is unknown. The noise generation, however, is primarily based on turbulence, which is dominated by the dynamics of the emanating shear layer at the single holes of the perforated plate. According to (Michalke 1965), the shear layer behavior can be characterized by the Strouhal number St. It is shown that for St < 0.25 the shear layer is unstable and strong excitation can be expected. In turn, stable behavior is found for St > 0.25. According to (Boij and Nilsson 2006), the Strouhal

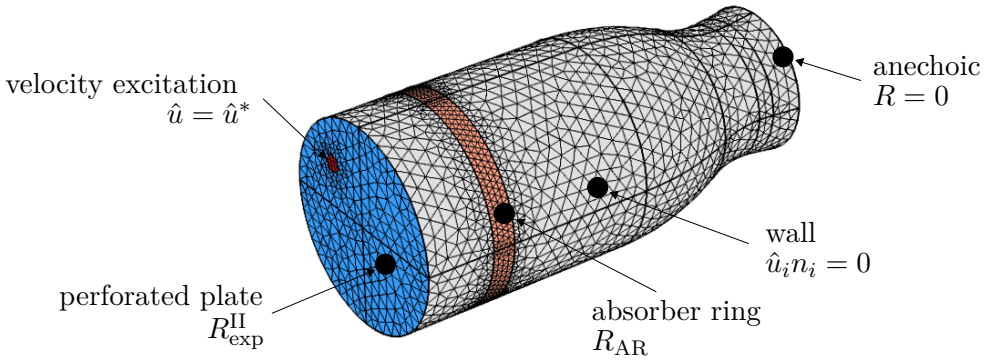

Fig. 4.25.: Numerical grid and boundary conditions for the acoustic simulation of the non-reactive test case with absorber ring.

number can be approximated by

$$\text{St} = \frac{\omega d_{\text{BL}}}{cM}, \tag{4.24}$$

where the boundary layer thickness d_{BL} at the separation edge is defined as 10 % of the upstream pipe radius in case of an area expansion. For the perforated plate its radius is used. For the highest considered frequency of 3000 Hz, a Strouhal number of 0.021 is found, which is well below the critical St number. In consequence, a constant amplitude modulation for acoustics is applied. The amplitude of the velocity excitation is scaled such that the resulting maximum amplitude in the frequency response coincides with the maximal amplitude in the experimental spectrum. For linear acoustics, such a scaling procedure is allowed.

For the determination of the frequency response, the reflection coefficient of the perforated plate needs to be applied for the considered entire frequency range. Below the cut-on frequency of the T_1 mode, longitudinal modes dominate the acoustic field. The reflection coefficient for longitudinal excitation is taken from (Kathan 2013) and shown in App. I. Furthermore, it is assumed that transverse mode motion dominates in the high frequency regime and the reflection coefficient for the T_1 mode can therefore directly be applied. This assumption is justified by the fact that the nozzle provides high damping for longitudinal modes.

As described in Sec. 2.7.4, the detailed absorber inlet regions are not resolved but the reflection coefficient of each single absorber R_{SA} is mapped onto the corresponding shell surface, see Fig. 4.26. The mapping is represented in form of an equivalent reflection coefficient for the absorber ring R_{AR}. The shell width is set equal to the cavity diameter.

The transformation of a reflection coefficient of a single absorber R_{SA} into R_{AR} is based on conservation of fluctuating mass and reads

$$R_{\text{AR}} = \frac{A_{\text{S}} Z_{\text{SA}} - N_{\text{SA}} A_{\text{SA}}}{A_{\text{S}} Z_{\text{SA}} + N_{\text{SA}} A_{\text{SA}}}, \tag{4.25}$$

where Z_{SA} denotes the impedance of a single absorber. Furthermore, A_{S} and A_{SA} denote

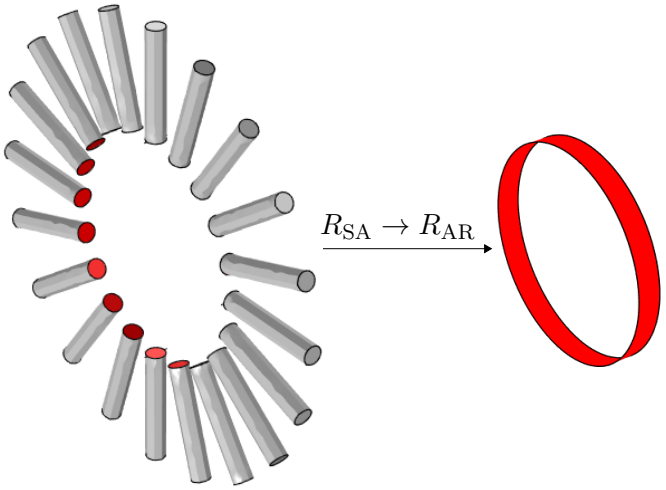

Fig. 4.26.: Mapping of the single absorbers onto the circular shell surface.

the areas of the shell surface and single absorber inlet, see App. J, and N_{SA} is the number of absorbers in the ring.

The reflection coefficient of the absorber cavities is not given experimentally and is therefore determined from theoretical models. Different absorber models are proposed e.g. in (Cárdenas 2014; Cárdenas and Polifke 2011; Ingard 1953; Ko 1971; Laudien et al. 1995; Pieringer 2008; Rienstra 2006; Tam and Auriault 1996). All these models contain certain parameters which can either be linked to further relations or need to be calibrated on the basis of experimental results or sophisticated numerical procedures. The presented results are based on the quarter wave model suggested in (Laudien et al. 1995). It defines the impedance by

$$Z_{\mathrm{SA}}\,\bar{\rho}\,c = 2\left(1+\epsilon_{\mathrm{nl}}+\frac{l_A}{D_A}\right)\sqrt{2\,\mu\bar{\rho}\,\omega}+\mathrm{i}\bar{\rho}\,c\,\cot\left(\frac{l_e\,\omega}{c}\right). \tag{4.26}$$

In Eq. (4.26), ϵ_{nl} denotes a non-linear resistance factor and l_e an effective length, which takes inertia effects into account and is approximately given by (Munjal 1987)

$$l_e = \frac{4}{3\pi}D_A \approx 0.424\,D_A. \tag{4.27}$$

The non-linear resistance factor is a major source of uncertainty. As originally proposed in (Garrison et al. 1969) and discussed in (Cárdenas 2014), ϵ_{nl} may vary over several orders of magnitude depending on the SPL. In the present test case, maximal pressure amplitudes of up to approximately 167 dB (5000 Pa) are observed close to the eigenfrequencies, which results in $\epsilon_{\mathrm{nl}} = \mathcal{O}(10^2)$ (Kathan 2013). For other frequencies, the SPL is considerably lower and ϵ_{nl} reduces accordingly. Throughout this investigation the non-linear factor is set to $\epsilon_{\mathrm{nl}} = 10$.

The reflection coefficient R_{AR} for the considered cavity lengths is shown in Fig. 4.27 in terms of amplitude and phase. At the quarter wave eigenfrequency of the cavities, which is given under the conditions that the imaginary part of the impedance in Eq.

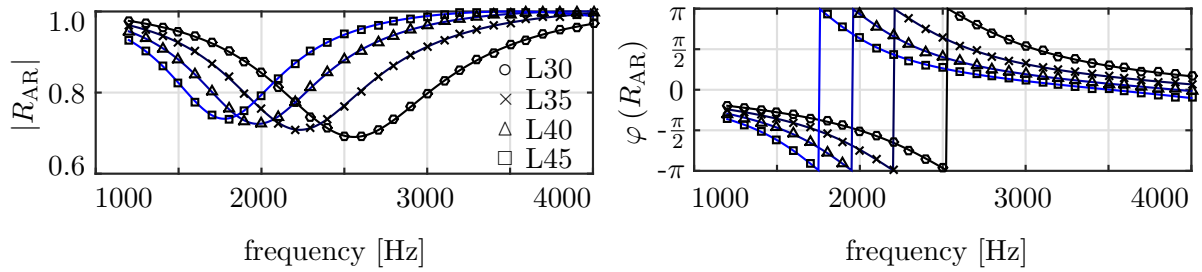

Fig. 4.27.: Amplitude (top) and phase (bottom) of the absorber ring reflection coefficient.

(4.26) is zero, low reflection amplitudes and an anti-phase behavior of ingoing and outgoing waves are observed. Hence, for T_1 eigenfrequencies of the system close to the quarter wave eigenfrequency of the cavities, acoustic dissipation can be expected. However, the influence of the absorber ring is not only restricted to the quarter wave eigenfrequency, but a rather broad spectrum of low amplitude and phase modulation might also influence other modes.

It is known that the absorber damping properties are based on different physical processes (Cárdenas 2014). Within the cavities, viscous boundary layer dissipation reduces acoustic amplitudes. In case of a standing mode pattern in the cavities for resonant frequencies, viscous dissipation is especially effective. At the cavity mouth, acoustic fluctuations modulate shear layers instabilities, which produce vortical structures and thereby dissipate acoustic energy. Furthermore, at resonant conditions inside the cavities, an out-of-phase relation between ingoing and outgoing wave is established, see Fig. (4.27). Consequently, a destructive effect of the outgoing wave on the transverse mode is realized, which directly reduces the T_1 amplitude in the chamber.

The dissipation of acoustic energy due to both boundary layer effects and the generation of vortical structures is modeled in form of viscous dissipation in Eq. (4.26). The different coefficients including the non-linear resistance can therefore be seen as enhanced viscous dissipation factors.

With an increase of the cavity length, the quarter wave eigenfrequency is reduced and the range of minimum reflection amplitude is shifted towards lower frequencies. Optimized damping can therefore be expected if the T_1 system eigenfrequency and the quarter wave eigenfrequency coincide. The cavity length is then given by

$$l_A = \frac{c}{4 f_{T_1}} = \frac{\pi}{4 s_{10}} D_{cc} \approx 0.427\, D_{cc}, \tag{4.28}$$

which results in a theoretical optimum length for the considered chamber configuration of $l_{A,\mathrm{opt}} = 39.24$ mm.

Studies from literature (Oschwald and Marpert 2001; Oschwald et al. 2008a; Schulze et al. 2015a) show that the decoupled consideration of chamber and absorber dynamics is not the optimal design procedure. Essentially, the coupled system determines the T_1 eigenfrequency and absorbers should be tuned that these eigenfrequencies are damped in an optimal way. The development of powerful absorber rings can therefore only be

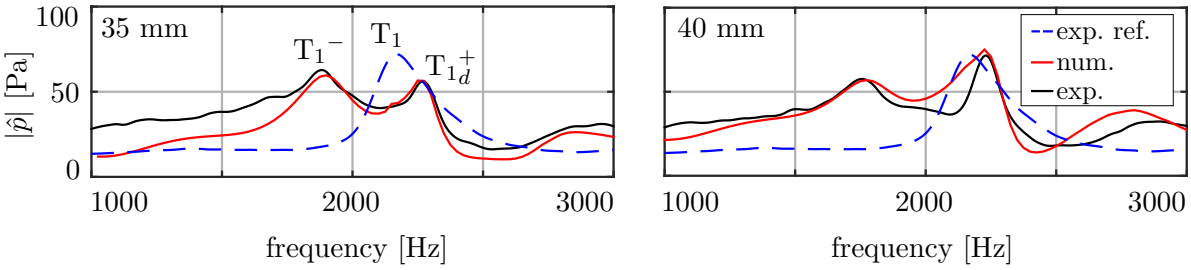

Fig. 4.28.: Frequency response of $|\hat{p}|$ [Pa] for 35 mm (left) and 40 mm cavity length (right) in comparison to the reference case without absorber ring: experimental findings and numerical results.

performed iteratively by reevaluating the system eigenfrequencies and damping rates after each modification of the absorber ring design and Eq. (4.28) can only be used as an initial approximation. For this purpose, fast procedures are desirable.

If several modes propagate at high amplitude simultaneously, the cavity lengths may be distributed asymmetrically around the circumference. Attenuation of amplitudes is then effective over a wider frequency range. Such arrangements are, however, not considered here. Nevertheless, such a configuration can be easily set-up and analyzed using the presented CFD/CAA approach.

The computational grid is shown in Fig. 4.25. The resolution is refined in the vicinity of the excitation and close to the absorber ring in order to provide smooth transition to the neighboring wall conditions.

4.3.2.3. Frequency Response for Absorber Ring Position 1

The frequency response is studied for the absorber ring position P1, cf. Fig. 4.24. For this arrangement, the two absorber lengths $l_A = 35$ mm and $l_A = 40$ mm are considered. Furthermore, the experimentally measured frequency response without absorbers (i.e. $l_A = 0$ mm) is also taken into account as reference configuration in order to illustrate the effects of the absorber ring. The frequency responses for the different absorber lengths are shown in Fig. 4.28.

First, the frequency response with absorber ring is compared to the numerical findings (num.) and the experimental results (exp.). Overall, good agreement is obtained. Characteristic peak values in the spectrum and corresponding eigenfrequencies are very well predicted, which implies that excitation amplitude and system damping characteristics are adequately modeled when the amplitudes are dominated by an eigenmode. For non-resonant frequencies, however, discrepancies are observed. Apparently, the assumption of negligible contributions from longitudinal modes is not fully correct within these frequency ranges.

In the next step, the frequency responses with absorber ring are compared to the findings of the reference case without absorber ring. It can be seen in Fig. 4.28, that a separation of the fundamental T_1 mode into two neighboring modes occurs. The sepa-

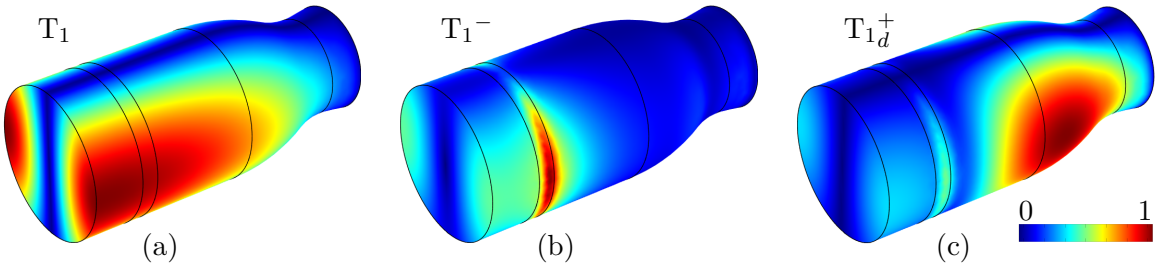

Fig. 4.29.: Mode shapes for configuration P1 in terms of normalized $|\hat{p}|$ under excitation for the peak frequencies in the spectra, cf. Fig. 4.28. (a): Reference case without absorber. (b) and (c): With an absorber cavity length of 35 mm.

rated modes are commonly referred to as $T_1{}^-$ and $T_1{}^+$ (Kathan 2013; Oschwald and Farago 2008; Oschwald et al. 2008a; Schulze et al. 2015a). The nomenclature $T_1{}^-$ denotes an additional acoustic mode, which is not present for the system without absorber ring. For the sake of clarity, the notation $T_1{}^+$ is also introduced. The corresponding acoustic mode is, however, still associated with the original T_1 mode.

To the author's knowledge, the separation of the T_1 peak in the spectrum into $T_1{}^-$ and $T_1{}^+$ is not fully understood today. Analytical results are studied in (Oschwald et al. 2008a), which, however, do not fully explain the phenomenon. The LEE results presented in this thesis allow a more detailed investigation. For that purpose, the pressure shapes for different modes identified in the spectra are studied in Fig. 4.29.

Clearly, the absorber ring significantly influences the mode shapes. While an approximately constant pressure distribution in the chamber is established for the T_1 mode in the reference case (a), high pressure amplitudes are only found directly at the absorber ring surface for the $T_1{}^-$ mode (b). Therefore, the $T_1{}^-$ mode exists primarily in the absorber ring section. The increased cross-sectional area due to the absorber cavities allows for the appearance of $T_1{}^-$ mode at reduced frequencies, which is in accordance with the frequency response data. With increasing cavity lengths, the $T_1{}^-$ mode frequency decreases, since the cross-sectional area becomes larger. In fact, for an absorber length of $l_A = 35$ mm, the eigenfrequency of the $T_1{}^-$ mode is approximatively 1880 Hz and reduces in case of an absorber length of $l_A = 40$ mm to roughly 1760 Hz.

Fig. 4.29 (c) reveals a mode shape, which predominantly exists downstream of the absorber ring and is commonly identified with $T_1{}^+$. However, to be more precise, this mode is referred to as T_{1d}^+ for future reference indicating that another mode exists, which primarily appears upstream of the absorber ring.

In terms of eigenfrequency, a shift of the T_{1d}^+ mode towards higher frequencies is observed in the spectra, see Fig. 4.28. This behavior can be explained by the reduced axial extent of the mode shape due to the influence of the absorber ring.

4.3.2.4. Eigenfrequencies and Damping Rates for Absorber Ring Position 1

The capabilities of the LEE to determine the eigenfrequency and damping rates under the influence of the absorber ring for different cavity lengths is studied next. In this study, the absorber ring is located close to the perforated plate, i.e. in position 1, cf. Fig. 4.24.

(Kathan 2013; Schulze et al. 2015a) report high damping rates for the $T_1{}^-$ mode for all considered cavity lengths. Probably, the strong attenuation of the $T_1{}^-$ mode is attributed to the fact that its eigenfrequency is cut-off in the regions next to the absorber ring section leading to a high imaginary part of the associated wave number, see Sec. 2.5. Consequently, the $T_1{}^-$ mode is uncritical in terms of thermoacoustic instabilities and therefore not further considered. A more detailed analysis can be found in (Schulze et al. 2015a). In this study, only the $T_1{}^+$ is taken into account. First, the focus is on the T_{1d}^+ mode, which shows high amplitudes predominantly in the section downstream of the absorber ring, cf. Fig. 4.29.

In the acoustic simulation, the excitation boundary condition is replaced by the reflection coefficient of the perforated plate $R_{\mathrm{exp}}^{\mathrm{II}}$, cf. Fig. 4.25, and the eigenvalue problem is solved using different cavity lengths. The reflection coefficients of the perforated plate and of the absorber ring are evaluated at the frequency $f_{\mathrm{T}_{1d}^+}$.

The experimental findings and numerical results for the T_{1d}^+ mode in terms of eigenfrequencies and damping rates for increasing cavity lengths are presented in Fig. 4.30. Altogether, very good agreement can be observed between the experimental data (exp., red line) and the numerically determined eigenfrequencies and damping rates (num. part. reflect., blue line). The good comparison again shows that the LEE together with the applied boundary treatment is well suited for the predictions of absorbers under grazing flow conditions for transverse acoustic motion. It can also be concluded that the evaluation procedure of the reflection coefficients of the perforated plate and the absorber ring at $f_{\mathrm{T}_{1d}^+}$ is adequate.

The numerically determined eigenfrequencies show constant but small discrepancies to the experimental data, which are, however, below 2 % deviation. The discrepancies originate from the missing influence of dome coupling, as already explained in Sec.

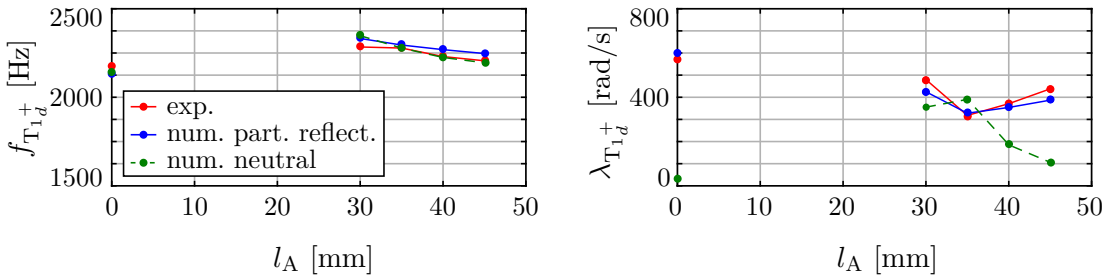

Fig. 4.30.: Eigenfrequency (left) and damping rate (right) of the T_{1d}^+ mode for configuration P1: Experimental findings and numerical results both for the partially reflecting inlet and the neutral inlet.

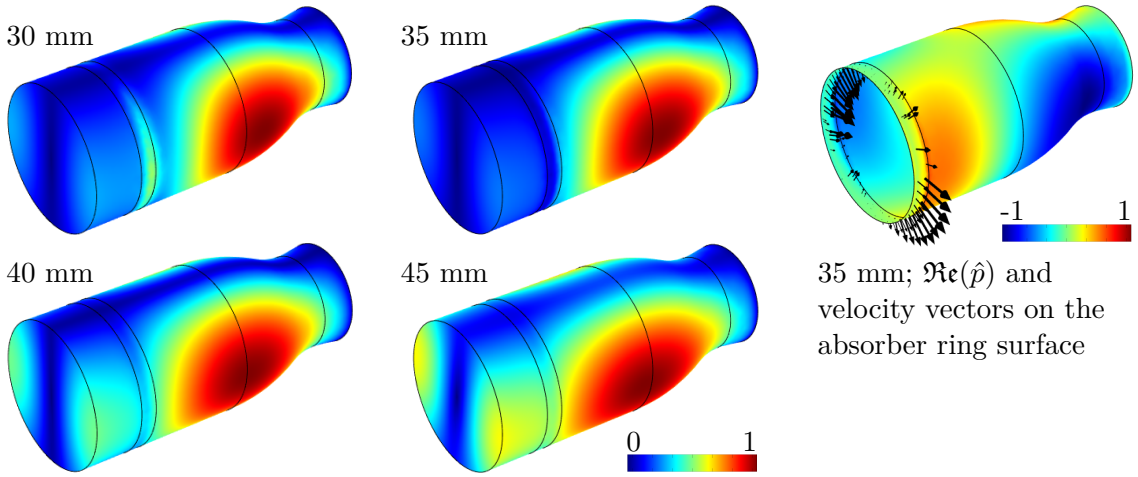

Fig. 4.31.: Mode shapes $T_{1_d^+}$ for different cavity lengths l_A in terms of normalized $|\hat{p}|$ and $\mathfrak{Re}(\hat{p})$ for 35 mm length (right) for configuration P1.

4.2.2.3. For 35 mm excellent agreement is observed. Concerning the damping rates, excellent agreement is observed for 35 mm and 40 mm, while small deviations are found for 30 mm and 45 mm. These discrepancies can be explained by the missing influence of the dome coupling and accompanied changes in eigenfrequency and therefore in R_{AR} elevated at $\omega_{T_{1_d^+}}$. Nevertheless, the small errors can be tolerated.

The results show, that the $T_{1_d^+}$ eigenfrequency is shifted towards higher frequencies with a maximum change of 9 % in comparison to the reference case without absorber ring (i.e. $l_A = 0$ mm). For increasing cavity length the shift decreases and the eigenfrequency tends towards the reference T_1 mode frequency, which is explained by the reduced influence of the absorber ring.

In contrary to expectations, the damping rates of the $T_{1_d^+}$ mode are significantly reduced for the entire range of cavity lengths in comparison to the reference case without absorber ring. The strongest reduction of 44 % is found for 35 mm. For higher cavity lengths the damping rate tends towards the reference value of the T_1 mode again.

Reduced damping rates could be explained by amplification properties of the absorber ring. As a result from the interaction of grazing flow and acoustic fluctuations at the cavity mouth, so-called whistling effects might in principle lead to an energy transfer into the $T_{1_d^+}$ mode (Lacombe et al. 2011). On the basis of acoustic intensity balancing, (Kathan 2013) and (Schulze et al. 2015a) show, however, that the considered absorber ring configuration is not capable of acoustic amplification.

To explain both increased eigenfrequencies and reduced damping rates, the shapes of the $T_{1_d^+}$ mode in terms of pressure amplitude $|\hat{p}|$ are studied in Fig. 4.31. In comparison to the reference T_1 mode, see Fig. (4.29), the shape is significantly altered by the absorber ring influence. The mode exists predominantly downstream of the absorber ring and shows only small amplitudes in the upstream part. The spatial separation effect is especially intense for 35 mm. For this cavity length, the strongest reduction of damping rates is found, cf. Fig. 4.30. For 45 mm length, in turn, higher pressure

amplitudes are present in the upstream part and a weaker reduction of the damping rate is observed.

The spatial separation of the $T_1{}^+$ mode can be explained by the impact of the absorbers on the mode propagation in the absorber ring cross-section. Two mechanisms are identified: On the one hand, the $T_{1_d}^+$ is not in resonance within the absorber ring section due to enlarged virtual diameter in this region. On the other hand, high transverse velocities at the absorber inlets and accompanied dampening effects restrict the axial propagation across the ring element. The velocities are illustrated in Fig. 4.31 (right) in form of arrows at the absorber ring surface. Furthermore, the impact on $\mathfrak{Re}(\hat{p})$ shows the distinct separation of the mode structure at the absorber interface.

Due to the spatial separation, the axial dimension of the $T_{1_d}^+$ mode is reduced. A shortened longitudinal component leads to higher eigenfrequencies, which is confirmed in Fig. 4.30 (left). For increasing cavity lengths, the separation effects gets weaker and the eigenfrequencies therefore converge towards to reference T_1 mode frequency.

Furthermore, the spatial separation effect shields the $T_{1_d}^+$ mode from the perforated plate. As the main contribution to acoustic dissipation originates from the inlet, its damping effect is reduced accordingly. Therefore, the reduction of the damping rate results from the weakened impact of the perforated plate. The stronger the absorber ring's influence, the more intense the separation and consequently the reduction of the damping rates. This explains the minimum value found for a cavity length of 35 mm.

In order to support the hypothesis of the spatial mode separation, the absorber ring's impact is investigated for an energetically neutral inlet condition for configuration P1. For this purpose, inlet boundary condition is prescribed according to Eq. (2.96). In this configuration, the shielding effect may not result in reduced damping rates, since the inlet does not provide acoustic dissipation. The corresponding mode shapes are illustrated in Fig. 4.32. The numerical results in terms of eigenfrequencies and damping rates are presented in Fig. 4.30 (num. neutral, green dashed line) together with the findings for the partially reflecting inlet data.

Neutral inlet conditions do not considerably influence the eigenfrequencies. Overall, good agreement between the experimental results and the numerical findings on the basis of the partially reflecting boundary condition as well as on the neutral inlet is obtained.

In comparison to the reference case with neutral inlet and a damping rate of $\lambda_{T_1} = 37$ rad/s, see Tab. 4.3 case (I), the incorporation of the absorber ring leads to tremendously increased damping rates for all cavity lengths. Consistently, the strongest impact is provided by a cavity length of 35 mm. In this situation, the damping rate increases by a factor of approximately 10. The damping rates even exceed the values found in case of a partially reflecting inlet. Also, for increasing cavity lengths the damping rate tends towards the reference again.

Interestingly, as the inlet does not provide damping, higher amplitudes are observed in the upstream part compared to the case with partially reflecting inlet, cf. Fig. 4.31 with Fig. 4.32. Furthermore, in the upstream part another mode is found, which is consequently referred to as $T_{1_u}^+$. Since this mode is subjected to the highly dissipating

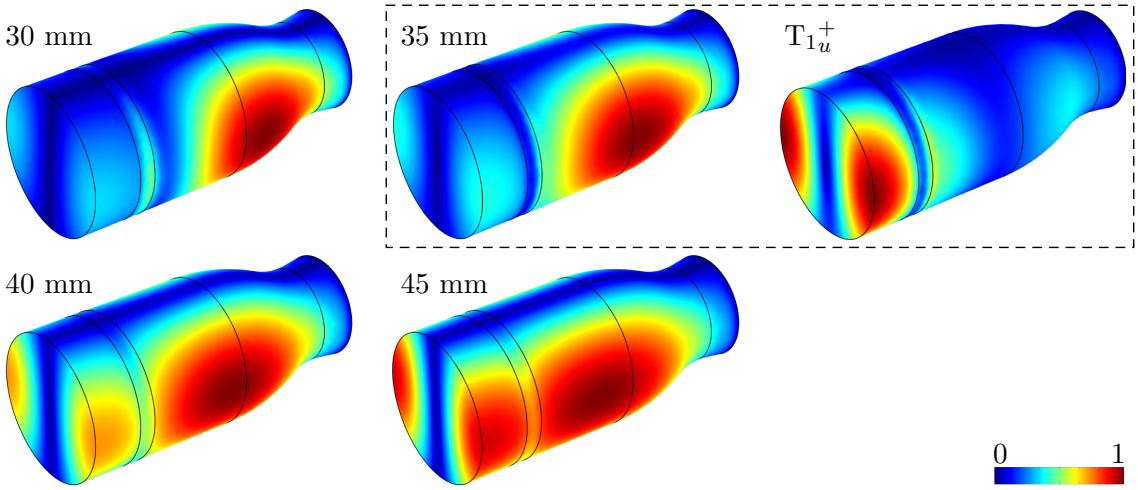

Fig. 4.32.: Mode shapes for different cavity lengths l_A and an neutral inlet boundary condition in case of configuration P1: $T_{1_d}^+$ and $T_{1_u}^+$ (right) modes in terms of normalized $|\hat{p}|$.

inlet in reality as well as to the absorber ring, damping rates are significantly higher than for the $T_{1_d}^+$ mode. Therefore, the $T_{1_u}^+$ mode is not considered in more detail for configuration P1.

In summary, an absorber ring increases damping rates for neutral inlet conditions, while the combination with a highly dissipating inlet causes reduced damping rates compared to the respective reference configuration. In both cases, the shielding effect decouples the $T_{1_d}^+$ mode from the inlet with very different influences on the damping rates. Furthermore, the shielding effect hypothesis is supported by the fact that approximately equivalent damping rates are found for 30 mm and 35 mm cavity length, for which the spatial separation is most intense, cf. Fig. 4.30 (right). In this situation the $T_{1_d}^+$ mode is almost completely separated and becomes therefore independent from the inlet.

Overall, highest damping rates are found for a shorter cavity length than theoretically predicted according to Eq. 4.28, which is in accordance with results presented in (Oschwald and Marpert 2001) and (Schulze et al. 2015a).

4.3.2.5. Eigenfrequencies and Damping Rates for Absorber Ring Position 2

As explained before, the upstream $T_{1_u}^+$ mode is subject to significant damping for configuration P1 with the partially reflecting inlet condition. Locating the absorber ring further downstream, however, increases the mode volume and therefore influences the mode separation. In this section, the absorber ring is located at the end of the chamber close to the nozzle and the impact on eigenfrequencies and damping rate is investigated on the basis of the partially reflecting inlet condition.

For configuration P2, experimental reference values for a validation are not yet available. Therefore, only numerical findings are presented and discussed.

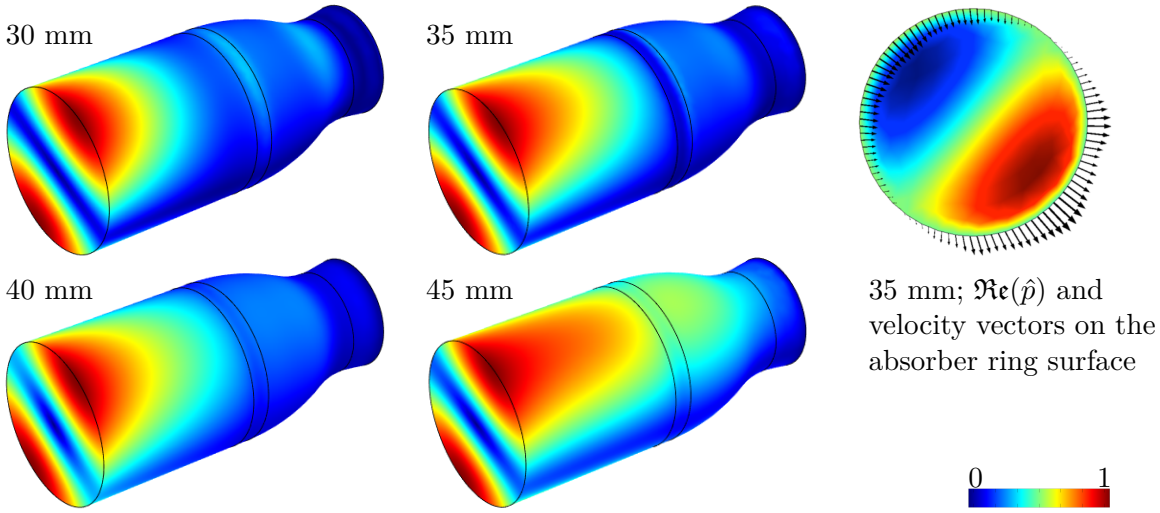

Fig. 4.33.: Mode shapes $T1_u^+$ for different cavity lengths l_A and partially reflecting inlet in terms of normalized $|\hat{p}|$ and $\mathfrak{Re}(\hat{p})$ for 35 mm length (right) for configuration P2.

In Fig. 4.33 the $T1_u^+$ mode shapes are presented for different cavity lengths. The mode shapes exist in almost the entire chamber and are separated from the nozzle. Highest amplitudes are present directly at the inlet. For increasing cavity lengths, significant pressure amplitudes reach further into the chamber, indicating that the strongest separation exists for 30 mm. For 45 mm, the lowest intensity of separation is observed due to the weak influence of the absorber ring.

The $T1_d^+$ mode exists in the nozzle part (not shown). However, due to its small axial extent and the varying cross-sectional area in the nozzle, the $T1_d^+$ mode is strongly damped and therefore not considered here.

The influence of the absorber ring on the eigenfrequency of the $T1_u^+$ mode is presented in Fig. 4.34 (left). In comparison to configuration P1, the shift in eigenfrequency to increased values is larger, which is explained by a stronger reduction of axial extent due to the decoupling of the entire nozzle part. Furthermore, a trend towards the reference solution is not present. The decoupling of the nozzle part is quite significant resulting to strong frequency shifts for already low influences of the absorber ring.

In Fig. 4.34 (right) a significant increase of the damping rate of the $T1_u^+$ mode is visible. Especially for 35 mm and 40 mm extremely high values are found. For even higher cavity lengths, the damping rate tends towards the reference value. Similar observations were reported in (Schulze et al. 2015a).

Since in configuration P2 the shielding of the $T1_u^+$ mode from the dissipating inlet is not present, both inlet and absorber ring contribute to damping. The damping rates are thus significantly higher than for configuration P1. In consequence, in case of a highly dissipating perforated plate, enhanced damping due to absorber devices can be achieved by realizing a substantial distance between absorber ring and the inlet.

The mode distribution in the cross-section of the absorber ring position for a cavity

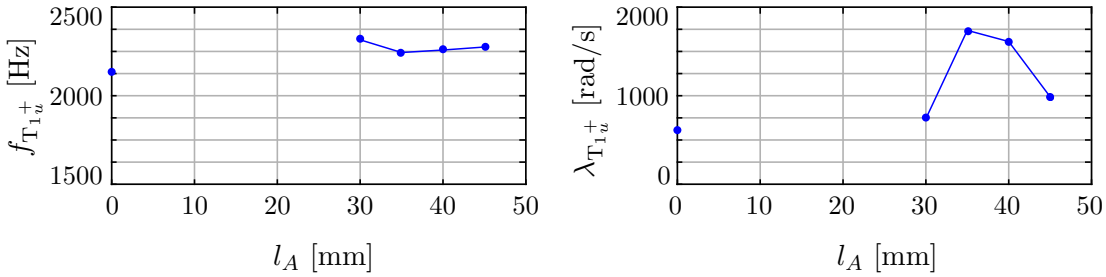

Fig. 4.34.: Numerical results: Eigenfrequency (left) and damping rate (right) of the T_{1u}^+ mode for configuration P2.

length of 35 mm is shown in Fig. 4.33 (right). The transverse velocity arrows indicate a strong interaction with the cavities. As explained for the GIT test case, high transverse velocity results in strong dissipating influence. Furthermore, $\mathfrak{Re}(\hat{p})$ shows that directly at the cavity mouth pressure is low for this phase instant, which again illustrates the decoupling mechanism between upstream and downstream modes.

4.4. Remarks for the Non-Reactive Acoustic Analyses

For the development of a combustion stability prediction tool for rocket engines, LEE in frequency space and in time domain as well as modeling strategies for nozzles, dome coupling and resonating cavities under grazing flow conditions were introduced and validated on the basis of non-reactive test cases. Furthermore, insights into relevant acoustic phenomena were generated. The main conclusions for the methodology's application to rocket engines are briefly summarized:

1. For linear acoustic analysis, frequency space LEE provide shorter turnaround times and allow for more accurate boundary condition modeling than time domain simulation. The unidirectional coupling between mean flow and acoustics is sufficient to capture the relevant effects. The accuracy of time domain consideration depends substantially on the FIR and IIR filter quality, respectively.
2. The generation of boundary conditions for transverse modes is complicated due to insufficient data available around the eigenfrequencies. Possible approximation strategies are explained.
3. Nozzle acoustics are accurately described on the basis of both frequency space and time domain simulations. The incorporation of the nozzle volume into the field discretization should be preferred.
4. The dome coupling concept is successfully validated for longitudinal and transverse wave propagation both in frequency space and time domain. The coupling is necessary to determine correctly the eigenfrequencies, while damping rates agree excellently with experimental comparison data on the basis of a coupling describing single reflection coefficient. The results show that all boundary conditions need to be accurately modeled.

5. Frequency space transformed LEE provide stable solution procedures for boundary conditions under grazing flow situations both for longitudinal and transverse wave propagation. Frequency response, eigenfrequencies and damping rates agree excellently with experimental validation data. The description of absorbers in form of an equivalent homogeneously distributed impedance allows for an adequate incorporation of the cavity effects on wave propagation.
6. For grazing flow situations, rather coarse grid resolutions are sufficient to capture the cavity effect on the wave propagation. For the considered GIT test case, the detailed mean flow profiles and the effective impedance boundary condition do not relevantly influence the results.
7. Significant changes in the mode shape should be expected due to the influence of absorber rings. Spatial mode separation and accompanied shielding effects tremendously change the system dynamics leading possibly to increased eigenfrequencies and reduced damping rates when highly dissipating boundary conditions are decoupled from the mode. In terms of flame dynamics, the impact of a different mode shape has to be carefully addressed.

The non-reactive acoustic analysis show that the frequency space LEE are highly suited the description of acoustic propagation in rocket engines. Therefore, the investigations on the reactive test case presented in the next sections are based on LEE in frequency space exclusively. However, it is believed that time domain considerations are advantageous for non-linear investigations, cf. Sec. 3.4.

5 Validation Data for Reactive Conditions

The focus is now on realistic rocket engine conditions including combustion. The purpose of Chapter 5 is to introduce a suitable test chamber for which reliable validation data is available. The measurements are used as a validation base for the numerical stability assessment procedure, which is explained and applied to the test chamber in the following Chapters.

In this thesis, the so-called combustion chamber D (in German **B**renn**k**ammer **D**) rocket engine configuration operated at the German Aerospace Center (DLR) in Lampoldshausen is used as test chamber. The BKD has been studied in the framework of the French-German Rocket Engine Stability Research Initiative (REST). The latest simulation results were presented at the 3rd REST Modeling Workshop in 2014 in Vernon, France (Gröning 2014). Different numerical methodologies were used reaching from hybrid approaches (Kaess et al. 2014; Schulze et al. 2014c) to high-performance computations using Large Eddy Simulations (LES) (Urbano et al. 2014). However, none of the simulations were capable of predicting the correct stability behavior.

5.1. Rocket Test Chamber BKD

The BKD is a fully equipped H_2/O_2 driven rocket chamber in a downscaled configuration. It operates at typical upper stage rocket engine conditions (thrust level 25 kN, chamber pressure 60-80 bar). The experimental test configuration is shown in Fig. 5.2 and Fig. 5.3. It consists of the water-cooled cylindrical combustion chamber (diameter: 80 mm, length: 215 mm), the thrust nozzle and the injection system.

The arrangement of the propellant domes is shown in Fig. 5.1. Essentially, the O_2 dome is conically shaped with a central igniter tube element. Two feed lines provide O_2 from the tanks. The H_2 dome is cylindrical and fuel is provided by six inflows. The cryogenic injection system comprises 42 coaxial injectors, which provide H_2/O_2 as propellants. The injectors are arranged in three concentric rings with 6, 12 and 24 elements, see Fig. 5.2 (right).

The injector geometry is shown in Fig. 5.3. The interface between dome and injector consists of an orifice, which leads to a drastic pressure reduction. Accordingly the orifice

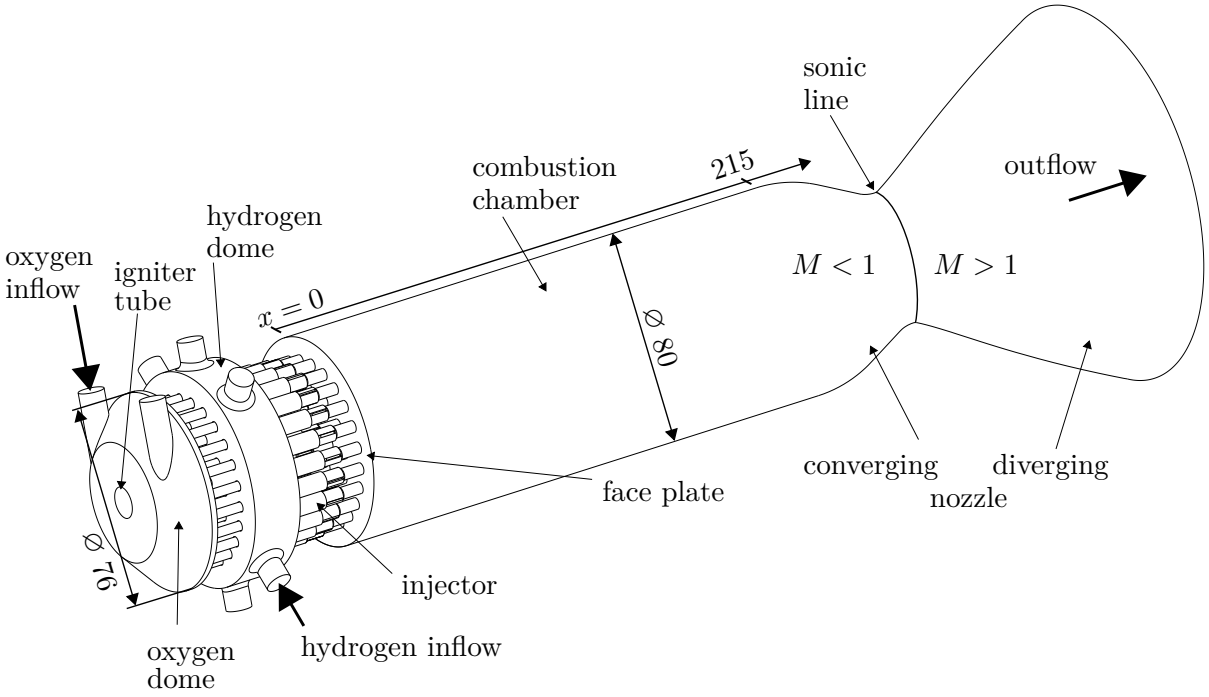

Fig. 5.1.: BKD test chamber configuration with details of the injection system in the injector head and chamber dimensions (Gröning and Oschwald 2014). Dimensions are given in [mm].

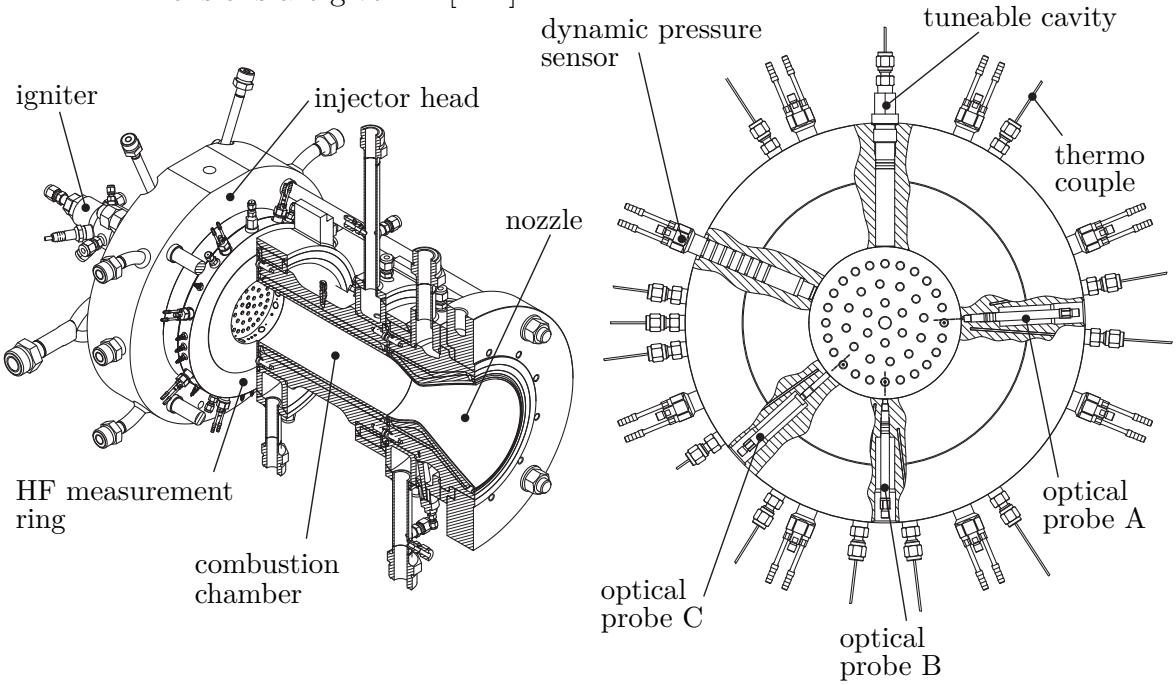

Fig. 5.2.: BKD combustion chamber and equipment, adapted from (Gröning et al. 2014) and (Gröning et al. 2015a).

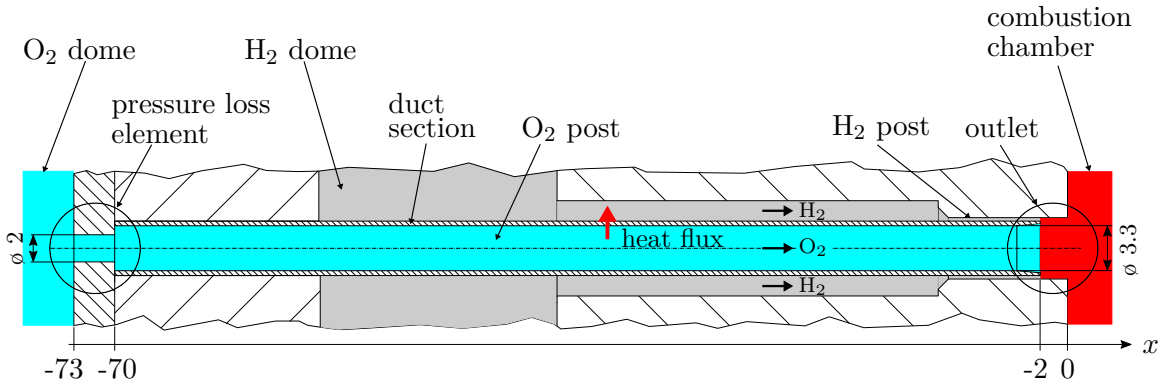

Fig. 5.3.: BKD injector geometry and propellant flow. Axial coordinates are given in [mm].

is referred to as pressure loss element. Afterwards, O_2 is delivered to the chamber through a long cylindrical O_2 post. The dimensions are given in Fig. 5.3. Before the propellants are brought into contact in the recess, the O_2 flow is subjected to a slight radial spread in order to improve mixing. The radial spread is realized by a conically shaped O_2 post outlet and the cone is defined by the so-called taper angle. H_2 is injected into the chamber co-axially to the O_2 through a thin ring surface. Such co-axial injector types are often used for cryogenic O_2/H_2 driven rocket engines (Sutton and Biblarz 2001).

A HF measurement ring is implemented into the experimental BKD configuration. The ring is located at the face plate, see Fig. 5.2 (right) and is equipped with eight dynamic pressure sensors, which are distributed equidistantly around the circumference. The dynamic pressure sensors record pressure fluctuations directly at the wall. Furthermore, three optical probes are mounted to the HF measurement ring, which are used to record OH* radiation intensity (Gröning et al. 2015a). Additionally, a tuneable cavity can be activated to analyze the damping effect of an absorber on acoustic amplitudes (Gröning et al. 2013a).

Various publications by Gröning et al. (Gröning et al. 2012, 2013a,b, 2014, 2015a,c) show that high pressure amplitudes of several bar peak-to-peak occur at distinct operation conditions. It is explained in (Gröning et al. 2012) that strong oscillations appear *self-excited* and originate from high amplitudes of the first transverse mode oscillating at frequencies of approximately 10 kHz. In subsequent campaigns, the same stability behavior was observed. This showed that the instability can be reliably generated and that distinct load point specifications are given, at which high acoustic amplitudes occur in the chamber. Such a *linear* onset of the first transverse mode instability indicates the BKD as a highly suitable test configuration for the numerical stability assessment procedure applied in this thesis.

5.2. Operating Conditions

The thermoacoustic behavior of the BKD test chamber is analyzed for four different load points (LP), which were suggested in (Gröning et al. 2014) and are summarized in Tab. 5.1 in terms of propellant mass flow rates $\dot{m}_{H_2/O_2}$, oxidizer to fuel ratio (ROF), dome temperatures T_{H_2/O_2} and dome pressures, p_{H_2/O_2}. Furthermore, the experimentally observed stability behavior is given. For future reference, further characteristic quantities are calculated and discussed in the following as well.

The chamber pressure p_{cc} for the different load points is not given in (Gröning et al. 2014). For its determination, an iterative procedure is employed (Schulze et al. 2014a; Schulze and Sattelmayer 2015a) using the CEA software package developed by Gordon and McBride (McBride and Gordon 1994). For the calculations, the mass flows of H_2 and O_2 are required. Results show that LP1 and LP2 operate at 70 bar, while 80 bar chamber pressure is calculated for LP3 and LP4, see Tab. 5.1. The findings agree well with experimental measurements, see (Gröning et al. 2013b).

The differences in mass flow lead to a ROF variation for the LP. For LP1 the ROF is given with 4, while LP2-4 operate at a higher ROF of 6. The considered ROF range agrees with typical values used in industrial rocket engine applications (Sutton and Biblarz 2001). The ROF affects species composition of educts as well as of products within the entire chamber. The stoichiometric ROF_{st} for H_2/O_2 is eight. In consequence, all LP operate in rich mode, i.e. an excess of fuel is present. LP2-4 are closer to stoichiometry than LP1. The effects of ROF on the reactive flow and on the acoustics will be investigated later on the basis of CFD results in Sec. 7.4.

Fuel excess is often applied to keep unreacted and lightweight hydrogen molecules in the products leading to increased thrust efficiency. However, studies show that the resulting oxidizer deficit can lead to an oxidizer dominated flame dynamic behavior (Sattelmayer et al. 2015b; Schulze et al. 2016b). Consistent with these findings (Gröning et al. 2015b) identify that the O_2 dynamic behavior governs the onset of an instability in case of the BKD test chamber. In fact, the BKD operates unstable if one of the O_2 injector eigenfrequencies coincides with the first transverse mode frequency in the chamber.

Tab. 5.1 shows that the temperature in the domes is higher for O_2 than for H_2. The thin wall between O_2 and H_2 in the injector is furthermore made of copper providing high heat conductivity. In consequence, the injection temperatures are not necessarily the same as the dome temperatures since heat is transported from O_2 to H_2 along the injector length, see Fig. 5.3. The effect of heat transport on the injection temperatures will be further investigated in Sec. 7.1. However, the calculated H_2 injection temperates are already given in Tab. 5.1 in order to derive further quantities at injection. As it will be explained in Sec. 7.1, the O_2 temperature does not relevantly changes along the O_2 post. In consequence, the O_2 injection temperature is the same as in the dome.

In Tab. 5.1 the injection velocities and Mach numbers for H_2 and O_2 are also specified.

The injection velocity is determined on the basis of the mass conservation law, viz.

$$u_{\mathrm{H_2,inj/O_2,inj}} = \frac{\dot{m}_{\mathrm{H_2/O_2}}}{\rho_{\mathrm{H_2/O_2}} \cdot A_{\mathrm{H_2/O_2}}}, \tag{5.1}$$

where $A_{\mathrm{H_2/O_2}}$ denote the respective injection areas and $\rho_{\mathrm{H_2/O_2}}$ the densities at injection. The mass flows of H_2 and O_2 are given in Tab. 5.1. Density is taken from the NIST database (Linstrom and Mallard 2015) for the given chamber pressure p_{cc} and the injection temperatures, cf. Tab. 5.1. For the determination of the Mach number according to Eq. (2.40), speed of sound is also taken from the NIST database. It can be seen that the injection velocity of O_2 is small for all LP. Therefore, the Mach numbers are also low. As the mass flow is larger for LP3 and LP4, the O_2 injection velocities are slightly higher than for LP1 and LP2. Furthermore, an increased injection temperature results in a slightly larger injection velocity of O_2 for LP4 than in case of LP3.

In contrast to O_2, H_2 is injected with high velocities and correspondingly high Mach numbers, cf. Tab. 5.1. The velocity is maximum for LP1, since H_2 mass flow is the highest. Interestingly, the H_2 injection velocities for the unstable LP2 and LP4 are essentially the same, although H_2 mass flow of LP2 is smaller than of LP4. It can easily be verified that the smaller pressure and slightly lower temperature in case of LP2 results in a reduced density at injection, which is just sufficient to match the injection velocities with LP4. It can be concluded that similar H_2 injection velocities

Tab. 5.1.: Load points and stability behavior for the BKD test chamber from (Gröning et al. 2014) as well as additionally calculated quantities.

load point	LP1	LP2	LP3	LP4
from (Gröning et al. 2014)				
$\dot{m}_{\mathrm{H_2}}$ [kg/s]	1.11	0.84	0.96	0.96
$\dot{m}_{\mathrm{O_2}}$ [kg/s]	4.44	5.04	5.77	5.75
ROF [-]	4	6	6	6
$T_{\mathrm{H_2}}$ [K]	93.67	94.90	47.62	95.66
$T_{\mathrm{O_2}}$ [K]	111.78	111.48	107.68	111.42
$p_{\mathrm{H_2}}$ [bar]	100.03	89.66	90.12	102.92
$p_{\mathrm{O_2}}$ [bar]	78.41	81.11	91.89	94.10
stability [-]	stable	unstable	stable	unstable
additionally calculated quantities				
$u_{\mathrm{H_2,inj}}$ [m/s]	408	324	137	330
$u_{\mathrm{O_2,inj}}$ [m/s]	9.91	11.22	12.58	12.76
$\dot{I}_{\mathrm{H_2,inj}}$ [N]	10.79	6.49	3.14	7.55
$\dot{I}_{\mathrm{O_2,inj}}$ [N]	1.05	1.35	1.73	1.74
$M_{\mathrm{H_2,inj}}$ [-]	0.475	0.372	0.149	0.370
$M_{\mathrm{O_2,inj}}$ [-]	0.013	0.015	0.016	0.016
$T_{\mathrm{H_2,inj}}$ [K]	87.69	91.28	48.1	91.98
p_{cc} [bar]	70.12	70.00	80.22	80.04

are present at the onset of an instability in the BKD test chamber. Furthermore, the hypothesis of the requirement of a particular H_2 injection velocity for the occurrence of an instability is supported by the fact that unstable operation is not present for LP3. Although the same mass flow is provided and the same chamber pressure is present for LP3 as for LP4, the injection velocity is significantly lower. The smaller H_2 injection temperature in case of LP3 leads to a 2.4 times higher density in comparison to LP4 and, in consequence, the injection velocity is reduced, cf. Eq. (5.1).

The sensitivity of the BKD stability becomes obvious by comparing again LP3 and LP4. A difference of only 50 K in H_2 injection temperature determines between stable and unstable operation. The numerical modeling of the BKD test chamber needs to capture the effects of such small differences throughout the entire stability assessment procedure.

In Tab. 5.1, the injection momentum of H_2 and O_2 is also reported. The injection momentum $\dot{I}$ is given by

$$\dot{I}_{H_2,\mathrm{inj}/O_2,\mathrm{inj}} = \dot{m}_{H_2/O_2} \cdot u_{H_2,\mathrm{inj}/O_2,\mathrm{inj}}, \tag{5.2}$$

where the mass flow through a single injector is used. It can be seen that the injection momentum of H_2 is larger than for O_2. The difference is especially high for LP1. In contrast, the lowest differences of the injection momentum between H_2 and O_2 is present for LP3. The low difference is based on the small injection velocity of H_2 in case of LP3.

Furthermore, large differences in H_2 injection momentum between the LP is present. The lowest H_2 injection velocity in case of LP3 also leads to the smallest injection momentum.

5.3. Verification of BKD's Stability Behavior

The stability behavior of LP1-4 is determined on the basis of normalized PDF (Probability Density Function) plots of the measured pressure amplitudes. The PDF describes the amplitude density distribution contained in the dynamic pressure signals. An instability is present if a high density of non zero amplitudes is found in the PDF. For the generation of the PDF, the time series data is band-pass filtered around the first transverse mode. Subsequently, the PDF distribution is calculated in MATLAB. The dynamic pressure recordings were kindly provided by Prof. Dr. Michael Oschwald, DLR Lampoldshausen (priv. comm.).

Fig. 5.4 presents the PDF for LP1-4. For each LP, eight dynamic pressure sensor signals are measured in the HF measurement ring, cf. Fig. 5.2. Pressure signals measured at opposite locations in the HF measurement ring are equally colored. One can clearly distinguish the characteristics between LP1/3 (left column) and LP2/4 (right column). In case of LP1 and LP3, the amplitude density maximum is zero indicating that only insignificant amplitudes are present. In consequence, the BKD test chamber operates stable for LP1/3 in the experiments, cf. Tab. 5.1.

In contrast, LP2/4 show a higher density of significant amplitudes in the signals

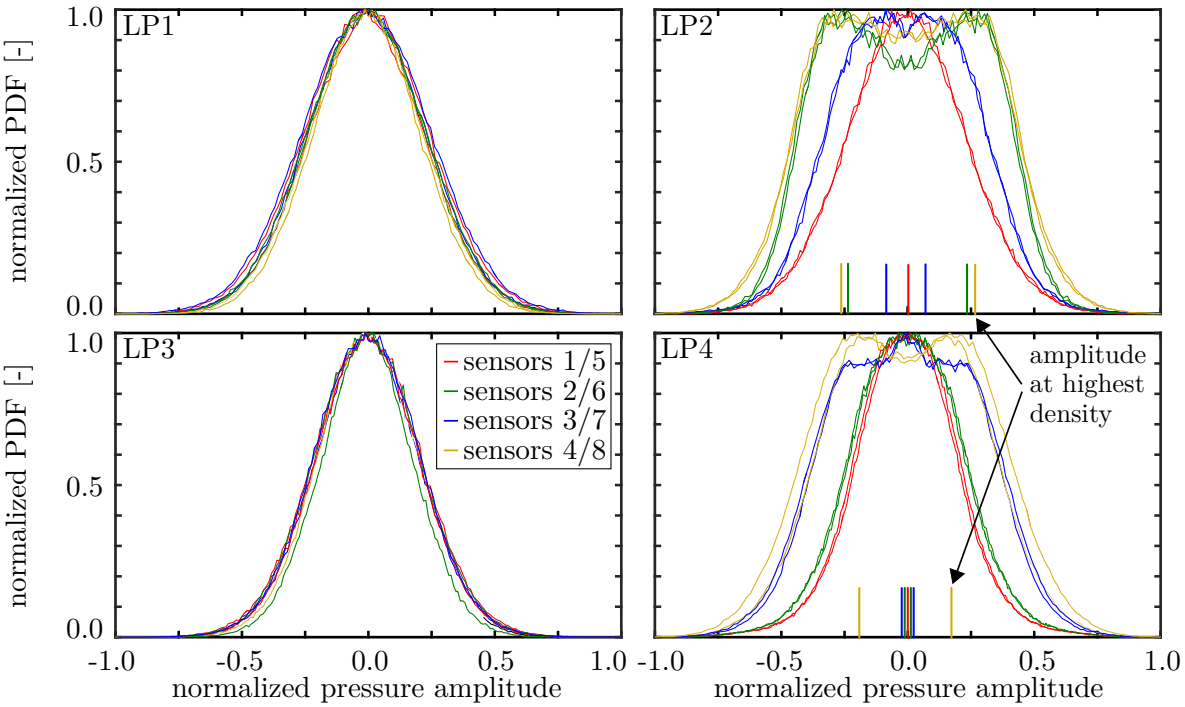

Fig. 5.4.: Normalized PDF of LP1-4 for eight sensors. The dynamic pressure measurements were kindly provided by Prof. Dr. Michael Oschwald, DLR Lampoldshausen.

indicating the presence of an instability. The amplitude at which the highest density is found is also indicated.

In case of LP2, the dynamic pressure data recorded at the oppositely located sensors 3/7 as well as at the sensors 4/8 contain the highest densities of large amplitudes. Lower maximal amplitude densities are measured with the sensors 2/6. Lastly, only insignificant amplitudes are contained in the signals of the sensors 1/5. Each of the sensor pairs shows a symmetrical PDF distribution around the zero amplitude axis. The symmetric distributions and the different maximal amplitude densities indicate a standing first transverse mode. A higher tendency of the presence of a standing mode were also concluded by (Gröning et al. 2013b).

A rather ambiguous PDF is determined for LP4. The signals of the sensors 4/8 again contain a high density of large amplitudes, which indicate unstable operation. However, the sensors 1/5 and 2/6 do not measure significant amplitudes. Furthermore, the PDF based on the signals of the sensors 3/7 show a maximum density at zero amplitude, but contain also a wide distribution of higher amplitude densities. Therefore, the presence of an instability is not as clear as for LP2. Nevertheless, BKD operation under LP4 is considered as unstable. More detailed analysis of the pressure signals conducted in (Gröning et al. 2013b) supports this conclusion.

5.4. Determination of Linear Growth and Damping Rates

As it will be explained in the next Chapter in more detail, the goal of the stability assessment procedure conducted in this thesis is to simulate BKD's thermoacoustic behavior for low amplitudes of the first transverse mode. This especially implies that acoustic propagation cannot be described under high amplitude limit-cycle conditions. A comparison of numerical results and measurements is therefore limited to eigenfrequencies and damping rates. However, measurements conducted in case of unstable operation are naturally performed at high amplitudes. Hence, it is necessary to extract the damping rate for the first transverse mode from the dynamic pressure signals in case of low and of high amplitude operation.

To the author's knowledge, damping rates were not given in literature for the BKD test chamber. In order to provide suitable comparison data for the validation of the stability assessment procedure, the damping rates are determined from the dynamic pressure signals and presented in this thesis. For this purpose, two methods are applied for mutual verification: Lorentzian profile fitting and parameter extraction method. Both methods are based on the stochastic forcing of the first transverse mode due to the presence of noise, which is generated by the highly turbulent reactive flow.

5.4.1. Lorentzian Fitting

The Lorentzian fitting is based on the Fourier transform of an exponentially decaying signal, which is given in terms of acoustic power density. Therefore, it is only applicable to signals measured under stable operation conditions, i.e. for low amplitudes. Regularly, the PSD signal is employed, which is defined by the square of pressure amplitude. The PSD of a decaying signal in frequency space, i.e. the Lorentzian profile, is given by (Bronstein et al. 2005; Kathan 2013)

$$\mathrm{PSD}(\omega) \sim \frac{\lambda}{\lambda^2 + (\omega - \omega^s)^2}, \tag{5.3}$$

where ω^s denotes the angular eigenfrequency and λ the damping rate.

Since the Lorentzian profile is defined in Fourier space, see Eq. (5.3), harmonic excitation can be used to determine experimentally the profile. However, the entire frequency spectrum is generated more efficiently using broad-band noise excitation, which is naturally present in the chamber. In consequence, the measured dynamic pressure signal can directly be employed without additional external excitation. The PSD generated from each dynamic pressure sensor signal are averaged in order to reduce random influences. The averaged PSD was provided by Stefan Gröning, DLR Lampoldshausen (priv. comm.). Subsequently, the damping rate and eigenfrequency can be obtained from the fit of the Lorentzian profile to the averaged PSD. It is found, however, that the procedure is more robust when the eigenfrequency ω^s is known eigenfrequency is used and only the damping rate is kept as fitting parameter. The eigenfrequencies of the first transverse mode for LP1-4 are taken from (Gröning et al. 2013b). The imple-

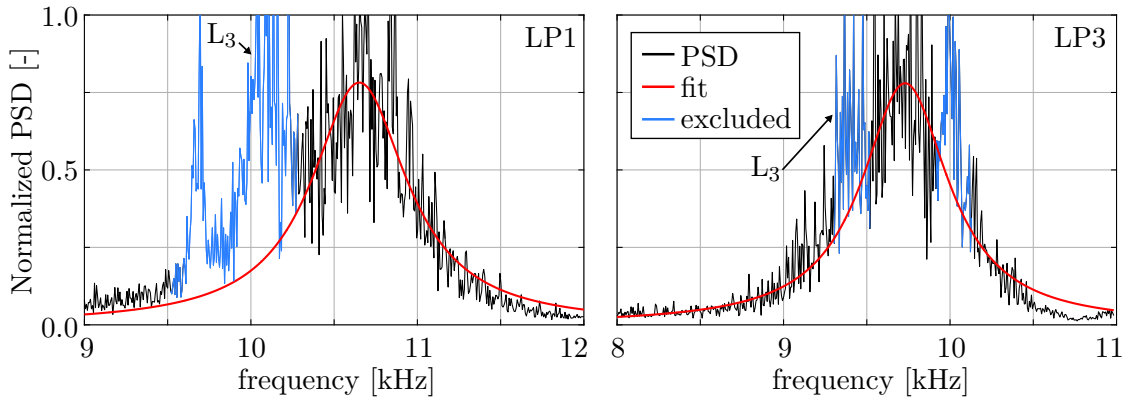

Fig. 5.5.: Averaged and normalized PSD, Lorentzian fits and excluded data for LP1 (left) and LP3 (right).

mentation of the Lorentzian fitting method into MATLAB was successfully validated in (Haimerl 2013) on the basis of a generic test case proposed in (Nicoud et al. 2007).

The averaged and normalized PSD is shown for the stable LP1 (left) and LP3 (right) in Fig. 5.5. Three peaks are observed in the considered frequency range. The spectrum associated with the first transverse mode is identified by the corresponding eigenfrequency. Furthermore, the numerical results presented in Sec. 7.3 reveal that one of the neighboring peaks is associated to the third longitudinal mode in the chamber L_3. The third sharp peak could not be identified in the eigenfrequency studies. The peak frequency probably coincides with the second longitudinal mode of the O_2 injector configuration (Gröning et al. 2015b).

The appearance of two additional modes close to the eigenfrequency of the first transverse mode complicates the application of the Lorentzian fitting. The profile according to the relation (5.3) holds true only for a single mode spectrum. In consequence, the frequency range with significant contributions to the PSD originating from the modes at neighboring frequencies are excluded for the fitting procedure. The corresponding excluded frequency range is highlighted in blue in Fig. 5.5.

Overall, a good agreement between the averaged PSD distributions and the Lorentzian fits for the first transverse mode is obtained for LP1 and LP3. Discrepancies occur in the higher frequency range. The deviations probably originate from an asymmetric distribution of the spectrum. Introducing a weighting function to control the accuracy in the different frequency ranges and forcing the fit to be more accurate in the higher frequency range, reduces the deviations, but increases the fitting errors for low frequencies. For the final results the higher frequency range is more weighted for LP1, since the PSD at lower frequencies is possibly distorted by the L_3 and O_2 injector modes. In contrast, for LP3 the lower frequencies are weighted more intensely, since the overall fitting quality is higher in this range. The used fitting algorithm also calculates the 95 % confidence interval, which gives a measure of the fitting quality. For a small interval, the fit matches the original data with high accuracy. In contrast, a large interval indicates that the nominal results might be rather inaccurate.

The determined damping rates using Lorentzian fitting for LP1 and LP3 are given

Tab. 5.2.: Damping rates λ for LP1-4: Results of the Lorentzian fitting procedure and of the parameter extraction method using mode $A(t)$ and $B(t)$.

λ [rad/s]	Lorentzian fitting	parameter extraction method $A(t)$	parameter extraction method $B(t)$
LP1	2199 ± 63	[200; 500]	[200; 500]
LP2	n.a.	[−40; −30]	[−40; −30]
LP3	2011 ± 13	[180; 390]	[180; 390]
LP4	n.a.	[−31; −29]	[−40; −37]

in Tab. 5.2 together with the 95 % confidence intervals. The results show that the first transverse mode is slightly stronger damped for LP1 than in case of LP3. The higher damping rate originates from the wider PSD spectrum, cf. Fig. 5.5. Overall, rather small confidence intervals are calculated indicating accurate fitting. The interval in case of LP1 is larger than for LP3. The slightly reduced accuracy for LP1 is explained by the larger frequency range excluded from the PSD data. In consequence, there is less data available for an accurate fitting procedure.

For comparison, the damping rates obtained from the parameter extraction method are also already given in Tab. 5.2. The underlying algorithm and the findings are explained in the next section.

5.4.2. Parameter Extraction Method

Originally, the parameter extraction method was applied to the investigation of HF mode dynamics in gas turbine combustors (Bothien et al. 2015; Noiray and Schuermans 2012, 2013) and has not been applied to rocket engine acoustics before. The procedure is derived on the basis of complex theoretical considerations, which cannot be illustrated in detail in this thesis. In the following, the focus is limited on the description of the general approach and on the applied algorithm.

Essentially, the method is based on the assumption that the amplitude dynamic can be described by the following differential equations (Noiray and Schuermans 2012):

$$\frac{\partial A(t)}{\partial t} = -\lambda A(t) + s(t) + \frac{\Gamma}{A(t)} - K A(t)^3, \tag{5.4}$$

where $A(t)$ denotes the amplitude of the clockwise rotating component of the first transverse mode, cf. Eq. (2.47). The term $s(t)$ in Eq. (5.4) denotes uncorrelated white noise excitation due to the turbulent reactive flow. Furthermore, the white noise background in the system leads to a systematic excitation, which can be interpreted as an inherently present driver of acoustic amplitudes. In fact, it can be shown that the systematic noise excitation influences the decay of acoustic amplitudes in time, when the amplitudes are sufficiently small, see App. K. The systematic noise excitation is described by the third term on the r.h.s. in Eq. (5.4) with Γ being the noise intensity.

Finally, K denotes a coefficient of the cubic (non-linear) saturation term, see also Eq. (3.48), which is relevant for high amplitudes.

The same differential equation also describes the amplitude dynamic of the anti-clockwise rotation component, which is referred to as mode component $B(t)$, cf. Eq. (2.47), viz.

$$\frac{\partial B(t)}{\partial t} = -\lambda B(t) + s(t) + \frac{\Gamma}{B(t)} - KB(t)^3. \tag{5.5}$$

The parameters λ, Γ and K do not necessarily have to be the same for $A(t)$ and $B(t)$. Moreover, the eigenfrequencies can be different. (Zahn et al. 2016) show that e.g. the influence of absorbers can lead to such non-degenerate mode dynamics. The pressure field $p'(t)$ is finally composed of the mode components $A(t)$ and $B(t)$, cf. Eq. (2.47). The composition of these modes is then referred to as first transverse mode.

(Noiray and Schuermans 2012) show that the differential equation according to Eq. (5.4) for $A(t)$ and Eq. (5.5) for $B(t)$ are valid if the mode amplitudes $A(t)/B(t)$ vary slowly with respect to the acoustic period. The goal of the method is to extract the parameters λ, Γ and K of Eq. (5.4) and Eq. (5.5) from dynamic pressure measurements. In the following, the method is further explained on the basis of the mode component $A(t)$ only. For the mode component $B(t)$, the procedure is the same and hence not presented in detail.

For sufficiently long dynamic pressure measurements in time, it can be assumed that the systematic noise excitation dominates over random noise excitation (priv. comm. with B. Schuermans, GE Power). In this case, the governing differential equations reduces to

$$\frac{\partial A(t)}{\partial t} = -\lambda A(t) + \frac{\Gamma}{A(t)} - KA(t)^3, \tag{5.6}$$

As the random noise excitation is hence irrelevant in the following, systematic noise excitation is simply referred to as noise excitation.

According to Eq. (5.6), the time variation of the amplitude $A(t)$ is influenced by the damping rate, noise excitation and non-linear cubic saturation. For small amplitudes, noise excitation dominates, initiating the possible onset of a linearly unstable combustion driven feedback cycle (second term on the r.h.s.). When an acoustic mode is initially excited by noise and the amplitudes reach a certain level, the second term on the r.h.s. becomes less relevant. In this situation, the strength of the overall damping and amplification of the mode determines if acoustic amplitudes decay, i.e. $\lambda > 0$, or grow, i.e. $\lambda < 0$, in time (first term on the r.h.s.). In case of stable operation, damping constantly counteracts noise excitation and the amplitudes remain small. For increasing amplitudes, in turn, the noise excitation gets more and more irrelevant and the flame feedback dominates the amplification. Decreased amplification strength and possibly enhanced damping capabilities due to non-linear effects reduces the growth of amplitudes and the limit cycle is finally reached (third term on the r.h.s.). For the analyses of amplitude dynamics in gas turbines (Noiray and Schuermans 2013) apply a cubic

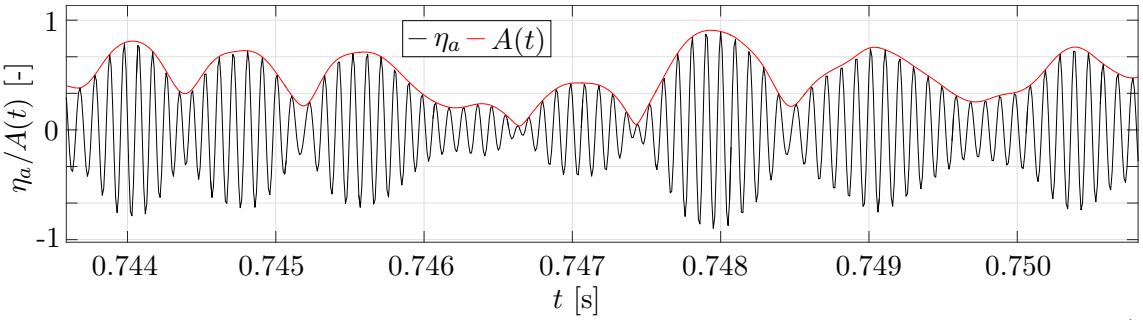

Fig. 5.6.: Normalized Fourier coefficient η_a and Hilbert transform amplitude $A(t)$.

saturation law. In this thesis, it is assumed that cubic saturation is also valid for the amplitude dynamics in rocket engines.

For the extraction of the time-invariant parameters, the dynamic pressure signals need to be decomposed into the components $A(t)$ and $B(t)$. Evaluating Eq. (2.26) and Eq. (2.47) at the chamber wall yields in time domain

$$p'(\theta, t) = \eta_a(t)\cos(\theta) + \eta_b(t)\sin(\theta), \tag{5.7}$$

with

$$\eta_a(t) = A(t)\cos(\omega^s\, t + \phi_a(t)), \tag{5.8}$$

and

$$\eta_b(t) = B(t)\cos(\omega^s\, t + \phi_b(t)), \tag{5.9}$$

where it is assumed that $A(t)$ and $B(t)$ as well as the phases $\phi_a(t)$ and $\phi_b(t)$ depend on time. Furthermore, the Fourier coefficients $\eta_a(t)$ and $\eta_b(t)$ are introduced. Essentially, $A(t)$ and $B(t)$ denote the envelopes of the corresponding Fourier coefficients.

First, the Fourier coefficients are determined using linear algebra

$$\underline{\underline{\eta}}_{a/b} = \underline{\underline{P}}\,\underline{\underline{\theta}}^T \left[\underline{\underline{\theta}}\,\underline{\underline{\theta}}^T\right]^{-1}, \tag{5.10}$$

where the matrix $\underline{\underline{P}}$ contains the dynamic pressure signals and $\underline{\underline{\theta}}$ the $\sin(\theta)/\cos(\theta)$ terms, cf. Eq. (5.7). For this step, the band-pass filtered dynamic pressure data recorded at eight locations in the HF measurement ring is used, cf. Fig. 5.2 (right). The data is filtered around the eigenfrequency of the first transverse mode employing a Butterworth band-pass filter of second order. In the second step, the envelopes $A(t)/B(t)$ are determined by applying the Hilbert transform to the Fourier coefficients. Fig. 5.6 shows a short interval of the time signal in terms of the Fourier coefficient η_a and its envelope $A(t)$. It can be seen that the amplitudes are reconstructed with very high accuracy. Finally, $A(t)$ and $B(t)$ as well as their time derivatives are used to fit the parameters λ, Γ and K in an optimization procedure. For unstable operation, i.e. in the presence of high amplitudes in case of LP2 and LP4, the fitting is based on Eq. (5.6). In contrast, for stable operation in case of LP1 and LP3, only low amplitudes are present and the

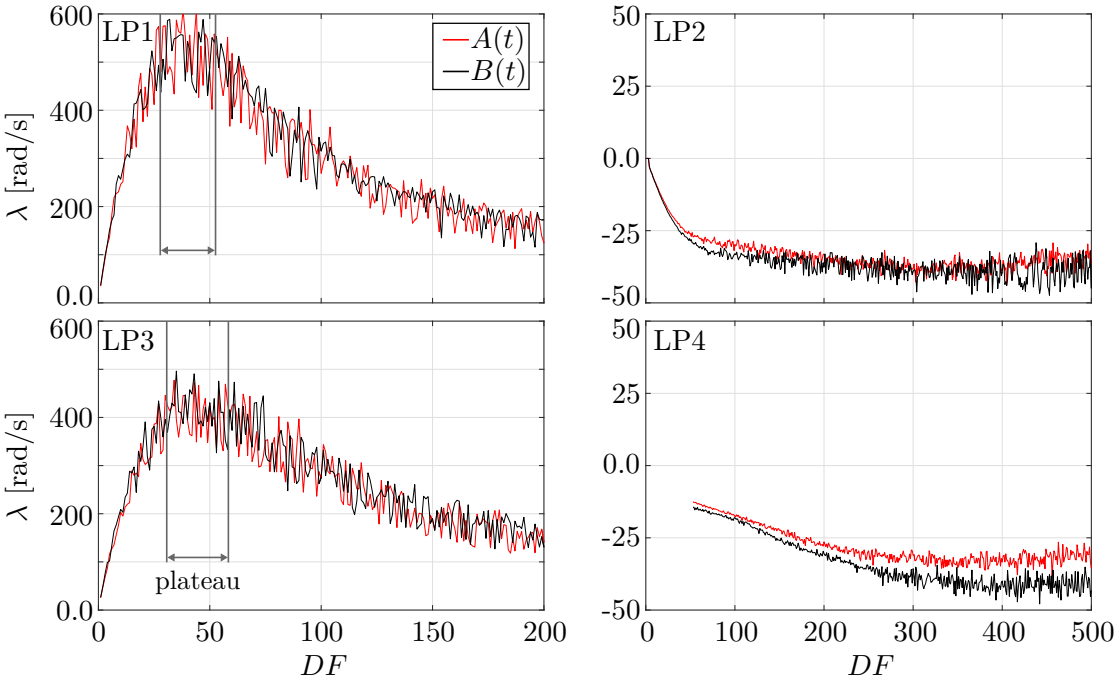

Fig. 5.7.: Damping rate λ over down-sampling factor DF for LP1-4.

cubic saturation term in Eq. (5.6) is therefore dropped yielding a reduced form of the governing differential equation:

$$\frac{\partial A(t)}{\partial t} = -\lambda A(t) + \frac{\Gamma}{A(t)}. \tag{5.11}$$

The generation of time derivatives of $A(t)$ and $B(t)$ is problematic. Essentially, $A(t)$ and $B(t)$ are superimposed by artificial high-frequency components, which significantly impair the numerical differentiation, cf. Eq. (5.4) and Eq. (5.6). To resolve this issue, a systematic reduction of data sampling frequency in order to filter artificial frequency components is made (priv. comm. with B. Schuermans, GE Power). An integer-valued down-sampling factor DF is introduced for this purpose. Therefore, the reduced sampling frequency is generally given by

$$f_{DF} = \frac{100 \text{ kHz}}{DF}, \tag{5.12}$$

with $DF = 1, 2, 3, 4, \ldots$. The experimental sampling frequency of 100 kHz was reported in (Gröning et al. 2015b). The usage of integers allows for a simple application of down-sampling, since the DF-th values in the discrete pressure data series can easily be extracted. A down-sampling factor of e.g. 50 reduces the sampling frequency to only 2 kHz. However, as the consequence of applying a systematic down-sampling a range for each parameter λ, Γ and K is determined.

First, the findings in terms of damping rates are presented. Fig. 5.7 (left) shows λ for both modes $A(t)$ and $B(t)$ in case of LP1 and LP3 for an interval of DF = 1-200.

Beyond a DF of 200, the damping rate does not change significantly. Therefore, higher down-sampling rates do not have to be considered. In general, a positive λ confirm stable operation for LP1 and LP3. The wide interval of DF, however, leads to a large range of damping rates. Initially, a steep increase of λ is found for small down-sampling factors. This behavior can be attributed to the presence of artificial high-frequency components and therefore inaccurate fitting results. With increasing DF, the high-frequency components are more and more filtered out leading to the formation of a plateau of λ, cf. Fig. 5.7. Varying the down-sampling factor in this plateau region does not alter relevantly the damping rate. The maximum value is defined as the upper limit of the λ range. If the down-sampling factor is further increased, a reduction of the damping rate is observed until it converges towards a rather constant value, which is defined as the lower limit of the λ range.

The damping rate variations over DF in case of LP2 and LP4 are shown in Fig. 5.7 (right). In contrast to LP1 and LP3, λ directly converges towards a constant value without the formation of an intermediate plateau. The calculated λ range is therefore smaller than in case of LP1 and LP3. However, higher DF are required in order to reach a constant λ. In fact, an interval of DF = 1-500 is used. In general, negative damping rates are determined confirming the presence of an instability for LP2 and LP4, cf. Fig. 5.4.

The calculated λ ranges for LP1-4 using the parameter extraction method are given in Tab. 5.2. For the stable LP1 and LP3 the ranges read $\lambda = [200; 500]$ rad/s and $\lambda = [180; 390]$ rad/s, which are one order of magnitude smaller than the findings based on the Lorentzian fitting procedure. These discrepancies are difficult to explain using only the available dynamic pressure data. However, they could be related to the influence of non-linear effects, which might emerge in case of operation conditions close to the stability limit (Noiray 2016). Furthermore, the presence of several peaks in close proximity to the T_1 eigenfrequency in the PSD, cf. Fig. 5.5, might additionally influence the computation of the damping rate and hence lead to different results using the Lorentzian fitting procedure and the parameter extraction method. A detailed analysis of the methods used for the determination of the damping rate is hence required, which is however out of the scope of this thesis.

The negative damping rates in case of an instability are one order of magnitude smaller than the positive damping rates for stable operation, if the results based on the parameter extraction method are considered as reference. In fact, for LP2 a range of $\lambda = [-40; -30]$ rad/s is determined for mode $A(t)$ and mode $B(t)$. A similar range is calculated for LP4. However, according to the results, the LP4 damping rates of the modes $A(t)$ and $B(t)$ are not the same. The damping rate range for mode $B(t)$ is $\lambda = [-40; -37]$ rad/s, which is slightly more negative than the range of $\lambda = [-31; -29]$ rad/s for mode $A(t)$. The inequality of λ for $A(t)$ and $B(t)$ in case of LP4 is difficult to interpret, but it might be related to non-linear mode interaction. The more negative damping rates for mode $B(t)$ suggest that this mode exhibits a stronger initial growth after the onset of an instability. Furthermore, the negative damping rates of LP2 and LP4 are close to the stability limit, which is defined by $\lambda = 0$ rad/s. Therefore, the initial growth of acoustic amplitudes is rather weak for these LP.

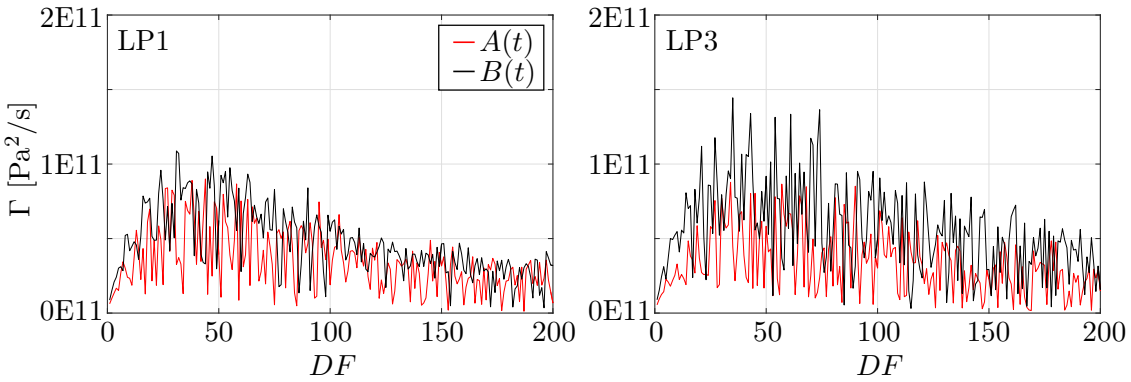

Fig. 5.8.: Noise intensity Γ [Pa^2/s] over down-sampling factor DF for LP1 and LP3.

The parameter extraction methods also provides ranges for the noise intensity Γ as well as for the non-linear saturation coefficient K. These quantities are analyzed next.

The noise intensity Γ is shown over the down-sampling factor DF for modes $A(t)$ and $B(t)$ in case of LP1 and LP3 is shown in Fig. 5.8. A similar shape as for the damping rate is found, cf. Fig. 5.7. High-frequency components in the low DF regime also affect the calculation of Γ. A high order of magnitude of $\mathcal{O}(11)$ is found. LP1 and LP3 show similar noise intensities. Consequently, the acoustics amplitudes are excited by noise with similar strength for LP1 and LP3.

As already explained, the noise excitation term in Eq. (5.6) (second term on the r.h.s.) is irrelevant in case of LP2 and LP4, since high amplitudes are present. Therefore, the fitting procedure does not deliver reasonable results for Γ, since the dynamics are completely dominated by the first and third term in Eq. (5.6). In consequence, the noise intensity for LP2 and LP4 cannot be analyzed.

Finally, the non-linear saturation coefficient K is discussed. As high amplitudes are present for LP2 and LP4, K can only be determined for these LP. The findings are shown in Fig. 5.9. After the strong variation for low DF, constant values are found for higher DF. The values of K are not the same for mode $A(t)$ and mode $B(t)$. As explained before, non-linear mode interaction might be the reason.

The order of magnitude of the non-linear saturation coefficient is small. In fact, K is of the order of $\mathcal{O}(-9)$ for LP2. For LP4, K is calculated one order of magnitude smaller, i.e. $\mathcal{O}(-10)$. Hence, non-linear saturation seems to be stronger for LP2.

To show that the calculated K are plausible, the orders of magnitude of the different terms in Eq. (5.6) are analyzed exemplary for LP2. As noise excitation is irrelevant for the unstable LP, the second term on the r.h.s is dropped for this investigation.

The amplitudes vary with several bar for unstable operation (Gröning et al. 2013b), i.e. of the order of $\mathcal{O}(5)$. A time scale can be concluded from the fact that the variations of the envelopes $A(t)$ and $B(t)$ are slow in comparison to the acoustic period of the first transverse mode (Noiray and Schuermans 2012), cf. Fig. 5.6. As the first transverse mode oscillates with approximately 10 kHz, the acoustic time scale is $\mathcal{O}(-4)$. A conservative guess for the time scale of the variations of the amplitudes $A(t)$ and $B(t)$

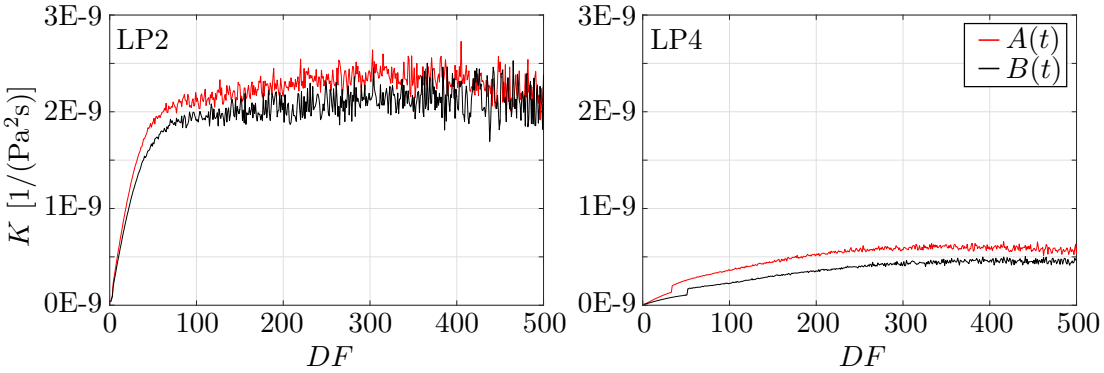

Fig. 5.9.: Non-linear saturation coefficient K [1/(Pa^{2}s)] over down-sampling factor for LP2 and LP4.

is therefore $\mathcal{O}[-3; -2]$. In the following, $\mathcal{O}(-2)$ is used. The damping rate for LP4 is of the order $\mathcal{O}(1)$, cf. Tab. 5.2. Finally, the order of K is given in Fig. 5.9 (left) with $\mathcal{O}(-9)$.

The orders of magnitude are now compared in Eq. (5.13). The first line shows the governing differential equation again. The second line indicates the corresponding orders of magnitude of each individual parameter as well as of the amplitude. Furthermore, the time scale is shown. Finally, the third line presents the multiplication of the single orders of magnitude and the time scale for each individual term. Essentially, the orders are well balanced indicating that the order of magnitude of K is in fact plausible. Its very low order is balanced by the cubic dependence on the amplitude in the last term of Eq. (5.6). The overall order of magnitude of Eq. (5.6) is $\mathcal{O}[6; 7]$.

$$\begin{array}{ccccc} \dfrac{\partial A(t)}{\partial t} & = & -\lambda \cdot A(t) & - & K \cdot A(t)^3, \\ \dfrac{\mathcal{O}(5)}{\mathcal{O}(-2)} & & \mathcal{O}(1) \cdot \mathcal{O}(5) & & \mathcal{O}(-9) \cdot \mathcal{O}(5)^3 \\ \mathcal{O}(7) & & \mathcal{O}(6) & & \mathcal{O}(6) \end{array} \tag{5.13}$$

6 Stability Assessment Procedure

Thermoacoustic processes are unsteady and contain complex flame - acoustic interactions. Moreover, realistic rocket engines are equipped with a high number of injectors. The simulation of the temporal behavior of pressure and temperature inside the combustion chamber is therefore highly challenging. In this thesis, a hybrid approach is used to reduce computational turn-around times. For this purpose, the methodology employed in Chap. 4 is extended to account for reactive conditions. In consequence, the reduction of the LEE to only four equations in three-dimensional space under isentropic conditions is no longer applicable. Instead, the full set of the LEE under non-isentropic conditions needs to be solved. Furthermore, the extension concerns two additional aspects: The determination of representative mean flows including combustion as well as the modeling of the feedback term $\hat{\dot{q}}$ in the energy equation of the LEE.

In this section, the followed methodology is first illustrated and the stability assessment procedure is subsequently presented. The different steps are exemplified by means of the BKD test chamber, cf. Chap. 5. The analyses of BKD's thermoacoustic behavior is afterwards presented in the next Chapter.

As explained in Chap. 1, transverse modes are most destructive for rocket engine operation, since longitudinal modes are strongly damped by the convective transport in the thrust nozzle (Morgenweck et al. 2010). Hence, the stability assessment procedure is developed to be applicable for transverse modes. High amplitude operation for LP2 and LP4 in case of the BKD is associated with the first transverse mode, cf. Sec. 5.2. In consequence, the focus is on the first transverse mode in the following.

6.1. Extended Methodology for the Incorporation of Reactive Flow into the Simulation

In this first section, the extended methodology for the incorporation of the reactive flow into the simulations is introduced. Special attention is paid towards to minimization of the computational turnaround times. For this purpose, the scope of the stability assessment procedure is explained next.

6.1.1. Scope of the Stability Assessment Procedure

The amplitude dynamics of the clockwise rotating and anti-clockwise rotating mode depend on the interplay of damping rate, noise excitation and non-linear saturation, see Sec. 5.4.2 and especially Eq. (5.6). However, the *linear* stability is determined from the interplay of noise excitation and damping rate exclusively. Initial noise excitation leads to an exponential growth of amplitudes only if the damping rate is negative. Since the damping rate describes the temporal behavior of acoustics at small amplitudes, λ can be calculated on the basis of linear equations. For this purpose, amplitude-dependent effects are neglected and noise is not included in the acoustic simulations. Hence, the amplitudes are assumed to be already large enough that noise excitation can be neglected, but still small enough that non-linearity does not play a role. In consequence, the governing differential equations under consideration read

$$\frac{\partial A(t)}{\partial t} = -\lambda A(t) \tag{6.1}$$

and

$$\frac{\partial B(t)}{\partial t} = -\lambda B(t), \tag{6.2}$$

which are in fact linear relations and describable with linearized equations, cf. Eq. (5.4).

The goal of the stability assessment procedure presented in this thesis is to calculate the damping rate and to determine the linear stability of the BKD test chamber configuration using a hybrid approach. Therefore, the calculated damping rate λ is used to determine whether noise excitation leads to growing or decaying amplitudes in time.

The damping rate λ of the first transverse mode is potentially influenced by the entire thrust system. As discussed in Chap. 4, damping originates from the nozzle and from the dome coupling, see Sec. 4.1 and Sec. 4.2, as well as from the influence of absorbers, see Sec. 4.3.2. Since the damping capabilities of each of these components depend on the complex frequency, also the chamber geometry and speed of sound indirectly affect λ, cf. Eq. (2.60). Especially the influence of speed of sound shows that the reactive flow might significantly change the overall damping in comparison to non-reactive conditions. Additionally, the dynamic heat release contributes to damping or amplification. When the Rayleigh criterion is fulfilled, see Eq. (2.104), flame dynamics might lead to negative damping rates and ultimately result in the growth of amplitudes in time. In consequence, the computation of the damping rate requires the incorporation of the entire combustion chamber and injection system into the acoustic simulations.

6.1.2. Separation of Scales

Although the calculation of λ is based on the simulation at small amplitudes only, the computation of the spatiotemporal fluiddynamic behavior of the entire rocket engine under this condition is still accompanied by extreme computational efforts. This can be seen from the comparison of the scales of acoustics and of the reactive flow.

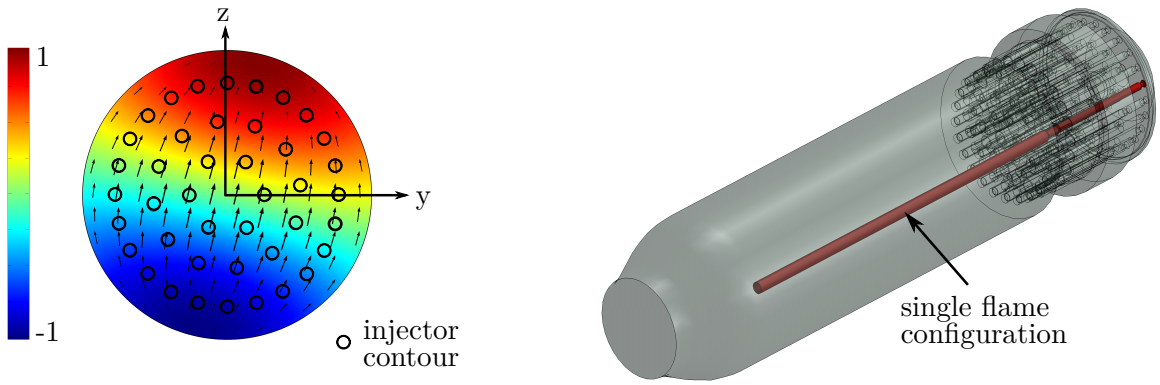

Fig. 6.1.: Left: First transverse mode structure in terms of normalized acoustic pressure (real part) and transverse velocity vector field together with injector contours. Right: Exemplary single flame configuration in the BKD test chamber.

The spatial scale of the first transverse mode corresponds to the chamber diameter. In contrast, combustion depends on mixing length scales, which are several order of magnitudes smaller than the chamber diameter. The acoustic time scale is given by the inverse of the acoustic period. Depending on chamber radius, combustion temperatures and propellant combination, transverse mode pressure typically oscillates between 1 kHz and 10 kHz yielding an acoustic time scale of $[10^{-4}; 10^{-3}]$ s. Furthermore, damping rates might be very small resulting in large time durations to be simulated in order to identify the growth or decay of the acoustic amplitudes, if the thermoacoustic system is close to the stability limit. In fact, negative damping rates for the BKD test chamber were calculated between -30 rad/s and -40 rad/s, see Tab. 5.2. Simulations need to capture such slow amplitude growth to assess the system stability. In contrast, the time scale of reaction is very small. For cryogenic H_2/O_2 driven propulsion at high pressures, the mixing process is limiting the time scale of combustion, yielding typical time scales of the order of 10^{-6} s, see Sec. 6.2.3.2. In consequence, the simulation of the internal reactive flow in the chamber including acoustic times scales requires enormous numbers of time steps, while the necessary grid refinement for the computation of turbulent combustion resolves acoustic spatial scales excessively.

To reduce turnaround times, a hybrid approach is applied to assess combustion stability in this thesis. The basic concept is to separate the spatial and temporal scales of acoustic propagation from those of the reactive flow. The separation leads to two significant advantages over fully coupled simulations. On the one hand, the acoustic propagation can be calculated using linearized conservation equations on coarse grids. Linearized equations also naturally describe the basic differential equation according to Eq. (6.1). On the other hand, optimized procedures for the simulation of the reactive flow field can be applied. The coupling of the reactive flow computation with the acoustic simulation is realized by two means. Firstly, the reactive flow field is converted into a mean flow, which is subsequently employed as linearization point for the acoustic equations. Therefore, the influence of the mean flow on the acoustic propagation is accounted for. Secondly, acoustically modulated heat release is incorporated into the

acoustic simulation in form of a feedback model. The parameters of the feedback model are determined in CFD simulations of the reactive flow using the steady mean flow result as initial solution.

The separated simulation of acoustic propagation and of reactive flow allows to further reduce computational efforts concerning the mean flow generation and determination of the feedback model parameters. Typically, industrial rocket engines are equipped with a high number of injectors resulting in thin flame structures, see Fig. 6.1 (left). The radial dimension of a flame corresponds to the radius of the injector, which is, in turn, much smaller than the radius of the chamber. Hence, the flame can be considered as acoustically compact in radial direction with respect to the first transverse mode, see Fig. 6.1 (left). That is, the acoustic wave length is much larger than the radial flame spread. In fact, for the considered BKD test chamber the ratio of injector to chamber radius amounts approximatively 0.06. In consequence, constant acoustic amplitudes in radial direction on single flame scale can be assumed. Such radially compact flame domains are referred to as single flame configurations. Radial acoustic compactness simplifies the necessary simulation domain in two respects.

Firstly, the first transverse mode shape and corresponding eigenfrequency primarily depend on the radially averaged mean flow quantities. Due to the presence of a high number of flame structures, which are compactly packed, it is assumed that the average of the mean flow quantities over the entire chamber cross-section corresponds to the average over a single flame configuration. In consequence, the radially averaged mean flow is determined from single flame simulation results. In the subsequent acoustic simulations, only the axial dependence of the mean flow quantities is included and radially averaged quantities are used.

Secondly, the radial compactness allows for the determination of feedback model parameters on the basis of single flame configurations as well. For this purpose, the single flame configurations are subjected to acoustic excitation, which mimics the influence of acoustic fluctuations in the chamber on the single flame. Afterwards, the response in terms of heat release modulation is extracted and employed to parameter calibration procedures.

6.1.3. Essential Steps of the Stability Assessment Procedure

In summary, the stability assessment procedure consists of four essential steps:

1. Generation of a representative mean flow using RANS CFD. The computational setup and the governing equations will be introduced in Sec. 6.2.
2. Determination of the open loop (i.e. $\hat{\dot{q}} = 0$) mode shape and eigenfrequency of the first transverse mode from acoustic simulations, see Sec. 6.3 and Sec. 6.4.
3. Simulation of a single flame configuration under acoustic excitation using URANS CFD and extraction of the response model parameters. This step is presented in Sec. 6.5. The mode shape to be excited is taken from the previous open loop acoustic simulations.

4. Determination of the closed loop (i.e. $\hat{\dot{q}} \neq 0$) mode shape, eigenfrequency as well as damping rate of the first transverse mode from acoustic simulations on the basis of the previously calculated response model parameters. The damping rate is used to assess the linear stability of the first transverse mode. This final step is explained in Sec. 6.6.

In the following, the necessary step to conduct the stability assessment procedure are explained in detail. First, the simulation of a single flame configuration under unexcited conditions is explained and the computation of the mean flow is presented.

6.2. Single Flame Simulation and Mean Flow Computation

The acoustic simulations are based on a representative mean flow. For its computation, a steady state simulation is performed for a single flame configuration. It is assumed that flame-flame interaction is negligible and that cooling effects at the wall do not alter the flame structure at near-wall locations. It is furthermore presumed that the total mass flow of propellants is equally distributed across all injectors. Equal mass flows are justified by the effect of the splitter plate in the dome leading to a homogenized propellant inflow, see (Sutton and Biblarz 2001) and Fig. 1.1. Since acoustic fluctuations are not included at this stage of the stability assessment procedure, the simulation of each single flame configuration in the chamber yields equal results. In consequence, the location of the single flame to be simulated can be chosen arbitrarily, cf. Fig. 6.1.

6.2.1. Computational Domain and Boundary Conditions

A single flame configuration comprises a part of the O_2 dome, one O_2 injector as well as a part of the combustion chamber, which is referred to as chamber section. The single flame configuration is shown in Fig. 6.1 (right) in red color. However, any other single flame configuration can be chosen for the determination of the mean flow.

The H_2 injection system is not included into the computational domain. Its impact on the chamber acoustics is assumed to be irrelevant, since high H_2 injection Mach numbers and a small H_2 injection area lead to a strong acoustic decoupling of the H_2 injection system from the combustion chamber, cf. Tab. 5.1.

The diameters of the virtual chamber and O_2 domains were chosen to conserve the area ratios between the propellants' injection area and the chamber cross-section as well as O_2 dome cross-section. At the outlet of the single flame configuration, the nozzle cannot be included. The computational domain is therefore confined to the inlet plane of the convergent nozzle part. Furthermore, rotational symmetry of the reactive field is assumed. In consequence, two-dimensional simulations can be conducted, reducing computational turn-around times substantially further.

The used rotationally symmetrical computational domain is shown in detail in Fig. 6.2. The O_2 mass flow is imposed at the inlet of the O_2 dome and the H_2 mass flow is applied to the corresponding surface at the inlet to the recess, cf. Tab. 5.1. However,

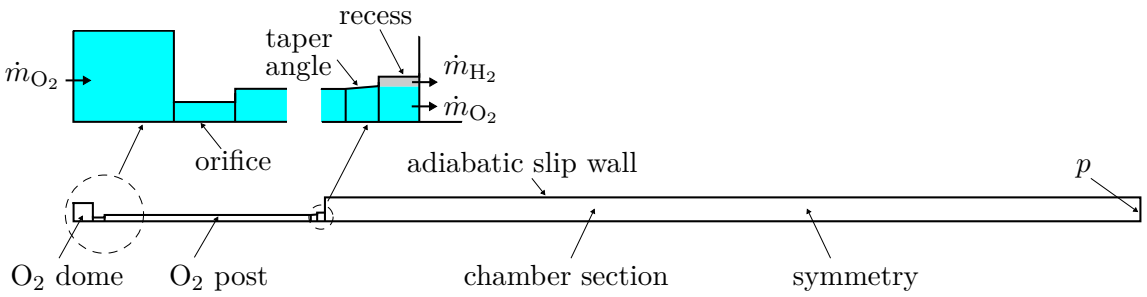

Fig. 6.2.: Computational domain for the single flame simulation.

the temperature of H_2 directly at injection into the recess is usually unknown, as only the dome temperatures are provided, cf. Tab. 5.1. In order to provide consistent H_2 injection temperatures at the boundary condition, cf. Fig. 6.2, a pre CFD simulation of the injection system including both the O_2 and H_2 injector taking conjugated heat transfer into account is conducted. From the results the injection temperature of H_2 is extracted and afterwards applied to the single flame simulation.

Since the nozzle is not included into the computational domain, pressure needs to be set at the outlet of the chamber, see Fig. 6.2. It is chosen such that the experimental chamber pressure, which is measured directly at the face plate, see Fig. 5.2, is realized in the simulation. In order to maintain the three-dimensionality of the reactive flow, rotational symmetry conditions are imposed on the flanges of the computational domain. The virtual free surfaces in the O_2 dome and in the chamber section are modeled as adiabatic, free-slip walls. In contrast, adiabatic no-slip conditions are imposed on wall surfaces of the injector, recess and face plate.

A disadvantage of the single flame domain simulations is that the consumption rates and heat release rates calculated by the combustion model cannot be validated on the basis of the computed chamber pressure. In reality, the chamber pressure is a consequence of the volume expansion due to combustion and the termination with the choked nozzle. As it will be shown in Sec. 6.2.4, the generation of the mean flow for the acoustic simulation allows to validate the combustion model in a subsequent step.

For the BKD test chamber single flame configuration, the computational domain is resolved with a total number of approximately 1×10^6 nodes. The computational grid is refined in the mixing and reaction zone O_2 and H_2.

In the next sections, the governing equations for the simulation of non-premixed combustion in a highly turbulent environment under the influence of real gas effects as encountered in the BKD test chamber are introduced. The simulations were conducted in ANSYS CFX 15.0 using RANS.

6.2.2. Real Gas Description

The usage of H_2/O_2 as propellants in the upper stage rocket engines is motivated by their high reactivity and the low molecular weight of the resulting combustion pro-

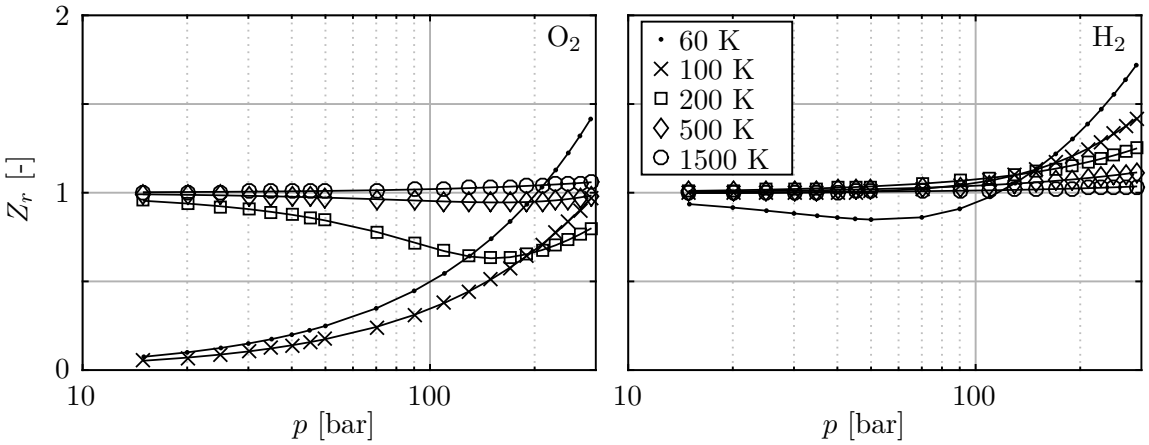

Fig. 6.3.: Real gas factor over pressure for different temperatures in case of pure O_2 (left) and H_2 (right) (Linstrom and Mallard 2015).

ducts (Sutton and Biblarz 2001; Turner 2005). Compact tanks are realized through the propellant's liquidation, which demands extremely low temperatures. It is therefore necessary to operate high efficient engines under *cryogenic* conditions. Propellants like O_2 and H_2 in liquid form provide very high amounts of energy per unit mass whereby the amount of fuel to be carried aboard decreases.

For high pressures and low injection temperatures, the ideal gas relation between thermodynamic state quantities becomes more and more inaccurate. Essentially, the volume of the molecule and the intermolecular forces relevantly influence density and pressure. For modeling internal rocket flows with combustion, such discrepancies between ideal gas and real gas behavior need to be accounted for, especially in the region of injection. To quantify the influence of real gas effects, the real gas factor Z_r is employed

$$Z_r = \frac{pV}{n\mathcal{R}T}. \tag{6.3}$$

If $Z_r = 1$, the ideal gas equation is obtained. Otherwise, real gas effects influence the thermodynamic state quantities. The deviation of Z_r from unity can be used to determine the significance of real gas effects.

Fig. 6.3 shows Z_r for pure O_2 and H_2 over pressure for different temperatures. O_2 needs to be treated as a real gas for a considerably wide range of temperatures and pressures. Especially, for very low temperatures, real gas effects significantly alter the thermodynamic behavior. In contrast, H_2 converges to ideal gas behavior already at lower temperatures. However, slight deviations from unity are still observed for pressures between 50-100 bar for a significantly large temperature range.

The different behavior of O_2 and H_2 is explained by their respective critical points: For moderate pressures ($p < 7p_c$), real gas effects are irrelevant if $T > 2\,T_c$ (Sattelmayer 2012). As shown in Tab. 6.1, the critical temperature for H_2 is considerably lower than for O_2. The criterion is met for H_2 already at approximately 70 K. With increasing pressure, ideal gas modeling is more and more inadequate.

Tab. 6.1.: Critical point, acentric factor and gas constant for O_2 and H_2 (Linstrom and Mallard 2015).

	T_c [K]	p_c [bar]	ρ_c [kg/m^3]	acentric factor ω_a	$\mathcal{R}$ [J/(kg K)]
O_2	154.6	50.43	436.1	0.0222	259.8
H_2	33.15	12.96	31.26	-0.219	4124

6.2.2.1. Real Gas Equations of State

The discrepancies between ideal gas and real fluid behavior originate from two effects: Real molecules have a finite volume as well as attract and repel each other, respectively. At high pressure and low temperature, intermolecular distance is short and attractive forces become significant. Such conditions are present in the feed system and injection region in the combustion chamber of cryogenic rocket engines.

Based on the ideas of (Van der Waals 1910), cubic equations of state (EOS) are used to describe real gas behavior generally in form of

$$(p + p_a)(v - b) = \mathcal{R}T. \tag{6.4}$$

Herein, p_a denotes the cohesion pressure, which reflects the influence of intermolecular forces on fluid pressure, and b the co-volume of the molecules, which reduces the effective fluid volume.

The effects of cohesion pressure and co-volume determine the deviation of Z_r from unity. If pressure and temperature are low, the intermolecular distance is still large enough that attractive forces dominate and the influence of the co-volume is weak. Consequently, the pressure predicted by the ideal gas law is too large and Z_r is hence smaller than unity. In contrast, if pressure is high, the intermolecular distance is small leading to a more significant influence of the co-volume and the molecules repel each other. Consequently, the volume predicted by the ideal gas law is too high and Z_r thus becomes larger than unity.

The cohesion pressure depends on the number of molecule collisions with the walls as well as on the influence of intermolecular forces on the intensity of collision. With decreasing specific volume, the number of collisions increases and intensity reduces. Both effects increase the cohesion pressure, which is therefore given by

$$p_a = \frac{a}{f(v^2)}, \tag{6.5}$$

where a is an empirically given coefficient and depends on species and temperature.

Different forms of Eq. (6.4) exist. Tab. 6.2 summarizes the empirical correlations for cohesion pressure and co-volume for ideal gas, Peng-Robinson (PR) (Peng and Robinson 1976) and Soave-Redlich-Kwong (SRK) (Soave 1972). In comparison to earlier forms (Redlich and Kwong 1949), PR and SRK improve accuracy by including the acentric factor ω_a, which reflects the deviation of the molecule form from ideal spherical shape.

Tab. 6.2.: Comparison of ideal gas, Peng-Robinson and Soave-Redlich-Kwong equation of state (Poling et al. 2001).

	Ideal gas (IG)	Peng-Robinson (PR)	Soave-Redlich-Kwong (SRK)
p_a	0	$\frac{a(T)}{v^2+2vb-b^2}$	$\frac{a(T)}{v^2+vb}$
$a(T)$	-	$a_0\left[1+n\left(1-\sqrt{T/T_c}\right)\right]^2$	$a_0\left[1+n\left(1-\sqrt{T/T_c}\right)\right]^2$
a_0	-	$0.45724\ \frac{\mathcal{R}^2T_c^2}{p_c}$	$0.42748\ \frac{\mathcal{R}^2T_c^2}{p_c}$
n	-	$0.37464+1.54226\,\omega_a-0.26993\,\omega_a^2$	$0.480+1.574\,\omega_a-0.176\,\omega_a^2$
b	0	$0.0778\frac{\mathcal{R}T_c}{p_c}$	$0.08664\frac{\mathcal{R}T_c}{p_c}$

In general, the forms of PR and SRK are similar, with the most significant difference being the definition of cohesion pressure.

6.2.2.2. Caloric Equation of State, Entropy and Speed of Sound

In the simulations, the caloric quantities need to be determined. The difference of internal energy e to an arbitrary reference state in terms of temperature and specific volume is calculated in a three-step process. First, an isothermal change of state v_{ref} to $v\to\infty$ is calculated at T_{ref} in order to ensure ideal gas conditions for the second step. Herein, the difference in internal energy due to the temperature change T_{ref} to T is computed under isochoric, ideal gas conditions, which are denoted with $()_0$. Finally, a second isothermal change of state accounts for the correct specific volume, i.e. $v\to\infty$ to v. The entire process reads:

$$e(T,v)-e(T_{\mathrm{ref}},v_{\mathrm{ref}})= \tag{6.6}$$
$$\int_{v_{\mathrm{ref}}}^{\infty}\left(T\left(\frac{\partial p}{\partial T}\right)_v-p\right)dv_{T_{\mathrm{ref}}}+\int_{T_{\mathrm{ref}}}^{T}c_{v,0}dT-\int_{v}^{\infty}\left(T\left(\frac{\partial p}{\partial T}\right)_v-p\right)dv_T.$$

Internal energy at the reference state is set to zero, i.e. $e(T_{\mathrm{ref}},v_{\mathrm{ref}})=0$. In the following, it is assumed that the reference state is in the ideal gas regime. In this case, the first integral in Eq. (6.6) is obsolete.

Enthalpy h is classically given by

$$h=e+pv. \tag{6.7}$$

The same procedure as for internal energy is performed for entropy s:

$$s(T,v)-s(T_{\mathrm{ref}},v_{\mathrm{ref}})= \tag{6.8}$$
$$\int_{v_{\mathrm{ref}}}^{\infty}\left(\frac{\partial p}{\partial T}\right)_v dv_{T_{\mathrm{ref}}}+\int_{T_{\mathrm{ref}}}^{T}\frac{c_{p,0}}{T}dT-\mathcal{R}\ln\left(\frac{p}{p_{\mathrm{ref}}}\right)-\int_{v}^{\infty}\left(\frac{\partial p}{\partial T}\right)_v dv_T.$$

Specific heat capacity c_v at isochoric conditions is generally defined by the change of internal energy with temperature. Using Eq. (6.6), c_v is given by

$$c_v = \left(\frac{\partial e}{\partial T}\right)_v = c_{v,0} - \frac{\partial}{\partial T}\left(T\left(\frac{\partial p}{\partial v}\right)_v - p\right), \tag{6.9}$$

where the differentials are evaluated on the basis of the EOS. The explicit equations are given in App. L. The isochoric specific heat capacity at ideal gas conditions $c_{v,0}$ is evaluated from the NASA polynomials (Burcat 1984; Burcat and Gardiner 2000; McBride et al. October 1993).

Using the volume expansivity β and isothermal compressibility $\mathcal{K}_T$, the isobaric specific heat capacity can be calculated (Anderson 2003)

$$c_p = c_v + vT\frac{\beta^2}{\mathcal{K}_T}, \tag{6.10}$$

where the coefficients are given by

$$\beta = -\frac{\left(\frac{\partial p}{\partial T}\right)_v}{v\left(\frac{\partial p}{\partial v}\right)_T}, \tag{6.11}$$

and

$$\mathcal{K}_T = -\frac{1}{v\left(\frac{\partial p}{\partial v}\right)_T}. \tag{6.12}$$

Combining Eq. (6.10) - Eq. (6.12) yields for c_p

$$c_p = c_v - T\frac{\left(\frac{\partial p}{\partial T}\right)_v^2}{\left(\frac{\partial p}{\partial v}\right)_T}. \tag{6.13}$$

The explicit forms of the differentials are given in App. L.

Finally, the speed of sound c is calculated for real gases by

$$c = \sqrt{-v^2\frac{c_p}{c_v}\left(\frac{\partial p}{\partial v}\right)_T} = \sqrt{\frac{c_p}{c_v}\left(\frac{\partial p}{\partial \rho}\right)_T}. \tag{6.14}$$

For the prediction of combustion stability, it is essential to correctly describe compressibility. For acoustic propagation, the isentropic compressibility is relevant, which is given by

$$\mathcal{K}_s = -\frac{1}{v\left(\frac{\partial p}{\partial v}\right)_s} = \frac{1}{\frac{1}{v}\left(\frac{\partial p}{\partial \rho}\right)_s} = \frac{1}{\rho\left(\frac{\partial p}{\partial \rho}\right)_s}. \tag{6.15}$$

According to Eq. (2.37), the isentropic chance of p with respective to ρ is given by the speed of sound, i.e.

$$\left(\frac{\partial p}{\partial \rho}\right)_s = c^2. \tag{6.16}$$

Therefore, the isentropic compressibility according to Eq. (6.15) reads

$$\mathcal{K}_s = \frac{1}{\rho c^2}. \tag{6.17}$$

In consequence, in order to validate the prediction of the isentropic compressibility by real gas EOS, density and speed of sound needs to be compared to reference data. The comparison is shown next.

6.2.2.3. Comparison of Equation of States

To evaluate the applicability of the different EOS to cryogenic rocket engine simulations, the predicted density is compared to the NIST (National Institute of Standards and Technology) database (Linstrom and Mallard 2015). Density ($\rho = 1/v$) is determined by solving the cubic Eq. (6.4) iteratively. In order to calculate the correct root, the initial value is set according to the reference value from NIST database.

The density is shown in Fig. 6.4 (left) for pure O_2 and in Fig. 6.5 (left) for pure H_2 in case of 60, 70 and 80 bar over a typical temperature range for cryogenic injection. In accordance with Z_r, cf. Fig. 6.3, the deviations between ideal gas and real gas behavior are already present at 200 K for O_2, while H_2 can reasonably be described by ideal gas relations down to approximately 85 K.

In case of O_2, the ideal gas law strongly underpredicts density for temperatures below 200 K. At typical injection temperatures of around 100-115 K, the error reads approximately 80 % for the considered pressures. In general, the real gas EOS describe density significantly more accurate. However, PR leads to overpredictions in the relevant temperature range of up to 12 %. Overall, SRK provides a higher accuracy with a maximum error of 7 % at approximately 150 K. For H_2, SRK provides very accurate density predictions, while PR deviates considerably from the NIST database.

To further validate the EOS for the description of acoustic propagation in the cryogenic regime, speed of sound is considered in Fig. 6.4 (right) for pure O_2 and in Fig. 6.5 (right) for pure H_2, cf. Eq. (6.17). In case of the consideration as an ideal gas, unacceptable discrepancies are found for O_2 in the lower temperature range. Above 300 K, the error is below 1 %. PR and SRK describe speed of sound accurately down to 160 K. For lower temperatures, the prediction of speed of sound is getting more and more inaccurate. At typical injection temperatures, the error of PR and SRK is approximately 16-20 %.

For H_2, the ideal gas description of speed of sound substantially deviates from the NIST database below approximately 65 K. Considerable differences between NIST and

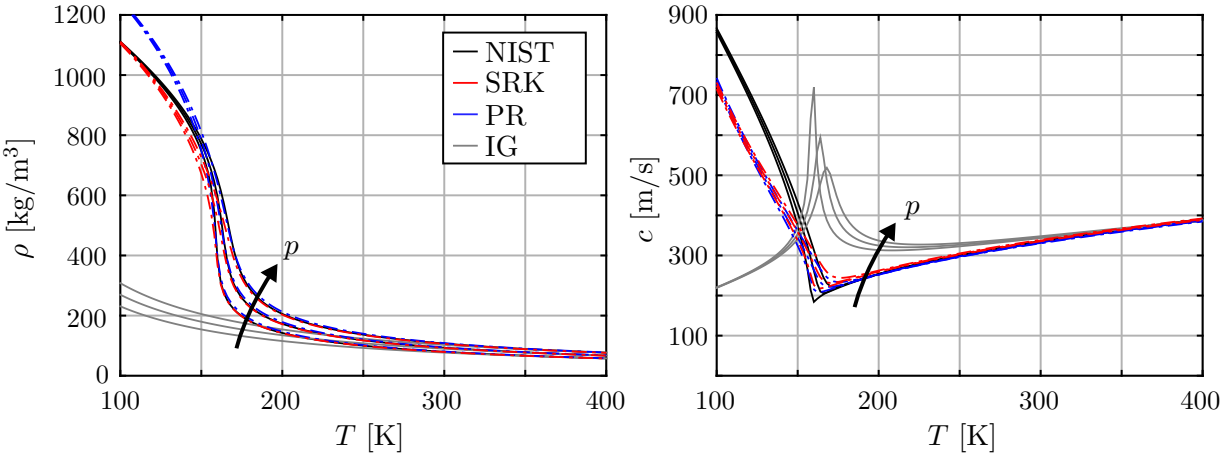

Fig. 6.4.: Density (left) and speed of sound (right) for pure O_2 and comparison between NIST database, SRK EOS, PR EOS and ideal gas law for 60, 70 and 80 bar.

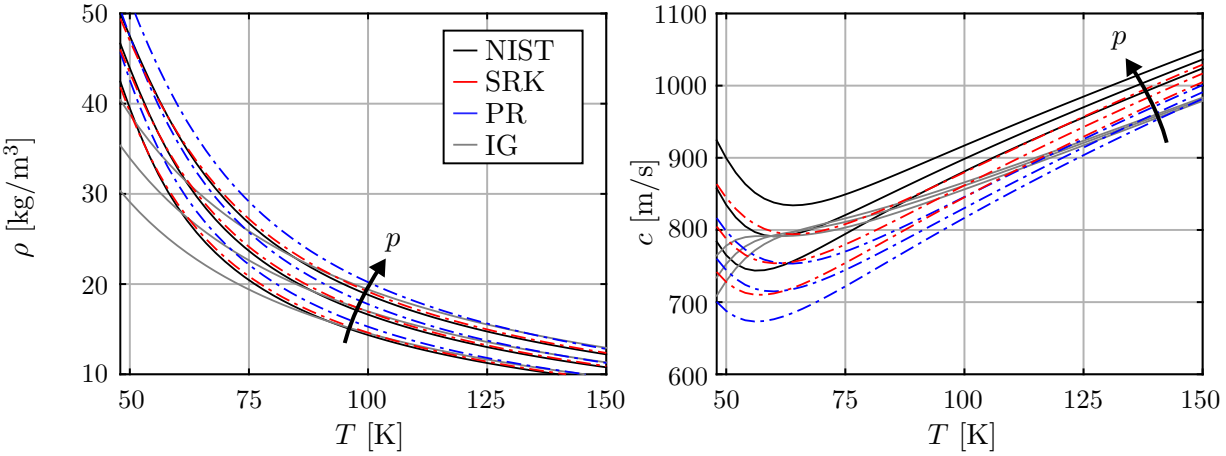

Fig. 6.5.: Density (left) and speed of sound (right) for pure H_2 and comparison between NIST database, SRK EOS, PR EOS and ideal gas law for 60, 70 and 80 bar.

ideal gas are also present for higher temperatures. The differences can be explained by a real gas factor of approximately 1.03-1.05 in this particular range. PR and SRK are, however, capable of providing higher accuracy, but deviations of 3-4 % still occur.

For the description of cryogenic O_2/H_2 flow including acoustic propagation with the ideal gas law results in unacceptable deviation for density and for speed of sound and hence for isentropic compressibility in the feed and injection region, see Eq. (6.17). On the one hand, incorrectly described density at the propellant inlets affects the injection momentum and consequently alters the flame length. On the other hand, discrepancies in speed of sound modify the characteristic impedance of the fluid affecting the system eigenfrequencies.

Additionally, Fig. 6.6 shows the isobaric and isochoric heat capacities for O_2 in case of 60, 70 and 80 bar in the low temperature regime. It can be seen that enormous amounts of energy must be supplied to increase the O_2 temperature in the injection region. In particular, c_p peaks close to 150 K, which can be regarded as equivalent to the evaporation process for liquid propellants.

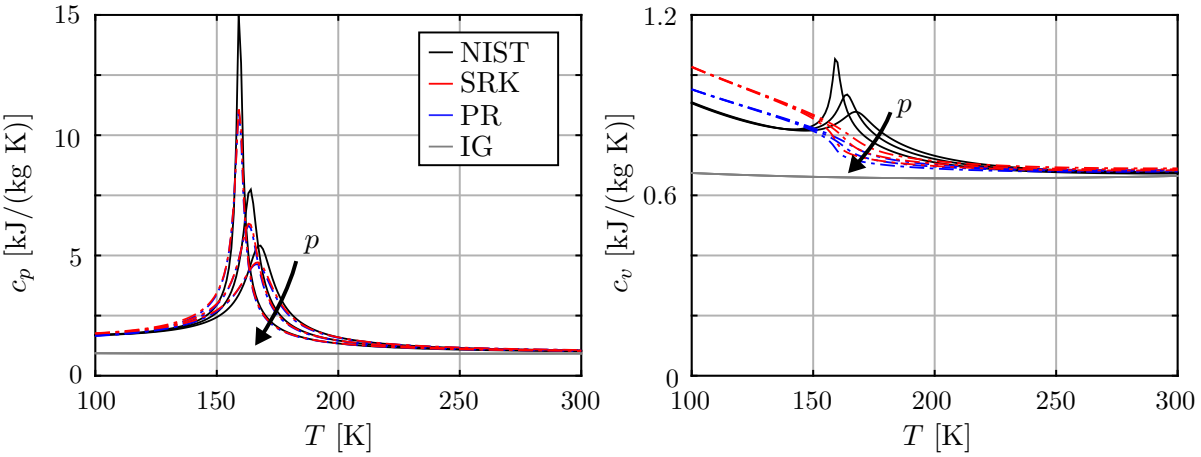

Fig. 6.6.: Specific heat capacity at isobaric (left) and isochoric (right) conditions for pure O_2 at 60, 70 and 80 bar.

Based on the comparisons, SRK is found to be the best choice for simulating cryogenic rocket flow and is used in the CFD simulations. However, the substantial error of 16-20 % for O_2 in terms of the speed of sound needs to be carefully addressed when performing simulations under acoustic excitation.

Improvements might be achieved by using the extension of Abudour (Abudour et al. 2012, 2013; Matheis et al. 2016), which is a volume-translation method and bases on the PR EOS. It could be shown, that density is accurately matched and the deviations for speed of sound are reduced to approximately 5 %. However, Abudour's extension is not implemented into the current ANSYS CFX software package used in this thesis.

6.2.3. Multi-Component Flow and Combustion

The governing field equations for the simulation of the reactive flow in the single flame configuration are presented next. The equations are based on the general set of the multi-component Navier-Stokes equations (2.1)-(2.7) and the SRK EOS to explicitly describe equation (2.8).

Simulations in ANSYS CFX 15.0 are based on enthalpy, which alters the energy equation (2.3):

$$\frac{\partial(\rho h)}{\partial t} + \frac{\partial(\rho u_i h)}{\partial x_i} = \frac{\partial p}{\partial t} + u_i \frac{\partial p}{\partial x_i} + \frac{\partial}{\partial x_i}\left(\sigma \frac{\partial T}{\partial x_i} + \sum_k^N \Gamma_k h_k \frac{\partial Y_k}{\partial x_i}\right) + (\tau_{ij} - p\delta_{ij}) \frac{\partial u_i}{\partial x_j}. \tag{6.18}$$

Enthalpy h is defined for reactive flow by

$$h = e + \frac{p}{\rho} + \sum_k^N \Delta h_k^0 Y_k, \tag{6.19}$$

and contains the chemical enthalpy $\sum_k^N \Delta h_k^0 Y_k$, where h_k^0 denotes the mass formation enthalpy of k-th species.

6.2.3.1. Turbulence Modeling and Mixing

Due to the small propellant injection areas with the high density of O_2 and with the high injection velocity of H_2, the propellant flows are turbulent, see Fig. 5.3 and Tab. 5.1. The influence of turbulence on the reactive flow field needs to be included into the simulation. However, to avoid the resolution of turbulent scales in the computations, the effect of turbulent fluctuations is modeled. The modeling approach is present in the following.

For the modeling of turbulence, the governing equations need to be rewritten in averaged form. First, this averaging process is explained. Introducing mass-weighted ensemble averages of a quantity $\tilde{\phi}$, the so-called Favre averages, according to

$$\tilde{\phi} = \frac{\overline{\rho\phi}}{\bar{\rho}} \tag{6.20}$$

yields

$$\phi = \tilde{\phi} + \phi'', \tag{6.21}$$

where ϕ'' denotes the fluctuating quantities. It holds that $\widetilde{\phi''} = 0$. Using Eq. (6.21), the averaged equations are derived next.

For the sake of readability, only the average of the unresolved scales are explicitly highlighted, while ($\tilde{}$) is otherwise dropped. In this notation, mass conservation is not changed, cf. Eq. (2.1). The momentum equation yields:

$$\frac{\partial(\rho u_j)}{\partial t} + \frac{\partial(\rho u_i u_j)}{\partial x_i} + \frac{\partial p}{\partial x_j} = \frac{\partial \tau_{ij}}{\partial x_i} - \frac{\partial(\rho\widetilde{u_i'' u_j''})}{\partial x_i}, \tag{6.22}$$

where the unresolved (Reynolds) stresses are modeled by

$$-(\rho\widetilde{u_i'' u_j''}) = \mu_\mathrm{t}\left(\frac{\partial u_i}{\partial x_j} + \frac{\partial u_j}{\partial x_i}\right) - \frac{2}{3}\delta_{ij}\left(\rho k_\mathrm{t} + \mu_\mathrm{t}\frac{\partial u_k}{\partial x_k}\right), \tag{6.23}$$

which increases the viscous dissipation in order to include the dissipating character of small turbulent scales. The turbulent viscosity is calculated from

$$\mu_\mathrm{t} = C_\mu \rho \frac{k_\mathrm{t}^2}{\epsilon}, \tag{6.24}$$

where k_t denotes turbulent kinetic energy, ϵ turbulent dissipation rate and C_μ a model constant. In this thesis, the two equation turbulence model $k_\mathrm{t} - \epsilon$ is applied to determine turbulence kinetic energy and turbulent dissipation rate. For this purpose, two additional transport equations are solved for k_t and ϵ

$$\frac{\partial}{\partial t}(\rho k_\mathrm{t}) + \frac{\partial}{\partial t}(\rho u_i k_\mathrm{t}) = \frac{\partial}{\partial x_j}\left[\left(\mu + \frac{\mu_\mathrm{t}}{\sigma_{k_\mathrm{t}}}\right)\frac{\partial k_\mathrm{t}}{\partial x_j}\right] + P_{k_\mathrm{t}} - \rho\epsilon \tag{6.25}$$

$$\frac{\partial}{\partial t}\left(\rho\epsilon\right)+\frac{\partial}{\partial t}\left(\rho u_i\epsilon\right)=\frac{\partial}{\partial x_j}\left[\left(\mu+\frac{\mu_\mathrm{t}}{\sigma_\epsilon}\right)\frac{\partial\epsilon}{\partial x_j}\right]+\frac{\epsilon}{k_\mathrm{t}}\left(C_{\epsilon1}P_{k_\mathrm{t}}-C_{\epsilon2}\rho\epsilon\right), \tag{6.26}$$

where P_{k_t} accounts for the production of turbulence by viscous forces and is given by

$$P_{k_\mathrm{t}}=\mu_\mathrm{t}\left(\frac{\partial u_i}{\partial x_j}+\frac{\partial u_j}{\partial x_i}\right)\frac{\partial u_j}{\partial x_j}-\frac{2}{3}\frac{\partial u_k}{\partial x_k}\left(3\mu_\mathrm{t}\frac{\partial u_k}{\partial x_k}+\rho k_\mathrm{t}\right), \tag{6.27}$$

cf. (ANSYS 2014a,b).

The $k_\mathrm{t}-\epsilon$ turbulence model is known to capture accurately separated flows (Speziale and Thangam 1992), which is necessary to simulate adequately the pressure drop over the injectors. Herein, transport equations are solved for k_t and ϵ at each iteration step and appropriate boundary conditions need to be imposed. It is referred to (ANSYS 2014a,b; Poinsot and Veynante 2005) for detailed information.

Conservation of enthalpy in averaged form reads

$$\frac{\partial(\rho h)}{\partial t}+\frac{\partial(\rho u_i h)}{\partial x_i}=\frac{\partial p}{\partial t}+\frac{\partial}{\partial x_i}\left(\sigma\frac{\partial T}{\partial x_i}+\sum_k^N \Gamma_k h_k\frac{\partial Y_k}{\partial x_i}-\rho\widetilde{u_i''h''}\right)+\tau_{ij}\frac{\partial u_i}{\partial x_j}, \tag{6.28}$$

where the turbulent enthalpy fluxes are determined from a gradient transport assumption by

$$-\rho\widetilde{u_i''h''}=\frac{\mu_\mathrm{t}}{\mathrm{Pr_t}}\frac{\partial h}{\partial x_i}, \tag{6.29}$$

where $\mathrm{Pr_t}$ denotes the turbulent Prandtl number, which is set to 0.9 in CFX.

The species transport equation in averaged form is given by

$$\frac{\partial\rho Y_k}{\partial t}+\frac{\partial(\rho u_i Y_k)}{\partial x_i}=\frac{\partial}{\partial x_i}\left(\Gamma_k\frac{\partial Y_k}{\partial x_i}-\rho\widetilde{u_i''Y_k''}\right)+\dot{\omega}_k, \tag{6.30}$$

and the turbulent species flux reads

$$-\rho\widetilde{u_i''Y_k''}=\Gamma_t\frac{\partial Y_k}{\partial x_i}=\frac{\mu_\mathrm{t}}{\mathrm{Sc_t}}\frac{\partial Y_k}{\partial x_i}, \tag{6.31}$$

where Γ_t denotes the turbulent diffusion coefficient, which is modeled as the ratio between turbulent viscosity and the turbulent Schmidt number $\mathrm{Sc_t}$. In CFX, the turbulent Schmidt number is set equal to the turbulent Prandtl number.

To reduce computational efforts for the calculation of energy and mass diffusion, the laminar Lewis number of each component is set to unity, i.e.

$$\mathrm{Le}_k=\frac{\sigma}{c_p\Gamma_k}=1 \tag{6.32}$$

In consequence, the molar diffusion coefficient Γ_k is substituted by the bulk viscosity in Eq. (6.30) and the enthalpy Eq. (6.28) reduces to

$$\frac{\partial(\rho h)}{\partial t} + \frac{\partial(\rho u_i h)}{\partial x_i} = \frac{\partial p}{\partial t} + \frac{\partial}{\partial x_i}\left(\left[\frac{\sigma}{c_p} + \frac{\mu_\mathrm{t}}{\mathrm{Pr_t}}\right]\frac{\partial h}{\partial x_i}\right) + \tau_{ij}\frac{\partial u_i}{\partial x_j}. \tag{6.33}$$

(Poinsot and Veynante 2005) argues that laminar diffusive fluxes for species and enthalpy are often irrelevant in comparison to turbulent transport. In consequence, the first term on the r.h.s. of Eq. (6.30) as well as the second term on the r.h.s. of Eq. (6.33) are small and could be neglected. However, CFX also describes the laminar fluxes. The necessary transport properties are given in App. M.

In the simulations, the different components share velocity, pressure, temperature and turbulence fields. For the determination of the bulk motion, density and transport properties of the single species are deduced from mixing. Under real gas conditions, non-ideal mixing rules apply (Kwak and Mansoori 1986). (Poschner and Pfitzner 2010) show that real gas mixing rules insignificantly influence the field results under typical rocket engine conditions. This could be due to the fact that the mixing region coincides with the reaction zone. Consequently, mixing takes place at high temperatures, at which ideal gas rules are valid. Based on these conclusions, ideal gas mixing rules are used in this thesis.

Ideal mixing rules calculate the mass fraction weighted average of quantity ϕ. Therefore, ϕ is given by

$$\phi = \sum_k^N Y_k \phi_k. \tag{6.34}$$

Eq. (6.34) is applied to material properties such as laminar viscosity μ, laminar thermal heat conductivity σ, heat capacities c_p, c_v, but also to derivatives of the EOS, i.e. $\left(\frac{\partial p}{\partial v}\right)_T$ and $\left(\frac{\partial p}{\partial T}\right)_v$, which are calculated from the real gas EOS.

6.2.3.2. Combustion Modeling

The propellants are converted into products under heat release by non-premixed combustion in the chamber. For the CFD simulation of the singe flame configuration, cf. Fig. 6.2, for steady state as well as under acoustic excitation, the strong influence of the heat release on the flow field needs to be modeled. In the following, the chosen modeling approach is explained.

In case of the BKD test chamber, O_2 and H_2 are injected close to critical temperature and pressure conditions, cf. Tab. 5.1 and Fig. 6.3. Hence, combustion is characterized as transcritical and supercritical, respectively. In this state, phase changes do not occur and classical subprocesses such as atomization and evaporation of droplets are not present. Instead, with increasing pressure rising above the critical point, the surface tension is progressively lowered, and a gas-like jet behavior emerges including complex gas/gas-like mixing with high diffusivity (Chehroudi 2012; Hickey and Ihme 2013).

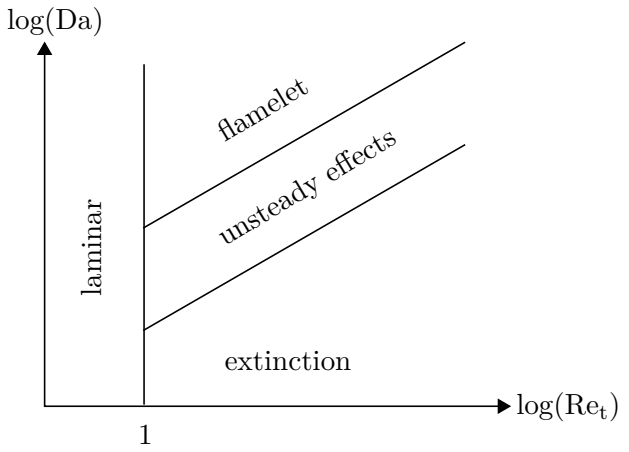

Fig. 6.7.: Regimes of turbulent non-premixed combustion in terms of the Damköhler number Da and the turbulent Reynolds number $\mathrm{Re_t}$, adapted from (Poinsot and Veynante 2005).

As atomization and evaporation are absent, the combustion in supercritical state is dominated by two processes. First, the propellants need to be brought into contact. In non-premixed flames, the propellants are transported into the reaction zone by diffusion in the mixing zone. In the second step, the mixed propellants react in the reaction zone leading to the formation of the combustion products. Usually, the flame front is located where the propellants are mixed stoichiometrically (Poinsot and Veynante 2005).

The mixing and reaction zones are strongly influenced by turbulence. For example, the presence of turbulent vorticies leads to flame wrinkling, which imposes strain on the mixing and reaction zones potentially leading to quenching. However, if the chemical reactions are fast compared to the turbulent time scales, the mixing and reaction zone follows the flow structures and quenching is unlikely to occur. This example shows that the choice of a suitable combustion model depends on the present ratio of time scales between chemical reaction and mixing. Since mixing is dominated by turbulence, the ratio is given by the time scales of turbulence τ_t to chemical reaction τ_c. The ratio corresponds to the Damköhler number (Poinsot and Veynante 2005):

$$\mathrm{Da} = \frac{\tau_\mathrm{t}}{\tau_\mathrm{c}}. \tag{6.35}$$

On the basis of the Da number and the turbulent Reynolds number $\mathrm{Re_t}$, (Poinsot and Veynante 2005) suggest a classification of non-premixed combustion regimes. The turbulent Reynolds number is a measure of the impact of large scale turbulent vorticies on the flow field. The classification in form of a combustion diagram is shown in Fig. 6.7. For turbulent Reynolds numbers below unity, combustion is laminar and hence not of interest for the combustion modeling in rocket engines. In the higher $\mathrm{Re_t}$ range, (Poinsot and Veynante 2005) distinguish between three regimes:

- For high Da numbers, the turbulence integral time scale τ_t is large compared to the time scale of chemical reaction τ_c, cf. Eq. (6.35). In consequence, chemistry

is fast enough to reach chemical equilibrium and the flame front follows the flow structures as a whole. The inner flame structure corresponds locally to a steady laminar flamelet solution comprising the mixing and reaction zones. Maximal temperature and reaction rates are in agreement with the corresponding laminar flame configuration (Poinsot and Veynante 2005). Since chemistry is fast, the flamelet structure is retained although large vorticies wrinkle the flame front. Furthermore, the reaction zone is substantially smaller than the mixing zone for large Da numbers (Poinsot and Veynante 2005).

- For Da numbers on an intermediate level, the time scales of turbulence and chemistry are approximately the same. In this situation, turbulent motion interacts with the reaction process and unsteady effects become relevant. For example, the rate of conversion of educts to combustion products might be too low to consume all reactants delivered to the reaction zone. In consequence, the accumulation of reactants in the reaction zone lowers the local temperatures and local extinction due to quenching may occur. In order to describe such unsteady effects, finite rate chemistry needs to be included.
- If the chemical time scale is large compared to the turbulent time scale, the strain imposed on the reaction zone by the turbulent vorticies is too intense for the reaction to proceed and quenching occurs in a wide spatial range in the reaction zone leading to flame extinction.

The limiting Da numbers for each regime depend on the turbulent Reynolds number. As shown in Fig. 6.7, the limiting Da numbers for the different regimes increase linearly in a log-log representation. Therefore, with increasing impact of large turbulent vorticies, chemistry needs to be faster in order to prevent the flame from extinction.

According to (Poinsot and Veynante 2005), the high Da number range and hence the flamelet combustion regime is given in most technical applications. For instance, (Nan et al. 2007) show that for the propellant combination CH_4/O_2 under 10 MPa in a typical injection configuration, the laminar flamelet regime is present and the combustion is dominated by mixing in the entire flowfield. Since the reactivity of the propellant combination H_2/O_2 is even higher than for CH_4/O_2 (Joos 2006; Singla et al. 2007), it can be reasonably assumed that thin flame structures and mixing controlled combustion are present in the BKD test chamber for the considered load points, cf. Tab. 5.1. Another indication that chemistry plays a secondary role in the BKD chamber is given in (Török 2015), where it is shown that the interaction of turbulence and chemistry is negligible for the simulation of a H_2/O_2 driven rocket engine under 6 MPa (Habiballah and Zurbach 2001).

To confirm the presence of high Da numbers and hence the validity of the flamelet approach in case of the BKD test chamber for LP1-4, the chemical and turbulent time scales are determined and compared. First, the chemical time scale is determined. (Peters 2000) shows that strain rates at extinction can be used to estimate the time scale of the chemical reaction. With increasing strain, the reaction zone gets thinner, until heat conduction towards oxidizer and fuel sides leads to heat fluxes, which exceed the heat generation due to chemical reaction and extinction occurs. Essentially, a balance

between the diffusion time scale, which is defined by the scalar dissipation rate at excitation χ_q, and the chemical time scale τ_c is present (Peters 2000):

$$\tau_\mathrm{c} = \frac{Z_\mathrm{st}^2(1-Z_\mathrm{st})^2}{\chi_\mathrm{q}}, \tag{6.36}$$

where Z_st denotes the stoichiometric mixture fraction, which is 1/9 for H_2/O_2. Extinction strain rates a_q are given in (Fiala and Sattelmayer 2014; Wang et al. 2013). Following (Peters 2000), strain rates are transformed into scalar dissipation rates by

$$\chi_q = \frac{a_q}{\pi} \exp\left(-2\left[\mathrm{erfc}^{-1}(2Z_\mathrm{st})\right]^2\right). \tag{6.37}$$

In consequence, the time scale of chemical reaction for the H_2/O_2 combustion in the BKD is given by $\tau_\mathrm{c} = \mathcal{O}(10^{-9})$ s for typical pressures of 60-80 bar.

In the next step, a turbulence integral time scale is determined. According to (Peters 2000; Poinsot and Veynante 2005), turbulent time scales are given by kinetic energy and turbulent dissipation rate as $\tau_\mathrm{t} = k_\mathrm{t}/\epsilon$, which can be determined from the turbulence model on the basis of the simulation results, cf. Eq. (6.25) and Eq. (6.26). Simulations reveal turbulent times scales of $\tau_\mathrm{t} = \mathcal{O}(10^{-6})$-$\mathcal{O}(10^{-5})$ s.

In comparison, the turbulence integral time scale τ_t is approximately 3-4 orders of magnitude larger than the chemical time scale τ_c. It is therefore concluded that the time scale of chemical reaction is sufficiently shorter than the time scale of turbulence for high Da numbers. According to Fig. 6.7, the BKD combustion zones are hence dominated by flamelet structures. Furthermore, the mixing and reaction zones are thin. Large turbulent vorticies may wrinkle the flame front, but the inner flamelet structures are retained.

Modeling combustion on the basis of laminar flamelet structures is very effective. Essentially, the combustion modeling can be decomposed into two problems: the description of the flow field including the mixing process and the simulation of the laminar flame structure (Poinsot and Veynante 2005). The flamelet solution can be obtained using laminar counter-flow diffusion flame simulations, (Fiala and Sattelmayer 2014). From the flamelet results, look-up tables are generated listing e.g. species mass fraction and density in terms of mixture fraction, its variance and scalar dissipation rate (Mastorakos 2001). These quantities are provided by the CFD simulation linking the mixing process to the laminar flamelet structure.

For the simulation of the steady state field of a BKD single flame configuration, the usage of a flamelet model and the tabulation of density and mass fraction is sufficient. Such an approach is referred to as primitive variable method (Poinsot and Veynante 2005). However, to determine Flame Transfer Functions according to Eq. (2.103), the heat release rate is required. For the calculation of the heat release rate, (Poinsot and Veynante 2005) suggest the usage of a reaction rate approach. Herein, the reaction rates are determined from the laminar counter-flow diffusion flamelet results and tabulated for the look-up in the subsequent CFD simulation. On the basis of the simulated reaction rates, the heat release rates can be calculated.

During the development of the stability assessment procedure, the applicability of the reaction rate based flamelet modeling approach for the determination of Flame Transfer Functions was investigated. For this purpose, steady state CFD simulations of a single flame configuration of the BKD test chamber, cf. Fig. 6.2, were conducted on the basis of the primitive variable method and the heat release rate was included additionally into the flamelet look-up table and monitored during the CFD runs. Finally, the volume integrated heat release rate $\dot{Q}_{\text{flamelet}}$ was compared to the power output calculated on the basis of the enthalpy differences between outlet and inlet. According to energy conservation, under adiabatic conditions, the difference in enthalpy between inlet and outlet should be the same as the volume integrated heat release rate $\dot{Q}_{\text{flamelet}}$, i.e.

$$(\dot{m}h)_{\text{outlet}} - (\dot{m}h)_{\text{inlet}} = \dot{Q}_{\text{flamelet}}. \tag{6.38}$$

However, a significant discrepancy between the volume integrated heat release rate $\dot{Q}_{\text{flamelet}}$ and the enthalpy difference was found. It was concluded that the heat release rate cannot reliably be determined on the basis of the flamelet combustion model. The discrepancies can probably be explained by the insufficient resolution of the laminar flamelet structures in the CFD simulations. To avoid an increase of simulation times by applying higher grid resolutions, a different combustion model than the flamelet approach was chosen.

As explained before, it is assumed that combustion in the BKD test chamber is fully controlled by mixing. For this situation, (Magnussen and Mjertager 1967) suggested the application of the Eddy Dissipation Model (EDM), that relates the reaction rates directly to the integral turbulence time scale τ_{t}. Assuming a one-step chemistry, i.e.

$$\frac{1}{2}\text{O}_2 + \text{H}_2 \rightarrow \text{H}_2\text{O}, \tag{6.39}$$

the reaction rates are given by

$$\dot{\omega}_{\text{k,EDM}} = (\nu''_{\text{k}} - \nu'_{\text{k}})\ \mathbf{W}_{\text{k}}\ A_{\text{EDM}}\ \tau_{\text{t}}\ \min\left(\rho\ \frac{Y_{\text{O}_2}}{\frac{1}{2}\mathbf{W}_{\text{O}_2}}, \rho\ \frac{Y_{\text{H}_2}}{\mathbf{W}_{\text{H}_2}}\right), \tag{6.40}$$

and

$$\dot{\omega}_{\text{k,EDM}} = (\nu''_{\text{k}} - \nu'_{\text{k}})\ \mathbf{W}_{\text{k}}\ A_{\text{EDM}}\ \frac{k_{\text{t}}}{\epsilon}\ \min\left(\rho\ \frac{Y_{\text{O}_2}}{\frac{1}{2}\mathbf{W}_{\text{O}_2}}, \rho\ \frac{Y_{\text{H}_2}}{\mathbf{W}_{\text{H}_2}}\right), \tag{6.41}$$

respectively.

In Eq. (6.41), A_{EDM} denotes a model constant, $\mathbf{W}$ the molar mass and the index $()_{\text{k}}$ states H_2, O_2 and H_2O, respectively. Furthermore, ν'/ν'' denote the stoichiometric conditions of the educts and products. For stoichiometry, it holds that the concentrations of the reactants altered by the stoichiometric coefficients are equal, i.e.

$$\frac{1}{2}[\text{O}_2] = [\text{H}_2], \tag{6.42}$$

cf. Eq. (6.39). Eq. (6.42) can be rewritten such that

$$\rho \frac{Y_{O_2}}{\frac{1}{2}\mathbf{W}_{O_2}} = \rho \frac{Y_{H_2}}{\mathbf{W}_{H_2}}, \tag{6.43}$$

which corresponds to the terms inside the minimum function in Eq. (6.41). Therefore, if one of the reactants is deficient, the reaction rate is limited by its respective mass fraction. For instance, if a H_2 excess is present:

$$\rho \frac{Y_{O_2}}{\frac{1}{2}\mathbf{W}_{O_2}} < \rho \frac{Y_{H_2}}{\mathbf{W}_{H_2}}, \tag{6.44}$$

and the reaction rate e.g. for water according to Eq. (6.41) yields

$$\dot{\omega}_{H_2O,EDM} = \mathbf{W}_{H_2O}\, A_{EDM}\, \frac{k_t}{\epsilon}\, 2\, \rho\, \frac{Y_{O_2}}{\mathbf{W}_{O_2}}. \tag{6.45}$$

In contrast, if an O_2 excess is present,

$$\rho \frac{Y_{O_2}}{\frac{1}{2}\mathbf{W}_{O_2}} > \rho \frac{Y_{H_2}}{\mathbf{W}_{H_2}}, \tag{6.46}$$

and the reaction rate reads

$$\dot{\omega}_{H_2O,EDM} = \mathbf{W}_{H_2O}\, A_{EDM}\, \frac{k_t}{\epsilon}\, \rho\, \frac{Y_{H_2}}{\mathbf{W}_{H_2}}. \tag{6.47}$$

The EDM model assumes that the reactants are burned very fast until the deficient one is fully consumed. However, due to the complete absence of chemistry in the EDM model, the calculated reaction rates are usually to large (Joos 2006) yielding unrealistically high temperatures in the reaction zone. Essentially, the EDM model does not calculate chemical equilibrium conditions for the given chamber pressure but only the single step according to Eq. (6.39) is taken into account.

In order to reach more realistic chemical equilibrium conditions and to obtain adiabatic combustion temperatures for the reaction of H_2 and O_2, the dissociation of water is also included into the simulation, i.e.

$$H_2O \rightarrow OH + H. \tag{6.48}$$

The dissociation of water is an endothermic reaction, which consumes considerably amounts of energy. This reaction strongly depends on temperature. Therefore, the dissociation reaction rate is modeled in form of an Arrhenius type term according to

$$\dot{\omega}_{k,FR} = (\nu''_k - \nu'_k)\ \frac{\rho\, Y_{H_2O}}{\mathbf{W}_{H_2O}}\, \mathbf{W}_k\, A_{FR}\, e^{-\frac{E_{FR}}{\mathcal{R}\cdot T}}, \tag{6.49}$$

with the constants $A_{FR} = 3.5{\cdot}10^9\ s^{-1}$ and $E_{FR}/\mathcal{R} = 52{,}900$ K (Knab et al. 1999). In Eq. (6.49) the index k denotes H_2O, OH and H, respectively. The capability of this simple dissociation model to obtain realistic flame temperatures was demonstrated for the

combustion simulation of the propellant combination MMH (Monomethylhydrazine) and NTO (Nitrogen Tetroxide) by several authors in the past (Aichner et al. 2012; Knab et al. 1998, 1999; Schmid 2009).

Altogether, the reaction rate source terms for the different species in Eq. (6.30) are given by

$$\begin{aligned}
\dot{\omega}_{\mathrm{H_2,EDM}} &= -\rho\, \mathbf{W}_{\mathrm{H_2}}\, A_{\mathrm{EDM}}\, \frac{k_\mathrm{t}}{\epsilon}\, \min\left(\frac{Y_{\mathrm{O_2}}}{\frac{1}{2}\mathbf{W}_{\mathrm{O_2}}}, \frac{Y_{\mathrm{H_2}}}{\mathbf{W}_{\mathrm{H_2}}}\right), \\
\dot{\omega}_{\mathrm{O_2,EDM}} &= -\frac{1}{2}\rho\, \mathbf{W}_{\mathrm{O_2}}\, A_{\mathrm{EDM}}\, \frac{k_\mathrm{t}}{\epsilon}\, \min\left(\frac{Y_{\mathrm{O_2}}}{\frac{1}{2}\mathbf{W}_{\mathrm{O_2}}}, \frac{Y_{\mathrm{H_2}}}{\mathbf{W}_{\mathrm{H_2}}}\right), \\
\dot{\omega}_{\mathrm{H_2O,EDM+FR}} &= \rho\, \mathbf{W}_{\mathrm{H_2O}}\, A_{\mathrm{EDM}}\, \frac{k_\mathrm{t}}{\epsilon}\, \min\left(\frac{Y_{\mathrm{O_2}}}{\frac{1}{2}\mathbf{W}_{\mathrm{O_2}}}, \frac{Y_{\mathrm{H_2}}}{\mathbf{W}_{\mathrm{H_2}}}\right) - \rho Y_{\mathrm{H_2O}}\, A_{\mathrm{FR}}\, \mathrm{e}^{-\frac{E_{\mathrm{FR}}}{\mathcal{R}\cdot T}}, \\
\dot{\omega}_{\mathrm{OH,FR}} &= \frac{\rho\, Y_{\mathrm{H_2O}}}{\mathbf{W}_{\mathrm{H_2O}}}\, \mathbf{W}_{\mathrm{OH}}\, A_{\mathrm{FR}}\, \mathrm{e}^{-\frac{E_{\mathrm{FR}}}{\mathcal{R}\cdot T}}, \\
\dot{\omega}_{\mathrm{H,FR}} &= \frac{\rho\, Y_{\mathrm{H_2O}}}{\mathbf{W}_{\mathrm{H_2O}}}\, \mathbf{W}_{\mathrm{H}}\, A_{\mathrm{FR}}\, \mathrm{e}^{-\frac{E_{\mathrm{FR}}}{\mathcal{R}\cdot T}}.
\end{aligned} \tag{6.50}$$

The validity of the modeling approach with the reaction rates according to Eq. (6.50) will be verified on the basis of flame temperatures in Sec. 7.1.

Eq. (6.41) reveals that the EDM reaction rates are completely dominated by turbulent quantities. For strong turbulent motion, the turbulent kinetic energy k_t is high providing intense mixing. Therefore, high turbulent kinetic energy leads to an intense transport of reactants to the reaction zone and consequently to large reaction rates. In contrast, viscous dissipation of turbulent motion on small scales reduces the intensity of reactant mixing. Hence, with increasing turbulent dissipation rates ϵ, the reaction rates decrease.

The turbulent quantities in the reactive flow field are influenced by different sources for turbulence. This can be realized by the vorticity equation, which is derived from the momentum equation by applying the rotational operator to each single term. For reasons of simplicity, the vorticity equation is not derived from the Favre averaged momentum equation but from the instantaneous momentum Eq. (2.2) (Williams 1974):

$$\frac{\partial \xi_i}{\partial t} = \xi_j \frac{\partial u_i}{\partial x_j} - \xi_i \frac{\partial u_j}{\partial x_j} + \varepsilon_{ijk} \frac{1}{\rho^2} \frac{\partial \rho}{\partial x_j} \frac{\partial p}{\partial x_k} + \varepsilon_{ijk} \frac{\partial}{\partial x_j}\left(\frac{1}{\rho}\frac{\partial \tau_{km}}{\partial x_m}\right) \tag{6.51}$$

In Eq. (6.51), especially the third and forth terms on the r.h.s. contribute to the production and dissipation of vorticity. The third term describes the generation of vorticity due to misaligned gradients of density and pressure. This effect is referred to as baroclinic torque. In contrast, the fourth term accounts for the dissipation of vorticity viscosity and contributes to the turbulent dissipation rate ϵ. As the vorticity equation is directly obtained by the rotation of the momentum equation, which is solved for in averaged form in the CFD simulation, the effects of baroclinic torque and viscous vorticity dissipation are accounted for in the computation and contained in k_t and the dissipation rate ϵ, see Eq. (6.22) - (6.26). In consequence, the influences of these effects on mixing and hence on the reaction rate are accounted for by the EDM model.

A drawback of the EDM/FR combustion modeling approach is that minor species are not simulated. Especially for the validation of combustion simulations on the basis of experimental measurements, the radiation of the minor species OH* molecule is often considered. Such validation procedures cannot be conducted using the EDM/FR model. (Fiala 2015; Fiala and Sattelmayer 2015b) propose a procedure to determine OH* radiation in turbulent flames considering self-absorption effects, which is based on the flamelet approach. The applicability of the procedure is demonstrated in (Schulze et al. 2016a).

6.2.4. Mean Flow Computation

The procedure of converting the single flame simulation results to an adequate mean flow for the subsequent acoustic simulation affects the stability assessment in multiple ways. Firstly, due to the cut-on condition according to Eq. (2.60), the eigenfrequency of the first transverse mode depends directly on the speed of sound and Mach number. Speed of sound, in turn, depends on pressure, density and species composition as well as on their respective specific heat capacities, see Eq. (6.14). The conversion procedure necessarily needs to conserve the effect of these quantities on acoustic propagation. If eigenfrequencies are inaccurately simulated, reflection coefficient boundary conditions are evaluated at incorrect frequencies, cf. Eq. (2.75). In consequence, discrepancies in terms of amplitude and phase of the reflection coefficient can significantly alter the stability predictions.

Secondly, the mean flow fields directly affect the mode shapes of pressure and transverse velocity. Incorrect amplitude and phase distributions of pressure and transverse velocity influence the dynamic flame response and lead to inaccurate Flame Transfer Functions. In the subsequent stability analysis, flame feedback might be too weak or too strong. According to the Rayleigh integral, see Eq. (2.105), incorrectly computed amplitude and phase distributions of pressure might attribute to wrongly described amplification of acoustic amplitudes by the heat release fluctuations.

For the adequate mean flow generation, a second CFD simulation is performed, which includes the entire combustion chamber and the nozzle. In this simulation, the chemical reaction is not modeled but the reacting rates are taken from the single flame simulation as input. For this purpose, radially averaged reaction rates are evaluated at 300 equidistantly distributed axial locations in the steady single flame CFD. It is again assumed that the radial average on single flame scale is equivalent to the chamber cross-sectional average, see Sec. 6.1.

The absence of a detailed description of combustion and the usage of radially averaged reaction rates substantially reduces computational turn-around times and allows for the computation of the entire chamber. The simulation is based on axis-symmetrically discretized compressible non-linear Euler equations and does not account for turbulence. At the outlet, supersonic conditions are imposed. At the inlet, species composition in terms of mass fractions according to the load point's specific ratio of oxidizer to fuel (ROF) is imposed and the full mass flow of propellants is applied. The inlet temperature is evaluated from the single flame simulation and determined as the radial average at

Fig. 6.8.: O_2 mass fraction of the mean flow for the acoustic simulation together with its detailed distribution in the single flame case.

the face plate. Since averaged inlet temperatures at the face plate are already elevated, real gas effects do not relevantly affect the results. The conversion procedure generates the entire set of radially averaged mean flow quantities and a consistent nozzle flow is obtained. Simulation times are limited to a few minutes.

The applied conversion procedure allows for the validation of the reaction rates calculated in the single flame simulations. Since the choked nozzle flow is included into the second CFD simulation, the calculated chamber pressure is a measure of the correctness of the reaction rates, cf. Tab. 5.1. In case of accurately computed chamber pressures, it can be concluded that the combustion model applied to the single flame simulations accurately predicts reaction rates and therefore heat release.

Fig. 6.8 illustrates the conversion procedure in terms of O_2 mass fraction. While the single flame simulation describes small-scaled structures in detail, the mean flow for the acoustic simulation accounts for the radial average. For instance, it can be seen that the length of the combustion zone is well conserved during the conversion procedure.

6.3. Determination of Dome Coupling Scattering Matrices

In order to acoustically couple the combustion chamber with the O_2 dome in the acoustic simulations, the scattering matrix for the injectors is required, see Sec. 4.2. Although experimental procedures are available for their determination, cf. Sec. 4.2, scattering matrices are not of interest during the development and operation of rocket engines. In consequence, experimentally determined scattering matrices are usually not available. Therefore, reflection and transmission coefficients need to be calculated using analytical and numerical procedures.

In this thesis, the scattering matrix for the dome coupling is determined on the basis of an acoustic network model for a single injector configuration, cf. Sec. 2.7.5. For this purpose, the single injector configuration is decomposed into its elementary components consisting of area changes, straight duct elements and impedance changes. As long as longitudinal wave propagation is present in the injector it is sufficient to apply acoustic two-poles, cf. Sec. 2.7.5 and (Bade 2014; Gentemann et al. 2003). Therefore, the local acoustic coupling between the chamber and the dome side is described two ingoing and two outgoing waves.

The scattering properties of each of these components can be described by semi ana-

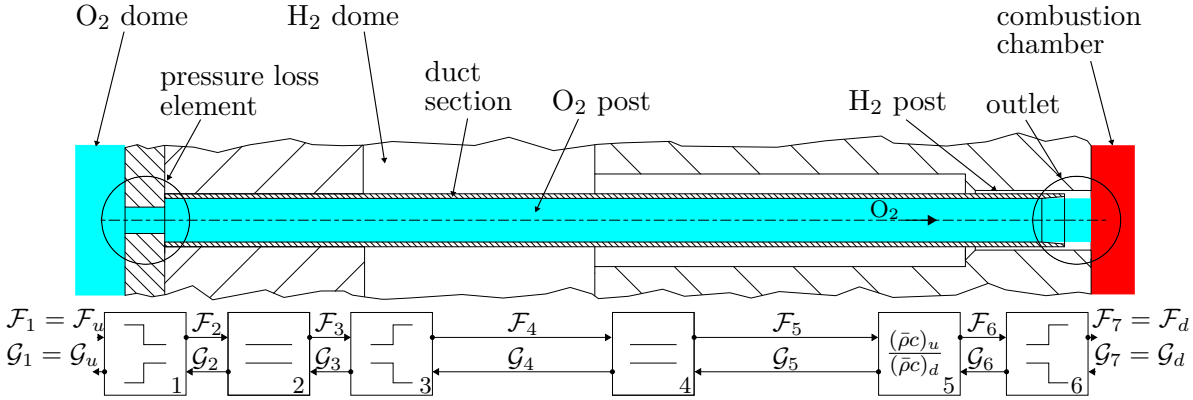

Fig. 6.9.: BKD injector configuration and corresponding network model.

lytical/empirical element scattering matrices, each of which are of the form according to Eq. (2.92). The scattering matrix of the entire injector configuration is then given by the connection of the components.

Fig. 6.9 shows again the geometrical arrangement of a BKD injector together with the corresponding series of acoustic elements. The single injector configuration is decomposed into the following components, see also 5.3. The pressure loss element is modeled as an ensemble of an area change with acoustic losses, a straight duct element and another area change with acoustic losses. These three components corresponds to the elements 1-3 in Fig. 5.3. The relevant cross-section of the O_2 dome on single injector scale is set according to the number of injector elements, i.e. to 1/42 of the entire dome cross-section. The O_2 post is described as duct element, see element 4. The junction of O_2, H_2 and the combustion products is modeled as change of characteristic impedance $(\bar{\rho}c)$, where $()_u$ denotes pure O_2 and $()_d$ the locally present average of O_2, H_2 and combustion products, see element 5. This element is referred to as impedance change element. The averaging of the characteristic impedance is performed directly at the face plate in the combustion chamber. Furthermore, the taper angle is neglected in the network model. Finally, the area change from the O_2 injector to the combustion chamber is again modeled including acoustic losses, see element 6. The explicit representation of each element scattering matrix is given in the App. B.3.

The H_2 injection system is not accounted for in the network model. Since H_2 is injected into the chamber through a very thin annular slit, see Fig. 5.2 and with high velocity, cf. Tab. 5.1. In consequence, the acoustic energy transferred from the chamber into the H_2 injection system is assumed to be negligible, cf. Sec. 6.2.1.

Finally, the reflection and transfer coefficients of the acoustic network model are given by the assembly of all elements 1-7, cf. Fig. 6.9. For the assembling, the Riemann invariants in the chamber are first expressed by the Riemann invariants before the last area jump, viz.

$$\begin{pmatrix} \mathcal{F}_d \\ \mathcal{G}_u \end{pmatrix} = \mathrm{SM}_6^{\mathrm{AC}} \begin{pmatrix} \mathcal{F}_6 \\ \mathcal{G}_6 \end{pmatrix}, \tag{6.52}$$

The Riemann invariants $\mathcal{F}_6$ and $\mathcal{G}_6$ upstream of the area change element 6 are determined by the element scattering matrix 5 and the corresponding waves further upstream $\mathcal{F}_5$ and $\mathcal{G}_5$. Assembling all element scattering matrices in this manner finally yields the injector scattering matrix by multiplication, i.e.

$$\begin{pmatrix} \mathcal{F}_d \\ \mathcal{G}_u \end{pmatrix} = \prod_{k=1}^{6} \mathrm{SM}_{7-k} \begin{pmatrix} \mathcal{F}_u \\ \mathcal{G}_d \end{pmatrix}. \tag{6.53}$$

see also Eq. (2.93).

The injector scattering matrix is therefore explicitly given by

$$\mathrm{SM} = \mathrm{SM}_6^{\mathrm{AC}} \cdot \mathrm{SM}_5^{\rho c} \cdot \mathrm{SM}_4^{\mathrm{DE}} \cdot \mathrm{SM}_3^{\mathrm{AC}} \cdot \mathrm{SM}_2^{\mathrm{DE}} \cdot \mathrm{SM}_1^{\mathrm{AC}}, \tag{6.54}$$

For the evaluation of the elementary scattering matrices in Eq. (6.54), mean flow quantities are required, cf. App. B.3. These quantities are extracted from the mean flow simulations on the basis of a single flame configuration, cf. Sec. 7.1.2.

6.4. Acoustic Simulation

The generated mean flow is subsequently applied to the first acoustic simulation. The computational setup is illustrated in Fig. 6.10, which is similar to the simulations performed under non-reactive conditions in Chap. 4. The computational domain comprises the chamber with the nozzle and the O_2 dome volume, which is acoustically coupled with the chamber via a scattering matrix. In contrast to the experimental BKD configuration, the igniter tube inside of the O_2 dome is neglected, since its impact on the acoustic propagation in the dome is assumed to be irrelevant, cf. Fig. 5.1. At the walls, slip conditions are prescribed, see Eq. (2.74). Furthermore, the axial length of the divergent nozzle part and its radial spread is reduced in order to minimize the computational domain. Non-reflective boundary conditions are imposed at the outlet of the nozzle, cf. Eq. (2.99). Since the H_2 injection system is assumed to be acoustically decoupled from the chamber, the H_2 dome is not included into the computational domain, see also Sec. 6.2.1.

Additionally, Fig. 6.10 indicates further applicable boundary conditions. In the O_2 dome, the reflection coefficients R_{F} of the O_2 feed lines from the tanks could be imposed. However, as it will be shown in Sec. 7.3, the acoustic coupling of the dome with the chamber is weak and only insignificant amplitudes are present in the dome volume in case of the BKD test chamber. As the dome is therefore decoupled from the chamber to a great extent, the O_2 lines do not influence the chamber acoustics. In consequence, for the acoustic analyses of the BKD test chamber, the feed line boundaries are substituted by simple slip wall conditions. However, it might be necessary to include the reflection coefficient of the feed lines for different systems.

A second applicable boundary condition is indicated in the chamber, see Fig. 6.10: the location of an absorber ring and its corresponding boundary surface, cf. Fig. 5.2 and Fig. 5.1. The capabilities to take the influence of an absorber ring in form an

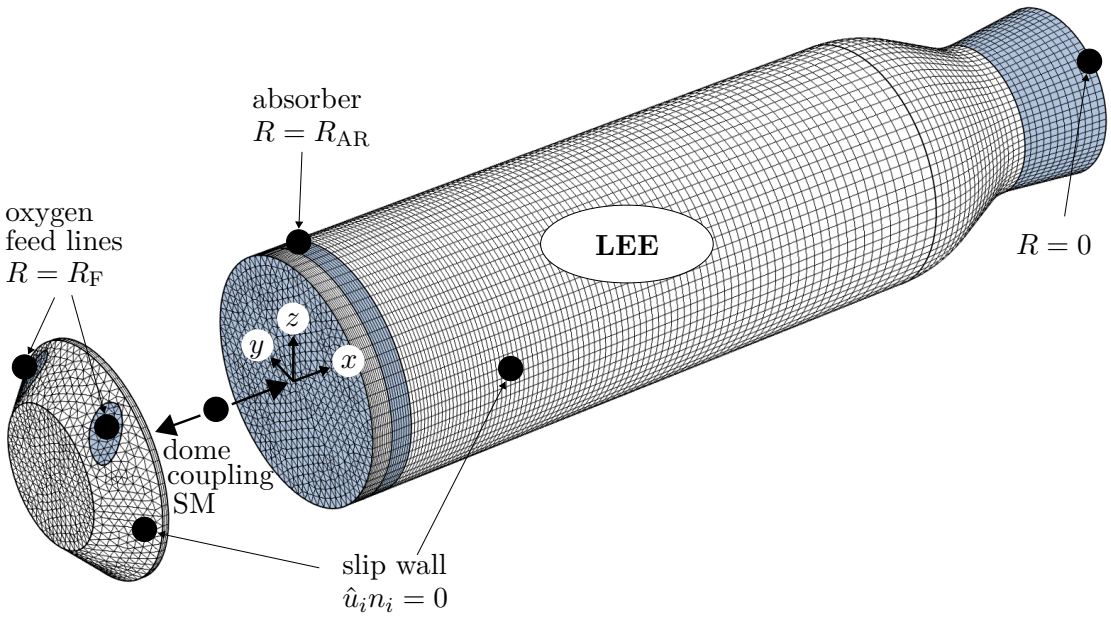

Fig. 6.10.: Computational domain, boundary conditions and grid for the acoustic simulation.

reflection coefficient R_{AR} into account in the acoustic simulations was shown in Sec. 4.3.2. However, in the acoustic analyses presented in the next Chapter, the absorber ring is not activated. Therefore, the possibility of including an absorbing ring is shown illustratively, but it is not used in this thesis. In the concluding Chapter of this thesis, a suitable test configuration with absorbers is suggested for further validation of the stability assessment procedure, see Chap. 8.

The computational grid for the acoustic simulation is shown in Fig. 6.10. Triangular element types are used in cross-section, while in axial direction hexahedral element types are included. To resolve the axial mean flow gradients, the grid is finest in the injection region and successively coarsened in axial direction. In the nozzle, the grid is again axially refined in order to account for the reduced wavelength of reflected waves due to the increase in Mach number. For the BKD test chamber approximately 130,000 finite elements are included leading to an overall number of approximately 340,000 DOF.

In the combustion chamber, the full set of LEE is solved, cf. Eq. (2.30) - (2.32). The previously simulated mean flow quantities are included into the acoustic simulation as follows. The distributions of mean pressure and velocity is taken from the mean flow computation of the entire chamber, see Sec. (6.2.4). However, due to radial averaging of the speed of sound and of the density, compressibility is not conserved during the conversion of the single flame results to the mean flow, see Sec. 6.2.4. In consequence, if speed of sound and density were taken from the previously simulated mean flow, acoustic propagation and therefore eigenfrequencies would not correctly be calculated in the acoustic simulations. To guarantee that compressibility is conserved, its radial

average is calculated on the basis of the single flame results and transferred into the acoustic simulation. As acoustic propagation is an isentropic process (Anderson 2003), isentropic compressibility is averaged. The radially averaged isentropic compressibility $\widetilde{\widetilde{\mathcal{K}}}_s$ is given by

$$\widetilde{\widetilde{\mathcal{K}}}_s = \widetilde{\widetilde{(\rho c^2)^{-1}}}, \tag{6.55}$$

cf. Eq. (6.17).

Inserting the definition of speed of sound according to Eq. (6.14) into Eq. (6.55) yields

$$\widetilde{\widetilde{\mathcal{K}}}_s = \widetilde{\widetilde{\left(\frac{c_p}{c_v} p\right)^{-1}}}. \tag{6.56}$$

In Eq. (6.56), ideal gas conditions are assumed, since the radially averaged temperatures at the inlet are already sufficiently high for real gas effects to be negligible, see Sec. 6.2.4.

The isentropic compressibility in the acoustic simulation (CAA) should be the same as the average in the single flame configuration, i.e.

$$\frac{1}{\rho_{\mathrm{CAA}} c^2_{\mathrm{CAA}}} = \widetilde{\widetilde{\left(\frac{c_p}{c_v} p\right)^{-1}}}. \tag{6.57}$$

In order to conserve compressibility, either ρ_{CAA} or c^2_{CAA} needs to be adapted to fulfill Eq. (6.57). For the calculation presented in the next Chapter, c^2_{CAA} is set equal to the radial average of the single flame simulation, and ρ_{CAA} is finally given by

$$\rho_{\mathrm{CAA}} = \widetilde{\widetilde{c^{-2}}} \widetilde{\widetilde{\left(\frac{c_p}{c_v} p\right)}}. \tag{6.58}$$

Finally, in the acoustic simulation, the radial averaged values as well the ρ_{CAA} correspond to the mean flow quantities, i.e.

$$\rho_{\mathrm{CAA}} \rightarrow \bar{\rho}; \;\; \widetilde{\widetilde{p}} \rightarrow \bar{p}; \;\; \widetilde{\widetilde{u}}_i \rightarrow \bar{u}_i \tag{6.59}$$

The isentropic exponent κ in the LEE is calculated by

$$\kappa = \widetilde{\widetilde{\left(\frac{c_p}{c_v}\right)}}. \tag{6.60}$$

Since density is altered through the conversion procedure, cf. Eq. (6.58), the characteristic impedance $\mathcal{Z}$ in the acoustic simulation is no longer the same as in the single flame CFD, cf. Eq. (2.42). The adaption of density is especially drastic in the injection region. However, the scattering matrix for the dome coupling is generated on the basis

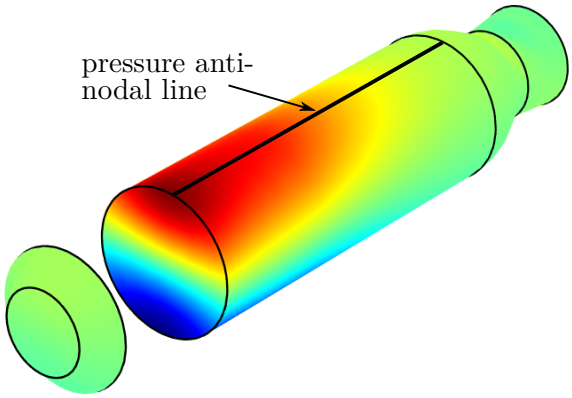

Fig. 6.11.: First transverse mode shape in terms of normalized pressure $\mathfrak{Re}(\hat{p})$ and the respective anti-nodal lines in the chamber.

of $\mathcal{Z}$ in the single flame configuration. In consequence, the change in $\mathcal{Z}$ needs to be accounted for in the scattering matrix. For this purpose, the acoustic network model is extended by another change of characteristic impedance element $(\bar{\rho}c)$. The scattering matrix is hence given by

$$\mathrm{SM} = \mathrm{SM}^{\rho c}_{\mathrm{CFD}\rightarrow\mathrm{CAA}} \cdot \mathrm{SM}^{\mathrm{AC}}_{6} \cdot \mathrm{SM}^{\rho c}_{5} \cdot \mathrm{SM}^{\mathrm{DE}}_{4} \cdot \mathrm{SM}^{\mathrm{AC}}_{3} \cdot \mathrm{SM}^{\mathrm{DE}}_{2} \cdot \mathrm{SM}^{\mathrm{AC}}_{1}, \tag{6.61}$$

cf. Eq. (6.54).

In the dome, quiescent flow conditions and isentropic acoustic propagation are assumed. In consequence, the reduced set of LEE (2.30) - (2.32) is solved in the dome volume. Necessary thermodynamic properties are determined from pressure and temperature, cf. Tab. 5.1 using the NIST database (Linstrom and Mallard 2015).

To determine the eigenfrequency and the mode shape of the first transverse mode, the acoustic simulation is performed in form of an eigenvalue problem, see Sec. 3.2.2.2. The turnaround times of the acoustic simulation depends on the number of DOF to solve for, but also on the convergence properties. In general, the solution process does not only solve for physical modes, also spurious solutions are calculated. These spurious solutions immensely reduce the convergence process of the acoustic simulations. However, it was found that the eigenvalue solution process for only a few (e.g. four) eigenfrequencies and the restriction of the initial setting to an approximation of the eigenfrequency, which can be obtained from experiments or from the cut-on condition, see Eq. (2.60), yields already reasonably fast convergence procedures.

At this stage, acoustic simulations can be performed for the open loop system, i.e. in the absence of dynamic heat release $(\hat{q})$. Such simulations are conducted in order to determine the eigenfrequency and the mode shape of the first transverse mode. Fig. 6.11 shows a typical mode shape in the chamber and the dome indicating a first transverse mode structure at the face plate and a decaying pressure amplitude in axial direction. The pressure distribution of this particular mode will be investigated in more detail in Sec. 7.3.2.

(Schwing 2013) shows that the mode shape of the first transverse mode is not rele-

vantly changed by the influence of the flame feedback in a model gas turbine combustor. In consequence, the mode shape of the open loop system can be used to determine the axial distribution of the complex pressure amplitude $\hat{p}$ along the anti-nodal pressure line of the closed loop system, cf. Fig. 6.11. The axial pressure distributions of amplitude and phase are subsequently implemented into the excitation procedure, which is employed to study the dynamic heat release response to acoustic modulation on the basis of the single flame simulations. The complete excitation methodology and the subsequent generation of Flame Transfer Functions is presented in the next section.

6.5. Modeling of the Dynamic Heat Release Rate $\hat{\dot{q}}$

In order to calculate the eigenfrequency and damping rate of the closed system, cf. Eq. (6.1), the fluctuating heat release source term due to acoustic modulation needs to be modeled and incorporated into the LEE energy equation, cf. Eq. (2.32). In the following, its modeling is presented.

The impact of the fluctuating heat release on the acoustic propagation is described by the Rayleigh integral, which was introduced in Sec. 2.8. To establish suitable feedback models, the Rayleigh integral Ra is studied. Since the flame is compact in radial direction, it is sufficient to analyze Ra on the basis of a single flame configuration, cf. Sec. 6.1.

In general, the Rayleigh integral of the single flame (SF) configuration is given by Eq. (2.105)

$$\mathrm{Ra}_{\mathrm{SF}} = \frac{1}{T_s}\int_{T_s}\int_{V_{\mathrm{SF}}} \dot{q}' p' \, dV \, dt = \frac{1}{T_s}\int_{T_s}\int_{V_{\mathrm{SF}}} (\dot{q} - \bar{\dot{q}})\, p' \, dV \, dt. \tag{6.62}$$

Radial compactness allows to develop acoustic pressure in radial direction in a Taylor series and to truncate after the linear term, i.e.

$$p' = \breve{p}' + \frac{\partial \breve{p}'}{\partial \xi}\xi, \tag{6.63}$$

where it is assumed that the local ξ coordinate is aligned with the transverse velocity, cf. Fig. 6.12. In Eq. (6.63), $(\breve{})$ denotes the pressure on the axis of the single injector domain. Using Eq. (6.63), the Rayleigh integral can be written as

$$\mathrm{Ra}_{\mathrm{SF}} = \frac{1}{T_s}\int_{T_s}\int_{V_{\mathrm{SF}}} \left(\dot{q}\breve{p}' + \dot{q}\frac{\partial \breve{p}'}{\partial \xi}\xi - \bar{\dot{q}}\breve{p}' - \bar{\dot{q}}\frac{\partial \breve{p}'}{\partial \xi}\xi \right) dV \, dt. \tag{6.64}$$

Assuming that the pressure gradient $\frac{\partial \breve{p}'}{\partial \xi}$ is constant in axial direction and that the flame oscillates as a whole in transverse direction, (Sattelmayer et al. 2015a) show that $\mathrm{Ra}_{\mathrm{SF}}$ can be written as

$$\mathrm{Ra}_{\mathrm{SF}} = \frac{1}{T_s}\int_{T_s}\int_{V_{\mathrm{SF}}} \breve{p}'\dot{q} \, dV \, dt + \frac{1}{T_s}\int_{T_s}\int_{V_{\mathrm{SF}}} \bar{\dot{q}}\, \Delta'_{\mathrm{fl}} \frac{\partial \breve{p}'}{\partial \xi} \, dV \, dt, \tag{6.65}$$

where Δ'_{fl} denotes the displacement of the flame due to the influence of the transverse acoustic velocity. The first term in Eq. (6.65) can be rewritten

$$\frac{1}{T_s}\int_{T_s}\int_{V_{\mathrm{SF}}} \breve{p}'\,\dot{q}\,dV\,dt = \frac{1}{T_s}\int_{T_s}\int_{V_{\mathrm{SF}}} \breve{p}'(\bar{\dot{q}}+\dot{q}')\,dV\,dt = \frac{1}{T_s}\int_{T_s}\int_{V_{\mathrm{SF}}} \breve{p}'\dot{q}'\,dV\,dt, \tag{6.66}$$

since the average of $\breve{p}'\,\bar{\dot{q}}$ in time is zero. Furthermore, (Hertweck 2016; Hertweck et al. 2016) show that the second term in Eq. (6.65) corresponds to

$$\int_{V_{\mathrm{SF}}} \bar{\dot{q}}\,\Delta'_{\mathrm{fl}}\,\frac{\partial \breve{p}'}{\partial \xi}\,dV\,dt = \int_{V_{\mathrm{SF}}} \breve{p}'\,\frac{\bar{\dot{q}}}{\kappa\bar{p}}\,\breve{p}'\,dt\,dV - \int_{V_{\mathrm{SF}}} \breve{p}'\Delta'_{\mathrm{fl}}\frac{\partial \bar{\dot{q}}}{\partial \xi}\,dV\,dt. \tag{6.67}$$

Overall, the Rayleigh integral of the single flame domain is finally given by

$$\mathrm{Ra}_{\mathrm{SF}} = \frac{1}{T_s}\int_{T_s}\int_{V_{\mathrm{SF}}} \breve{p}'\dot{q}'\,dV\,dt + \frac{1}{T_s}\int_{T_s}\int_{V_{\mathrm{SF}}} \breve{p}'\,\frac{\bar{\dot{q}}}{\kappa\bar{p}}\,\breve{p}'\,dt\,dV - \frac{1}{T_s}\int_{T_s}\int_{V_{\mathrm{SF}}} \breve{p}'\Delta'_{\mathrm{fl}}\frac{\partial \bar{\dot{q}}}{\partial \xi}\,dV\,dt. \tag{6.68}$$

According to Eq. (6.68), the Rayleigh integral contains different coupling types. The second term describes the heat release fluctuations due to isentropic variation of the acoustic density and therefore of the specific volume of the heat release zone (Zellhuber et al. 2014). The third term relates the heat release fluctuations to the flame displacement due to transverse acoustic velocity Δ'_{fl}. If Δ'_{fl} and $\breve{p}'$ are in phase, the flame is periodically displaced towards higher pressure, which drives the feedback loop (Sattelmayer et al. 2015a). Finally, the first term in Eq. (6.68) is associated with the direct influence of pressure fluctuations on the flame dynamics (Sattelmayer et al. 2015a).

In general, the coupling types described in Eq. (6.68) influence each other. For example, while the flame is displaced in transverse direction, heat release is modulated simultaneously by the direct influence of pressure fluctuations. In consequence, the contribution to $\mathrm{Ra}_{\mathrm{SF}}$ by the motion of the flame is not only based on the displacement of the mean heat release $\bar{\dot{q}}$, but also on the displacement of the fluctuating heat release $\dot{q}'$, which is generated by pressure coupling. However, such interactions of coupling types would occur as third order terms in the Rayleigh integral, e.g.

$$\mathrm{Ra}_{\mathrm{SF}} \sim \frac{1}{T_s}\int_{T_s}\int_{V_{\mathrm{SF}}} \breve{p}'\cdot f(\Delta'_{\mathrm{fl}}\,\breve{p}')\,dV\,dt. \tag{6.69}$$

Third order relations in the Rayleigh integral suggest second order fluctuating heat release source terms, i.e.

$$\dot{q}' \sim f(\Delta'_{\mathrm{fl}}\,\breve{p}'). \tag{6.70}$$

However, second order terms are neglected in the framework of linearized Euler equations, cf. Eq. (2.11) - Eq. (2.13). In consequence, the interaction of the coupling mechanisms is not accounted for in the modeling of the heat release source term.

For the application of the feedback models derived on the basis of the Rayleigh integral, Eq. (6.68) is transformed into frequency space. The time average over one

acoustic period is calculated in frequency space by Eq. (2.71). Eq. (6.68) can be given in frequency space by

$$\mathrm{Ra}_{\mathrm{SF}} = \frac{1}{2}\mathfrak{Re}\left[\int_{V_{\mathrm{SF}}} \breve{\hat{p}}^{*}\hat{\dot{q}}\,dV + \int_{V_{\mathrm{SF}}} \breve{\hat{p}}^{*}\,\frac{\bar{\dot{q}}}{\kappa\bar{p}}\,\breve{\hat{p}}\,dV - \int_{V_{\mathrm{SF}}} \breve{\hat{p}}^{*}\hat{\Delta}_{\mathrm{fl}}\frac{\partial\bar{\dot{q}}}{\partial\xi}\,dV\right]. \tag{6.71}$$

Herein, $\breve{\hat{p}}^{*}$ denotes the conjugated $()^{*}$ complex pressure amplitude ($\hat{}$) on the single flame domain axis ($\breve{}$).

When the interaction of the coupling types is neglected, the fluctuating heat release of the first term in Eq. (6.71) originates from the direct influence of pressure exclusively. The impact of pressure fluctuations on heat release is described in form of a non-dimensionalized Flame Transfer Function, i.e. the first term in Eq. (6.71) is written as

$$\breve{\hat{p}}^{*}\cdot\hat{\dot{q}} = \breve{\hat{p}}^{*}\,\mathrm{FTF}\frac{\bar{\dot{q}}}{\bar{p}}\,\breve{\hat{p}}, \tag{6.72}$$

and hence

$$\mathrm{Ra}_{\mathrm{SF}} = \frac{1}{2}\mathfrak{Re}\left[\int_{V_{\mathrm{SF}}} \breve{\hat{p}}^{*}\,\mathrm{FTF}\frac{\bar{\dot{q}}}{\bar{p}}\,\breve{\hat{p}}\,dV + \int_{V_{\mathrm{SF}}} \breve{\hat{p}}^{*}\,\frac{\bar{\dot{q}}}{\kappa\bar{p}}\,\breve{\hat{p}}\,dV - \int_{V_{\mathrm{SF}}} \breve{\hat{p}}^{*}\hat{\Delta}_{\mathrm{fl}}\frac{\partial\bar{\dot{q}}}{\partial\xi}\,dV\right]. \tag{6.73}$$

It can be seen that the first term as well the second term in Eq. (6.73) are pressure sensitive and can therefore be combined. Furthermore, a Flame Transfer Functions $\mathrm{FTF}^{\mathrm{p}}$ is defined such that it contains the influence of direct pressure coupling as well as the impact of the isentropic change of density and hence pressure on the heat release fluctuations, cf. Eq. (6.68), viz.

$$\mathrm{Ra}_{\mathrm{SF}} = \frac{1}{2}\mathfrak{Re}\left[\int_{V_{\mathrm{SF}}} \breve{\hat{p}}^{*}\,\underbrace{\left(\mathrm{FTF}+\frac{1}{\kappa}\right)}_{\mathrm{FTF}^{\mathrm{p}}}\frac{\bar{\dot{q}}}{\bar{p}}\breve{\hat{p}}\,dV - \int_{V_{\mathrm{SF}}} \breve{\hat{p}}^{*}\hat{\Delta}_{\mathrm{fl}}\frac{\partial\bar{\dot{q}}}{\partial\xi}\,dV\right]. \tag{6.74}$$

The last term in Eq. (6.73) depends on the flame displacement $\hat{\Delta}_{\mathrm{fl}}$. In a realistic scenario, the flame does not necessarily follow the acoustic displacement entirely, i.e. $\hat{\Delta}_{\mathrm{fl}} \neq \hat{\Delta}_{\mathrm{ac}}$, cf. (Sattelmayer et al. 2015a). To model such slip effects, the ratio of flame displacement to acoustic displacement is introduced via

$$\mathrm{FTF}^{\Delta} = \frac{\hat{\Delta}_{\mathrm{fl}}}{\hat{\Delta}_{\mathrm{ac}}} \tag{6.75}$$

Inserting Eq. (6.75) into Eq. (6.74) and expressing the acoustic displacement by the transverse velocity following (Klingen 2013) by

$$\hat{\Delta}_{\mathrm{ac}} = \frac{\breve{\hat{v}}}{\mathrm{i}\omega} \tag{6.76}$$

yields

$$\mathrm{Ra}_{\mathrm{SF}} = \frac{1}{2}\mathfrak{Re}\left[\int_{V_{\mathrm{SF}}} \breve{p}^{*}\,\mathrm{FTF}^{\mathrm{p}}\frac{\bar{\dot{q}}}{\bar{p}}\breve{\hat{p}}\,dV - \int_{V_{\mathrm{SF}}} \breve{p}^{*}\,\underbrace{\frac{\mathrm{FTF}^{\Delta}}{\mathrm{i}\omega}\frac{\partial\bar{\dot{q}}}{\partial\xi}}_{\mathrm{FTF}^{\mathrm{v}}}\breve{v}\,dV\right]. \tag{6.77}$$

In Eq. (6.77), FTF^{Δ} is combined with frequency ω and the mean flow gradient of the heat release in order to formulate a Flame Transfer Function in terms of transverse velocity $\mathrm{FTF}^{\mathrm{v}}$. In this notation, $\mathrm{FTF}^{\mathrm{v}}$ carries a dimension.

Finally, the general Rayleigh integral form of a single flame configuration is given by

$$\mathrm{Ra}_{\mathrm{SF}} = \frac{1}{2}\mathfrak{Re}\left[\int_{V_{\mathrm{SF}}} \breve{p}^{*}\,\underbrace{\mathrm{FTF}^{\mathrm{p}}\frac{\bar{\dot{q}}}{\bar{p}}\breve{\hat{p}}}_{\hat{\dot{q}}^{\mathrm{p}}}\,dV - \int_{V_{\mathrm{SF}}} \breve{p}^{*}\,\underbrace{\mathrm{FTF}^{\mathrm{v}}\breve{v}}_{\hat{\dot{q}}^{\mathrm{v}}}\,dV\right]. \tag{6.78}$$

According to Eq. (6.78) the fluctuating heat release rate is given by the sum of a pressure and a transverse velocity sensitive term. Each term individually contributes to the overall fluctuating heat release. The contribution of pressure is given by

$$\frac{\hat{\dot{q}}^{\mathrm{p}}}{\bar{\dot{q}}} = \mathrm{FTF}^{\mathrm{p}}\frac{\breve{\hat{p}}}{\bar{p}}, \tag{6.79}$$

which is referred to as *pressure coupling*. It can be seen that Eq. (6.79) is related to the pressure fluctuation on the single flame domain axis. Furthermore, Eq. (6.79) implies that the pressure fluctuation is distributed constantly in the single flame domain cross-section. In consequence, $\mathrm{FTF}^{\mathrm{p}}$ needs to be extracted from an environment with constant pressure in radial and circumferential direction.

The contribution to the overall fluctuating heat release by transverse velocity is given by

$$\hat{\dot{q}}^{\mathrm{v}} = \mathrm{FTF}^{\mathrm{v}}\breve{\hat{v}}, \tag{6.80}$$

which is referred to as *velocity coupling* in the following. Here, the acoustic coupling quantity $\breve{\hat{v}}$ is also constant over the cross-section.

Pressure and velocity coupling are based on constant respective acoustic fluctuations in radial and circumferential direction within the single flame domain. For the sake of readability, the indicator $(\breve{})$ is hence dropped in the following.

Goal of the acoustically excited single flame simulations is to determine the Flame Transfer Functions $\mathrm{FTF}^{\mathrm{p}}$ and $\mathrm{FTF}^{\mathrm{v}}$ using URANS computations. (Schmid 2014) presents an effective methodology for the separate determination of $\mathrm{FTF}^{\mathrm{p}}$ and $\mathrm{FTF}^{\mathrm{v}}$. Essentially, single flame configurations are simulated in two unique locations in the chamber under acoustic excitation, see also Fig. 6.12: (1) A single flame configuration within the pressure anti-node of the first transverse mode in the chamber. This location

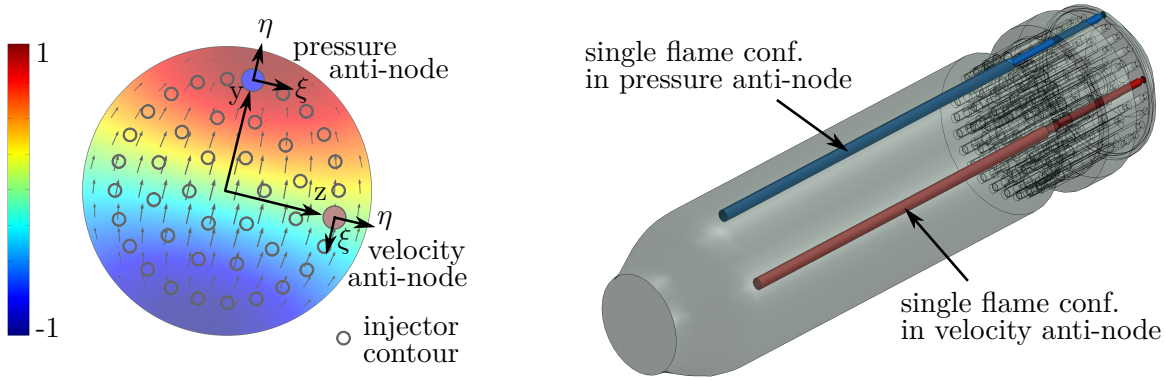

Fig. 6.12.: Left: First transverse mode structure in terms of normalized acoustic pressure (real part) and transverse velocity vector field together with injector contours and locations of the pressure anti node and the transverse velocity anti-node. Right: Single flame configurations in the pressure anti-nodal line and in the transverse velocity anti-nodal line.

is subjected to pressure fluctuations only while velocity fluctuations are absent. The corresponding single flame domain is shown in blue in Fig. 6.12. In general, different feedback mechanisms might potentially be initiated by pressure fluctuations. (2) A single flame configuration within the velocity anti-node, which is dominated by transverse velocity fluctuations and acoustic pressure amplitudes are zero. The respective domain is highlighted in red in Fig. 6.12. (Schmid 2014) argues that for the transverse mode, axial velocity fluctuations are small compared to the transverse velocity fluctuations. In consequence, $\mathrm{FTF}^{\mathrm{v}}$ relates the fluctuating heat release only to the transverse velocity fluctuations.

For all single flame configurations not located in an anti-node of pressure or of transverse velocity, it is assumed that the individual $\mathrm{FTF}^{\mathrm{p}}$ and $\mathrm{FTF}^{\mathrm{v}}$ are the same as for the reference flames located in the respective anti-node. Hence, the heat release fluctuations due to pressure coupling as well due to velocity coupling can simply be superimposed, cf. Eq. (6.79).

For the simulations with excitation, the same governing equations as for the steady state single flame computations are used, cf. Sec. 6.2. However, the excitation method is additionally implemented into the computational setup and unsteady simulations are conducted. According to the Nyquist criterion (Oppenheim et al. 1999), the sampling rate has to be at least two times the eigenfrequency of the first transverse mode in order to resolve sufficiently the acoustic fluctuations in time. As the first transverse mode oscillates with approximately 10 kHz, cf. Sec. 5.1, the sampling frequency should be at least 20 kHz, which corresponds to an acoustic period of 5×10^{-5} s. In the simulations, the sampling rate corresponds to the computational time step. For the simulations of the single flame configurations with excitation a time step of 4×10^{-6} s is used. Therefore, the Nyquist criterion is fulfilled.

The excitation method is not the same for the simulations of pressure and velocity

coupling. Hence, the individual methods will be explained in the next section separately. The general procedure is, however, similar. The simulations are started with the steady state results as initial solution, cf. Sec. 6.2. A series of time steps without excitation is conducted first in order to filter out artificial perturbations in the fields originating from the sudden change from steady state to transient computations. Subsequently, the excitation amplitude is slowly and linearly increased. Typically a number of five acoustic periods is employed to reach the targeted amplitude. The excitation frequency is known from the previous acoustic simulations and corresponds to the eigenfrequency of the first transverse mode, cf. Sec. 6.4. During the simulation, the fluctuations of pressure, transverse velocity and heat release are monitored as soon as constant amplitudes are reached. Amplitude and phase of the fluctuations are finally employed to determine the Flame Transfer Functions.

In general, the amplitude and phase of the Flame Transfer Functions depend on amplitude. As the single flame simulations with excitation are based on non-linear equations, the influence of the acoustic amplitude on the heat release fluctuations is fully described. In order to generate Flame Transfer Functions which can consistently be applied to the linear stability assessment procedure, small excitation amplitudes are used. According to (Sutton and Biblarz 2001), smooth combustion and hence small amplitudes is given for pressure fluctuations below 5 %. Therefore, for the investigations of pressure coupling, the maximal amplitude of 3 % of the mean pressure is used in the simulations. For velocity coupling, the velocity amplitude of excitation is set such that it corresponds to a pressure amplitude of also 3 %, see Sec. 6.5.2.

Furthermore, the axial profiles of the mean flow quantities might change if high amplitudes are present. In consequence, also the mode shapes and eigenfrequencies can be affected. In fact, both amplitude-dependent Flame Transfer Functions and mean flow might contribute to non-linear saturation resulting in limit cycle operation. The possibilities of performing non-linear stability assessments on the basis of the proposed stability assessment procedure was already discussed in Sec. 3.

6.5.1. Pressure Coupling and FTF^{p} Modeling

The simulation of pressure coupling is performed for a single flame configuration located in the pressure anti-node, cf. Fig. 6.12. Therefore, the excitation method is implemented such that the corresponding shapes of pressure amplitude and phase along the anti-nodal pressure line in axial direction are adequately imposed on the single flame, cf. Fig. 6.11. For this purpose, (Schmid 2014) suggests the application of a harmonically varying mass source term to the adiabatic slip wall in the chamber section, see Fig. 6.2. In consequence, mass is periodically injected and extracted from the chamber. In order to impose only pressure fluctuations, the source terms are constant around the circumference in a cylindrical chamber section, see. Fig. 6.13. However, amplitude and phase of the source term change in axial direction, in order to impose the pressure shape which was previously calculated in the pressure anti-nodal line, see Fig. 6.11. The strength of the source term excitation corresponds to the arrow length in Fig. 6.13, where a reduction in axial direction is assumed. In order to inject no foreign matter,

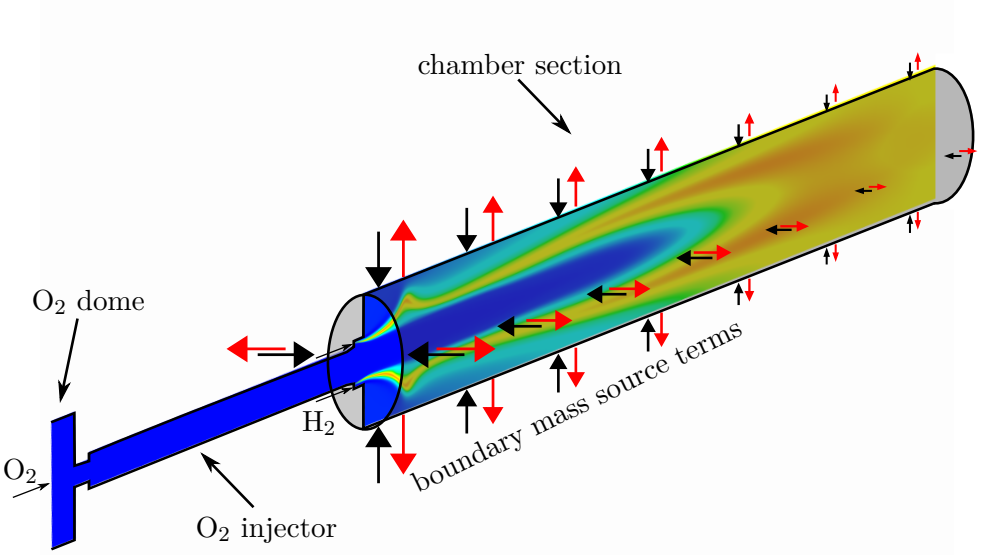

Fig. 6.13.: Illustration of the pressure coupling excitation method. The field shows the temperature and the arrows indicate the periodic compression and decompression of the single flame configuration.

the source term is imposed such that the injected and extracted compound correspond to the locally present species composition in the domain.

Fig. 6.13 shows that only the chamber section of the single flame configuration is subjected to excitation. This is reasoned by the fact that only insignificant pressure amplitudes are present in the O_2 dome. Low acoustic amplitudes were measured in the experiments (priv. comm. with S. Gröning, DLR Lampoldshausen). In the O_2 injector, however, high acoustic amplitudes are present. In fact, (Gröning et al. 2015b) describe a significant impact of the O_2 injector dynamics on combustion stability. Therefore, the O_2 injector is fully included in the computational domain. The injector acoustics are excited by the fluctuating pressure in the chamber section. Furthermore, the O_2 dome is included in order to establish a well-defined boundary for the acoustic propagation in the O_2 injector upstream.

In the O_2 injector, the pressure is approximately the same as in the chamber and temperature corresponds to the O_2 injection condition, cf. Fig. 5.1. The real gas factor Z_r of O_2 in the injector is therefore approximately 0.23 - 0.26, cf. Fig. 6.3. In consequence, real gas effects significantly affect the injector dynamics. It was shown in Sec. 6.2.2.3, however, that e.g. the speed of sound of O_2 is described 16-20 % too low using the SRK EOS for these pressure and temperature conditions. It can therefore not be expected that eigenfrequencies of the injector are accurately simulated. Since neither improved real gas EOS, cf. Sec. 6.2.2.3, nor the possibility of tabulating the thermodynamic states for the usage in the simulation are available in the current version of ANSYS CFX, a different strategy is followed. To recover the acoustic properties of the O_2 injector, the discrepancies in speed of sound are circumvented by adapting the O_2 post length such that the injector eigenfrequencies are corrected, cf. Fig. 6.2. Since only

longitudinal modes are relevant, which are proportional to

$$f \sim \frac{c}{l_{\text{post}}}, \tag{6.81}$$

the discrepancies in c can simply be corrected by reducing l_{post} such that the error in c is compensated. The necessary length reduction directly corresponds to the error in c of 16-20 % depending on the load point. Fluid dynamic properties such as the pressure drop over the entire injector are not affected, since the pressure loss element is not changed and l_{post} is still enough long to establish a fully developed flow on the O_2 post.

The derivation of the explicit source term of mass is based on the pressure distribution for an uniform flow in the combustion chamber, see Sec. 2.4. The time variation of pressure for the first transverse mode is therefore given by

$$p'(x,\xi,t) = \mathfrak{Re}(P_{\mathrm{T}_1}(x)\,\Theta_{\mathrm{T}_1}(\xi)\,R_{\mathrm{T}_1}(r)e^{\mathrm{i}\omega t}). \tag{6.82}$$

For a single flame configuration, only the axial and azimuthal direction are relevant. The radial ansatz function $R_{\mathrm{T}_1}(r)$ is set to one, viz.

$$p'(x,\xi,t) = \mathfrak{Re}(A_e\,P_{\mathrm{T}_1}(x)\,\cos(k_{\mathrm{T}_1}\xi)\,e^{\mathrm{i}\omega t}), \tag{6.83}$$

where A_e denotes the excitation amplitude and ξ the local coordinate in circumferential direction, cf. Fig. 6.12. Furthermore, $P_{\mathrm{T}_1}(x)$ contains the axial pressure distributions in amplitude and phase, which are extracted from the previous acoustic simulation results along the anti-nodal pressure line, cf. Fig. 6.11. In order to fully control the excitation amplitude with A_e, the amplitude of $P_{\mathrm{T}_1}(x)$ is normalized. In contrast, to retain the correct phase distribution is axial direction, $\varphi(P_{\mathrm{T}_1}(x))$ is not changed. The pressure of excitation is finally given by

$$p'(x,\xi,t) = \mathfrak{Re}(A_e\cos(k_{\mathrm{T}_1}\xi)\,[\mathfrak{Re}(P_{\mathrm{T}_1}(x)) + \mathrm{i}\mathfrak{Im}(P_{\mathrm{T}_1}(x))]\,[\cos(\omega t) + \mathrm{i}\sin(\omega t)]), \tag{6.84}$$

and consequently

$$p'(x,\xi,t) = A_e\cos(k_{\mathrm{T}_1}\xi)\,[\mathfrak{Re}(P_{\mathrm{T}_1}(x))\cos(\omega t) - \mathfrak{Im}(P_{\mathrm{T}_1}(x))\sin(\omega t)]\,. \tag{6.85}$$

For the application of a mass source term on the boundary, $p'(x,\xi,t)$ needs to be converted into a corresponding velocity fluctuation. Using the linearized momentum equation in ξ-direction according to Eq. (2.12) in the absence of mean flow and volume source terms ($\mathcal{S}'_{u_i} = 0$) yields

$$\frac{\partial w'(x,t)}{\partial t} = -\frac{1}{\bar{\rho}}\frac{\partial p'(x,\xi,t)}{\partial \xi}, \tag{6.86}$$

and therefore

$$w'(x,t) = \frac{A_e\,k_{\mathrm{T}_1}}{\bar{\rho}\,\omega}\,\sin(k_{\mathrm{T}_1}\xi)\,[\mathfrak{Re}(P_{\mathrm{T}_1}(x))\sin(\omega t) + \mathfrak{Im}(P_{\mathrm{T}_1}(x))\cos(\omega t)]\,, \tag{6.87}$$

if it is assumed that the ξ direction in the pressure anti-node coincides with the global z coordinate, see Fig. 6.12 (left).

Fluctuating mass flow per unit boundary area $\dot{m}_e$ is given by Eq. (2.96). In consequence, the source term $\dot{m}'_{\mathrm{e}}$ on the boundary reads

$$\dot{m}'_{\mathrm{e}} = \bar{\rho} w'(x,t). \tag{6.88}$$

Inserting Eq. (6.87) into Eq. (6.88) finally yields the fluctuating mass source term per unit boundary area

$$\dot{m}'_{\mathrm{e}} = \bar{\rho} w'(x,t) = \frac{A_e \, k_{\mathrm{T_1}}}{\omega} \, \sin(k_{\mathrm{T_1}} \xi) \left[\mathfrak{Re}(P_{\mathrm{T_1}}(x)) \sin(\omega t) + \mathfrak{Im}(P_{\mathrm{T_1}}(x)) \cos(\omega t) \right], \tag{6.89}$$

where the wave number is given by

$$k_{\mathrm{T_1}} = \frac{\omega}{c}. \tag{6.90}$$

The excitation amplitude is defined by A_e. However, as the pressure distribution of $P_{\mathrm{T_1}}(x)$ is not constant in axial direction, A_e corresponds to the maximum amplitude in the system. As exemplarily indicated in Fig. 6.11, the maximum pressure is present at the face plate. For the investigation of the non-linear dependency of the mean flow on pressure amplitude, A_e can gradually be increased.

In order to not change the chosen excitation amplitude, the speed of sound in Eq. (6.90) is set constant. For this purpose, a volume averaged speed of sound is determined on the basis of the steady state mean flow results.

As shown in Fig. 6.13, the applied pressure excitation method is constant in circumferential direction and hence axis-symmetrical. Therefore, it is not necessary to simulate the entire three-dimensional cylindrical configuration, but the same two-dimensional computational domain as for the steady state computation is employed, cf. Fig. 6.2. The mass source term according to Eq. (6.89) is imposed on the adiabatic slip wall in the chamber section. Furthermore, to apply the pressure fluctuations consistently on the chamber, the pressure at the outlet has to be varied accordingly. Hence, the outlet boundary condition is modified to

$$p = \bar{p} + p'(x, \xi, t), \tag{6.91}$$

where $\bar{p}$ corresponds to the pressure applied in the steady state simulation, cf. Fig. 6.2. Moreover, $p'(x, \xi, t)$ is given by Eq. (6.85) and evaluated at the location of the outlet.

Finally, the Flame Transfer Functions $\mathrm{FTF}^{\mathrm{p}}$ are calculated from the dynamic results of the simulation according to Eq. (6.79). In general, the single flame simulations with excitation allow to determine the relationship between pressure and heat release at every location in the domain. However, such an approach is not followed in this thesis since a local relation between pressure and heat release appears unphysical. If combustion is perturbed due to the influence of pressure fluctuation e.g. at a location x_1, but the perturbation is transported convectively with the flow before heat is actually released at

a location x_2, then $\hat{\dot{q}}(x_2)$ can not be related to the pressure fluctuation at x_2. Specifically, when $\hat{p}$ is non constant in space, amplitude and phase of $\hat{p}(x_1)$ and $\hat{p}(x_2)$ are not the same. In consequence, $\mathrm{FTF^p}$ determined on the basis of $\hat{p}(x_2)$ instead of $\hat{p}(x_1)$ will be incorrect in terms of amplitude and phase. In fact, as $\hat{\dot{q}}(x_2)$ is initiated at location x_1, it must be related to $\hat{p}(x_1)$. If $\mathrm{FTF^p}$ is simply determined at each location according to Eq. (6.79), the spatial separation of initiation and effect is not accounted for.

$\mathrm{FTF^p}$ contains different coupling mechanisms. The governing coupling mechanisms will be explained together with the $\mathrm{FTF^p}$ results in the next Chapter in case of the BKD, see Sec. 7.5. It will be shown, however, that the mechanisms occur in spatially separated regions. Hence, for each region in which a coupling mechanism occurs, a separate $\mathrm{FTF^p}$ is calculated. Within the individual regions, $\mathrm{FTF^p}$ is not determined on each location, but a single $\mathrm{FTF^p}$ is calculated, which describes the complete coupling mechanism in terms of amplitude and phase. $\mathrm{FTF^p}$ is therefore referred to as $\mathrm{FTF^p_{mech}}$ in the following. For its calculation, the volume integrated heat release rate fluctuations are determined first, i.e.

$$\hat{\dot{Q}}^{\mathrm{p}} = \int_{V_{\mathrm{mech}}} \hat{\dot{q}}^{\mathrm{p}} \, dV_{\mathrm{mech}}, \tag{6.92}$$

and

$$\bar{\dot{Q}} = \int_{V_{\mathrm{mech}}} \bar{\dot{q}} \, dV_{\mathrm{mech}}, \tag{6.93}$$

where V_{mech} corresponds to the volume in which the coupling mechanism is present. In consequence, the volume integrated heat release fluctuations are given by

$$\frac{\hat{\dot{Q}}^{\mathrm{p}}}{\bar{\dot{Q}}} = \mathrm{FTF^p_{mech}} \frac{\hat{p}(x_{\mathrm{ref}})}{\bar{p}(x_{\mathrm{ref}})}, \tag{6.94}$$

cf. Eq. (6.79). $\mathrm{FTF^p_{mech}}$ is then calculated by

$$\mathrm{FTF^p_{mech}} = \frac{\hat{\dot{Q}}^{\mathrm{p}}}{\bar{\dot{Q}}} \frac{\bar{p}(x_{\mathrm{ref}})}{\hat{p}(x_{\mathrm{ref}})}. \tag{6.95}$$

In the acoustic simulation, the volumetric heat release rate is required. Therefore, $\hat{\dot{Q}}$ is divided by the respective volume, i.e.

$$\hat{\dot{q}}^{\mathrm{p}} = \frac{\hat{\dot{Q}}^{\mathrm{p}}}{V_{\mathrm{mech}}} = \mathrm{FTF^p_{mech}} \frac{\hat{p}(x_{\mathrm{ref}})}{\bar{p}(x_{\mathrm{ref}})} \frac{\bar{\dot{Q}}_{\mathrm{mech}}}{V_{\mathrm{mech}}}. \tag{6.96}$$

$\mathrm{FTF^p_{mech}}$ needs to be determined for each region in the system, in which a pressure coupling mechanism occurs. Finally, Eq. (6.96) is implemented into the acoustic simulation code in order to the describe the influence of pressure coupling on stability.

6.5.2. Velocity Coupling and $\mathrm{FTF^v}$ Modeling

In general, the same methodology is followed for the simulation of the velocity coupling as for pressure coupling. The response of heat release to transverse velocity fluctuations is simulated for a single flame configuration in the anti-velocity nodal line, which

is located 90° shifted circumferentially to the anti-nodal pressure line, cf. Fig. 6.12 (left). Amplitude and phase distribution of the transverse velocity is extracted from the previous acoustic simulation results and imposed on the single flame configuration. However, in order to impose the velocity fluctuations on the single flame configuration without the modulation of pressure, a different excitation method needs to be employed than for pressure coupling. Instead of a mass source term at the boundaries, (Schmid 2014) suggests the application of a harmonically varying volumetric force term to the entire single flame chamber section volume. The force mimics the influence of transverse velocity fluctuations on the local flow field including the flame. In consequence, the fluid in the single flame configuration is pushed harmonically through the domain, see. Fig. 6.14.

The volumetric force term corresponds to a source term in the ξ-momentum equation, cf. Fig 6.12 (left) to see the local frame of reference. Furthermore, as pressure fluctuations are not present and mean velocity is zero in ξ direction, the ξ-momentum equation reads, cf. Eq. (2.31)

$$\frac{\partial v'(x,\xi,t)}{\partial t} = \frac{S_\xi}{\bar{\rho}}, \tag{6.97}$$

assuming that the local ξ coordinate coincides with the global y coordinate in the velocity anti-node, cf. Fig. 6.12 (left). In consequence, the source term is given by

$$S_\xi = \bar{\rho}\frac{\partial v'(x,\xi,t)}{\partial t}. \tag{6.98}$$

The term on the r.h.s. of Eq. (6.98) can be further developed using the pressure excitation method, cf. Eq. (6.82) - Eq. (6.86). In comparison to the pressure anti-node, pressure is shifted by 90° in circumferential direction in the velocity anti-node, i.e.

$$S_\xi = \bar{\rho}\frac{\partial v'(x,\xi,t)}{\partial t} = -\frac{\partial}{\partial \xi}\left(-A_e \sin(k_{\mathrm{T}_1}\xi)\left[\mathfrak{Re}(P_{\mathrm{T}_1}(x))\cos(\omega t) - \mathfrak{Im}(P_{\mathrm{T}_1}(x))\sin(\omega t)\right]\right). \tag{6.99}$$

Finally, the volumetric source term for transverse velocity excitation is given by

$$\mathcal{S}_\xi = A_e\, k_{\mathrm{T}_1}\cos(k_{\mathrm{T}_1}\xi)\left[\mathfrak{Re}(P_{\mathrm{T}_1}(x))\cos(\omega t) - \mathfrak{Im}(P_{\mathrm{T}_1}(x))\sin(\omega t)\right]. \tag{6.100}$$

The volumetric source term of momentum according to Eq. (6.100) has a similar structure as the boundary source term for pressure excitation, cf. Eq. (6.89). Both pressure and velocity excitation methods are derived on the basis of the amplitude and phase distribution of pressure in the anti-nodal pressure line $P_{\mathrm{T}_1}(x)$, cf. Fig. 6.11. In consequence, the parameter A_e applies for both the amplitude of pressure excitation and of transverse velocity excitation. In the latter case, A_e can be regarded as an equivalent pressure amplitude, although only transverse velocity fluctuations are imposed on the single flame configuration. Particularly, A_e corresponds to the pressure amplitude, which would be present in the anti-pressure node. Hence, when the same is set

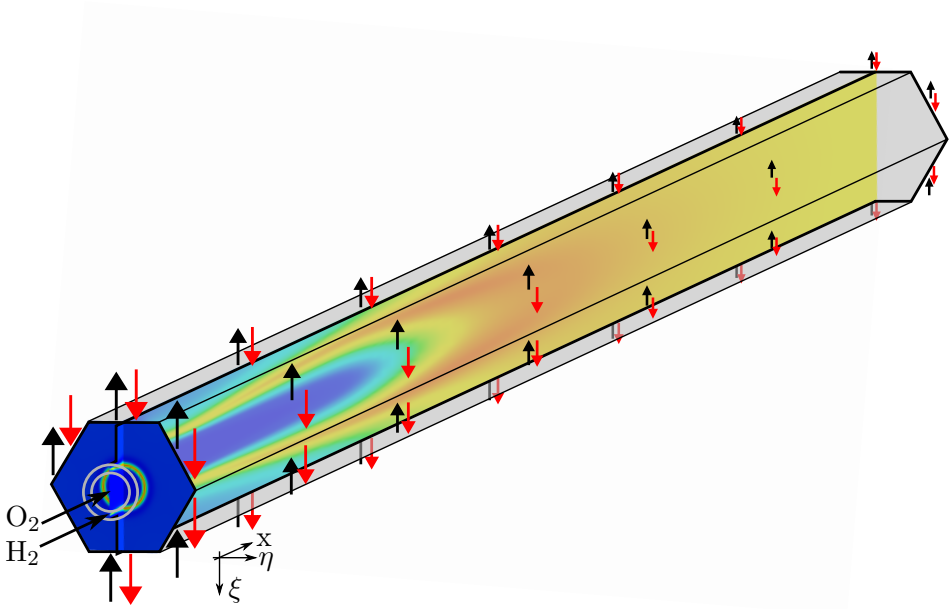

Fig. 6.14.: Illustration of the velocity coupling excitation method. The field shows the temperature. The black and red arrows indicate the direction of the transverse acoustic velocity at two time instants, which differ by half an acoustic period.

for A_e in case of pressure velocity excitation, the individual Flame Transfer Functions can directly be compared even for higher amplitudes. For low amplitudes, comparability is always given as long as linearity is not violated. Furthermore, the effects on the mean flow through acoustic fluctuations at higher (but equal) amplitudes can also be compared.

The computational domain for the application of transverse velocity excitation is shown in Fig. 6.14. The source term of momentum S_ξ is applied within the entire single flame configuration in ξ direction, see Fig. 6.14. The arrows indicate the strength of the source term excitation. As pressure decays in axial direction, cf. Fig. 6.11, also transverse velocity excitation strength gets reduced. In order to not generated acoustic pressure fluctuations in domain, opposing boundaries are set periodically in terms of mass flow. However, since the transverse velocity excitation method cannot be applied axis-symmetrically, three-dimensional simulations are necessary. To also reflect the periodicity between neighboring single-flame configurations, the computational domain is hexagonally shaped in cross-section.

In case of transverse velocity excitation, the injector is acoustically not active. This can be shown by the axial momentum balance at the injector outlet at a position of $x = -2$ mm, see. Fig. 5.3. As the Mach number is small in the injector, convective terms can be neglected in the momentum equation for the following analysis, cf. Tab. 5.1. Also, volumetric source terms are not present at the injector outlet. The axial

momentum equation at the injector outlet is therefore given by (cf. Eq. (2.12))

$$\frac{\partial u'(x,t)}{\partial t} = -\frac{1}{\bar{\rho}}\frac{\partial p'(x,t)}{\partial x} + \frac{\rho'(x,t)}{\bar{\rho}^2}\frac{\partial \bar{p}}{\partial x}. \tag{6.101}$$

As pressure is not excited in the chamber section, $p'(x,t) = \rho'(x,t) = 0$, and consequently

$$\frac{\partial u'(x,t)}{\partial t} = 0. \tag{6.102}$$

Therefore, both pressure and velocity fluctuations are zero at the injector outlet. Hence, the injector dynamics are irrelevant for the simulation of velocity coupling. To reduce computational turn-around times, the injector is not included into the computational domain for the simulation of velocity coupling. Instead, the O_2 mass flow and the temperature are imposed on the boundary condition of the O_2 inflow, which is located at the inlet to the recess, see Fig. 6.14.

As explained before, the displacement of the flame towards elevated pressure may drive the feedback taking into account possible slip between acoustic and flame displacement, see (6.75). Due to symmetrical transverse velocity excitation conditions within each half acoustic period, modulated heat release fluctuations occur at double excitation frequency. A direct coupling between the transverse velocity and heat release fluctuations for the considered eigenfrequency of the system is therefore not possible in the linear regime. In consequence, only the displacement of the flame can contribute to a fluctuating heat release source term driving the amplitude of the first transverse mode.

From the dynamic results of the single flame configuration with transverse velocity excitation, FTF^{Δ} according to Eq. (6.75) is deduced. For this purpose, the flame displacement Δ'_{fl} as well as the acoustic displacement Δ'_{ac} is monitored and afterwards converted into their frequency space form, i.e. $\hat{\Delta}_{\mathrm{fl}}$ and $\hat{\Delta}_{\mathrm{ac}}$.

The flame displacement $\hat{\Delta}_{\mathrm{fl}}$ is calculated as the center of gravity of heat release over the entire single flame chamber domain (Schmid 2014)

$$\hat{\Delta}_{\mathrm{fl}} = \mathcal{F}\left(\frac{\int_{V_{\mathrm{SF}}} \xi\, \dot{q}\, dV}{\frac{1}{T_s}\int_{T_s}\int_{V_{\mathrm{SF}}} \dot{q}\, dV\, dt}\right). \tag{6.103}$$

For example, if the flame is not displaced in ξ direction, heat release $\dot{q}$ is distributed symmetrically with respect to the η axis, see Fig. 6.12. In this situation, the enumerator of Eq. (6.103) and consequently $\hat{\Delta}_{\mathrm{fl}}$ are zero. However, as soon as the transverse velocity fluctuations move the flame in ξ direction, the unsymmetrical distribution of $\dot{q}$ yields a non-vanishing displacement $\hat{\Delta}_{\mathrm{fl}}$.

The acoustic displacement $\hat{\Delta}_{\mathrm{ac}}$ is determined at a reference position close to the outlet of the computational domain. At this location combustion is complete and a realistic acoustic displacement in the light product gas on the center axis is obtained. In the reaction zone the acoustic displacement is altered through the dense O_2 core and a

measurement at this location would therefore lead to inadequate FTF^{Δ}. However, the decreasing excitation in axial direction reduces the acoustic displacement towards the outlet, see Fig. 6.11 and 6.14. To provide realistic acoustic reference displacements at the measurement position, another computation is conducted, where a source term with constant amplitude is imposed on the domain. The constant amplitude of the source term corresponds to the maximal amplitude used in the first computation.

To finally incorporate the velocity coupling according to Eq. (6.77) into the acoustic simulation, the gradient of the mean heat release field $\frac{\partial \bar{\dot{q}}}{\partial \xi}$ is necessary. However, as argued by (Schmid 2014), the spatially small-scaled mean heat release field cannot be resolved fully in the acoustic simulations. Instead, (Schmid 2014) suggests the usage of a pseudo heat release field, which can be resolved with typical acoustic grids. This pseudo heat release field is defined that the Rayleigh integral according to Eq. (6.77) is conserved. In consequence the driving effect of acoustic amplitudes by velocity coupling is maintained. The detailed mapping procedure is comprehensively described in (Schmid 2014). The source term reads:

$$\hat{\dot{q}}^{\mathrm{v}} = -\frac{1}{2}\,\mathrm{FTF}^{\Delta}\frac{\pi^2\bar{\dot{Q}}_{\mathrm{SF}}}{(\pi^2-4)V_{\mathrm{SF}}}\frac{-\pi\xi\sin\left(\frac{\pi}{R_{\mathrm{SF}}}\sqrt{\xi^2+\eta^2}\right)}{R_{\mathrm{SF}}\sqrt{\xi^2+\eta^2}}\cdot\frac{\hat{v}}{\mathrm{i}\Omega}, \tag{6.104}$$

where R_{SF} denotes the radius of the chamber section in the single flame configuration. In Eq. (6.104) it is assumed that the ξ direction coincides with the acoustic velocity vector. For the usage in a Cartesian frame of reference in the cross-section of the entire chamber, ξ, η coordinates are transformed into y, z coordinates.

The source term according to Eq. (6.104) is constant in axial direction. However, fluctuating heat release can only appear if combustion takes place. It is therefore assumed, that the shape of the amplitude of $\hat{\dot{q}}^{\mathrm{v}}$ in axial direction corresponds qualitatively to the distribution of the mean heat release rate. The shape of the amplitude is incorporated by weighting the source term with a shape function $\mathfrak{s}(x)$. Hence, the final source term is given by

$$\hat{\dot{q}}^{\mathrm{v}} = \frac{1}{2}\,\mathrm{FTF}^{\Delta}\frac{\pi^2\bar{\dot{Q}}_{\mathrm{SF}}}{(\pi^2-4)V_{\mathrm{SF}}}\frac{\pi\xi\sin\left(\frac{\pi}{R_{\mathrm{SF}}}\sqrt{\xi^2+\eta^2}\right)}{R_{\mathrm{SF}}\sqrt{\xi^2+\eta^2}}\cdot\frac{\hat{v}}{\mathrm{i}\Omega}\cdot\mathfrak{s}(x). \tag{6.105}$$

The shape function is formulated as

$$\mathfrak{s}(x) = \frac{1}{\bar{\dot{Q}}_{\mathrm{SF}}}\bar{\dot{q}}_{\mathrm{SF},r}(x), \tag{6.106}$$

where $\bar{\dot{Q}}_{\mathrm{SF}}$ denotes the volume integrated heat release, i.e.

$$\bar{\dot{Q}}_{\mathrm{SF}} = \int_{V_{\mathrm{SF}}}\bar{\dot{q}}_{\mathrm{SF}}\,dV, \tag{6.107}$$

and $\bar{\dot{q}}_{\mathrm{SF},r}(x)$ the over the chamber cross-section integrated distribution of the volumetric heat release in axial direction. The volume integration of $\mathfrak{s}(x)$ yields

$$\int_{V_{\mathrm{SF}}}\mathfrak{s}(x)dV = \int_{L_{\mathrm{SF}}}\frac{1}{\bar{\dot{Q}}_{\mathrm{SF}}}\cdot\bar{\dot{q}}_{\mathrm{SF},r}\,dx = \frac{1}{\bar{\dot{Q}}_{\mathrm{SF}}}\int_{L_{\mathrm{SF}}}\bar{\dot{q}}_{\mathrm{SF},r}\,dx = \frac{1}{\bar{\dot{Q}}_{\mathrm{SF}}}\cdot\bar{\dot{Q}}_{\mathrm{SF}} = 1. \tag{6.108}$$

In consequence, the volume integration of the shape function is unity.

In the acoustic simulations, a separate source term according to Eq. (6.104) is included at each flame location, cf. Fig. 5.2. Therefore, the acoustic grid needs to be refined such that it resolves the spatial dependency of the source term at each of the 42 flames sufficiently.

6.6. Assessment of Linear Stability

In the final step of the stability assessment procedure, acoustic simulations in form of eigenvalue studies are conducted for the closed loop system. This last step is illustrated in Fig. 6.15.

Essentially, the same computational setup as for the open loop system is used, see Sec. 6.4 and especially Fig. 6.10. Since only low amplitude operation is analyzed, it is assumed that the mean flow $\bar{\phi}(x)$ is the same both for the open loop and for the closed loop system. Furthermore, the scattering matrix SM is used to acoustically couple the chamber with the O_2 dome. However, in order to close the feedback loop, the source terms of fluctuating heat release for pressure and velocity according to Eq. (6.96) and Eq. (6.105), viz.

$$\hat{\dot{q}} = \hat{\dot{q}}^{\mathrm{p}} + \hat{\dot{q}}^{\mathrm{v}}. \tag{6.109}$$

is also included into the acoustic simulations. The source terms are based on $\mathrm{FTF}^{\mathrm{p}}_{\mathrm{mech}}$ and FTF^{Δ}, cf. Fig. 6.15. Optionally, the reflection coefficients of an absorber ring or of the O_2 feed lines on the O_2 dome could be incorporated.

Since the Flame Transfer Functions as well as the scattering matrix and reflection coefficients depend on frequency, the complex frequency can only be found iteratively, cf. Sec. 3.2.2.2. Initially, all transfer functions are evaluated at the open loop eigenfrequency. Afterwards, amplitude and phase of the transfer functions are updated according to the new eigenfrequency Ω_n with each iteration n and acoustic simulations are conducted until the relative changes of both ω_n and λ_n are below a certain threshold δ, i.e.

$$\left| \frac{\omega_{n+1} - \omega_n}{\omega_n} \right| < \delta \tag{6.110}$$

and

$$\left| \frac{\lambda_{n+1} - \lambda_n}{\lambda_n} \right| < \delta. \tag{6.111}$$

In this thesis a convergence criterion of $\delta = 0.03$ is applied, which corresponds to the relative deviations from the mean value of the 95 % confidence interval calculated by the Lorentzian fitting for the damping rates of LP1, cf. Tab. 5.2.

During the iterative procedure, the transfer functions are evaluated at the complex frequencies of the intermediate iterations Ω_n. As discussed in Sec. 3.3.1, the accuracy of

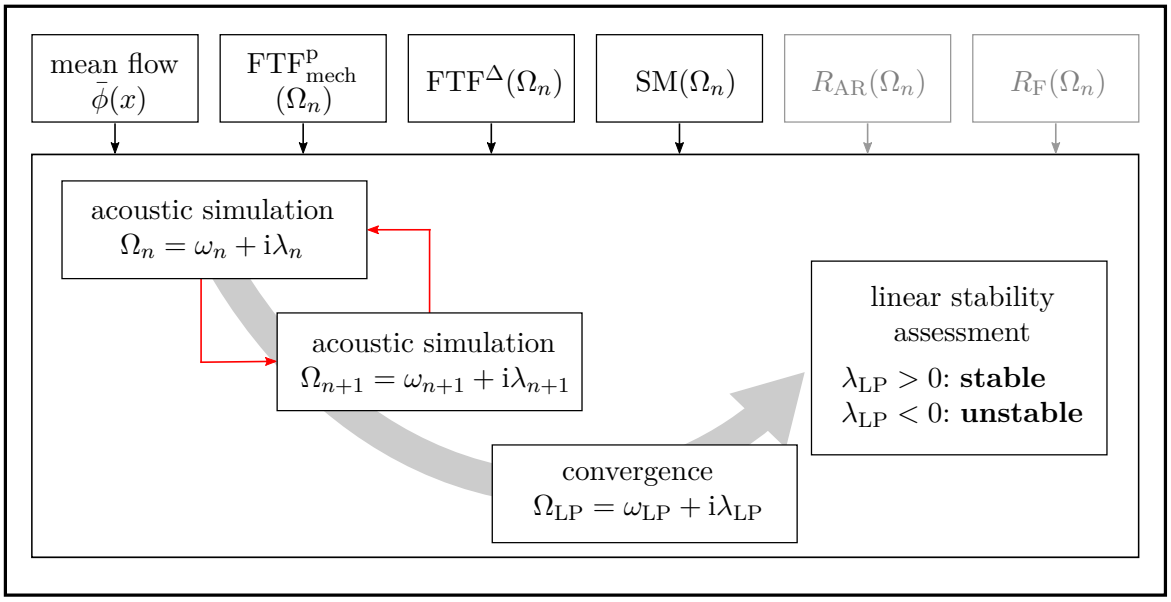

Fig. 6.15.: Linear stability assessment procedure.

amplitude and phase of the transfer functions depends on the ratio between ω_n and λ_n. If λ_n is comparably large, the inaccuracy of the amplitudes and phases might be rather high possibly leading to failed convergence. The used iterative procedure is therefore especially robust, if the damping rate is low in comparison to the eigenfrequency.

From the complex frequency Ω_{LP}, the linear stability is determined by assessing the damping rate for each load point, see Sec. (2.3). A negative damping rate, i.e. $\lambda_{\mathrm{LP}} < 0$ indicates that the initial excitation by noise leads to a linear growth of acoustic amplitudes due to the driving by the flame, cf. Eq. (6.1). In contrast, if $\lambda_{\mathrm{LP}} > 0$, damping of acoustic amplitudes is stronger than the amplification by flame feedback. In consequence, amplitudes initially excited by noise are constantly damped and the system operates stable.

As already shown in Sec. 5.4, the damping rates of the considered LP for the BKD test chamber operation are in fact very low in comparison to the eigenfrequency. For the unstable LP2 and LP4, the damping rates are even close to the stability limit. As it will be shown in the next Chapter, the calculated damping rates are in good agreement with the experimentally determined λ_{LP}. In consequence, rapid convergence is obtained during the stability assessment procedures.

7 Thermoacoustic Characterization of the Test Chamber BKD

The stability assessment procedure introduced in Chap. 6 is validated on the basis of the BKD test chamber, see Chap. 5. The validation of the procedure is conducted on different levels. First, mean flow profiles are simulated by CFD and validated in terms of combustion temperatures and of static pressures in the O_2 dome. Afterwards, the scattering matrices for the coupling of the chamber with the O_2 dome are presented. Using the mean flow profiles and the dome coupling scattering matrices for LP1-4, the eigenfrequencies for the open loop system are simulated and subsequently compared to experimental findings. For this purpose, the eigenfrequencies up to the first radial mode are evaluated.

Afterwards, the focus is on the first transverse mode dynamics in the BKD test chamber. A sensitivity study of the first transverse mode eigenfrequencies on injection conditions, i.e. on H_2 injection temperature as well as on ROF, is performed and the numerical findings are verified. The sensitivity study reveals both the necessary accuracy of the calculations for the adequate determination of eigenfrequencies and the suitability of the hybrid approach for the description of acoustic propagation in the BKD test chamber.

In the next step, Flame Transfer Functions for pressure coupling and velocity coupling are presented for LP1-4. For the validation of the FTF only limited experimental comparison data is available. Finally, the closed loop systems for LP1-4 are simulated and the damping rates for the first transverse mode are compared to the experimental validation data, which was generated on the basis of Lorentzian fitting and the parameter extraction method presented in Sec. 5.4.

The goal of this Chapter is not only the comparison of simulated eigenfrequencies and damping rates to experimental findings. Additionally, the thermoacoustic properties of the BKD test chamber derived from the numerical results are investigated. Particularly, the mode structure of the first transverse mode is analyzed and its impact on the stability is discussed.

7.1. Mean Flow Fields

Since the steady state fields of a single flame configuration are the basis for the following acoustic simulations and excited CFD computations, their results are analyzed first. The computational setup and the governing equations for the simulation of the single flame configuration were described in Sec. 6.2.

7.1.1. Injection Temperatures of H_2 and O_2

As explained in Sec. 6.2, the H_2 injector and H_2 dome are not included into the steady state, single flame configuration simulations. However, the H_2 temperature can change along the H_2 post e.g. due to the heat flux originating from the O_2 and other effects. In order to reveal the influence of the H_2 injection system on the injection temperature of H_2 and O_2, simulations of the BKD injection system with conjugated heat transfer were conducted (Demmelmair 2014).

The computed injection temperatures of H_2 are given in Tab. 7.1. Unexpectedly, the H_2 injection temperatures are in fact lower than the dome temperatures for LP1, LP2 and LP4, although heat is actually transferred from the warmer O_2 to the H_2, cf. Tab. 5.1. An increase in temperature along the H_2 post was only found for LP3.

The reduction of H_2 temperature along the H_2 post in case of LP1, LP2 and LP4 can be explained by the strong increase in velocity and the accompanied reduction in static enthalpy. Assuming that H_2 is at rest in the dome, the energy conservation between the dome and the location of injection in terms of enthalpy is given by

$$c_{p,\mathrm{H_2}}|_{\bar{T}_{\mathrm{ref}}}^{\bar{T}_{\mathrm{H_2}}} \cdot \bar{T}_{\mathrm{H_2}} = c_{p,\mathrm{H_2}}|_{\bar{T}_{\mathrm{ref}}}^{\bar{T}_{\mathrm{H_2,inj}}} \cdot \bar{T}_{\mathrm{H_2,inj}} + \frac{\bar{u}_{\mathrm{H_2,inj}}^2}{2} - \frac{\dot{Q}}{\dot{m}_{\mathrm{H_2}}}, \tag{7.1}$$

where $c_{p,\mathrm{H_2}}|_{\bar{T}_{\mathrm{ref}}}^{\bar{T}}$ denotes the isobaric heat capacity averaged over the respective temperature interval. In the following, it is assumed that the enthalpy at $\bar{T}_{\mathrm{ref}}$ is zero. The term on the l.h.s. of Eq. (7.1) describes the total enthalpy, the terms on the r.h.s. the static enthalpy and the kinetic energy at the H_2 injector outlet as well as the heat transferred from O_2 to H_2 with the heat flux $\dot{Q}$. Assuming that the averaged isobaric heat capacities are the same, i.e. $c_{p,\mathrm{H_2}}|_{\bar{T}_{\mathrm{ref}}}^{\bar{T}_{\mathrm{H_2}}} = c_{p,\mathrm{H_2}}|_{\bar{T}_{\mathrm{ref}}}^{\bar{T}_{\mathrm{H_2,inj}}} = c_{p,\mathrm{H_2}}$, Eq. (7.1) can be rearranged yielding the temperature at injection

$$\bar{T}_{\mathrm{H_2,inj}} = \bar{T}_{\mathrm{H_2}} + \frac{\dot{Q}}{\dot{m}_{\mathrm{H_2}} c_{p,\mathrm{H_2}}} - \frac{\bar{u}_{\mathrm{H_2,inj}}^2}{2 c_{p,\mathrm{H_2}}}. \tag{7.2}$$

Tab. 7.1.: Comparison of H_2 temperatures in the dome and at injection for LP1-4.

load point	LP1	LP2	LP3	LP4
$\bar{T}_{\mathrm{H_2}}$ [K]	93.67	94.90	47.62	95.66
$\bar{T}_{\mathrm{H_2,inj}}$ [K]	87.69	91.28	48.1	91.98

Eq. (7.2) shows that if the injection velocity is high, the reduction of the static enthalpy may dominate over the increase of total enthalpy by the heat input. In fact, for LP1, LP2 and LP4, high injection velocities are present, cf. Sec. 5.2 and Tab. 5.1.

In contrast, H_2 is injected with low velocity in case of LP3 and the reduction of the static enthalpy and therefore temperature is low. In consequence, the heat transferred to H_2 leads to a small temperature increase along the H_2 post in case of LP3. However, the temperature increase is very small. Therefore, it can be concluded that the heat flux $\dot{Q}$ from the O_2 to H_2 is small.

Moreover, since O_2 is not accelerated along the O_2 post, its temperature is only affected by the heat transfer to the H_2. However, since the heat flux $\dot{Q}$ is small, the O_2 temperatures cannot change significantly. For this reason, the computed O_2 injection temperatures are not shown since they correspond to the O_2 temperatures in the dome, cf. Tab. 5.1.

For the steady state mean flow simulations and also for the following excited CFD computations, the H_2 temperatures presented in Tab. 7.1 are imposed at the H_2 injection boundary, cf. Fig. 6.2.

7.1.2. O_2 Dome and Injector Flow

The O_2 flow in the O_2 dome and injector is visualized as surface plots. In each analyses, the visualization surface corresponds to a half symmetry plane of the single flame configuration.

The distributions of pressure (top) and Mach number (bottom) in the O_2 dome and injector passage are shown in Fig. 7.1 for LP1-4. First, the pressure fields are analyzed. At the injector outlet, the pressure corresponds to the chamber pressure p_{cc}, cf. Tab. 5.1. Along the O_2 post length, the pressure is approximately constant. Finally, a high pressure drop is present at the pressure loss element. The pressure drop is established due to streamline curvature as well as due to shear layer effects. Highest pressure values are found in the O_2 dome.

In the CFD simulations, the pressure is imposed as boundary condition at the outlet of the chamber section, cf. Fig. 6.2. In consequence, the numerically determined dome pressure can be used as a validation base of the computations. The comparison of the simulated and the experimental dome pressures is shown in Tab. 7.2. It can be seen that the relative error is at most 2.6 % in case of LP2. Considering that the O_2 injection system is dominated by real gas effects, which are described by the SRK EOS with limited accuracy in terms of density, the deviations between numerical results and experimental measurements are acceptable, cf. Sec. 6.2.2.3.

To quantify the pressure drop over the O_2 injection system, the ratio of p_{cc} to p_{O_2} is given in Tab. 7.2 as well. Overall, the pressure is reduced by approximately 10 %, if the chamber pressure is taken as reference. For LP1, the pressure ratio is slightly higher. This is caused by the lower mass flow of O_2 through the injector, cf. Tab. 5.1. In contrast, since the O_2 mass flows are higher for LP3 and LP4 than for LP1, the pressure reduction is slightly larger than 10 % for LP3/4. Since the pressure is constant

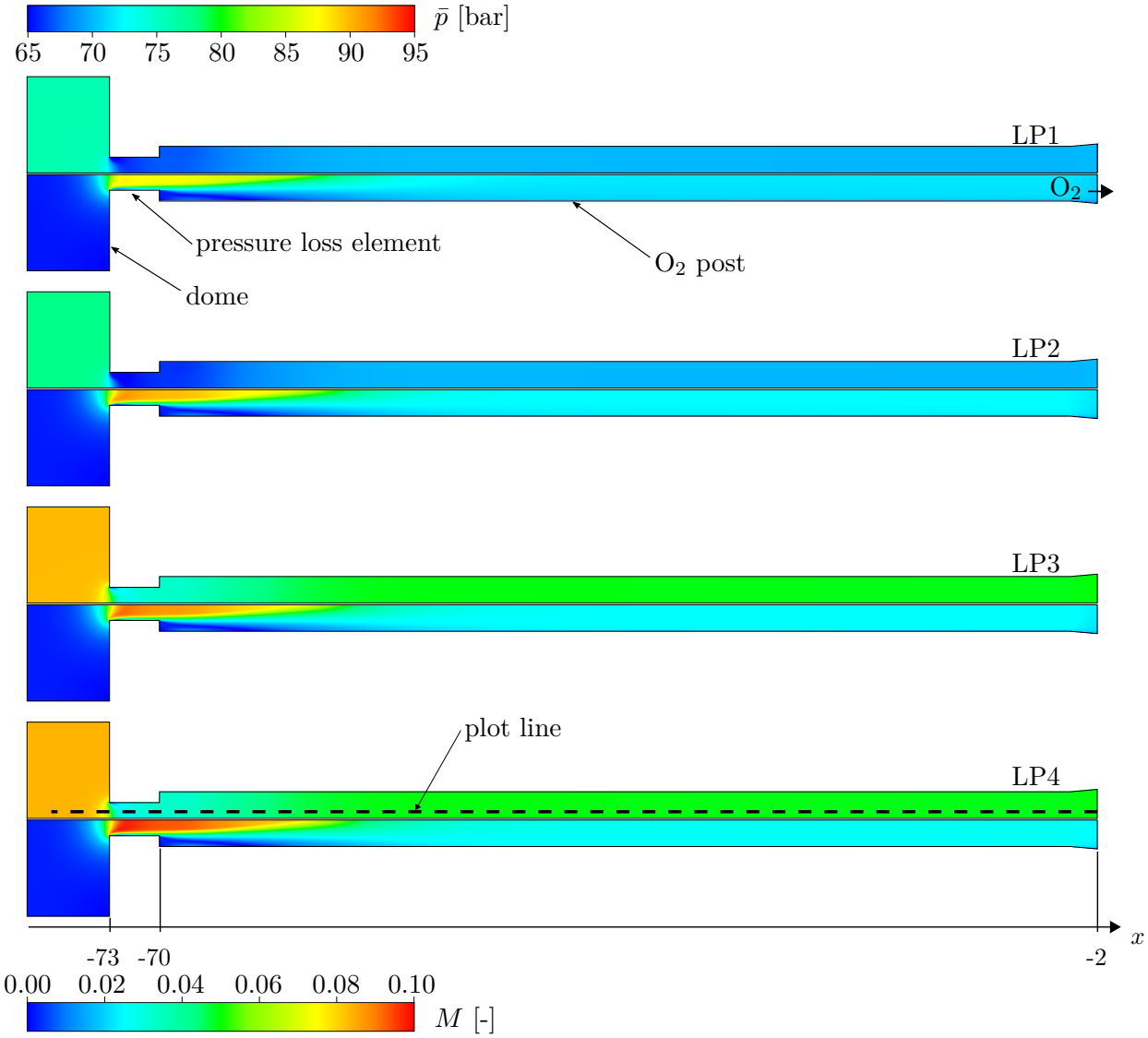

Fig. 7.1.: Pressure $\bar{p}$ (top) and Mach number M (bottom) in the O_2 dome and injector for LP1-4. Axial coordinates are given in [mm].

Tab. 7.2.: Validation of simulated dome pressure and ratio of chamber pressure to dome pressure.

load point		LP1	LP2	LP3	LP4
$\bar{p}_{O_2}$ experiment	[bar]	78.4	81.11	91.9	94.10
$\bar{p}_{O_2}$ simulation	[bar]	76.5	79.0	91.0	92.2
relative error	%	2.4	2.6	1.0	2.0
$\bar{p}_{cc}/\bar{p}_{O_2}$	[−]	0.92	0.89	0.88	0.87

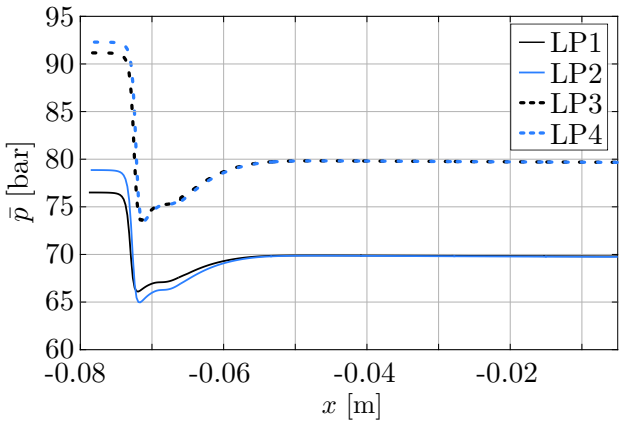

Fig. 7.2.: Pressure in the O_2 injection system for LP1-4 along the plot line, see Fig. 7.1.

in the O_2 post, the pressure ratio over the O_2 injection system essentially corresponds to the pressure ratio of the pressure loss element, cf. Fig. 7.1. The pressure distributions in the O_2 dome and in the $O2_2$ injector for LP1-4 are also visualized in Fig. 7.2. The corresponding plot line is shown in Fig. 7.1 as dash shape. Fig. 7.2 shows that the pressure is approximately constant in the injector. Furthermore, the high pressure drop across the pressure loss element is visible.

In the next step, the Mach number distributions in the O_2 injection system are discussed, see Fig. 7.1 (bottom). Overall, the distributions are similar for LP1-4. Maximal Mach numbers are found in the pressure loss element. Directly downstream of the pressure loss element, a jet structure forms. According to the mass flow rates of O_2, cf. Tab. 5.1, the Mach numbers in the pressure loss element and the jet lengths increase from LP1 to LP4. At the injector outlet, low Mach numbers are reached again.

The shown Mach numbers in the O_2 injection system are approximately 30 % higher than in reality, cf. Tab. 5.1. These deviations are based on the inaccurately described speed of sound of O_2 by the real gas SRK EOS, cf. Sec. 6.2.2.3. However, as the static pressure in O_2 dome is simulated with sufficient accuracy, cf. Tab. 7.2, the deviations in the Mach number seem to be acceptable.

7.1.3. Reactive Field in the Chamber

The reactive flow in the chamber section is now investigated by means of the fields of temperature and O_2 mass fraction. The visualization surface again corresponds to a half symmetry plane of the single flame configuration. Fig. 7.3 shows the half-section surface plots for LP1-4 between the recess and the outlet for the single flame configuration.

In general, for all load points the temperature and mass fraction distributions are similar. O_2 is concentrated in the center and H_2 is injected co-axially. Consequently, the highest temperatures are reached within the reaction zone, which is located in the mixing zone between O_2 and H_2. A recirculation zone is formed at the face plate, which results in a radial spread of the mixing and combustion zone approximately two

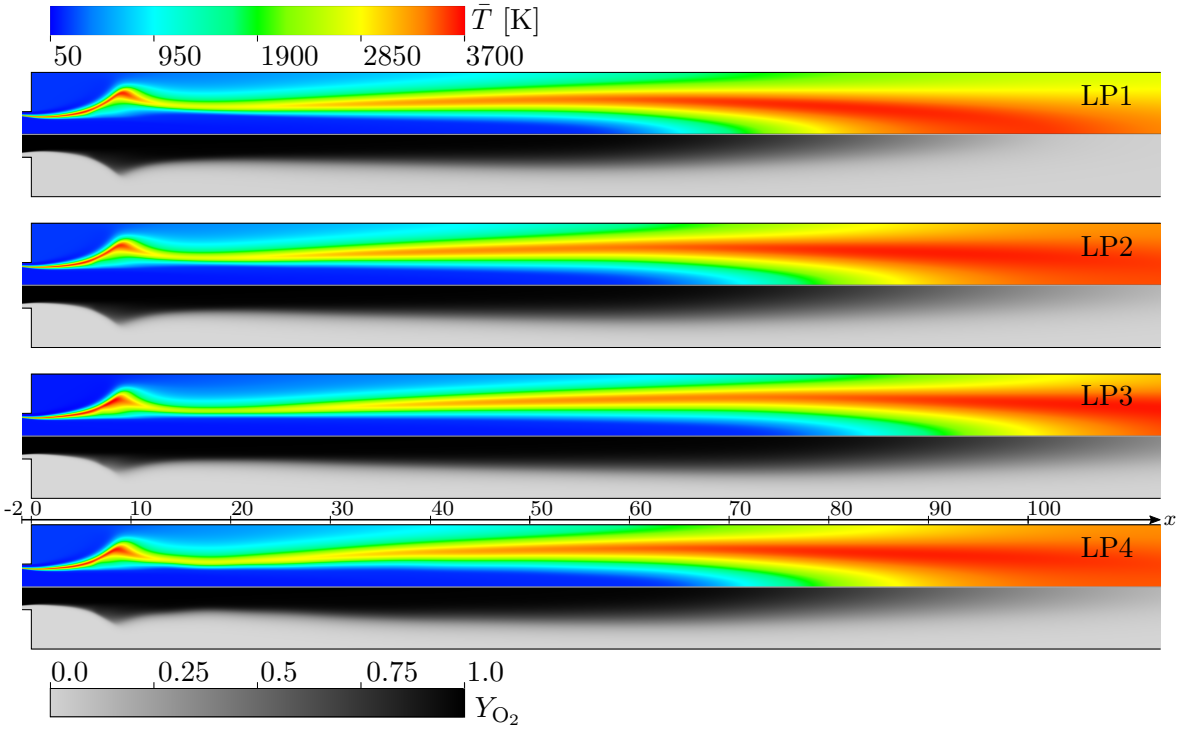

Fig. 7.3.: Temperature (top) and mass fraction of O_2 (bottom) in the chamber section for LP1-4. The axial dimensions are given in [mm].

injector diameters downstream of the face plate. In the region between injection and radial spread, the shear velocities between the O_2 and H_2 are highest and turbulent mixing is therefore intense. High temperatures are reached again at the end of the O_2 core and further downstream. The maximum temperature is approximately 3600 K, which is in very good agreement with the adiabatic flame temperatures. Therefore, the chosen coupled EDM/FR combustion model is capable of predicting meaningful maximal temperatures, cf. Sec 6.2.3.2. It is concluded that the EDM/FR combustion model is appropriate to describe the reactive flow in the BKD test chamber under steady state conditions.

Since O_2 is deficient, cf. Sec. 5.2, the flame length can be associated with the length of the O_2 core, see Fig. 7.3. Hence, Fig. 7.3 reveals that LP1 exhibits the shortest flame length, while the O_2 penetration into the system is highest for LP3. Interestingly, the unstable load points LP2/4, although operated at different pressures and propellant mass flows, see Tab. 5.1, show very similar flame lengths. Apparently, the similarity is based on equal inlet temperatures of O_2 and H_2 together with the same ROF.

For the subsequent acoustic simulations, radially averaged mean flow profiles are generated, cf. Sec. 6.4. A comprehensive comparison of the radially averaged flow quantities for LP1-4 is presented in App. N.

7.2. Dome Coupling Properties

In this section, the scattering matrices of the acoustic coupling between the dome and the chamber are presented and discussed. The presentation of the scattering matrices is subdivided into the following two steps:

First, the individual scattering matrices of the impedance change element and the pressure loss element are analyzed in order to reveal their influences on the scattering behavior between the chamber and the dome, cf. Sec. 6.3 and Fig. 6.9.

Afterwards, the complete dome coupling scattering matrices are presented for LP1-4. For this purpose, the scattering matrices are calculated on the basis of the acoustic network model described in Sec. 6.3, cf. Eq. (6.53). For the evaluation of the network model, the necessary mean flow quantities such as pressure changes across the network elements and axial velocities are taken from the mean flow simulation results.

7.2.1. Scattering Matrices of the Impedance Change Element and the Pressure Loss Element

The individual scattering matrices of the impedance change element and the pressure loss element are investigated. For the analysis of the impedance change element, its transfer matrix representation, cf. Eq. (B.8), is transformed into the scattering matrix form. This yields

$$\mathrm{SM}^{\rho c} = \begin{pmatrix} \dfrac{2\frac{(\bar{\rho}c)_u}{(\bar{\rho}c)_d}}{\frac{(\bar{\rho}c)_u}{(\bar{\rho}c)_d}+1} & \dfrac{\frac{(\bar{\rho}c)_u}{(\bar{\rho}c)_d}-1}{\frac{(\bar{\rho}c)_u}{(\bar{\rho}c)_d}+1} \\ \dfrac{1-\frac{(\bar{\rho}c)_u}{(\bar{\rho}c)_d}}{\frac{(\bar{\rho}c)_u}{(\bar{\rho}c)_d}+1} & \dfrac{2}{\frac{(\bar{\rho}c)_u}{(\bar{\rho}c)_d}+1} \end{pmatrix}. \tag{7.3}$$

The scattering matrix for the characteristic change of impedance according to Eq. (7.3) is real-valued frequency independent.

In case of the BKD test chamber, the change of characteristic impedance between the O_2 post and the recess, which is filled with O_2/H_2 and combustion products, is immense. Specifically, the steady state simulations reveal a characteristic impedance ratio between the O_2 post and recess of approximately $\frac{(\bar{\rho}c)_u}{(\bar{\rho}c)_d} \approx 12$ for all LP. Therefore, the scattering matrix according to Eq. (7.3) yields quantitatively

$$\mathrm{SM}^{\rho c} = \begin{pmatrix} T_u & R_d \\ R_u & T_d \end{pmatrix} = \begin{pmatrix} 1.85 & 0.85 \\ -0.85 & 0.15 \end{pmatrix}. \tag{7.4}$$

Eq. (7.4) shows that the acoustic waves are asymmetrically transmitted by the impedance change element. In fact, the downstream transmission coefficient is 0.15, indicating only low transmission of acoustic waves through the impedance change element

from downstream into the O_2 post. In contrast, acoustic waves originating from the O_2 post and hence from the dome actually exhibit an increase of the amplitude by a factor of 1.85. The reflection coefficients establish that the sum of transmission amplitude and reflection amplitude is unity. Therefore, the transmission coefficient upstream T_u is larger than one and the reflection coefficient upstream R_u is negative indicating a phase change of π of the reflected wave. Since the transmission coefficient downstream is below one, the reflection coefficient downstream R_d is positive indicating high reflection without phase change. Since the transmission amplitude downstream is low, the amplitude of the reflection coefficient downstream is high. In terms of absolute values, the reflection coefficients upstream and downstream are equal.

Next, the scattering matrix of the pressure loss element is analyzed. For its calculation, the acoustic network model is reduced to only the first area change, the duct element in the pressure loss element and the second area change, cf. Fig. 6.9. Therefore, the scattering matrix of the pressure loss element is calculated by

$$\mathrm{SM} = \mathrm{SM}_3^{\mathrm{AC}} \cdot \mathrm{SM}_2^{\mathrm{DE}} \cdot \mathrm{SM}_1^{\mathrm{AC}}. \tag{7.5}$$

The scattering matrix of the pressure loss element on the basis of the network model according to Eq. (7.5) in terms of amplitude and phase is shown in Fig. 7.4 and Fig. 7.5. The scattering matrix is only considered in the frequency range between 8 kHz and 12 kHz. It can be seen that the amplitudes and phases are almost constant over the frequency range. The frequency independent behavior can be explained by the axial compactness of the pressure loss element.

In case of the pressure loss element, the amplitude of the transmission coefficient downstream $|T_d|$ is also small. In consequence, acoustic waves approaching the pressure loss element from the O_2 post are weakly transmitted into the O_2 dome. Low transmission downstream is explained by the high area ratio between the injectors and the O_2 dome. However, the low transmission through the pressure loss element from downstream to upstream is not compensated by high reflection amplitudes downstream. In fact, the amplitude of the reflection coefficient downstream $|R_d|$ is only approximately 0.25. (Schulze et al. 2014d; Wagner et al. 2013b) explain that the low amplitudes of the reflection coefficient downstream may originate from the generation of vortical structures due to the interaction of the longitudinal wave with the emanating jet structure in the mean flow. Such a jet structure is also present downstream of the pressure loss element, cf. 7.1. The generation of vortical structures is associated with the dissipation of acoustic energy, cf. Sec. 2.2. In consequence, the low reflection properties at the downstream side of the pressure loss element can be explained by the partial dissipation of the incident wave.

On the upstream side of the pressure loss element, the amplitude of both the transmission coefficient $|T_u|$ and the reflection coefficient $|R_u|$ are high. The intense reflection and transmission of the Riemann invariants can be explained by the large area ratio between the O_2 dome and the injectors.

Due to the influence of the mean flow on the scattering of acoustic waves and the different areas between the O_2 dome and the injectors, the scattering matrix of the

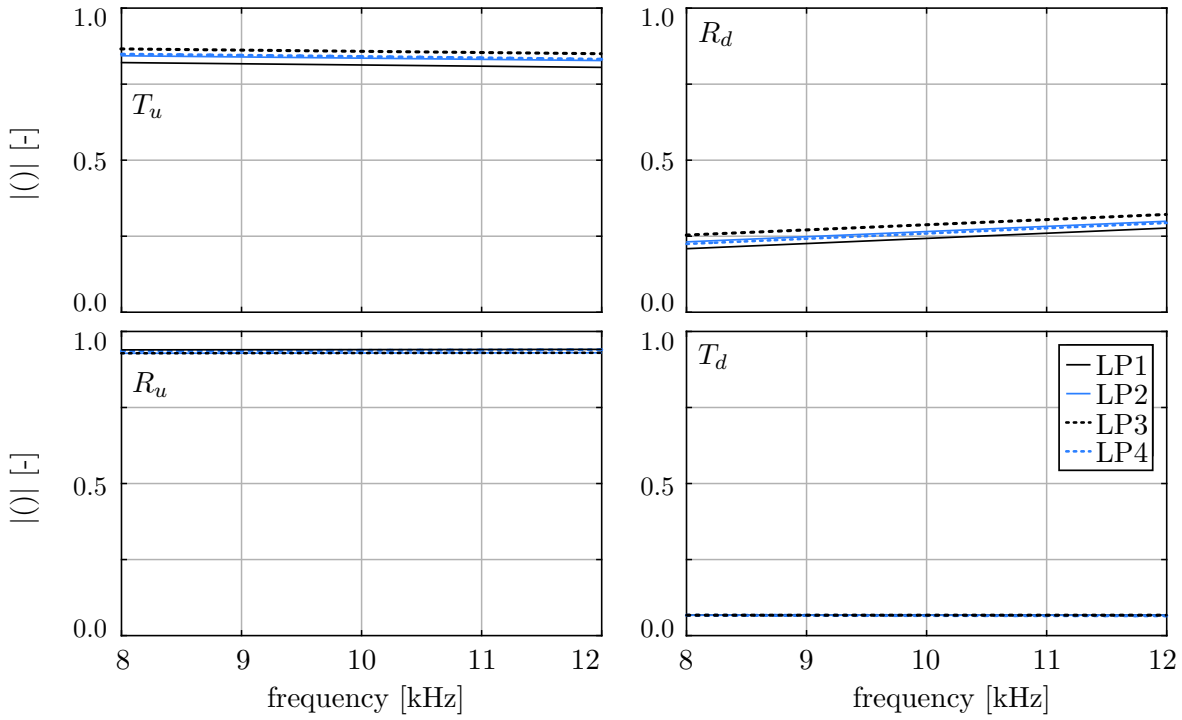

Fig. 7.4.: Pressure loss element scattering matrix amplitudes for LP1-4.

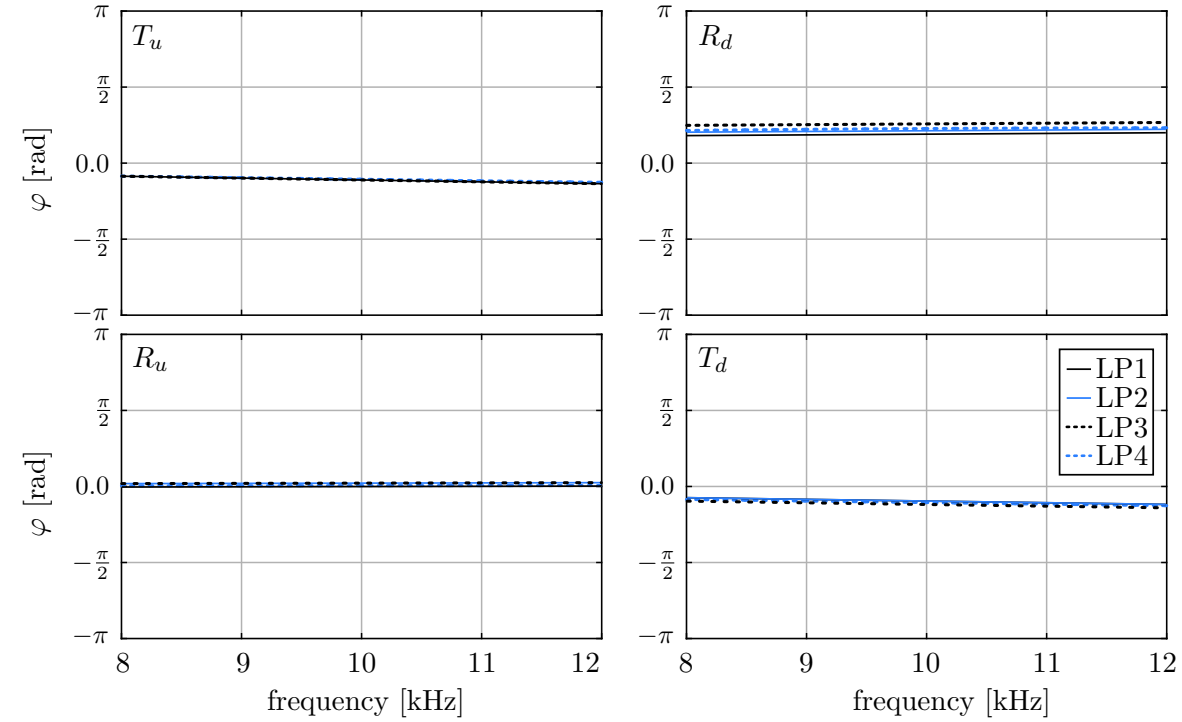

Fig. 7.5.: Pressure loss element scattering matrix phases for LP1-4

pressure loss element is not symmetrical in terms of both amplitudes and phases. While the coefficients on the upstream side show high amplitudes and almost zero phases, the downstream coefficients provide low amplitudes and considerable deviations of the phases from zero.

7.2.2. Dome Coupling Scattering Matrices

The dome coupling scattering matrices for LP1-4 calculated on the basis of the acoustic network model are shown for a frequency range from 4-11 kHz in terms of amplitude and phase in Fig. 7.6 and Fig. 7.7, respectively. Overall, a similar behavior is observed for all LP.

The transmission coefficient downstream T_d shows very small amplitudes indicating that only insignificant portions of acoustic energy are transmitted from the combustion chamber into the O_2 dome. Several effects are responsible for that. Firstly, the high area ratio between the injectors and the chamber and dome, respectively. Secondly, the low amplitudes of the transmission coefficient downstream of the impedance change element and of the pressure loss element. Both reduce the overall transmission of acoustic waves from the chamber to the dome, cf. Eq. (7.4) and Fig. 7.4.

In comparison, the transmission coefficient upstream T_u provides considerably higher amplitudes than T_d, see Fig. 7.6. The larger amplitudes in turn can be explained by the higher transmission amplitudes from upstream in case of the impedance change element and the pressure loss element, cf. Eq. (7.4) and Fig. 7.4.

Because of the low amplitudes of the transmission coefficient downstream $|T_d|$, small fluctuations of acoustic pressure and velocity are expected in the dome volume. In fact, according to (Gröning 2015), only insignificant pressure amplitudes in the dome are observed experimentally. However, the low transmission of acoustic energy from the chamber into the dome does not imply that amplitudes are also small in the O_2 post. Essentially, the amplitude of T_d describes only the transmission through the injector into the dome, but not which amplitudes are present in the O_2 post.

The unequal amplitudes of the transmissions coefficients upstream and downstream $|T_u|$ and $|T_d|$ of the impedance change element and the pressure loss element also explain the asymmetrical transmission of acoustic waves from upstream and downstream at the face plate.

Fig. 7.6 reveals high amplitudes of the reflection coefficient downstream R_d in the entire frequency range indicating that the acoustic waves in the chamber are almost completely reflected at the face plate. The strong reflection is based on the small area ratio between the O_2 post and the chamber of approximately 0.071, cf. Fig. 5.1 and Fig. 5.3.

Furthermore, the reflection coefficient upstream R_u provides lower amplitudes than R_d within the considered frequency range, see Fig. 7.6. The lower reflections upstream are explained by the higher transmission from the dome to the chamber.

An asymmetrical behavior as for the amplitudes is not observed for the phases, cf.

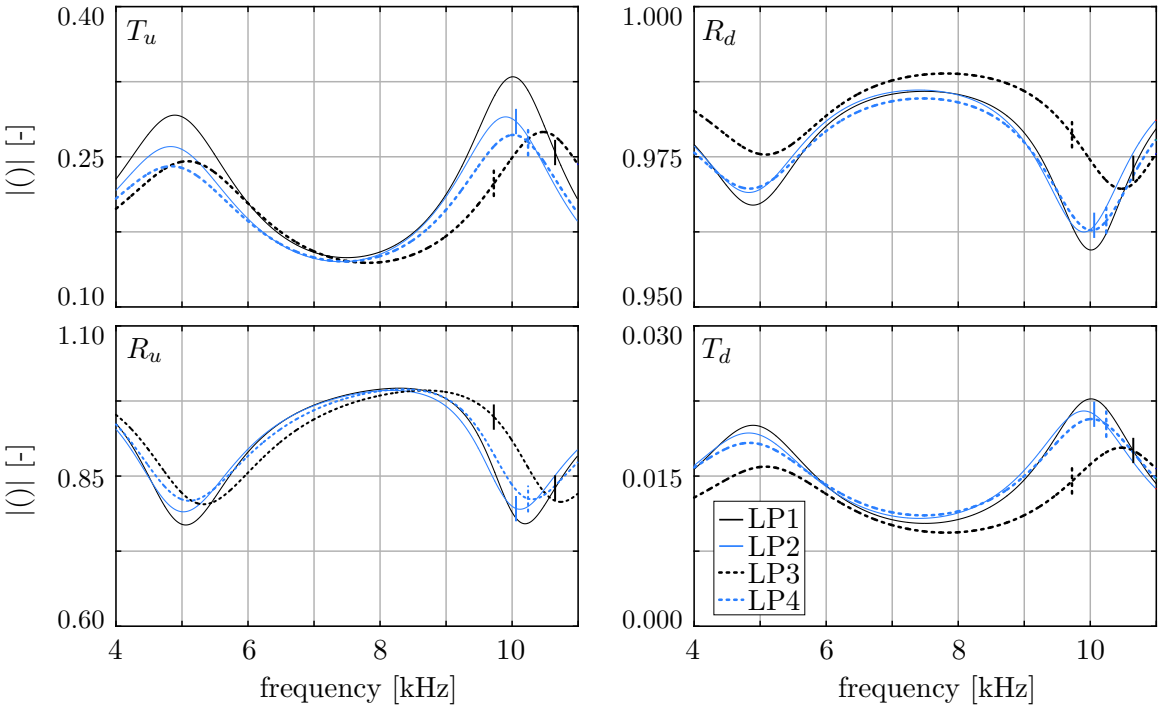

Fig. 7.6.: Dome coupling scattering matrix amplitudes for LP1-4.

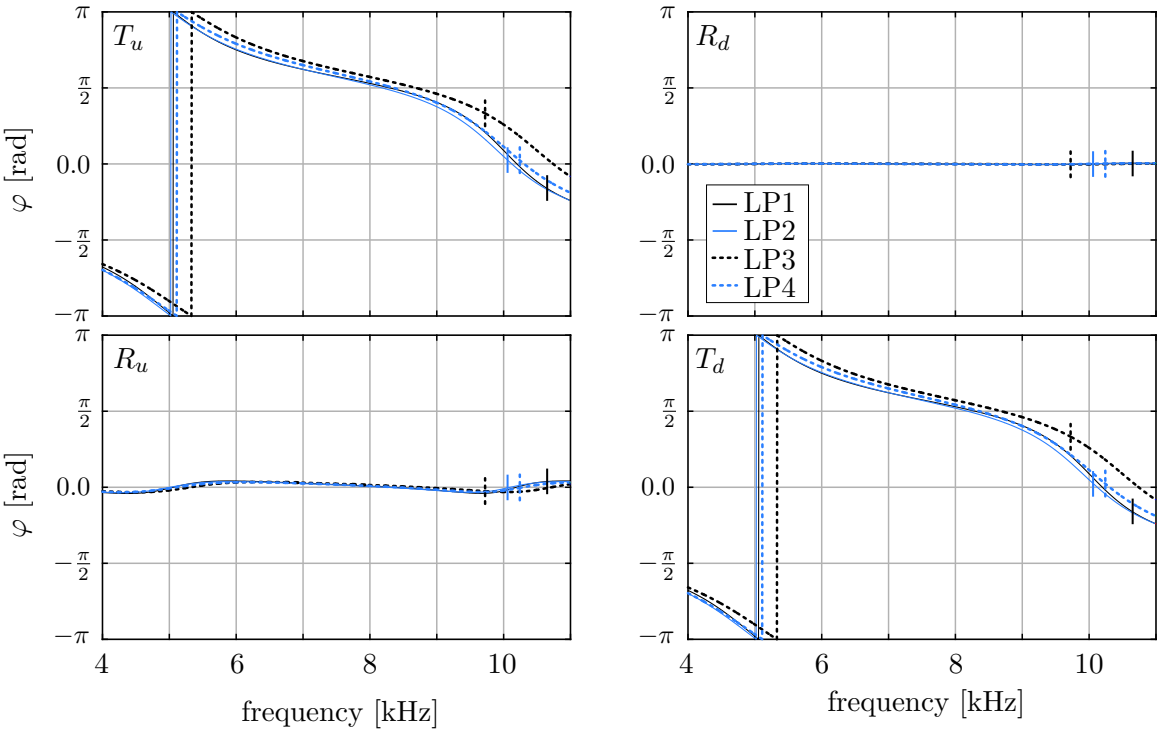

Fig. 7.7.: Dome coupling scattering matrix phases for LP1-4.

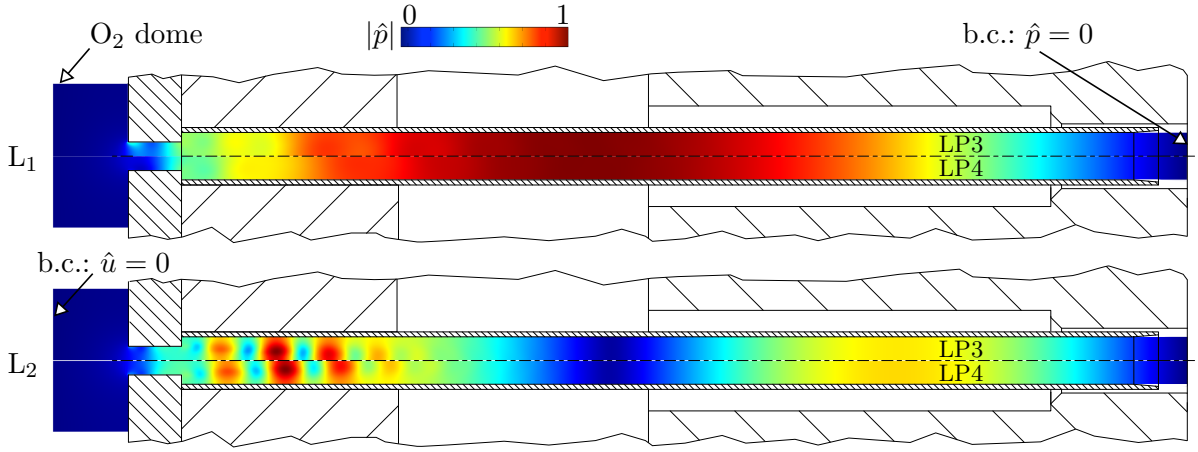

Fig. 7.8.: First and second longitudinal modes of the O_2 injector in terms of normalized pressure amplitude $|\hat{p}|$ for LP3 (top) and LP4 (bottom).

Fig. 7.7. Essentially, the reflection coefficients R_d and R_u show almost zero phase in the entire frequency range. Therefore, acoustic waves are reflected without a change in phase both at the dome side as well as at the chamber side of the face plate. This behavior can also be explained by the high area ratio between the injectors and the chamber and dome, respectively, cf. Fig. 5.2 (right).

In contrast, significant phase changes are observed in the transmission coefficients T_u and T_d, see Fig. 7.7. With increasing frequency, the phases decrease. Interestingly, approximately at 5 kHz and at 10 kHz, phase differences of π and zero, respectively, are found for LP1-4. Such phase differences between incident and transmitted wave indicate the presence of an acoustic eigenmode of the injector.

To visualize the mode shapes of the eigenfrequencies in the injector, eigenvalue studies are conduced using the CFD/CAA methodology introduced in Chap. 2 and Chap. 3. In the acoustic simulations, the CFD results of the single flame configuration are used as mean flow, see Sec. 7.1. The CFD results are directly used and a radial average is not generated. This allows to capture the influence of the detailed mean flow structure in the injector on the acoustic propagation.

For the acoustic simulations, the impedance change in the recess due to the presence of O_2, H_2 and combustion products as well as the area change between the O_2 post and the chamber are not included. This is not fully consistent with the acoustic network model, where these elements are accounted for. However, a stable LEE solution for the multi-species flow under reactive conditions could not be obtained. Nevertheless, the LEE results reveal the mode shapes for the eigenfrequencies at 5 kHz and 10 kHz approximatively. In the simulations, the axial acoustic velocity is set to zero as inlet boundary condition at the dome side. At the outlet of the injector, the acoustic pressure is set to zero. The remaining boundary conditions are prescribed as slip walls, cf. Eq. (2.72). The inlet and outlet boundary condition are indicated in Fig. 7.8.

Fig. 7.8 shows the simulated mode shapes for the eigenfrequencies at approximately

5 kHz (top) and 10 kHz (bottom) for LP3 and LP4 in terms of the normalized pressure amplitude. The eigenfrequency at 5 kHz corresponds to the first longitudinal mode L_1. Furthermore, the eigenfrequency at 10 kHz corresponds to the second longitudinal mode L_2. Interestingly, downstream of the pressure loss element, vorticity structures are formed, which may influence the injector eigenfrequencies due to backscattering effects (Gikadi et al. 2012). Furthermore, the generation of these vortical structures also explains the dissipation of acoustic waves at the pressure loss element yielding low downstream reflection amplitudes, cf. Sec. 7.2.1.

Since the axial acoustical velocity is set to zero at the inlet of the computational domain, pressure amplitudes should be present in the O_2 dome. However, due to the low transmission properties of the pressure loss element, the acoustic waves are only insignificantly transmitted through the orifice. This behavior can be seen for the L_1 and for the L_2 modes. Hence, the low transmission of pressure amplitude predicted in the acoustic simulations confirm the low amplitudes of the transmission coefficient downstream T_d of the dome coupling scattering matrix, cf. Fig. 7.6. Furthermore, high amplitudes are present in the O_2 post.

In Fig. 7.6 and Fig. 7.7 also the eigenfrequencies of the first transverse mode in the chamber are indicated as small vertical lines for LP1-4. The eigenfrequencies of the first transverse mode will be investigated in detail in Sec. 7.3. It can be seen that the eigenfrequencies of the first transverse mode coincide well with the eigenfrequencies of the second longitudinal mode L_2 in the injector for LP2 and LP4. As explained in Sec. 5.2, the BKD test chamber operates unstable for these operating conditions. Apparently, in case of unstable BKD operation, the frequency of the second longitudinal mode L_2 in the injector coincides with the first transverse mode frequency in the chamber. These conclusions were also presented in (Gröning et al. 2015b).

7.3. Eigenfrequencies and Mode Shapes

The eigenfrequencies and mode shapes of the BKD test chamber are analyzed. First, the eigenfrequencies up to the first radial mode are simulated and compared to experimental findings. Furthermore, the corresponding mode shapes are visualized. Afterwards, the focus is drawn towards the first transverse mode in the chamber.

For the acoustic simulations, the scattering matrices presented in Fig. 7.6 and Fig. 7.7 are imposed as boundary conditions at the O_2 dome side and the chamber side, cf. Fig. 6.10. For this purpose, the reflection and transmission coefficients are additionally evaluated at higher frequencies on the basis of the acoustic network model. Furthermore, the mean flow fields are generated on the basis of the CFD results, cf. Sec. 7.1, using the mean flow conversion procedure, cf. Sec. 6.2.4.

7.3.1. BKD Eigenfrequencies and Visualization of Mode Shapes

The eigenfrequencies of the BKD test chamber up to the first radial mode frequency are presented in Fig. 7.9 together with the measured PSD (black line). The PSD data

is provided by (Gröning et al. 2013b). The acoustic eigenfrequencies appear as peaks in the PSD. For the validation of the acoustic simulations, the numerically determined eigenfrequencies are plotted into the PSD (colored vertical lines), see Fig. 7.9.

Overall, very good agreement is achieved between the peak frequencies in the PSD and the simulated eigenfrequencies for all LP. It is therefore concluded that the hybrid LEE approach based on the mean flow conversion procedure and the dome coupling description captures the relevant influences on the eigenfrequencies accurately. Moreover, the applied numerical grid size is sufficient to resolve to acoustic scales up to approximately 25 kHz, cf. Fig 6.10.

In general, different mode classes are contained in the considered frequency range. The individual mode classes are indicated by color in Fig. 7.9. Each higher-order mode class contains a number of longitudinally combined modes. Each eigenfrequency is therefore denoted by its mode class and, if necessary, by its longitudinal order in Fig. 7.9, cf. Sec. 2.4. The identification of the mode classes and longitudinal order is based on the mode shapes, which are revealed by the numerical simulations.

For the investigation of the mode classes, a selection of the different mode shapes in case of LP4 is shown in Fig. 7.10 and Fig. 7.11. The mode shapes for the other LP are similar. For the visualization, the normalized real part of pressure $\mathfrak{Re}(\hat{p})$ (left column) and the normalized pressure amplitude $|\hat{p}|$ (right column) are used. The presentation in form of amplitude and real part is chosen since they contain different information. In general, the amplitude describes the maximum pressure fluctuation at each location. Hence, the amplitude can be used to identify the regions of relevant acoustic activity. In contrast, the real part $\mathfrak{Re}(\hat{p})$ represents the actual pressure fluctuation $p'(t)$ for $t = 0$, cf. Eq. (2.26), and hence describes the amplitude altered by the phase.

The first three modes found for all LP at the lowest frequencies of approximately 3 kHz, 6 kHz and 9-10 kHz (red vertical lines in Fig. 7.9), correspond to the longitudinal modes L_1 - L_3, see Fig. 7.10. The longitudinal order can clearly be identified in the amplitude plots showing the distinct number of pressure nodes. As explained in Sec. 1 and shown in Sec. G for non-reactive conditions, intense acoustic losses based on the convective transport in the nozzle prevent longitudinal modes from becoming a threat for the engine's operation. Therefore, the longitudinal modes are not further investigated.

For frequencies above approximately 10 kHz, higher-order modes are present. Specifically, the first and second transverse mode classes as well as the radial mode class can be found in the PSD for all LP, see Fig. 7.9.

The lowest eigenfrequency in the T_1 mode class is denoted with T_1^α in Fig. 7.9 as well as in Fig. 7.10 and is found at approximately 10 kHz for all LP. Its special denotation originates from its particular amplitude structure. Remarkably, the T_1^α mode shows significant amplitudes only in the region close to the face plate and a strong amplitude decay in axial direction, see Fig. 7.10. The decay is stronger in the amplitude plot than in the real part plot. It can also be seen that the amplitudes of this particular mode are already very small one chamber diameter downstream of the face plate.

Above the T_1^α mode frequency, the first transverse modes are referred to as $T_1^\beta L_x$

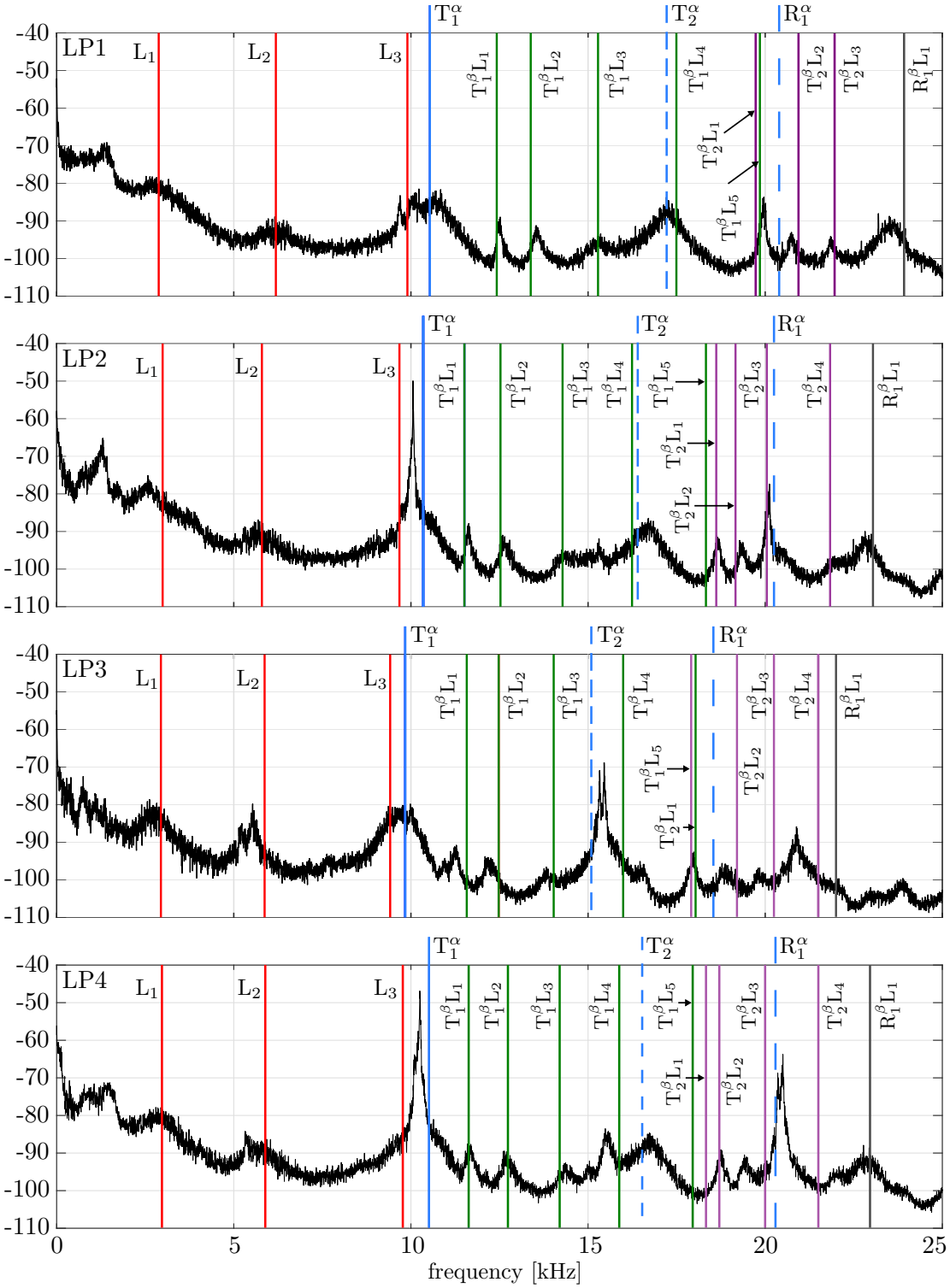

Fig. 7.9.: Experimental PSD (black) given in [dB/Hz] and numerically determined eigenfrequencies for LP1-4. Different mode classes are indicated by color. Experimental results from (Gröning et al. 2014).

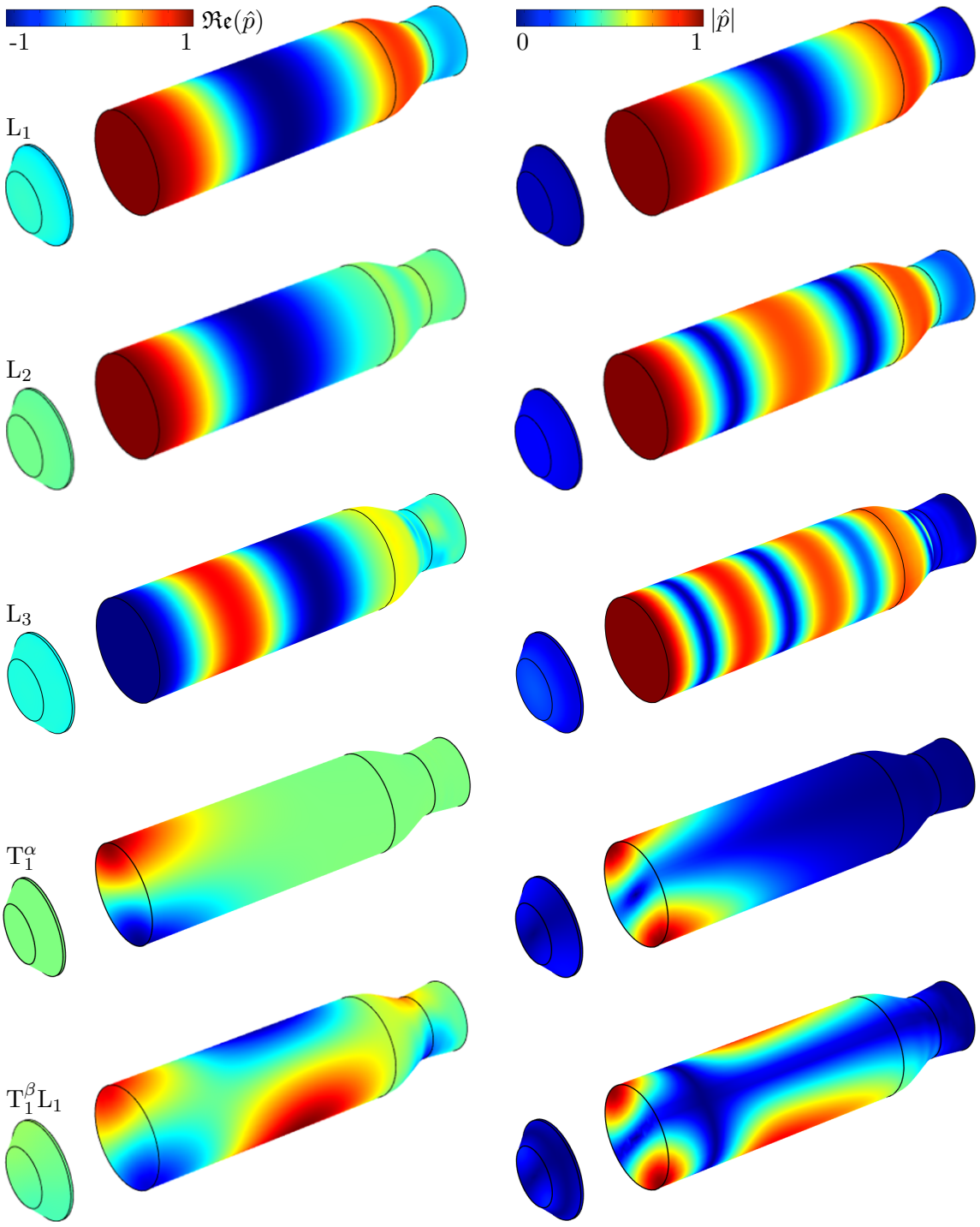

Fig. 7.10.: Selection of mode shapes up to the first radial mode in terms of normalized real part (left) and absolute value (right) for the example of LP4 (1/2).

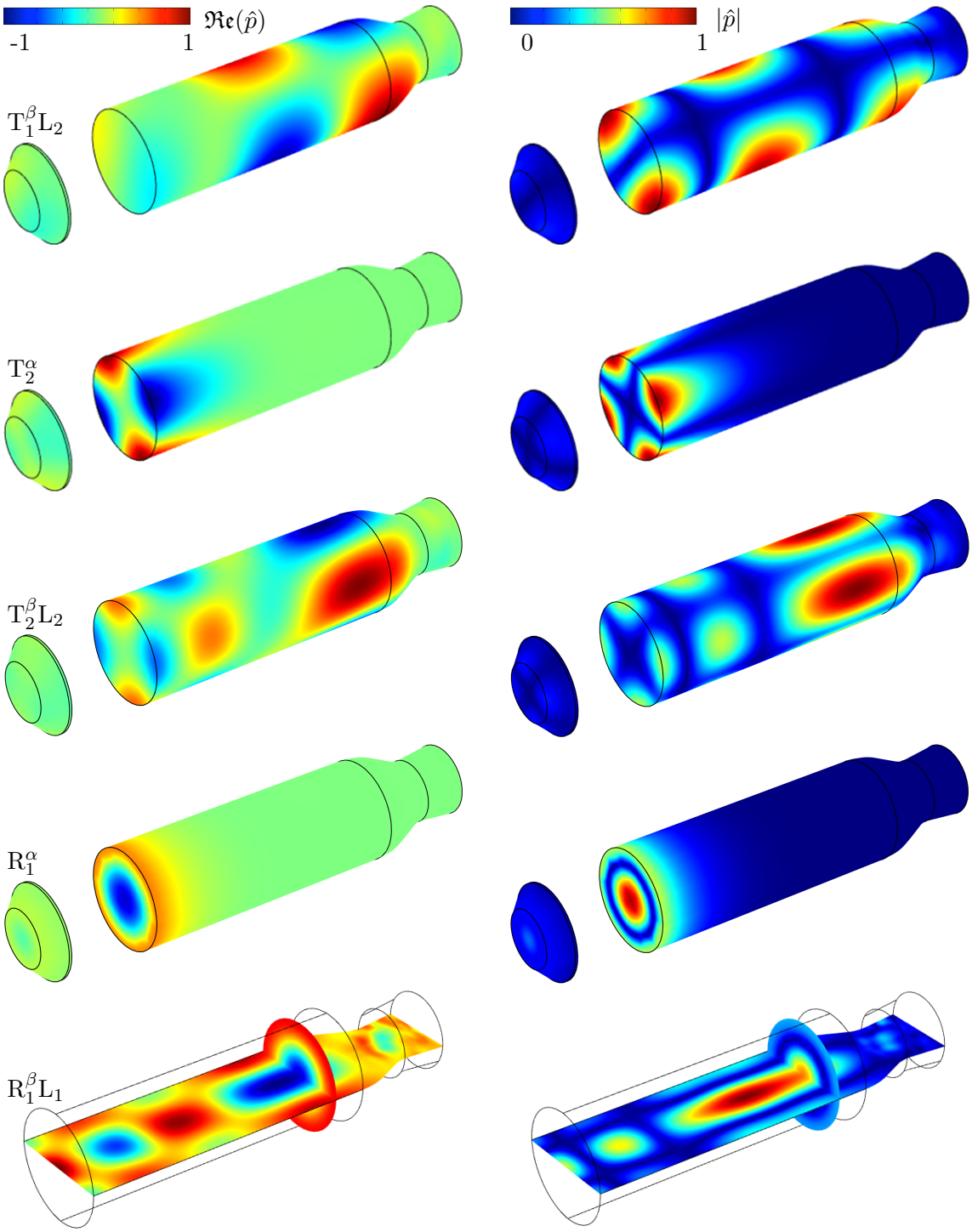

Fig. 7.11.: Selection of mode shapes up to the first radial mode in terms of normalized real part (left) and absolute value (right) for the example of LP4 (2/2).

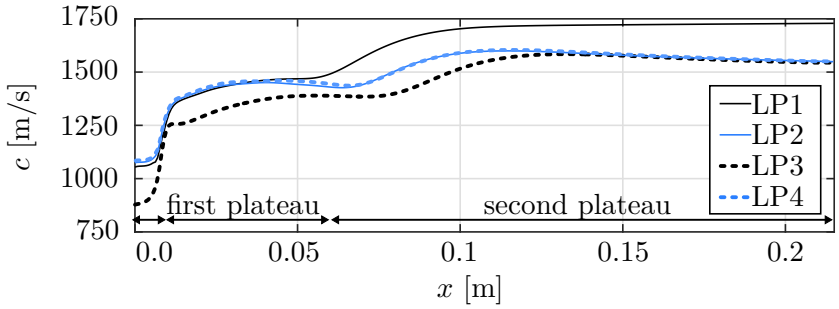

Fig. 7.12.: Axial distributions of speed of sound along the pressure anti-nodal line for LP1-4 as well as the indication of two plateau regions in the chamber.

(green vertical lines in Fig. 7.9). The corresponding mode shapes of $T_1^\beta L_1$ and $T_1^\beta L_2$ are shown in Fig. 7.10 and Fig. 7.11. In comparison to the T_1^α mode, the $T_1^\beta L_x$ modes exhibit significant amplitudes within the entire chamber. Furthermore, the real parts of the $T_1^\beta L_1$ and $T_1^\beta L_2$ modes show high pressure fluctuations in the entire chamber.

To explain the significantly different pressure amplitude structures of the T_1^α and the $T_1^\beta L_x$ modes, the axial distribution of the speed of sound in the chamber is analyzed, see Fig. 7.12. The speed of sound is determined by the cross-sectional average of the single flame CFD results, cf. Sec. 7.1. Fig. 7.12 shows that the chamber can be divided into three regions, each with a characteristic speed of sound distribution. In a first short region, speed of sound is dominated by the injected propellants and the lowest speed of sound is found. A first plateau of c is reached after the short increase of speed of sound and coincides with the location of the O_2 core jet, cf. Fig. 7.3. In this first plateau region, the speed of sound is influenced by the propellants with low temperature and hence with low speed of sound as well as by high temperatures in the combustion zone, cf. Fig. 7.3. Therefore, a moderate mean speed of sound is present. In the region further downstream, a second plateau forms. The second plateau is dominated by the hot combustion products and, in consequence, by a high speed of sound.

The different pressure amplitude distributions of the T_1^α and the $T_1^\beta L_x$ modes can now be explained by the changed cut-on frequencies for the first transverse mode class in the different regions. The cut-on condition depends on the speed of sound and thus differs between the different plateaus, cf. Eq. (2.60). In the regions of injection and of the first plateau, the cut-on frequency is lowest. Significant amplitudes of the T_1^α mode are only present in these regions, cf. Fig. 7.10 and Fig. 7.12. In contrast, the cut-on frequency in the second plateau region is higher and, in consequence, the T_1^α mode is cut-off restricting its further propagation in downstream direction. In contrast, the eigenfrequencies of the $T_1^\beta L_x$ modes are higher than of T_1^α, and the $T_1^\beta L_x$ modes can propagate both in the second as well as in the first plateau region. Significant $T_1^\beta L_x$ mode amplitudes are hence present in the entire chamber volume.

In general, the T_1^α modes may appear also in combined form with longitudinal modes. However, as the axial dimension of the T_1^α mode is small, cf. Fig. 7.10, the first combined mode would occur at very high frequencies. Within the considered frequency range, such a combination of the T_1^α mode with a longitudinal mode could not be identified in the

acoustic simulations. In consequence, this mode is simply referred to as T_1^α. In contrast, the $T_1^\beta L_x$ modes exist in the entire chamber and, in fact, several combined modes were found in the acoustic simulations, cf. Fig. 7.9. In Fig. 7.10 and Fig. 7.11 the $T_1^\beta L_1$ and $T_1^\beta L_2$ modes are illustrated. The longitudinal order $()_x$ is given by the number of pressure nodes in the amplitude plots, cf. Fig. 7.10 and Fig. 7.11. An explanation for the chosen nomenclature of the $T_1^\beta L_x$ modes, is presented in App. O.

The characteristic distribution of the speed of sound in the chamber equivalently affects further higher-order mode classes. The decomposition of a higher-order mode class into the $()^\alpha$ mode and the $()^\beta L_x$ modes is therefore generally valid in case of the BKD test chamber. In fact, in the PSD for LP1-4, the T_2^α as well as the R_1^α modes are indicated and the corresponding mode shapes are shown in Fig. 7.11. Significant amplitudes of the T_2^α and the R_1^α modes are only observed close to the face plate. In contrast, the $T_2^\beta L_x$ (purple vertical lines in Fig. 7.9) as well as the $R_1^\beta L_1$ (gray vertical line in Fig. 7.9) modes exhibit high amplitudes in the entire chamber. The $T_2^\beta L_2$ and $R_1^\beta L_1$ modes are illustrated in Fig. 7.11. For the $R_1^\beta L_1$ mode, two slices in the chamber are shown in order to indicate the significant amplitudes in the interior of the chamber volume.

Since the conclusions concerning the influence of speed of sound on the mode shapes drawn for the T_1 mode class appear to be generally valid and the focus of this thesis is on the first transverse mode, the T_2 and R_1 mode classes are not further discussed.

After the identification of the chamber eigenfrequencies in the PSD, shown in Fig. 7.9, the influences of the operating conditions for LP1-4 are investigated. In comparison, the eigenfrequencies of the unstable LP2 and LP4 are very similar due to the similar mean flow fields. As explained in Sec. 5.2, the injection conditions of the propellants for LP2 and LP4 are almost identical. Furthermore, the flame length is essentially the same, cf. Sec. 7.1. In consequence, comparable distributions of speed of sound and density are present in the chamber explaining the similarity of the eigenfrequencies. Interestingly, the difference in chamber pressure between LP2 (70 bar) and LP4 (80 bar) seems to be of minor relevance for the acoustic properties of the BKD test chamber, cf. Tab. 5.1.

The eigenfrequencies of the $()^\alpha$ modes in case of LP3 occur at lower frequencies compared to the other LP. This is due to the fact that the H_2 injection temperature in case of LP3 is approximately halved compared to the other LP, cf. Tab. 5.1. A reduced injection temperature leads to a lower speed of sound and, in consequence, to a lower eigenfrequency, cf. Fig. 6.5.

In contrast, the eigenfrequencies of the $()^\alpha$ modes in case of LP1 are slightly higher than for LP2 and LP4. However, the injection temperatures are similar. The increased eigenfrequencies can be explained by the higher speed of sound in the regions of injection and of the first plateau. In turn, the higher speed of sound can be attributed to the elevated temperatures, originating from intensified combustion due to the higher H_2 injection velocity in case of LP1, cf. 5.1. The higher injection velocity leads to stronger shear forces between the propellants and thus more intense mixing. The effect of the H_2 injection velocity will be explained in more detail in Sec. 7.4.1.

As explained in Sec. 5, the high amplitudes in case of unstable BKD operation are

associated with the first transverse mode. From the PSD plots and the acoustic simulation results, it can be concluded which particular T_1 mode exhibits high amplitudes. In Fig. 7.9 high amplitudes are observed for the T_1^α modes in case of LP2 and LP4.

Since the T_1^α mode has been identified as critical in terms of thermoacoustic stability in the BKD test chamber, the focus is on this particular mode in the following.

7.3.2. Investigation of T_1^α Mode Shapes

Since the potentially unstable T_1^α mode shows an unexpected pressure amplitude distribution in the chamber, cf. Fig. 7.10, its shape is further analyzed and compared for the different LP. In particular, the strong axial decay is discussed.

7.3.2.1. Mode Shape Amplitude Distributions

First, the simulated T_1^α eigenfrequencies are validated by means of the experimental data given in (Gröning et al. 2013b), see Tab. 7.3. The numerical results agree well with the experimental data. The maximal deviation is 2.8 % in case of LP2. These rather small deviations may originate from uncertainties in both data sources, simulation and experiment. For example, the inaccurate description of the O_2 speed of sound in the chamber on the basis of the real gas SRK EOS might lead to such small deviations, Sec. 6.2.2.3.

When the distributions of the normalized T_1^α pressure amplitude in the chamber for LP1-4 are compared, similar shapes are observed, see Fig. 7.13. High amplitudes are concentrated in the region close to the face plate and the strong axial amplitude decay is present. Furthermore, in the O_2 dome only insignificant pressure amplitudes are found. The very weak transmission of acoustic pressure from the chamber to the O_2 dome can be explained by the low amplitude of the downstream transmission coefficient $|T_d|$ of the dome coupling scattering matrix, cf. Sec. 7.2 and especially Fig. 7.6.

For the quantitative investigation of the decaying amplitudes in the chamber, the axial pressure amplitude distributions in the anti-nodal pressure lines for LP1-4 are compared, see Fig. 7.14 (top). Since the appearance of high amplitudes at the face plate as well as the absence of relevant amplitudes further downstream can be explained by the speed of sound changes in the chamber, cf. Sec. 7.3.1, the axial distribution of c is also shown in Fig. 7.14 (bottom).

Tab. 7.3.: Eigenfrequencies of the T_1^α mode for LP1-4: Experimental findings (Gröning et al. 2013b), simulation results and relative deviations.

load point		**LP1**	**LP2**	**LP3**	**LP4**
experiment	Hz	10,651	10,059	9723	10,242
simulation	Hz	10,535	10,348	9796	10,375
relative deviation	%	1.1	2.8	0.7	1.3

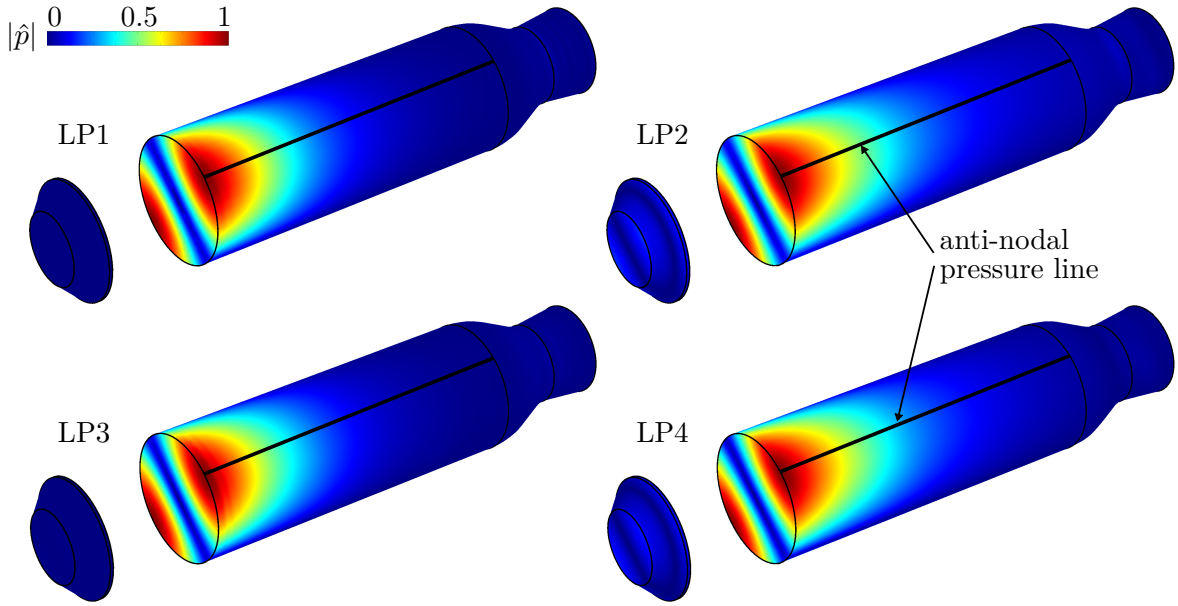

Fig. 7.13.: T_1^{α} mode shapes in terms of normalized pressure amplitudes for LP1-4 as well as anti-nodal pressure lines.

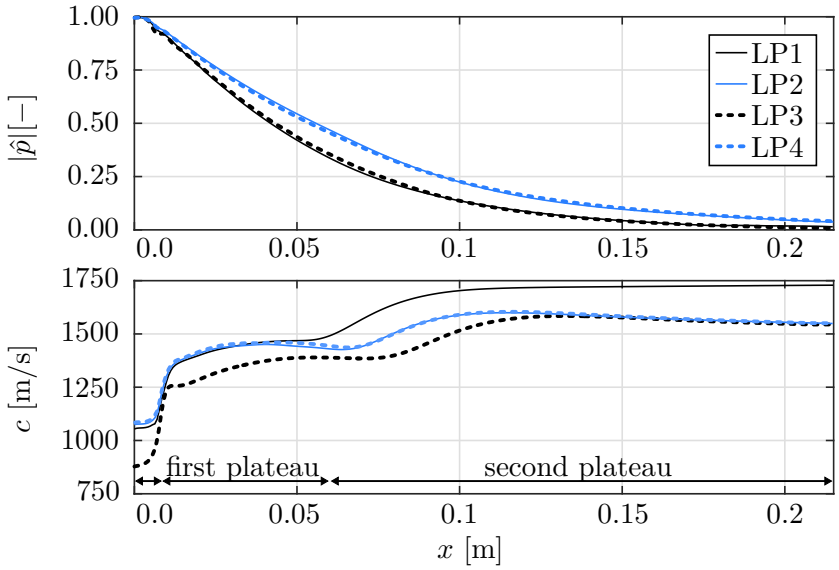

Fig. 7.14.: Axial distributions of the normalized pressure amplitude (top) and speed of sound (bottom) along the pressure anti-nodal line.

As explained in Sec. 7.3.1, the T_1^{α} mode predominantly exists in the regions of injection and of the first plateau of c in the chamber. However, the first plateau region has a different shape for LP1-4. For LP2 and LP4 an almost identical first plateau with a rather constant speed of sound is found. In turn, the change of the speed of sound within the first plateau region is stronger in case of LP3. Furthermore, the transition from the first plateau to the second plateau occurs a certain distance further downstream for LP3 than for LP2 and LP4. Finally, the axial dimension of the first plateau

is shorter for LP1 than for LP2 and LP4.

The larger axial lengths of the first plateau in case of LP2 and LP4 yield a prolongation of the T_1^α mode in the chamber. For LP1, the short plateau region leads to a more compact mode and therefore a faster decay of the amplitude in axial direction, see Fig. 7.14 (top). Interestingly, the shape of the axial pressure amplitude distribution in case of LP3 is the same as for LP1, although these LP have very different flame lengths, see Sec. 7.3.

7.3.2.2. Analysis of Axial Decay Rates

Finally, the decay rate of the T_1^α mode in axial direction is determined. The amplitude decay establishes due to increase of the speed of sound and hence due to the cut-off of the mode in axial direction, see Sec. 7.3.1. In consequence, the increase of speed of sound in axial direction leads to transformation of the T_1^α mode into an evanescent mode, cf. Sec. 2.5.

The determination of the axial decay rate is based on the wave number, see Sec. 2.43. In general, $k_{T_1^\alpha}^{x\pm}$ is a mode parameter attributed to the T_1^α mode. However, as M and c vary in space, $k_{T_1^\alpha}^{x\pm}$ is treated as a field variable. As only the axial dependence of the mean flow quantities is incorporated into the acoustic simulations, cf. Sec. 6.4, $k_{T_1^\alpha}^{x\pm}$ varies only in x-direction.

The imaginary part of the wave number in positive direction, i.e. $\mathfrak{Im}(k_{T_1^\alpha}^{x+})$ is shown in Fig. 7.15 (top) together with the axial distribution of speed of sound (bottom), which is equivalent to Fig. 7.14 (bottom). The corresponding imaginary part of the wave number in negative direction, i.e. $\mathfrak{Im}(k_{T_1^\alpha}^{x-})$, is equivalent in absolute value but carries the opposite sign, cf. Fig. 2.1.

In Fig. 7.15 (top), it can be seen that in the region close to the face plate the imaginary part is zero. In consequence, the propagation of the T_1^α is not restricted and high amplitudes are therefore present, see Fig. 7.10 and Fig. 7.13. A sudden and intense increase of $\mathfrak{Im}(k_{T_1^\alpha}^{x+})$ is found at approximately one chamber radius downstream of the face plate. The increase appears very abrupt. This effect will be discussed later in more detail. Interestingly, for the stable LP1 and LP3, $\mathfrak{Im}(k_{T_1^\alpha}^{x+})$ increases in axial direction almost monotonically to maximal values of approximately 25 [1/m], with only a small decreasing zone in between. In consequence, the T_1^α modes decay along almost the entire chamber length. This behavior is explained by the also almost monotonically increasing c.

For the unstable LP2 and LP4 speed of sound reaches a first plateau. In contrast to the distributions of in case of LP1 and LP3, c decreases again after the first plateau region. The reduction is sufficient for the cut-on condition to be fulfilled again. In consequence, the $\mathfrak{Im}(k_{T_1^\alpha}^{x+})$ is again zero. Even further downstream, speed of sound increases and $\mathfrak{Im}(k_{T_1^\alpha}^{x+})$ rises to a maximal value of approximately 18 [1/m], which is considerably lower than the maximum for LP1 and LP3.

In conclusion, it is shown that the T_1^α mode is subjected to axial decay due to the

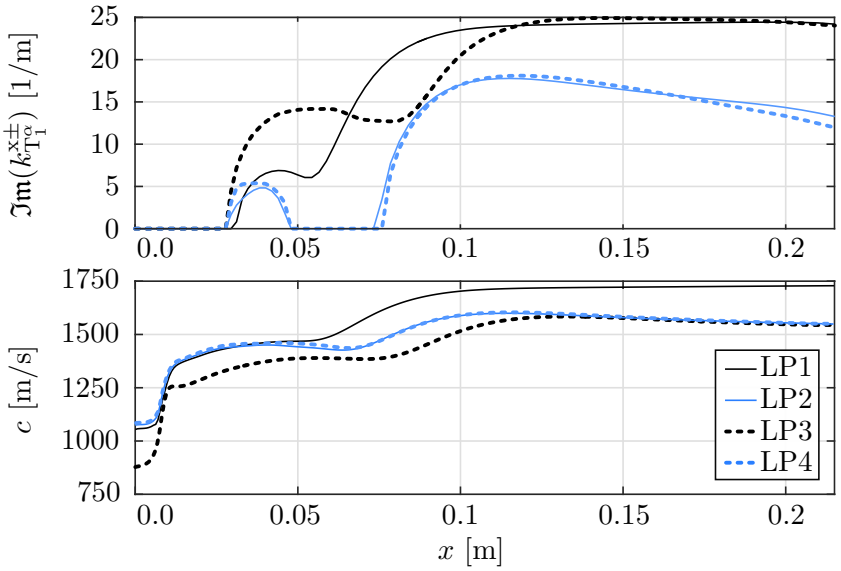

Fig. 7.15.: Axial distributions of $\mathfrak{Im}(k_{T_1^\alpha}^{x\pm})$ [1/m] (top) and speed of sound [m/s] (bottom) for LP1-4.

axial variation of speed of sound. Significantly higher axial decay rates are found in case of LP1/3.

The increase of $\mathfrak{Im}(k_{T_1^\alpha}^{x+})$ as soon as the cut-on condition is reached is remarkable. To further investigate the cut-on condition, $\mathfrak{Im}(k_{T_1^\alpha}^{x+})$ is plotted over c in case of the LP2 eigenfrequency and a constant axial mean velocity of $\bar{u} = 230$ m/s in Fig. 7.16. It can be seen that $\mathfrak{Im}(k_{T_1^\alpha}^{x+})$ significantly increases as soon as the cut-off condition is reached. The shape is similar to the behavior plotted in Fig. 7.15 (top). It can be shown that the change of $\mathfrak{Im}(k_{T_1^\alpha}^{x+})$ with respect to c at cut-on is infinitely large, see App. P. In consequence, the drastic changes of $\mathfrak{Im}(k_{T_1^\alpha}^{x+})$ in axial direction, cf. Fig. 7.16, are based on only small changes of c.

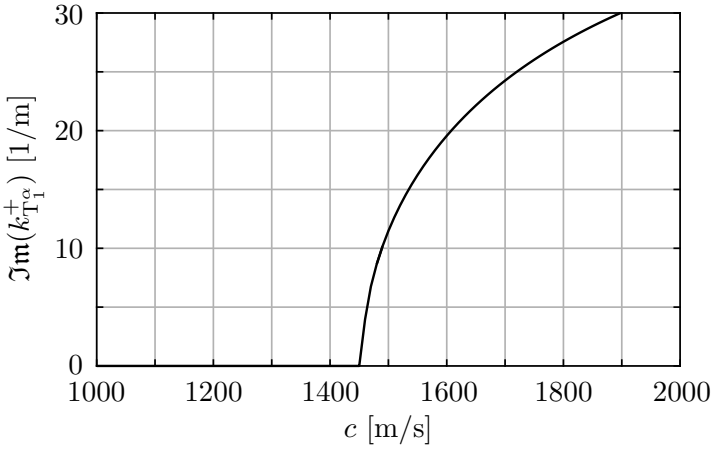

Fig. 7.16.: Dependency of $\mathfrak{Im}(k_{T_1^\alpha}^{+})$ on c for constant $\bar{u} = 230$ m/s.

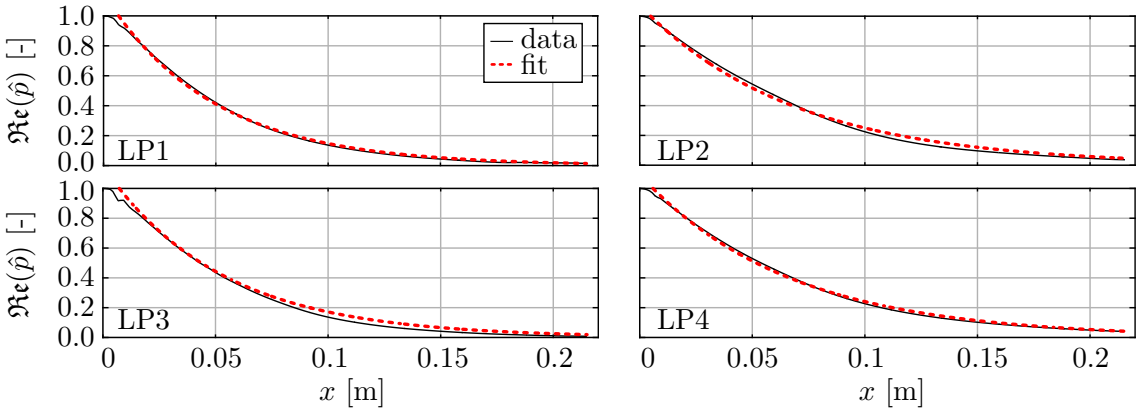

Fig. 7.17.: Normalized real part of complex pressure amplitude along anti-nodal line and exponential fits for LP1-4.

Further analyses are performed to show the quantitative agreement between the imaginary part of the wave number and the decay rate of acoustic pressure in axial direction. For that purpose, the real-part distribution $\Re\mathfrak{e}(\hat{p})$ of the normalized acoustic pressure along the anti-nodal line in axial direction is assumed to be of the form

$$\Re\mathfrak{e}(\hat{p}) = \mathcal{A}e^{-\mathrm{i}k_\mathrm{f}x}, \tag{7.6}$$

where $\mathcal{A}$ denotes an (irrelevant) amplitude and k_f an axial wave number. Fitting Eq. (7.6) to the normalized distribution of $\Re\mathfrak{e}(\hat{p})$ reveals k_f for LP1-4. The normalized $\Re\mathfrak{e}(\hat{p})$ data as well as the fits are shown for LP1-4 in Fig. 7.17. Overall, a very good agreement between the fits and the axial distributions of acoustic pressure is obtained. Minor deviations are found for LP2 and LP3. The acoustic pressure distributions and the fits show that LP1 and LP3 exhibit a stronger decay in axial direction.

To compare the fitted results to the imaginary part of the wave number, the axial $\Im\mathfrak{m}(k^{\mathrm{x}+}_{\mathrm{T}^\alpha_1})$ distribution is averaged, cf. Fig. 7.15. For this purpose, only the volume upstream of the initial occurrence of $\Im\mathfrak{m}(k^{\mathrm{x}+}_{\mathrm{T}^\alpha_1}) > 0$ is taken into account. The comparison of the fitted results and averaged $\Im\mathfrak{m}(k^{\mathrm{x}+}_{\mathrm{T}^\alpha_1})$ is presented in Tab. 7.4, showing very good agreement. Hence, the decay of pressure amplitudes in axial direction in regions where the T^α_1 mode is not able to freely propagate can directly be linked to the cut-off condition.

For the stable LP1/3 higher imaginary parts of the axial wave numbers are found.

Tab. 7.4.: Comparison of $\Im\mathfrak{m}(k^{\mathrm{x}+}_{\mathrm{T}^\alpha_1})$ with the axial decay rates of the fits k_f.

	k_f [1/m]	$\Im\mathfrak{m}(k^{+}_{\mathrm{T}^\alpha_1})$ [1/m]
LP1	20.7	20.3
LP2	14.8	13.8
LP3	19.5	19.2
LP4	14.7	14.2

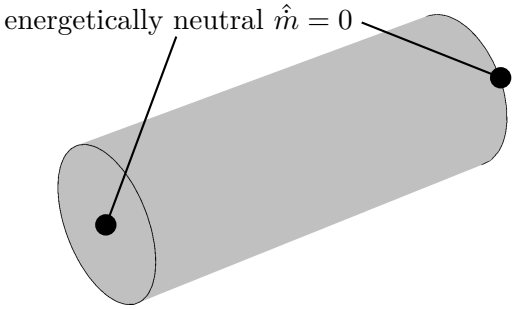

Fig. 7.18.: Computational domain as well as energetically neutral inlet and outlet boundary conditions for the investigation of the mean flow influence on the T_1^α mode damping rates.

According to the results, a reduction of acoustic pressure of approximately 20-21 [1/m] is present. In contrast, weaker decay is present for the unstable LP2/4 with imaginary parts reduced by approximately 30 % in comparison to LP1/3.

7.3.2.3. Influence of the Mean Flow on the T_1^α Mode Damping

As shown in the last section, the variation of speed of sound in the chamber leads to a strong axial decay of the T_1^α mode amplitudes. Apparently, the spatial variations of the mean flow quantities have a large influence on the amplitude behavior. Therefore, it is now investigated whether the mean flow alters the damping of the acoustic amplitudes, i.e. the change of the amplitudes in time. The investigations are conducted for LP4.

In order to reveal the impact of the mean flow on the damping rate λ, a reduced computational domain comprising only the cylindrical combustion chamber is considered. The O_2 dome and the nozzle are not included. The face plate and the outlet boundary condition are set energetically neutral according to Eq. (2.96) to only include the damping effects of the mean flow. Furthermore, the dynamic heat release rate $\hat{\dot{q}}$ is set to zero, i.e. the open loop system is analyzed. In this situation, the acoustic intensity flux I_i^a is zero at all boundaries and the fluctuating energy according to Eq. (2.63) reduces to

$$\frac{\partial E}{\partial t} + \frac{\partial(\bar{\rho}\bar{u}_i T' s')}{\partial x_i} = \mathcal{D}. \tag{7.7}$$

In consequence, the change of the fluctuating energy E depends only on the convection of temperature and entropy fluctuations across the boundaries and the source term $\mathcal{D}$, which describes the impact of the mean flow on the damping within the chamber. Moreover, the fluctuating energy E and its temporal derivative can directly be related

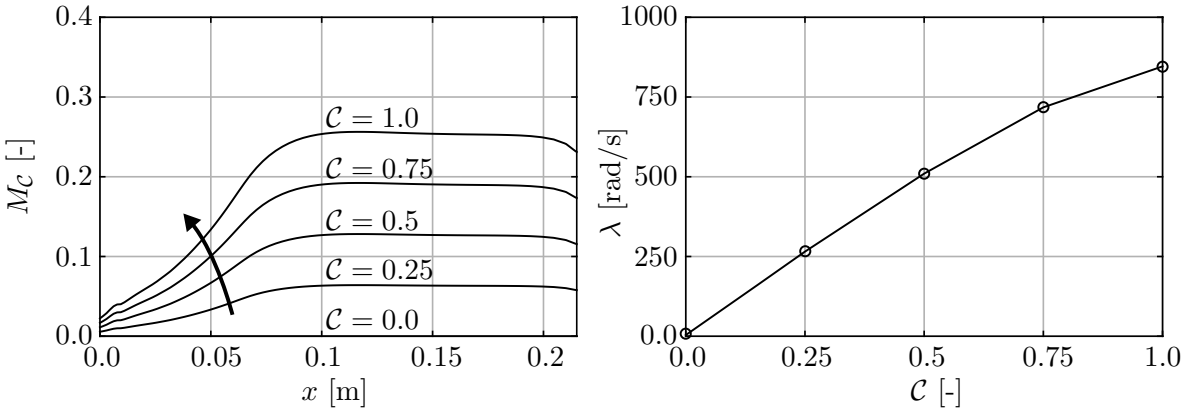

Fig. 7.19.: Distribution of the Mach number $M_\mathcal{C}$ for different prefactors $\mathcal{C}$ (left) and T_1^α mode damping rates for the different distributions of $M_\mathcal{C}$ depending on the prefactor $\mathcal{C}$ (right).

to the damping rate by (Fiala 2010)

$$\lambda = -\frac{1}{2}\frac{\frac{\partial E}{\partial t}}{E}. \tag{7.8}$$

In consequence, in order to analyze the influence of the mean flow on damping, the change of the fluctuating energy E needs to be revealed.

The influence of the mean flow on the damping rate is investigated in three steps. First, the mean flow quantities are set constant in the combustion chamber. For this purpose, a spatially averaged speed of sound c, density $\bar{\rho}$, isentropic exponent κ and pressure $\bar{p}$ is imposed. Furthermore, the Mach number M is set to zero. Secondly, the axial dependencies of $c, \bar{\rho}, \kappa$ and $\bar{p}$ are included. However, the Mach number remains zero. Finally, on the basis of the axially dependent $c, \bar{\rho}, \kappa$ and $\bar{p}$, the Mach number is gradually increased until the full velocity in the chamber is reached. To establish similarly shaped Mach number profiles, the mean axial velocity is scaled with a constant prefactor $\mathcal{C}$, i.e.

$$M_\mathcal{C}(x) = \mathcal{C}M(x) = \frac{\mathcal{C}\bar{u}(x)}{c(x)}, \tag{7.9}$$

where $\bar{u}(x)$ and $M(x)$ denote the unscaled mean axial velocity and Mach number, respectively. The different Mach number distributions $M_\mathcal{C}$ for $\mathcal{C} = 0, 0.25, 0.5, 0.75$ and 1.0 are shown in Fig. 7.19 (left).

Initially, the first transverse mode shape and the corresponding damping rate for a homogeneous speed of sound distribution and a zero Mach number, i.e. $\mathcal{C} = 0$, is discussed. The mode shape is shown in Fig. 7.20 (left). It can be seen that the pressure amplitudes are constant in axial direction and an axial decay is not present. This is explained by the constant speed of sound and hence unchanged cut-on frequency in axial direction. Furthermore, due to the absence of mean flow gradients, entropy and vorticity fluctuations s' and ξ' cannot be generated, cf. Eq. (2.24) and Eq. (2.25).

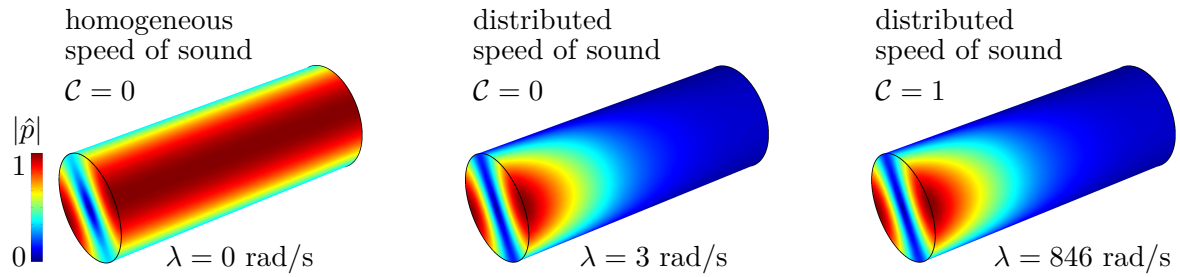

Fig. 7.20.: Normalized pressure amplitude plots of the first transverse mode shape in the reduced chamber domain for different distributions of speed of sound and prefactors $\mathcal{C}$.

Therefore, the source term $\mathcal{D}$ according to Eq. (2.66) becomes zero and the fluctuating energy balance according to Eq. (7.7) reduces to

$$\frac{\partial E}{\partial t} = 0. \tag{7.10}$$

Eq. (7.10) shows that in case of constant mean flow quantities and zero Mach number the change of the fluctuating energy is zero. In consequence, the damping rate is zero, cf. Eq. (7.8). This is also confirmed by the acoustic simulations, cf. Fig. 7.20 (bottom/left). Even for a non-zero but spatially constant Mach number in the chamber, vorticity and entropy modes cannot be generated and the damping rate is therefore zero, cf. Eq. (2.24) and Eq. (2.25).

In the next step, the mode shape and the damping rate in case of axially distributed $c, \bar{\rho}, \kappa$ and $\bar{p}$ but with zero Mach numbers, i.e. $\mathcal{C} = 0$, is analyzed. The simulated mode shape is shown in Fig. 7.20 (middle). Since the speed of sound is now changes in axial direction and corresponds to the profile shown in Fig. 7.12 for LP4, the spatial decay of the pressure amplitudes is present. Therefore, the mode shape is similar to the T_1^α shape for the complete mean flow with a non-zero Mach number, i.e. for $\mathcal{C} = 1$. For this configuration, entropy and vorticity modes can be generated, cf. Eq. (2.24) and Eq. (2.25). However, since the mean axial velocity is zero, the source term $\mathcal{D}$ contains only two terms, viz.

$$\mathcal{D} = -s'\bar{\rho}u_i'\frac{\partial \bar{T}}{\partial x_i} - \frac{\bar{\dot{q}}T'^2}{\bar{T}^2}. \tag{7.11}$$

In turn, since $\bar{u} = 0$, the convective transport of entropy fluctuations across the outlet boundary condition according to Eq. (7.7) is zero. The acoustic simulations show that the resulting damping rate is very small, i.e. $\lambda = 3$ rad/s. In consequence, although axial mean flow gradients are present and the acoustic amplitudes strongly decay in axial direction, the damping rate is hardly influenced.

In the final step, the Mach number is gradually increased until the unscaled mean profile is reached. The mode shape for the unscaled situation, i.e. $\mathcal{C} = 1$, is shown in Fig. 7.20 (right). A very similar shape is observed as for the case with $\mathcal{C} = 0$ and axially distributed $c, \bar{\rho}, \kappa$ and $\bar{p}$, cf. Fig. 7.20 (middle). Apparently, the mode shape is

predominantly determined by the distribution of speed of sound. However, with a non-zero Mach number, the source term $\mathcal{D}$ contains a variety of terms, each contributing to the change of the fluctuating energy and hence to the damping rate, cf. Eq. (2.66).

The change of the damping rate with increasing Mach number is shown in Fig. 7.19 (right). A strong increase of the damping rate with rising prefactor $\mathcal{C}$, cf. Eq. (7.9), can be observed. Fig. 7.19 (right) suggests that the increase of the damping rate is approximatively proportional to the prefactor $\mathcal{C}$ and hence to the Mach number.

It can be concluded that the mean flow leads to a strong increase of the damping rate only if an axial mean velocity and gradients of $c, \bar{\rho}, \kappa$ and $\bar{p}$ are present. In this situation, the interaction of the acoustic fluctuations with the mean flow gradients results in the generation of vorticity and entropy modes, cf. Eq. (2.24) and Eq. (2.25), and the source term $\mathcal{D}$ according to Eq. (2.66) leads to a change of the fluctuating energy and hence to an increase of the damping rate.

7.4. Impact of the Injection Conditions on T_1^α and $\mathrm{T}_1^\beta\mathrm{L}_1$ Eigenfrequencies

The LP for stable and unstable operation in case of the BKD test chamber reveal that small variations of the H_2 temperature at injection as well as different ROF tremendously affect the stability of the system, cf. Tab. 5.1. In fact, the H_2 temperature at injection differs by only 50 K between LP3 and LP4, but high amplitudes are observed only for LP4. In contrast, the injection temperature of H_2 is approximately the same for LP1 and LP2. However, high amplitudes during operation are only present for LP2 with the higher ROF.

A strong influence of the H_2 injection temperature on combustion stability was also pointed out in (Conrad et al. 1968; Nunome et al. 2008, 2011; Wanhainen and Morgan 1969; Wanhainen et al. 1966, 1968). However, in contrast to the observations in the BKD test chamber, unstable operation was observed for reduced H_2 injection temperatures.

(Gröning et al. 2014) suggest that the variation of the H_2 injection temperature changes speed of sound in the chamber and therefore alters the eigenfrequencies of the acoustic modes. For a specific speed of sound in the chamber and, in consequence, for a specific H_2 injection temperature, the T_1^α eigenfrequency is just right for an instability to occur. In a recent publication, (Gröning et al. 2015b) show that the BKD test chamber operates unstable if the T_1^α eigenfrequency coincides with an eigenfrequency of the O_2 post, cf. Sec. 7.2. In turn, (Gröning et al. 2014) determine experimentally that for a ramp-wise change of the H_2 injection temperature, high amplitudes of the T_1^α mode are only observed at approximately 95 K. Consequently, in case of ROF 6, only a H_2 injection temperature of approximately 95 K results in an unstable BKD test chamber operation, cf. Tab. 5.1.

For a successful assessment of linear stability, it is essential for the numerical simulations to capture the influence of the H_2 injection temperature and of the ROF on the mode dynamics. The purpose of the first part of this section is to test the stability

assessment procedure in terms of its capabilities to predict the effect of small H_2 injection temperature variations on the eigenfrequencies. In particular, the eigenfrequencies of the potentially unstable T_1^α mode but also of the $T_1^\beta L_1$ mode are simulated and compared to experimental results.

The influence of the H_2 injection temperature on the eigenfrequencies is experimentally investigated in ramping procedures. Herein, the H_2 temperature was successively changed from approximately 40 K to 135 K (Gröning et al. 2014). The procedure was performed for different ROF. However, in the present study concerning the influence of the H_2 injection temperature on the eigenfrequencies only a ROF of 6 is considered, since it corresponds to LP3 and LP4, cf. Tab. 5.1. Furthermore, the chamber pressure is kept constant at approximately 80 bar.

The T_1^α and $T_1^\beta L_1$ mode eigenfrequencies can also be influenced by the ROF. Therefore, matching eigenfrequencies of the T_1^α mode with the O_2 post could also be established for a specific ROF. Therefore, in the second part of this study a variation of ROF is numerically calculated while the H_2 injection temperature is kept constant at approximately 96 K. Furthermore, the chamber pressure is kept constant at approximately 80 bar. Experimental comparison data is taken from (Gröning et al. 2013b).

The simulation procedure for the calculation of the eigenfrequencies corresponds to first and second step of the stability assessment procedure, see Sec. 6.1. Therefore, the acoustic simulations are performed for the open loop system, i.e. the dynamic heat release fluctuations are not accounted for. In the first step, steady state CFD simulations are conducted and afterwards converted into a mean flow for the subsequent acoustic simulations. In the CFD simulations, the influences of heat transfer and flow acceleration on the H_2 injection temperature at the recess are neglected, since the attributed temperature change along the H_2 post length is small, see Sec. 7.1. In the second step, acoustic simulations are performed to reveal the T_1^α and $T_1^\beta L_1$ eigenfrequencies. For the acoustic simulations, the numerical setup described in Sec. 6.4 is applied.

7.4.1. Influence of the H_2 Temperature on T_1^α and $T_1^\beta L_1$ Eigenfrequencies

In this first study, the H_2 injection temperature $\bar{T}_{H_2}$ was varied in a range of 40-140 K in steps of 20 K and its impact on the T_1^α and $T_1^\beta L_1$ eigenfrequencies is analyzed. The chosen temperature range includes LP3 and LP4, cf. Tab. 5.1. The simulated results furthermore reveal the change of the eigenfrequencies for temperatures beyond the H_2 injection temperature of LP4.

To begin with, the T_1^α and the $T_1^\beta L_1$ mode eigenfrequencies for the variation of $\bar{T}_{H_2}$ are compared to experimental findings in Fig. 7.21 (top/left). In the following, these frequencies will be referred to as $f_{T_1^\alpha}$ and $f_{T_1^\beta L_1}$. Very good agreement is achieved for the entire $\bar{T}_{H_2}$ range for both $f_{T_1^\alpha}$ and $f_{T_1^\beta L_1}$. Hence the stability assessment procedure with the chosen mean flow modeling approach is capable of capturing the influences of small H_2 injection temperature variations on the eigenfrequencies accurately.

Now the behavior of $f_{T_1^\alpha}$ and $f_{T_1^\beta L_1}$ with increasing $\bar{T}_{H_2}$ is analyzed. Fig. 7.21 (top/left)

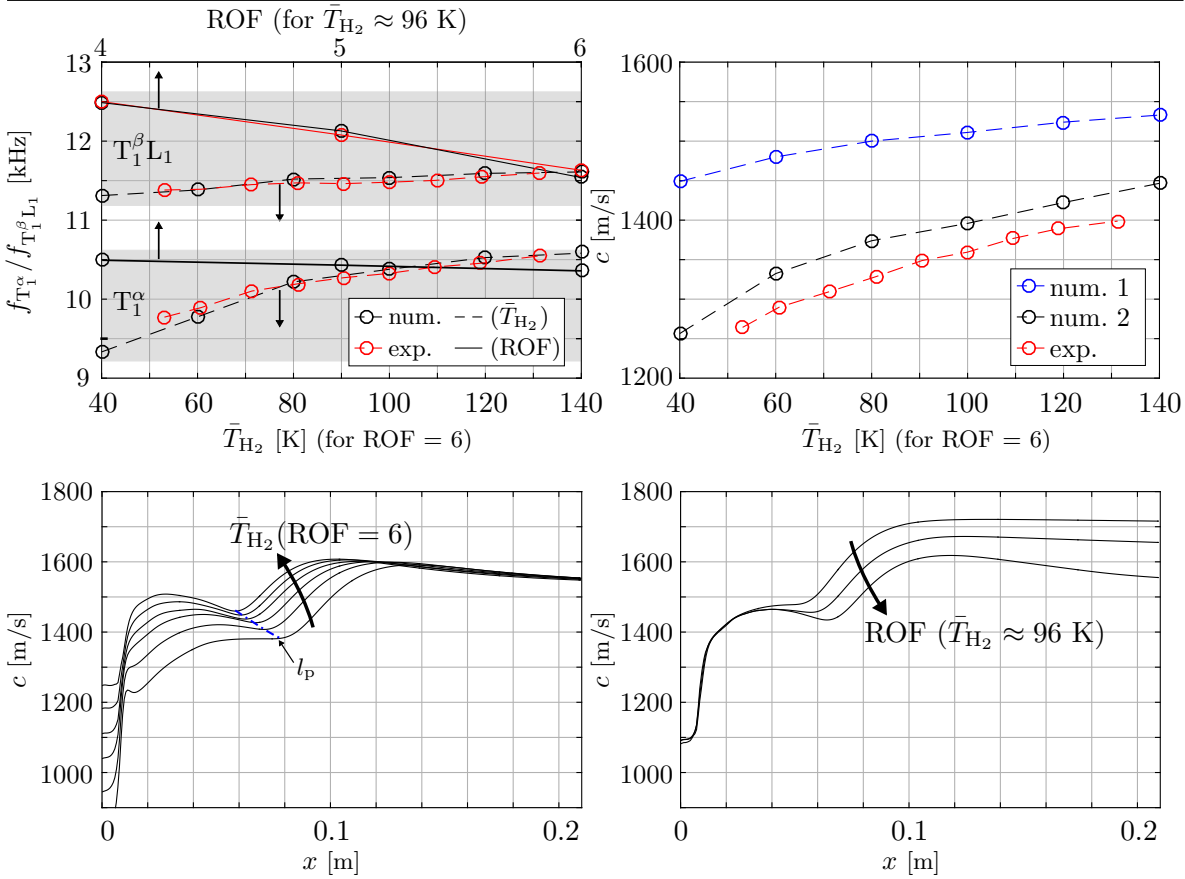

Fig. 7.21.: Top: Variation of eigenfrequencies $f_{T_1^\alpha}/f_{T_1^\beta L_1}$ (left) and speed of sound c (right) with $\bar{T}_{H_2}$. Bottom: Spatial dependence of speed of sound for different H_2 injection temperatures $\bar{T}_{H_2}$ (left) and ROF (right); Experimental results from (Gröning et al. 2014).

shows that $f_{T_1^\alpha}$ increases by almost 20 % between 40 K and 140 K (with $f_{T_1^\alpha}$ at 40 K being the reference). This increase is immense since the remaining injection parameters are unchanged.

Interestingly, $f_{T_1^\alpha}$ does not depend linearly on $\bar{T}_{H_2}$. In fact, the change of $f_{T_1^\alpha}$ with $\bar{T}_{H_2}$ is more significant for lower temperatures, and less for higher $\bar{T}_{H_2}$. Similarly, $f_{T_1^\beta L_1}$ also increases with the injection temperature of H_2. However, the change between 40 K and 140 K is lower than that of the $f_{T_1^\alpha}$ mode and is given by approximately 2.6 %.

To explain the behavior of $f_{T_1^\alpha}$ and $f_{T_1^\beta L_1}$ for increasing H_2 injection temperatures, the distribution of the speed of sound in the chamber is analyzed. For this purpose, the spatial dependency of speed of sound in axial direction is shown in Fig. 7.21 (bottom/left) for the different $\bar{T}_{H_2}$. It can be seen that the general distribution of c is similar to Fig. 7.14 consisting of a short injection zone with low values as well as a first and a second plateau. However, with higher $\bar{T}_{H_2}$, the speed of sound at injection and in the first plateau region is considerably increased. This can be explained by two effects. Firstly, speed of sound of H_2 increases directly with $\bar{T}_{H_2}$ above approximately 65 K, see Fig. 6.5 (right). In consequence, higher injection temperatures lead to elevated values of c in the

injection and combustion zone. Additionally, according to Fig. 6.5 (right), c decreases with increasing temperatures below 65 K suggesting that the eigenfrequency should decrease in this temperature range. However, combustion rapidly rises temperature above 65 K and the effect of the very low temperatures is hence irrelevant.

The second effect originates from an indirect influence of $\bar{T}_{H_2}$ on the speed of sound. Essentially, increasing $\bar{T}_{H_2}$ reduces density at injection $\bar{\rho}_{H_2}$, see Fig. 6.5 (left). However, as the mass flow of H_2 is not changed, decreasing density leads to higher injection velocity according to mass conservation:

$$\underbrace{\dot{m}_{H_2}}_{\approx \text{const.}} \sim \underbrace{\bar{\rho}_{H_2,\text{inj}}}_{\downarrow} \cdot \underbrace{\bar{u}_{H_2,\text{inj}}}_{\uparrow} . \tag{7.12}$$

A higher injection velocity in turn results in stronger shear forces in the mixing and combustion zone between H_2 and O_2, see Fig. 7.3, and therefore more intense turbulent mixing. Ultimately, the turbulent kinetic energy in the mixing zone increases resulting in higher reaction rates according to the EDM combustion model, cf. Eq. (6.41). In consequence, higher temperatures and hence increased speed of sound are present in the mixing and reaction zone.

In Fig. 7.21 (bottom/left), it can also be seen that the length of the first plateau region is reduced with increasing $\bar{T}_{H_2}$. As explained in Sec. 7.3.1, the length of the first plateau is associated with the axial dimension of the O_2 core. Since O_2 is the deficient species, cf. Tab. 5.1, the flame length is directly associated with the O_2 core dimension. The reduction of the O_2 core length can be explained by the presence of higher reaction rates due to more intense mixing with higher H_2 injection velocities, cf. Eq. (7.12). Essentially, increased reaction rates result in a faster consumption of the propellants. Therefore, the O_2 core dimension and hence the flame length gets reduced. In consequence, also the length of the first plateau region is smaller.

The injection velocities of H_2 are illustrated together with the lengths of the O_2 core as well as of the first plateau region in Fig. 7.22. The injection velocities are calculated from mass conservation cf. Eq. (5.1). The lengths of the O_2 core and first plateau are determined as follows:

- The O_2 core length l_{O_2} is extracted from the CFD mean flow results. The length is defined at the axial position where the O_2 mass fraction on the axis of the single flame configuration is reduced to 0.99, cf. Fig. 7.3.
- The length of the first plateau l_p is measured on the basis of the axial distributions of the speed of sound, see Fig. 7.21 (bottom/left). Since l_p is associated with the length of the O_2 core, it is defined at the axial location where the influence of the O_2 core on the speed of sound vanishes. This location corresponds to the start of the transition zone between the first and second plateau regions. In consequence, l_p is defined at the axial location where the distributies speed of sound shows a minimum point, which is found directly before the transition from the first to the second plateau region, see Fig. 7.21 (bottom/left).

The H_2 injection velocity $\bar{u}_{H_2,\text{inj}}$ as well as the lengths l_{O_2} and l_p are now analyzed, see Fig. 7.22. An almost linear increase of $\bar{u}_{H_2,\text{inj}}$ from approximately 100 m/s to almost

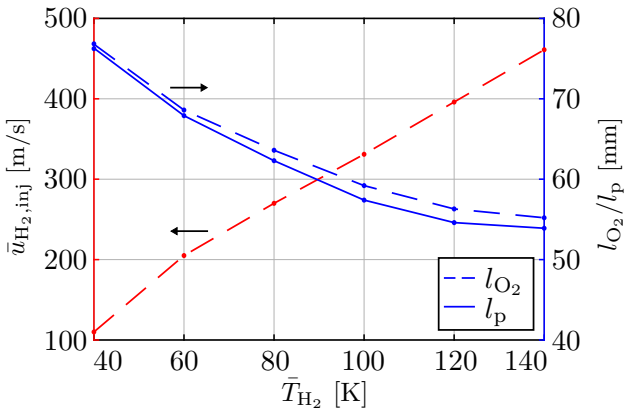

Fig. 7.22.: Injection velocity of H_2 together with the lengths of the O_2 core and of the first plateau of c in dependence of the injection temperature.

500 m/s with rising $\bar{T}_{H_2}$ can be seen. The linear increase can be explained by the change of the injection density with injection temperature. Since H_2 can approximatively be treated as an ideal gas for the considered injection conditions, cf. Fig. 6.3, the dependency of the injection velocity on the injection temperature $\bar{T}_{H_2}$ can be derived on the basis of Eq. (7.12)

$$\bar{u}_{H_2,inj} \sim \frac{\dot{m}_{H_2}}{\bar{\rho}_{H_2}} = \dot{m}_{H_2} \frac{\mathcal{R}\bar{T}_{H_2}}{\bar{p}_{cc}} \sim \dot{m}_{H_2}\bar{T}_{H_2}. \tag{7.13}$$

Eq. (7.13) shows the linear dependency of the injection velocity of H_2 on the injection temperature. Small deviations from the linear behavior are given in Fig. 7.22, which are caused by the slightly non-ideal gas behavior of H_2 at small temperatures, see Fig. 6.3.

Fig. 7.22 also shows that the lengths of the first plateau region l_p and of the O_2 core l_{O_2} are almost identical. This reveals that the first plate region indeed coincides with the O_2 core length and that the reduction of l_p and l_{O_2} is a direct consequence of the increasing injection velocities $\bar{u}_{H_2,inj}$ with $\bar{T}_{H_2}$. However, Fig. 7.22 shows that the length reduction becomes less significant with increasing $\bar{T}_{H_2}$. This can be explained by the reduced relative change of injection velocity with increasing $\bar{T}_{H_2}$ and hence by the reducing relative increase of turbulent kinetic energy, which finally leads to a reduced increase of the reaction rates, cf. Eq. (6.41).

Due to the reduction of the O_2 core length with increasing $\bar{T}_{H_2}$, the transition from the first plateau of c into the second plateau is shifted further upstream. In consequence, the length of the second plateau is increased. However, the speed of sound in the second plateau region is not influenced by $\bar{T}_{H_2}$. This can be explained by the fact that combustion is complete before the location of the second plateau. Hence, the species composition and, in consequence, temperature and speed of sound, are given by the chemical equilibrium, which in turn depends on ROF and chamber pressure exclusively. Both quantities are constant for the variation of the $\bar{T}_{H_2}$ injection temperature and the speed of sound in the second plateau region is hence the same.

The weak reduction of c along the second plateau length is due to the dissociation

of water. As the combustion model does not describe the recombination of OH and H to H_2O, the dissociation reaction permanently reduces the temperature and hence the speed of sound in the second plateau region, see Eq. (6.50). The missing recombination is unphysical and reveals a disadvantage of the combustion model. However, the very good agreement of the eigenfrequencies shows that the influence on acoustic propagation is negligibly weak.

The axial distributions of speed of sound now explain the behavior of $f_{T_1^\alpha}$ as well as of $f_{T_1^\beta L_1}$ with increasing injection temperature of H_2. The T_1^α exists predominantly in the regions of injection and of the first plateau, see Sec. 7.3.2.1. Therefore, the immense increase of $f_{T_1^\alpha}$ is explained by the strong raise of speed of sound in these particular regions, see Fig. 7.21 (bottom/left). Furthermore, the T_1^α eigenfrequency is directly influenced by the length reduction of the first plateau region. In fact, the reduction shortens the mode structure, leading to an additional increase of $f_{T_1^\alpha}$.

In contrast, the $T_1^\beta L_1$ mode exists within the entire chamber, see Sec. 7.3.1 and is hence influenced by the speed of sound in the regions of injection, of the first plateau as well as of the second plateau. Therefore, $f_{T_1^\beta L_1}$ depends on an averaged speed of sound over the entire chamber length. Since the speed of sound in the second plateau region is not changed with varying $\bar{T}_{H_2}$, the relative change of the axially averaged speed of sound is not as large as the relative change of speed of sound in the first plateau region, see Fig. 7.21 (bottom/left). In consequence, the increase of $f_{T_1^\beta L_1}$ is lower compared to the increase of $f_{T_1^\alpha}$ with raising $\bar{T}_{H_2}$. The T_1^α mode eigenfrequency is hence more sensitive towards variations of $\bar{T}_{H_2}$ than the $T_1^\beta L_1$ mode eigenfrequency.

Finally, the differently strong changes of $f_{T_1^\alpha}$ with increasing $\bar{T}_{H_2}$ at lower and higher H_2 injection temperatures are explained, respectively. Essentially two effects lead to the less significant increase of $f_{T_1^\alpha}$ at higher $\bar{T}_{H_2}$, see Fig. 7.21 (bottom/left):

Firstly, the axial distribution of c within the region of the first plateau shows that the increase of c becomes less significant with raising $\bar{T}_{H_2}$. This behavior originates from two influences: On one hand, the increase of speed of sound of H_2 at injection becomes less significant for increasing $\bar{T}_{H_2}$. On the other hand, the intensification of combustion reduces, since the relative increase of the injection velocity decreases. This behavior can also be reasoned by the less significant reduction of l_{O_2} and l_p, see Fig. 7.22. In consequence, the reduced intensification of combustion leads to a less strong increase of temperatures and hence of the speed of sound in the region of the first plateau.

Secondly, since the reduction of l_{O_2} and l_p becomes less significant with $\bar{T}_{H_2}$, the increase of $f_{T_1^\alpha}$ due to the axial length shortening of the mode shape also contributes to a less significantly increase of $f_{T_1^\alpha}$, cf. Fig. 7.22.

A non-linear increase of the eigenfrequency with increasing $\bar{T}_{H_2}$ at lower and higher H_2 injection temperatures can also be observed for the $T_1^\beta L_1$ mode. However, this effect is substantially weaker than for the T_1^α mode. As explained before, the $T_1^\beta L_1$ mode frequency depends also on the speed of sound in the second plateau region. Since speed of sound in this region is the same for all considered $\bar{T}_{H_2}$, the overall change of $f_{T_1^\beta L_1}$

with $\bar{T}_{\mathrm{H_2}}$ is weak. In consequence, the less significant increase of $f_{\mathrm{T_1^\beta L_1}}$ in the higher $\bar{T}_{\mathrm{H_2}}$ range can hardly be recognized in Fig. 7.21.

Lastly, a comparison of the simulation results with experimental findings on the basis of speed of sound is presented. (Gröning et al. 2014) calculate a characteristic speed of sound based on experimentally determined $\mathrm{T_1^\alpha}$ eigenfrequencies and the cut-on condition (Eq. 2.60) with $M = 0$. The findings are shown in Fig. 7.21 (top/right). It can be seen that speed of sound increases with $\bar{T}_{\mathrm{H_2}}$. Furthermore, a less significant increase in the higher temperature range can be observed. In consequence, the general trend of the characteristic speed of sound is qualitatively in agreement with the behavior of the $\mathrm{T_1^\alpha}$ and $\mathrm{T_1^\beta L_1}$ eigenfrequencies, cf. Fig. 7.21 (top/left). Ultimately, the characteristic speed of sound should be reproducible from the mean flow simulation results, i.e. from the distributions shown in Fig. 7.21 (bottom/left).

Firstly, the entire chamber volume is used to calculate an averaged c from the mean flow CFD results. The findings are presented in Fig. 7.21 (top/right) in blue (num. 1) and compared to the experimental result (exp.). Although the general trend is captured, considerable discrepancies can be observed. Apparently, using the entire chamber volume for the determination of the averaged speed of sound is not correct.

Secondly, the axial extent is limited to l_p, i.e. only the region of existence of the $\mathrm{T_1^\alpha}$ mode is taken into account for the generation of the averaged speed of sound. The results are shown in black (num. 2) in Fig. 7.21 (top/right). In this case, the discrepancies are substantially reduced and only a small but constant deviation is left. The less significant increase of c in the higher $\bar{T}_{\mathrm{H_2}}$ range is excellently reproduced.

The comparison shows that only the speed of sound within the region defined by the first plateau length l_p and hence in the region of the O_2 core is relevant for the calculation of the $\mathrm{T_1^\alpha}$ eigenfrequency. In turn, this evidently shows that this particular mode shape is only present within the axial region limited by l_p.

7.4.2. Influence of ROF on $\mathrm{T_1^\alpha}$ and $\mathrm{T_1^\beta L_1}$ Eigenfrequencies

In this second study, the influence of the ROF on the $\mathrm{T_1^\alpha}$ and $\mathrm{T_1^\beta L_1}$ mode eigenfrequencies was investigated. For this purpose, three operating conditions were chosen. The corresponding load points are presented in Tab. 7.5. Essentially, the LP only differ in ROF and correspondingly in the mass flows of H_2 and O_2. Both the H_2 injection temperature of approximately 96 K and the chamber pressure of approximately 80 bar is the same for the three LP.

First, the simulated eigenfrequencies are compared to the experimental validation data in Fig. 7.21 (top/left). However, validation data is only available for the $\mathrm{T_1^\beta L_1}$ mode. An excellent agreement is found. Therefore, the applied stability assessment procedure is capable to capture the impact of different ROF on the eigenfrequencies accurately.

In Fig. 7.21 (top/left), it can be seen that both $f_{\mathrm{T_1^\alpha}}$ and $f_{\mathrm{T_1^\beta L_1}}$ reduce with increasing ROF. The reduction is considerably stronger for the $\mathrm{T_1^\beta L_1}$ mode with approximately 7.5

Tab. 7.5.: Load point definitions for the ROF variations (Gröning 2015).

LP		ROF = 4	5	6
$\dot{m}_{H_2}$	kg/s	1.27	1.08	0.96
$\dot{m}_{O_2}$	kg/s	5.09	5.42	5.75
T_{H_2}	K	96.79	96.69	95.66
T_{O_2}	K	114.08	112.62	111.42
chamber pressure p_{cc}	bar	80.94	80.87	80.04
$u_{H_2,inj}$	m/s	472	401	357
$u_{O_2,inj}$	m/s	13.6	14.4	15.2
($u_{H_2,inj}$ - $u_{O_2,inj}$)	m/s	459	387	342

% (with the eigenfrequency for ROF 4 being the reference) than for the T_1^α mode with approximately 2.4 %. Due to the low number of eigenfrequencies calculated, a general trend cannot be recognized, but a rather linear dependency of the eigenfrequency on ROF seems to be likely.

For the explanation of the differently strong changes of $f_{T_1^\beta L_1}$ and $f_{T_1^\alpha}$, the distributions of speed of sound in the chamber are again analyzed. Fig. 7.21 (bottom/right) shows the axial distributions of c for a variation of ROF $= 4, 5, 6$ according to Tab. 7.5.

Directly at injection, only insignificant speed of sound differences are observed. Essentially, this region is dominated by equally distributed reactants. Furthermore, the temperature of the reactants is not changed in this region for the different ROF. Also the region of the first plateau is dominated by similar values of speed of sound. However, with raising ROF the length of the first plateau region l_p increases. This is explained by two effects:

Firstly, the mass flow of O_2 increases with ROF, see Tab. 7.5. Therefore, the injection velocity of O_2 and, in consequence, O_2 momentum increases. A higher O_2 momentum leads to a larger penetration depth into the chamber and increases the length of the first plateau region.

Secondly, the mass flow of H_2 reduces with ROF and hence the velocity of H_2 injection lowers, see Tab. 7.5. The injection velocities are determined on the basis of mass conservation according to Eq. (5.1). Since the increase of the O_2 injection velocity is comparably low, the velocity difference between H_2 and O_2 reduces with increasing ROF, see Tab. 7.5. However, the velocity differences directly affect the shear forces between the propellants. In consequence, with increasing ROF, shear forces and hence turbulent kinetic energies are reduced. Ultimately, the turbulent mixing of H_2 and O_2 becomes less intense and the reaction rates are lowered, cf. Eq. (6.41). Less intense combustion results in a slower consumption of the propellants and the overall flame length gets larger.

Fig. 7.21 (bottom/right) shows that in the region of the second plateau, a significant reduction of c is observed with ROF, although ROF increases towards stoichiometry ($ROF_{st} = 8$). This is surprising, since increasing ROF lead to higher temperatures in

this region and, in consequence, speed of sound should rise. To investigate the behavior of the speed of sound in the second plateau region, the definition of c for an ideal gas is analyzed, viz.

$$c = \sqrt{\kappa \frac{\mathfrak{R}}{\mathbf{W}} \bar{T}}, \tag{7.14}$$

where $\mathfrak{R}$ denotes the universal gas constant. Eq. (7.14) shows that speed of sound in the second plateau region does not only depend on temperature, but also on the isentropic exponent and the molar mass. Both κ and $\mathbf{W}$ in turn depend on species composition and hence on chemical equilibrium for the given ROF and pressure. As pressure is constant, only the dependency on ROF is left. Additionally, κ also depends on temperature.

In general, the combustion products provide a higher molar mass, which leads to a reduction of c. However, as fuel excess is present, an increasing ROF also leads to higher temperatures, which in turn elevate c, cf. Eq. (7.14). In consequence, the influences of temperature and of molar mass $\mathbf{W}$ on c counteract.

To discriminate between the different influences on the speed of sound, each dependency is investigated. For this purpose, the change of speed of sound in terms of κ, $(\mathfrak{R}/\mathbf{W})$ and $\bar{T}$ is determined separately, and the relative change of c with each quantity is calculated with the speed of sound for ROF 4, c_{ROF4}, as the reference. The relative changes are given by

$$\begin{aligned}
\delta_{\bar{T}} &= \frac{\sqrt{\kappa_{\mathrm{ROF4}} \left(\frac{\mathfrak{R}}{\mathbf{W}}\right)_{\mathrm{ROF4}} \bar{T}} - c_{\mathrm{ROF4}}}{c_{\mathrm{ROF4}}} \qquad
\delta_{\mathbf{W}} = \frac{\sqrt{\kappa_{\mathrm{ROF4}} \left(\frac{\mathfrak{R}}{\mathbf{W}}\right) \bar{T}_{\mathrm{ROF4}}} - c_{\mathrm{ROF4}}}{c_{\mathrm{ROF4}}} \\
\delta_{\kappa} &= \frac{\sqrt{\kappa \left(\frac{\mathfrak{R}}{\mathbf{W}}\right)_{\mathrm{ROF4}} \bar{T}_{\mathrm{ROF4}}} - c_{\mathrm{ROF4}}}{c_{\mathrm{ROF4}}} \qquad
\delta_{c} = \frac{\sqrt{\kappa \left(\frac{\mathfrak{R}}{\mathbf{W}}\right) \bar{T}} - c_{\mathrm{ROF4}}}{c_{\mathrm{ROF4}}}
\end{aligned} \tag{7.15}$$

The relative changes of the speed of sound according to Eq. (7.15) are calculated using the CEA software package (McBride and Gordon 1994). Hence, chemical equilibrium is assumed in the region of the second plateau. The comparison is shown in Fig. 7.23 for increasing ROF. For illustrative purposes an extended ROF range up to stoichiometric conditions is shown.

It can be seen that the relative changes of the speed of sound with molar mass, i.e. $\delta_{\mathbf{W}}$, and with the isentropic exponent, δ_{κ}, are negative. In consequence, for increasing ROF the influences of κ and $\mathbf{W}$ lead to a reduction of the speed of sound. In contrast, $\delta_{\bar{T}}$ is positive leading to an increase of speed of sound.

Obviously, the speed of sound is mostly influenced by the molar mass, which therefore dominates the behavior of c. Since δ_c is negative, c reduces with increasing ROF, see Fig. 7.23. Moreover, δ_{κ} is also slightly negative, leading to a stronger reduction of c. This

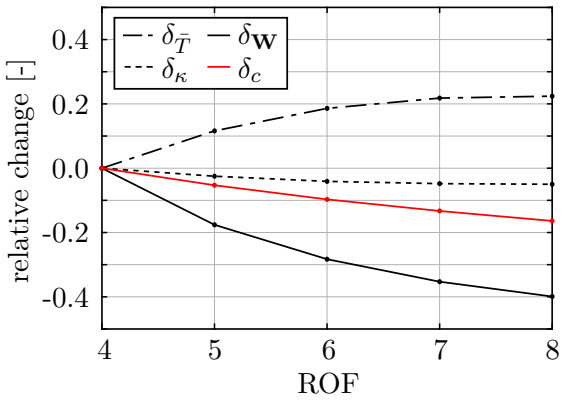

Fig. 7.23.: Relative changes of speed of with ROF in terms of temperature, isentropic exponent and molar mass.

behavior does not necessarily needs to be the same for other propellant combinations, since the interplay of temperature and molar mass with ROF at chemical equilibrium might be different.

In order to verify if the combustion model provides adequate equilibrium temperatures and speed of sounds, the CFD results for ROF = 4-6 are compared to the CEA findings, see Tab. 7.6. For this purpose, averaged temperatures and speed of sound are generated on the basis of the CFD results. In the averaging process, only the region of the second plateau is accounted for, cf. Fig. 7.21 (bottom/right). Excellent agreement is achieved indicating that the chosen models for H_2/O_2 combustion and water dissociation, cf. Eq. (6.50) are suitable for the simulation of the mean flows. Furthermore, the excellent comparison shows that chemical equilibrium conditions are indeed reached in the BKD test chamber. The fact that equilibrium conditions are reached might be explained by the relatively large length to diameter ratio, cf. Fig. 5.1.

Finally, the effect of ROF on the T_1^α and $T_1^\beta L_1$ mode eigenfrequencies can be explained on the basis of the distributions of speed of sound in the chamber, cf. Fig. 7.21 (top/left) and (bottom/right). The extension of the O_2 core length influences the T_1^α eigenfrequency twofold: On the one hand, the axial extent of the T_1^α increases leading to a lower eigenfrequency. On the other hand, the averaged speed of sound in the first plateau region is reduced, as the minimum speed of sound is lower in the first plateau region, cf. Fig. 7.21 (bottom/right). In consequence, $f_{T_1^\alpha}$ gets further reduced. The T_1^α is not influenced by the strong reduction of c in the second plateau region, since the mode is cut-off in this region and hence negligible amplitudes are present, cf. 7.3.2.1.

Tab. 7.6.: Comparison of simulation results and CEA: Temperature and speed of sound for ROF = 4-6.

CFD / CEA	ROF = 4	5	6
$\bar{T}$ [K]	2912 / 2950	3281 / 3293	3435 / 3499
c [m/s]	1714 / 1707	1654 / 1637	1553 / 1569

However, the overall impact of the increasing O_2 core length is low and the decrease of the $f_{T_1^\alpha}$ is hence moderate, cf. Fig. 7.21 (top/left).

In contrast, the $T_1^\beta L_1$ mode is influenced by the strong reduction of c in the second plateau region, due to the distribution of high amplitudes in the entire chamber, see Fig. 7.10. In consequence, the reduction of speed of sound with rising ROF leads to the strong reduction of $f_{T_1^\beta L_1}$ as depicted in Fig. 7.21 (top/left).

In summary, the simulations with small variations of the H_2 injection temperature and of the ROF show that the stability assessment procedure based on the EDM/FR combustion model and the acoustic simulation with LEE on the basis of the radially constant mean flow, is adequate to capture the influences of $\bar{T}_{H_2}$ and ROF on the eigenfrequencies of the T_1^α and $T_1^\beta L_1$ modes. The T_1^α mode eigenfrequency is highly sensitive towards the H_2 injection temperature, which changes the distribution of speed of sound in the flame region. However, the T_1^α mode sensitivity on ROF is rather low. In contrast, the $T_1^\beta L_1$ mode eigenfrequency strongly depends on ROF, which changes the chemical equilibrium in the rear part of the chamber in terms of temperature and speed of sound. Furthermore, the $T_1^\beta L_1$ mode is only moderately affected by the injection temperature of H_2.

7.5. Flame Dynamics and Flame Transfer Functions

The focus is now on the flame dynamics in the BKD test chamber. The goal is to simulate a single flame configuration under acoustic excitation and to determine the Flame Transfer Functions for the subsequent usage in the acoustic simulations of the closed loop system. The methodology was introduced in Sec. 6.5. For the computations, the real gas SRK EOS, the $k_t - \epsilon$ turbulence model as well as the combined EDM/FR combustion model are applied, cf. Sec. 6.2.3.1 and Sec. 6.2.3.2.

The flame dynamic behavior in terms of heat release rate fluctuations is studied in terms of pressure coupling, cf. Sec. 6.5.1 and transverse velocity coupling, cf. Sec. 6.5.2. First pressure coupling is studied and FTF^p are presented.

7.5.1. Pressure Coupling

For the investigation of pressure coupling, a single flame configuration located in the pressure anti-nodal line is simulated, cf. Fig. 6.12 and Fig. 6.11. For the simulations, the single flame CFD setup as described in Sec. 6.2 is used. In order to impose the excitation, mass source terms on the boundaries of the chamber section are applied, see Fig. 6.13. The explicit form of the boundary source term is shown in Eq. (6.89). Pressure excitation is not imposed in the dome section, since the change of the characteristic impedance from the recess into the O_2 post as well the pressure loss element scattering properties prevent acoustic waves from traveling upstream into the dome volume, cf. Sec. 7.2.

For the pressure excitation in the single flame configuration with the source term

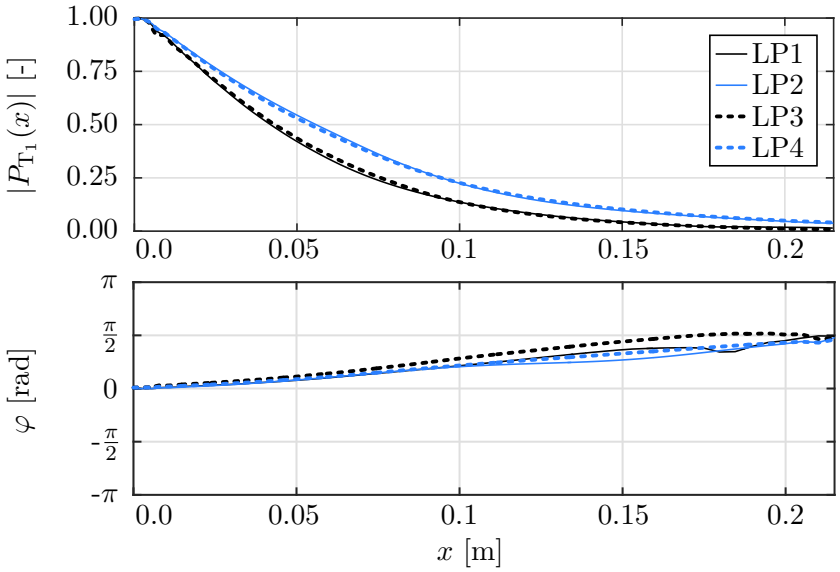

Fig. 7.24.: Axial distributions of $P_{T_1}(x)$ in terms of normalized amplitude (top) and phase (bottom) along the pressure anti-nodal line for the application to pressure coupling.

according to Eq. (6.89), the excitation amplitude is set to 3 % of the mean pressure, cf. Sec. 6.5. The excitation frequency ω is set to the eigenfrequency of the T_1^α mode. The eigenfrequencies for LP1-4 were presented in Tab. 7.3. Since the eigenfrequency might still change in the closed loop system due to the influence of the flame feedback, the Flame Transfer Functions are determined for a certain frequency range around the eigenfrequencies in Tab. 7.3. The frequency variation can not be performed for large deviations from the T_1^α mode eigenfrequency, since the mode shapes change with frequency altering the pressure distribution in the pressure anti-nodal line (Schmid 2014). In this situation, the applied source term according to Eq. (6.89) is no longer valid.

For the application of the source term according to Eq. (6.89), the axial pressure distribution $P_{T_1}(x)$ in the pressure anti-nodal line needs to be specified. As explained in Sec.6.5.1, $P_{T_1}(x)$ is determined on the basis of the acoustic simulations of the open loop system. Therefore, $P_{T_1}(x)$ is extracted from the anti-nodal lines of the T_1^α mode as indicated in Fig. 7.13.

The distributions of $P_{T_1}(x)$ in terms of amplitude and phase for LP1-4 are shown in Fig. 7.24. The normalized pressure amplitudes are the same as already presented in Fig. 7.14 and were discussed comprehensively in Sec. 7.3.2. However, the phases are presented in Fig. 7.24 for the first time. For the sake of comparison, the reference phase is set zero at the inlet, i.e. at $x = 0.0$ m. It can be seen that the phase distributions for LP1-4 are almost the same. The phases increase approximatively linearly in axial direction. At higher axial locations, the phases show deviations from the linear behavior. However, as pressure amplitudes are low in this region, the phases are rather irrelevant. Amplitude and phase of $P_{T_1}(x)$ are applied to the boundary source in term according to Eq. (6.89) and are hence the basis for the investigations of the pressure coupling.

On the basis of the CFD simulations with pressure excitation, the Flame Transfer Functions $\mathrm{FTF}^{\mathrm{p}}_{\mathrm{mech}}$ are determined, cf. Eq. (6.96). In consequence, the $\mathrm{FTF}^{\mathrm{p}}_{\mathrm{mech}}$ are given by

$$\mathrm{FTF}^{\mathrm{p}}_{\mathrm{mech}} = \hat{\dot{q}}^{\mathrm{p}} \cdot \frac{\hat{p}(x_{\mathrm{ref}})}{\bar{p}(x_{\mathrm{ref}})} \cdot \frac{\bar{\dot{Q}}}{V_{\mathrm{mech}}}. \tag{7.16}$$

Eq. (7.16) shows that the heat release fluctuation $\hat{\dot{q}}^{\mathrm{p}}$, the pressure fluctuation $\hat{p}(x_{\mathrm{ref}})$ and its mean value $\bar{p}(x_{\mathrm{ref}})$ at a reference position x_{ref} as well as the mean heat release rate $\bar{\dot{Q}}$ needs to be determined from the CFD simulations. However, as explained in Sec. 6.5.1, different coupling mechanisms might be present in the chamber. Furthermore, these mechanisms need to be separated in terms of their spatial appearance in order to determine the $\mathrm{FTF}^{\mathrm{p}}_{\mathrm{mech}}$ for each region. Therefore, the CFD results are investigated first to identify the governing coupling mechanisms. These investigations are presented next.

7.5.1.1. Coupling Mechanisms

For the identification of the coupling mechanisms in case of pressure excitation, the fluctuating heat release field needs to be studied. As explained in Sec. 6.2.3.2, the forward reaction of O_2 and H_2 to H_2O is fully controlled by turbulent mixing. In turn, turbulent mixing is described by the turbulent kinetic energy k_{t} and the turbulent dissipation rate ϵ, cf. Eq. (6.41). In consequence, the dynamics of the heat release rate can be analyzed on the basis of the fluctuating fields of these turbulent quantities. The influence of the dissociation of water is can be neglected for this purpose, since it is predominantly relevant in the rear part of the chamber where only low pressure amplitudes are present, cf. Fig. 7.24.

The identification of the coupling mechanisms is presented on the basis of LP4 for a frequency of 10,500 Hz. Fig. 7.25 shows the spatial distributions of the phase-resolved turbulent kinetic energy k_{t} (top) and dissipation rate ϵ (bottom) under pressure excitation conditions over one acoustic period.

Two characteristic regions with intense fluctuations of k_{t} and ϵ can be identified. The fluctuations are especially strong in the k_{t} distributions. The first region with high activity is located in close proximity to the face plate and covers approximately the initial 6 % of the chamber's length. The second region is located further downstream with a larger extent in axial direction than the first region. The intense variations of turbulent kinetic energy in these regions lead to high fluctuations of the heat release rate. Apparently, these two regions play a crucial role for the flame dynamics in terms of pressure coupling.

On the basis of the analysis of the fluctuating k_{t} and ϵ fields, two spatially separated regions for the determination of the Flame Transfer Functions are defined. The first region is referred to as *nearfield* due to its location near the face plate, whereas the second region is referred to as *farfield*. The nearfield covers the axial distance from 0 mm to 13 mm and the farfield from 13 mm to 215 mm. For each region, individual

	LP1	LP2	LP3	LP4
x_n [mm]	7.5	7.5	7.5	7.5
x_f [mm]	69	79	90	79

Tab. 7.7.: Axial reference locations for the determination of fluctuating pressure in the nearfield and farfield.

Flame Transfer Functions are determined and denoted by $\mathrm{FTF}_\mathrm{n}^\mathrm{p}$ for the nearfield and $\mathrm{FTF}_\mathrm{f}^\mathrm{p}$ for the farfield.

For the determination of the $\mathrm{FTF}_\mathrm{n}^\mathrm{p}$ and $\mathrm{FTF}_\mathrm{f}^\mathrm{p}$, the volume integrated heat release fluctuations are determined from the excited CFD simulations. For the integration the respective volumes of each field are used. In the next step, the volume integrated heat release rates are related to pressure fluctuations at individual reference locations x_n for the nearfield and x_f for the farfield, cf. Eq. (7.16). The choice of the reference locations is not unique and appears to be somewhat arbitrary. Since the amplitude and the phase of the imposed pressure excitation are not constant in axial direction, cf. Fig. 7.24, the choice of the reference location influences $\mathrm{FTF}_\mathrm{n}^\mathrm{p}$ and $\mathrm{FTF}_\mathrm{f}^\mathrm{p}$. Therefore, the reference locations need to be carefully chosen.

For the determination of the $\mathrm{FTF}_\mathrm{n}^\mathrm{p}$ and $\mathrm{FTF}_\mathrm{f}^\mathrm{p}$, the pressure fluctuations are monitored at the following reference locations: Since the nearfield is small, the pressure is approximatively constant in this region. In consequence, x_n can be defined at any location in the nearfield. Eventually, x_n is located in the center of nearfield region, cf. Fig. 7.25. In contrast, the pressure fluctuations are not constant in the farfield. A reasonable choice for the fluctuating pressure measurement position x_f is the region with the highest heat release variations in the farfield. This region coincides with the highest amplitudes of turbulent kinetic energy. This location can be identified in the phase-resolved distributions of k_t, cf. Fig. 7.25. The axial reference locations for the measurements of the pressure fluctuations in the nearfield x_n and for the farfield x_f are presented in Tab. 7.7 for LP1-4.

After the identification of the regions with high turbulent kinetic energy fluctuations and hence intense heat release rate modulation, the involved coupling mechanisms are discussed. The physical coupling mechanisms in the nearfield were already described in (Schulze et al. 2014b). Essentially, pressure fluctuations in the nearfield generate velocity fluctuations in the O_2 and H_2 injection planes. These velocity fluctuations in turn perturb the shear layer between O_2 and H_2. The shear layer perturbations are convected downstream, harmonically increasing and decreasing the intensity of propellant mixing, which results in variations of k_t and ϵ and finally in fluctuations of the heat release rate. Furthermore, velocity fluctuations in the O_2 and H_2 injection zones lead to fluctuating mass flow rates, which modulate the heat release rate as well. Finally, perturbed mixing zones and accompanied flame wrinkling effects lead to variations of the flame surface, which additionally modulates the heat release rates.

The variations of k_t in the farfield cannot be explained by shear layer effects due to

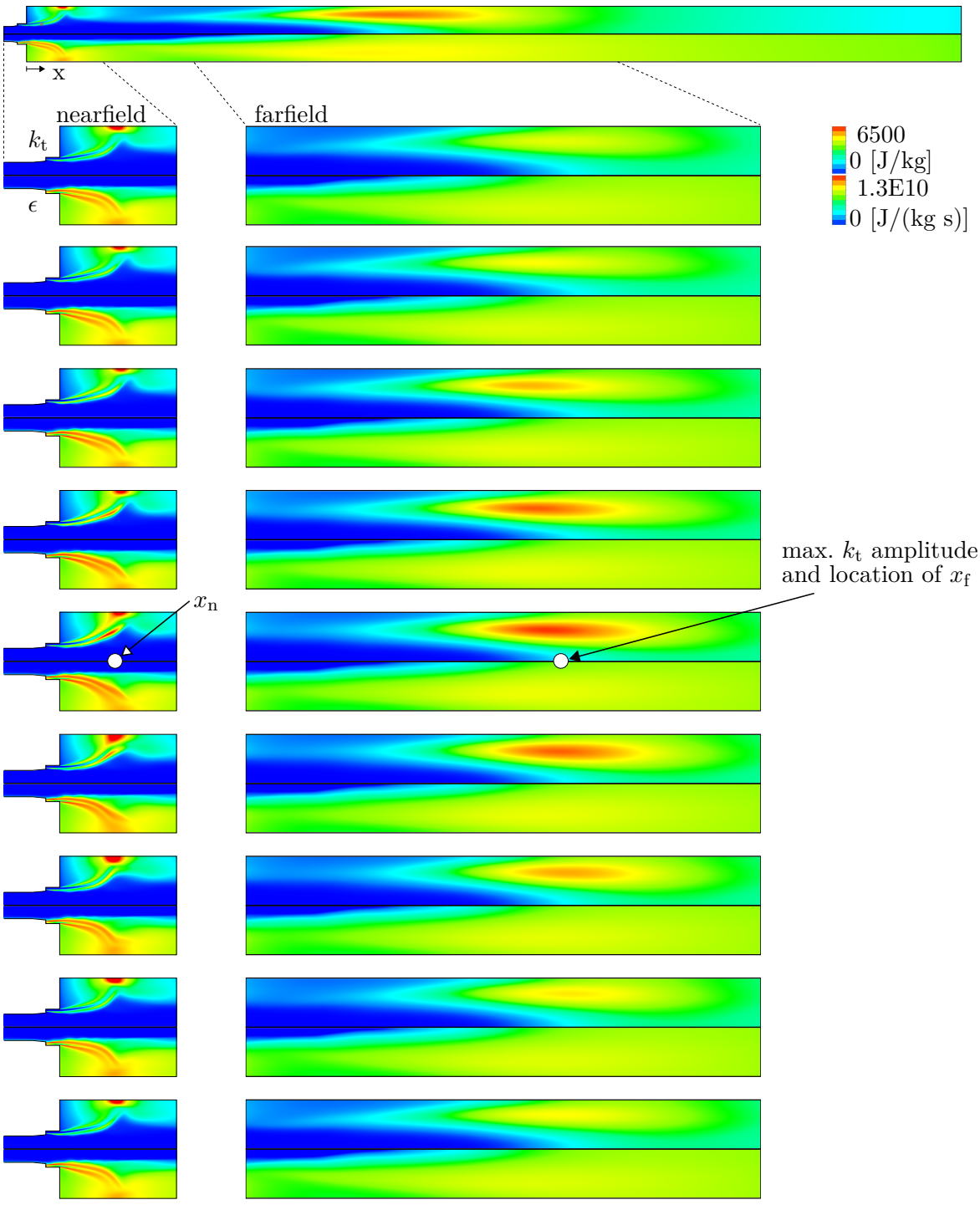

Fig. 7.25.: Phase-resolved turbulent kinetic energy k_t (top half) and turbulent dissipation rate ϵ (bottom half) under pressure excitation conditions for a frequency of 10,500 Hz. The reference locations x_n and x_f for the measurement of the pressure fluctuations are also shown.

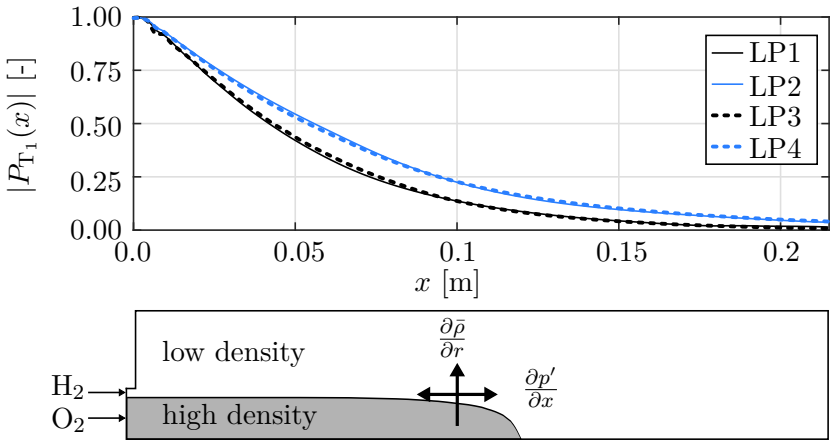

Fig. 7.26.: Top: Axial distributions of $P_{T_1}(x)$ in terms of normalized amplitude. Bottom: Illustration of baroclinique torque effects in the single flame configuration.

their large axial length scale. The simulation results reveal that the intense fluctuations of k_t in the farfield originate from baroclinique torque. This effects establishes due to the misaligned mean flow density gradients in radial direction and the axial acoustic pressure gradients, cf. Fig. 7.26 (bottom). The radial mean flow density gradient is caused by the high density differences between the dense O_2 core and the surrounding light H_2 and combustion products, cf. Fig. 7.3. According to Eq. (6.51), this misalignment of the radial density gradients and the axial acoustic pressure gradient periodically increases and reduces vorticity by

$$\frac{\partial \xi'_{i,b}}{\partial t} = \varepsilon_{ijk} \frac{1}{\bar{\rho}^2} \frac{\partial \bar{\rho}}{\partial x_j} \frac{\partial p'}{\partial x_k}. \tag{7.17}$$

The fluctuating vorticity leads to a periodic intensification and reduction of turbulent kinetic energy and hence of turbulent mixing. Ultimately, also the heat release rate is modulated (Schulze et al. 2014b).

The spatial separation of the coupling mechanisms into a nearfield and a farfield has been observed for all load points and frequencies. However, the intensity of the nearfield and farfield coupling is different for each load point. To analyze the differences, the Flame Transfer Functions for pressure coupling are presented and discussed next.

7.5.1.2. Flame Transfer Functions for Pressure Coupling

On the basis of the spatial separation into nearfield and farfield, individual transfer functions are defined and evaluated from the transient simulations. The results are compared in Fig. 7.27 in terms of the FTF_n^p in the nearfield (left column) and the FTF_f^p (right column) in the farfield in terms of amplitude (red) and phase (blue) for the frequencies between 9500 and 11,000 Hz.

Since the nearfield is small, it can be assumed that it is acoustically compact. Furthermore, the baroclinique torque effects in the farfield are independent of convective transport, since the modulation of turbulent mixing immediately leads to heat release due to the fully mixing controlled combustion model, see Sec. 6.2.3.2. In consequence, the phase of FTF^{p}_{n} and FTF^{p}_{f} can be used to determine directly whether the acoustic amplitudes are amplified ($|\varphi_{FTF^{p}_{n,f}}| < \frac{\pi}{2}$) or damped ($|\varphi_{FTF^{p}_{n,f}}| > \frac{\pi}{2}$), see Sec. 2.8. The $\frac{\pi}{2}$ phase limits are highlighted in black dot-and-dashed lines in Fig. 7.27.

To evaluated the influence of the injector dynamics, $FTF^{p}_{n/f}$ are presented on the basis of both simulations with and without injector. When the injector is absent, the respective domain is excluded and only the recess length is incorporated in the computational domain. Essentially, O_2 and H_2 are injected in the same plane. The mass flow of O_2 is then imposed directly at the recess leading to only small fluctuations of axial acoustic velocity at the inlet. These velocity fluctuations originate from varying pressure and therefore density fluctuations at the inlet.

In the following, the $FTF^{p}_{n/f}$ for nearfield and farfield are discussed separately.

7.5.1.3. Nearfield FTF^{p}_{n}

First, the FTF^{p}_{n} in the nearfield are discussed, see Fig. 7.27 (left). The phase values are rather constant over frequency for all LP. In turn, the amplitudes seem to depend only slightly on frequency, where LP3 shows the strongest variations. The highest amplitude of approximately 1.7 is found for LP3 for the case without injector.

In the realistic case with injector the amplitudes are generally reduced. LP3 exhibits the strongest reduction and LP1 shows the highest amplitudes of approximately 1.05. For LP3, the lowest amplitudes of approximately 0.3 are found. Rather similar amplitudes of 0.7-0.8 are observed for LP2/4. Concerning the phase values, the injector dynamics lead to a shift towards smaller values, leading to a more in phase behavior of heat release fluctuations and pressure fluctuations. The phase shift is largest for LP1, while the shifts is similarly smaller for LP2-4.

In a recent publication, simultaneous measurements of dynamic pressure and intensity of OH* radiation are used to determine experimentally a phase relation between the pressure and heat release fluctuations for LP1 and LP4 (Gröning et al. 2015a). It is assumed that OH* intensity can be used as an indicator for heat release. As shown in Fig. 5.2, the measurement ring is located directly at the face plate and OH* measurements are therefore restricted to the nearfield. Furthermore, the probes provide a narrow optical access, each is focused on a single flame region, see Fig. 5.2. Therefore, the results allow for a comparison with the computationally determined FTF^{p}_{n} in the nearfield in terms of the phase values. However, on the basis of the OH* measurements, the amplitude of heat release fluctuations cannot be determined. In consequence, experimental validation data is not available for the amplitude of the FTF^{p}_{n}.

Optical probes record the line-of-sight integrated radiation. In consequence, the determined phase between pressure and OH* radiation may originate from a flame ensemble, which is located within the integration path. However, (Fiala 2015; Fiala and Sattel-

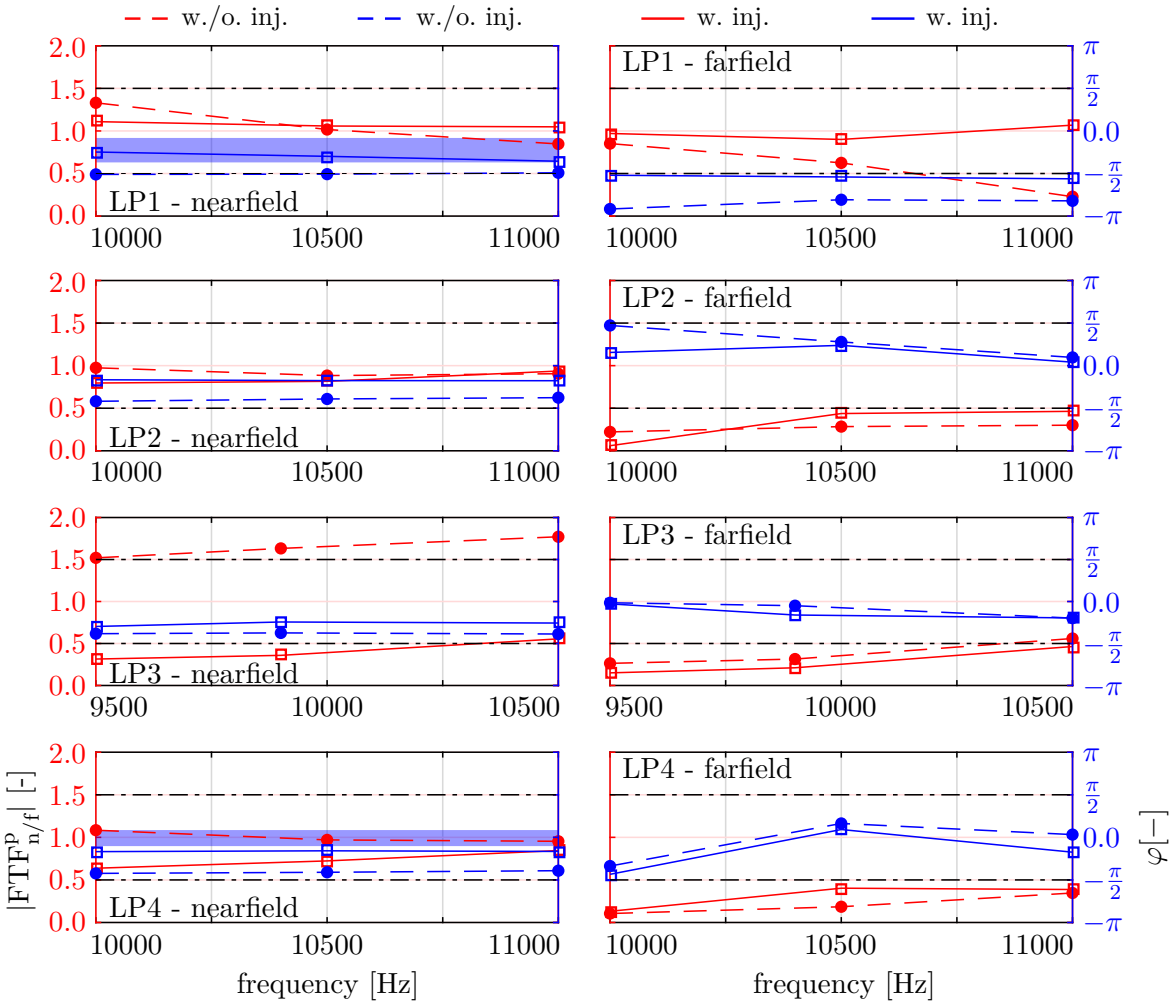

Fig. 7.27.: Flame Transfer Functions for the nearfield FTF_n^p (left) and farfield FTF_f^p (right) for LP1-4 with injector (solid lines) and without injector (dotted lines) in terms of amplitude (red) and phase (blue). Experimental phase values are highlighted in transparent blue.

mayer 2015b; Schulze et al. 2016a) show that OH* radiation at elevated pressure is subjected to intense self-absorption. It is therefore assumed that the measured radiation originates only from the nearest flame, at which the optical probe is aligned. A direct comparison between experimental findings and numerical results in terms of the FTF_n^p phase in the nearfield is therefore justified.

As shown in (Gröning et al. 2015a), statistical methods are used to determine the phase relation between OH* intensity and the dynamic pressure signal. In consequence, a specific phase value between the OH* intensity and pressure cannot be given. Instead, an interval with the highest number of samples of the phase between OH* intensity and dynamic pressure is presented (Gröning et al. 2015a).

For the measurements of OH*, three optical probes are used, see Fig. 5.2. For the comparison of the experimentally determined phase relation between OH* and the pressure

		response factor nearfield		response factor farfield	
	frequency [Hz]	w. inj.	w/o. inj.	w. inj.	w/o. inj.
LP1	10,535	0.610	-0.025	0.114	-0.515
LP2	10,348	0.702	0.274	0.321	0.182
LP3	9796	0.227	0.587	0.167	0.287
LP4	10,375	0.648	0.270	0.386	0.161

Tab. 7.8.: Response factor (RF) of LP1-4 for nearfield and farfield. The results without injector are also reported for the purpose of comparison.

fluctuations, the given intervals of the three optical probes are averaged. The phase intervals are highlighted in Fig. 7.27 for LP4 and LP1 in transparent blue. It can be seen that for LP1 the numerical phase values are in excellent agreement with the experimental findings. For the unstable LP4, the numerical phase is slightly too low but overall in good agreement with the experimental data. Altogether, the numerical methodology seems to be capable to capture the relevant time lags in the nearfield. Furthermore, the necessity of the decomposition into nearfield and farfield is evident. Without this decomposition, the spatially averaged phase would not match the experimental data and would lead to an incorrect representation of the phase relation.

For the direct comparison of the $\mathrm{FTF}_{\mathrm{n}}^{\mathrm{p}}$ between the LP1-4, the representation in terms of amplitude and phase is not adequate. Instead, the comparison is based on the response factor, see Sec. 2.8. As explained before, the compactness of the nearfield makes the RF suitable for comparing the Flame Transfer Functions based on a single quantity. Essentially, the higher the response factor, the higher the potential to drive the thermoacoustic feedback loop. The response factors are evaluated at the T_1^{α} eigenfrequency of each LP, see Tab. 7.3 and are presented in Tab. 7.8.

The highest response factor is found for LP2, while LP3 shows the lowest value. Interestingly, the two unstable LP exhibit similar response factors, which are slightly higher than for LP1. In comparison, the injector's influence constitutes approximately a doubling of the response factors for LP2 and LP4.

7.5.1.4. Farfield $\mathrm{FTF}_{\mathrm{f}}^{\mathrm{p}}$

In the following, the $\mathrm{FTF}_{\mathrm{f}}^{\mathrm{p}}$ of the farfield is discussed. The frequency dependence of the $\mathrm{FTF}_{\mathrm{f}}^{\mathrm{p}}$ is stronger than in the nearfield, see Fig. 7.27 (right column). Overall, the amplitudes are lower in the farfield than in the nearfield. The highest amplitude of approximately 1.0 in case of the system with injector is found for LP1. The injector influence generally leads to increased amplitudes in the farfield except for LP3, where the amplitudes are reduced. While the phase only changes moderately for LP3/4, a stronger impact is found for LP2 at low frequencies. The strongest impact is found for LP1. The phase values without injector are out-of-phase, while the injector dynamic leads to a phase difference of approximately $\pi/2$, which is close to the limit between amplifying and dampening influence.

	frequency	$\lvert Y_{\mathrm{CFD}}\rvert$
LP1	10 535	1.26
LP2	10 348	1.43
LP3	9 796	1.37
LP4	10 375	1.71

Tab. 7.9.: Amplitude of the O_2 injector admittance Y determined on the basis of the excited CFD simulations.

Next, the response factors of the farfield are discussed, see Tab. 7.8. In general, the same trend as for the nearfield is observed. While the response factor for LP3 is reduced due to the influence of the injector, LP2 and LP4 are approximately doubled, indicating a stronger feedback. In case of LP1, the injector actually leads to a different sign of RF. In fact, due to the influence of the injector, the RF of LP1 becomes slightly positive leading to a weak amplification of acoustic amplitudes.

7.5.1.5. Influence of the O_2 Injector

The significantly different flame responses for the simulations including the O_2 post can be explained on the basis of the O_2 injector dynamics. Specifically, the applied pressure modulation generates axial velocity fluctuations at the O_2 injector outlet. These fluctuations are convected downstream, which, as explained before, initiate different coupling mechanisms in the nearfield. A more detailed analysis on the convective transport process can be found in (Schulze et al. 2014b).

To indicate the impact of the O_2 post on the Flame Transfer Functions, its admittance is compared for the different load points in Tab. 7.9. High absolute values of Y lead to strong axial velocity fluctuations. The highest absolute value is found for LP4, indicating a strong influence of the O_2 post on the flame dynamics. For LP2 a moderate absolute value is found, which is slightly higher as for LP1 and LP3. Consequently, the stable LP are subjected to the lowest velocity fluctuations at the O_2 post outlet. However, the difference between LP2 and LP3 is not significant.

In conclusion the injector dynamics leads to a doubling of the response factor for the unstable LP2/4. In contrast, for the stable LP3, the injector dynamics lead to a reduction of the response factor for nearfield and farfield. Therefore, the injector dynamic is crucial for the adequate characterization of the flame dynamics and consequently for meaningful stability assessments.

7.5.2. Velocity Coupling

In the next step, the flame behavior under transverse velocity modulation is investigated. As explained in Sec. 6.5, transverse acoustic velocity fluctuations displace the flame and hence the heat release in the direction of increasing acoustic pressure. As it can be

seen in Eq. (6.73), the displacement of the flame $\hat{\Delta}_{\mathrm{fl}}$ yields a positive contribution to the overall Rayleigh integral and thus drives the feedback loop.

For the investigation of the flame displacement, a single flame configurations is subjected to transverse velocity fluctuations, cf. Fig. 6.14. As described in Sec. 6.5.2, the three-dimensional simulations are conducted with a momentum source term applied to the domain. The source term definition is given in Eq. (6.100). Since the source term for the generation of transverse velocity fluctuations was derived on the basis of the pressure excitation method, it depends on the axial pressure distribution $P_{\mathrm{T}_1}(x)$. In consequence, the axial distribution of the source term corresponds qualitatively to the shape of $P_{\mathrm{T}_1}(x)$, which is shown in Fig. 7.24. The excitation amplitude is set to 3 % pressure equivalent amplitude, cf. Sec. 6.5.2.

Goal of the CFD simulations under transverse acoustic excitation is to determine the Flame Transfer Functions FTF^{Δ}, see Eq. (6.75). Hence, the flame and the acoustic displacement need to be monitored. The flame displacement is defined by Eq. (6.103) and the transverse velocity displacement is measured in a second CFD simulation with a constant excitation amplitude in the rear part of the chamber, cf. Sec. 6.5.2. First, the effect of slip between the flame and the acoustic displacement is explained. Afterwards, the FTF^{Δ} are presented and discussed.

7.5.2.1. Slip Effect between Flame and Acoustic Displacement

The slip effect between the displacement of the flame and the acoustic displacement is explained on the basis of Fig. 7.28. It show a cross-sectional slice of a single flame configuration at an axial location of $x = 0.05$ m, Fig. 7.28 (top). Fig. 7.28 (bottom) compares the heat release rates without excitation (left) and the distribution for transverse acoustic forcing with 10,500 Hz. In the illustration of the heat release rate distribution under forced conditions also the transverse acoustic velocity vector field is indicated by arrows.

For the steady state case without excitation, the zone of intense heat release is almost circular, see Fig. 7.28 (bottom/left). Small deviations from a circular shape originate from the hexagonal shaped cross-sectional area. The heat release occurs within a thin mixing and reaction zone between the O_2 in the center and the surrounding H_2.

When transverse acoustic velocity fluctuations are imposed on the single flame configuration, the shape of the heat release rate distribution changes in comparison to the steady state field, see Fig. 7.28 (bottom/right). It shows the heat release rate and the velocity vector field at the instant of highest velocity in upwards direction. The maximal velocity is approximatively 25 m/s. In this situation, the field of $\dot{q}$ is squeezed and the center of gravity of the flame according to Eq. (6.103) is displaced upwards. Since the acoustic velocity displaces the flame towards higher acoustic pressure, the Rayleigh integral according to Eq. (6.65) is positive yielding an energy transfer into the feedback loop.

Essentially, the flattening of the heat release zone is based on different displacement amplitudes in regions of different density. The inner O_2 core with high density is hardly

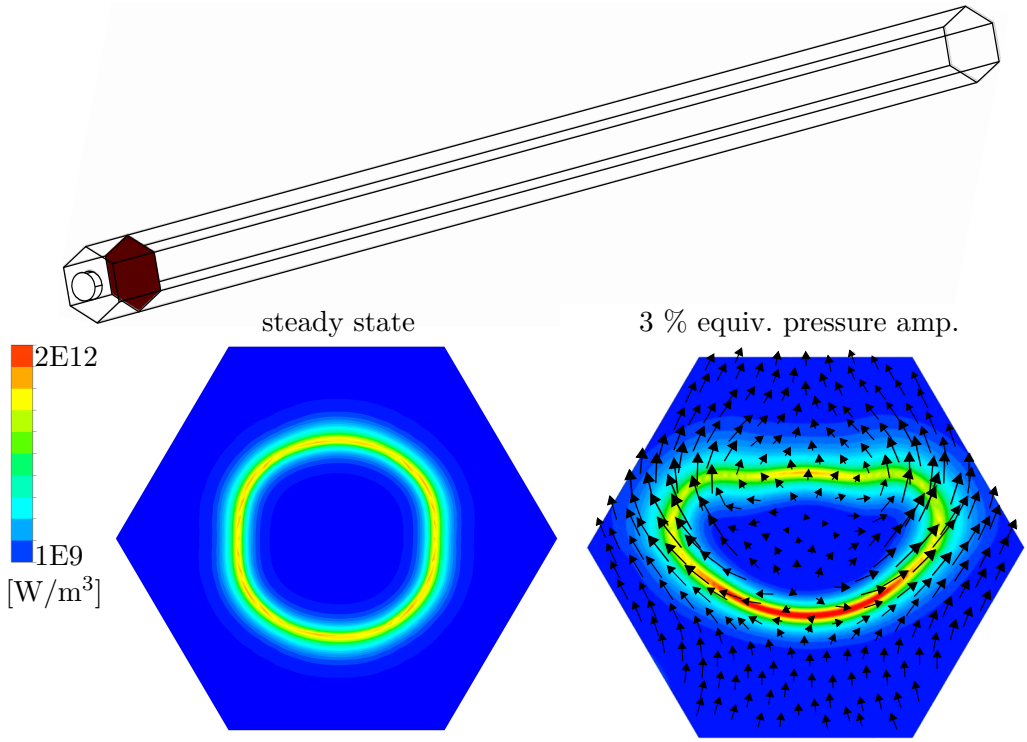

Fig. 7.28.: Top: Visualization plan. Bottom/left: Volumetric heat release rate $\dot{q}$ under steady state conditions. Bottom/right: Volumetric heat release rate $\dot{q}$ and transverse velocity vector field under transverse acoustic forcing conditions with 10,500 Hz and 3 % pressure equivalent excitation amplitude.

displaced in transverse direction. In contrast, the light H_2 and combustion products in the outer circular area are displaced significantly stronger, see Fig. 7.28 (bottom). In consequence, the acoustic streamlines bend around the O_2 core. Due to the periodic vertical displacement, an accumulation of H_2 and products occurs on both sides of the O_2 core leading to an horizontal expansion of the reaction zone. Due to mass conservation, the regions below and above the inner O_2 core get smaller, leading to a compression in vertical direction.

In Fig. 7.28 (bottom/right), increased heat release rates on the *windward* side of the dense O_2 core are observed. The increased heat release rates on the windward side originate from intensified turbulent mixing, which in turn is explained by higher shear forces between the weakly displaced dense O_2 core in the center and the strongly displaced light H_2 and combustion products in the outer circular area. Essentially, higher shear forces due to large velocity differences between O_2 and H_2 as well as combustion products result in an increased turbulent kinetic energy k_t and, in consequence, higher reactions rates and hence heat release rates, cf. Eq. (6.41).

However, according to the definition of the center of gravity of the flame (Eq. (6.103)),

the increased heat release rates on the windward side reduce the flame displacement. This reduction of the flame displacement in comparison to the acoustic displacement is referred to as slip. Since the windward side changes periodically with the direction of the transverse acoustic velocity, the slip effect reduces the overall flame displacement at each instant in time.

The Flame Transfer Functions for velocity coupling FTF^{Δ} describes the slip effect by the ratio of Flame Displacement $\hat{\Delta}_{\mathrm{fl}}$ and acoustic displacement $\hat{\Delta}_{\mathrm{ac}}$, cf. Eq. (6.75). In general, the FTF^{Δ} is a complex-valued quantity, since the maximum flame displacement and the highest acoustic displacement do not necessarily need to be in phase. In the following, the Flame Transfer Functions for velocity coupling are presented.

7.5.2.2. Flame Transfer Functions of Velocity Coupling

To quantify the driving potential of flame displacement, the Flame Transfer Function FTF^{Δ} according to Eq. (6.75) is determined. The displacement of the flame's center of gravity is determined according to Eq. (6.103). As explained in Sec. 6.5.2, the acoustic displacement is measured at a position close to the outlet of the computational domain. Specifically, it is determined at

$$\hat{\Delta}_{\mathrm{ac}} = \hat{\Delta}_{\mathrm{ac}}(x_{\Delta} = 200 \text{ mm}). \tag{7.18}$$

At this location combustion is complete and a realistic acoustic displacement in the light product gas on the center axis is present. However, the acoustic displacement is not determined from the same excited CFD simulation as the displacement of the flame's center of gravity, cf. Sec. 6.5.2. Instead, a second excited CFD simulation is conducted using a excitation source term with constant amplitude in axial direction. The excitation amplitude is chosen such that it corresponds to the excitation amplitude at a reference location in the first excited CFD simulation. The reference location is defined where the strongest displacement of the flame's center of gravity has been observed in the first CFD simulation.

In case of the BKD test chamber, the strongest displacement of flame's center of gravity has been found at $x = 40$ mm for LP1-4. In consequence, the source term for transverse velocity excitation for the second computation is given by

$$S_{\xi} = -\frac{\partial}{\partial \xi}\left(-A_e \sin(k_{\mathrm{T}_1}\xi)\left[\mathfrak{Re}(P_{\mathrm{T}_1}(40 \text{ mm}))\cos(\omega t) - \mathfrak{Im}(P_{\mathrm{T}_1}(40 \text{ mm}))\sin(\omega t)\right]\right), \tag{7.19}$$

The FTF^{Δ} is presented in Fig. 7.29 for LP1-4 in terms of amplitude and phase. The considered frequency range is the same as already used for the presentation of the $\mathrm{FTF}^{\mathrm{p}}_{\mathrm{n}}$ and $\mathrm{FTF}^{\mathrm{p}}_{\mathrm{f}}$, see Fig. 7.27.

It can be seen in Fig. 7.29, that both amplitude and phase of FTF^{Δ} are approximatively independent of frequency. Furthermore, LP2-4 show similar amplitudes, while lowest amplitudes are observed for LP1. However, the amplitudes reach at most 0.5,

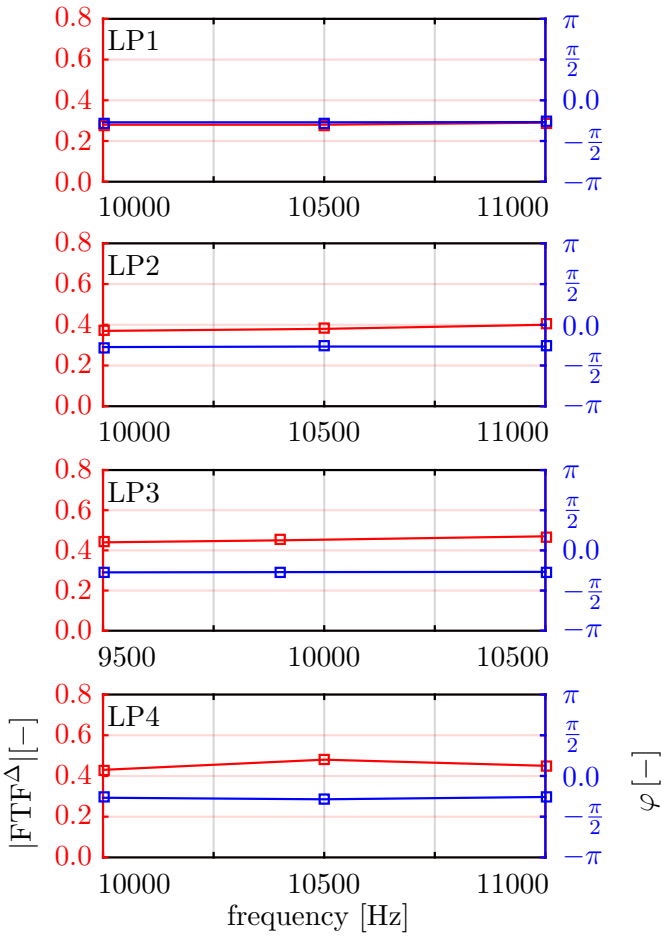

Fig. 7.29.: Displacement Flame Transfer Functions FTF^{Δ} for LP1-4 in terms of amplitude (red) and phase (blue).

indicating a strong slip between flame displacement and acoustic displacement. In consequence, the influence of increased heat release rates at the windward side of the O_2 core, cf. Fig. 7.28, significantly reduces the overall displacement of the flame's center of gravity. Moreover, an approximately constant phase of $-\frac{1}{4}\pi$ exists for all LP over the considered frequencies. Consequently, the maximal acoustic displacement and the displacement of the flame's center of gravity are not in phase.

7.5.3. Heat Release Source Terms for Pressure Coupling and Velocity Coupling in the Acoustic Simulations

In the acoustic simulations of the closed loop system, the fluctuating heat release source terms for pressure coupling according to Eq. (6.96) in the nearfield using $\mathrm{FTF}_{\mathrm{n}}^{\mathrm{p}}$ and farfield employing $\mathrm{FTF}_{\mathrm{f}}^{\mathrm{p}}$, see Fig. 7.27, are applied spatially decoupled in accordance with their regions of definition, see Sec. 7.5.1.1. The distributions of the fluctuation source terms for pressure and velocity coupling are shown in Fig. 7.30.

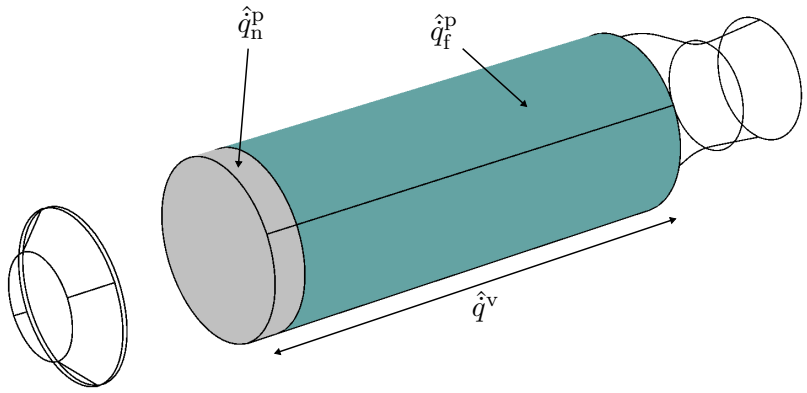

Fig. 7.30.: Fluctuating heat release source terms due to pressure coupling in the nearfield and farfield as well as due to velocity coupling in the entire chamber.

In consequence, the source terms for pressure coupling are explicitly given by

$$\hat{q}^{\mathrm{p}} = \begin{cases} \hat{q}^{\mathrm{p}}_{\mathrm{n}} = \mathrm{FTF}^{\mathrm{p}}_{\mathrm{n}} \frac{\hat{p}(x_{\mathrm{n}})}{\bar{p}(x_{\mathrm{n}})} \frac{\bar{\dot{Q}}_{\mathrm{n}}}{V_{\mathrm{n}}} & \text{if } 0\,\mathrm{mm} \leq x < 0.013\,\mathrm{mm} \\ \hat{q}^{\mathrm{p}}_{\mathrm{f}} = \mathrm{FTF}^{\mathrm{p}}_{\mathrm{f}} \frac{\hat{p}(x_{\mathrm{f}})}{\bar{p}(x_{\mathrm{f}})} \frac{\bar{\dot{Q}}_{\mathrm{f}}}{V_{\mathrm{f}}} & \text{if } 0.013\,\mathrm{mm} \leq x \leq 0.215\,\mathrm{mm}. \end{cases} \tag{7.20}$$

and the source term for velocity coupling is given

$$\hat{q}^{\mathrm{v}} = \frac{1}{2}\,\mathrm{FTF}^{\Delta} \frac{\pi^2 \bar{\dot{Q}}_{\mathrm{SF}}}{(\pi^2-4)V_{\mathrm{SF}}} \frac{\pi\xi \sin\left(\frac{\pi}{R_{\mathrm{SF}}}\sqrt{\xi^2+\eta^2}\right)}{R_{\mathrm{SF}}\sqrt{\xi^2+\eta^2}} \cdot \frac{\hat{v}}{\mathrm{i}\Omega} \cdot \mathfrak{s}(x) \;\text{ if }\; 0.0\,\mathrm{mm} \leq x \leq 0.215\,\mathrm{mm}, \tag{7.21}$$

cf. Eq. (6.105). The complete fluctuating heat release source term for the application in the acoustic simulations is finally given by the sum of $\hat{q}^{\mathrm{p}}$ and $\hat{q}^{\mathrm{v}}$, i.e.

$$\hat{q} = \hat{q}^{\mathrm{p}} + \hat{q}^{\mathrm{v}}. \tag{7.22}$$

7.5.4. Rayleigh Integrals

To reveal the different contributions of pressure coupling in the nearfield and farfield as well as of the velocity coupling to the amplification of acoustic amplitudes, the individual Rayleigh integrals are calculated and compared to each other. In comparison to the response factor, the Rayleigh integral takes the detailed distribution of the acoustic pressure in the system into account and indicates the temporally averaged energy transfer into the feedback loop over one acoustic cycle, cf. Eq. (2.104).

The Rayleigh integrals are calculated on the basis of the frequency space definition according to Eq. (2.105). In consequence, the Rayleigh integrals for the pressure coupling in the nearfield $\mathrm{Ra}^{\mathrm{p}}_{\mathrm{n}}$ and in the farfield $\mathrm{Ra}^{\mathrm{p}}_{\mathrm{f}}$ as well as for the velocity coupling Ra^{v}

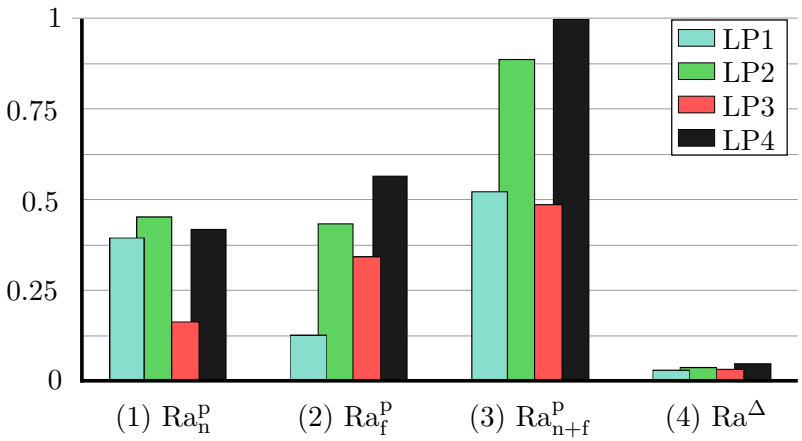

Fig. 7.31.: Comparison of normalized Rayleigh integrals for LP1-4 in terms of: (1) Nearfield, (2) Farfield, (3) Nearfield + farfield, (4) Displacement.

are given by

$$\mathrm{Ra}^{\mathrm{p}}_{\mathrm{n}} = \frac{1}{2}\mathfrak{Re}\int_{V_{\mathrm{n}}} \hat{q}^{\mathrm{p}}_{\mathrm{n}} \cdot \hat{p}^{*} dV, \tag{7.23}$$

$$\mathrm{Ra}^{\mathrm{p}}_{\mathrm{f}} = \frac{1}{2}\mathfrak{Re}\int_{V_{\mathrm{f}}} \hat{q}^{\mathrm{p}}_{\mathrm{f}} \cdot \hat{p}^{*} dV, \tag{7.24}$$

$$\mathrm{Ra}^{\mathrm{v}} = \frac{1}{2}\mathfrak{Re}\int_{V_{cc}} \hat{\dot{q}}^{\mathrm{v}} \cdot \hat{p}^{*} dV. \tag{7.25}$$

In case of pressure coupling, the Flame Transfer Functions with injector are used, cf. Fig. 7.27.

In Eq. (7.23) - (7.25), the different heat release source terms and the acoustic pressure are evaluated from the acoustic simulations of the closed loop system, i.e. from the simulations with $\hat{\dot{q}}$ included in the energy equation of the LEE. The source term definitions and the respective volume integration zones for the pressure coupling in the nearfield and farfield as well as for the velocity coupling are given in Sec. 7.5.3.

In Fig. 7.31 the volume-integrated Ra for the different coupling types are shown for LP1-4. Additionally, the sum of pressure coupling in nearfield and farfield $\mathrm{Ra}^{\mathrm{p}}_{\mathrm{n+f}}$ is presented in order to compare it to the Rayleigh integral of the velocity coupling Ra^{v}. The values are normalized by the maximum value, which is given by the sum $\mathrm{Ra}^{\mathrm{p}}_{\mathrm{n+f}}$ for LP4.

In the nearfield, the unstable LP2/4 show similar $\mathrm{Ra}^{\mathrm{p}}_{\mathrm{n}}$ values, which are only slightly higher than in case of LP1. The lowest value of approximately two thirds smaller than for LP2 is found for LP3. Interestingly, the highest flame length establishes in case of LP3, which might be the reason for the low driving potential in its nearfield. The order of increasing $\mathrm{Ra}^{\mathrm{p}}_{\mathrm{n}}$ corresponds to the order of increasing response factors for the nearfield, see Tab. 7.8. In the farfield the highest $\mathrm{Ra}^{\mathrm{p}}_{\mathrm{f}}$ is found for LP4. LP2 shows a driving potential of approximately 12 % less than for LP4. Substantially lower values are found for LP1 and LP3. The comparison between the total Ra values for pressure

coupling $\mathrm{Ra}^{\mathrm{p}}_{\mathrm{n+f}}$ and velocity coupling Ra^{Δ} indicates that the contribution of the velocity coupling to the amplification of acoustic amplitudes is far less significant.

Overall, it can be seen that all Ra are positive. This shows that each coupling type contributes to the amplification of acoustic amplitudes. Furthermore, for each coupling type, LP2 and LP4 provide the highest Rayleigh integrals. In consequence, the overall driving potential of acoustic amplitudes is higher for LP2 and LP4 than for LP1 and LP3.

Interestingly, unstable BKD operation is observed in case of LP2 and LP4, which provide the highest Rayleigh integrals, cf. Tab. 5.1. In consequence, unstable operation might be explained by the stronger heat release feedback for these specific load point specifications.

7.6. Stability Behavior of the BKD Test Chamber

In this final section, the numerical linear stability assessments for the BKD test chamber are conducted for the T^{α}_{1} mode for the different LP. First, the damping rates for the closed loop system calculated on the basis of the stability assessment procedure are compared to experimental validation data. Afterwards, the influences of the nozzle and the dome coupling on the damping rates are revealed and the contributions to the amplifications of acoustic amplitudes by pressure coupling and velocity coupling are determined. Finally, sensitivity studies concerning the dependency of the damping rate on the grid resolution and on the stability coefficient α_{τ} of the numerical stabilization method are presented.

7.6.1. Linear Stability Assessment

The stability assessment is performed for LP1-4, cf. Tab. 5.1. For this purpose, the previously presented dome coupling scattering matrices, see Sec. 7.2, and FTF for pressure and velocity coupling, see Sec. 7.5, are included into the acoustic simulation and the complex eigenfrequencies of the closed loop system are solved.

As explained in Sec. 3.3.1, the dome coupling scattering matrix and the FTF need to be evaluated at the complex frequency Ω for the acoustic simulation of the closed loop system. For this purpose, complex fits of the reflection and transmission coefficients as well of the FTF are required, cf. Eq. (3.21). However, the experimental results reveal that the order of magnitude of the T^{α}_{1} mode eigenfrequencies (in [Hz]) is $\mathcal{O}(4)$, which is considerable larger than the order of magnitude of the damping rates. In fact, if the parameter extraction method is considered as reference, λ (in [rad/s]) is of the order of $\mathcal{O}(2)$ for the stable LP and of $\mathcal{O}(1)$ for the unstable LP, cf. Tab. 5.2. According to Sec. 3.3.1, these large scale differences allow to reduce the dependency of the scattering matrix elements and of the FTF to only the frequency ω, cf. Eq. (3.24). This dependency is already available from the previously presented scattering matrix investigations, cf. Sec. 7.2, and FTF analyses, cf. Sec. 7.5. Hence, it is not necessary to generate complex-valued fits.

Tab. 7.10.: Comparison of λ [rad/s] between numerical results calculated on the basis of the stability assessment procedure and the experimental findings.

λ [rad/s]	Stability assessment procedure	Lorentzian fitting	Parameter extraction method $A(t)$	Parameter extraction method $B(t)$
LP1	420	2199 ± 63	[200; 500]	[200; 500]
LP2	-14	n.a.	[−40; −30]	[−40; −30]
LP3	155	2011 ± 13	[180; 390]	[180; 390]
LP4	-24	n.a.	[−31; −29]	[−40; −37]

In general, the mode shape might change due to the presence of feedback. In consequence, the determination of the FTF on the basis of excitation procedures has to be performed iteratively until convergence is achieved. It could be shown, however, that the mode shapes are only irrelevantly changed if the fluctuating heat release source term is included. Essentially, a comparable amplitude distribution is calculated and the phase is altered only slightly in the rear part of the chamber, see App. Q. The effect on the FTF in both nearfield and farfield is therefore very low and iterations are hence not performed to reduce computational turnaround times.

In order to reach a converged acoustic solution, a maximum of 3-5 Arnoldi iteration steps are typically necessary, cf. Sec. 3.2.2.2, yielding a simulation time of 5-8 min on a 6x3.0 GHz core machine with 64 Gbyte RAM. It is found that the results in terms of eigenfrequency convergences rapidly with respect to the dependence on ω, see Sec. 3.2.2.2. Already the second iteration yields converged results, reducing computational turnaround times considerably.

The eigenfrequencies of the T_1^α mode were already validated and found in excellent agreement with experimental findings, see Tab. 7.3. Since in this section acoustic simulations of the closed loop system are conducted, the influence of the fluctuating heat release source term on the eigenfrequencies can be determined. It is found that the relative change of the eigenfrequencies between the open and closed loop system is considerably below 1 %. Therefore, in the following only the damping rates are further analyzed.

The damping rates determined from the stability assessment procedure are compared to the experimental findings, which were determined on the basis of the Lorentzian fitting and the parameter extraction method (see Sec. 5.4), in Tab. 7.10. It can be seen that the prediction by the stability assessment procedure is in agreement with the experimentally observed stability behavior. For LP1 and LP3 positive damping rates are predicted confirming stable operation. Furthermore, for LP2 and LP4 negative damping rates are found. Negative damping rates indicate the onset of an instability for the T_1^α mode, cf. Eq. (6.1). High amplitudes are also observed for LP2 and LP4 in the experimental procedures, cf. Sec. 5.1.

The quantitative comparison of the numerical results and the experimental evaluations shows that a good match for λ is obtained, if the parameter extraction method is

considered as reference. For LP1, the stability assessment procedure predicts $\lambda = 420$ rad/s, which lies well within the λ range calculated on the basis of the parameter extraction method. A larger discrepancy is found for LP3. The numerical result is slightly lower than the finding of the parameter extraction method. However, considering the spectrum of complex process involved in the thermoacoustic feedback loop and the made assumption for the development of the stability assessment procedure, see. Sec. 6.1, the relative deviation of approximately 14 % from the lower limit of the range determined with the parameter extraction method, appears to be within expected error margins.

As already discussed, the damping rates for the stable LP1 and LP3 computed on the basis of the Lorentzian fitting procedure are signifiantly larger than the results calculated with the parameter extraction method. In consequence, the discrepencies between the Lorentzian fitting results and the numerical findings are equally large. Although this cannot be considered as proof for the validity of the parameter extraction method, the numerical results nevertheless suggest that the Lorentzian fitting procedure overestimates the damping rates.

For the unstable LP, experimental validation data is only available from the parameter extraction method, see Sec. 5.4.2. While the numerical results are quantitatively slightly too low, the order of magnitude is well simulated. Quantitatively, the predicted (negative) damping rates for LP2 and LP4 are approximatively 50 % too low. The small stability margins for LP2 and LP4 are well predicted by the stability assessment procedure showing again its capability of capturing minor changes in the operation conditions.

7.6.2. Identification of Main Contributors to Damping and Amplification

The stability assessment procedure is now deployed to identify the main contributors to the gain and loss of acoustic energy in the system. For this purpose, the eigenvalue studies are repeated including and excluding individual components to evaluate their impact on the damping rate. The comparison is based on the calculated λ.

The different contributions of each damping and amplification mechanism are shown in Fig. 7.32 for LP1-4. The stability limit (i.e. $\lambda = 0$) is shown in the center of the plot. Since damping effects increase λ, they are plotted in positive λ direction. In contrast, amplification effects reduce λ and are therefore negative. The quantitative comparison of the different contributions is given in App. R. In the following, Fig. 7.32 is explained and discussed in detail.

For each LP the damping rate for the open loop and the closed loop system are determined. The damping rate for the closed loop system corresponds to the results already presented in Tab. 7.10. Therefore, the closed loop contains all damping and amplification effects. In contrast, the open loop system does not include the dynamic heat release rate fluctuations. This is realized by setting the fluctuating heat release source term zero

$$\hat{\dot{q}} = 0. \tag{7.26}$$

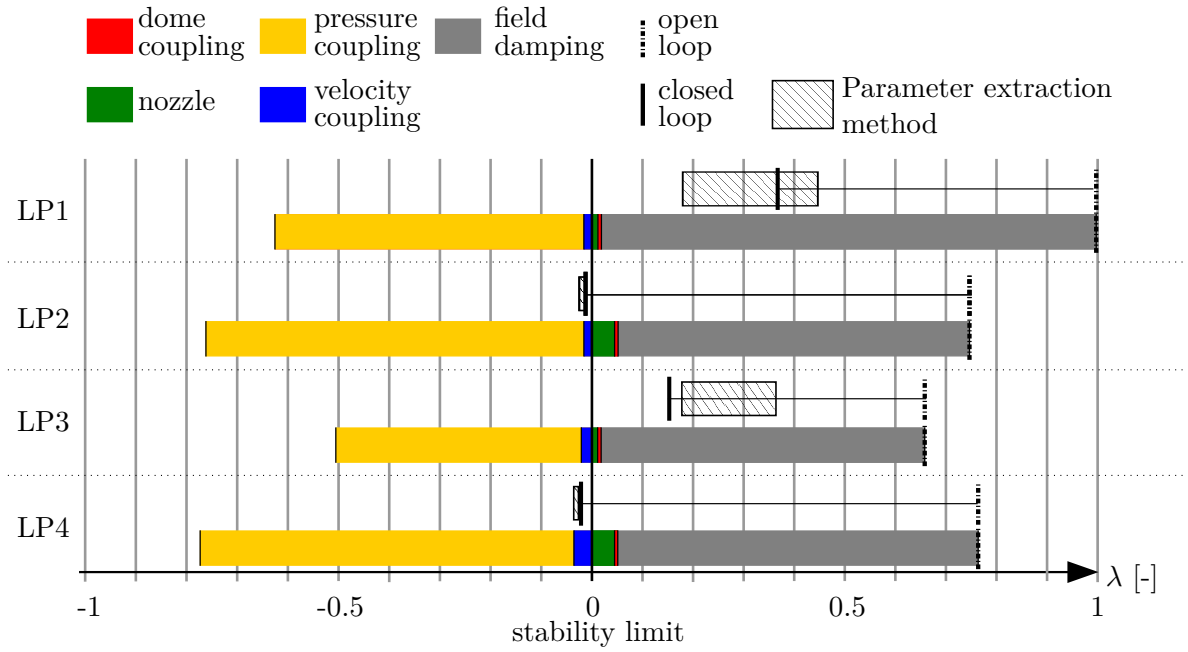

Fig. 7.32.: Individual contributions of damping and amplification effects for the T_1^{α} mode and LP1-4 visualized on the basis of the normalized damping rate. For the parameter extraction method, mode $A(t)$ is used. The quantitative comparison is given in App. R.

In the absence of the dynamic heat release rate fluctuations, only positive damping rates are calculated, indicating damped systems. Furthermore, the difference between the open loop and the closed system reveals the impact of the fluctuating heat release due to pressure and velocity coupling.

The lowest damping rate for the open loop system is found for LP1. This lowest damping rate is used for the normalization of the damping rates presented in Fig. 7.32. Therefore, the normalized damping rate of the open loop system of LP1 is unity. The normalization of the damping rates using the reference damping rate of the open loop system of LP1 allows to compare the influences of the different damping and amplification effects between the LP.

In Fig. 7.32, two rows are shown for each LP. In the first row, the normalized damping rates for the open loop (vertical black dash-and-dotted line) and closed loop systems (vertical black line) are presented. Furthermore, the ranges of the computed damping rates using the parameter extraction method are plotted. It can again be seen that the numerical results of the closed loop system agree well with the findings on the basis of the parameter extraction method. The Lorentzian fitting results are not shown due to the large deviations from the numerical results.

In the second row, the individual contributions to damping and amplification, respectively, are shown. The individual contributions are indicated by different colors. In the

following, the individual contributions are discussed.

7.6.2.1. Dampening Effects

First, the influences of the nozzle and of the dome coupling are investigated. For this purpose, acoustic simulations are performed with the fluctuating heat release source term $\hat{\dot{q}}$ included, but the nozzle and dome coupling, respectively, are excluded. Afterwards, the change in damping rate in comparison to the full system including both the nozzle and the dome coupling, is determined.

To exclude the influences of the nozzle and the dome coupling on the damping rates, the corresponding boundary conditions are set energetically neutral, see Fig. 7.33. In case of the dome coupling, the O_2 dome is removed from the computational domain and the energetically neutral condition in terms of the reflection coefficient according to Eq. (2.97) is imposed at face plate. However, although the dome is not included into the acoustic simulation, the FTF for pressure coupling determined with the O_2 injector included are nevertheless used, cf. Sec. 7.5.1.2. In consequence, dome coupling only describes the damping effect inherently described by the acoustic scattering matrix between the chamber and the O_2 dome, see Sec. 7.2.2.

In contrast, to exclude the nozzle from the simulation, the nozzle volume is removed from the computational domain and only the cylindrical combustion chamber and the O_2 dome are retained. At the outlet of the combustion chamber the energetically neutral boundary conditions according to Eq. (2.97) is applied.

The contributions of the nozzle damping and the dome coupling to the damping rate of the open loop system are presented in normalized form in Fig. 7.32 for LP1-4. The influence of the dome nozzle damping is plotted in green and the impact of the dome coupling is plotted in red. It can be seen that the influence of the dome coupling on the damping rate is very weak for all LP. In fact, in comparison to the open loop damping rate, its influence is well below 1 %.

The damping contribution of the nozzle differs between the LP. For the stable LP1 and LP3, the contribution is similarly low and is comparable to the contribution of the dome coupling. The low influence can be explained by the short axial length of the T_1^α mode in case of these LP, cf. Fig. 7.14 (top). The short axial extent in turn can be explained by the strong axial decay. This leads to insignificant pressure amplitudes at the downstream boundary condition. In consequence, the nozzle is spatially decoupled from the T_1^α mode and can thus not influence the T_1^α mode damping. In contrast, since the axial decay is less significant for LP2 and LP4, higher pressure amplitudes are present at the nozzle, cf. Fig. 7.14 (top). In consequence, a higher impact of the nozzle on acoustic damping is present for these LP.

Fig. 7.32 reveals that the contributions of the dome coupling and of the nozzle on the open loop damping rates are low. Therefore, a significant contribution to the present damping of the T_1^α mode must originate from additional effects. These additional contributions are colored in gray and referred to as field damping. The physical mechanisms leading to field damping were discussed in Sec. 7.3.2.3.

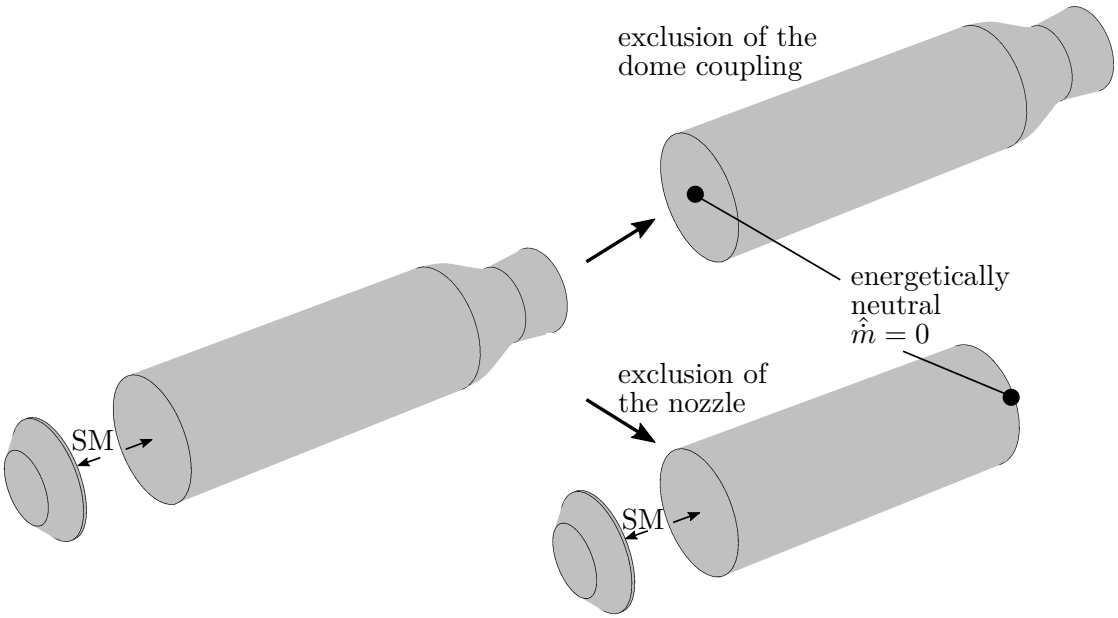

Fig. 7.33.: Computational domains and energetically neutral boundary conditions for the determination of the influences of the nozzle and the dome coupling on the damping rates.

7.6.2.2. Amplification Effects

The overall contribution of the dynamic heat release to the amplification of the acoustic amplitudes can be determined from the difference in the damping rate between the open loop system and the closed loop system. By incorporating either the pressure coupling or the velocity coupling sequentially into the acoustic simulation, the different contributions can be separated. The subsequent incorporation of each coupling is realized by including the respective fluctuating heat release source terms individually.

First, only the fluctuating heat release source term for the pressure coupling according to Eq. (7.20) is included into the acoustic simulation and the damping rate is calculated. For this purpose, the Flame Transfer Functions calculated with the O_2 injector included are used. This reveals only the influence of the pressure coupling on the damping rate of the closed loop system. The contribution is shown in yellow in Fig. 7.32. Subsequently, only the source term for velocity coupling according to Eq. (7.21) is included into the acoustic simulations. From the determined damping rate, the contribution of velocity coupling can be determined. The contributions are highlighted in blue in Fig. 7.32.

Finally, the main contributor to amplification can be revealed. It can be seen in Fig. 7.32 that the amplification due to pressure coupling is more significant than velocity coupling. This conclusion is in agreement with the Rayleigh integrals, see Fig. 7.31.

7.6.3. Final Remarks on the Stability Assessment

In Fig. 7.32, the small stability margins can be recognized for LP2/4. These small margins show the importance of each single contributor to damping and amplification. Although the main contributors are essential to detect the correct order of magnitude, the effects of nozzle damping or transverse velocity coupling might still be the crucial factor for meaningful stability predictions.

Having the contributions of the damping and amplification effects separated, the reasons for the stability behavior of LP1-4 can be revealed. It can be seen in Fig. 7.32 that it is the stronger amplification by the dynamic heat release rate fluctuations together with the moderate overall damping which lead to negative damping rates for LP2 and LP4. In contrast, intense damping and only moderate flame feedback in case of LP1 are not sufficient to reach a negative damping rate. In consequence, initial noise excitation is constantly damped and high amplitudes can therefore not develop. Interestingly, although the overall damping is lowest for LP3, the weak flame feedback prevents the acoustic amplitude from growing in time. This might be explained by unequal eigenfrequencies of the T_1^α mode in the chamber and the L_2 mode in the O_2 injector and hence by the low influence of the O_2 injector the flame feedback.

The presented evaluations of the contributions to damping and amplification are only approximatively. Essentially, a mutual dependence exists. For example, a slightly changed spatial distribution of pressure amplitudes due to the absence of feedback also affects the influence of the nozzle on damping. As already explained, however, the influence of feedback on the mode shape is very small, cf. App. Q.

7.6.4. Sensitivity Studies

Finally, the dependencies of the eigenfrequency and the damping rate on the numerical grid resolution and stabilization coefficient α_τ of the stabilized finite element method, cf. Sec. 3.2.1, are studied. Furthermore, the necessary accuracy of the FTF in terms of amplitude and phase is evaluated in order to determine the error tolerances in the dynamic CFD simulations.

7.6.4.1. Dependence of T_1^α Mode Eigenfrequency and Damping Rate on Grid Resolution and Stability Coefficient

As already presented for the non-reactive conditions, the sensitivity of the eigenfrequency f and the damping rate λ towards the grid resolution and the stability coefficient α_τ is studied, cf. Sec. 4.2.2.4. For illustrative purposes, the T_1^α mode in case of LP2 is chosen. The findings are presented in Fig. 7.34.

Within the considered DOF range the eigenfrequency is almost constant. In consequence, the used grid size is absolutely sufficient to accurately capture the eigenfrequencies of the T_1^α mode. In contrast, λ strongly oscillates within the lower DOF range and convergences to a rather constant value above approximately 300,000. As already

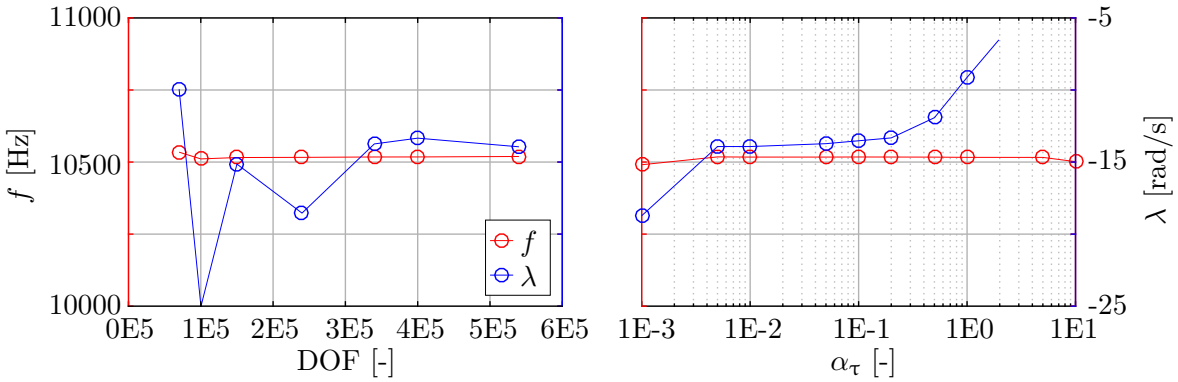

Fig. 7.34.: Grid convergence analysis (left) and dependency of eigenfrequency on the stabilization coefficient (right).

said, 340,000 DOF are finally used to conduct the stability assessments. This number of DOF represents a reasonable trade-off between computational turnaround times and numerical accuracy and consistency.

The dependence on α_τ is found similar to the behavior in case of the non-reactive test case, see Sec. 4.2.2.4. The eigenfrequency does not show relevant changes within the entire considered α_τ range. For the damping rate, an intermediate range with constant results is identified, which is in very good agreement with the corresponding region of constant values found for the non-reactive test case, cf. Fig. 4.17. Below this range, the damping rate tends towards more unstable predictions, while higher values of α_τ lead to artificially high damping generated by the numerical discretization.

The sensitivity studies both for the non-reactive test case, cf. Sec. 4.2.2.4 as well as for the reactive BKD test chamber reveal that the stabilization coefficient should be chosen from the range of α_τ = [1E-2; 1E-1] in order to provide negligible influence of numerical stabilization on acoustic damping as well as on eigenfrequencies. Therefore, this α_τ range is recommended for future studies using the frequency space transformed LEE together with GLS stabilization technique. Throughout this thesis a value of $\alpha_\tau = 0.1$ was used, yielding reasonable results.

7.6.4.2. Dependency of Damping Rate on FTF$^{\mathrm{p}}$

In this section, the dependency of the damping rate on the Flame Transfer Functions are revealed. For this purpose, only pressure coupling is taken into account since it is the main contributor to the amplification of acoustic amplitudes, cf. Fig. 7.32. To show the dependency of the damping rate on the FTF$^{\mathrm{p}}$, amplitude and phase of FTF$^{\mathrm{p}}_{\mathrm{n}}$ as well as of FTF$^{\mathrm{p}}_{\mathrm{n}}$ are varied within a range of $\delta = \pm 20\%$ for LP2. The results are shown in Fig. 7.35. The stability limit of $\lambda = 0$ is indicated by the dash-dotted line. It is used to determine the tolerable deviation in terms of amplitude and phase to still predict the correct stability behavior. Furthermore, the arrows indicate the reduction or increase of amplitude and phase, respectively.

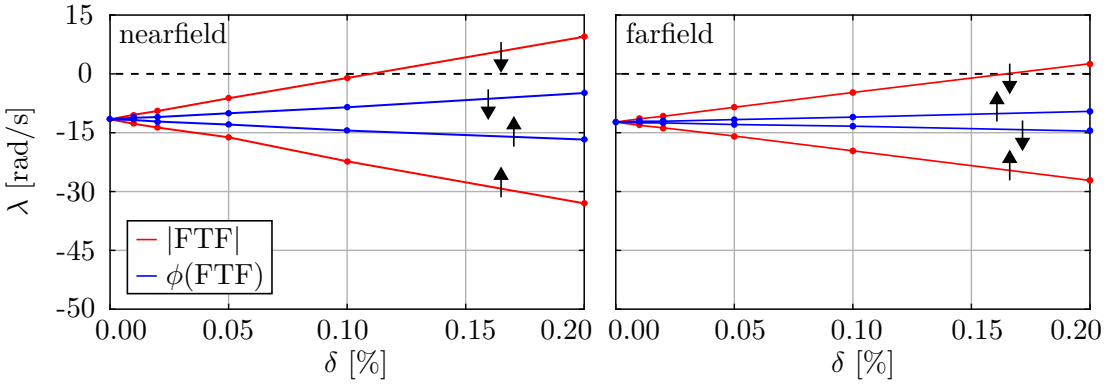

Fig. 7.35.: Dependency of λ on amplitude and phase of $\mathrm{FTF}_{\mathrm{n}}^{\mathrm{p}}$ and $\mathrm{FTF}_{\mathrm{f}}^{\mathrm{p}}$.

First, the sensitivity of the nearfield $\mathrm{FTF}_{\mathrm{n}}^{\mathrm{p}}$ is discussed. The dependency of the damping rate on the variation of amplitude and phase of $\mathrm{FTF}_{\mathrm{n}}^{\mathrm{p}}$ is shown in Fig. 7.35. It is observed that the damping rate depends linearly on the changes of both amplitude and phase for the considered range. An increasing amplitude hence lead linearly to higher damping rates, while its reduction reduces the damping rate by the same factor.

Since the phase of $\mathrm{FTF}_{\mathrm{n}}^{\mathrm{p}}$ is negative, a reduction leads to a more stable behavior and vice versa, cf. Fig. 7.27. In general, the same almost linear behavior is found. However, the dependence of λ on the relative change of the phase is weaker in comparison to the amplitude dependence. In consequence, a higher accuracy for the amplitude is more important than for the phase to correctly determine the stability behavior in the nearfield.

Overall, to correctly predict the linear stability, an accuracy of approximately 10 % is necessary in terms of amplitude. As the sensitivity towards the phase is less important, a reduced accuracy can be tolerated.

A similar behavior is found for the farfield FTF. As the phase of $\mathrm{FTF}_{\mathrm{f}}^{\mathrm{p}}$ is positive, an increase leads to reduced damping rates, cf. Fig. 7.27. The overall dependence of λ on the relative changes of amplitude and phase in the farfield is lower than in the nearfield. Ultimately, the tolerable discrepancies in order to still predict the correct stability behavior is higher and given by approximately 16 %.

8 Conclusions and Future Work

A CFD/CAA methodology for the assessment of linear stability in rocket engines was introduced. The stability assessment procedure is capable of describing the acoustic propagation within the combustion chamber, the nozzle and the propellant domes on the basis of realistic axially distributed mean flows. Furthermore, the acoustic effects of small subcomponents such as injectors and resonating cavities in absorber ring arrangements can be included in the stability assessment in form of frequency dependent reflection coefficient boundary conditions and scattering matrices. The procedure is implemented such that a high flexibility is maintained to rapidly evaluate the influence of redesigned components or to determine the impact of substituted propellant combinations on stability. The quick evaluation process is obtained through scale separation, allowing for coarse grids in the acoustic simulations, the calibration of mean flow profiles and dynamic flame response models based on single flame configurations and the application of frequency space transformed linearized Euler equations, which provide significant advantages over time domain calculations for complex acoustic analyses in the linear regime.

The methodology is extensively validated for non-reactive, ambient conditions. The focus is on the dome coupling, nozzle acoustics as well as the influence of resonating cavities for longitudinal and transversal mode propagation under grazing flow conditions. Validation data is taken both from literature and from own experiments. Frequency space transformed LEE simulations based on stabilized Finite Element discretizations are highly suited to achieve consistent and reliable procedures as well as accurate results in terms of eigenfrequencies and damping rates. The findings show that the applied scattering matrix approach for the acoustic coupling of the chamber with the oxidizer dome describes the relevant dynamic effects adequately. Furthermore, absorber rings significantly alter the HF propagation in terms of mode separation and spatial shielding effects, which tremendously change the system dynamics possibly leading to reduced damping rates and increased eigenfrequencies.

The stability prediction quality is demonstrated on the basis of DLR's cryogenic H_2/O_2 BKD test chamber, which operates under realistic rocket engine conditions and shows self-sustained high amplitude combustion instabilities under certain operating conditions. The Soave-Redlich-Kwong real gas equation of state and a combined combustion model consisting of a mixing controlled Eddy-Dissipation Model for the forward reaction and kinetically controlled dissociation reaction are used to simulate the mean flow and to determine feedback models for two experimentally observed stable (LP1/3)

and two unstable (LP2/4) operating conditions. Furthermore, the injection conditions are varied to study the influence of the H_2 injection temperature and ROF on the first transverse eigenfrequency. The following conclusions are drawn:

- The first transverse mode class is decomposed into a face plate near T_1^α mode and the $T_1^\beta L_x$ mode, which exhibits high amplitudes in the entire chamber. The decomposition is based on the variation of speed of sound in axial direction. Only the T_1^α mode is found linearly unstable.
- The damping rates for the stable LP1/3 are one order of magnitude larger than for the unstable LP2/4, which are in turn found very close to the stability limit. The order of magnitudes of the damping rates are confirmed by the parameter extraction method. Even quantitative agreement is given. However, the Lorentzian fitting results suggest one order of magnitude larger damping rates for the stable load points.
- The linear stability is well predicted by the CFD/CAA approach. Therefore, the necessary sensitivity and accuracy in terms of injection conditions, related field mechanisms and boundary treatment are established.
- The usage of single flame configurations for the generation of axially distributed mean flow profiles and Flame Transfer Functions is justified and the assumption of radial compactness provides acoustically consistent results.
- O_2 injector dynamics are found important for the characterization of Flame Transfer Functions.
- Due to the good agreement of the simulated damping rates with experimental validation data, it can be concluded that URANS simulations are sufficient to capture the relevant flame dynamic effects.
- A comparison of the impact of each included damping and amplification mechanism on the damping rate reveals that a correct prediction of stability margins requires the incorporation of each contributor.
- Pressure coupling is the main contributor to amplification. A compact region close to the face plate is identified, in which dynamic heat release is dominated by shear layer mechanisms. This region spatially coincides well with the T_1^α. In the region further downstream, dynamic heat release is driven by baroclinique torque. Transverse velocity coupling is significantly weaker.
- Substantial damping is generated by the interaction of the acoustic fluctuations with the mean flow. This effect is essential to include into the simulation in order to reveal the linear stability.
- The T_1^α eigenfrequency is significantly affected by the H_2 injection temperature. Higher injection temperatures lead to reduced flame lengths, to increased speed of sound and hence to higher eigenfrequencies.
- The T_1^β eigenfrequency significantly depends on chemical equilibrium species composition and speed of sound in the chamber's rear part. Increasing ROF towards stoichiometry reduces speed of sound and therefore the eigenfrequency. Accurate

results for the ROF dependent eigenfrequencies shows that the chosen combustion modeling provides meaningful flame temperatures and species composition.

- Although LP2/4 operate at different pressure and total power output, similar flame lengths, acoustic pressure distributions in the chamber, Rayleigh integrals and linear (negative) damping rates are found both experimentally and numerically. The similarity is due to comparable injection temperatures of H_2 and ROF.

The following future work is proposed to extend the capabilities and provide further validation:

- For the generation of a reliable validation base from the dynamic pressure measurements concerning the damping rates, the validity of the parameter extraction method and the Lorentzian fitting procedure for the considered BKD test configuration should be carefully revealed. Afterwards, the numerical results need to be re-evaluated.
- The linear stability assessment should be tested for different propellant combinations. In (Schmid 2014; Schmid et al. 2014), FTF for MMH/NTO are readily available, but comprehensive stability investigations have not been performed yet. The flexibility of the stability assessment procedure might also be tested on the basis of GCH_4/O_2 (Celano et al. 2015).
- In order to simulate limit cycle amplitudes, non-linearity could be gradually incorporated in terms of flame dynamics, acoustic propagation and further non-linear models for the dome coupling as well as for absorber devices. Non-linear disturbance equations are especially suited for this purpose (Köglmeier et al. 2014b). The influence of an amplitude dependent mean flow should also be investigated. The mean flow at different amplitudes could be extracted from acoustically excited single flame simulations. First indications of reduced flame lengths with increasing amplitude were presented in this thesis. Finally, the relevance of each non-linear component should be evaluated on the basis of experimental data recorded in high pressure limit cycle conditions. The BKD HF-7 test case is recommended as validation base (Gröning et al. 2013b; Gröning 2014).
- Reduced order models offer the possibility to efficiently evaluated the stability assessment procedure in time domain. This will allow for the incorporation of random noise excitation and non-linear mode interaction as well as the analysis of standing and rotating mode effects (Hummel et al. 2015, 2016).
- The absorber impact on damping and on mode shapes should be reevaluated under reactive conditions. (Gröning et al. 2015c) presented a suitable BKD test case configuration.
- In future rocket engine systems the pressure drop over the injectors will be reduced in order to maximize efficiency. This demands a re-evaluation of the acoustic relevance of the feed and injection system including the dome and feed lines (Knab and Riedmann 2016).
- Although good comparison of linear damping rates was obtained, the simulated Flame Transfer Function remain a source of uncertainty. A thorough comparison

to experimental measurements is absolutely necessary. (Fiala 2015; Fiala and Sattelmayer 2015b) and (Schulze et al. 2016a) suggest the validation on the basis of OH* radiation as well as of Blue Radiation (Fiala and Sattelmayer 2015a), which requires a flamelet combustion model. Furthermore, LES simulations are suggested to validate the adequateness of URANS by comparison.

- An improved real-gas equation should be included into the CFD simulations in order to consistently analyze of the O_2 injector dynamics (Abudour et al. 2013).

APPENDIX

A LEE Compact Matrix Notation

The LEE's compact matrix notation is given by:

$$\mathcal{R} = \mathcal{L}(\hat{\underline{\phi}}) - \hat{\underline{\mathcal{S}}} = \Omega\hat{\underline{\phi}} + \underline{\underline{A}}\,\frac{\partial\hat{\underline{\phi}}}{\partial x} + \underline{\underline{B}}\,\frac{\partial\hat{\underline{\phi}}}{\partial y} + \underline{\underline{C}}\,\frac{\partial\hat{\underline{\phi}}}{\partial z} + \underline{\underline{D}}\,\hat{\underline{\phi}} - \underline{\underline{Q}}\,\hat{\underline{\phi}} - \hat{\underline{\mathcal{S}}} = 0, \tag{A.1}$$

with the primary variables

$$\hat{\underline{\phi}} = (\hat{\rho}, \hat{u}, \hat{v}, \hat{w}, \hat{p})^T. \tag{A.2}$$

The matrices and the load vector read:

$$\underline{\underline{A}} = \begin{pmatrix} \bar{u} & \bar{\rho} & 0 & 0 & 0 \\ 0 & \bar{u} & 0 & 0 & \frac{1}{\bar{\rho}} \\ 0 & 0 & \bar{u} & 0 & 0 \\ 0 & 0 & 0 & \bar{u} & 0 \\ 0 & \kappa\bar{p} & 0 & 0 & \bar{u} \end{pmatrix}, \; \underline{\underline{B}} = \begin{pmatrix} \bar{v} & 0 & \bar{\rho} & 0 & 0 \\ 0 & \bar{v} & 0 & 0 & 0 \\ 0 & 0 & \bar{v} & 0 & \frac{1}{\bar{\rho}} \\ 0 & 0 & 0 & \bar{v} & 0 \\ 0 & 0 & \kappa\bar{p} & 0 & \bar{v} \end{pmatrix}, \; \underline{\underline{C}} = \begin{pmatrix} \bar{w} & 0 & 0 & \bar{\rho} & 0 \\ 0 & \bar{w} & 0 & 0 & 0 \\ 0 & 0 & \bar{w} & 0 & 0 \\ 0 & 0 & 0 & \bar{w} & \frac{1}{\bar{\rho}} \\ 0 & 0 & 0 & \kappa\bar{p} & \bar{w} \end{pmatrix} \tag{A.3}$$

$$\underline{\underline{D}} = \begin{pmatrix} \frac{\partial\bar{u}_i}{\partial x_i} & \frac{\partial\bar{\rho}}{\partial x} & \frac{\partial\bar{\rho}}{\partial y} & \frac{\partial\bar{\rho}}{\partial z} & 0 \\ -\frac{1}{\bar{\rho}^2}\frac{\partial\bar{p}}{\partial x} & \frac{\partial\bar{u}}{\partial x} & \frac{\partial\bar{u}}{\partial y} & \frac{\partial\bar{u}}{\partial z} & \frac{1}{\bar{\rho}} \\ -\frac{1}{\bar{\rho}^2}\frac{\partial\bar{p}}{\partial y} & \frac{\partial\bar{v}}{\partial x} & \frac{\partial\bar{v}}{\partial y} & \frac{\partial\bar{v}}{\partial z} & 0 \\ -\frac{1}{\bar{\rho}^2}\frac{\partial\bar{p}}{\partial z} & \frac{\partial\bar{w}}{\partial x} & \frac{\partial\bar{w}}{\partial y} & \frac{\partial\bar{w}}{\partial z} & 0 \\ 0 & \frac{\partial\bar{p}}{\partial x} - \frac{\bar{p}}{\kappa-1}\frac{\partial\kappa}{\partial x} & \frac{\partial\bar{p}}{\partial y} - \frac{\bar{p}}{\kappa-1}\frac{\partial\kappa}{\partial y} & \frac{\partial\bar{p}}{\partial z} - \frac{\bar{p}}{\kappa-1}\frac{\partial\kappa}{\partial z} & \kappa\frac{\partial u_i}{\partial x_i} + \frac{\bar{u}_i}{\kappa-1}\frac{\partial\kappa}{\partial x_i} \end{pmatrix} \tag{A.4}$$

$$\underline{\underline{Q}} = (\kappa - 1)\begin{pmatrix} 0 & 0 & 0 & 0 & 0 \\ 0 & 0 & 0 & 0 & 0 \\ 0 & 0 & 0 & 0 & 0 \\ 0 & 0 & 0 & 0 & 0 \\ 0 & 0 & \frac{\partial\bar{q}}{\partial y}\frac{\mathrm{FTF^v}}{\Omega} & \frac{\partial\bar{q}}{\partial z}\frac{\mathrm{FTF^v}}{\Omega} & \mathrm{FTF^p} \end{pmatrix} \tag{A.5}$$

$$\underline{\mathcal{S}} = \begin{pmatrix} \hat{\mathcal{S}}_\rho \\ \hat{\mathcal{S}}_u \\ \hat{\mathcal{S}}_v \\ \hat{\mathcal{S}}_w \\ \hat{\mathcal{S}}_p \end{pmatrix} \tag{A.6}$$

B Supplement for Rocket Engine Acoustics

B.1. Roots s_{mn} of Bessel Function Derivative

Mode	m	n	s_{mn}
T1	1	0	1.8412
T2	2	0	3.0540
R1	0	1	3.8318
T3	3	0	4.2013
T4	4	0	5.3175
T5	5	0	6.3160
R2	0	2	7.0155
T6	6	0	7.5018
T7	7	0	8.5781
T8	8	0	9.6475

B.2. Definition of R, Z and Y

B.2.1. Definition

Inlet/Outlet:

$$R_{mn} = \frac{\hat{F}_{mn} + \hat{G}_{mn} \pm (\kappa^+_{mn}\hat{F}_{mn} + \kappa^-_{mn}\hat{G}_{mn})}{\hat{F}_{mn} + \hat{G}_{mn} \mp (\kappa^+_{mn}\hat{F}_{mn} + \kappa^-_{mn}\hat{G}_{mn})} \tag{B.1}$$

$$Y_{mn} = \mp\frac{\kappa^+_{mn}\hat{F}_{mn} + \kappa^-_{mn}\hat{G}_{mn}}{\hat{F}_{mn} + \hat{G}_{mn}} \tag{B.2}$$

$$Z_{mn} = Y^{-1}_{mn} = \mp\frac{\hat{F}_{mn} + \hat{G}_{mn}}{\kappa^+_{mn}\hat{F}_{mn} + \kappa^-_{mn}\hat{G}_{mn}} \tag{B.3}$$

B.2.2. Conversion Rules: R, Z and Y

Independent of the mode shape holds:

Output \ Input	R	Z	Y
R	-	$\frac{Z-1}{Z+1}$	$-\frac{Y-1}{Y+1}$
Z	$-\frac{R+1}{R-1}$	-	Y^{-1}
Y	$-\frac{R-1}{R+1}$	Z^{-1}	-

B.3. Analytical Scattering Matrices for Longitudinal Wave Propagation

B.3.1. Transfer Matrices

B.3.1.1. Duct Element

$$\begin{pmatrix} \frac{\hat{p}}{\bar{\rho}c} \\ \hat{u} \end{pmatrix}_d = \underbrace{\frac{1}{2}\begin{pmatrix} e^{-\mathrm{i}k^+L} + e^{\mathrm{i}k^-L} & e^{-\mathrm{i}k^+L} - e^{\mathrm{i}k^-L} \\ e^{-\mathrm{i}k^+L} - e^{\mathrm{i}k^-L} & e^{-\mathrm{i}k^+L} + e^{\mathrm{i}k^-L} \end{pmatrix}}_{\mathrm{TM}^{\mathrm{DE}}} \begin{pmatrix} \frac{\hat{p}}{\bar{\rho}c} \\ \hat{u} \end{pmatrix}_u \tag{B.4}$$

where L denotes the duct length. From Eq. (2.43) follows

$$k^{\pm} = \pm \frac{k}{1 \pm M}. \tag{B.5}$$

B.3.1.2. Area Change with Loss

$$\begin{pmatrix} \frac{\hat{p}}{\bar{\rho}c} \\ \hat{u} \end{pmatrix}_d = \underbrace{\begin{pmatrix} 1 & (1 - \zeta_l - \alpha_A^2)M_u - \mathrm{i}kl_{\mathrm{eff}} \\ -\mathrm{i}l_{\mathrm{red}}M_d & \alpha_A \end{pmatrix}}_{\mathrm{TM}^{\mathrm{AC}}} \begin{pmatrix} \frac{\hat{p}}{\bar{\rho}c} \\ \hat{u} \end{pmatrix}_u \tag{B.6}$$

where

$$\zeta_l = \frac{\Delta\bar{p}}{\frac{\bar{\rho}}{2}\bar{u}^2}; \quad \alpha_A = \frac{A_u}{A_d}. \tag{B.7}$$

Furthermore, l_{eff}, l_{red} take streamline and inertia effects into account Gentemann et al. (2003).

B.3.1.3. Change of Characteristic Impedance

According to (Bade 2014):

$$\begin{pmatrix} \frac{\hat{p}}{\bar{\rho}c} \\ \hat{u} \end{pmatrix}_d = \underbrace{\begin{pmatrix} \frac{(\bar{\rho}c)_u}{(\bar{\rho}c)_d} & 0 \\ 0 & 1 \end{pmatrix}}_{\mathrm{TM}^{\rho c}} \begin{pmatrix} \frac{\hat{p}}{\bar{\rho}c} \\ \hat{u} \end{pmatrix}_u \tag{B.8}$$

B.3.1.4. Transformation of Transfer Matrix into Scattering Matrix

I:

$$\mathrm{TM}_{fg} = \Omega_T \cdot \mathrm{TM} \cdot \Omega_T^{-1} \tag{B.9}$$

with

$$\Omega_T = \frac{1}{2} \begin{pmatrix} 1 & 1 \\ 1 & -1 \end{pmatrix} \tag{B.10}$$

II:

$$\mathrm{SM} = \frac{1}{\mathrm{TM(2,2)}_{fg}} \begin{pmatrix} \mathrm{TM(1,1)}_{fg}\mathrm{TM(2,2)}_{fg} - \mathrm{TM(1,2)}_{fg}\mathrm{TM(2,1)}_{fg} & \mathrm{TM(1,2)}_{fg} \\ -\mathrm{TM(2,1)}_{fg} & 1 \end{pmatrix} \tag{B.11}$$

B.4. Mass Flow Inlet

The mass flow rate $\dot{m}$ through a surface S is given by

$$\dot{m} = \int_S \rho u_i n_i dS. \tag{B.12}$$

For zero flux, the mass flow rate needs to vanish on the entire surface, $\dot{m} = 0$, viz.

$$\rho u_i n_i = 0. \tag{B.13}$$

Linearization of Eq. (B.13) yields

$$\left(\bar{\rho}\hat{u}_i + \hat{\rho}\bar{u}_i\right) n_i = 0. \tag{B.14}$$

Inserting Eq. (B.14) into Eq. (2.79) gives

$$R_{mn} = \frac{\hat{p}_{mn} + \hat{\rho}_{mn}\, c\, \bar{u}_i n_i}{\hat{p}_{mn} - \hat{\rho}_{mn}\, c\, \bar{u}_i n_i}. \tag{B.15}$$

Using Eq. (2.37) yields

$$R_{mn} = \frac{c + \bar{u}_i n_i}{c - \bar{u}_i n_i}. \tag{B.16}$$

Assuming an axially oriented inlet surface (i.e. $n_i = n_x = -1$), the reflection coefficient is finally given by

$$R_{mn} = R = \frac{1-M}{1+M}. \tag{B.17}$$

At an outlet the reflection coefficient reads accordingly

$$R_{mn} = R = \frac{1+M}{1-M}. \tag{B.18}$$

B.5. Periodic Mean of Acoustic Intensity using the Admittance

The starting point for this derivation is Eq. (2.70). For the sake of better readability, the indicator $()^a$ for acoustic fluctuation is dropped here. Applying Eq. (2.71) to Eq. (2.70) the periodic average reads

$$< I_i > = \frac{1}{2}\mathfrak{Re}\left(\hat{p}^*\hat{u}_i\right) + \frac{1}{2}\mathfrak{Re}\left(\bar{u}_i\frac{\hat{p}^*\hat{p}}{\bar{\rho}c^2}\right) + \frac{1}{2}\mathfrak{Re}\left(\bar{\rho}\bar{u}_j\hat{u}_j^*\hat{u}_i\right) + \frac{1}{2}\mathfrak{Re}\left(\frac{\hat{p}^*}{c^2}\bar{u}_j\hat{u}_j\bar{u}_i\right). \tag{B.19}$$

Inserting the definitions of admittance (2.90) and Mach number (2.40) yields

$$< I_i > = \frac{1}{2}\mathfrak{Re}\left(\frac{\hat{p}^*\hat{p}}{\bar{\rho}c}Y\right) + \frac{1}{2}\mathfrak{Re}\left(M\frac{\hat{p}^*\hat{p}}{\bar{\rho}c}\right) + \frac{1}{2}\mathfrak{Re}\left(M\frac{\hat{p}^*\hat{p}}{\bar{\rho}c}|Y|^2\right) + \frac{1}{2}\mathfrak{Re}\left(M^2\frac{\hat{p}^*\hat{p}}{\bar{\rho}c}Y\right). \tag{B.20}$$

Identifying

$$\hat{p}^*\hat{p} = |\hat{p}|^2 \tag{B.21}$$

yields

$$< I_i >= \frac{1}{2}\frac{|\hat{p}|^2}{\bar{\rho}c}\left[\mathfrak{Re}(Y)(1+M^2) + M|Y|^2 + M\right]. \tag{B.22}$$

C Non-reactive Nozzle Acoustics

C.1. Proof: Nozzle Admittance is homogeneously distributed in cross-section

Considering frequency ranges in which only longitudinal ($mn = 00$) and the first transverse ($mn = 10$) modes are present, Eq. (2.41) reduces to

$$\hat{p}(x, r, \theta) = P_{00}(x)R_{00}(r)\Theta_{00}(\theta) + P_{10}(x)R_{10}(r)\Theta_{10}(\theta). \tag{C.1}$$

The axial acoustic velocity component $\hat{u}$ is given by

$$\hat{u}(x, r, \theta) = U_{00}(x)R_{00}(r)\Theta_{00}(\theta) + U_{10}(x)R_{10}(r)\Theta_{10}(\theta), \tag{C.2}$$

where the term $U_{mn}(x)$ is expressed by conservation of momentum according to Eq. (2.50) as a function of the axial pressure gradient

$$U_{mn}(x) = f\left(\frac{dP_{mn}(x)}{dx}\right). \tag{C.3}$$

Thus, Eq. (C.2) may be rewritten as

$$\hat{u}(x, r, \theta) = f\left(\frac{dP_{00}(x)}{dx}\right)R_{00}(r)\Theta_{00}(\theta) + f\left(\frac{dP_{10}(x)}{dx}\right)R_{10}(r)\Theta_{10}(\theta). \tag{C.4}$$

Expressing the admittance defined by Eq. (2.90), using Eq. (2.41) and (C.4) yields

$$Y\bar{\rho}c = \frac{f\left(\frac{dP_{00}(x)}{dx}\right)R_{00}(r)\Theta_{00}(\theta)}{P_{00}(x)R_{00}(r)\Theta_{00}(\theta) + P_{10}(x)R_{10}(r)\Theta_{10}(\theta)} + \tag{C.5}$$

$$\frac{f\left(\frac{dP_{10}(x)}{dx}\right)R_{10}(r)\Theta_{10}(\theta)}{P_{00}(x)R_{00}(r)\Theta_{00}(\theta) + P_{10}(x)R_{10}(r)\Theta_{10}(\theta)}. \tag{C.6}$$

The admittance for the first transverse mode only reads

$$Y_{10}\bar{\rho}c = \frac{f\left(\frac{dP_{10}(x)}{dx}\right)R_{10}(r)\Theta_{10}(\theta)}{P_{10}(x)R_{10}(r)\Theta_{10}(\theta)} = \frac{f\left(\frac{dP_{10}(x)}{dx}\right)}{P_{10}(x)}. \tag{C.7}$$

Comparing Eq. (C.6) and Eq. (C.7) shows that the admittance for the first transverse mode does not depend on r and θ and is therefore homogeneously distributed in cross-section. However, the total admittance defined by $\hat{p}$ and $\hat{u}$ in Eq. (C.6) depend on x, r and θ.
The total admittance Y can be expressed as a linear combination of the form

$$Y = aY_{00} + bY_{10}, \tag{C.8}$$

where Y_{00} is additionally given by

$$Y_{00} = \frac{1}{\bar{\rho}c} \frac{f\left(\frac{dP_{00}(x)}{dx}\right)}{P_{00}(x)}. \tag{C.9}$$

Equating coefficients of Eq. (C.6) and Eq. (C.8) using Eq. (C.7) and Eq. (C.9) yields

$$\frac{f\left(\frac{dP_{00}(x)}{dx}\right) R_{00}(r)\theta_{00}(\phi)}{P_{00}(x)R_{00}(r)\theta_{00}(\phi) + P_{10}(x)R_{10}(r)\theta_{10}(\phi)} \stackrel{!}{=} a \frac{f\left(\frac{dP_{00}(x)}{dx}\right) R_{00}(r)\theta_{00}(\phi)}{P_{00}(x)R_{00}(r)\theta_{00}(\phi)} \tag{C.10}$$

and

$$\frac{f\left(\frac{dP_{10}(x)}{dx}\right) R_{10}(r)\theta_{10}(\phi)}{P_{00}(x)R_{00}(r)\theta_{00}(\phi) + P_{10}(x)R_{10}(r)\theta_{10}(\phi)} \stackrel{!}{=} b \frac{f\left(\frac{dP_{10}(x)}{dx}\right) R_{10}(r)\theta_{10}(\phi)}{P_{10}(x)R_{10}(r)\theta_{10}(\phi)}. \tag{C.11}$$

Therefore, the coefficients a and b are given by

$$a = \frac{P_{00}(x)R_{00}(r)\theta_{00}(\phi)}{P_{00}(x)R_{00}(r)\theta_{00}(\phi) + P_{10}(x)R_{10}(r)\theta_{10}(\phi)} = \frac{\hat{p}_{00}}{\hat{p}} \tag{C.12}$$

and

$$b = \frac{P_{10}(x)R_{10}(r)\theta_{10}(\phi)}{P_{00}(x)R_{00}(r)\theta_{00}(\phi) + P_{10}(x)R_{10}(r)\theta_{10}(\phi)} = \frac{\hat{p}_{10}}{\hat{p}}. \tag{C.13}$$

Eq. (C.7)-(C.13) show that the mode admittances Y_{mn} must be superimposed proportional to the pressure amplitudes' ratio of each mode $\hat{p}_{mn}$ and the total acoustic pressure amplitude $\hat{p}$. The determination of the pressure amplitude ratio requires a mode decomposition of the acoustic field.

C.2. Rapid Determination of the Frequency with Maximal Nozzle Admittance

As suggested in (Schulze et al. 2013a), the characteristic nozzle admittance is a direct consequence of the superposition of the acoustic waves in the chamber and reflected waves from the nozzle. It is shown that the frequencies at which maximal admittance values appear can be linked to the convergent nozzle length. Highest values are therefore

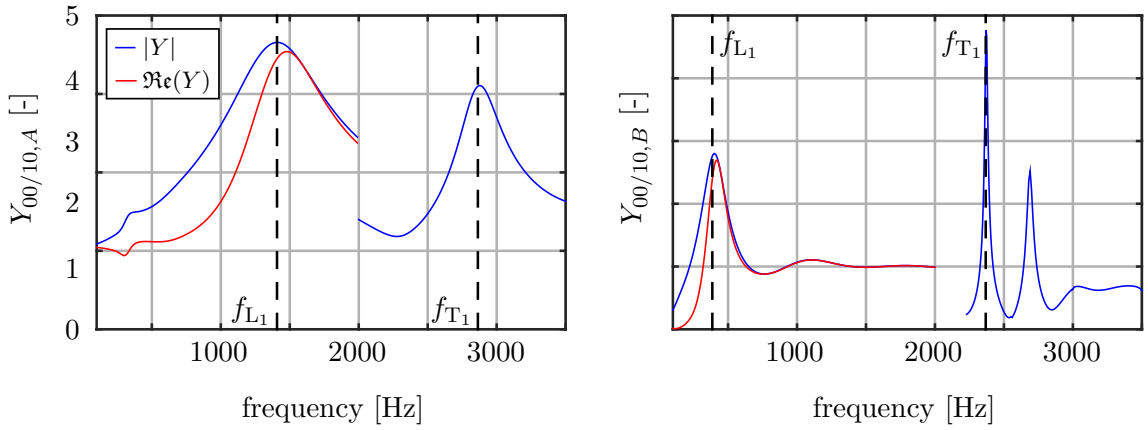

Fig. C.1.: Amplitude and real part of admittance for nozzle A (left) and nozzle B (right) in terms of the first longitudinal mode (low frequency range) and the first transverse mode (high frequency range).

expected when incident and reflected wave superimpose most constructively, which is the case for eigenfrequencies of the nozzle. Using an averaged speed of sound c and Mach number M, it is empirically found that the frequency at which the first longitudinal mode shape fits into the convergent nozzle part can be approximated by

$$f_{\mathrm{L}_1} = \frac{c(1+M^2)}{4l}, \tag{C.14}$$

where l again denotes the convergent nozzle part length. Eq. (C.14) corresponds to the first eigenfrequency of the nozzle altered by the mean flow. Quantitatively, the frequency is given for nozzle A by

$$f_{\mathrm{L}_1,\mathrm{A}} = 1476\,\mathrm{Hz}, \tag{C.15}$$

and for nozzle B by

$$f_{\mathrm{L}_1,\mathrm{B}} = 386\,\mathrm{Hz}. \tag{C.16}$$

The large difference is explained by the very different nozzle lengths, see Tab. 4.1.

In Fig. C.1, the analytically found frequencies are compared to the amplitude and real part of the admittance for nozzle A and B in the low frequency range. Clearly, the predicted frequencies excellently match the frequencies at which the maximum amplitude of the admittance occurs. Furthermore, the real part maximum is located closely to the predicted frequency, which indicates that the phase is close to zero in this particular frequency range. A phase of zero confirms the appearance of the first longitudinal mode structure in the convergent nozzle part.

Deriving an equivalent equation for the determination of the admittance peak frequency for the T_1 mode is drastically more complicated due to the complex reflection

pattern inside the nozzle. However, it is found empirically that the corresponding frequency can be determined on the basis of the cut-on frequency of the T_1 mode and the peak frequency for the L_1 mode, viz.

$$f_{T_1} = f_{T_1}^{co} + \frac{f_{L_1}}{2}. \tag{C.17}$$

The comparison of the analytical results with the nozzle admittance for the T_1 mode in the high frequency range of nozzle A and B is also presented in Fig. C.1, showing very good agreement.

The rather simple Eq. (C.14) and Eq. (C.17) allow to establish high damping capabilities by rapidly maximizing the admittance. Assuming invariant mean speed of sound and Mach numbers, the impact of a modified nozzle length in terms of admittance peak frequency changes can directly be evaluated. Such prediction methods are especially useful in the iterative design process of novel engines.

D Geometrical Specifications of the Perforated Plate

	value
hole diameter	3 mm
separation	4 mm
thickness	2 mm
area ratio	51 %
Mach number	0.4

E Dome Coupling

For frequencies well below the T_1 cut-on frequency, the experimentally determined and numerically reconstructed scattering matrix is shown. Furthermore, the IIR-filter representation is illustrated.

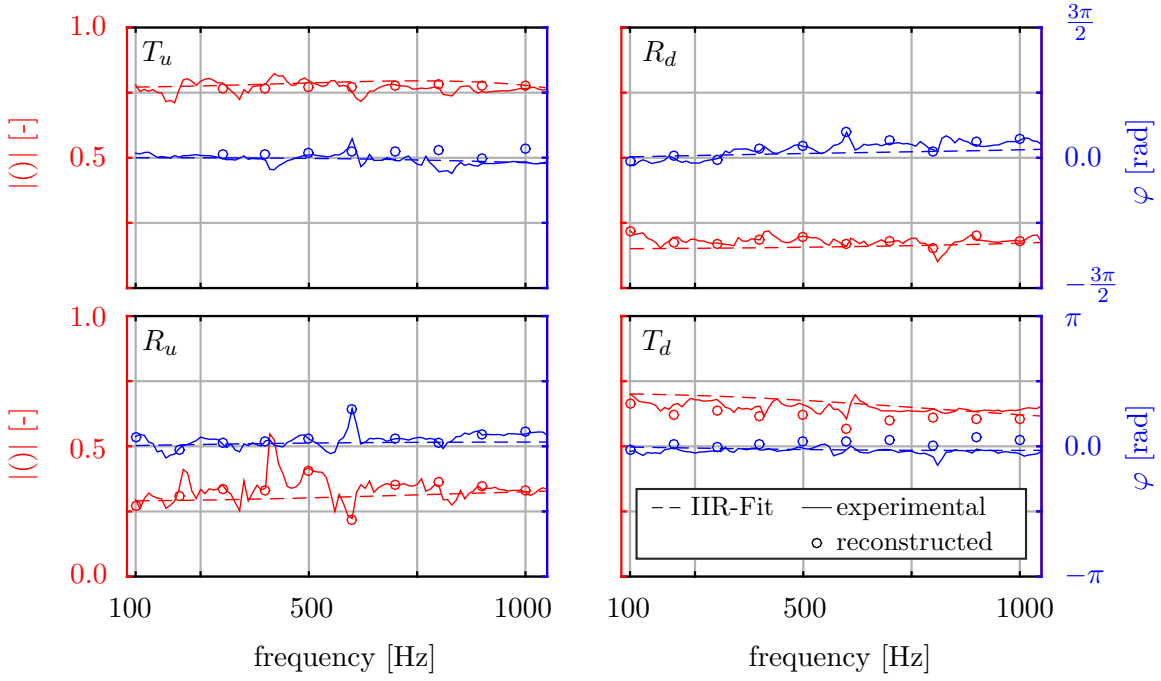

Fig. E.1.: Experimental and numerically reconstructed scattering matrix for longitudinal excitation.

F T_1 Mode Filter Coefficients for Perforated Plate

F.1. Reflection Coefficient

Tab. F.1.: IIR filter coefficients for $R_{\mathrm{IIR}}^{\mathrm{II}}$.

	0	1	2
b_k	2.1657E-1	2.3457E-1	8.7522e-03
a_k	1.0	6.1325E-1	-

F.2. Scattering Matrix

Tab. F.2.: IIR filter coefficients for $R_{\mathrm{IIR}}^{\mathrm{II}}$.

		0	1	2	3	4	5
T_u	b_k	8.2352E-1	1.7227E-1	1.5956e-1	-	-	-
	a_k	1.0	-	-	-	-	-
R_d	b_k	-3.7452E-2	-3.7452E-2	-3.7452E-2	-3.7452E-2	-3.7452E-2	-3.7452E-2
	a_k	1.0	2.6616E0	4.0399E0	3.8162E0	2.1595E0	7.0701E-1
R_u	b_k	1.4988E-1	1.4092E-1	1.8186E-1	-	-	-
	a_k	1.0	7.0373E-1	8.9264E-1	-	-	-
T_d	b_k	0.6	-	-	-	-	-
	a_k	1.0	-	-	-	-	-

G L Modes – Non-Reactive Case

For the non-reactive test case the complex frequency of the L_1 mode is determined. Tab. G.1 presents the findings for eigenvalue studies in frequency space and for time domain consideration. Good agreement is achieved.

Tab. G.1.: Mode frequency f [Hz] and damping rate λ [rad/s] for the L_1 mode of the non-reactive test case.

	f	λ
Time domain	1069[7]	1145
Frequency space	999	1003

Fig. G.1 shows the corresponding mode shape. The axially oriented wave motion is clearly visible.

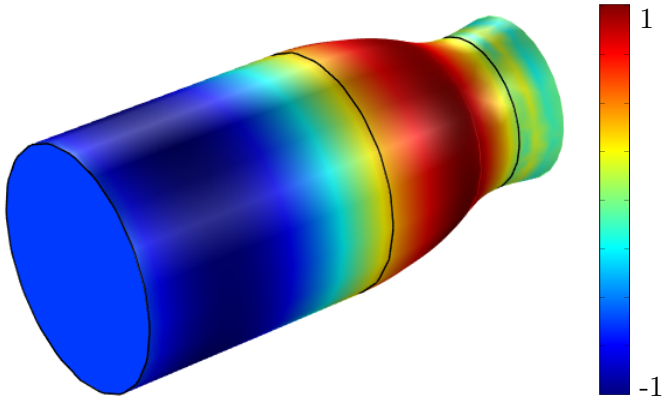

Fig. G.1.: Mode shape of the L_1 mode in terms of $\mathfrak{Re}(\hat{p})$.

[7] see Morgenweck (2013)

H GIT Test Case

H.1. Computational Grids

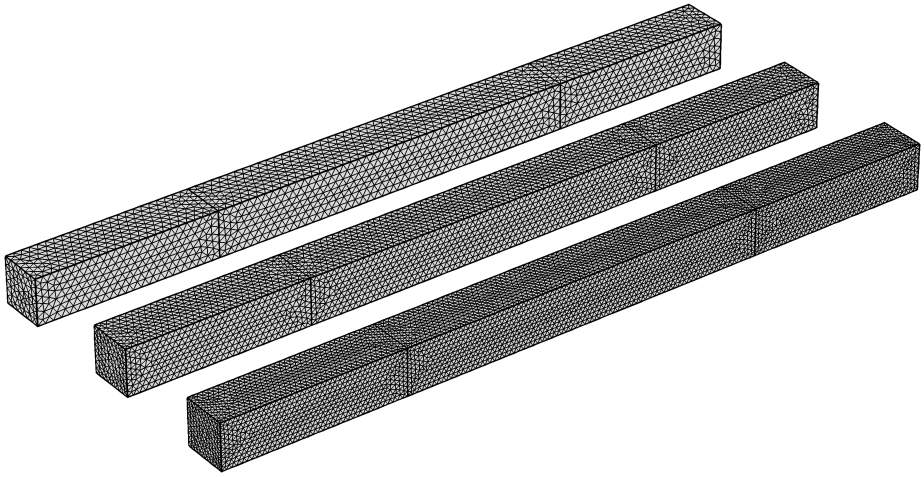

Fig. H.1.: Numerical grids for the GIT convergence study (From left to right: Coarse, medium and fine).

H.2. Results for Lower Mach Numbers

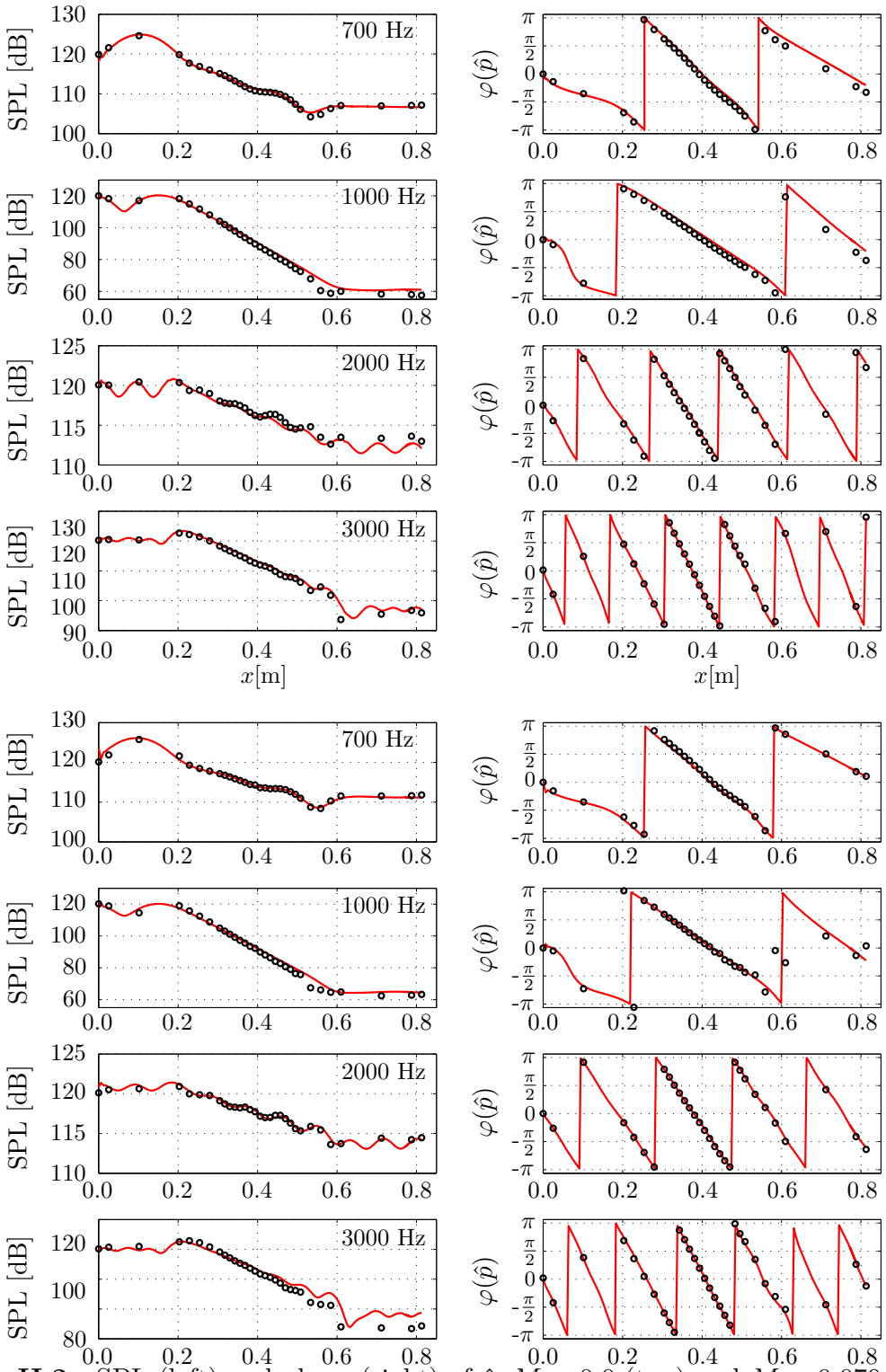

Fig. H.2.: SPL (left) and phase (right) of $\hat{p}$; $M = 0.0$ (top) and $M = 0.079$ (bottom): Exp. data (∘) and num. results (–).

I Perforated Plate: Reflection Coefficients

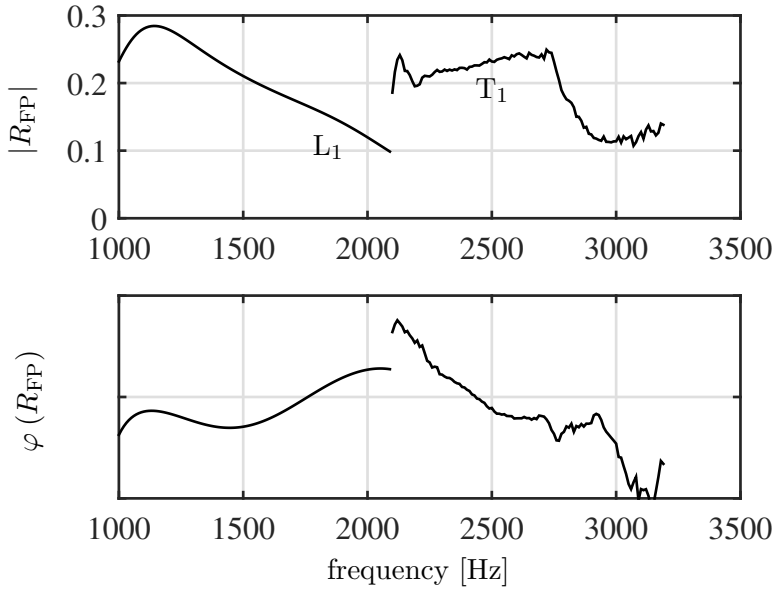

Fig. I.1.: Amplitude (top) and phase (bottom) of the reflection coefficient at the face plate Kathan (2013).

J Derivation of Equivalent Absorber Ring Reflection Coefficient

An equivalent absorber ring reflection coefficient R_{AR}, which can be imposed on the corresponding circular shell surface $()_{\mathrm{S}}$, is defined such that fluctuating mass is conserved, viz.

$$N_{\mathrm{SA}}\hat{\dot{m}}_{\mathrm{SA}} + \hat{\dot{m}}_{\mathrm{wall}} = \hat{\dot{m}}_{\mathrm{S}}, \tag{J.1}$$

where N_{SA} denotes the number of single absorbers in the ring. The fluctuating mass flow through the wall is zero. Using the linearized mass equations yields

$$\bar{\rho}\hat{u}_i n_i N_{\mathrm{SA}} A_{\mathrm{SA}} + \hat{\rho}\bar{u}_i n_i N_{\mathrm{SA}} A_{\mathrm{SA}} = \bar{\rho}\hat{u}_i n_i A_{\mathrm{S}}. \tag{J.2}$$

The Mach number within the absorber cavities is zero, which reduces mass conservation further to

$$\bar{\rho}\hat{u}_i n_i N_{\mathrm{SA}} A_{\mathrm{SA}} = \bar{\rho}\hat{u}_i n_i A_{\mathrm{S}}. \tag{J.3}$$

The fluctuating velocity is replaced by the acoustic admittance, viz.

$$\bar{\rho}\frac{Y_{\mathrm{SA}}\hat{p}}{\bar{\rho}c} N_{\mathrm{SA}} A_{\mathrm{SA}} = \bar{\rho}\frac{Y_{\mathrm{AR}}\hat{p}}{\bar{\rho}c} A_{\mathrm{S}}, \tag{J.4}$$

and acoustic compactness at the absorber inlet interface reduces to

$$Y_{\mathrm{SA}} N_{\mathrm{SA}} A_{\mathrm{SA}} = Y_{\mathrm{AR}} A_{\mathrm{S}}, \tag{J.5}$$

and

$$Y_{\mathrm{AR}} = \frac{N_{\mathrm{SA}} A_{\mathrm{SA}}}{A_{\mathrm{S}}} Y_{\mathrm{SA}}. \tag{J.6}$$

In form of a reflection coefficient this reads

$$R_{\mathrm{AR}} = -\frac{N_{\mathrm{SA}} A_{\mathrm{SA}} Y_{\mathrm{SA}} - A_{\mathrm{S}}}{N_{\mathrm{SA}} A_{\mathrm{SA}} Y_{\mathrm{SA}} + A_{\mathrm{S}}} \tag{J.7}$$

and on the basis of an impedance Z_{SA}

$$R_{\mathrm{AR}} = \frac{A_{\mathrm{S}} Z_{\mathrm{SA}} - N_{\mathrm{SA}} A_{\mathrm{SA}}}{A_{\mathrm{S}} Z_{\mathrm{SA}} + N_{\mathrm{SA}} A_{\mathrm{SA}}}, \tag{J.8}$$

respectively.

K Effect of Systematic Noise Excitation

To show the effect of systematic noise excitation, a damped signal of a clock-wise rotating mode $A(t)$ is considered for small amplitudes. The dynamics of $A(t)$ is then described by the differential equation (5.11).

First, the dynamics with the systematic noise excitation not included is analyzed. In this case the differential equation reduces to

$$\frac{\partial A(t)}{\partial t} = -\lambda A(t). \tag{K.1}$$

The solution of Eq. (K.1) describes the well known exponential decay of $A(t)$ in time, i.e

$$A(t) = A_0 e^{-\lambda t}. \tag{K.2}$$

According to Eq. (K.2), $A(t)$ approaches zero for $t \to \infty$.

In contrast, if the systematic noise excitation is included, the differential equation is

$$\frac{\partial A(t)}{\partial t} = -\lambda A(t) + \frac{\Gamma}{A(t)}, \tag{K.3}$$

cf. Eq. (5.11). For $t \to \infty$ it holds that

$$\frac{\partial A(t)}{\partial t} = 0, \tag{K.4}$$

and thus

$$0 = -\lambda A(t \to \infty) + \frac{\Gamma}{A(\to \infty)}, \tag{K.5}$$

which yields

$$A(t \to \infty) = \sqrt{\frac{\Gamma}{\lambda}}. \tag{K.6}$$

Eq. (K.6) shows that the influence of systematic noise excitation with intensity Γ leads to a non-zero final state of $A(t)$ for $t \to \infty$.

L Additional Real Gas Relations

L.1. Internal Energy

Ideal gas:

$$e - e_0 = 0 \tag{L.1}$$

Peng-Robinson:

$$e - e_0 = \frac{1}{b\sqrt{8}} \left[a(T) - T \frac{\partial a(T)}{\partial T} \right] \ln \left(\frac{2(v+b) - b\sqrt{8}}{2(v+b) + b\sqrt{8}} \right) \tag{L.2}$$

with

$$\frac{\partial a(T)}{\partial T} = -\frac{a_0\, n}{T\, T_c} \left(1 + n \left(1 - \sqrt{T/T_c} \right) \right) \tag{L.3}$$

Soave-Redlich-Kwong:

$$e - e_0 = \frac{1}{b} \left[a(T) - T \frac{\partial a(T)}{\partial T} \right] \ln \left(\frac{v}{v+b} \right) \tag{L.4}$$

with

$$\frac{\partial a(T)}{\partial T} = -\frac{a_0\, n}{T\, T_c} \left(1 + n \left(1 - \sqrt{T/T_c} \right) \right) \tag{L.5}$$

L.2. Isochoric Specific Heat Capacity

Ideal gas:

$$c_v = c_{v,0} \tag{L.6}$$

Peng-Robinson:

$$c_v = c_{v,0} - \frac{T}{b\sqrt{8}} \frac{\partial^2 a(T)}{\partial T^2} \ln \left(\frac{2(v+b) - b\sqrt{8}}{2(v+b) + b\sqrt{8}} \right) \tag{L.7}$$

with

$$\frac{\partial^2 a(T)}{\partial T^2} = \frac{a_0\, n^2}{2\, T\, T_c} + \frac{a_0 n}{2}\left(1 + n\left(1 - \sqrt{T/T_c}\right)\right)\, T_c\, (T\, T_c)^{-1.5} \tag{L.8}$$

Soave-Redlich-Kwong:

$$c_v = c_{v,0} - \frac{T}{b}\frac{\partial^2 a(T)}{\partial T^2}\ln\left(\frac{v}{v+b}\right) \tag{L.9}$$

with

$$\frac{\partial^2 a(T)}{\partial T^2} = \frac{a_0\, n^2}{2\, T\, T_c} + \frac{a_0 n}{2}\left(1 + n\left(1 - \sqrt{T/T_c}\right)\right)\, T_c\, (T\, T_c)^{-1.5} \tag{L.10}$$

L.3. Isobaric Specific Heat Capacity

Ideal gas:

$$c_p = c_{p,0} \tag{L.11}$$

Peng-Robinson:

$$c_p = c_v - T\frac{\left(\frac{\partial p}{\partial T}\right)_v^2}{\left(\frac{\partial p}{\partial v}\right)_T} \tag{L.12}$$

with

$$\left(\frac{\partial p}{\partial T}\right)_v = \frac{\mathcal{R}}{v-b} - \frac{a_0 n\left(1 + n\left(1 - \sqrt{T/T_c}\right)\right)}{\sqrt{T\, T_c}(v^2 + 2bv - b^2)} \tag{L.13}$$

and

$$\left(\frac{\partial p}{\partial v}\right)_T = -\frac{\mathcal{R}T}{(v-b)^2} + \frac{2a(T)(v+b)}{(v^2+2bv-b^2)^2} \tag{L.14}$$

Soave-Redlich-Kwong:

$$c_p = c_v - T\frac{\left(\frac{\partial p}{\partial T}\right)_v^2}{\left(\frac{\partial p}{\partial v}\right)_T} \tag{L.15}$$

with

$$\left(\frac{\partial p}{\partial T}\right)_v = \frac{\mathcal{R}}{v-b} - \frac{a_0 n\left(1 + n\left(1 - \sqrt{T/T_c}\right)\right)}{\sqrt{T\, T_c}(v[v-b])} \tag{L.16}$$

and

$$\left(\frac{\partial p}{\partial v}\right)_T = -\frac{\mathcal{R}T}{(v-b)^2} + \frac{a(T)(2v+b)}{(v[v-b])^2} \tag{L.17}$$

M Molecular Transport Properties

Standard models are employed to calculate the material properties of the single species. As already described, heat capacities at ideal gas state are evaluated from NASA polynomials. Species viscosity is determined from the Rigid Non Interacting Sphere model, which is given by elementary kinetic theory according to (Hirschfelder et al. 1954):

$$\mu = 26.69 \frac{\sqrt{\mathbf{W}T}}{\sigma_d^2}, \tag{M.1}$$

where $\mathbf{W}$ denotes the molar mass and σ_d the collision diameter. Following (Chung et al. 1984), σ_d can be calculated from

$$\sigma_d = 0.809 \sqrt[3]{v_{m,c}}, \tag{M.2}$$

where $v_{c,m}$ denotes the critical molar volume.

Lastly, thermal conductivity is calculated based on the Modified Euken Model (Poling et al. 2001):

$$\frac{\sigma}{\mu c_v} = 1.32 + \frac{1.77\mathcal{R}}{c_v}. \tag{M.3}$$

N Axial Distributions of Mean Quantities for LP1-4

The next page shows the mean quantities' axial distribution for LP1-4. For this purpose, the quantities are radially averaged and taken from the single flame CFD computations.

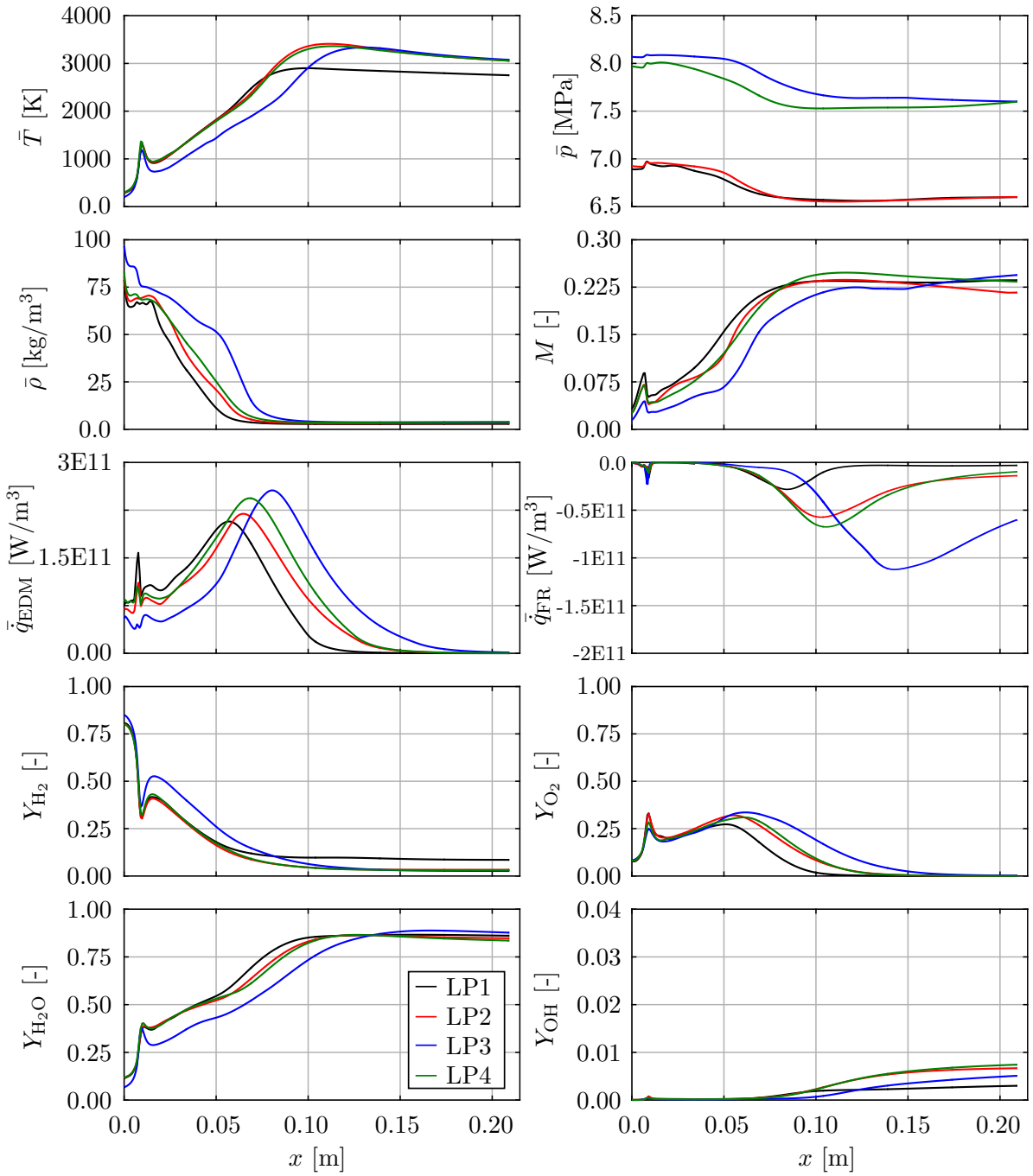

Fig. N.1.: Axial distributions of mean quantities for LP1-4.

O $T_1^\beta L_x$ Modes in the BKD Test Chamber

To explain the chosen nomenclature of the $T_1^\beta L_x$ modes, the corresponding mode shapes are further investigated. For this purpose, the first four mode shapes, i.e. $T_1^\beta L_1$ - $T_1^\beta L_4$ are calculated and compared in App. O (left column). For the investigations, the $T_1^\beta L_x$ mode shape is divided into two sections. The division is indicated by the red line in Fig. O.1. The first section in the chamber comprises the region between the face plate and the first pressure amplitude node. In this section, a similar amplitude distribution as for the T_1^α mode is identified for $T_1^\beta L_1$ - $T_1^\beta L_4$, see also Fig. 7.11. With increasing longitudinal order, the axial dimension of the first section, and hence of the T_1^α equivalent mode shape, reduces. In the second section, a typical combination of a first transverse mode and a longitudinal mode is found. With increasing longitudinal order, the second section becomes larger and a higher number of pressure amplitude nodes is present. In consequence, the $T_1^\beta L_x$ mode can be interpreted as a complex combination of a T_1^α equivalent mode, which is only present in the region with low speed of sound before the first amplitude pressure node, and a conventional T_1 mode structure in the second section of the chamber combined with a longitudinal mode. The nomenclature $T_1^\beta L_x$ is chosen to discriminate these modes from the T_1^α mode.

In order to verify that the $T_1^\beta L_x$ mode shapes in the second section of the chamber actually correspond to a classical combined mode, acoustic simulations are conducted taking only the second region of the chamber into account. The computational domain comprises the region between the first pressure amplitude node and the nozzle outlet. The location of the first pressure amplitude node is taken from the acoustic simulation results of the entire chamber, see Fig. O.1 in App. O (left column). Furthermore, to reduce complexity, a uniform mean flow with zero Mach number is assumed, cf. Sec. 2.4. Representative conditions are established by applying a constant speed of sound, which is generated by averaging over the second chamber section on the basis of the single flame CFD results. At the inlet, the amplitude pressure node is described by setting acoustic pressure zero. At the outlet of the nozzle, velocity is set zero. The simulated mode shapes are shown in Fig. O.1 (right column). A clear first transverse mode structure is found in cross-section. Furthermore, it can be seen that identical amplitude distributions in axial direction are calculated in comparison to the mode shapes of the full chamber (left column in Fig. O.1). Between the inlet and the nozzle throat location, a clear longitudinal mode structure establishes. In conclusion, the $T_1^\beta L_x$

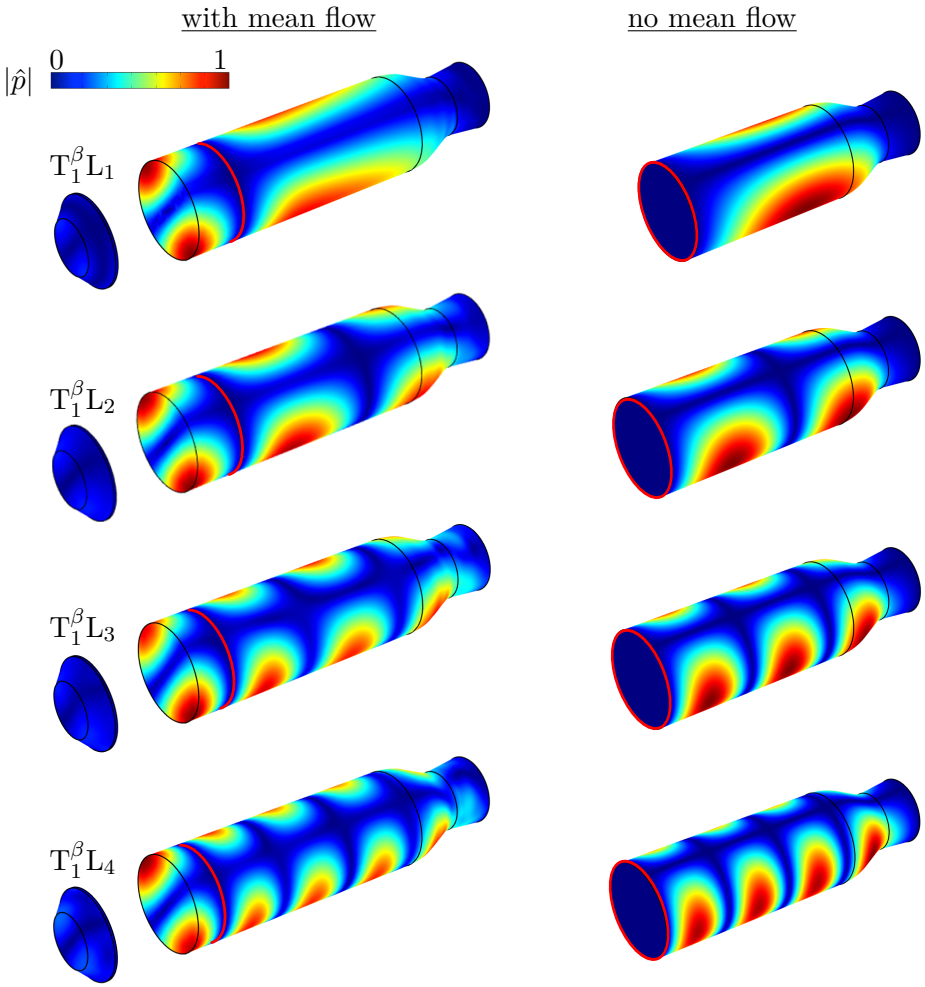

Fig. O.1.: Left: First four $T^\beta L_x$ modes shapes simulated with mean flow. Right: Mode shapes downstream of the first pressure node without mean flow.

mode shapes in the second chamber section correspond to the classical combination of a first transverse mode and a longitudinal mode.

P Derivative of $\mathfrak{Im}(k^{+}_{\mathrm{T}^{\alpha}_{1}})$ at Cut-on

Using the definition Eq. (2.43), the axial wave number in positive direction is expressed as

$$k^{+}_{\mathrm{T}^{\alpha}_{1}} = \frac{c\,\omega_{\mathrm{T}^{\alpha}_{1}}}{c^2-\bar{u}^2}\sqrt{1-A_k^2(c^2-\bar{u}^2)}, \tag{P.1}$$

where only the second term is accounted for since the first term cannot be become imaginary. Furthermore, the constant

$$A_k = \frac{s_{10}}{R_{cc}\,\omega_{\mathrm{T}^{\alpha}_{1}}} \tag{P.2}$$

is introduced.
The derivation with respect to c is given by

$$\frac{\partial k^{+}_{\mathrm{T}^{\alpha}_{1}}}{\partial c} = \frac{\omega_{\mathrm{T}^{\alpha}_{1}}(c^2-\bar{u}^2)-2c^2\omega_{\mathrm{T}^{\alpha}_{1}}}{(c^2-\bar{u}^2)^2}\sqrt{1-A_k^2(c^2-\bar{u}^2)} - \frac{c\,\omega_{\mathrm{T}^{\alpha}_{1}}}{c^2-\bar{u}^2}\frac{A_k^2 c}{\sqrt{1-A_k^2(c^2-\bar{u}^2)}}. \tag{P.3}$$

Evaluating the derivative at the cut-on condition, i.e. for

$$A_k^2(c^2-\bar{u}^2)=1, \tag{P.4}$$

yields

$$\left.\frac{\partial k^{+}_{\mathrm{T}^{\alpha}_{1}}}{\partial c}\right|_{A_k^2(c^2-\bar{u}^2)=1} = 0-(\infty), \tag{P.5}$$

which proves that $\mathfrak{Im}(k^{+}_{\mathrm{T}^{\alpha}_{1}})$ strongly increases when a mode is cut-off.

Q Open and Closed Loop Mode Shapes

Fig. Q.1 shows a comparison of the axial pressure distribution in the anti-nodal line in case of the T_1^α mode for the open loop and the close loop system. It can be seen that both amplitude and phase are in good agreement. In consequence, the flame feedback does not relevantly influences the mode shape.

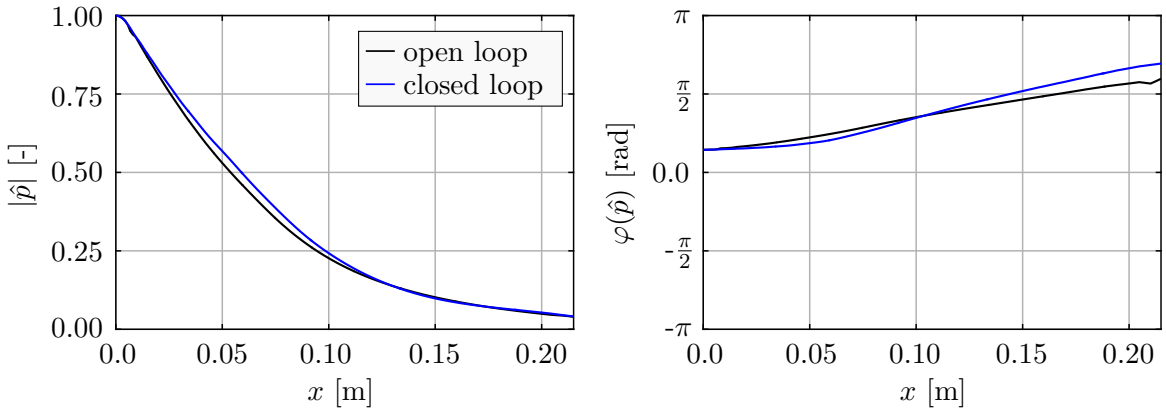

Fig. Q.1.: Comparison of the axial pressure distribution for the T_1^α mode for the open loop and the closed loop system.

R Quantitative Contributions of Damping and Amplification Effects for LP1-4

Tab. R.1 summarizes the contributions to damping and amplification quantitatively for LP1-4. The visualization is presented in Fig. 7.32.

Tab. R.1.: Relative contributions of the different damping and amplification effects to the closed loop damping rate. Normalization with the open loop damping rate for LP1.

λ [-]	Pressure coupling	Velocity coupling	Nozzle damping	Dome coupling	Field damping	Open loop	Closed loop
LP1	-0.611	-0.015	0.012	0.007	0.981	**1**	0.373
LP2	-0.751	-0.016	0.045	0.007	0.698	0.748	-0.015
LP3	-0.488	-0.021	0.011	0.007	0.642	0.660	0.151
LP4	-0.761	-0.035	0.045	0.006	0.714	0.765	-0.022

Supervised Student Theses

Im Rahmen dieser Dissertation entstanden am *Lehrstuhl für Thermodynamik* der *Technischen Universität München* in den Jahren 2012 bis 2016 unter wesentlicher wissenschaftlicher und inhaltlicher Anleitung des Autors die im Folgenden aufgeführten studentischen Arbeiten, in welchen verschiedene Fragestellungen zu den in dieser Arbeit behandelten Themengebieten untersucht wurden und deren Ergebnisse in Teilen in das vorliegende Dokument eingeflossen sind. Der Autor dankt allen Studierenden für ihr Engagement bei der Unterstützung dieser wissenschaftlichen Arbeit.

Several student theses emerged from the research project behind the present work, listed below. These student projects were conducted at the *Lehrstuhl für Thermodynamik*, *Technische Universität München*, in the years 2012 through 2016 under close supervision of the author of this Ph.D. thesis with regard to academic, professional, and context-related concerns. The author would like to express his sincere gratitude to all formerly supervised students for their commitment and support of this research project and of the Ph.D. thesis at hand.

Student (date)	Thesis title
Niccolò A. Ciarlini (B.T., 31/10/2014)	Implementation of a displacement model for the investigation of thermoacoustic stability in rocket engines
Manuel Demmelmair (B.T., 30/9/2014)	Analytische und numerische Bestimmung der Temperaturverteilung in einem H_2/O_2-Zufuhrsystem eines Raketenmotors
Christoph Aumiller (M.T., 2/7/2014)	Eigenfrequenzanalysen für die Beurteilung der linearen Stabilität von thermoakustischen Problemstellungen in Raketenmotoren
Max Zahn (M.T., 6/11/2013)	URANS-Simulations for the Analysis of H_2/O_2-Flame Dynamics under Supercritical Conditions
Markus Stoll (B.T., 31/10/2013)	Linearized Euler and Navier-Stokes Equations for Determining Scattering Behavior of Acoustic Absorbers in Rocket Motors
Michael Haimerl (B.T., 25/10/2013)	Bestimmung von Dämpfungskoeffizienten für numerische akustische Felder mit dem Lorenzverfahren

Previous Publications

Wesentliche Teile dieser Dissertation wurden vom Autor bereits vorab als Konferenz- und Zeitschriftenbeiträge sowie im Rahmen von Berichten veröffentlicht. Alle relevanten Vorveröffentlichungen sind entsprechend der gültigen Promotionsordnung ordnungsgemäß gemeldet und anschließend aufgeführt. Sie sind deshalb nicht zwangsläufig im Detail einzeln referenziert. Vielmehr wurde bei der Referenzierung eigener Vorveröffentlichungen Wert auf Verständlichkeit und inhaltlichen Bezug gelegt.

Significant parts of this Ph.D. thesis have been published by the author beforehand in conference proceedings, journal papers, and reports. All of these relevant prior printed publications are registered according to the valid doctoral regulations and listed below. However, not all of them are quoted explicitly everywhere as they are part of this present work being official documents. Whether these personal prior printed publications were referenced, depended on maintaining comprehensibility and providing all necessary context.

2016:

1. M. Schulze, T. Hummel, N. Klarmann, F. Berger, B. Schuermans, and T. Sattelmayer: Prediction of Linear High-Frequency Stability in Gas Turbine Combustors with Linearized Euler Equations. *Proceedings of ASME Turbo Expo 2016*, GT2016-57818, Seoul, South Korea, June 13-17, 2016.
2. M. Zahn, M. Schulze, C. Hirsch, and T. Sattelmayer: Impact of Quarter Wave Tube Arrangement on Damping of Azimuthal Modes, Analysis and Validation, *Proceedings of ASME Turbo Expo 2016*, GT2016-56450, Seoul, South Korea, June 13-17, 2016.
3. M. Schulze and T. Sattelmayer: Linear Stability Assessment of a Cryogenic Rocket Engine, *International Symposium on Thermoacoustic Instabilities in Gas Turbines and Rocket Engines: Industry meets Academia*, Munich, Germany, May 30-June 2, 2016.
4. M. Schulze, T. Fiala, and T. Sattelmayer: Radiation-Based Validation of Combustion Simulations and Comparison to Heat Release in Rocket Engines, *AIAA SciTech Aerospace Science Meeting*, San Diego, USA, 2016.
5. M. Schulze, M. Schmid, and T. Sattelmayer: Influence of Atomization Quality Modulation on Flame Dynamics in a Hypergolic Rocket Engine, *International*

Journal of Spray and Combustion Dynamics 0(0), 1-16, 2016.

2015:

6. A. Chemnitz, M. Schulze, and T. Sattelmayer: RANS Simulations of a GCH4/GOx Single Element Combustor. *Proceedings of the Summer Program Sonderforschungsbereich Transregio 40*, 2015.
7. M. Schulze and T. Sattelmayer: Frequency Domain Simulations for the Determination of Liner Effects on Longitudinal Wave Propagation, *International Journal of Aeroacoustics* 14(7), 1025-1047, 2015.
8. T. Hummel, M. Schulze, B. Schuermans, and T. Sattelmayer: Reduced Order Modeling of Transversal and Non-Compact Combustion Dynamics. *22nd International Congress on Sound and Vibration*, 2015.
9. T. Sattelmayer, M. Schmid, and M. Schulze: Impact of Injector Mass Flow Fluctuations on Combustion Dynamics in Liquid Engines. *Journal of Spacecraft and Rockets* 52 (5), 2015, 1417-1429.
10. T. Sattelmayer, M. Schmid, and M. Schulze: Interaction of Combustion with Transverse Velocity Fluctuations in Liquid Rocket Engines. *Journal of Propulsion and Power* 31 (4), 2015, 1137-1147.
11. M. Schulze, R. Kathan, and T. Sattelmayer: Impact of Absorber Ring Position and Cavity Length on Acoustic Damping. *Journal of Spacecraft and Rockets* 52 (3), 2015, 917-927.
12. M. Schulze and T. Sattelmayer: Flame Dynamics in Supercritical H_2/O_2 Rocket Combustion Systems. In: Adams, N. A., Radespiel, R., Sattelmayer, T., Schröder, W., Weigand, B. (Hrsg.): *Annual Report, Sonderforschungsbereich/Transregio 40*, 2015.
13. M. Schulze and T. Sattelmayer: Eigenvalue Analysis for the Prediction of Initial Growth Rates of Thermoacoustic Instability in Rocket Motors. *53rd AIAA Aerospace Sciences Meeting*, 2015.
14. M. Schulze and T. Sattelmayer: A Comparison of Time and Frequency Domain Descriptions of High Frequency Acoustics in Rocket Engines with Focus on Dome Coupling. *Aerospace Science and Technology* (Volume 45), 2015, 165-173.
15. C. Temmler, M. Schulze, and T. Sattelmayer: Acoustic Scattering Matrices for Higher-Order Modes for Simple Orifice Configurations with Flow. *21st AIAA/CEAS Aeroacoustics Conference*, 2015.
16. M. Zahn, M. Schulze, C. Hirsch, M. Betz, and T. Sattelmayer: Frequency Domain Predictions of Acoustic Wave Propagation and Losses in a Swirl Burner with Linearized Navier-Stokes Equations. *Proceedings of the ASME Turbo Expo 2015*, GT2015-42723.

2014:

17. M. Schulze and T. Sattelmayer: Low-Order Modelling of the Non-Local Acoustic Reacting Combustion Chamber-Dome Interface in Rocket Engines. *19th American Institute of Aeronautics and Astronautics International Space Planes and Hypersonic Systems and Technologies Conference*, American Institute of Aeronautics and Astronautics, 2014.
18. M. Schulze, M. Schmid, and T. Sattelmayer: Eigenvalue Analysis for the Prediction of Initial Growth Rates of a Thermoacoustic Instability - HF-7 Test Case. *Proceedings of the 3rd REST Workshop on Combustion Instability Modeling*, Vernon, France, 2014.
19. M. Schulze, A. Urbano, M. Zahn, M. Schmid, T. Sattelmayer, and M. Oschwald: Thermoacoustic Feedback Analysis of a Cylindrical Combustion Chamber under Supercritical Conditions. *50th AIAA/ASME/SAE/ASEE Joint Propulsion Conference*, 2014.
20. M. Schulze, M. Wagner, and T. Sattelmayer: Acoustic Scattering Properties of Perforated Plates and Orifices with Stratified flow - HF-8 test case. *Proceedings of the 3rd Workshop on Combustion Instability Modeling*, Vernon, France, 2014.
21. M. Schulze, M. Zahn, M. Schmid, and T. Sattelmayer: About Flame-Acoustic Coupling Phenomena in Supercritical H2/O2 Rocket Combustion Systems. *63. Deutscher Luft- und Raumfahrtkongress*, Augsburg, Germany, 2014.
22. W.C. Ullrich, M. Schulze, and T. Sattelmayer: Fundamental Indirect Noise Generation by Interactions between Entropy, Vorticity and Acoustic Waves in the Context of Aero Engine Applications. Internoise 2014, 43rd Int. Congress on Noise Control Engineering.
23. M. Schulze: Definition of Test Case HF-8. *Proceedings of the 3rd REST Workshop on Combustion Instability Modeling*, Vernon, France, 2014.

2013:

24. M. Schmid, R. Blumenthal, M. Schulze, W. Polifke, and T. Sattelmayer: Quantitative stability analysis using real-valued frequency response data. *Journal of Engineering for Gas Turbines and Power* (135/12), 2013, 121601.
25. M. Schulze, J. Gikadi, and T. Sattelmayer: Acoustic Admittance Prediction of two Nozzle Designs of different length using Frequency Domain Simulations. *5th European Conference for Aeronautics and Space Sciences*, 2013.
26. M. Schulze, M. Schmid, D. Morgenweck, S. Köglmeier, and T. Sattelmayer: A Conceptional Approach for the Prediction of Thermoacoustic Stability in Rocket Engines. *49th AIAA/ASME/SAE/ASEE Joint Propulsion Conference*, San Jose, California, USA, 2013.
27. A. Urbano, M. Schulze, M. Zahn, M. Schmid, T. Sattelmayer, and M. Oschwald: Investigations on Thermoacoustic Feedback on a Representative Test Chamber Configuration. *Proceedings of the Summer Program*, Sonderforschungsbereich

Transregio 40, 2013.

28. M. Wagner, M. Schulze, and T. Sattelmayer: Experimental Investigation of Acoustic Properties of Orifices and Perforated Plates in the High Mach Number Regime. *20th International Congress on Sound and Vibration* (ICSV), 2013.
29. M. Wierman, S. Beinke, W. Anderson, M. Oschwald, M. Schulze, M. Zahn, and T. Sattelmayer: Investigation of Modeling and Post-Processing Methods for Combustion Instability Experiments. *Proceedings of the Summer Program Sonderforschungsbereich Transregio 40*, 2013.

2012:

30. J. Gikadi, M. Schulze, J. Schwing, S. Föller, and T. Sattelmayer: Linearized Navier-Stokes and Euler Equations for the Determination of the Acoustic Scattering Behaviour of an Area Expansion. *18th AIAA/CEAS Aeroacoustics Conference*, 2012.
31. M. Schulze, D. Morgenweck, and T. Sattelmayer: Dämpfung akustischer Wellen durch Absorber in Raketentriebwerken. *61. Deutscher Luft- und Raumfahrtkongress*, 2012.

List of Figures

1.1 Vulcain II rocket engine configuration, adapted from (Kathan 2013). . . 2

2.1 Amplitudes and phases of $\hat{F}_{10}$ and $\hat{G}_{10}$ in axial direction for different frequencies. 18
2.2 Illustration of dome coupling with complex acoustic scattering processes involved. 26
2.3 Illustration of the scattering matrix (SM) approach. 27
2.4 Interplay between wave propagation inside the chamber and dynamic heat releaser rate. 31

3.1 Procedure for the iterative determination of the eigenfrequency and the corresponding mode shape. 42
3.2 Point-wise data of R (real part) for frequencies ω and confidence circle in the ω, λ-plane, adapted from (Schmid 2014). Furthermore, a exemplary continuous fit is shown in red. 44

4.1 Geometry and Mach number distribution of nozzle A (left) and nozzle B (right). 56
4.2 Left: Location of the excitation, boundary conditions and computational grid. Right: Shape of the excitation function. 57
4.3 Distribution of spatial monitor points $I, J, K = (10, 8, 10)$ in the cylindrical part of nozzle A. 58
4.4 Energy ratio of the extracted modes and the entire acoustic energy in the specified volume between x = 50-107 mm for nozzle A. 59
4.5 Admittances of nozzle A (top) and nozzle B (bottom). Left: First longitudinal mode ($mn = 00$). Right: First transverse mode ($mn = 10$). . . . 60
4.6 Direct LEE computation results compared to the application of the fit of the nozzle admittance: Real part for the longitudinal mode evaluated at different damping rates. 62
4.7 Extended non-reactive rocket engine system (left) and pipe element with perforated plate (right). 64
4.8 Comparison of scattering matrices of the perforated plate for the longitudinal and first transverse modes calculated from experimental measurements in the simple pipe element, cf. Fig. 4.7 (right). 65
4.9 Computational grid for frequency space (left) and time domain solver (right). 66

4.10 Comparison between experimental findings and reconstructed data for the scattering matrix SM in case of T_1 mode propagation. 67
4.11 Distribution of normalized $|(\hat{\mathcal{F}}_{10})|$ at the interfacing surfaces (left) as well as axial distribution of $\hat{\mathcal{F}}_{10}$ in terms of amplitude and phase (right) for a frequency of 2110 Hz. 68
4.12 Step-wise approach for the modeling of dome coupling: Computational domain and inlet boundary treatment for I-III. 69
4.13 Extended computational domain including dome coupling. 70
4.14 Experimentally evaluated reflection coefficient for the cases (I)-(III) together with their IIR filter representation. 71
4.15 T_1 scattering matrix for the perforated plate: Experimental findings, IIR filter representation and reconstruction in time domain for case (III). . . 72
4.16 Mode shapes of case (II) (left) and case (III) (right) taken from the eigenvalue studies: Normalized pressure amplitudes $|\hat{p}|$ (top) and its real part $\mathfrak{Re}(\hat{p})$ (bottom). 75
4.17 Dependence of T_1 eigenfrequency and damping rate on stabilization coefficient α_τ for mode A_2 and mode B_2. 76
4.18 Detailed illustration of the GIT test case including the location of the liner, boundary conditions, microphone positions as well as the Mach number profile in the duct (Jones et al. 2005). Dimensions are given in [mm]. 78
4.19 Exit (top) and liner (bottom) impedances in terms of resistance (left) and reactance (right) for different Mach numbers (Jones et al. 2005). . . 80
4.20 Cut-plane used to visualize pressure distribution (gray). Visualization lines used to plot surface normal velocity (red) and to compare numerical and experimental pressure values (blue). 83
4.21 Pressure distribution $\mathfrak{Re}(\hat{p})$ for $M = 0.0$ (top) and $M = 0.172$ (bottom) together with liner surface normal acoustic velocity (arrows). 84
4.22 SPL (left) & phase (right) of $\hat{p}$; $M = 0.172$ (top) & $M = 0.255$ (bottom): Exp. ( ); coarse grid ( ), medium grid ( ), fine grid ( ); effective imped. ( ). 86
4.23 Comparisons of constant Mach number distribution and detailed profile for SPL (left) and phase (right): experimental values ( ); constant Mach number ( ); detailed Mach number profile ( ). 87
4.24 Experimental test configuration and computational domain (red) for absorber ring positions P1 (left) and P2 (right). 89
4.25 Numerical grid and boundary conditions for the acoustic simulation of the non-reactive test case with absorber ring. 90
4.26 Mapping of the single absorbers onto the circular shell surface. 91
4.27 Amplitude (top) and phase (bottom) of the absorber ring reflection coefficient. 92
4.28 Frequency response of $|\hat{p}|$ [Pa] for 35 mm (left) and 40 mm cavity length (right) in comparison to the reference case without absorber ring: experimental findings and numerical results. 93

4.29 Mode shapes for configuration P1 in terms of normalized $|\hat{p}|$ under excitation for the peak frequencies in the spectra, cf. Fig. 4.28. (a): Reference case without absorber. (b) and (c): With an absorber cavity length of 35 mm. 94
4.30 Eigenfrequency (left) and damping rate (right) of the $T_{1_d}^+$ mode for configuration P1: Experimental findings and numerical results both for the partially reflecting inlet and the neutral inlet. 95
4.31 Mode shapes $T_{1_d}^+$ for different cavity lengths l_A in terms of normalized $|\hat{p}|$ and $\mathfrak{Re}(\hat{p})$ for 35 mm length (right) for configuration P1. 96
4.32 Mode shapes for different cavity lengths l_A and an neutral inlet boundary condition in case of configuration P1: $T_{1_d}^+$ and $T_{1_u}^+$ (right) modes in terms of normalized $|\hat{p}|$. 98
4.33 Mode shapes $T_{1_u}^+$ for different cavity lengths l_A and partially reflecting inlet in terms of normalized $|\hat{p}|$ and $\mathfrak{Re}(\hat{p})$ for 35 mm length (right) for configuration P2. 99
4.34 Numerical results: Eigenfrequency (left) and damping rate (right) of the $T_{1_u}^+$ mode for configuration P2. 100

5.1 BKD test chamber configuration with details of the injection system in the injector head and chamber dimensions (Gröning and Oschwald 2014). Dimensions are given in [mm]. 104
5.2 BKD combustion chamber and equipment, adapted from (Gröning et al. 2014) and (Gröning et al. 2015a). 104
5.3 BKD injector geometry and propellant flow. Axial coordinates are given in [mm]. 105
5.4 Normalized PDF of LP1-4 for eight sensors. The dynamic pressure measurements were kindly provided by Prof. Dr. Michael Oschwald, DLR Lampoldshausen. 109
5.5 Averaged and normalized PSD, Lorentzian fits and excluded data for LP1 (left) and LP3 (right). 111
5.6 Normalized Fourier coefficient η_a and Hilbert transform amplitude $A(t)$. 114
5.7 Damping rate λ over down-sampling factor DF for LP1-4. 115
5.8 Noise intensity Γ [Pa^2/s] over down-sampling factor DF for LP1 and LP3. 117
5.9 Non-linear saturation coefficient K [$1/(Pa^2s)$] over down-sampling factor for LP2 and LP4. 118

6.1 Left: First transverse mode structure in terms of normalized acoustic pressure (real part) and transverse velocity vector field together with injector contours. Right: Exemplary single flame configuration in the BKD test chamber. 121
6.2 Computational domain for the single flame simulation. 124
6.3 Real gas factor over pressure for different temperatures in case of pure O_2 (left) and H_2 (right) (Linstrom and Mallard 2015). 125
6.4 Density (left) and speed of sound (right) for pure O_2 and comparison between NIST database, SRK EOS, PR EOS and ideal gas law for 60, 70 and 80 bar. 130

6.5 Density (left) and speed of sound (right) for pure H_2 and comparison between NIST database, SRK EOS, PR EOS and ideal gas law for 60, 70 and 80 bar. 130
6.6 Specific heat capacity at isobaric (left) and isochoric (right) conditions for pure O_2 at 60, 70 and 80 bar. 131
6.7 Regimes of turbulent non-premixed combustion in terms of the Damköhler number Da and the turbulent Reynolds number Re_t, adapted from (Poinsot and Veynante 2005). 135
6.8 O_2 mass fraction of the mean flow for the acoustic simulation together with its detailed distribution in the single flame case. 142
6.9 BKD injector configuration and corresponding network model. 143
6.10 Computational domain, boundary conditions and grid for the acoustic simulation. 145
6.11 First transverse mode shape in terms of normalized pressure $\mathfrak{Re}(\hat{p})$ and the respective anti-nodal lines in the chamber. 147
6.12 Left: First transverse mode structure in terms of normalized acoustic pressure (real part) and transverse velocity vector field together with injector contours and locations of the pressure anti node and the transverse velocity anti-node. Right: Single flame configurations in the pressure anti-nodal line and in the transverse velocity anti-nodal line. 152
6.13 Illustration of the pressure coupling excitation method. The field shows the temperature and the arrows indicate the periodic compression and decompression of the single flame configuration. 154
6.14 Illustration of the velocity coupling excitation method. The field shows the temperature. The black and red arrows indicate the direction of the transverse acoustic velocity at two time instants, which differ by half an acoustic period. 159
6.15 Linear stability assessment procedure. 163

7.1 Pressure $\bar{p}$ (top) and Mach number M (bottom) in the O_2 dome and injector for LP1-4. Axial coordinates are given in [mm]. 168
7.2 Pressure in the O_2 injection system for LP1-4 along the plot line, see Fig. 7.1. 169
7.3 Temperature (top) and mass fraction of O_2 (bottom) in the chamber section for LP1-4. The axial dimensions are given in [mm]. 170
7.4 Pressure loss element scattering matrix amplitudes for LP1-4. 173
7.5 Pressure loss element scattering matrix phases for LP1-4 173
7.6 Dome coupling scattering matrix amplitudes for LP1-4. 175
7.7 Dome coupling scattering matrix phases for LP1-4. 175
7.8 First and second longitudinal modes of the O_2 injector in terms of normalized pressure amplitude $|\hat{p}|$ for LP3 (top) and LP4 (bottom). 176
7.9 Experimental PSD (black) given in [dB/Hz] and numerically determined eigenfrequencies for LP1-4. Different mode classes are indicated by color. Experimental results from (Gröning et al. 2014). 179

7.10 Selection of mode shapes up to the first radial mode in terms of normalized real part (left) and absolute value (right) for the example of LP4 (1/2). 180
7.11 Selection of mode shapes up to the first radial mode in terms of normalized real part (left) and absolute value (right) for the example of LP4 (2/2). 181
7.12 Axial distributions of speed of sound along the pressure anti-nodal line for LP1-4 as well as the indication of two plateau regions in the chamber. 182
7.13 T_1^α mode shapes in terms of normalized pressure amplitudes for LP1-4 as well as anti-nodal pressure lines. 185
7.14 Axial distributions of the normalized pressure amplitude (top) and speed of sound (bottom) along the pressure anti-nodal line. 185
7.15 Axial distributions of $\mathfrak{Im}(k^{\mathrm{x}\pm}_{\mathrm{T}_1^\alpha})$ [1/m] (top) and speed of sound [m/s] (bottom) for LP1-4. 187
7.16 Dependency of $\mathfrak{Im}(k^{+}_{\mathrm{T}_1^\alpha})$ on c for constant $\bar{u} = 230$ m/s. 187
7.17 Normalized real part of complex pressure amplitude along anti-nodal line and exponential fits for LP1-4. 188
7.18 Computational domain as well as energetically neutral inlet and outlet boundary conditions for the investigation of the mean flow influence on the T_1^α mode damping rates. 189
7.19 Distribution of the Mach number $M_{\mathcal{C}}$ for different prefactors $\mathcal{C}$ (left) and T_1^α mode damping rates for the different distributions of $M_{\mathcal{C}}$ depending on the prefactor $\mathcal{C}$ (right). 190
7.20 Normalized pressure amplitude plots of the first transverse mode shape in the reduced chamber domain for different distributions of speed of sound and prefactors $\mathcal{C}$. 191
7.21 Top: Variation of eigenfrequencies $f_{\mathrm{T}_1^\alpha}/f_{\mathrm{T}_1^\beta \mathrm{L}_1}$ (left) and speed of sound c (right) with $\bar{T}_{\mathrm{H}_2}$. Bottom: Spatial dependence of speed of sound for different H_2 injection temperatures $\bar{T}_{\mathrm{H}_2}$ (left) and ROF (right); Experimental results from (Gröning et al. 2014). 194
7.22 Injection velocity of H_2 together with the lengths of the O_2 core and of the first plateau of c in dependence of the injection temperature. 196
7.23 Relative changes of speed of with ROF in terms of temperature, isentropic exponent and molar mass. 201
7.24 Axial distributions of $P_{\mathrm{T}_1}(x)$ in terms of normalized amplitude (top) and phase (bottom) along the pressure anti-nodal line for the application to pressure coupling. 203
7.25 Phase-resolved turbulent kinetic energy k_{t} (top half) and turbulent dissipation rate ϵ (bottom half) under pressure excitation conditions for a frequency of 10,500 Hz. The reference locations x_{n} and x_{f} for the measurement of the pressure fluctuations are also shown. 206
7.26 Top: Axial distributions of $P_{\mathrm{T}_1}(x)$ in terms of normalized amplitude. Bottom: Illustration of baroclinique torque effects in the single flame configuration. 207

7.27 Flame Transfer Functions for the nearfield FTF_n^p (left) and farfield FTF_f^p (right) for LP1-4 with injector (solid lines) and without injector (dotted lines) in terms of amplitude (red) and phase (blue). Experimental phase values are highlighted in transparent blue. 209
7.28 Top: Visualization plan. Bottom/left: Volumetric heat release rate $\dot{q}$ under steady state conditions. Bottom/right: Volumetric heat release rate $\dot{q}$ and transverse velocity vector field under transverse acoustic forcing conditions with 10,500 Hz and 3 % pressure equivalent excitation amplitude. 213
7.29 Displacement Flame Transfer Functions FTF^{Δ} for LP1-4 in terms of amplitude (red) and phase (blue). 215
7.30 Fluctuating heat release source terms due to pressure coupling in the nearfield and farfield as well as due to velocity coupling in the entire chamber. 216
7.31 Comparison of normalized Rayleigh integrals for LP1-4 in terms of: (1) Nearfield, (2) Farfield, (3) Nearfield + farfield, (4) Displacement. 217
7.32 Individual contributions of damping and amplification effects for the T_1^{α} mode and LP1-4 visualized on the basis of the normalized damping rate. For the parameter extraction method, mode $A(t)$ is used. The quantitative comparison is given in App. R. 221
7.33 Computational domains and energetically neutral boundary conditions for the determination of the influences of the nozzle and the dome coupling on the damping rates. 223
7.34 Grid convergence analysis (left) and dependency of eigenfrequency on the stabilization coefficient (right). 225
7.35 Dependency of λ on amplitude and phase of FTF_n^p and FTF_f^p. 226

C.1 Amplitude and real part of admittance for nozzle A (left) and nozzle B (right) in terms of the first longitudinal mode (low frequency range) and the first transverse mode (high frequency range). 239

E.1 Experimental and numerically reconstructed scattering matrix for longitudinal excitation. 242

G.1 Mode shape of the L_1 mode in terms of $\mathfrak{Re}(\hat{p})$. 244

H.1 Numerical grids for the GIT convergence study (From left to right: Coarse, medium and fine). 245
H.2 SPL (left) and phase (right) of $\hat{p}$; $M = 0.0$ (top) and $M = 0.079$ (bottom): Exp. data ( ) and num. results ( ). 246

I.1 Amplitude (top) and phase (bottom) of the reflection coefficient at the face plate Kathan (2013). 247

N.1 Axial distributions of mean quantities for LP1-4. 254

O.1 Left: First four $T^{\beta}L_x$ modes shapes simulated with mean flow. Right: Mode shapes downstream of the first pressure node without mean flow. 256

Q.1 Comparison of the axial pressure distribution for the T_1^{α} mode for the open loop and the closed loop system. 258

List of Tables

3.1 Summary and comparison of time domain and frequency space simulation techniques. 52

4.1 Specifications, flow conditions and the cut-on frequencies and of the nozzles A and B. 56
4.2 Polynomial orders for the cases (I)-(III) and each scattering matrix element for the perforated plate. 71
4.3 Comparison of eigenfrequencies f [Hz] and damping rates λ [rad/s] for the considered cases (I)-(III). The experimental data of (III) is also used for the comparison with the numerical results of (II) and of (III)/filter . 73
4.4 Operational conditions for the GIT test case. 79

5.1 Load points and stability behavior for the BKD test chamber from (Gröning et al. 2014) as well as additionally calculated quantities. . . . 107
5.2 Damping rates λ for LP1-4: Results of the Lorentzian fitting procedure and of the parameter extraction method using mode $A(t)$ and $B(t)$. . . 112

6.1 Critical point, acentric factor and gas constant for O_2 and H_2 (Linstrom and Mallard 2015). 126
6.2 Comparison of ideal gas, Peng-Robinson and Soave-Redlich-Kwong equation of state (Poling et al. 2001). 127

7.1 Comparison of H_2 temperatures in the dome and at injection for LP1-4. 166
7.2 Validation of simulated dome pressure and ratio of chamber pressure to dome pressure. 168
7.3 Eigenfrequencies of the T_1^α mode for LP1-4: Experimental findings (Gröning et al. 2013b), simulation results and relative deviations. 184
7.4 Comparison of $\mathfrak{Im}(k_{T_1^\alpha}^{x+})$ with the axial decay rates of the fits k_f. 188
7.5 Load point definitions for the ROF variations (Gröning 2015). 199
7.6 Comparison of simulation results and CEA: Temperature and speed of sound for ROF = 4-6. 201
7.7 Axial reference locations for the determination of fluctuating pressure in the nearfield and farfield. 205
7.8 Response factor (RF) of LP1-4 for nearfield and farfield. The results without injector are also reported for the purpose of comparison. 210
7.9 Amplitude of the O_2 injector admittance Y determined on the basis of the excited CFD simulations. 211

7.10 Comparison of λ [rad/s] between numerical results calculated on the basis of the stability assessment procedure and the experimental findings. . . 219

F.1 IIR filter coefficients for $R_{\mathrm{IIR}}^{\mathrm{II}}$. 243
F.2 IIR filter coefficients for $R_{\mathrm{IIR}}^{\mathrm{II}}$. 243

G.1 Mode frequency f [Hz] and damping rate λ [rad/s] for the L_1 mode of the non-reactive test case. 244

R.1 Relative contributions of the different damping and amplification effects to the closed loop damping rate. Normalization with the open loop damping rate for LP1. 259

References

M. Åbom. A note on the experimental determination of acoustical two-port matrices. *Journal of Sound and Vibration*, 155(1):185 – 188, 1992.

M. Åbom and H. Bodén. Error Analysis of Two-Microphone Measurements in Ducts with Flow. *The Journal of the Acoustical Society of America*, 83(6):2429–2438, 1988.

A. M. Abudour, S. A. Mohammad, R. L. R. Jr., and K. A. Gasem. Volume-translated Peng-Robinson equation of state for saturated and single-phase liquid densities. *Fluid Phase Equilibria*, 335:74 – 87, 2012. ISSN 0378-3812. doi: http://dx.doi.org/10.1016/j.fluid.2012.08.013.

A. M. Abudour, S. A. Mohammad, R. L. R. Jr., and K. A. Gasem. Volume-translated Peng-Robinson equation of state for liquid densities of diverse binary mixtures. *Fluid Phase Equilibria*, 349:37 – 55, 2013. doi: http://dx.doi.org/10.1016/j.fluid.2013.04.002.

T. Aichner, H. Riedmann, B. Kniesner, and O. Knab. Development of an Advanced Global MMH/NTO Combustion Model for CFD Application. In *Space Propulsion*, number 2356608. AAAF-ESA-CNES, Mai 2012.

P. R. Amestoy, I. S. Duff, J.-Y. L'Excellent, and J. Koster. A Fully Asynchronous Multifrontal Solver Using Distributed Dynamic Scheduling. *SIAM Journal on Matrix Analysis and Applications*, 23(1):15–41, 2001. doi: 10.1137/S0895479899358194. URL `http://dx.doi.org/10.1137/S0895479899358194`.

J. D. Anderson. *Modern compressible flow: with historical perspective*, volume McGraw-Hill series in aeronautical and aerospace engineering. McGraw-Hill, 2003.

I. ANSYS. ANSYS CFX-Solver Modeling Guide - ANSYS CFX Release 15.0. *Canonsburg, PA, USA*, 2014a.

I. ANSYS. ANSYS CFX-Solver Solver Guide - ANSYS CFX Release 15.0. *Canonsburg, PA, USA*, 2014b.

C. Ashcraft, 1999. URL `http://www.netlib.org/linalg/spooles/spooles.2.2.html`.

S. Bade. *Messung und Modellierung der thermoakustischen Eigenschaften eines modularen Brennersystems für vorgemischte Systeme*. PhD thesis, Technische Universität München, 2014.

G. L. Beau, S. Ray, S. Aliabadi, and T. Tezduyar. SUPG finite element computation of compressible flows with the entropy and conservation variables formulations. *Computer Methods in Applied Mechanics and Engineering*, 104(3):397 – 422, 1993. ISSN 0045-7825. doi: http://dx.doi.org/10.1016/0045-7825(93)90033-T. URL `http://www.sciencedirect.com/science/article/pii/004578259390033T`.

W. Bell and B. Zinn. The prediction of three-dimensional liquid-propellant rocket nozzle admittances. (73N17807):68, 1973.

H. Bodén and M. Åbom. Influence of Errors on the Two-Microphone Method for Measuring Acoustic Properties in Ducts. *Journal of the Acoustical Society of America*, 79(2):541–549, 1986.

S. Boij and B. Nilsson. Scattering and absorption of sound at flow duct expansions. *Journal of Sound and Vibration*, 289(3):577 – 594, 2006. ISSN 0022-460X. doi: 10.1016/j.jsv.2005.02.017.

M. R. Bothien, N. Noiray, and B. Schuermans. Analysis of Azimuthal Thermo-acoustic Modes in Annular Gas Turbine Combustion Chambers. *Journal of Engineering for Gas Turbines and Power, ASME*, 137(6), 2015. doi: doi:10.1115/1.4028718.

J. Brear, F. Nicoud, M. Talei, A. Giauque, and E. R. Hawkes. Disturbance energy transport and sound production in gaseous combustion. *Journal of Fluid Mechanics*, 707:53–73, 9 2012. ISSN 1469-7645. doi: 10.1017/jfm.2012.264. URL `http://journals.cambridge.org/article_S0022112012002649`.

I. Bronstein, K. Semendjajew, G. Musiol, and H. MÃ$\frac{1}{4}$hlig. *Taschenbuch der Mathematik*. Verlag Harri Deutsch, Frankfurt am Main, 6. edition, 2005. ISBN 3-8171-2006-0.

A. Burcat. Thermochemical Data for Combustion Calculations. In J. Gardiner, WilliamC., editor, *Combustion Chemistry*, pages 455–473. Springer US, 1984. ISBN 978-1-4684-0188-2. doi: 10.1007/978-1-4684-0186-8_8. URL `http://dx.doi.org/10.1007/978-1-4684-0186-8_8`.

A. Burcat and J. Gardiner, WilliamC. Ideal Gas Thermochemical Data for Combustion and Air Pollution Use. In J. Gardiner, W.C., editor, *Gas-Phase Combustion Chemistry*, pages 489–538. Springer New York, 2000. ISBN 978-1-4612-7088-1. doi: 10.1007/978-1-4612-1310-9_5. URL `http://dx.doi.org/10.1007/978-1-4612-1310-9_5`.

A. Cárdenas. *Influence of Enhanced Heat Transfer in Pulsating Flow on the Damping Characteristics of Resonator Rings*. PhD thesis, Technische Universität München, 2014.

A. Cárdenas and W. Polifke. Study of Enhanced Heat Transfer in Generic Configurations of Pulsating Flow. 2011.

M. Celano, S. Silvestri, G. Schlieben, C. Kirchberger, and O. Haidn. Injector Characterization for a GOX-GCH4 Single Element Combustion Chamber. In *EUCASS Advances in Aerospace Sciences, Progress in Propulsion Physics, Vol. 9*, 2015.

B. Chehroudi. Recent Experimental Efforts on High-Pressure Supercritical Injection for Liquid Rockets and Their Implications. *International Journal of Aerospace Engineering, Article ID 121802*, 2012:31, 2012. doi: doi:10.1155/2012/121802.

T. H. Chung, L. L. Lee, and K. E. Starling. Applications of kinetic gas theories and multiparameter correlation for prediction of dilute gas viscosity and thermal conductivity. *Industrial & Engineering Chemistry Fundamentals*, 23(1):8–13, 1984. doi: 10.1021/i100013a002. URL `http://dx.doi.org/10.1021/i100013a002`.

E. W. Conrad, H. E. Bloomer, J. P. Wanhainen, and D. W. Vincent. Interim summary of liquid rocket acoustic-mode-instability studies at a nominal thrust of 20 000 pounds. In *Technical Note TN D-4968, NASA*, 1968.

F. E. C. Culick. Combustion instabilities in liquid-fuelled propulsion systems. *AGARD Conference on Combustion instabilitites in liquid-fuelled propulsion systems*, 1988.

F. E. C. Culick. Unsteady Motions in Combustion Chambers for Propulsion Systems. *NATO RTO AGARDograph AG-AVT-039*, 2006.

F. Culick and V. Yang. *Overview of Combustion Instabilities in Liquid-Propellant Rocket Engines*. American Institute of Aeronautics and Astronautics, 1995.

J. W. Delfs, M. Bauer, R. Ewert, H. A. Grogger, M. Lummer, and T. G. W. Lauke. Technical report, Deutsches Zentrum für Luft- und Raumfahrt - Institut für Aerodynamik und Strömungstechnik Abteilung Technische Akustik, 2008.

J. W. Demmel. *Applied Numerical Linear Algebra*. Society for Industrial and Applied Mathematics, Philadelphia, PA, USA, 1997. ISBN 0-89871-389-7.

M. Demmelmair. *Analytische und numerische Bestimmung der Temperaturverteilung in einem H2/O2-Zufuhrsystem eines Raketenmotors*. Master's thesis, Technische Universität München, 2014.

J. Donea and A. Huerta. *Finite Element Methods for Flow Problems*. Finite Element Methods for Flow Problems. John Wiley & Sons, 2003. ISBN 9780471496663. URL `http://books.google.de/books?id=S4URqrTtSXoC`.

K. Ehrenfried. Skript zur Vorlesung Strömungsakustik I. In *Technische Universität Berlin*, 2003.

Enseeiht, 2015. URL `http://mumps.enseeiht.fr/`.

R. Ewert and W. Schröder. Acoustic perturbation equations based on flow decomposition via source filtering. *Journal of Computational Physics*, 188(2):365 – 398, 2003. ISSN 0021-9991. doi: http://dx.doi.org/10.1016/S0021-9991(03)00168-2.

R. Ewert, M. Meinke, and W. Schröder. Computation of Sound Radiation from a Trailing Edge Applying Acoustic Perturbation Equations. In *3rd Swing Aeroacoustics Workshop, Stuttgart, Germany, Aerodynamisches Institut, RWTH Aachen*, 2002a.

R. Ewert, M. Meinke, and W. Schröder. Computation of Trailing Edge Noise via LES and Acoustic Perturbation Equations. In *8th AIAA/CEAS Aeroacoustics Conference and Exhibit, Breckenridge, Colorado*, 2002b.

T. Fiala and T. Sattelmayer. Nonpremixed Counterflow Flames: Scaling Rules for Batch Simulations. *Journal of Combustion*, 2014:7, Jun 2014. doi: 10.1155/2014/484372.

T. Fiala. *Bestimmung der Dämpfung akustischer Wellen in einer Raketenbrennkammer*. Master's thesis, Technische Universität München, 2010.

T. Fiala. *Radiation from High Pressure Hydrogen-Oxygen Flames and its Use in Assessing Rocket Combustion Instability*. PhD thesis, Technische Universität München, 2015.

T. Fiala and T. Sattelmayer. Modeling of the Continuous (Blue) Radiation in Hydrogen Flames. *International Journal of Hydrogen Energy*, 2015a. doi: 10.1016/j.ijhydene.2015.10.045.

T. Fiala and T. Sattelmayer. Assessment of existing and new modeling strategies for the simulation of OH* radiation in high-temperature flame. *CEAS Space Journal*, 2015b. doi: 10.1007/s12567-015-0107-z.

S. Föller and W. Polifke. Determination of acoustic transfer matrices via Large Eddy Simulation and system identification. volume No. AIAA-2010-3998, 2010.

S. Föller and W. Polifke. Identification of aero-acoustic scattering matrices from large eddy simulation. Application to a sudden area expansion of a duct. *Journal of Sound and Vibration*, 331(13):3096 – 3113, 2012. ISSN 0022-460X. doi: 10.1016/j.jsv.2012.01.004. URL `http://www.sciencedirect.com/science/article/pii/S0022460X12000247`.

S. Föller, R. Kaess, and W. Polifke. Determination of acoustic scattering coefficients via LES and system identification. *Springer Verlag, in 'High Performance Computing in Science and Engineering'*, pages 243–255, 2010.

M. L. Frezzotti, A. Terracciano, F. Nasuti, S. Hester, and W. E. Anderson. Low-order model studies of combustion instabilitites in a DVRC combustor. In *50th AIAA/ASME/SAE/ASEE Joint Propulsion Conference*, 2014.

G. Garrison, A. Schnell, C. Baldwin, and P. Russell. Suppression of Combustion Oscillations with Mechanical Damping Devices. Technical report, Interim Report PWA FR-3299, Pratt & Whitney Aircraft, Box 2691, West Palm Beach, Florida 33402, 1969.

A. M. G. Gentemann, A. Fischer, S. Evesque, and W. Polifke. Acoustic Transfer Matrix Reconstruction and Analysis for Ducts with Sudden Area Changes. *9th AIAA/CEAS Aeroacoustics Conference and Exhibit AIAA 2003-3142*, 2003.

J. Gikadi. *Prediction of Acoustic Modes in Combustors using Linearized Navier-Stokes Equations in Frequency Space*. PhD thesis, Technische Universität München, 2014.

J. Gikadi, M. Schulze, J. Schwing, S. Föller, and T. Sattelmayer. Linearized Navier-Stokes and Euler Equations for the Determination of the Acoustic Scattering Behaviour of an Area Expansion. In *18th AIAA/CEAS Aeroacoustics Conference*, number AIAA-2012-2292, 2012.

J. Gikadi, W. C. Ullrich, T. Sattelmayer, and F. Turrini. Prediction of the Acoustic Losses of a Swirl Atomizer Nozzle Under Non-Reactive Conditions. In *Proceedings of ASME Turbo Expo 2013*, number GT2013-95449, San Antonio, USA, 2013.

J. Gikadi, S. Föller, and T. Sattelmayer. Impact of turbulence on the prediction of linear aeroacoustic interactions: Acoustic response of a turbulent shear layer. *Journal of Sound and Vibration*, 333(24):6548 – 6559, 2014. ISSN 0022-460X. doi: http://dx.doi.org/10.1016/j.jsv.2014.06.033. URL `http://www.sciencedirect.com/science/article/pii/S0022460X14005392`.

S. Gröning. Definition of BKD Load Points with Different ROF. private correspondence, 2015.

S. Gröning and M. Oschwald. LOX/H2-Combustion with self-sustained acoustic excitation: HF-7 test case. In *Proceedings of the 3rd REST Modelling Workshop, Vernon, France*, 2014.

S. Gröning, M. Oschwald, and T. Sattelmayer. Selbsterregte tangentiale Moden in einer Raketenbrennkammer unter repräsentativen Bedingungen. In *Deutscher Luft- und Raumfahrtkongress, Berlin, Germany*, 2012.

S. Gröning, M. Oschwald, and T. Sattelmayer. Einfluss einer Kavität auf das Druckfeld der ersten tangentialen Mode einer Raketenbrennkammer unter repräsentativen Bedingungen. In *Deutscher Luft- und Raumfahrtkongress, Stuttgart, Germany*, 2013a.

S. Gröning, D. Suslov, M. Oschwald, and T. Sattelmayer. Stability Behaviour of a Cylindrical Rocket Engine Combustion Chamber Operated with Liquid Hydrogen and Liquid Oxygen. In *5th European Conference for Aerospace Sciences (EUCASS)*, 2013b.

S. Gröning, D. Suslov, J. Hardi, and M. Oschwald. Influence of hydrogen temperature on the acoustics of a rocket engine combustion chamber operated with LOX/H2 at representative conditions. In *Space Propulsion Conference, Cologne, Germany*, 2014.

S. Gröning. HF-7 Test Case: LOX/H2-Combustion with self-sustained acoustic excitation. Technical report, 3rd REST Workshop on Combustion Instability Modeling, Rocket Engine Stability Research Initiative, French-German Research on High Frequency Combustion Instability, 2014.

S. Gröning, J. Hardi, D. Suslov, and M. Oschwald. Analysis of phase shift between oscillations of pressure andflame radiation intensity of self-excited combustion instabilities. In *6th European Conference For Aerospace Sciences (EUCASS)*, 2015a.

S. Gröning, J. S. Hardi, D. Suslov, and M. Oschwald. Injector-driven combustion instabilities in a hydrogen/oxygen rocket combustor. *Accepted for Publication in Journal of Propulsion and Power*, 2015b.

S. Gröning, P. Losco, J. S. Hardi, and M. Oschwald. Effect of an acoustic absorber on self-exicted combustion instabilities of the first tangential resonance mode. *Sonderforschungsbereich/Transregio 40 - Annual Report*, 2015c.

M. Habiballah and S. Zurbach. Test Case RCM-3, Mascotte single injector, 60 bar. *2nd International Workshop on Rocket Combustion Modeling*, 2001.

M. Haimerl. *Bestimmung von Dämpfungskoeffizienten für numerische akustische Felder mit dem Lorenzverfahren*. Master's thesis, Technische Universität München, 2013.

D. Harrje and F. Reardon. *Liquid propellant rocket combustion instability*. Number NASA-SP-194 in 19720026079. NASA, 1972.

M. Hertweck. *Einfluss der Flammenposition auf transversale hochfrequente akustische Moden in zylindrischen Brennkammern*. PhD thesis, Technische Universität München, 2016.

M. Hertweck, F. Berger, T. Hummel, and T. Sattelmayer. Impact of the Heat Release Distribution on Transverse Thermoacoustic Driving in Premixed Swirl Flames. *submitted to International Journal of Spray and Combustion Dynamics*, 2016.

J.-P. Hickey and M. Ihme. Supercritical mixing and combustion in rocket propulsion. *Center of Turbulence Research, Annular Research Briefs*, 2013.

J. Hirschfelder, C. Curtiss, R. Bird, and U. of Wisconsin. Theoretical Chemistry Laboratory. *Molecular theory of gases and liquids*. Structure of matter series. Wiley, 1954. ISBN 9780471400653. URL `https://books.google.de/books?id=HQtRAAAAMAAJ`.

A. Huber and W. Polifke. Time-domain Impedance Boundary Conditions for Computational Fluid Dynamics. In *2nd GACM Colloquim on Computational Mechanics, Germany*, 2007.

T. J. Hughes, L. P. Franca, and M. Balestra. A new finite element formulation for computational fluid dynamics: V. Circumventing the babuška-brezzi condition: a stable Petrov-Galerkin formulation of the stokes problem accommodating equal-order interpolations. *Computer Methods in Applied Mechanics and Engineering*, 59(1):85 – 99, 1986. ISSN 0045-7825. doi: http://dx.doi.org/10.1016/0045-7825(86)90025-3. URL `http://www.sciencedirect.com/science/article/pii/0045782586900253`.

T. J. Hughes, L. P. Franca, and G. M. Hulbert. A new finite element formulation for computational fluid dynamics: VIII. The galerkin/least-squares method for advective-diffusive equations. *Computer Methods in Applied Mechanics and Engineering*, 73(2):173 – 189, 1989. ISSN 0045-7825. doi: http://dx.doi.org/10.1016/0045-7825(89)90111-4. URL `http://www.sciencedirect.com/science/article/pii/0045782589901114`.

T. Hummel, M. Schulze, B. Schuermans, and T. Sattelmayer. Reduced Order Modeling of Transversal and Non-Compact Combustion Dynamics. 2015.

T. Hummel, C. Temmler, B. Schuermans, and T. Sattelmayer. Reduced-Order Modeling of Aeroacoustic Systems for Stability Analyses of Thermoacoustically Noncompact Gas Turbine Combustors. *Journal of Engineering for Gas Turbines and Powerl*, 138: 051502–1–11, 2016.

U. Ingard. On the Theory and Design of Acoustic Resonators. *The Journal of the Acoustical Society of America*, 25(6):1037–1061, 1953. doi: http://dx.doi.org/10.1121/1.1907235.

M. Jones and W. W. D. Nark. Effects of Flow Profile on Educed Acoustic Liner Impedance. In *16th AIAA/CEAS Aeroacoustics Conference, Stockholm, Sweden*, 2010.

M. Jones, W. Watson, M. Tracy, and T. Parrott. Comparison of Two Waveguide Methods for Educing Liner Impedance in Grazing Flow. *AIAA Journal*, 42(2):232–240, 2003.

M. Jones, W. Watson, and T. Parrott. Benchmark Data for Evaluation of Aeroacoustic Propagation Codes with Grazing Flow. In *11th AIAA/CEAS Aeroacoustics Conference, Monterey, California*, 2005.

F. Joos. Technische Verbrennung Verbrennungstechnik, Verbrennungsmodellierung, Emissionen, 2006. URL `http://www.worldcat.org/search?qt=worldcat_org_all&q=3540343334`.

R. Kaess, A. Huber, and W. Polifke. A Time-Domain Impedance Boundary Condition for Compressible Turbulent Flow. In *14th AIAA/CEAS Aeroacoustics Conference (29th AIAA Aeroacoustics Conference)*, number AIAA-2008-2921, Vancouver, Canada, May 5 – 7 2008. AIAA/CEAS.

R. Kaess, S. Köglmeier, M. Schmid, and T. Sattelmayer. Linearized Euler Calculation of Acoustics of a Rocket Combustion Chamber. In *HF2 Testcase*. 2nd REST Modeling Workshop, Ottobrunn, Germany, 2010.

R. Kaess, S. Köglmeier, R. Behr, O. Knab, and T. Sattelmayer. Test Case HF-7: Simulation of the HF-7 Test Case Using a Combined URANS-CAA Approach. In *Proceedings of the 3rd REST Workshop on Combustion Instability Modeling, SNECMA, Vernon*, 2014.

R. Kathan. Experimental Investigation of the Test Case HF-2. In *Proceedings of the 2nd REST Modelling Workshop*, 2010.

R. Kathan. Test case HF-2: Acoustics of a rocket motor model with choked nozzle. In *Proceedings of the 2nd REST Modelling Workshop*, 2010, EADS Astrium, Ottobrunn.

R. Kathan. *Verlustmechanismen in Raketenbrennkammern*. PhD thesis, Technische Universität München, 2013.

R. Kathan, D. Morgenweck, R. Kaess, and T. Sattelmayer. Validation of the Computation of Rocket Nozzle Admittances with Linearized Euler Equations. In *4th European Conference For Aerospace Sciences*, 2011.

J. Keller and E. Zauner. On the use of Helmholtz resonators as sound attenuators. *Zeitschrift für angewandte Mathematik und Physik ZAMP*, 46(3):297–327, 1995. ISSN 0044-2275. doi: 10.1007/BF01003552. URL `http://dx.doi.org/10.1007/BF01003552`.

A. Kierkegaard, S. Boij, and G. Efraimsson. A frequency domain linearized Navier-Stokes equations approach to acoustic propagation in flow ducts with sharp edges. *The Journal of the Acoustical Society of America*, 127(2):710–719, 2010. doi: 10.1121/1.3273899.

B. Klingen. *Fouriertransformation für Ingenieur- und Naturwissenschaften*. Springer-Lehrbuch. Springer Berlin Heidelberg, 2013. ISBN 9783642567759. URL `https://books.google.de/books?id=_K_3BQAAQBAJ`.

O. Knab and H. Riedmann. Definition and Evaluation of Advanced Rocket Thrust Chamber Demonstrator Concepts. In *SFB TRR 40 3rd Funding Period Proposal*, 2016.

O. Knab, D. Preclik, and D. Estublier. Flow Field Prediction Within Liquid Film Cooled Combustion Chambers of Storable Bi-Propellant Rocket Engines. In *34th AIAA/ASME/SAE/ASEE Joint Propulsion Conference and Exhibit*. American Institute of Aeronautics and Astronautics, 1998.

O. Knab, A. Fröhlich, and D. Wennerberg. Design Support for Advanced Storable Propellant Engines by ROCFLAM Analyses. In *35th Joint Propulsion Conference and Exhibit*. American Institute of Aeronautics and Astronautics, 1999.

S.-H. Ko. Sound Attenuation in Lined Rectangular Ducts with Flow and Its Application to the Reduction of Aircraft Engine Noise. *The Journal of the Acoustical Society of America*, 50(6A):1418–1432, 1971. doi: http://dx.doi.org/10.1121/1.1912784.

S. Köglmeier, R. Kaess, D. Morgenweck, K. Vollmer, R. Kathan, and T. Sattelmayer. Rapid Approach for the Prediction of Complex Acoustic Resonance Frequencies in Rocket Combustion Chambers. In *Proceedings of the 2nd REST Modelling Workshop*, 2010.

S. Köglmeier, R. Kaess, and T. Sattelmayer. Numerical Investigation on Nonlinear Acoustics in Liquid Rocket Combustion Instability. In *4th European Conference for Aerospace Sciences, Saint Petersburg, Russia*, 2011.

S. Köglmeier, R. Kaess, D. Morgenweck, P. Tudisco, and T. Sattelmayer. Modelling of Acoustic Absorbers for Liquid Rocket Combustion Chambers. In *Space Propulsion Conference, Cologne, Germany*, 2014a.

S. Köglmeier, R. Kaess, and T. Sattelmayer. Determination of Acoustic Scattering Matrices Using Nonlinear Disturbance Equations. In *20th AIAA/CEAS Aeroacoustics Conference, Atlanta, USA*, 2014b.

T. Kwak and G. Mansoori. Van der waals mixing rules for cubic equations of state. Applications for supercritical fluid extraction modelling. *Chemical Engineering Science*, 41(5):1303 – 1309, 1986. ISSN 0009-2509. doi: http://dx.doi.org/10.1016/0009-2509(86)87103-2.

R. Lacombe, P. Moussou, and Y. Aurégan. Whistling of an orifice in a reverberating duct at low Mach number. *The Journal of the Acoustical Society of America*, 130(5): 2662–2672, 2011. doi: 10.1121/1.3641427. URL `http://link.aip.org/link/?JAS/130/2662/1`.

E. Laudien, R. Pongratz, R. Pierro, and D. Preclik. Experimental Procedures Aiding the Design of Acoustic Cavities. *Progress in Astronautics and Aeronautics.American Institute of Aeronautics and Astronautics, V. Yang and W. Anderson*, 1995.

R. B. Lehoucq, D. C. Sorensen, and C. Yang. ARPACK Users Guide: Solution of Large Scale Eigenvalue Problems by Implicitly Restarted Arnoldi Methods., 1997.

B. Leitenberger. *Europäische Trägerraketen Band 1: Von der Diamant zur Ariane-4 – Europas steiniger Weg in den Orbit*. Books on Demand, 2013. ISBN 9783848297849. URL `https://books.google.de/books?id=CZ4wAQAAQBAJ`.

S. K. Lele. Compact Finite Difference Schemes with Spectral-like Resolution. *Journal of Computational Physics*, 103:16–42, November 1992. doi: 10.1016/0021-9991(92)90324-R.

X. Li and F. Thiele. Numerical Computation of Sound Propagation in Lined Ducts by Time-Domain Impedance Boundary Conditions. In *10th AIAA/CEAS Aeroacoustics Conference, Manchester, UK*, 2004.

P. Linstrom and W. Mallard. NIST Chemistry WebBook, NIST Standard Reference Database Number 69. *National Institute of Standards and Technology, Gaithersburg MD, 20899, http://webbook.nist.gov*, 2015.

L. Long. A Nonconservative Nonlinear Flowfield Splitting Method for 3-D Unsteady Fluid Dynamics. In *6th AIAA/CEAS Aeroacoustics Conference, Maui, Hawaii, USA*, 2000.

T. Lung and A. Doige. A Time-Averaging Transient Testing Method for Acoustic Properties of Piping Systems and Mufflers with Flow. *The Journal of the Acoustical Society of America*, 73 (3)(867-876), 1983.

B. F. Magnussen and B. Mjertager. On mathematical modeling of turbulent combustion. *16th Symp. (Int.) on Combustion, The Combustion Institute, Pittsburgh*, pages 719–727, 1967.

T. E. E. Mastorakos. *Turbulent Combustion Modeling*. Number 1. Springer Netherlands, 2001. doi: 10.1007/978-94-007-0412-1.

J. Matheis, H. Müller, C. Lenz, M. Pfitzner, and S. Hickel. Volume translation methods for real-gas computational fluid dynamics simulations. *The Journal of Supercritical Fluids*, 107:422 – 432, 2016. doi: http://dx.doi.org/10.1016/j.supflu.2015.10.004.

B. McBride and S. Gordon. Computer Program for Calculation of Complex Chemical Equilibrium Compositions and Applications. 1994.

B. McBride, S. Gordon, and M. Reno. Coefficients for Calculating Thermodynamic and Transport Properties of Individual Species. *NASA Report TM-4513*, October 1993.

J. Melcher and R. Morehead. Combustion Stability Characteristics of the Project Morpheus Liquid Oxygen/Liquid Methane Main Engine. In *50th AIAA/ASME/SAE/ASEE Joint Propulsion Conference, Cleveland, Ohio, United States*, 2014.

A. Michalke. On spatially growing disturbances in an inviscid shear layer. *Journal of Fluid Mechanics*, 23:521–544, 1965. doi: 10.1017/S0022112065001520.

D. Morgenweck. *Modellierung des Transferverhaltens im Zeitbereich zur Beschreibung komplexer Randbedingungen in Raketenschubkammern*. PhD thesis, Technische Universität München, 2013.

D. Morgenweck, J. Pieringer, and T. Sattelmayer. Numerical Determination of Nozzle Admittances in Rocket Engines. 2010.

D. Morgenweck, T. Sattelmayer, F. Fassl, and R. Kaess. Influence of Scaling Rules on the Loss of Acoustic Energy. *Journal of Spacecraft and Rockets*, 48:498–506, 2011. doi: 10.2514/1.4833.

M. L. Munjal and A. Doige. Theory of A Two Source-location Method for Direct Experimental Evaluation of the Four-Pole Parameters of an Aeroacoustic Element. *Journal of Sound and Vibration*, 141(2):323–333, 1990.

M. Munjal. *Acoustics of Ducts and Mufflers*. John Wiley & Sons, 1987.

M. K. Myers. On the Acoustic Boundary Condition in the Presence of Flow. *Journal of Sound and Vibration*, 71(8):429–434, 1980.

M. K. Myers. Transport of energy by disturbances in arbitrary steady flows. *Journal of Fluid Mechanics*, 226, 1991.

Z. Nan, R. Guillaume, and V. Yang. Supercritical Combustion of Liquid Oxygen (LOX) and Methane Stabilized by a Splitter Plate. In *45th AIAA Aerospace Sciences Meeting and Exhibit*, 2007. doi: doi:10.2514/6.2007-575.

F. Nicoud, L. Benoit, C. Sensiau, and T. Poinsot. Acoustic Modes in Combustors with Complex Impedances and Multidimensional Active Flames. *AIAA Journal*, 45(2): 426–441, 2012/10/28 2007. doi: 10.2514/1.24933. URL `http://arc.aiaa.org/doi/abs/10.2514/1.24933`.

N. Noiray. Linear Growth Rate Estimation from Dynamics and Statistics of Acoustic Signal Envelope in Turublent Combustors. In *Proceedings of ASME Turbo Expo: Turbine Technical Conference and Exposition, GT2016-58169*, 2016.

N. Noiray and B. Schuermans. Deterministic quantities characterizing noise driven Hopf bifurcations in gas turbine combustors. *International Journal of Non-Linear Mechanics*, 50:152–163, 2012. doi: 10.1016/j.ijnonlinmec.2012.11.008.

N. Noiray and B. Schuermans. On the dynamic nature of azimuthal thermoacoustic modes in annular gas turbine combustion chambers. *Proceedings of the Royal Society of London A: Mathematical, Physical and Engineering Sciences*, 469(2151), 2013. ISSN 1364-5021. doi: 10.1098/rspa.2012.0535.

Y. Nunome, M. Takahashi, A. Kumakawa, K. Miyazaki, S. Yoshida, and T. Onga. Highfrequency flame oscillation observed at a coaxial LOX/LH2 injector element. In *44th AIAA/ASME/SAE/ASEE Joint Propulsion Conference & Exhibit, AIAA 2008-4848*, 2008.

Y. Nunome, T. Onodera, M. Sasaki, T. Tomita, K. Kobayashi, and Y. Daimon. Combustion instability phenomena observed during cryogenic hydrogen injection temperature ramping tests for single coaxial injector elements. In *47th AIAA/ASME/SAE/ASEE Joint Propulsion Conference & Exhibit, AIAA 2011-6027*, 2011.

A. V. Oppenheim, R. W. Schafer, and J. R. Buck. *Discrete-time Signal Processing (2Nd Ed.)*. Prentice-Hall, Inc., Upper Saddle River, NJ, USA, 1999. ISBN 0-13-754920-2.

M. Oschwald and Z. Farago. Acoustics of Rocket Combustors Equipped with Absorber Rings. In *44th AIAA/ASME/SAE/ASEE Joint Propulsion Conference & Exhibit, Hartford*, 2008.

M. Oschwald and M. Marpert. On the acoustics of rocket combustors equipped with quarter wave absorbers. *Progress in Propulsion Physics*, 2:339–350, 2001.

M. Oschwald, Z. Farago, G. Searby, and F. Cheuret. Resonance Frequencies and Damping of a Combustor Acoustically Coupled to an Absorber. *Journal of Propulsion and Power*, 24:3:524–533, 2008a.

M. Oschwald, Z. Farago, G. Searby, and F. Cheuret. Resonance Frequencies and Damping of a Combustor Acoustically Coupled to an Absorber. *Journal of Propulsion and Power*, 24(3):524–533, 2012/10/30 2008b. doi: 10.2514/1.32313. URL `http://dx.doi.org/10.2514/1.32313`.

Y. Özyörük and L. Long. A Time-Domain Implementation of Surface Acoustic Impedance Condition with and without Flow. *American Institute of Aeronautics and Astronautics*, NAG1-1367, 1996.

Y. Özyörük and L. Long. Time-Domain Calculation of Sound Propagation in Lined Ducts with Sheared Flows. *AIAA Journal*, 38(5):768–773, 2012/10/28 2000. doi: 10.2514/2.1056. URL `http://arc.aiaa.org/doi/abs/10.2514/2.1056`.

Y. Özyörük, L. Long, and M. Jones. Time-Domain Numerical Simulation of a Flow-Impedance Tube. *Journal of Computational Physics*, 146(1):29 – 57, 1998. ISSN 0021-9991. doi: 10.1006/jcph.1998.5919. URL `http://www.sciencedirect.com/science/article/pii/S0021999198959198`.

C. Pankiewitz. *Hybrides Berechnungsverfahren für thermoakustische Instabilitäten von Mehrbrennersystemen*. PhD thesis, Technische Universität München, 2004.

C. Paschereit, B. Schuermans, W. Polifke, and O.Mattson. Theory of A Two Source-location Method for Direct Experimental Evaluation of the Four-Pole Parameters of an Aeroacoustic Element. *Journal of Engineering for Gas Turbines and Power*, 124: 239–247, 2002.

D.-Y. Peng and D. B. Robinson. A New Two-Constant Equation of State. *Industrial & Engineering Chemistry Fundamentals*, 15(1):59–64, 1976. doi: 10.1021/i160057a011.

N. Peters. *Turbulent Combustion*. Cambridge University Press, 2000. ISBN 9780511612701. URL `http://dx.doi.org/10.1017/CBO9780511612701`. Cambridge Books Online.

J. Pieringer. *Simulation selbsterregter Verbrennungsschwingungen in Raketenschubkammern im Zeitbereich*. PhD thesis, Technische Universität München, 2008.

J. Pieringer, T. Sattelmayer, and F. Fassl. Time-Domain Simulation of Liquid Rocket Combustion Instabilites. *The Combustion Institute, European Combustion Meeting (ECM2005), Louvain-la-Neuve, Belgium*, 2005.

T. Poinsot and D. Veynante. *Theoretical and Numerical Combustion*. Edwards, 2005.

W. Polifke, J. van der Hoek, and B. Verhaar. *Everything you always wanted to know about f and g*. 1997.

B. Poling, J. Prausnitz, and J. O'Connell. *The properties of gases and liquids*. McGraw-Hill, 2001. ISBN 9780070116825. URL `https://books.google.de/books?id=s_NUAAAAMAAJ`.

M. Poschner and M. Pfitzner. CFD-Simulation of the Injection and Combustion of LOX and H2 at Supercritical Pressures. In *48th AIAA Aerospace Sciences Meeting Including the New Horizons Forum and Aerospace Exposition*, 2010. doi: doi:10.2514/6.2010-1144.

R. J. Priem. Guidlines for Combustion Stability Specifications and Verification Procedures for Liquid Propellant Rocket Engines. *Chemical Propulsion Information Agency*, 1997.

J. G. Proakis and D. G. Manolakis. *Digital Signal Processing (3rd Ed.): Principles, Algorithms, and Applications*. Prentice-Hall, Inc., Upper Saddle River, NJ, USA, 1996. ISBN 0-13-373762-4.

P. Rao and P. Morris. Use of Finite Element Methods in Frequency Domain Aeroacoustics. *AIAA Journal*, 44(7):1643–1652, 2012/10/28 2006. doi: 10.2514/1.12932.

L. Rayleigh. The Theory of Sound. *Macmillan*, 1896.

O. Redlich and J. N. S. Kwong. On the Thermodynamics of Solutions. V. An Equation of State. Fugacities of Gaseous Solutions. *Chemical Reviews*, 44(1):233–244, 1949. doi: 10.1021/cr60137a013.

C. Richter, F. Thiele, X. Li, and M. Zhuang. Comparison of Time-Domain Impedance Boundary Conditions for Lined Duct Flows. *AIAA Journal*, 45(6):1333–1345, 2012/10/28 2007. doi: 10.2514/1.24945. URL `http://arc.aiaa.org/doi/abs/10.2514/1.24945`.

S. Rienstra. Impedance Models in Time Domain including the Extended Helmholtz Resonator Model. *12th AIAA/CEAS Aeroacoustics Conference (27th AIAA Aeroacoustics Conference), Cambridge, Massachusetts*, 2006.

T. Sattelmayer. Thermodynamik 1. In *lecture notes, Technical University of Munich*, 2012.

T. Sattelmayer, M. Schmid, and M. Schulze. Interaction of Combustion with Transverse Velocity Fluctuations in Liquid Rocket Engines. *Journal of Propulsion and Power*, 31(4):1137–1147, 2015a. doi: http://arc.aiaa.org/doi/abs/10.2514/1.B35529.

T. Sattelmayer, M. Schmid, and M. Schulze. Impact of Injector Mass Flow Fluctuations on Combustion Dynamics in Liquid Engines. *Journal of Spacecraft and Rockets*, 52 (5):1417–1429, 2015b. doi: 10.2514/1.A33287. URL `http://dx.doi.org/10.2514/1.A33287`.

O. Schenk and K. Gärtner. Solving unsymmetric sparse systems of linear equations with {PARDISO}. *Future Generation Computer Systems*, 20(3):475 – 487, 2004. ISSN 0167-739X. doi: http://dx.doi.org/10.1016/j.future.2003.07.011. URL `http://www.sciencedirect.com/science/article/pii/S0167739X03001882`. Selected numerical algorithms.

M. Schmid. *Modelling of Film Cooling and Decomposition in MMH/NTO Rocket Engines*. Diplomarbeit, EADS Astrium/TU Kaiserslautern/INSA Rouen, August 2009.

M. Schmid. *Thermoakustische Kopplungsmechanismen in Flüssigkeitsraketentriebwerken*. PhD thesis, Technische Universität München, 2014.

M. Schmid, R. Blumenthal, M. Schulze, W. Polifke, and T. Sattelmayer. Quantitative Stability Analysis Using Real-Valued Frequency Response Data. In *ASME Turbo Expo*, number GT2013-95459, San Antonio, Texas, USA, 2013a.

M. Schmid, R. Blumenthal, M. Schulze, W. Polifke, and T. Sattelmayer. Quantitative Stability Analysis Using Real Frequency Response Data. *J. Eng. Gas Turbines Power*, 135(1):121601, 2013b.

M. Schmid, S. Köglmeier, and T. Sattelmayer. Numerisches CFD/LEE -Verfahren zur Berechnung der Verbrennungsstabilität von Raketentriebwerken für die industrielle Anwendung - Schlussbericht. *Lehrstuhl für Thermodynamik/Airbus Defense and Space and German Space Agency*, 2014.

M. Schulze, D. Morgenweck, and T. Sattelmayer. Dämpfung akustischer Wellen durch Absorber in Raketentriebwerken. In *Deutscher Luft- und Raumfahrtkongress, Berlin*, 2012.

M. Schulze, J. Gikadi, and T. Sattelmayer. Acoustic Admittance Prediction of two Nozzle Designs of different length using Frequency Domain Simulations. In *5th European Conference for Aerospace Sciences (EUCASS)*, 2013a.

M. Schulze, M. Schmid, D. Morgenweck, S. Köglmeier, and T. Sattelmayer. A Conceptional Approach for the Prediction of Thermoacoustic Stability in Rocket Engines. In *49th AIAA/ASME/SAE/ASEE Joint Propulsion Conference, San Jose, California, USA*, 2013b.

M. Schulze, A. Urbano, M. Zahn, M. Schmid, T. Sattelmayer, and M. Oschwald. Thermoacoustic Feedback Analysis of a Cylindrical Combustion Chamber under Supercritical Conditions. In *50th AIAA/ASME/SAE/ASEE Joint Propulsion Conference, USA, Cleveland*, 2014a.

M. Schulze, M. Zahn, M. Schmid, and T. Sattelmayer. About Flame-Acoustic Coupling Phenomena in Supercritical H2/O2 Rocket Combustion Systems. In *Deutscher Luft- und Raumfahrtkongress, Augsburg, Germany*, 2014b.

M. Schulze. *Linearized Euler and Navier-Stokes Equations for the Determination of the Acoustic Scattering Behaviour of Area Expansion and Orifice*. Master's thesis, Technische Universität München, 2012.

M. Schulze and T. Sattelmayer. Low-Order Modelling of the Non-Local Acoustic Reacting Combustion Chamber-Dome Interface in Rocket Engines. In *19th AIAA International Space Planes and Hypersonic Systems and Technologies Conference*. American Institute of Aeronautics and Astronautics, 2014/06/20 2014. doi: doi:10.2514/6.2014-3086. URL `http://dx.doi.org/10.2514/6.2014-3086`.

M. Schulze and T. Sattelmayer. Eigenvalue Analysis for the Prediction of Initial Growth Rates of Thermoacoustic Instability in Rocket Motors. In *53rd AIAA Aerospace Sciences Meeting*. American Institute of Aeronautics and Astronautics, 2015/01/08 2015a. doi: doi:10.2514/6.2015-1606. URL `http://dx.doi.org/10.2514/6.2015-1606`.

M. Schulze and T. Sattelmayer. Frequency domain simulations for the determination of liner effects on longitudinal wave propagation. *International Journal of Aeroacoustics*, 14(7):1025–1047, 2015b.

M. Schulze, M. Schmid, and T. Sattelmayer. Eigenvalue Analysis for the Prediction of Initial Growth Rates of a Thermoacoustic Instability-HF7 Test Case. In *Proceedings of the 3rd REST Workshop on Combustion Instability Modeling, SNECMA, Vernon*, 2014c.

M. Schulze, M. Wagner, and T. Sattelmayer. Acoustic Scattering Properties of Perforated Plates and Orifices with Stratified flow-HF8 test case. In *Proceedings of the 3rd REST Workshop on Combustion Instability Modeling, SNECMA, Vernon*, 2014d.

M. Schulze, R. Kathan, and T. Sattelmayer. Impact of Absorber Ring Position and Cavity Length on Acoustic Damping. *Journal of Spacecraft and Rockets*, 2015a.

M. Schulze, M. Wagner, and T. Sattelmayer. Linearized Euler Equations for the Determination of Scattering Matrices for Orifice and Perforated Plate Configurations in the high Mach Number Regime. *Submitted to International Journal of Acoustics and Vibration*, 2015b.

M. Schulze, T. Fiala, and T. Sattelmayer. Radiation-Based Validation of Combustion Simulations and Comparison to Heat Release in Rocket Engines. In *54th AIAA Aerospace Sciences Meeting, San Diego*, 2016a.

M. Schulze, M. Schmid, and T. Sattelmayer. Influence of atomization quality modulation on flame dynamics in a hypergolic rocket engine. *International Journal of Spray and Combustion Dynamics*, 2016b. doi: 10.1177/1756827716648838. URL `http://scd.sagepub.com/content/early/2016/05/11/1756827716648838.abstract`.

J. Schwing. *Über die Interaktion von transversalen akustischen Moden, Strömung und drallstabilisierter Flamme in zylindrischen Flammrohren.* PhD thesis, Technische Universität München, 2013.

K. Shipley, W. Anderson, M. E. Harvazinski, and V. Sankaran. A Computational Study of Transverse Combustion Instability Mechanisms. In *50th AIAA/ASME/SAE/ASEE Joint Propulsion Conference*, 2014.

G. Singla, P. Scouflaire, J. Rolon, and S. Candel. Flame stabilization in high pressure LOx/GH2 and {GCH4} combustion. *Proceedings of the Combustion Institute*, 31(2):2215 – 2222, 2007. ISSN 1540-7489. doi: http://dx.doi.org/10.1016/j.proci.2006.07.094. URL `http://www.sciencedirect.com/science/article/pii/S1540748906000769`.

G. Soave. Equilibrium constants from a modified Redlich-Kwong equation of state. *Chemical Engineering Science*, 27(6):1197 – 1203, 1972. ISSN 0009-2509. doi: http://dx.doi.org/10.1016/0009-2509(72)80096-4. URL `http://www.sciencedirect.com/science/article/pii/0009250972800964`.

C. Speziale and S. Thangam. Analysis of an {RNG} based turbulence model for separated flows. *International Journal of Engineering Science*, 30(10):1379 – IN4, 1992. ISSN 0020-7225. doi: http://dx.doi.org/10.1016/0020-7225(92)90148-A.

G. P. Sutton and O. Biblarz. *Rocket Propulsion Elements.* John Wiley and Sons, 2001.

C. K. W. Tam and L. Auriault. Time-domain impedance boundary conditions for computational aeroacoustics. *AIAA Journal*, pages 917–923, 1996. doi: 10.2514/3.13168. URL `http://dx.doi.org/10.2514/3.13168`.

C. Temmler, M. Schulze, and T. Sattelmayer. Acoustic Scattering Matrices for Higher-Order Modes for Simple Orifice Configurations with Flow. In *21st AIAA/CEAS Aeroacoustics Conference, Dallas, USA*, 2015.

A. Török. *Computation of the Thermoacoustic Driving Capability of Rocket Engine Flames with Detailed Chemistry*. PhD thesis, Technische Universität München, 2015.

M. Turner. *Rocket and Spacecraft Propulsion: Principles, Practice And New Developments*. Springer Praxis Books / Astronautical Engineering. Springer, 2005. ISBN 9783540221906. URL `https://books.google.de/books?id=ja1ROyh4yPYC`.

W. C. Ullrich, J. Gikadi, C. Jörg, and T. Sattelmayer. Acoustic-entropy coupling behavior and acoustic scattering properties of a Laval nozzle. In *20th AIAA/CEAS Aeroacoustics Conference, Atlanta, USA*, 2014.

W. C. Ullrich and T. Sattelmayer. Transfer Functions of Acoustic, Entropy and Vorticity Waves in an Annular Model Combustor and Nozzle for the Prediction of the Ratio Between Indirect and Direct Combustion Noise. In *21st AIAA/CEAS Aeroacoustic Conference, Dallas, USA*, 2015.

A. Urbano, L. Selle, G. Staffelbach, B. Cuenot, T. Schmitt, S. Ducruix, and S. Candel. Large-Eddy Simulation of the HF-7 Test Case. In *Proceedings of the 3rd REST Workshop on Combustion Instability Modeling, Vernon*, 2014.

A. Urbano, L. Selle, G. Staffelbach, B. Cuenot, T. Schmitt, S. Ducruix, and S. Candel. Large Eddy Simulation of a Model Scale Rocket Engine. In *Ninth Mediterranean Combustion Symposium*, 2015.

J. Van der Waals. The equation of state for gases and liquids. Nobel Lectures in Physics, 1910.

M. Wagner, M. Schulze, and T. Sattelmayer. Experimental Investigation of Acoustic Properties of Orifices and Perforated Plates in the High Mach Number Regime. In *Proceedings of the ICSV, Bangkok, Thailand*, 2013a.

M. Wagner, M. Schulze, and T. Sattelmayer. Experimental Investigation of Acoustic properties of Orifices and Perforated Plates in the High Mach Number Regime. 2013b.

X. Wang, H. Huo, and V. Yang. Supercritical Combustion of General Fluids in Laminar Counterflows. In *51st AIAA Aerospace Sciences Meeting*, 2013. doi: doi:10.2514/6.2013-1165.

J. P. Wanhainen and C. J. Morgan. Effect of injection element radial distribution and chamber geometry on acoustic-mode instability in a hydrogen oxygen rocket. In *Technical Note TN D-5375, NASA*, 1969.

J. P. Wanhainen, H. C. Parish, and E. W. Conrad. Effect of propellant injection velocity on screech in 20 000-pound hydrogen-oxygen rocket engine. In *Technical Note TN D-3373, NASA*, 1966.

J. P. Wanhainen, C. E. Feiler, and C. J. Morgan. Effect of chamber pressure, flow per element, and contraction ratio on acoustic-mode instability in hydrogen-oxygen rockets. In *Technical Note TN D- 4733, NASA*, 1968.

J. Williams. *Fluid Mechanics*. George Allan & Unwin, 1974.

M. Zahn, M. Schulze, C. Hirsch, M. Betz, and T. Sattelmayer. Frequency Domain Predictions of Acoustic Wave Propagation and Losses in a Swirl Burner with Linearized Navier-Stokes Equations. In *Proceedings of ASME Turbo Expo: Turbine Technical Conference and Exposition*, 2015.

M. Zahn, M. Schulze, C. Hirsch, and T. Sattelmayer. Impact of Quarter Wave Tube Arrangement on Damping of Azimuthal Modes. In *Proceedings of ASME Turbo Expo: Turbine Technical Conference and Exposition, GT2016-56450*, 2016.

M. Zellhuber, J. Schwing, B. Schuermans, T. Sattelmayer, and W. Polifke. Experimental and Numerical Investigation of Thermo-Acoustic Sources Related to High-Frequency Instabilities. *International Journal of Spray and Combustion Dynamics*, Volume 6 (1):1–34, Mar 2014. doi: 10.1260/1756-8277.6.1.1.